Fermilab

FERMILAB-THESIS-2000-19

A NEXT-TO-LEADING-ORDER QCD ANALYSIS OF CHARGED CURRENT EVENT RATES FROM νN DEEP INELASTIC SCATTERING AT THE FERMILAB TEVATRON

by

JESSE M. GOLDMAN

B.A., Columbia University in the City of New York, 1995

AN ABSTRACT OF A DISSERTATION

Submitted in partial fulfillment of the

requirements for the degree

DOCTOR OF PHILOSOPHY

Department of Physics

College of Arts and Sciences

KANSAS STATE UNIVERSITY

Manhattan, Kansas

2000

ABSTRACT

This dissertation details the results of a NLO QCD analysis of νFe and $\overline{\nu}$Fe scattering at the Fermilab Tevatron. Recently an increasing number of measurements by a variety of experiments have led to a good understanding of the partonic contents of the nucleon. Accurate parameterisations of these contents and the fact that neutrino Deep Inelastic Scattering is an ideal probe of the nucleus allow for a unique understanding of QCD and related phenomena in the kinematic region for which $Q^2 > 5$ GeV^2 and $0.1 < x < 0.7$. Perturbative QCD and such non-perturbative effects as the EMC correction, the longitudinal structure function, R_L, and higher twist corrections are studied and χ^2 comparisons are made with the NuTeV charged current data sample. These comparisons indicate that a NLO perturbative QCD model combined with the EMC correction and higher twist best agrees with the NuTeV data. Using this resultant model and altering the cuts to include all data for which $0.003 < x < 0.7$ leads to a NLO measurement of the strange sea level, κ. Combining this result with the measurement of κ from the NuTeV dimuon analysis leads to limits on the Cabbibo-Kobayashi-Masakawa matrix element, V_{cs}, which are consistent with currently accepted values.

Acknowledgements

The best part of any thesis (next to working with PAW) is that in which the writer gets to acknowledge the help and support received from others on the way to its completion. I would like to take this opportunity, first and foremost, to thank my advisor, Tim Bolton. He is one of the finest physicists I've had the privilege to work with and I count myself extremely lucky to have been his student. His door was always open whenever I (or any of his students) had a questions or problems. He taught me to think critically about experimental problems as well as how to defend my solutions to an equally critical audience. That I leave Kansas State with a better understanding of high energy physics and how it's done is in large part due to his patience and advice. I am also grateful to Larry Weaver. Without his deep understanding of theory and his enthusiasm and ability for teaching, my first few years of graduate school would have been very rocky indeed. His door was also always open for academic questions or just a chat and the department is friendlier place because of him. My two NuTeV colleagues, Drew Alton and Max Goncharov have likewise had a great effect on my development as a physicist. Drew always had an uncanny feel for how experimental physics is done and it's my hope that I gain something approaching his ability someday. I'd also like to thank him for patiently answering many non-physics related questions of mine such as "How do I fix a backed up sink?" which came up periodically. He's an excellent teacher and I'm sure he'll go far in academia. Max was my other officemate and it's thanks to him that I've been able to figure out many of the finer mathematical points of my analysis. In addition, his perspective on life outside the united states has always led to interesting conversations and I'm glad he was often along for the ride on my frequent interminable road trips to Fermilab. I'd like to thank Todd Adams, K-State's post-doctoral representative on NuTeV for his perspective on my analysis and his willingness to "run interference" for our group up at Fermilab when things needed to be done. I thank the other HEP faculty members, Ron Sidwell, Bill Reay, and Noel Stanton for welcoming me into the group and I'm extremely indebted to our supremely capable administrative assistant, Kathleen Pierce. She was always

prepared to cut me down to size whenever I got above myself and she also made sure I got paid, which, in my opinion, was even more important. High energy physics work is very computer-intensive and I'm not sure how I would have finished my analysis *or* written my thesis if it hadn't been for Clay Crouch and, subsequently, Robert Illing keeping a vigilant eye on our cluster. Thanks guys. Thanks go also to the non-high-energy people in the department who've been my friends and have generally made life pleasant for me, even when it probably should have been. Particular thanks go to (in no special order) James and Junell Norris, Xiao-Min and Erin Lin, Alicia Allbaugh, Vince Needham, Chris Verzani, and Xavier and Karen Flechard. I would also like to mention several members of the K-State family who are no longer here, but who played important roles in my early life as a graduate student. I think Shih-Wen Yang, Arun Tripathi (even though he claimed to be from Ohio State), Dave Woods, and Daniel Mihalcea. Finally, I'd like to thank my family who encouraged me to seek a graduate education (or, at least, didn't really try to talk me out of it) and who were always willing to offer advice and encouragement when I needed it.

TABLE OF CONTENTS

LIST OF FIGURES

LIST OF TABLES

Chapter 1

Introduction

Since its inception in the 1970's, Quantum Chromodynamics (QCD) has been the most successful theory of intra-nucleon dynamics. The theory may be roughly divided into two components: *perturbative* and *non-perturbative* QCD. "Perturbative", in this context, refers to the mathematical procedure of expanding the expression for some physically measurable quantity, such as a structure function or cross-section, in a power-series with respect to some relevant parameter. In QCD this parameter is usually $\alpha_s(Q^2)$, the strong force coupling constant expressed as a function of the squared momentum transferred to the nucleon, Q^2. In addition to $\alpha_s(Q^2)$, the understanding of QCD requires, in turn, an understanding of the probability and momentum distributions of the nucleonic subparticles, known as *partons*, out of which protons and neutrons are constructed. These distributions are parameterized via what is known as a *parton distribution function* or PDF. The value of the PDF for a parton $p_i(x, Q^2)$ at a particular value of x and Q^2 (see below) is equal to the probability of finding parton p when an experiment is carried out in the appropriate (x,Q^2) kinematic range. Often, in lepton-nucleon (ℓN) scattering, the quantity of interest is not $p_i(x, Q^2)$, but $xp_i(x, Q^2)$ which is the fraction of the interaction momentum imparted to the struck proton or neutron carried by the parton in question. At low values of Q^2, $\alpha_s(Q^2)$ is large and multiplies the non-perturbative terms in the cross-section contained in the PDF. At high Q^2, $\alpha_s(Q^2)$ becomes small. In this perturbative region, a power series expansion can be made using α_s as the expansion coefficient. The differential cross-section, expanded in such a power series, is shown in terms of α_s and to next-to-leading-order in QCD in Equation 1.1.

$$\frac{d\sigma^{\ell N}(x, Q^2, E, \mu, c_{l/r})}{dxdQ^2} = \sum_{p_i=u,\overline{u},\cdots,g} \alpha_s^0(Q^2)\sigma_{p_i}^{\ell(0)}(x', E, \mu, c_{l/r})p_i^{(0)}\left(\frac{x}{x'}\right)$$
$$+ \sum_{p_i=u,\overline{u},\cdots,g} \alpha_s^0(Q^2)\int_x^1 dx'\,\hat{\sigma}_{p_i}^{\ell(0)}(x', E, \mu, c_{l/r})p_i^{(1)}\left(\frac{x}{x'}, Q^2\right)$$

$$+ \sum_{p_i=u,\overline{u},\cdots,g} \alpha_s^1(Q^2) \int_x^1 dx' \hat{\sigma}_{p_i}^{\ell(1)}(x', Q^2, E, \mu, c_{l/r}) \left\{ p_i^{(1)}\left(\frac{x}{x'}, Q^2\right) + p_i^{(2)}\left(\frac{x}{x'}, Q^2\right) \right\} \tag{1.1}$$

In Eq. 1.1, E is the energy of the incoming lepton and M is the mass of the nucleon, which is approximately 0.939 GeV/c^2. In the case of charged-current neutrino scattering, $E = E_{had} + E_\mu$, where E_{had} is the amount of hadronic energy deposited in the calorimeter by the interaction and E_μ is the energy carried away by the muon. The quantity $x = Q^2/2MEy$ is the Bjorken scaling variable (defined with respect to inelasticity $y = E_{had}/E_\nu$), Q^2 is the momentum transfer squared, and $\sigma_{p_i}^\ell$ is the leading-order differential cross-section corresponding to lepton scattering from parton p_i. In the term proportional to $\alpha_s(Q^2)$, $\hat{\sigma}_{p_i}^\ell$ is the hard-scattering coefficient for scattering from parton p_i. Standard Model couplings are indicated by $c_{l/r}$ and the hard-scattering factorization scale is denoted by μ. All information relating to perturbative QCD is contained in the hard-scattering coefficient whereas non-perturbative (soft) QCD is contained in the parton distribution functions p_i. The parenthetical superscripts on the quantities $\hat{\sigma}^\ell$, σ^ℓ, and p_i indicate the order in QCD to which they are calculated. The first term, $\sigma^{(000)}$ is the Quark Parton Model term in the perturbative expansion and rigorously obeys scaling such that it has no Q^2 dependence. The second term, σ^{001}, is the LO QCD piece of the cross-section which contains first order in $\log(Q^2/Q_0^2)$ scaling violations in the PDF component. The third term, containing σ^{111} and σ^{112}, comprises the NLO contribution to the cross-section. It provides the terms of order α_s and contains parton distributions evolved through order $\log^2(Q^2/Q_0^2)$ denoted by $p_i^{(1)}$ and $p_i^{(2)}$.

Experimentally, the above expression has the potential to answer many interesting questions.

- How does the parton distribution function affect the cross-section?
- How do nuclear effects such as the EMC correction affect the cross-section?
- What effect do electroweak radiative corrections have?
- Do non-perturbative effects such as higher-twist affect the cross-section?
- Does a change in (factorization scale) μ substantially affect the cross-section?

As the cross-section is proportional to the ℓN scattering event rate, tests of these corrections are made via the comparison of νN scattering data collected from the NuTeV experiment to a detailed Monte Carlo simulation. The MC takes as input parton distribution functions, convolves them systematically with the corrections and ultimately is compared directly to the data. Previous analyses by this collaboration (see, for example, Refs. 14 and 32), have performed a direct extraction of

structure functions using CCFR and NuTeV data in which the Monte Carlo is used to make extensive acceptance and smearing corrections to the data in an unavoidably model-dependent way.

Fundamentally, the most important open question investigated by this analysis is whether models of non-perturbative NLO QCD, exemplified by PDF sets fit to electroproduction data, can accurately describe νN scattering data when combined with a complete NLO perturbative cross-section calculation. Secondarily, the present technique is sensitive to changes in the QCD model outlined above allowing for clear statements in support of or against a particular "submodel" defined by the addition of, for example, higher twist to the base QCD model. In addition to this model sensitivity, the dependence of the NLO cross-section model at low values of x_{Bj} on m_c, the shape of the strange sea, $s(x, Q^2)$, and the Cabbibo-Kobayashi-Masakawa (CKM) matrix element, $|V_{cs}|^2$, allows for useful limits to be set on these quantities as well.

Chapter 2

Experimental Apparatus

The NuTeV experiment lies on the Fermilab NC beamline downstream from the new Sign Selected Quadrupole Train (SSQT) designed specifically for its ability to provide separate ν and $\overline{\nu}$ beams of high purity. Next to the NC beamline lies the NT or test beamline which was indispensible in the calibration of the NuTeV detector. The detector itself, in the experimental hall at Lab E/F, consists of two parts: the CCFR target calorimeter and the muon spectrometer (toroid), both with upgraded instrumentation and drift chambers.

2.1 Calorimeter

The NuTeV target calorimeter is 3m x 3m x 17.7m and weighs approximately 690 tons. It consists of 168 steel plates with 84 liquid scintillation counters and 42 drift chambers spaced evenly throughout its volume. It is designed to measure the hadronic shower energy, E_{had}, of νN interactions as well as the position of the interaction vertex. It is also used to find muon tracks resulting from νN charged current interactions and (to some extent) the energy of the resulting muon via multiple coulomb scattering [12]. The drift chambers have a spatial resolution of 500μm. The hadron energy resolution of the calorimeter is $\sigma(E)/E = 0.022 \oplus (0.86 \pm 0.01)/\sqrt{E}$ and the θ resolution is approximately 1.6×10^{-2} mr.

2.2 Toroid (Muon Spectrometer)

The toroid, or muon spectrometer, is used to measure the energy of muons resulting from charged current interactions in the calorimeter. It consists of three "carts" each containing eight cylindrical iron washers separated by gaps each containing five single

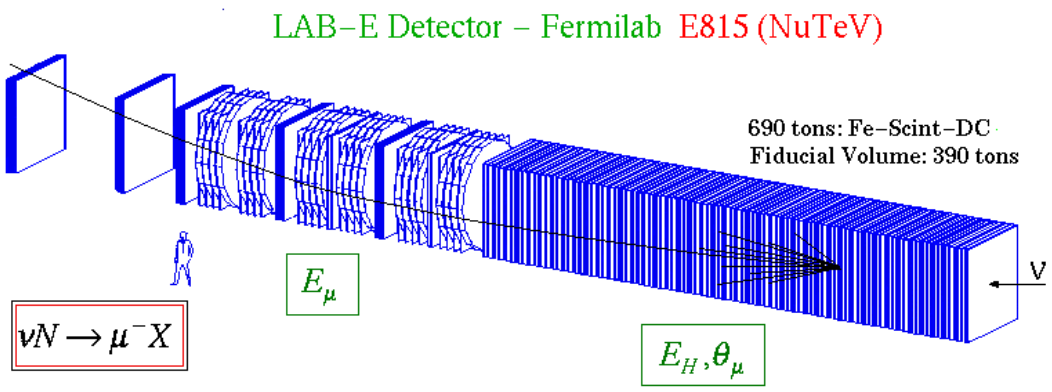

Figure 2.1: Lab E calorimeter and muon spectrometer

wire drift chambers. The three carts are spaced approximately 1.2 meters apart with the intervening drift chambers at roughly 7.6 centimeters from one another. A fourth and fifth set of similar drift chambers exists, at approximately 3 meters and 7 meters downstream of the toroid respectively, comprising what is known as the "Blue Cart". The drift chambers in the first three carts along with those in the Blue Cart provide the μ tracking information for the NuTeV detector. The single-wire drift chambers have a position resolution of 500μm, and the overall momentum resolution of the toroid spectrometer is $\sigma_p/p = 11\%$.

2.3 Test Beam

2.3.1 General Information

In order to improve hadron and muon calibration, NuTeV made use of a testbeam which ran continuously over the course of the experiment. The testbeam was laid out in the NT (formerly NK) beamline at a 42 mr angle with respect to the main (NC) neutrino beamline and was approximately 152 meters long. Figure 2.2 contains a schematic drawing of the test beamline. There were three different modes of running: electron, hadron, and muon. During the testbeam run, these modes were used for hadron energy response calibration, toroid magnetic field calibration (muon mode), electron energy response calibration, and positional detector response mapping with both hadrons and muons.

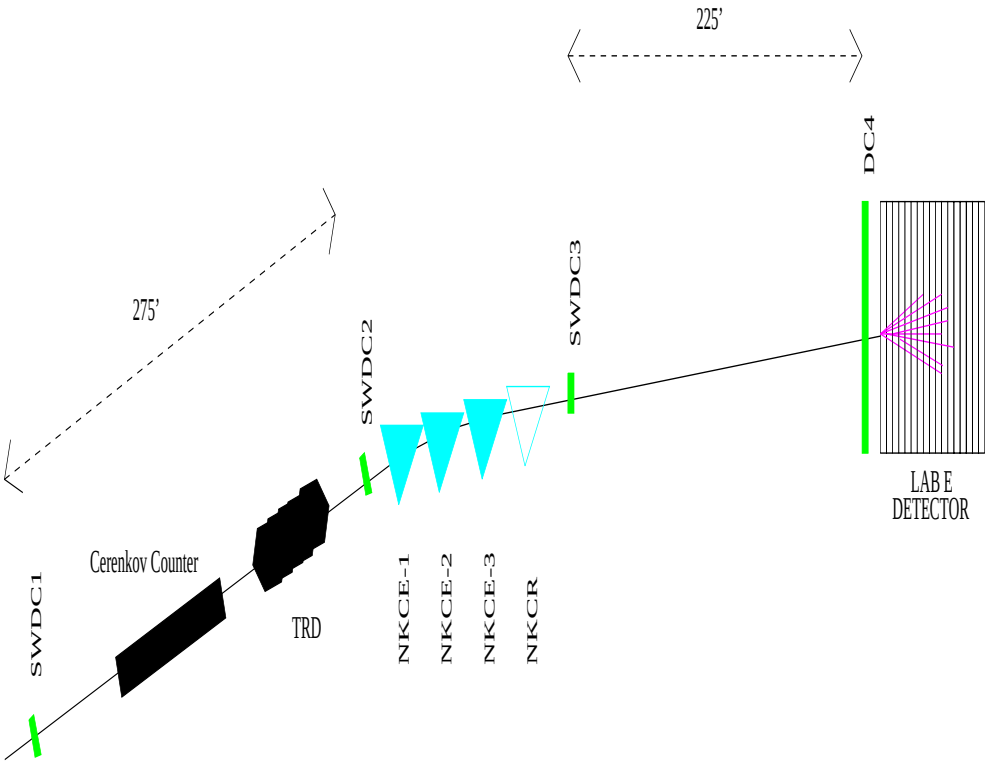

Figure 2.2: Testbeam layout

2.3.2 Technical Specifications and Layout

The testbeam consisted of a number of different elements including beam optics such as dipole and quadrupole magnets, drift chambers, an eight module transition radiation detector, and a cerenkov counter. Three different kinds of drift chambers were used. Four small chambers, named for their designer, John Krider, were designed for momentum tagging. They contained two x and two y planes each with an active area of 10.2cm×10.2cm and a resolution of 390μm. In addition, there was an E774 drift chamber and two NuTeV target chambers at the upstream end of lab E. Diagrams and descriptions of the NuTeV chambers can be found in Ref. 30. The E774 chamber had an active area of 35.6cm×35.6cm with a resolution of 250μm in each of its six planes and the NuTeV chambers had active areas of 3mx3m with approximately 500μm resolution (one plane each). The reason for the variety of chambers is the following. Since the testbeam could run in both straight-through and bent beam mode, it was necessary to have several chambers that were large enough to tag particles traveling down the beamline at relatively large distances from the beam axis. The Krider chambers were not large enough for this purpose and so provided extra information in bent-beam mode only. The E774 chambers and the NuTeV drift chambers were large enough and so could be used in both modes.

2.4 SSQT

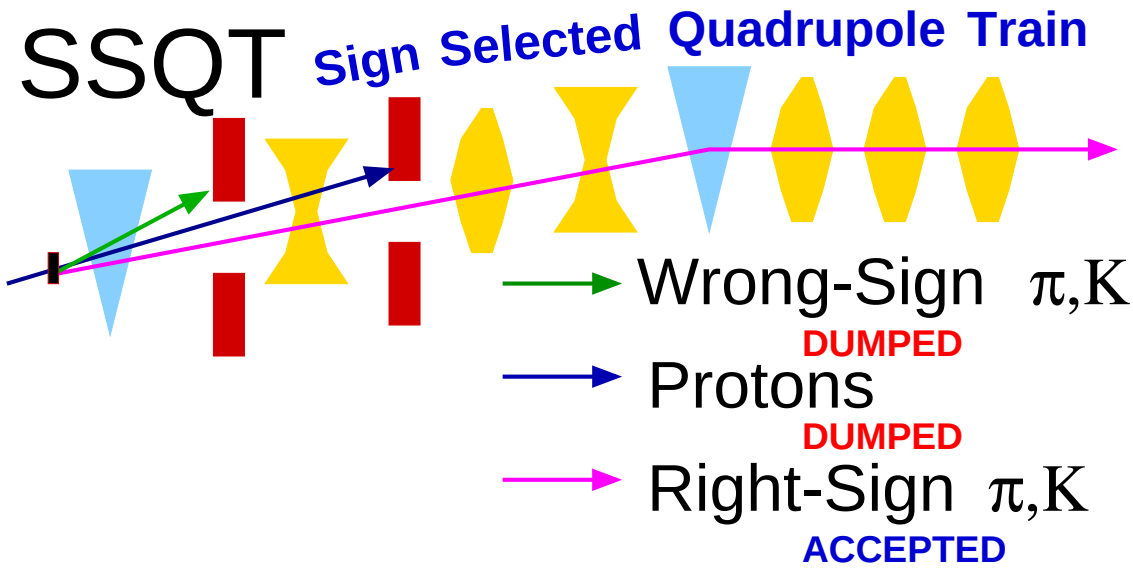

Figure 2.3: Schematic diagram of the SSQT

The SSQT (Sign Selected Quadrupole Train) was one of the most vital components of the experiment. It allowed for separate, high purity beams of neutrinos or anti-neutrinos with a flux of approximately 20 neutrinos or 4 anti-neutrinos per 10 trillion protons on the primary BeO target. The beamline was designed such that beam from the primary target was produced far upstream from, and at an angle to, the calorimeter. As a result, neutral particles, such as K_L's produced at the interaction vertex (shown above as the middle arrow leaving the target), traveled straight into a beam dump and did not continue down the beamline. Neutrino and anti-neutrino mode were chosen according to the sign of the current in the first dipole downstream of the target (first triangle on the left above) and positively and negatively charged beams could be either directed down the beamline or into a dump based on that dipole's polarity. In ν mode, the ratio $\overline{\nu}/\nu$ was 0.8×10^{-3} and in $\overline{\nu}$ mode, the ratio $\nu/\overline{\nu}$ was 4.8×10^{-3}. Neutrinos present in anti-neutrino mode running and anti-neutrinos in neutrino-mode running are said to have originated from "wrong sign" Pions or Kaons. The SSQT also incorporated extensive primary and secondary beamline monitoring via the Fermilab EPICURE system. With this system in place, it was possible to determine charged particle fluxes to a reasonable degree of accuracy at several places along the beamline.

2.5 Data Acquisition

The NuTeV Data Acquisition system (DAQ) was designed to maximize speed, accuracy, and flexibility. To achieve these goals, a system based on VME modules (acting as drivers for two CAMAC branches), a Motorola 68040 processor, and running VxWorks was developed [13]. The DAQ collected information from drift chambers wires and phototube cables that had been processed through the trigger logic and a bank of FERA ADC's. These data were then collected from the DAQ buffer and written out to Exabyte 8505 tapes in a format compatible with that of the CERN program library's (cernlib) ZEBRA data structure. Simultaneously, the information in the buffers could be served via TCP/IP to a network of Silicon Graphics workstations which were able to graphically monitor both the performance of the DAQ system and the values of the data being collected. This allowed for a great deal of real-time control as well as for ease of debugging.

2.6 Trigger

The NuTeV trigger was designed for versatility so as to provide information for a large variety of analysis topics. The signals to the trigger electronics came from the 4 phototubes at the corners of each counter. Signals from the phototubes were combined in various ways to produce useful information that were passed to the data acquisition system (DAQ). Table 2.1 contains a list of the different triggers and a short description of their functions. As there was a limit to the amount of information that the DAQ could store in a data bank, it was necessary to limit the time during which a given trigger could take data. This was accomplished through the use of gating.

2.6.1 Gates

Five different kinds of gates were used during a beam spill: the pedestal gate, cosmic ray gate, SIGX gate, fast gate, and the slow gate. The pedestal gate's function was to read out the electronics when there were no triggers, the cosmic ray gate activated the neutrino trigger when there was no beam (for cosmic ray background subtraction), and the SIGX gate was essentially the same as the cosmic ray gate, but it was used to study cosmic rays themselves. The two most important gates, for the purposes of this analysis, are the fast and slow gates. The fast gate contained the neutrino pings and was used in conjunction with the neutrino triggers. The slow gate contained the test beam and was necessary for the calibration of the detector. The gates were synched with the beam timing structure in order to make data collection more efficient. The total time during beam spill was approximately 1 second, an

interval further subdivided into fast spill, which consisted of five 4ms "buckets" or "pings", and slow spill which was the remainder of the interval. Figure 2.4 contains a diagram of beam spill intervals and gate layout. The reason for the ping structure during fast gate was that neutrino events often look like cosmic ray events. In order to maximize the probability of having an actual neutrino event take place during fast gate, it was necessary for the flux of neutrinos incident on the detector to be both short in duration and extremely intense to preclude the possibility of a cosmic ray event feeding into the neutrino sample.

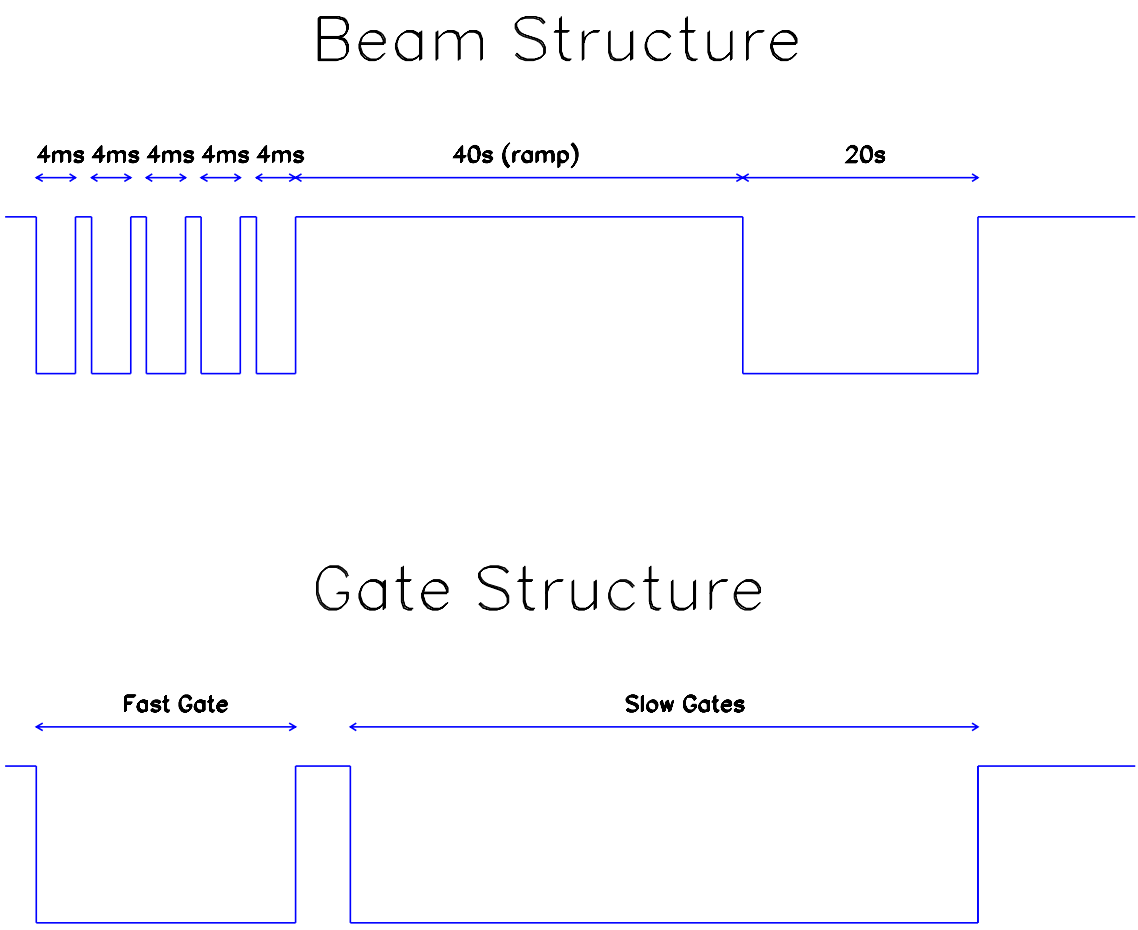

Figure 2.4: Schematic diagram of beam and gate timing structure

2.6.2 Trigger Logic

Signals from individual phototubes were called *lows*. The 4 lows from a given counter were summed to form the *combination low* for that particular counter. Combination lows were amplified by 10 and sent to an adc as *highs*. One other very important piece of logic was the *sbit* system. Sbits were made by amplifying the combination

lows by 100 and piping the resulting signal through a discriminator with a threshold of 150 mV or about 1/4 of a minimum ionizing particle (MIP). The actual value of 1 MIP is subject to calibration and has the approximate value of 0.212 GeV or, alternatively, 75 ADC counts [26]. There were 12 triggers, some of which were redundant or created for specific studies.

Trigger	*Name*	*Requirements*
1	Charged Current Trigger	• counters on upstream of washer 1 • counters on in both toroid gaps • no upstream veto
2	Neutral Current Trigger	• $E_{had} > 5$ GeV in 8 consecutive counters • $E_{had} > 0.15$ GeV in 2 out of 4 consecutive counters • no upstream veto
3	Range-Out/Exit Trigger	• 1/4 MIP in each of 16 non-consecutive counters • 4 GeV energy in any 8 adjacent counters • no upstream veto
4	Charged Current Trigger II	• shower energy • hits in first cart upstream of toroid • muon track through one toroid quadrant
5	Test Beam Trigger	• slow spill
6	Straight through μ Trigger	• hits in each cart and one toroid quadrant
8	Cosmic Ray Trigger	• 40 counter muon requirement
10,11,12	Pedestal Triggers	• No other triggers

Table 2.1: NuTeV trigger list with descriptions

Chapter 3

Theory

3.1 The Standard Model

The Standard Model specifies the forces via which all particles interact as well their basic properties. Of all current theories, the Standard Model (or SM) has been the most successful in describing experimental results.

3.1.1 The Four Forces

Elementary particles must interact via the mediation of forces. Currently, theory allows for four (listed here in descending order of strength):

- Strong
- Electromagnetic
- Weak
- Gravitational

In the late 1960's, Glashow, Salam, and Weinberg postulated that the electromagnetic and weak forces were related to each other. This became known as GWS theory, and it effectively reduces the number of independent forces to three. In this dissertation, gravity will be ignored bringing the total down to two: electroweak and strong. Each force has one or more mediators associated with it. These mediators, called intermediate vector bosons (vector because they have spin 1), are particles which transmit their respective forces between other elementary particles. For example, in the electromagnetic interaction:

$$e^+e^- \rightarrow e^+e^- \quad \text{(Bhabha scattering)}$$

the two electrons exchange a photon mediator. Table 3.1 contains a list of forces and their associated mediators. In the standard model, the relationship between all mediators ($W^{\pm}, Z^0, \gamma, g$) may be understood in terms of the language of group theory. The mediator for any interaction can be expressed as an element of a group reflecting a particular symmetry. An example of a group is, R, the rotation group, which contains the set of all rotations in three dimensional space. This group is also known as $SO(3)$, where S and O stand for special and orthogonal. An orthogonal matrix is one for which the inverse is equal to the transpose conjugate:

$$M^{-1} = \tilde{M}^*$$

The term "special" means that the matrix has determinant of 1. Therefore, the group $SO(3)$ contains matrices which are orthogonal, with determinant 1. These matrices are the mathematical operators for rotation about a point in three dimensional space. In its fundamental irreducible representation, $SO(3)$ contains three "generator" matrices which correspond to rotations around three orthogonal axes such as x, y, and z. More interesting within the context of this dissertation, is the special *unitary* matrix:

$$U^{-1} = U^{\dagger} = \tilde{U}^*$$

which is the complex analog of the orthogonal matrix. Of particular interest are the groups $U(1)$, $SU(2)$, and $SU(3)$ which play an important role in the standard model of weak and strong interactions. The number of generators associated with the group $U(n)$ is n^2 and the number associated with $SU(n)$ is $n^2 - 1$. Therefore, the three groups mentioned above have 1, 3, and 8 generators respectively. The $SU(2)\times U(1)$ group may be associated with the symmetries of the electromagnetic and weak forces and their mediators the photon, and the $W^{\pm}$ and Z^0 respectively. The $SU(3)$ group is a color group related to the strong interaction and its generators represent the gluons in a three color QCD scheme. A complete theory of neutrino scattering must combine these three groups since the electromagnetic, weak, and strong forces are all relevant in νN scattering. This is accomplished by forming the composite group $SU(3)\times SU(2) \times U(1)$.

3.1.2 Leptons

The lepton (meaning "light-weight") family contains one of the most familiar particles, the electron. In addition, the society of leptons contains two heavier versions of

Force	*Mediator*
Strong	g (Gluon)
Electroweak	γ,W^+,W^-,Z^0
Gravitational	G (Graviton)

Table 3.1: Standard Model forces and mediators

the electron, the muon (μ) and the tau (τ) as well as a neutrino (ν) corresponding to each. All leptons have anti-particles and are fermions with spin of 1/2. All particles carry what are known as quantum numbers which define a quantity that must be conserved in a given interaction. For leptons, the relevant quantum number is *lepton number* which is conventionally defined to be +1 for leptons and -1 for anti-leptons. Lepton number is conserved separately for e, μ, and τ. Leptons and their related neutrino are usually grouped in *weak isospin doublets* to indicate that they are connected via the charged weakly interacting intermediate vector boson, $W^{\pm}$. Table 3.2 lists leptons and their quantum numbers. Leptons interact with other particles via the electromagnetic and weak interactions but not via the strong interaction.

lepton	I_w	L_e	L_μ	L_τ	*Charge*	*Mediator*
e^-	+1	+1	0	0	-1	$W^{\pm}$,Z^0,γ
μ^-	+1	0	+1	0	-1	
τ^-	+1	0	0	+1	-1	
ν_e	-1	+1	0	0	0	$W^{\pm}$,Z^0
ν_μ	-1	0	+1	0	0	
ν_τ	-1	0	0	+1	0	

Table 3.2: Leptons and quantum numbers

3.1.3 Quarks

Most particles are not leptons, but rather, mesons ("middle-weight") or baryons ("heavy-weight") made up of quarks. Like leptons, quarks are spin 1/2 fermions and can interact weakly (ie. via the W and Z bosons). Unlike leptons, however, they also interact via the *strong* or "color" force mediated by the gluon (g). Below is a table of quarks and their charges.

QCD states that there are eight gluon mediators and that they differ only in color from each other. Quarks must have color in order to interact with the gluons. If these "colors" are chosen to be (r)ed, (g)reen, and (b)lue, then a given quark can be red, green, or blue, and a given gluon must share a color *and* an anti-color. Theory also specifies that all physical particles (leptons, baryons, and mesons) must be $SU(3)$ color singlets while gluons are contained in $SU(3)$ color octets. To satisfy these requirements, a particle composed either of a red, green, and a blue quark or,

quark	*Charge*	*Mediator*
u(p)	+2/3	γ
d(own)	-1/3	$W^{\pm}$,Z^0
c(harm)	+2/3	g
s(trange)	-1/3	
t(op)	+2/3	
b(ottom)	-1/3	

Table 3.3: Quarks

a color/$\overline{color}$ combination is defined to be colorless. For example, a proton contains two up quarks and a down quark among which all three colors must be represented to preserve color neutrality while a D_s^+, in the quark model, must be the linear combination:

$$c\overline{s}|_{r\overline{r}} + c\overline{s}|_{g\overline{g}} + c\overline{s}|_{b\overline{b}}$$

where each color subscript applies to either the c or s quark. It is the strong force between quarks and gluons which makes QCD at once complicated and interesting. All other forces in nature grow weaker as the distance between two particles grows. The strong force, however, grows *larger* the further apart the two particles are from each other. This means that, at very high energy scales or, alternatively, at very short distance scales at which quarks are bunched together in the nucleon, the strong force that binds them is practically non-existent. In other words, as the squared momentum transfer $Q^2 \to \infty$, $\alpha_s(Q^2) \to 0$. This is the principle of *asymptotic freedom* which states that deep inelastic scattering as a probe of the nucleus gives a picture of quarks that are almost free. The fact that the quarks are bound very loosely at high energies but tightly at low energies is quantified by the "running" of the strong coupling constant α_s with Q^2. At deep inelastic scattering (DIS) energies, quarks are essentially unbound, α_s is very small, and QCD calculations can be done in the relatively well understood perturbative framework.

3.2 Deep Inelastic Scattering

3.2.1 Neutrino-Nucleon Scattering Kinematics

A diagram of νN deep inelastic charged-current scattering is shown in Fig. 3.1. The diagram for neutral current scattering is similar, but, in place of the $W^{\pm}$ bosons, there is a Z^0 and the outgoing μ is replaced with a scattered ν. In general the cross-section for such an interaction will depend on several variables such as the

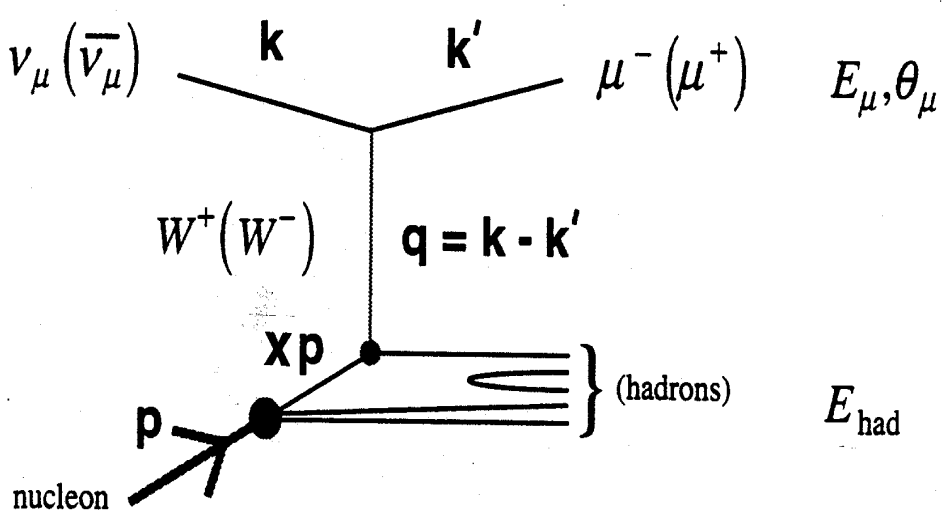

Figure 3.1: Neutrino-Nucleon Scattering Kinematics

squared momentum transfer Q^2, the scaling variable x, also known as "Bjorken x", and the inelasticity, y (see Eq. 3.1).

$$x = \frac{-q^2}{2q\cdot p}, \qquad y = \frac{p\cdot q}{p\cdot k}_{lab} \simeq \frac{1}{2}(1-\cos\theta_{CM}) = \left.\frac{E_{had}}{E_\nu}\right|_{lab} \tag{3.1}$$

In high energy scattering, the neutrino doesn't interact with the proton as a whole, but with the quarks and gluons inside. Each quark or gluon carries a specific fraction of the proton's overall momentum. The momentum fraction of the parton struck by the neutrino corresponds to x in Eq. 3.1. This quantity is also known as "Bjorken x" or x_{Bj}. Another quantity, y, called the *inelasticity* of the interaction, is related to the scattering angle of the outgoing μ or ν in the center-of-mass frame. In the lab frame, y is the fraction of the incoming neutrino's energy converted into hadronic energy in the target.

3.2.2 Neutral and Charged Currents

As mentioned above, neutrinos and quarks can interact via the exchange either of a $W^\pm$ or Z^0 boson. In the latter case, the interaction is referred to as a "Neutral

Particle	c_V	c_A
ν_e, ν_μ, ν_τ	$\frac{1}{2}$	$\frac{1}{2}$
e,μ, τ	$-\frac{1}{2} + 2\sin\theta_W$	$-\frac{1}{2}$
u,c,t	$\frac{1}{2} - \frac{4}{3}\sin^2\theta_W$	$\frac{1}{2}$
d,s,b	$-\frac{1}{2} + \frac{2}{3}\sin^2\theta_W$	$-\frac{1}{2}$

Table 3.4: Neutral Current coupling strength of quarks to neutrinos

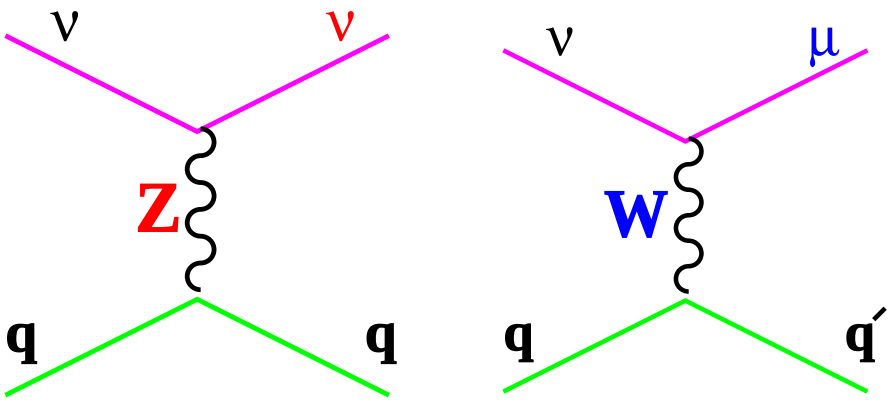

Figure 3.2: Tree level Feynman diagrams for NC and CC events

Current" (NC) interaction (since there is no electric charge exchanged) while the former case is a "Charged Current" (CC) interaction (see Figure 3.2). Weak interactions are mixtures of V±A (for vector plus/minus axial vector) couplings as opposed to the purely vector couplings of electromagnetic scattering. This means that the couplings of all particles to the W and Z bosons contain both vector and axial terms. As can be seen below in the mathematical expressions for the couplings, it is the interference term, $\alpha_w\gamma^\mu\gamma^5/\alpha_z c_A^i\gamma^\mu\gamma^5$, in the couplings which is the origin of the parity-violating behavior of weak interactions. The couplings are:

$$\alpha_w\gamma^\mu\left(1-\gamma^5\right) \qquad (W^\pm \text{ coupling})$$

$$\alpha_z\gamma^\mu\left(c_V^i - c_A^i\gamma^5\right) \qquad (Z^0 \text{ coupling}).$$

In the above expressions, α_w and α_z are the couplings to the W and Z bosons and have the approximate values (in dimensionless units) of 0.0076 and 0.01 respectively. For comparison, the value of the fine structure constant, $\alpha_{EM} = g_e^2/16\pi^2$, is 0.0073. The quantities c_V and c_A are the vector and axial components for coupling to the Z *only*, and i indicates the particle in question. Table 3.4 lists c_V and c_A for NC interactions. The γ matrices are the standard 4x4 matrices found in the Dirac equation.

3.2.3 Scattering Cross-Sections

The total $\nu(\overline{\nu})N$ scattering cross-section can be calculated from Fermi's Golden Rule which states:

$$d\sigma = \frac{|\mathcal{M}|^2}{\phi(E)} d\Omega_{space} \tag{3.2}$$

where $|\mathcal{M}|^2$ is the squared amplitude for the process in Fig. 3.1, $\phi(E)$ is the incident neutrino flux, and $d\Omega_{space}$ is a differential phase space factor. The amplitude contains all information about the scattering process. For QCD, the Feynman rules specify that:

$$|\mathcal{M}|^2 \propto L_{\mu\nu} W^{\mu\nu} \tag{3.3}$$

where $L_{\mu\nu}$ is the the lepton tensor describing the interaction at the vertex of the neutrino and the W boson and $W^{\mu\nu}$ is the hadronic tenser containing information about the hadronic vertex. The tensor $W^{\mu\nu}$ is a parameterization of an unknown quantity, interpreted in the parton model as the precise distribution of partons inside the nucleus. By contrast, the tensor $L_{\mu\nu}$, since it contains only information about the electroweak vertex, can be calculated exactly via Quantum Electrodynamics (QED) and the Glashow-Weinberg-Salam (GWS) theory of weak interactions. Eqs. 3.5 and 3.4 define these two tensors in terms of the momenta in Fig. 3.1.

$$W^{\mu\nu} = \mathcal{W}_1 g^{\mu\nu} + \frac{\mathcal{W}_2}{M^2} p^\mu p^\nu - i\epsilon^{\mu\nu\alpha\beta} \frac{\mathcal{W}_3}{2M^2} + \frac{q^\mu q^\nu \mathcal{W}_4}{M^2} + \mathcal{W}_5 \left(\frac{p^\mu q^\nu + q^\mu p^\nu}{M^2} \right) + i\mathcal{W}_6 \frac{(p^\mu q^\nu - q^\mu p^\nu)}{2M^2} \tag{3.4}$$

$$L_{\mu\nu} = k_\mu k_\nu^{'} + k_\mu^{'} k_\nu - g_{\mu\nu} k \cdot k^{'} \pm i\epsilon_{\mu\nu\lambda\sigma} k^\lambda k^{'\sigma} \tag{3.5}$$

The mathematical quantities $\mathcal{W}_{1-6}$ are functions of x and Q^2 and contributions to the amplitude from $\mathcal{W}_{4,5,6}$ are proportional to M_μ^2 and are ignored. Contraction of $L_{\mu\nu}$ and $W^{\mu\nu}$ results in the following expression:

$$|\mathcal{M}|^2_{\nu(\overline{\nu})} \propto 2EE^{'} \left\{ 2\sin^2\frac{\theta}{2} \mathcal{W}_1 + \cos^2\frac{\theta}{2} \mathcal{W}_2 \mp \mathcal{W}_3 \frac{(E+E^{'})}{M} \sin^2\frac{\theta}{2} \right\} \tag{3.6}$$

where E and $E^{'}$ refer to the initial and final state energies of the lepton and θ is the lepton scattering angle in the center of mass frame. Inserting Eq. 3.6 into Eq. 3.2 and including explicitly all proportionality factors leads to an expression for the $\nu/\overline{\nu}$ differential scattering cross-section (Eq. 3.7).

$$\frac{d^2\sigma^{\nu(\overline{\nu})}}{d\Omega_{space}dE'} = \frac{G_F^2 E'^2}{2\pi^2}\left(\frac{M_W^2}{M_W^2+Q^2}\right)^2 2EE'\left\{2\sin^2\frac{\theta}{2}\mathcal{W}_1 + \cos^2\frac{\theta}{2}\mathcal{W}_2 \mp \mathcal{W}_3\frac{(E+E')}{M}\sin^2\frac{\theta}{2}\right\} \tag{3.7}$$

In Eq. 3.7, the $\mathcal{W}$ are the structure functions for $\nu(\overline{\nu})N$ scattering. Making a change of variables from $(d\Omega_{space}, dE')$ to (dx, dy) and altering the structure function definitions to reflect modern notation gives Eq. 3.8 which is the general lorentz invariant expression for νN scattering.

$$\frac{d\sigma^{\nu(\overline{\nu})N}}{dxdy} = \frac{{G_F}^2 ME}{\pi(1+\frac{Q^2}{{M_W}^2})^2}\left[\left(1-y-\frac{Mxy}{2E}\right){F_2}^{\nu(\overline{\nu})} + \frac{y^2}{2}2x{F_1}^{\nu(\overline{\nu})} \pm y\left(1-\frac{y}{2}\right)x{F_3}^{\nu(\overline{\nu})}\right]. \tag{3.8}$$

In Eq. 3.8, x and y have their standard definitions, $Q^2 = -q^2$, and F_1, F_2, and F_3 are structure functions parameterizing our ignorance of how quarks and gluons are arranged inside the nucleon. While it is true that quarks and neutrinos are purely spin $\frac{1}{2}$ objects, there are longitudinal components in the total scattering cross-section due to quark-antiquark pair-production from gluons as well as quark effects which amount, effectively, to spin 0 objects in the nucleon at NLO (see Fig. 3.3). By separating Eq. 3.8 into pieces, more information can be obtained about how the angular dependence of the cross-section differs depending on whether the scattering particles are ν/q, $\nu/\overline{q}$, or some other combination. To this end, the following two assumptions are made:

- Structure Functions can be divided into longitudinal and transverse pieces
- They can, to all orders, be expressed as functionals of parton momentum distributions or parton structure functions. Specifically:

$$F_1(x,Q^2) = F_1[p^T(x,Q^2) + \overline{p^T}(x,Q^2)], \tag{3.9}$$

$$F_2(x,Q^2) = F_2[p^{T+L}(x,Q^2) + \overline{p^{T+L}}(x,Q^2)], \tag{3.10}$$

$$F_3(x,Q^2) = F_3[p^T(x,Q^2) - \overline{p^T}(x,Q^2)], \tag{3.11}$$

  where T=transverse, L=longitudinal. This is equivalent to the assumption that angular dependence is the same for structure functions to all orders in QCD.

In Eqs. 3.9, 3.10, and 3.11, the symbol p^T refers to the transverse quark and gluon distributions while p^{T+L} is the transverse and longitudinal quark and gluon distributions. For the case of F_3, the functional in Eq. 3.11 can be written as:

$$F_3(x,Q^2) = F_3[q^T(x,Q^2) - \overline{q^T}(x,Q^2)],$$

where the q^T are transverse quark distributions, since $g^T = \overline{g}^T$. Separating out the longitudinal and transverse pieces in Eq. 3.8:

$$\frac{d\sigma_L^{\nu(\overline{\nu})N}}{dxdy} = \frac{{G_F}^2 ME}{\pi(1+\frac{Q^2}{{M_W}^2})^2}\left(1-y-\frac{Mxy}{2E}\right){F_{2L}}^{\nu(\overline{\nu})}, \tag{3.12}$$

$$\frac{d\sigma_T^{\nu(\overline{\nu})N}}{dxdy} = \frac{{G_F}^2 ME}{\pi(1+\frac{Q^2}{{M_W}^2})^2}\left(1-y+\frac{y^2}{2}\right){F_{2T}}^{\nu(\overline{\nu})} \pm y\left(1-\frac{y}{2}\right)x{F_{3T}}^{\nu(\overline{\nu})}. \tag{3.13}$$

Applying the above assumptions about F_2 and F_3 to Eq. 3.13 and assuming that E is large in Eq. 3.12 leads to the following two relationships (for ν scattering):

$$\frac{d\sigma_T^{\nu N}}{dxdy} \simeq \left[p^T + \overline{p^T}\,(1-y)^2\right], \tag{3.14}$$

$$\frac{d\sigma_L^{\nu N}}{dxdy} \simeq (1-y)\left(p^L + \overline{p^L}\right). \tag{3.15}$$

Using these expressions and invoking symmetry:

$$\frac{d\sigma^{\nu q}}{dy} = \frac{d\sigma^{\overline{\nu q}}}{dy} \simeq 1, \tag{3.16}$$

$$\frac{d\sigma^{\overline{\nu} q}}{dy} = \frac{d\sigma^{\nu \overline{q}}}{dy} \simeq (1-y)^2, \tag{3.17}$$

$$\frac{d\sigma^{\nu q}}{dy} = \frac{d\sigma^{\nu \overline{q}}}{dy} \simeq (1-y). \tag{3.18}$$

3.2.4 The Parton Model at Leading Order

Up until this point, the discussion of cross-sections and partons has been rather casual and without detail. In order to understand Eq. 3.8, there must be a more detailed discussion of the quantities F_1, F_2, and F_3 which contain almost all of the physics. As has been seen previously, structure functions are a way of parameterizing the lack of knowledge about the contents of the proton and neutron. QCD specifies only that SF's must depend on a pair of kinematic variables defined for the scattering interaction. A customary choice is the pair (x, Q^2). The standard way to interpret structure functions, in leading order, is to view them as literal sums and differences of parton distribution functions. For each scattering process, structure functions are constructed which can then be used to form the appropriate portion of the total cross-section. Separating 3.8 by parton, there results:

$$\frac{d\sigma^{p(x)}}{dxdy} = f[x, y, E_{\nu(\overline{\nu})}, p(x)]. \tag{3.19}$$

As an example, suppose one is interested in charged current ν scattering from u and d type quarks only. From the discussion of weak couplings, it is known that CC interactions have coupling coefficients of 1. Since electromagnetic charge must be conserved, there remain only d and $\overline{u}$ quarks to scatter from. Also, keeping in mind the y dependence of $\nu(\overline{\nu})/q(\overline{q})$ scattering, the LO charged current Callan-Gross piece of the cross-section may be written,

$$\frac{d\sigma_0^{cc}}{dxdy} = d(x) + (1-y)^2\overline{u}(x). \tag{3.20}$$

Summing over this and other LO processes results in the total differential cross-section.

3.2.5 The Parton Model at Next to Leading Order

In a perturbative QCD expansion, the leading order cross-section includes quark parton model terms that are "0^{th}" order in α_s and parton evolution. Higher order terms in the series contain progressively higher and higher order terms of α_s coupled with higher order evolution terms (see Eq. 1.1). In general, NLO terms will be prefaced by α_s, NNLO by α_s^2, and so on. Since this thesis is concerned with NLO QCD formalism, the expression for α_s must itself be NLO. There are several different approaches that have been developed to describe next-to-leading-order parton behavior inside the nucleon. They differ in terms of QCD scale and the number of parton or quark flavors included in the PDF, but all incorporate the same formal-

ism for α_s which is dependent, not only on the order of the calculation, but on the number of quark flavors as well. The NLO expression for $\alpha_s(Q^2)$ is:

$$\frac{\alpha_s(\log \mu^2)}{4\pi} = \frac{1}{\beta_0 \log \mu^2/\lambda^2} - \frac{\beta_1}{\beta_0^3} \frac{\log\log \mu^2/\lambda^2}{\log^2 \mu^2/\lambda^2} + \dots \tag{3.21}$$

where,

$$\beta_0 = 11 - 2N_f/3, \quad \beta_1 = 102 - 38N_f/3. \tag{3.22}$$

In Eq. 3.21, N_f represents the number of parton flavors, μ is the factorization scale, and λ is the QCD scale, which varies between PDF sets and is on the order of 300 MeV.

3.2.6 Cross-Section Calculation Schemes

There are several approaches to calculating the NLO cross-section, each of which makes assumptions about the kinds of quarks contained in the parton, and what factorization scale to use. Two common approaches are the Fixed Flavor Scheme (FFS) used in this analysis, and the Variable Flavor Scheme (VFS). In the former, the number of parton flavors in the PDF set remains constant for all energies. As an example, in a 3 FFS scheme, the u, d, s, and g distributions are contained within the PDF set while heavy quark production and other high Q^2 and high E_ν processes are accounted for via "hard-scattering coefficients" (see Eq. 3.23). In the VFS scheme, the number of parton flavors in the PDF set depends on the energy of the incident probe. When a certain energy threshold is reached, the next largest quark (in terms of mass) is given a non-zero probability distribution. Two examples of such schemes are discussed below. One, known as the ACOT scheme, is variable flavor, while the GKR scheme, used in this analysis, is a three fixed flavor scheme.

ACOT Scheme

The ACOT scheme [6, 10], is a variable flavor approach to NLO QCD. Essentially, the NLO massive quark cross-section is calculated by summing over a convolution of parton distribution functions where the index of the sum varies depending on the relationship of the energy scale of the calculation [9] to the mass of any heavy quarks that are present. There are three regions of interest:

- $m_h \ll Q$: This is the energy scale for which the mass of the "heavy" quark of interest is, in fact, so much smaller than Q that it may be idealized as massless and can be included in the PDF in the same manner as the other partons.

- $m_h \gg Q$: In this region, the energy scale is so much smaller than the heavy quark mass that an intrinsic heavy quark distribution is impossible and a fixed flavor scheme in which the number of parton flavors remains 3 or 4 regardless of energy scale, is a better choice.

- $m_h \simeq Q$: This situation is well modeled since logarithms in the perturbative expansion of the form $log\frac{m_h}{\mu}$ are small. Here, μ is the QCD factorization scale common choices for which are Q^2 or the square of the final state muon's transverse momentum, p_T^2.

Independent of scheme, all NLO structure-function calculations must include extra Feynman diagrams in their hard-scattering coefficients that are not included in leading order calculations. These diagrams include gluon radiation from the quark leg of the diagram as well as boson-gluon fusion. Both LO and NLO diagrams are shown in Fig. 3.3. In the ACOT and other schemes, special attention must be paid to possible overlap between NLO and leading order diagrams. In particular, the LO boson-quark scattering diagram is also included in the NLO boson-gluon fusion diagram for the case in which the the scattering is from a gluon collinear with the quark momentum. Therefore, this particular term in the cross-section formalism must be subtracted from the total cross-section. This is done in different ways for different schemes but it must be done in all to avoid double counting [11]. A heavy charm quark analysis has already been done [6] using the ACOT scheme but it was clear that, for the purposes of this charged current analysis, the newer fixed flavor, massive quark scheme [8] in conjunction with the standard fixed flavor massless quark formalism [4] had several advantages among which were a great degree of consistency between massless and massive quark treatments, practicality, and simplicity of implementation. A description of the new procedure follows.

GKR/HW Fixed Flavor Scheme

The NLO cross-section model used in this analysis is a combination of several different, but similar, schemes appropriate for different parts of the cross-section. Table 3.5 shows the divisions. One of the most important differences between NLO and LO formalism is that, at NLO, structure functions can no longer simply be written as sums and differences of "raw" parton distributions. The factorization theorem (Eq. 3.23) states that NLO structure- functions for a particular parton evaluated at x and Q^2 are convolution integrals over the NLO parton distribution function and an appropriate hard- scattering (Wilson) coefficient.

$$F^j(x,Q^2) = \sum_i \int_x^1 \frac{dy}{y} \mathcal{C}^j(y, \overline{g}(Q^2)) p_i(x/y) \tag{3.23}$$

σ	*Formalism*
Massless u,d,s,g	Herrod/Wada ([4])
NC charm scattering	Glück/Godbole/Reya ([7])
CC charm production	Glück/Kretzer/Reya ([8])

Table 3.5: NLO cross-section pieces by formalism

In Eq. 3.23, j=1,3 (corresponding to structure function number), i={u,d,s,g}, $\mathcal{C}^j$ is the hard scattering or Wilson coefficient, and p_i is the appropriate parton distribution function. As can be seen, $F^i(x,Q^2)$ depends, not only on x and Q^2, but also on $p_i(x)$ evaluated at all other x values between x and 1. This is similar to the NLO evolution in Q^2 which occurs in the splitting functions used to derive the NLO parton distributions [4]. It is also important to note that the hard-scattering coefficient differs depending on which of $F_1, F_2,$ or F_3 is being calculated. The reason for this is that, in NLO, νq scattering is no longer simply a spin 1/2 on spin 1/2 interaction. Rather, a longitudinal component appears which is due mainly to quark pair-production from gluons (Fig. 3.3) and its associated effects on the NLO quark distributions. Therefore, the Callan-Gross approximation, $F_2 = 2xF_1$ no longer holds and the three structure functions must be calculated separately for each process of interest. Equation 3.23 as written applies generally to all of the NLO formalism discussed in this thesis. Of course, details (such as the Wilson coefficient) differ depending on whether the calculation is of structure functions for massless quarks, massless boson-gluon fusion, massive quarks, or massive boson-gluon fusion. For details, refer to Refs. 4 and 8. Like the ACOT scheme, the GKR/HW scheme effectively splits the structure functions into "LO" and "NLO" parts in order to facilitate standard subtraction of overlapping diagrams. This is only done for quark structure functions as there are no leading order gluon initiated diagrams. In the formalism of Ref. 4, the Wilson coefficient $\mathcal{C}^j$ takes the following form:

$$\mathcal{C}(y) \propto \delta(1-y) + \frac{g^2}{16\pi^2}\mathcal{C}^{(1)}(y). \tag{3.24}$$

Using just the first part of the $\mathcal{C}$ function in Eq. 3.23, there results, for a given parton distribution:

$$F^i_{\text{“}lo\text{”}} = \int_x^1 \frac{dy}{y}\delta(1-y)p_i(\frac{x}{y})$$

$$\Longrightarrow F^i_{\text{“lo”}} = p_i(x).$$

The "leading order" part of the NLO structure function is simply the NLO parton distribution function evaluated at x. Note that this piece is *not* identical to the LO

parton distribution function evaluated at x. The second term in $\mathcal{C}$ of order α_s is the properly subtracted NLO piece of the structure function. The Glück, Kretzer, and Reya and Herrod and Wada formalisms have several advantages over the ACOT calculation. Firstly, they are straightforward to implement in any programming language and are both extremely well documented. Essentially, both calculations are equivalent but for the inclusion of charm quark mass effects in the evolution kernel of the GKR formalism. Both postulate a massless strange quark which rids the theory of dependence on an extra arbitrary parameter. In addition, as mentioned, the GKR and HW formalisms explicitly separate the structure functions into a leading order collinear piece and a NLO non-collinear piece which accounts for the subtraction term mentioned above. Most importantly, the 3 Flavor Fixed scheme, common to both the GKR and HW calculations, has been shown to be accurate over a large range of Q^2 up to collider energies [34, 35], obviating complex, quark mass dependent NLO calculations.

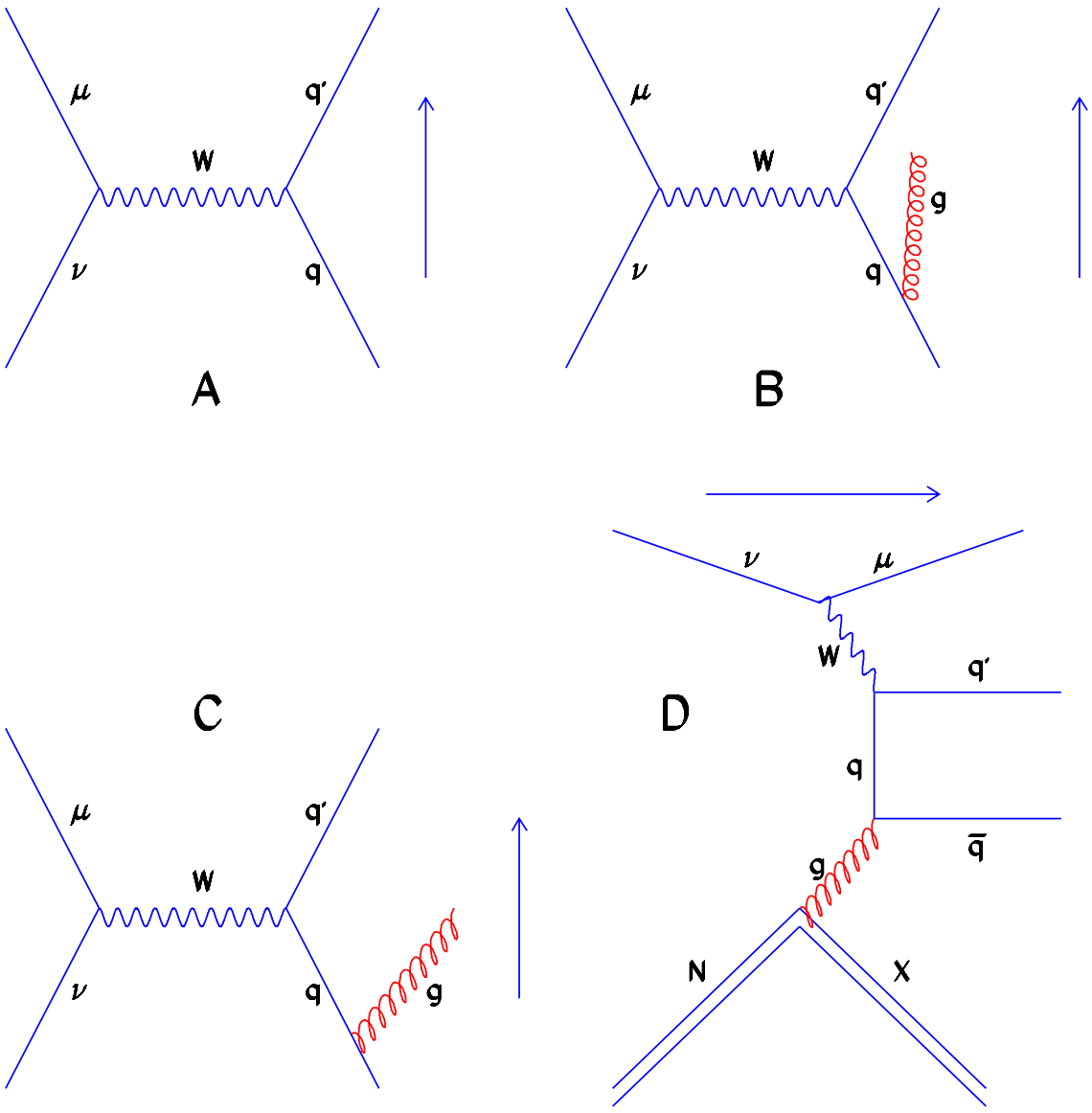

Figure 3.3: LO and NLO diagrams. A) LO quark scattering. B) LO quark scattering with collinear gluon. C) NLO quark scattering with hard gluon radiating from initial state quark leg. D) Boson-Gluon Fusion. The arrow indicates the direction, in momentum space, of the interaction.

Chapter 4

Monte Carlo Model

4.1 Numonte

The NuTeV Monte Carlo, known as NUMONTE, is a fast simulation of the NuTeV detector (see Section 2.1). Its purpose is to simulate kinematic distributions measured by the experiment. The term *fast* in this context refers to the fact that NUMONTE is a parameterized MC capable of generating and smearing events much more quickly than a "hit level" monte carlo based on such packages as GEANT. Speed is particularly important in this analysis due to the high number of events in the CC data sample and the need for numerous systematic and statistical studies. The inner workings of the MC simulation can be roughly divided into several parts: the flux simulation, event generation, cross-section model, smearing and resolution, and reweighting.

4.1.1 Flux

The purpose of NUMONTE is to simulate the events in the NuTeV data sample. In order to calculate the number of events one might expect with specific kinematics, it is necessary to understand as well as possible the ν and $\overline{\nu}$ flux incident on the front of the detector. Section 2.4 briefly describes the SSQT beamline used by NuTeV and highlights its advantages over mixed $\nu/\overline{\nu}$ beamlines. The construction of the beamline did not allow for an event-by-event measurement of the actual incident flux and so a beam monte carlo model was used. The most commonly used beam simulation was DECAY TURTLE [36], a simulation of the NuTeV SSQT beamline using purely beam-optical calculations to determine the $\nu/\overline{\nu}$ flux on the front face of the NuTeV detector as a function of position and energy. Due to secondary processes such as beam-scraping, however, DECAY TURTLE by itself is not able to reproduce accurately the measured distributions. This problem is solved

via an iterative procedure. First, a flux is generated from unaltered beam monte carlo. This flux is then used to generate distributions of the variable E_ν, which is sensitive to the flux. Figure 4.1 shows the ν and $\overline{\nu}$ E_ν distributions generated by NUMONTE. The lower energy peak corresponds to neutrinos from pion decay, while the higher peak corresponds to those from kaon decay. The flux (in terms of E_ν) is then parameterized as a function of four variables: $E_\pi, E_K, R_{\pi/K}$, and N. Here, E_π and E_K represent the energies of the π and K peaks respectively, $R_{\pi/K}$ is the ratio of the π and K peak energies, and N is a normalization factor. The MC E_ν distribution is then fit to the data distribution to yield values for the four parameters. The parameters are subsequently used to adjust the DECAY TURTLE output to produce the MC E_ν distribution once again and the whole process is repeated until the iterations converge. While this method produces distributions that are close to the data, it still does not properly account for such contributions to the neutrino flux as scraping and charm production in the beamline. In order to take these factors into account a complementary GEANT flux has been created which rigorously includes these processes [31]. This secondary flux is then combined with the DECAY TURTLE flux to produce a final flux.

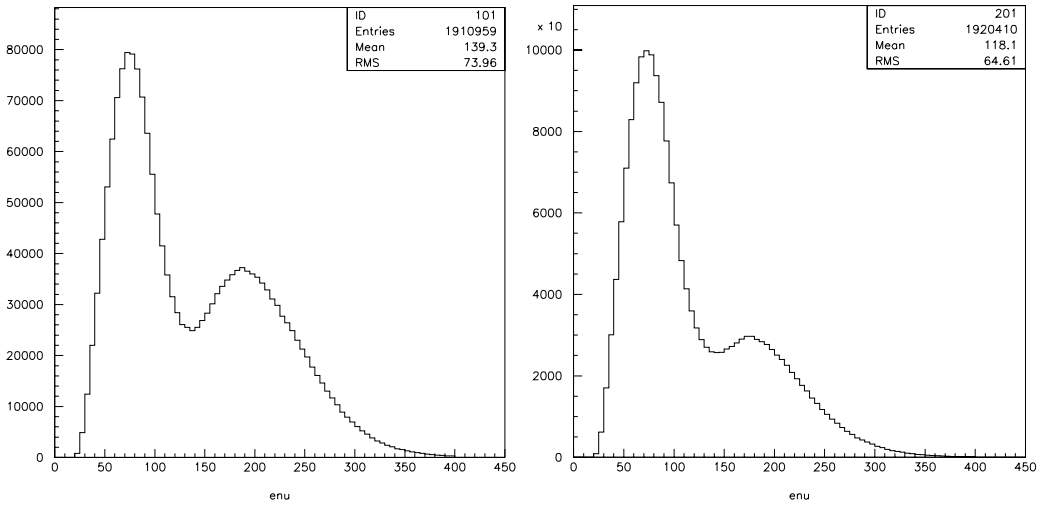

Figure 4.1: E_ν distribution of CC MC in ν and $\overline{\nu}$ mode

4.1.2 Event Generation

Event generation takes place in several steps:

1) Select a neutrino type, E_ν, and interaction point for the event from the generated flux distributions.

2) Determine kinematic variables ($x_{gen}, y_{gen}, Q^2_{gen}, E^{gen}_\mu, E^{gen}_{had}$) from the cross-section.

3) Calculate a weight for the event (see below).

The first two steps provide all of the kinematic variables necessary for the monte carlo to model the data. The third step requires some explanation. NUMONTE is a "weighted" monte carlo simulation in which each event is assigned a weight based on its physical characteristics. For example, the charged current weight for an event is defined to be:

$$wtcc = \frac{\sigma_{cc}^{\nu/\overline{\nu}}}{\sigma_{nc}^{\nu/\overline{\nu}} + \sigma_{cc}^{\nu/\overline{\nu}}} \tag{4.1}$$

Neutral current events were not generated in this analysis.

4.1.3 Target Mass and Slow Rescaling

Before an in-depth discussion of the NuTeV cross-section, two important kinematic effects on the model should be discussed, the target mass effect and the slow-rescaling correction.

Target Mass Correction

Figure 3.1 contains a schematic of the typical charged current νN interaction. In it, the variable p represents the initial 4-momentum of the target nucleon and k, the 4-momentum of the incident neutrino. The variable q is the momentum transferred to the nucleon via the $W^{\pm}$ boson. The kinematic variables x, y, and Q^2 have already been defined in section 3.2. From the definition of these variables,

$$(\xi p + q)^2 = m_q^2 \tag{4.2}$$

where ξ is the momentum fraction carried by the struck parton and m_q^2 represents the mass of the final state hadronic system. The definition given previously for x requires the following two assumptions.

- The invariant mass of the nucleon is much less than the 4-momentum transfer.

$$p^2 << Q^2.$$

- The invariant mass of the final hadronic system is zero.

$$(p^{\mu} + q^{\mu})(p_{\mu} + q_{\mu}) = 0. \tag{4.3}$$

Applying them results in the equality $\xi = x$. The kinematic range of the NuTeV experiment, however, is such that these assumptions are often untrue. Rather than derive a completely general expression for the scaling variable, it is preferable to make the above assumptions individually and combine the results in a more general expression afterwards. Such an expression suffers no great loss of accuracy while retaining a great deal of flexibility. For the case of light quark (u,d,s) production, the second assumption is true and the solution of equation 4.2 for ξ is:

$$\xi = \frac{2x}{1 + \sqrt{1 + \frac{4M^2x^2}{Q^2}}} \tag{4.4}$$

This form for the variable ξ is known as the Nachtmann variable and is used in place of the simple x_{Bj} variable in cross-section formulae as part of the *target mass* correction. A qualitative look at this equation indicates that it behaves as it should when $M^2/Q^2 \approx 0$. Allowing that the first assumption is true but that the second is not, ξ takes the form in Eq. 4.5.

$$\xi = x(1 + \frac{m_q^2}{Q^2}) \tag{4.5}$$

Replacing x_{Bj} with this variable applies the *slow rescaling* correction which is relevant to situations in which the final state of the charged-current interaction contains a heavy quark. In this analysis, the heavy quark mass in question is m_c. In the following discussion of the monte-carlo cross-section model, there are two sections, one dealing with the massless quark cross-section and the other dealing with the charm-production or "heavy quark" cross-section. In the former case, only the target mass correction is desirable since the up, down, and strange quarks are not heavy enough to require a slow-rescaling variable. The heavy quark cross-section, however, requires both target-mass and slow rescaling which has been implemented by supplying the scaling variable

$$\xi = \frac{2x}{1 + \sqrt{1 + \frac{4M^2x^2}{Q^2}}} \left(1 + \frac{m_q^2}{Q^2}\right) \tag{4.6}$$

to the cross-section. Mathematically speaking, this means that the differential cross-section is a function of ξ and y rather than of x and y. In order to ensure that the final cross-section depends on the proper variables, the kinematic factor in Eq. 4.7 must multiply the final cross-section:

$$\frac{d\sigma}{dxdy} = \frac{d\sigma}{d\xi dy}\frac{d\xi}{dx} \qquad \left(\frac{d\xi}{dx} = \frac{1}{1 + \frac{2x\xi M^2}{Q^2}}\right). \tag{4.7}$$

4.1.4 Cross Section Model

The NuTeV cross-section model is one of the largest components of NUMONTE. Given as inputs the kinematic variables and the event type, it calculates the structure functions and, ultimately, the cross-section corresponding to those inputs. For ease of use and to allow for flexibility, the model is divided up into pieces. A description of the leading order cross-section model can be found in Ref. 5. The NLO cross-section contains many important differences which are described here. Section 3.2.5 outlines the principles by which NLO structure functions can be calculated. This section will cover in more detail how each component of the next-to-leading-order cross-section is handled.

Parton Distribution Functions

Previous next-to-leading-order charm production and structure function analyses [6, 14] used parton distributions extracted from data from their own experiment. Others [15] used distributions extracted from global fits to many different experiments. The former approach has the obvious advantage that any MC simulation run with the native PDF's as input will match the experimental data extremely well. The use of outside PDF's, occasionally with sensible re-parameterization (see Sec. 4.1.5) however, leads to greater generality. There are two NLO PDF sets used in this analysis; one from the GRV collaboration [38] and one from the CTEQ collaboration [37]. Both were extracted using the fixed flavor scheme (FFS) using three quark flavors (u,d,s) and gluons.

Nuclear Effects

Until 1983, it was more or less assumed by the physics community that the nucleons contained in the nucleus were essentially free and that incident particles such as neutrinos or leptons would scatter from them incoherently. This would mean, in effect, that the structure function F_2^A could be related to the proton and neutron structure functions F_2^p and F_2^n by Eq. 4.8.

$$AF_2^A = ZF_2^p + (A - Z)F_2^n \tag{4.8}$$

Since then, a number of measurements by several collaborations indicate that this is not the case and that the ratio R_A of structure functions measured on an experiment with target mass number A to those measured on experiments with, for example, a deuteron target is *not* unity. In fact, this ratio varies with both x_{Bj} and, to a lesser extent, Q^2. These effects can be discussed separately according to the range of x_{Bj} in which they are important. The first of these, known as shadowing [16, 17],

is important in the very low x_{Bj} region and has the effect of lowering the structure function ratio discussed above such that:

$$R^A(x,Q^2) = \frac{F_2^A(x,Q^2)}{F_2^d(x,Q^2)} < 1 \tag{4.9}$$

where F_2^d is measured for the deuteron. Proton structure functions are not used because they do not take into account intra-nuclear effects which are present in deuterons and all heavy nuclei. Shadowing can be attributed to interactions between different bound nucleons mediated by their associated quarks and gluons. Experiment has not found any appreciable Q^2 or E_{had} dependence in shadowing. Although experiments differ on where exactly in x_{Bj} shadowing ceases to become important, a value that is often quoted is $x_{Bj} = 0.1$. Above that, another nuclear effect first noticed by the EMC collaboration at CERN in 1983 [18] becomes important. For $x_{Bj} < 0.2$, the ratio of structure functions $R_A(x,Q^2)$ demonstrates a rise above 1 followed by a dip below one for $0.2 < x_{Bj} < 0.7$. The EMC effect appears to be independent of Q^2 for $Q^2 > 5$ GeV^2. Below this limit, there is the possibility of some variation which occurs in conjunction with other low Q^2 effects such as shadowing and higher twist corrections of order $1/Q^2$. Various models have been proposed to explain the EMC effect. Among them are nucleon-nucleon correlation models, x_{Bj} rescaling models and QCD influenced Q^2 rescaling models. Brief descriptions of several of these can be found in Refs. 19 and 20. Above $x_{Bj} = 0.7$, the nucleons in the target move in a manner similar to the particles in a Fermi gas. These internucleon correlations affect the structure functions [39] and the effect is known as *Fermi smearing*. Events in this region are cut from this analysis.

Longitudinal Structure Function

As was shown in Sec. 3.2, the structure functions F_1, F_2, and xF_3 measured in νN deep inelastic scattering can be separated into transverse and longitudinal components. In the next-to-leading-order $\overline{MS}$ scheme, F_2 carries all of the longitudinal contribution to the cross-section while F_1 and xF_3 contain only transverse components. Expressing these structure functions in terms of parton distributions:

$$F_1(x) = q(x) + \overline{q}(x) + 2k^T(x), \tag{4.10}$$

$$F_2(x) = q(x) + \overline{q}(x) + 2k^L(x), \tag{4.11}$$

$$F_3(x) = q(x) - \overline{q}(x), \tag{4.12}$$

In Eqs. 4.10, 4.11, and 4.12, the $q(x)$ represent the quark distributions functions, $k^L(x)$ is the longitudinal contribution to the structure function from both quarks and gluons, and $k^T(x)$ is the transverse contribution to the structure function from gluons. The $\overline{MS}$ structure function scheme (or any scheme at NLO) incorporates this piece into F_2 via a Wilson or Hard-Scattering coefficient (Sec. 3.2). This composite F_2 represents the QCD prediction of longitudinal behavior in the NLO cross-section. At the present time, there exist a number of parameterizations of the ratio of F_1 to F_2 which can be applied to the NLO cross-section model in place of the QCD F_2. In these parameterizations, the *longitudinal structure function*, $R_L(x, Q^2)$ is defined by:

$$R_L(x, Q^2) = \frac{F_2(x, Q^2)\left(1 + \frac{2M_p x}{Ey}\right)}{2xF_1(x, Q^2)} - 1. \tag{4.13}$$

Given the definition in Eq. 4.13, F_2 can be replaced in all cross-section formulas by an expression containing only F_1 and R_L. The standard parameterization of R_L used by NuTeV is a fit to the world's data [21] called $R_{whitlow}$. Because $R_{whitlow}$ is a fit to data, it is, in principle, correct to all orders in QCD and implicitly contains many corrections not included in the theoretical R_{QCD}. However, $R_{whitlow}$ is extracted from electroproduction, not neutrino production, and may therefore differ from R_{QCD} as implemented here. Figure 4.2 contains comparisons of $R_{whitlow}$ and R_{QCD}.

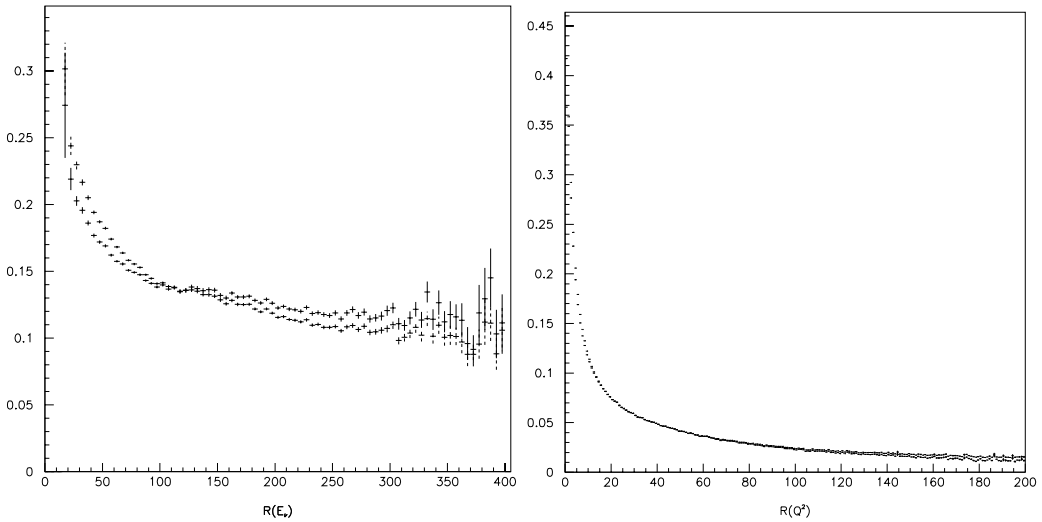

Figure 4.2: R_{QCD} vs. $R_{whitlow}$ (dashed) as a function of E_ν (left) and Q^2 (right).

Factorization Scale

NLO calculations, like LO and NNLO calculations, are only approximations to the truth. In perturbative QCD calculations, one attempts to calculate the contribution from terms that are of higher and higher order in α_s. The function of $\alpha_s(Q^2)$ (see Eq. 3.21) is to differentiate between interaction diagrams which represent hard, or perturbative, exchanges and soft scattering which is non-perturbative and cannot be calculated exactly. Roughly speaking, the diagrams falling into the hard-scattering category are included in the Wilson coefficient whereas the others are absorbed into the parton distribution functions. In a finite order series meant to approximate an exact calculation, the choice of factorization scale μ is more or less arbitrary and depends on a variety of factors such as what part of the cross-section one wishes to calculate. A common scale choice is Q^2 and this is what is chosen for the NLO massless quark structure function calculation. For NLO charm production however, one might choose a scale of $Q^2 + m_c^2$ since the cross-section is a function of the charm quark mass. Varying the factorization scale is another way to learn more about NLO physics. Alternatively, it could be seen as the application of a "scale uncertainty" [6] which can be evaluated as a systematic error.

Electroweak Radiative Corrections

Figure 3.3 shows some of the QCD LO and NLO Feynman diagrams which contribute to the structure functions at both LO and NLO. Their effects are included either in the PDF sets or in the hard-scattering coefficients. Not included, however, are electroweak radiative corrections. Diagrams in this category include loop corrections to the boson propagator, $\gamma/Z^0/W^{\pm}$ radiation from the final state quark, and electroweak box diagrams (see Fig. 4.3). Two independent calculations exist which provide these corrections. The calculation by Bardin [24, 25] includes 1-loop electroweak propagator corrections (NLO in QED/GWS) along with LO $\gamma/Z^0/W^{\pm}$ radiation from the quark leg. While this straightforward LO approach results in high accuracy for the EW component of the radiative corrections, the QCD and QCD-EW interference terms at LO introduce unwanted quark model dependence into the calculation. Any application of the Bardin corrections requires a choice of both Λ_{QCD} and quark masses. There also exists a calculation by Derujula [23] done in the leading-log approximation. The hallmark of this approach is that the value of the radiative corrections is determined in QCD only up to terms of order $\alpha_s \log(Q/m_q)$. Invoking the properties of logarithms, all terms dependent on a particular quark model cancel each other leaving a correction which, at reasonable values of Q^2, is both accurate and independent of quark masses. This advantage is balanced by the fact that the QED and EW radiative corrections in the NLL formalism are not quite as accurate as those calculated in LO.

Higher Twist

Currently, perturbative QCD is the foundation for calculation of cross-sections at any order. No other theory to date has had equal success at predicting observed phenomena. Nevertheless, theoretical calculation is severly limited once the physical nature of the nuclear processes in question cause kinematic quantities such as x and Q^2 to move to extreme values. At extremely high x, Fermi Motion is a substantial effect while at low values of Q^2, higher twist effects take precedence over the parton model and perturbative QCD. One particularly important low Q^2 effect is higher-twist [14, 27] which directly modifies the structure functions by adding terms containing increasing powers of $1/Q^2$. For the structure function F_i, this can be parameterized as follows:

$$F_i(x,Q^2)^{HT+DIS} = F_i(x,Q^2)^{DIS}\left(1+\frac{T_4(x)}{Q^2}+\frac{T_6(x)}{Q^4}+\ldots\right). \tag{4.14}$$

The terms containing $T_4(x)$ and $T_6(x)$ are referred to, respectively, as the *twist 4* and *twist 6* terms. Figures 4.4 and 4.5 show the twist-4 and twist-6 terms for $2xF_1$, F_2, and xF_3. The data in Figure 4.4 can be found in Ref. 28. Information about the program used to generate the theoretical curves can be found in Ref. 29. It should be emphasized that the functional form of $T_4(x)$, $T_6(x)$, and higher order terms is predicted from a model and that these terms have not yet been experimentally measured in νN scattering. SLAC/BCDMS data does exist, however, and is plotted in Fig. 4.4.

Massless Quark Structure Functions

Rewriting equation 3.23 from section 3.2.5 gives:

$$F^j(x,Q^2) = \sum_i \int_x^1 \frac{dy}{y}\mathcal{C}^j(y,\overline{g}(Q^2))p_i(x/y). \tag{4.15}$$

To calculate the structure functions for the light quarks (u,d,s), the definition of $\mathcal{C}$ [4] from Eq. 4.16 applies.

$$\mathcal{C}(y) = \delta(1-y)+\frac{g^2}{16\pi^2}\mathcal{C}^i(y) \tag{4.16}$$

The number i indicates that the Wilson Coefficient in question, when inserted into the above hard scattering equation will yield the structure function F_i where i runs from 1 to 3. The values of the coefficients $\mathcal{C}^i$ for quarks and gluons and a more

detailed discussion of the calculation of massless quark structure functions can be found in Sec. A.1 and Ref. 4.

Heavy Quark Structure Functions

Heavy quark structure functions are calculated along the same lines as their massless counterparts but for a few differences. The three structure functions, $F^{1,2,3}$, associated with charm production from massless quarks ($W^+s \rightarrow c$) and gluons ($W^+g \rightarrow c\overline{s}$ and $W^+s \rightarrow gc$) can be calculated from Eq. 4.17 (see Ref. 8).

$$\mathcal{F}_i^c(x,Q^2) = s^{'}(\xi,\mu^2) + \frac{\alpha_s(\mu^2)}{2\pi}\left\{\int_\xi^1 \frac{d\xi^{'}}{\xi^{'}}\left[H_i^q(\xi^{'},\mu^2,\lambda)s^{'}(\frac{\xi}{\xi^{'}},\mu^2) + H_i^g(\xi^{'},\mu^2,\lambda)g(\frac{\xi}{\xi^{'}},\mu^2)\right]\right\} \tag{4.17}$$

The structure functions $F^{1,2,3}$ are related to the $\mathcal{F}^{1,2,3}$ structure functions by the following relationships:

$$F_1^c = \mathcal{F}_1^c, F_2^c = 2\xi\mathcal{F}_2^c, F_3^c = 2\mathcal{F}_3^c.$$

where ξ is the slow rescaling variable of Eq. 4.5. The structure functions, once calculated, are then inserted into Eq. 3.8 to yield the differential cross-sections for the appropriate process and event type. Calculation of the heavy quark structure functions is outlined in greater detail in Sec. A.2.

4.1.5 Strange Sea Parameterization

Charm production makes up approximately 10% of the total charged current cross-section, much of it due to scattering from the strange sea. This makes the strange distribution of particular interest in this analysis. The size of the strange sea is often expressed by a parameter relating it either to the non-strange sea or to valence distributions. The first of these is called κ and can be expressed formally as:

$$\kappa_{pdf}(Q^2) = \frac{2\int_0^1 x s_{pdf}(x,Q^2)dx}{\int_0^1 x[\overline{u}_{pdf}(x,Q^2) + \overline{d}_{pdf}(x,Q^2)]dx} \tag{4.18}$$

The second of these parameters, η_s is a measure of the level of the strange sea relative to the level of the valence quarks:

$$\eta_s^{pdf}(Q^2) = \frac{2\int_0^1 x s_{pdf}(x,Q^2)dx}{\int_0^1 x[u_{pdf}(x,Q^2) + d_{pdf}(x,Q^2)]dx}. \tag{4.19}$$

In this thesis, the level of the strange sea is defined in terms of a "base" sea. This base sea is taken to be the theoretical prediction for the strange distribution taken directly from an appropriate, published PDF set (for example, CTEQ or GRV). The measured sea is the defined in terms of this base sea by:

$$< s^{'}(x,Q^2) >= (1+\varepsilon_s^{pdf}) < s_{pdf}(x,Q^2) > \tag{4.20}$$

A measurement of the number ε_s^{pdf} can be converted into a measurement of κ or η_s via the equations:

$$\kappa(Q^2) = \frac{2(1+\varepsilon_s)\int x s_{pdf}(x,Q^2)dx}{\int x[\overline{u}_{pdf}(x,Q^2)+\overline{d}_{pdf}(x,Q^2)]dx} \tag{4.21}$$

and

$$\eta_s(Q^2) = \frac{2(1+\varepsilon_s)\int x s_{pdf}(x,Q^2)dx}{\int x[u_{pdf}(x,Q^2)+d_{pdf}(x,Q^2)]dx} \tag{4.22}$$

Alterations to the strange sea constitute a significant change to the the cross-section model and are therefore considered as part of a "model" of charm production.

4.1.6 Reweighting

Although NUMONTE is a fast monte carlo relative to hit-level simulations of the NuTeV detector, it is still rather slow in absolute terms. To generate distributions with adequate statistics corresponding to a specific choice of of parton distribution set, m_c, or strange sea can take many hours. In order to avoid this potential bottleneck in the analysis, a reweighting procedure has been devised which greatly speeds up the process. First, a base model is chosen which corresponds to a reasonable set of choices for PDF, m_c, strange sea, and other relevant quantities. Then, a long monte carlo job is run with this model to produce a data file called a monte carlo data summary tape (DST), which is written to disk. This file contains generated and smeared kinematic variables, cross-sections, and other information for each generated event. To produce distributions resulting from alternate choices for these input variables, the monte carlo DST is used as input for a reweighting program which, given the desired model settings, can give a new weight to each event in the DST corresponding to the value of the cross-section implied by the new model. This new weight is defined in terms of the old and new cross-sections by the formula:

$$wtcc_{new}^{\nu(\overline{\nu})} = \frac{\sigma_{cc-new}^{\nu(\overline{\nu})}}{\sigma_{cc-old}^{\nu(\overline{\nu})}}. \tag{4.23}$$

The reweighting software uses much of the machinery present in the monte carlo which makes it possible to reweight the cross-section model with different choices for the parton distribution functions as well as QCD parameters. For the final analysis, 24,000,000 ν mode events were generated 7,935,564 of which passed cuts. Six million events were generated in $\overline{\nu}$ mode, 2,038,419 of which passed the cuts (see Sec. 5.3).

4.2 Smearing and Resolution

The ultimate goal of a monte carlo simulation is to produce distributions of event rates, kinematic variables, and other quantities which can be compared directly with data. In order to do this, quantities analogous to generated variables such as x_g, y_g , and Q_g^2 but which include such effects as detector resolution and smearing must be constructed. The value of the reconstructed/smeared hadron energy is calculated by smearing the generated hadron energy by the hadron energy resolution function:

$$\frac{\sigma_E}{E} = 0.022 \pm 0.001 \oplus \frac{0.86 \pm 0.01}{\sqrt{E}}. \tag{4.24}$$

Similarly, the generated muon energy is smeared by the toroid resolution function to produce the reconstructed E_μ. Angular and vertex smearing are carried out in a similar fashion. A more detailed discussion of smearing and resolution in the NuTeV detector can be found in Ref. 26. Once the reconstructed E_{had}, E_μ, E_ν, and θ have been calculated, they can be used to make reconstructed versions of the kinematic variables mentioned above. The error on the understanding of the absolute energy scale and the precise form of the resolution function is the source of an appreciable systematic effect on this analysis. Section 5.4 contains a discussion of how these systematic errors were evaluated.

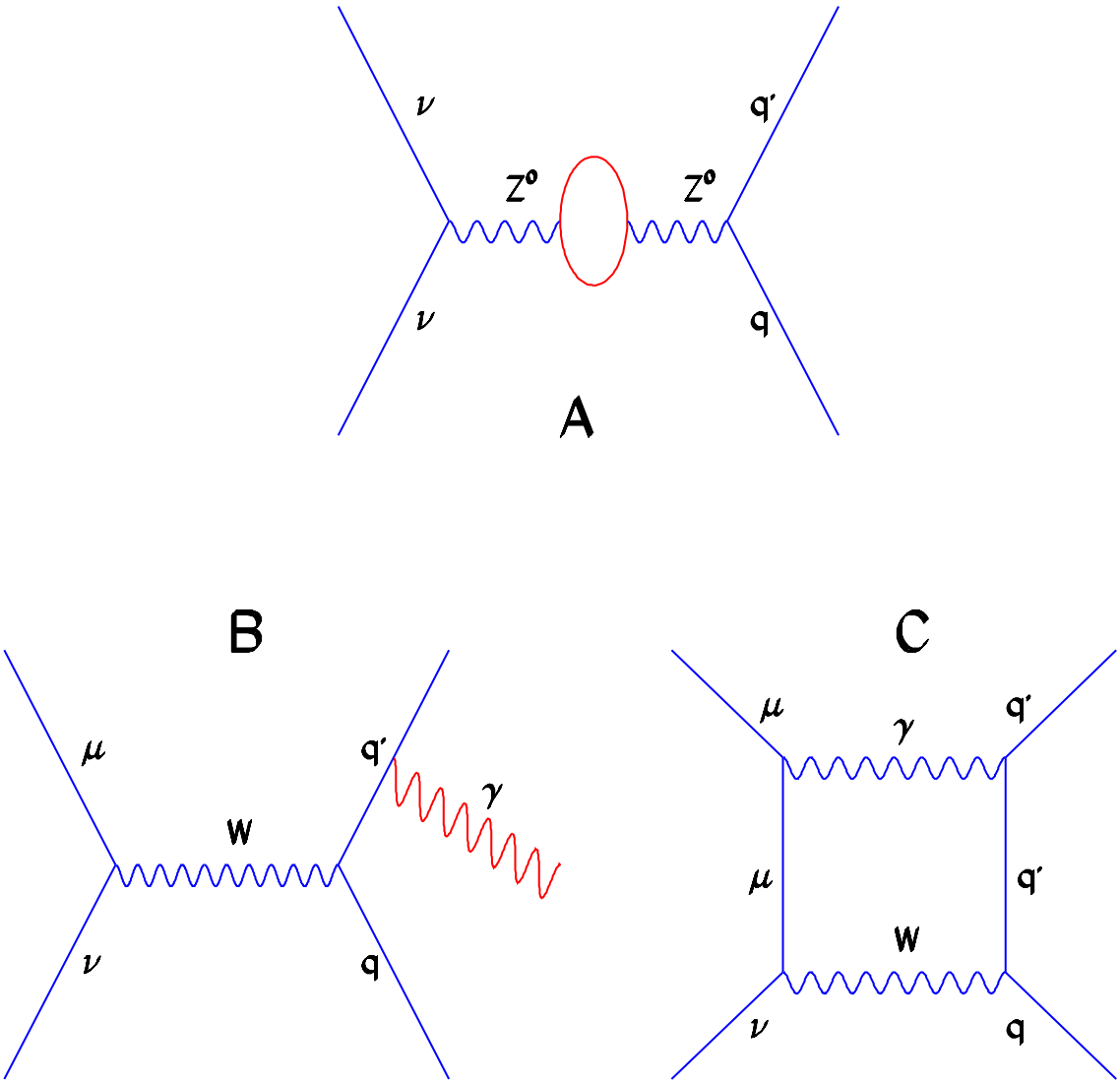

Figure 4.3: Radiative correction diagrams. A) Boson loop correction. B) Boson radiation from final state quark. C) Box diagram.

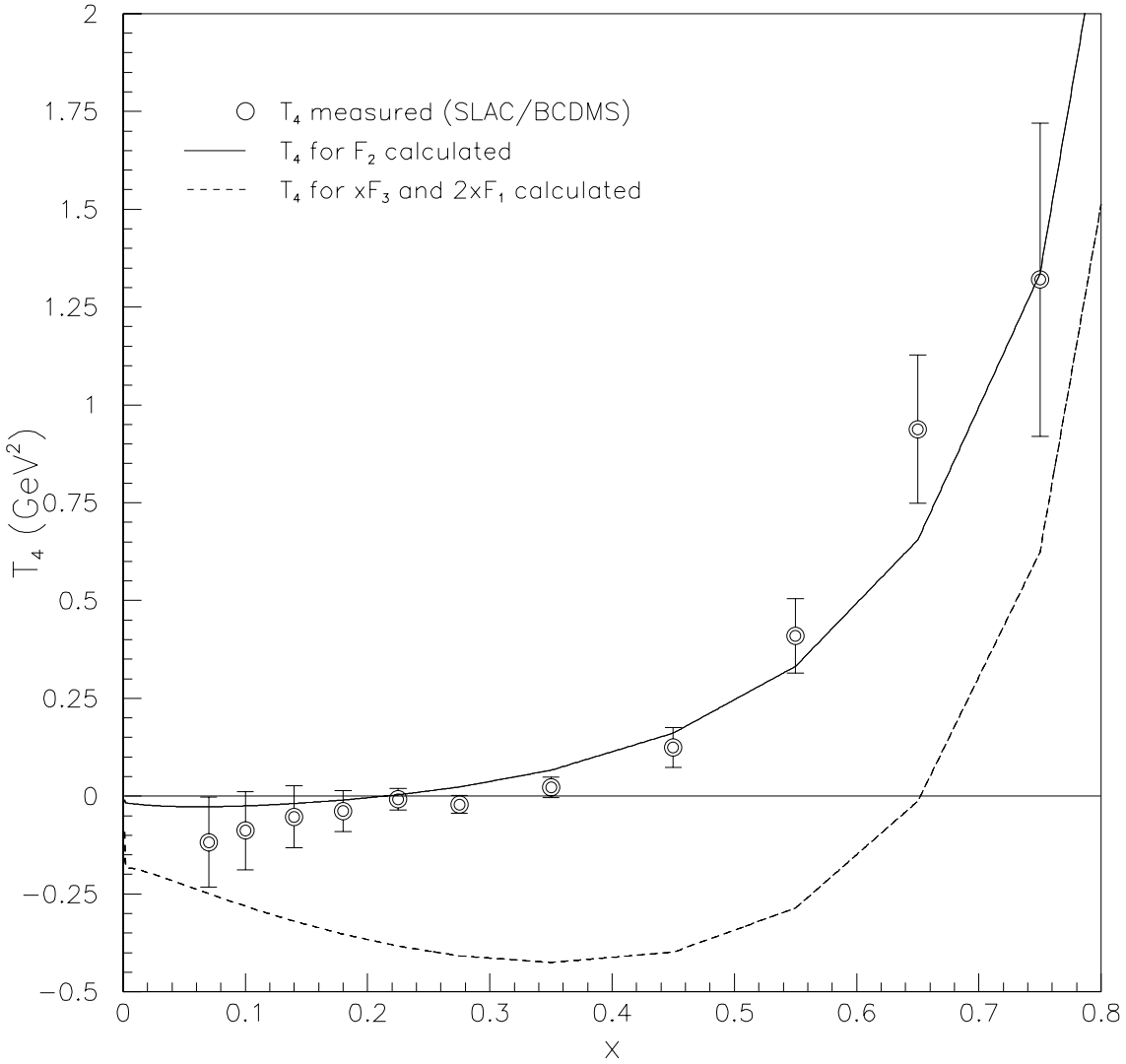

Figure 4.4: T_4 twist term ($Q^2 = 25$ GeV^2).

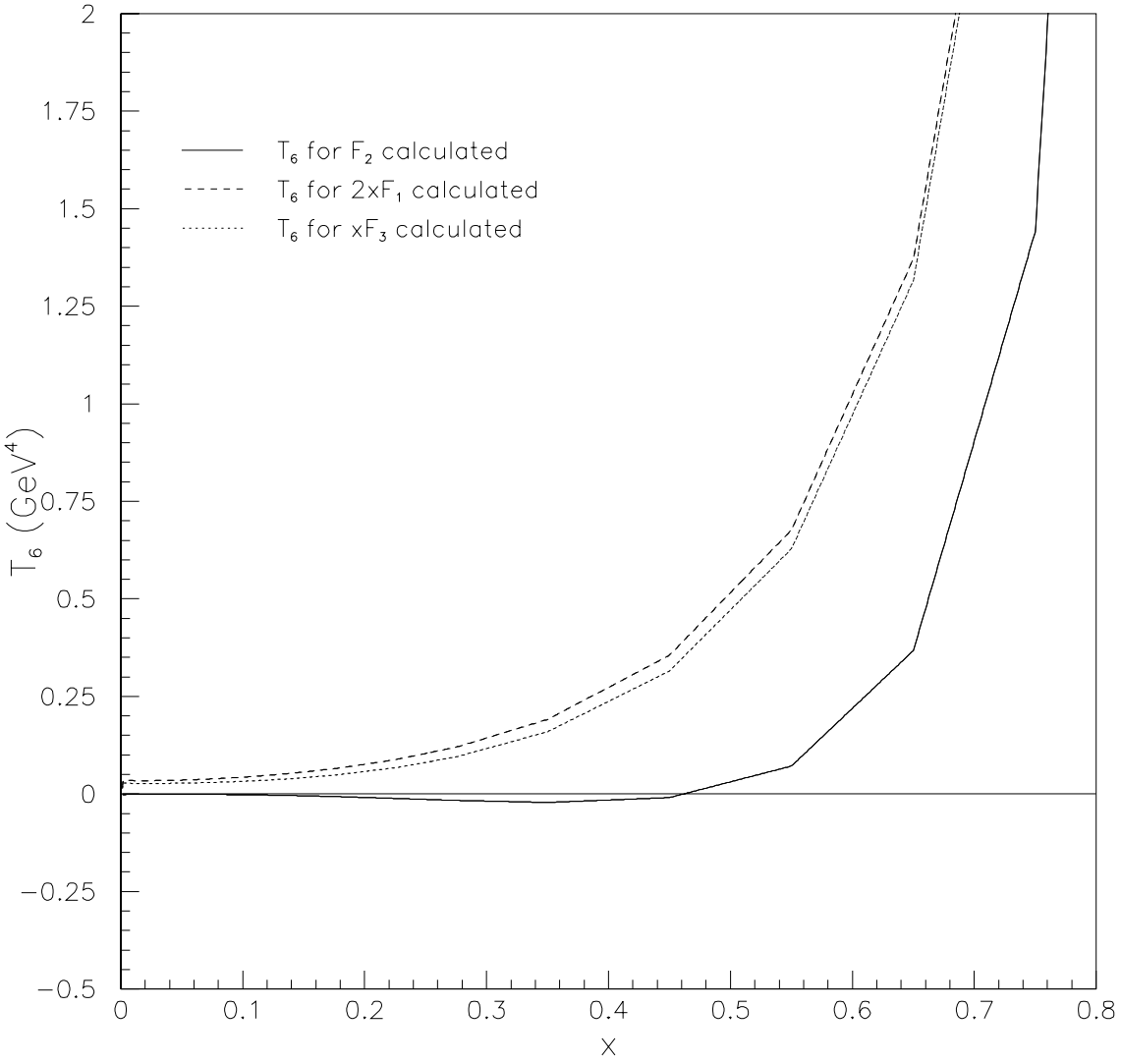

Figure 4.5: T_6 twist term ($Q^2 = 25$ GeV^2).

Chapter 5

Analysis

5.1 Charged Current Event Rates at NLO

The goal of this analysis is to further the understanding of QCD. Neutrinos are extremely useful particles in this respect as they are singularly well suited to the probing of the inner contents of the nucleon due to their very small mass and lack of electrical charge.

5.2 Charged Current Event Rate

The primary focus of this dissertation is the study of charged current event rates in the NuTeV detector as a means to see inside the nucleon. Cuts are applied (see Section 5.3) to the charged current data sample which is then separated into x, Q^2, and E_ν bins. Since raw event rates are sensitive to the absolute level of the flux, a fact which would introduce a large systematic error, they are converted into fractional event rates, defined by:

$$\eta_{ij} = \frac{N_{ij}}{\sum_{i,j} N_{ij}} \tag{5.1}$$

for each data and monte carlo bin. In addition to lessening the flux dependence of the monte carlo sample, the η variable also eliminates the need for an arbitrary normalization factor which would have to be put in to match the monte carlo peak with that of the data. The monte carlo η distributions can then be compared directly with the corresponding data distributions. In comparing the data to the monte carlo in this fashion, the following assumptions play an important role:

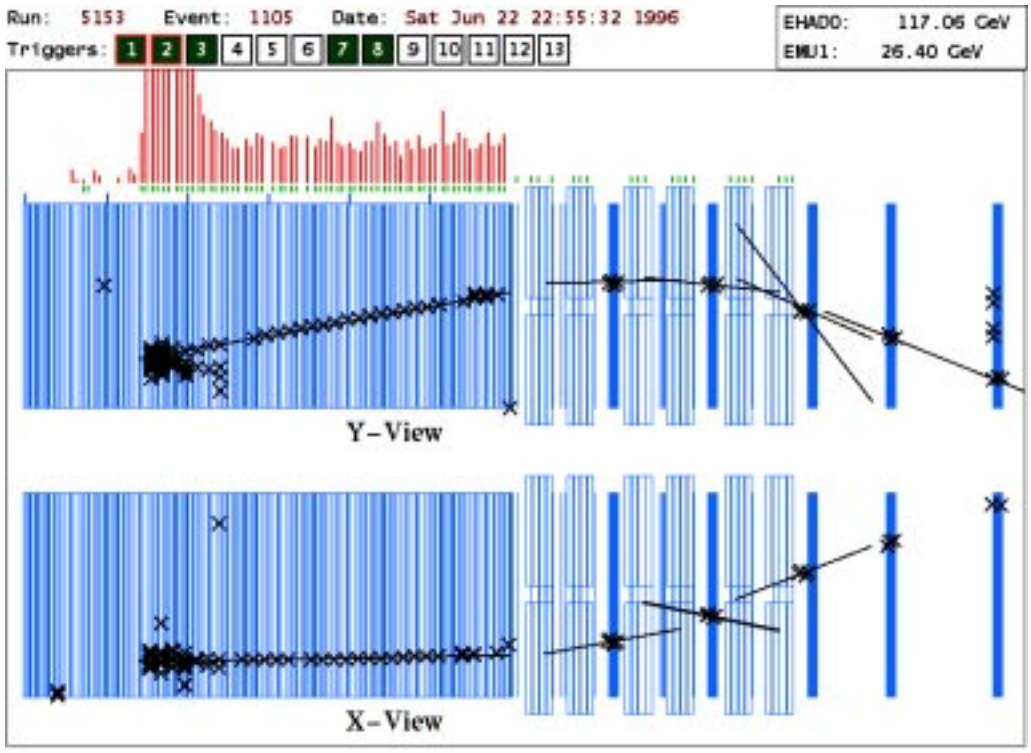

Figure 5.1: NuTeV Charged Current Event

- QCD is correct.
- Parton Distribution Functions are universal.
- $\nu/\overline{\nu}$ CC scattering is sensitive to the parameters m_c and $s(x, Q^2)$.

The first of these assumptions is of particular importance in a next-to-leading order QCD analysis due to the nature of the data to monte carlo comparisons in question. Ultimately, the NuTeV experiment measures, not cross-sections or structure functions, but event rates. In order to connect these rates with σ, F_1, F_2, and F_3, a detailed monte carlo simulation, which depends on a QCD model to determine what kinds of events it must generate, is necessary. Many different theoretical collaborations have published PDF sets fit to data from a large number of experiments. In order to create the structure functions and cross-sections, a theoretical calculation which takes NLO parton distributions as input and turns them into structure functions is required. Several such calculations are described in Sec. 3.2. The second assumption relates to the "universality" of parton distributions. Although parton distributions functions are fit from many different kinds of experiments, they should all reflect the same basic underlying reality. That is, the quark content of a nucleon depends on the Q^2 of the interaction and quantities such as x and y, but it cannot have to do with what experiment the the quark probability distributions are

extracted from or what kind of probe (ν,e^-, etc) is used. The third assumption will be discussed in more detail in a later section. An analysis of NuTeV charged current scattering data done using comparisons of η distributions is well suited to it's two main goals:

- Provide a quantitative measurement of the "goodness" of a QCD model.
- Measure QCD parameters.

It uses a large statistics charged current sample and avoids much of the complication of the structure function analysis by sidestepping the "unsmearing" phase entirely. Monte Carlo is generated, smeared, and compared directly to data. More information about the model components m_c and $s(x,Q^2)$ can be extracted from the η distributions. Both are low x phenomena and sensitivity to shifts in their values can be increased by constructing a quantity more directly proportional to the low x parton distributions in the nucleon. To construct such a quantity requires the identification of η^ν and $\eta^{\overline{\nu}}$ found in Eqs. 5.2 and 5.3 as,

$$\eta^\nu(x,Q^2) = k\frac{(1-y)F_2(x,Q^2) + \frac{y^2}{2}2xF_1(x,Q^2) + y(1-\frac{y}{2})xF_3(x,Q^2)}{\sigma_\nu}, \tag{5.2}$$

$$\eta^{\overline{\nu}}(x,Q^2) = k\frac{(1-y)F_2(x,Q^2) + \frac{y^2}{2}2xF_1(x,Q^2) - y(1-\frac{y}{2})xF_3(x,Q^2)}{\sigma_{\overline{\nu}}}, \tag{5.3}$$

which expressions are exactly correct in the limit of infinitesimally small energy bins. The number k is a proportionality constant taking into account energy corrections related to the flux.

$$k = \frac{E_\nu\phi(E_\nu)}{\int_{E_\nu} E_\nu\phi(E_\nu)}. \tag{5.4}$$

To proceed further, several simplifying assumptions are necessary.

- Quarks are massless, (such that $F_3^\nu = F_3^{\overline{\nu}}$).
- Cross-Section is transverse only ($F_2 = 2xF_1$).
- $\sigma_\nu = 2\sigma_{\overline{\nu}}$.

Using these assumptions, the following useful expression results:

$$\eta^+(x,Q^2) = 2\eta^\nu(x,Q^2) + \eta^{\overline{\nu}}(x,Q^2) \rightarrow k\frac{(1+(1-y)^2)F_2(x,Q^2)}{\sigma_{\overline{\nu}}}$$

and, ridding the right hand side of explicit y dependence,

$$\frac{\eta^+(x,Q^2)}{1+(1-y)^2} = k\frac{F_2(x,Q^2)}{\sigma_{\overline{\nu}}}. \tag{5.5}$$

What remains is a quantity proportional only to the *singlet* part of the cross-section and which is therefore sensitive to charm production and the strange sea. Similarly, a quantity proportional to the *non-singlet* (valence) component of the cross-section can be constructed.

$$\eta^-(x,Q^2) = 2\eta^\nu(x,Q^2) - \eta^{\overline{\nu}}(x,Q^2) \rightarrow k\frac{(1-(1-y)^2)xF_3(x,Q^2)}{\sigma_{\overline{\nu}}}$$

and, again, dividing out the y dependent factor:

$$\frac{\eta^-(x,Q^2)}{1-(1-y)^2} = k\frac{xF_3(x,Q^2)}{\sigma_{\overline{\nu}}}. \tag{5.6}$$

These two quantities, η^+ and η^-, are not only useful for charm and sea studies. Due to their sensitivity to singlet and non-singlet components of the cross-section, they can be used to determine the effects of non-QCD modifications (such as EMC and Higher-Twist corrections) on the corresponding structure functions. The outstanding question as to whether the EMC correction should be applied to xF_3 as well as $2xF_1$ and F_2 can be answered by looking at η^- information. These quantities also address theoretical questions relating to higher-twist. In the Dasgupta and Webber renormalon model (see Ref. 29), HT contributions for F_2 and xF_3 are different (Figs. 4.4, 4.5). Using η^-, this analysis can determine whether this calculation is consistent with the data, or whether the assumption that HT(xF_3)=HT(F_2) is justified.

5.2.1 Comparison of NLO to LO

Most previous analyses using the NuTeV detector have used leading-order cross-section models at the core of their monte-carlo simulations (see Section 4.1.4). The CCFR experiment used a private set of LO parton distribution functions known as BGPAR (for Buras-Gaemers parameterization) as the standard. The CCFR dimuon

analysis [6] used a NLO ACOT formalism (Sec. 3.2) for its charm production cross-section in conjunction with NLO Duke and Owens PDF's fit to the CCFR data [22]. The present analysis is the first to use a completely consistent NLO model both for the light and heavy (ie. charm production) pieces of the cross-section. It uses the Fixed Flavor Scheme (FFS) with three parton flavors along with the NLO Glück, Kretzer, and Reya (GKR) formalism which handles the calculation of heavy quark structure functions [8]. The light quark formalism is that of Herrod and Wada [4]. While the BGPAR and Duke/Owens parton parameterizations do fit the data fairly well, this is mainly due to the fact that they are parameterizations of similar data and no particular theoretical significance should be inferred.

5.2.2 Comparison of Parton Distribution Functions

The previous section described the rationale behind the comparison of results from a NLO CC analysis with those from a LO analysis. The study of the effect of a specific PDF on the results is closely related to this. Different parton distribution sets, while they may be fit to some of the same experimental data, make different theoretical assumptions and often cover slightly different ranges of x and Q^2. These differences, in turn, can lead to varying degrees of agreement with the data in different kinematic regions.

5.2.3 Extraction of QCD Parameters

The charged current production rate of both charm and light quarks is largely dependent on the size of the strange quark sea $s(x, Q^2)$. It is of great importance, therefore, that the level of $s(x, Q^2)$ be well understood. Fig 6.6 shows how the parameterization of $s(x, Q^2)$ can vary widely between PDF sets with respect to its overall level as well as shape. Recent analyses [6, 15, 44] have measured the strange sea level to within 20% with a leading order cross-section formalism. The χ^2 technique that forms the basis of this analysis provides a measurement of $s(x, Q^2)$ based on the likelihood that Monte Carlo distributions generated with the sea shifted by some fraction of its central value match the corresponding data distributions. This, together with the NLO cross-section model, the lack of smearing corrections, and relatively high statistics, leads to a good limit on $s(x, Q^2)$. Current measurements of m_c (see references above) are also at the 10-20% level.

Fitting

The fit for the charm mass and strange sea is performed by expanding $\chi^2_{model}[m_c, s(x, Q^2)]$ in the parabolic form shown in Eq. 5.7. The QCD model is chosen and then the pa-

Collaboration	m_c	κ
CCFR (LO)	$1.31\pm0.24\pm0.12$ GeV/c^2	$0.373^{+0.049}_{-0.043}$
CCFR (NLO)	$1.70\pm0.19\pm0.02$ GeV/c^2	$0.477^{+0.051-0.017}_{-0.043+0.036}$
CHARM II (LO)	$1.79^{+0.26}_{-0.28}\pm0.27$ GeV/c^2	$0.388^{+0.074}_{-0.061}\pm0.067$
NOMAD (LO)	$1.3^{+0.3+0.3}_{-0.3-0.3}$ GeV/c^2	$0.48^{+0.09+0.17}_{-0.07-0.12}$

Table 5.1: m_c and κ results from previous experiments

rameters m_c and $s(x,Q^2)$ are varied, resulting in a table of $m_c/s(x,Q^2)$ coordinates associated with a value of $\chi^2_\nu + \chi^2_{\overline{\nu}}$. It is possible to extract the values of Δm_c and $\Delta s(x,Q^2)$ as well as their associated errors via a fit to this table using the function of Eq. 5.7.

$$\begin{aligned}\chi^2_{model} = \chi^2_0 + V_{m_c^2}(\overline{\Delta m_c} - \Delta m_c)^2 + V_{ss^2}(\overline{\Delta ss} - \Delta ss)^2 + 2V_{m_c ss}(\overline{\Delta m_c} - \Delta m_c)(\overline{\Delta ss} - \Delta ss) \\ + V_{m_c^2 ss}(\overline{\Delta m_c} - \Delta m_c)^2(\overline{\Delta ss} - \Delta ss) + V_{m_c ss^2}(\overline{\Delta m_c} - \Delta m_c)(\overline{\Delta ss} - \Delta ss)^2 \\ + V_{m_c^2 ss^2}(\overline{\Delta m_c} - \Delta m_c)^2(\overline{\Delta ss} - \Delta ss)^2 \end{aligned} \tag{5.7}$$

In Eq. 5.7, the central values of the parameters are $m_c = 1.5$ GeV and $s(x,Q^2) = 1.0$. Assuming a reasonably parabolic function, the variance matrix of the fit is,

$$V = \begin{pmatrix} V_{m_c^2} & V_{m_c ss} \\ V_{m_c ss} & V_{ss^2} \end{pmatrix} \tag{5.8}$$

and the statistical errors and correlations of the parameters are defined by,

$$\sigma^2_{m_c} = V^{-1}_{m_c^2}, \quad \sigma^2_{ss} = V^{-1}_{ss^2}, \quad \sigma_{m_c ss} = V^{-1}_{m_c ss}.$$

Effects of the systematic errors are described in Sec. 5.4.

5.2.4 Extraction of $|V_{cs}|^2$

The Cabbibo-Kobayashi-Masakawa (CKM) matrix governs cross-generational quark mixing and is usually written in the form of a 3×3 unitary matrix V (not to be confused with V of Eq. 5.8):

$$V = \begin{pmatrix} V_{ud} & V_{us} & V_{ub} \\ V_{cd} & V_{cs} & V_{cb} \\ V_{td} & V_{ts} & V_{tb} \end{pmatrix} = \begin{pmatrix} 0.9753 & 0.2210 & 0.0032 \\ 0.2210 & 0.9745 & 0.0390 \\ 0.0085 & 0.0385 & 0.9993 \end{pmatrix}. \tag{5.9}$$

The element V_{12} of the matrix in Eq. 5.9 specifies the suppression factor applied to the production of parton 1 from parton 2. Numerical values are averaged [43]. For example, the values of V_{cs} and V_{us} indicate that neutrino scattering from a strange quark is very likely to produce a c quark but not nearly as likely to produce a u. Section 5.2.3 contains a discussion of the extraction of the QCD parameters, m_c and the level of the strange sea. As the data sample for this analysis is an inclusive (ie. charm *and* light quark production) charged current sample, the strange sea level measured can not, strictly speaking, be related to the quantity κ defined in Eq. 4.18, but rather, $\kappa_{inc}(|V_{us}|^2 + r_{cc}|V_{cs}|^2)$. The NuTeV dimuon analysis measures a related quantity, $B_c\kappa_{2\mu}\,|V_{cs}|^2$ in which the quantity B_c is the $c\to\mu$ branching ratio. Without making any assumptions about the mathematical properties of the CKM matrix (such as two or three generation unitarity), one can write the following equations:

$$B_c^{exp}|V_{cd}^0|^2 = B_c^{ext}|V_{cd}^{exp}|^2, \tag{5.10}$$

$$B_c^{exp}|V_{cs}^0|^2\kappa_{2\mu}^{exp} = B_c^{ext}|V_{cs}^{exp}|^2\ \widetilde{\kappa}, \tag{5.11}$$

$$(|V_{us}^0|^2 + r_{cc}|V_{cs}^0|^2)\kappa_{inc} = (|V_{us}^{exp}|^2 + r_{cc}|V_{cs}^{exp}|^2)\ \widetilde{\kappa}\ . \tag{5.12}$$

In Eqs. 5.10, 5.11, and 5.12, quantities labeled with a 0 superscript indicate theoretical values, those marked with "exp" are quantities to be extracted from a fit, and B_c^{ext} is an external [45] measured value of the dimuon branching ratio. Although this analysis is sensitive to both V_{us} and V_{cs}, the piece of the cross-section proportional to V_{cs} is suppressed by a factor:

$$r_{cc} = \frac{\sum s(\xi,Q^2)\left(1-\frac{m_c^2}{2ME_\nu\xi}\right))}{\sum s(x,Q^2)} \tag{5.13}$$

relative to the piece of the cross-section corresponding to light quark production from the strange sea. Accordingly, this factor, r_{cc}, multiplies $|V_{cs}|^2$ in Eq. 5.12. Using the information about the strange sea and B_c contained in both this analysis and the concurrent NuTeV dimuon analysis (as summarized in Eqs. 5.11 and 5.12) results in an expression for $|V_{cs}^{exp}|^2$ in terms of both theoretical and measured quantities:

$$|V_{cs}^{exp}|^2 = \frac{|V_{us}^0|^2/r_{cc}}{\left(1+\frac{|V_{us}^0|^2}{|V_{cs}^0|^2}\right)\frac{B_c^{ext}}{B_c^{exp}}\frac{\kappa_{inc}}{\kappa_{2\mu}}-1}. \tag{5.14}$$

The CKM matrix element V_{us}^0 has been well measured by other experiments and the PDG value can be used with Eq. 5.14 to provide a measurement of the parameter

V_{cs}^{exp}. The PDG values of V_{cd}^0 and V_{cs}^0 may also be used as nominal input values to Eq. 5.14.

5.3 Single Muon Sample

5.3.1 Standard Cuts

The cuts used in this analysis are, with a few minor changes, the same as those used in the concurrent NuTeV Structure Function analysis. The changes mainly center on the definition of the lower bounds of the Q^2 and energy cuts. In addition to the cuts outlined below, several more specific cuts were applied which will be discussed in the next section. Since NUMONTE is a parameterized monte carlo and does not model variables related to timing or tracking as a hit level monte carlo might, several of the following cuts are applied only to the data. This is noted next to the individual cut.

- **Gate Cut**

  Requires $0 \leq igate \leq 5$. This limits the events in the sample to those occuring during the fast gate (neutrino or anti-neutrino pings) and reduces contamination due to cosmic rays.

- **Trigger Cut**

  Requires Trigger 1. This is the charged current trigger mentioned in the previous chapter.

- **Place Cut**

  $20 < place < 80$. The standard E_{had} definition requires a 20 counter energy sum which necessitates the lower limit on place. The upper limit is used to screen out test beam muons, horizontal cosmic ray muons and other particles which might adversely affect the place distribution.

- **Vertex Cut**

  $|X, Y| < 50$ cm, where X and Y indicate the respective positions of the event vertex on the face of the detector. In this coordinate system, X=Y=0 is at the center. This cut is in place to:

  a) Remove events that are too close to the edge of the detector and which will result in lost E_{had}, E_{μ}.

  b) Eliminate events which occur in a region of the detector which is not well understood. For example, the NuTeV flux has not been tuned beyond 127 cm.

- **Timing Cut**

  This cut attempts to pick out all neutrino events with "bad times" such as backward-going events or events during which the time-to-digital converters (TDCs) were not working properly (data only).

- **Target Track Cut**

  Requires that a good track be found for any calorimeter muons (data only).

- **Toroid Front Face Radius Cut**

  $R_{tor}^{FF} < 162.6$ cm. Given the angle and position of the CC muon at the interaction vertex, this cut requires that its projected radius downstream at the front face of the toroid be no greater than 162.6 cm. This removes events from the sample that are too close to the edge of the calorimeter and complements the vertex cut.

- **Steel Cut**

  In an attempt to ensure a good measurement by the toroid of the muon energy, this cut requires that muons spend 80% of their time in the toroid steel. This percentage is based on a straight line fit from the interaction vertex.

- **Toroid Track Cut**

  Similar to the target track cut but applies to muons in the toroid (data only).

- **Good Fit Cut**

  Requires that fits to toroid muon tracks have a reasonable χ^2 (data only).

- **Two Gap Cut**

  Requires all muons in the toroid to pass through at least the first two toroid gaps. This allows for a better momentum measurement.

- **Angle Cut**

  $\theta_\mu < 0.15$ radians. This cut, along with the toroid FF cut, attempts to discard events in which charged current muons do not stay within the volume of the toroid.

- **Toroid Hole Cut**

  $R_{tor}^{FF} > 15.2$ cm and $\theta_\mu > 0.007$ radians. At the center of the toroid is a region in which measurements of p_μ are inaccurate because the magnetic field B is not well known. These two cuts attempt to remove events which are likely to enter this central area.

- **Muon Energy Cuts**

  10 GeV $< E_\mu <$ 600 GeV, $E_\mu^{TFF} > 3$ GeV. The first cut tries to ensure that, on the lower end, the event in question lies, in energy, above the efficiency

of the charged current trigger and, on the upper end, that the muon is of reasonable energy. The second cut (tied to the toroid front face) requires the muon to have enough energy to travel 2/3 of the way through the toroid.

- **Shower Containment Cut**

  Requires that the last counter in the hadron shower be at least six upstream of the toroid front face. Uncertainty in the algorithm used to determine the end of a shower could lead to mismeasurement of muon energy if the showers are allowed to get too close to the toroid.

- **Hadron Energy Cuts**

  10 GeV $< E_{had} <$ 600 GeV. Similar in purpose to E_μ cuts.

- Q^2 **Cut**

  $Q^2 <$ 1000 GeV^2. Values of Q^2 greater than 1000 typically indicated complete failure on the part of the analysis code to reconstruct the event. Bad events in this category are removed with this cut.

- **Neutrino Energy Cuts**

  20 GeV $< E_\nu <$ 600 GeV. Similar to E_μ/E_{had} cuts.

- **Muon Charge Cut**

  Requires that the charge of the leading muon be consistent with the beam polarity for that event. Its purpose is to remove wrong-sign ν events from the data sample.

Similar cuts have been used extensively both on NuTeV and on CCFR. A detailed study of their effects can be found in Ref. 14.

5.3.2 Analysis Specific Cuts

In addition to the general cuts above, several more cuts were applied after examination of the charged current data sample. These are:

- $0.003 < x < 1$,
- $1 < Q^2 <$ 200 GeV^2,
- $20 < E_\nu <$ 400 GeV,
- μ charge must be $\nu/\overline{\nu}$ mode appropriate and equal to toroid polarity.

Within these cuts, x, Q^2, and E_ν were further binned as shown in Table 5.2 and 5.3. The bins are logarithmic in x and Q^2, a reasonable choice since the QCD perturbation series is logarithmic in powers of these two variables. The E_ν cuts were chosen so as to place approximately equal numbers of events in all five energy bins. Applying these cuts as well as the structure function cuts results in a data sample containing 832,899 ν events and 240,774 $\overline{\nu}$ events. The MC sample contains 7,935,564 ν events and 2,038,419 $\overline{\nu}$ events or roughly 9.5 and 8.5 times the data sample respectively. Distributions of the kinematic variables can be seen in Figures 5.2, 5.3, and 5.4. The data in Figures 5.2 and 5.3 are displayed in the bins from Table 5.3.

Energy Bin 1	$20 < E_\nu < 62$ GeV
Energy Bin 2	$62 < E_\nu < 85$ GeV
Energy Bin 3	$85 < E_\nu < 129$ GeV
Energy Bin 4	$129 < E_\nu < 201$ GeV
Energy Bin 5	$201 < E_\nu < 400$ GeV

Table 5.2: Energy Bin Definitions

5.4 Systematic Errors

Reweighting monte-carlo with a particular model does not provide all information necessary to compare the model with the data. There are several systematic effects which must be accounted for. The largest of these are described below and include the muon and hadron energy scales, muon and hadron energy linearity, and muon dE/dx. Including the effects of these systematics in the model greatly improves agreement with data and, in a large number of bins, accounts for the disagreement between the two. The figures in Appendix C contain comparisons, for all E_ν, x, and Q^2 bins, of the data and the reference monte carlo (GRV98NLO with Higher Twist) with systematic error bands overplotted. Both ν and $\overline{\nu}$ are shown. In the figures, the central value monte carlo model is shown surrounded by error bands corresponding to the various systematic errors. Bands are calculated in the plots by adding the fractional errors on the model associated with a particular systematic in quadrature. Since this technique does not account for bin to bin correlations between systematics, it cannot reasonably be used when calculating the final effect of the systematics on a given model. For the model comparisons, systematics are floated and a fit is performed to the data using the testbeam as a constraint. Accordingly, plots showing data to monte carlo comparisons in the following sections have systematics rigorously incorporated into the monte carlo model and do not contain error bands. Taking the hadron energy scale as an example, a PDF set is selected, monte carlo is reweighted with E_{had} shifted by $\pm 1\%$, and χ^2's for the shifted model in both ν and $\overline{\nu}$ mode are calculated and summed. There now exist three summed χ^2's, the third

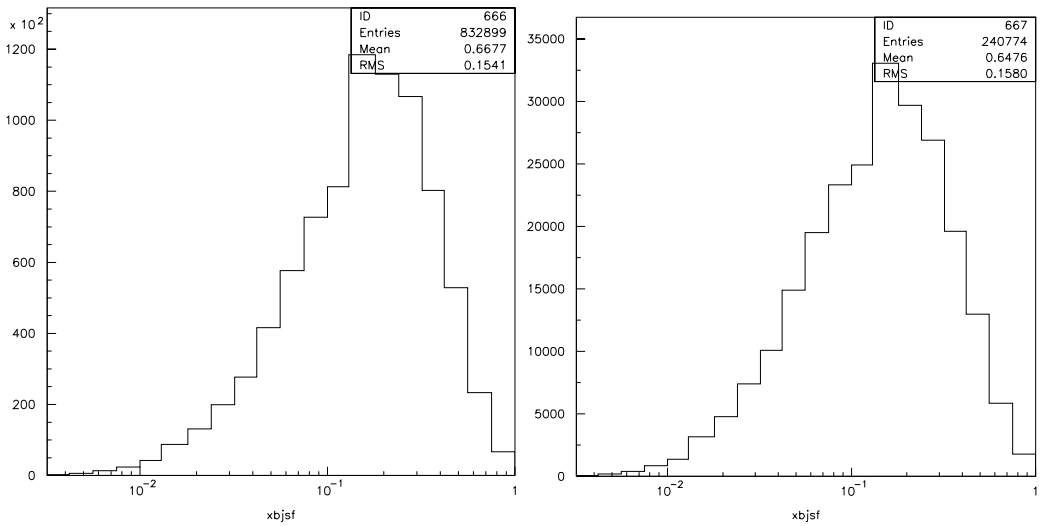

Figure 5.2: x_{Bj} distribution of CC Data in ν and $\overline{\nu}$ mode

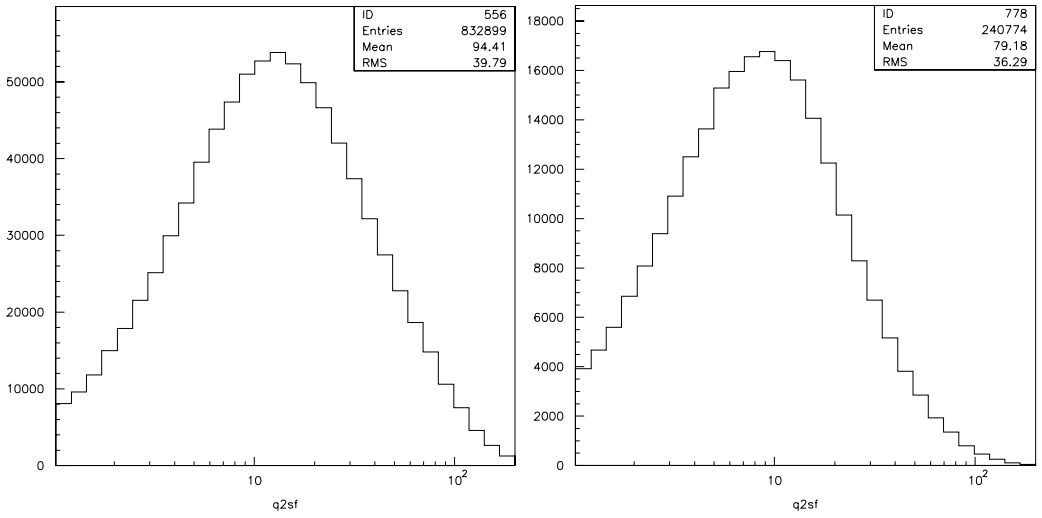

Figure 5.3: Q^2 distribution of CC Data in ν and $\overline{\nu}$ mode

being for the unshifted monte carlo These three points are then fit to a quadratic function of the form:

$$\chi^2 = \chi_0^2 + a\Delta E_{had} + b\Delta {E_{had}}^2 \tag{5.15}$$

where ΔE_{had} is the percentage shift in the quantity E_{had}. The χ^2 function is minimized subject to the constraint that the shift in E_{had} remain within the 0.43% limits determined by the testbeam. Figure 5.5 shows the results of such a fit for GRV98NLO. From the fit, $\Delta E_{had} = -0.004$ GeV which means that, for the GRV98NLO model, the data to monte carlo comparison implies a downward shift in the hadronic energy scale of 0.004 GeV. Similar fits are performed for the other systematics after which the fitted values of all systematic shifts are put back into the monte carlo which is reweighted once again. The resulting corrected model is used for the QCD comparisons. There are five sources of systematic error evaluated: E_{had} and E_μ scale uncertainties constrained by the testbeam to be within 0.43% and 1% of their nominal values, the muon dE/dx uncertainty also constrained to 1%, and the E_{had} and E_μ linearity uncertainties constrained to within 0.5%. The forms of the scale, linearity and dE/dx systematic errors are shown in Eqs. 5.16, 5.17, and 5.18 respectively.

$$\Delta E^{scale} = E^{recon} \times (\pm 1\%) \tag{5.16}$$

$$\Delta E^{linearity} = E^{gen} \times \left[\pm 0.5\% \left(\frac{E^{gen} - 50 \text{ GeV}}{50 \text{ GeV}} \right) \right] \tag{5.17}$$

$$\Delta E_\mu^{dE/dx} = (E_\mu^{recon} - E_{\mu ff}^{recon}) \times (\pm 1\%) \tag{5.18}$$

A brief discussion of muon dE/dx is appropriate here. While a muon's energy is measured by the toroid spectrometer, it loses a fair amount of its initial energy through ionization in the calorimeter. So, what NuTeV actually measures is, in fact, the "true" muon momentum minus the amount lost to ionization, known as dE/dx. It is impossible to measure the exact loss but, it can be modeled in the monte carlo [46], a necessary step before it is possible to make comparisons with the data. In Eq. 5.18, dE/dx is expressed as the difference between the reconstructed (toroid) E_μ and the value of the muons energy, $E_{\mu ff}$, at the front face of the toroid.

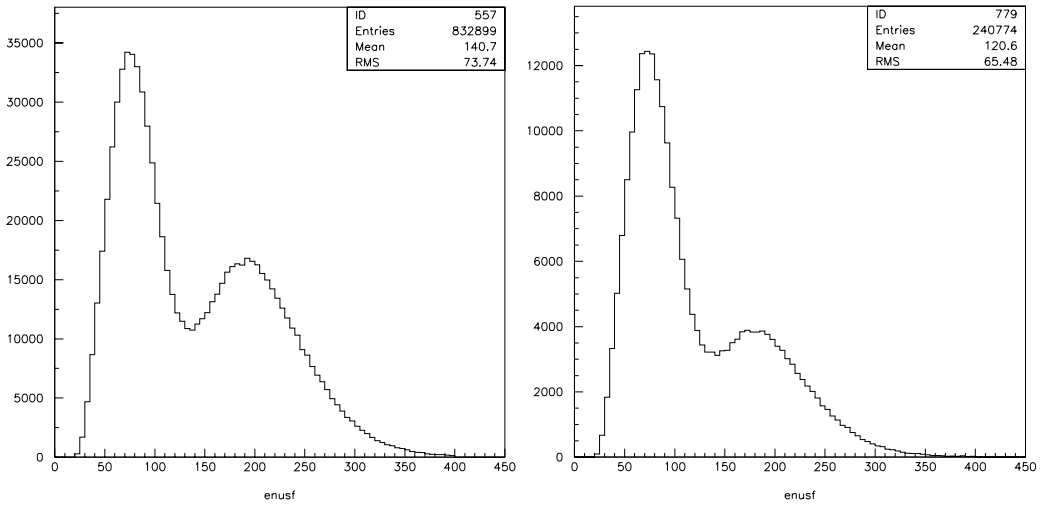

Figure 5.4: E_ν distribution of CC Data in ν and $\overline{\nu}$ mode

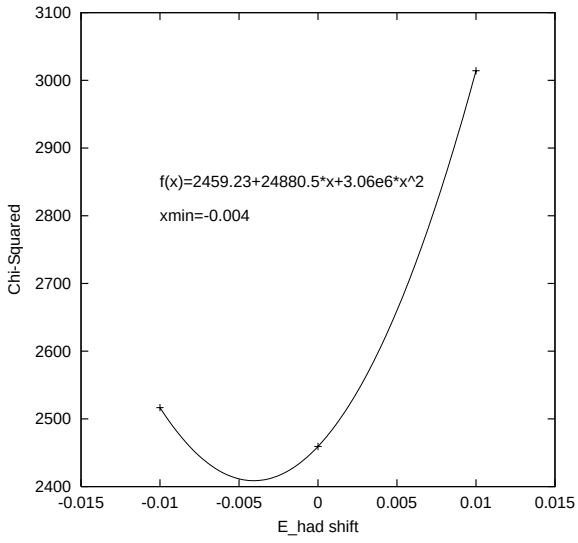

Figure 5.5: E_{had} scale systematic shift evaluated for GRV98NLO

Bin	x	Q^2
1	$0.0032 < x < 0.0037$	$1.02 < Q^2 < 1.22$ GeV^2
2	$0.0037 < x < 0.0042$	$1.22 < Q^2 < 1.45$ GeV^2
3	$0.0042 < x < 0.0049$	$1.45 < Q^2 < 1.73$ GeV^2
4	$0.0049 < x < 0.0056$	$1.73 < Q^2 < 2.07$ GeV^2
5	$0.0056 < x < 0.0065$	$2.07 < Q^2 < 2.47$ GeV^2
6	$0.0065 < x < 0.0075$	$2.47 < Q^2 < 2.94$ GeV^2
7	$0.0075 < x < 0.0087$	$2.94 < Q^2 < 3.5$ GeV^2
8	$0.0087 < x < 0.01$	$3.5 < Q^2 < 4.18$ GeV^2
9	$0.01 < x < 0.012$	$4.18 < Q^2 < 4.98$ GeV^2
10	$0.012 < x < 0.013$	$4.98 < Q^2 < 5.94$ GeV^2
11	$0.013 < x < 0.015$	$5.94 < Q^2 < 7.08$ GeV^2
12	$0.015 < x < 0.018$	$7.08 < Q^2 < 8.44$ GeV^2
13	$0.018 < x < 0.021$	$8.44 < Q^2 < 10.06$ GeV^2
14	$0.021 < x < 0.024$	$10.06 < Q^2 < 12.0$ GeV^2
15	$0.024 < x < 0.027$	$12.0 < Q^2 < 14.31$ GeV^2
16	$0.027 < x < 0.032$	$14.31 < Q^2 < 17.06$ GeV^2
17	$0.032 < x < 0.037$	$17.06 < Q^2 < 20.33$ GeV^2
18	$0.037 < x < 0.042$	$20.33 < Q^2 < 24.24$ GeV^2
19	$0.042 < x < 0.049$	$24.24 < Q^2 < 28.9$ GeV^2
20	$0.049 < x < 0.056$	$28.9 < Q^2 < 34.46$ GeV^2
21	$0.056 < x < 0.065$	$34.46 < Q^2 < 41.09$ GeV^2
22	$0.065 < x < 0.075$	$41.09 < Q^2 < 48.99$ GeV^2
23	$0.075 < x < 0.087$	$48.99 < Q^2 < 58.4$ GeV^2
24	$0.087 < x < 0.1$	$58.4 < Q^2 < 69.63$ GeV^2
25	$0.1 < x < 0.12$	$69.63 < Q^2 < 83.02$ GeV^2
26	$0.12 < x < 0.13$	$83.02 < Q^2 < 98.98$ GeV^2
27	$0.13 < x < 0.15$	$98.98 < Q^2 < 118.0$ GeV^2
28	$0.15 < x < 0.18$	$118.0 < Q^2 < 140.69$ GeV^2
29	$0.18 < x < 0.21$	$140.69 < Q^2 < 167.74$ GeV^2
30	$0.21 < x < 0.24$	$167.74 < Q^2 < 200.0$ GeV^2
31	$0.24 < x < 0.27$	
32	$0.27 < x < 0.32$	
33	$0.32 < x < 0.37$	
34	$0.37 < x < 0.42$	
35	$0.42 < x < 0.49$	
36	$0.49 < x < 0.56$	
37	$0.56 < x < 0.65$	
38	$0.65 < x < 0.75$	
39	$0.75 < x < 0.87$	
40	$0.87 < x < 1.0$	

Table 5.3: Bin Definitions

Chapter 6

Results

This analysis is a departure from previous analyses by the CCFR and NuTeV collaborations in the respect that it takes a macroscopic approach to the study of QCD parameters while, simultaneously, making a quantitative statement about the value of the QCD model itself. Accordingly, the first part of the analysis is devoted to the determination of what consitutes the best QCD model with respect to its agreement with the NuTeV charged current data sample. The most important underlying assumption in this approach is that parton distribution functions are universal, meaning that electroproduction measurements of the partonic contents of the proton and neutron are applicable to neutrino production (or hadroproduction) as well. This assumption allows for further comparison of the QCD model to determine whether adding such effects as higher twist, the EMC correction, or different parameterizations of the longitudinal structure function, improve or worsen χ^2 comparisons between data and monte carlo. This χ^2 value can be used to determine whether a particular model correction is warranted or not, a substantial difference from previous approaches which *assumed* a particular QCD model before attempting to extract physical quantities such as m_c and the strange sea level (κ), a procedure which constitutes the second part of this analysis.

6.1 Kinematic Regions

The most important region of kinematic phase space for model comparisons is the "QCD" region which contains those events for which $0.1 < x < 0.7$ and $Q^2 > 5$ GeV^2. At values of x below 0.1, the effects of charm production via scattering from the strange sea bring in quark mass dependence which causes greater uncertainty in the understanding of the pure QCD comparisons discussed here. Similarly, for $Q^2 < 5$ GeV^2, higher twist effects may become large, rendering the low Q^2 kinematic region less useful for analysis of QCD. Above $x = 0.7$, neutrino and anti-

neutrino probes see mostly valence quark distributions which are heavily subject to Fermi smearing, which washes out the underlying PDF information. These events are removed from the sample with the requirement $x < 0.7$. For the purposes of parameter extraction, however, these "QCD" cuts are too stringent since much of the sensitivity in the data to m_c and $s(x, Q^2)$ lies in the region $x < 0.1$. In order to ensure that the data and monte carlo samples are solidly within the deep inelastic scattering region, it is necessary to retain a cut of $Q^2 > 5$ GeV^2 while extending x down to the region below 0.1. The Fermi smearing region does not contain any useful contribution either to the model comparisons or to the parameter extraction and is not used in this analysis. Figure 6.1 is a schematic diagram of the kinematic regions discussed here. The parameter extraction region mentioned above is the sum of the "QCD Region" and "Low x/Q^2" regions in the figure. In Sec. 5.4, it was noted that the QCD Region was used to determine the size of the systematic errors. Since these errors are generally larger at low values of x, the exclusion of the low x region in their determination reduces their correlation with the charm production parameters, to which there is also a great deal of sensitivity for $x < 0.1$. Two CCFR structure function analyses [47, 48] have been performed which bracket the QCD kinematic region discussed here in the low x/Q^2 and high x/Q^2 regions respectively.

6.2 Model Comparisons

This section contains the results of the model comparisons including such effects as higher twist, the EMC effect, radiative corrections, factorization scale, and flux. Three kinds of information about each model are presented: a χ^2 table included in the appropriate section indicating which model agrees best with the data, a series of plots showing the χ^2/dof for several model changes as a function of E_ν, x, and Q^2 (see Appendix F) and, finally, the raw η distributions in x, Q^2, and E_ν bins for several models (see Appendices C and E). From the χ^2 tables in Appendix B and this chapter, it is clear that all model χ^2 values are greater than 1 per degree of freedom and do not correspond to a high statistical probability of that model being correct. It is important to note however that the PDF sets used in this analysis have not been tuned and that the systematic error model is relatively simple and incorporates only the largest five sources of calibration error. Taking this into consideration, both NLO PDF models used show very good agreement with the data across a wide spectrum of x, Q^2 and E_ν values. This agreement is, in most bins, better than that found between the LO BGPAR PDF model which was fit to CCFR data. It is expected that future generations of PDF's will provide increasingly good agreement between data and monte carlo. All χ^2 values shown in the context of model comparisons have been corrected for monte carlo statistical errors.

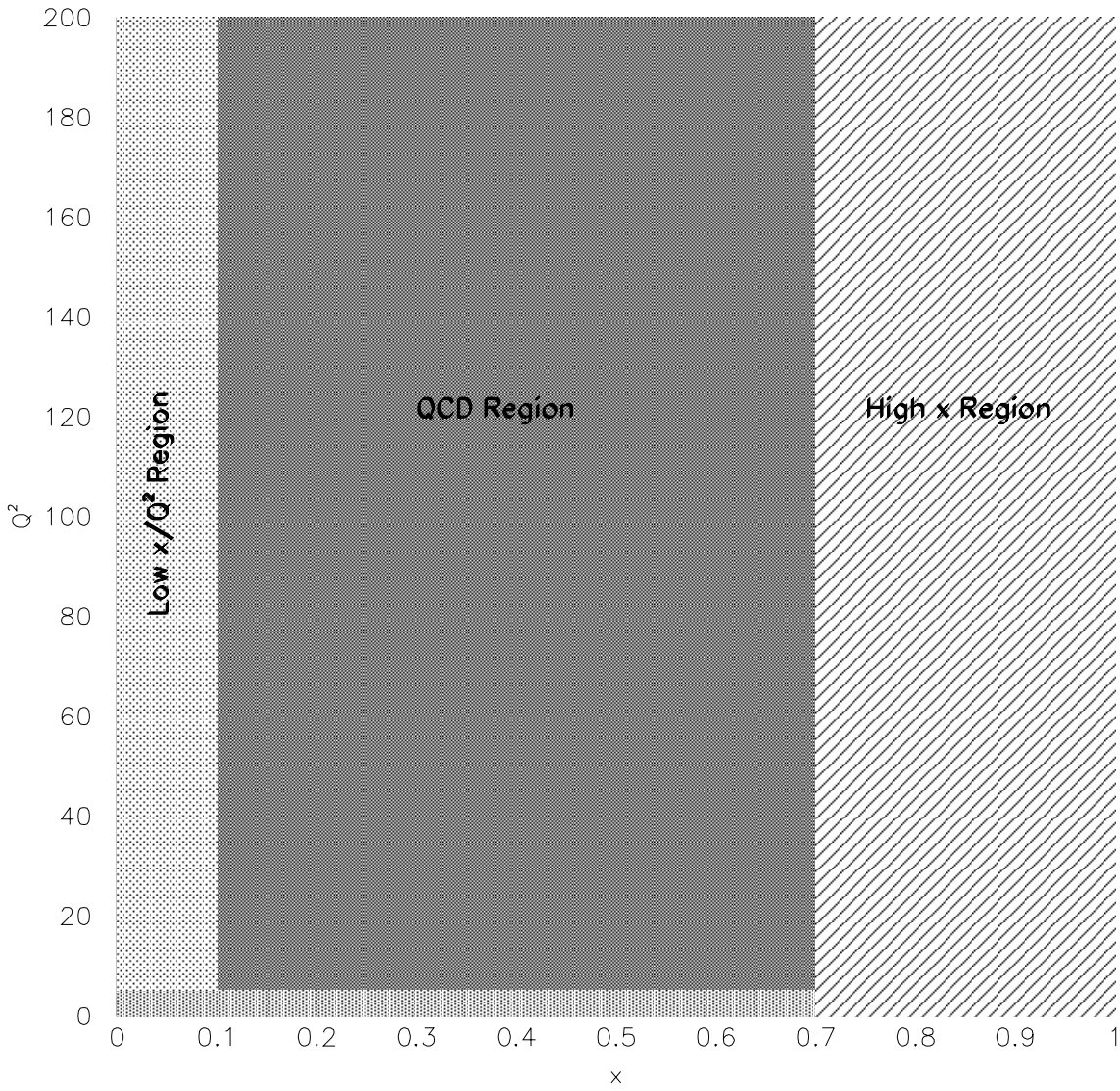

Figure 6.1: Kinematic region boundaries

Base Model

Before reweighting, a "base" model was chosen to which all other QCD models were compared. All models contain PDF's from one of three families: GRV, CTEQ, and BGPAR, which is a Buras-Gaemers fit to NuTeV structure function data. Another family, MRST, was considered as an alternative but was ultimately reject for several reasons. Among these are the fact that the most recent set, MRST99, does not currently exist in PDFLIB and is not readily available as an independent package. In addition, the current generation of MRST PDF's contain well known problems with charm production and are not extracted in a three flavor fixed scheme as are GRV98 and CTEQ5 PDF's. The NLO base models contain the following corrections:

- GRV98NLO or CTEQ5NLO PDF
- Longitudinal structure function equal to R_{QCD}
- EMC effect applied to singlet and non-singlet structure functions
- Bardin radiative corrections applied to the cross-section
- Factorization scale $\mu^2 = Q^2$ for heavy and light quark cross-sections
- DECAY TURTLE flux

The LO non-BGPAR base models are:

- GRV98LO or CTEQ5LO PDF
- Longitudinal structure function equal to $R_{Callan-Gross}$
- EMC effect applied to PDF's
- Bardin radiative corrections applied to the cross-section
- DECAY TURTLE flux

The BGPAR base model includes the EMC effect and the longitudinal structure function from the Whitlow parameterization. Bardin radiative corrections and DECAY TURTLE flux are standard as well. Any deviation from these base models is indicated by an abbreviation of the appropriate effect added to the base model. A list of these can be found in Table 6.1.

The standard set of modifications to the base models included higher twist, radiative corrections, longitudinal structure function, and the EMC correction. Studies to determine factorization scale, the effect of singlet and non-singlet distributions on

Model Effect	*Abbreviation*
Higher Twist	HT
Derujula Radiative Corrections	DRAD
Heavy Quark $\mu^2 = Q^2 + m_c^2$	SCALE
EMC Effect	EMC
EMC singlet	F2EMC
$R_{whitlow}$	R_{whit}
EMC singlet only	F2EMC
$HT_{xF_3} = HT_{F_2}$	$HT_{F_3F_2}$
GEANT Flux	GFLUX

Table 6.1: Model abbreviations

the EMC and higher twist, and flux affects were considered auxiliary studies and were performed using the best model determined from the standard modifications as a new base model. This model includes the following effects:

- GRV98NLO parton distributions
- EMC effect applied to all structure functions
- Longitudinal structure function $R_L = R_{QCD}$
- Derujula radiative Corrections
- Higher twist corrections

and is indicated by the abbreviation "GRV98NLO+EMC+HT+DRAD."

6.2.1 Comparison of LO with NLO

The NLO cross-section formalism represents a fairly radical departure from models used in previous incarnations of the NuTeV experiment. Compared with LO models, it offers increased sensitivity to electroweak and QCD parameters as well as a more cohesive and physically motivated approach to cross-section calculation. However, the fact that the LO CCFR cross-section model is very well understood and extensively tested makes a comparison of NLO to LO valuable. The three leading order models chosen for comparison were BGPAR, a Buras-Gaemers fit to CCFR (and subsequently NuTeV) data [33], GRV98LO, and CTEQ5LO. The last two were chosen for comparison with their NLO counterparts. Figures F.13 and F.14 show comparisons as a function of E_ν bin of GRV98NLO and LO PDFs respectively. BGPAR is included in these plots for reference. A listing of the E_ν, x, and Q^2 bins

used can be found in Tables 5.2 and 5.3. From these figures and their x and Q^2 binned counterparts, it is clear that in both ν and $\overline{\nu}$ mode, the NLO model is in good agreement with the data. In this analysis, the figure of merit associated with a given model is the value of the χ^2 summed over all bins and over both modes. These χ^2 values can be found in Table 6.2. Data to MC comparisons of $\eta^{\nu/\overline{\nu}}$ can be seen graphically in Appendix E. In addition to demonstrating that the NLO cross-section model fits the data better than the leading order model, Table 6.2 also determines the PDF distribution that best fits the data. In both modes and particularly ν mode, GRV98NLO is evidently a better QCD description than CTEQ5NLO. Although both parton sets were extracted in a 3 Flavor Fixed Scheme, they were fit to different experimental data sets and do not necessarily give precisely the same valence and sea quark predictions. For example, the CTEQ5NLO strange sea differs from the GRV98NLO strange sea in places by as much as a factor of two (see Fig. 6.6). These and other details will be discussed in Section 6.3.

Model	χ^2/dof	
	ν	$\overline{\nu}$
GRV98NLO+EMC	1168.80/860	974.48/831
CTEQ5NLO+EMC	1265.25/860	1006.37/831
GRV98LO+EMC	1646.59/860	1100.22/831
CTEQ5LO+EMC	1741.58/860	1177.40/831
BGPAR	1797.68/860	1124.08/831

Table 6.2: Model χ^2 for NLO-LO and PDF comparison

6.2.2 EMC Effect

Nuclear and non-QCD related phenomena such as the EMC and nuclear shadowing effects have been demonstrated experimentally and it is not the purpose of this thesis to verify or to rule out their existence. There are two questions to be answered here:

1) Does the EMC correction improve Data/MC agreement?

2) Should the EMC effect be applied to the non-singlet structure function (xF_3) in addition to the singlet structure functions ($2xF_1/F_2$)?

Figures F.19-F.24 show the difference in χ^2/dof resulting from application of the EMC effect to NLO structure functions. Although applying the EMC correction improves the overall model agreement, as expected, there is a quantitative difference between the relative improvement found in GRV98 and that in CTEQ5. Table 6.5 shows that, while the improvement is large for both ν and $\overline{\nu}$ for the former, it shrinks

substantially for the latter. The χ^2 values in the table and the η distributions in the plots indicate that the EMC correction is needed at NLO. To answer the second question, the GRV98NLO model with higher twist was chosen as the base PDF set due to its good agreement with the data. Table 6.3 contains χ^2 comparisons for these two models. These comparisons show that the data support the application of the EMC correction to xF_3. The variable η^-, defined in Sec. 5.2, since it is particularly sensitive to the non-singlet structure function, can be used to single out the part of the cross-section proportional to xF_3 and this sensitivity can be used as a check of the $\chi^2_{\nu/\overline{\nu}}$ comparison technique to determine whether application of the EMC correction to xF_3 is warranted. Table 6.4 confirms that the EMC correction should be applied to the non-singlet structure function. It is interesting to note that the agreement between the data and monte carlo, as quantified via $\chi^2_{\eta^-}/dof$ in the same table, is very close to 1. Because $\chi^2_{\eta^-}$ is sensitive to the non-singlet, or valence, part of the cross-section, this good agreement suggests that the theoretical valence quark distributions are better understood than their sea counterparts.

Model	χ^2/dof	
	ν	$\overline{\nu}$
GRV98NLO+EMC+HT+DRAD	1111.08/860	972.51/831
GRV98NLO+F2EMC+HT+DRAD	1148.91/860	1033.04/831

Table 6.3: Model χ^2 for EMC(singlet)/EMC(singlet+non-singlet) comparison

Model	χ^2/dof (η^-)
GRV98NLO	1110.66/831
GRV98NLO+EMC+HT+DRAD	899.51/831
GRV98NLO+F2EMC+HT+DRAD	961.33/831

Table 6.4: Model χ^2 for EMC(singlet)/EMC(singlet+non-singlet) comparison

Model	χ^2/dof	
	ν	$\overline{\nu}$
GRV98NLO+EMC	1168.80/860	974.48/831
GRV98NLO	1617.38/860	1146.11/831
CTEQ5NLO+EMC	1253.85/860	1006.37/831
CTEQ5NLO	1267.47/860	1035.42/831

Table 6.5: Model χ^2 for EMC comparison

6.2.3 Longitudinal Structure Function

The longitudinal structure function, R_L, is defined to be the ratio, σ_L/σ_T, of the longitudinal component of the deep inelastic ℓN scattering cross-section to the trans-

verse component (see Sec. 4.1.4). Equation 4.13 expresses it in terms of the structure functions F_1 and F_2. In the NLO formalism used here, R_L is incorporated into the hard-scattering coefficients for F_1 and F_2 and is therefore referred to as R_{QCD}. A parameterization of world data by Whitlow [21] also exists and is denoted by R_{whit}. Although R_L does not truly have meaning at LO, it has been applied to leading order structure functions as a "correction" meant to account for longitudinal components of the cross-section. The BGPAR set of parton distributions was extracted using R_{whit} to account for the differences known to exist in the data between F_2 and F_1, but LO PDF sets from other collaborations, such as GRV and CTEQ, do not incorporate these effects. Table 6.6 shows χ^2 comparisons of both NLO and LO models with and without R_L. In the NLO case, the longitudinal structure function is either R_{QCD} or R_{whit} and, in the LO case (non-BGPAR), the longitudinal structure function is either $R_{Callan-Gross}$ ($F_2 = 2xF_1$) or R_{whit}. BGPAR is shown for the purposes of comparison. Figures F.1-F.6 show the agreement between GRV98NLO and CTEQ5NLO and the data with R_{QCD} and R_{whit}. From these plots, it can be concluded that R_{QCD} is preferred by the data at NLO, as would be expected for a consistent NLO model. It is also clear that R_{whit} should not be used with pure LO PDF sets which are extracted assuming that the Callan-Gross relation is rigorously correct.

Model	χ^2/dof	
	ν	$\overline{\nu}$
GRV98NLO+EMC	1168.80/860	974.48/831
GRV98NLO+EMC (R_{whit})	1270.55/860	1016.40/831
CTEQ5NLO+EMC	1253.85/860	1006.37/831
CTEQ5NLO+EMC (R_{whit})	1377.47/860	1046.86/831
GRV98LO+EMC	1646.59/860	1100.22/831
GRV98LO+EMC (R_{whit})	3867.65/860	1607.04/831
CTEQ5LO+EMC	1741.58/860	1313.10/831
CTEQ5LO+EMC (R_{whit})	3965.32/860	1177.40/831
BGPAR	1797.68/860	1636.65/831

Table 6.6: Model χ^2 for R_L comparison

6.2.4 Higher Twist

The higher twist correction (see Sec. 4.1.4) used in this thesis is derived from a renormalon model [29]. It is one of several effects, including nuclear shadowing and target mass correction, which alter the model at low values of Q^2. Although higher twist effects are small, they provide, in a sense, an extra degree of freedom at low Q^2 and might therefore be expected to improve the overall agreement between data and MC, which, as can be seen in Table 6.7, they do. In addition, Figs. F.7-F.12 show the

relative improvement of the HT corrected NLO cross-section over the uncorrected model as a function of E_ν, x, and Q^2 bins. The improvement is substantial: almost 70 units of χ^2 in neutrino mode for both NLO PDF sets. Differences in the anti-neutrino χ^2 agreement are discussed below. These values indicate strongly that Higher Twist corrections should be applied for NLO QCD analyses. Figures 4.4 and 4.5 show that, in the Dasgupta and Webber renormalon formalism of higher twist, the twist-4 and twist-6 contributions to the higher twist correction are essentially the same for $2xF_1$ and xF_3, while the F_2 contribution differs markedly. There is no *a priori* reason to expect that this should be the case and so a modification of the model, by setting both twist contributions for $2xF_1/xF_3$ and F_2 equal to each other, is reasonable. Table 6.8 contains the $\chi^2_{\nu/\overline{\nu}}$ comparisons of the standard renormalon model and the altered model in which higher twist corrections for all structure functions are equal. The difference between the summed χ^2's of the two models is approximately two units, not enough to distinguish one from the other. Using the variable η^-, with its higher sensitivity to xF_3, however, results in the χ^2 values found in Table 6.9. The difference between the two models moves up to eight units of χ^2, suggesting that the higher twist corrections may be the same for all structure functions. As in the case of the EMC correction, the model agreement using $\chi^2_{\eta^-}/dof$ is very good. This confirms that the valence distributions used in this analysis are well modeled. A feature of the model comparisons shown in Table 6.7 is the slight worsening of data/MC agreement in $\overline{\nu}$ mode for GRV98NLO when higher twist effects are added. This feature is not well understood and could result from one of several effects. The difference in agreement between GRV98NLO and CTEQ5NLO when low Q^2 effects (such as Higher Twist) are applied to the monte carlo indicates that the GRV98NLO PDF's themselves may require some adjustment in this kinematic region. Additionally, the limited number of systematics incorporated into the model comparisons might cause a skewing of the agreement at low Q^2 in anti-neutrino mode. To resolve this apparent (slight) inconsistency, it is useful to look at the model χ^2 constructed from the quantity η^+ which, in contrast to η^-, is sensitive to sea quark distributions. Table 6.10 contains such χ^2 values for both GRV98NLO and CTEQ5NLO supporting the addition of higher twist corrections to the NLO model.

Model	χ^2/dof	
	ν	$\overline{\nu}$
GRV98NLO+EMC	1168.80/860	974.48/831
GRV98NLO+EMC+HT	1114.51/860	979.65/831
CTEQ5NLO+EMC	1253.85/860	1006.37/831
CTEQ5NLO+EMC+HT	1186.28/860	1003.37/831

Table 6.7: Model χ^2 for Higher Twist comparison

Model	χ^2/dof	
	ν	$\overline{\nu}$
GRV98NLO+EMC+HT+DRAD	1110.93/860	972.51/831
GRV98NLO+EMC+$HT_{F_2xF_3}$+DRAD	1121.33/860	963.96/831

Table 6.8: Model χ^2 for $HT_{F_2xF_3}$ comparison

Model	$\chi^2/dof\ (\eta^-)$
GRV98NLO+EMC+HT+DRAD	899.51/831
GRV98NLO+EMC+$HT_{F_2xF_3}$+DRAD	892.28/831

Table 6.9: η^- χ^2 for $HT_{F_2xF_3}$ comparison

6.2.5 Radiative Corrections

Table 6.11 shows the χ^2 comparisons for models with Bardin and Derujula radiative corrections. The χ^2 values shown indicate a slight improvement in the model comparisons using Derujula over those with Bardin calculations. Although the improvement is not enough to conclude that Derujula radiative corrections are better than those calculated by Bardin, the χ^2 values suggest that they are at least comparable. This result is interesting as no measurements have been carried out to date that have determined the one radiative correction set compares to the other.

6.2.6 Factorization Scale

Although the distinction between perturbative and non-perturbative QCD is not always clear cut (since the range of kinematic variables is continuous), the QCD factorization scale, μ^2, is generally used to determine whether a particular Feynman diagram belongs in the hard-scattering coefficient, or whether it should be absorbed into a parton distribution function. Because the QCD perturbation series is calculated to finite order, the choice for μ^2 is essentially arbitrary and can be chosen so as to make calculation as convenient as possible. In the NLO scheme employed here, the factorization scale for massless quarks is defined to be Q^2 for all QCD models. The factorization scale "model" test applies only to heavy (in this case charm) quark production. The charm production piece of the cross-section was calculated alternately with factorization scales $\mu^2 = Q^2$ and $\mu^2 = Q^2 + m_c^2$. Table 6.12 contains χ^2 comparisons of the model (GRV98NLO+HT+DRAD) with $\mu^2 = Q^2$ for both light and heavy quark cross-section pieces to the model (GRV98NLO+HT+DRAD+SCALE), in which $\mu^2 = m_c^2 + Q^2$ for the heavy quark structure functions. The table shows that using a modified factorization scale for heavy quarks does not lead to substantial improvement in the χ^2 value.

Model	χ^2/dof (η^+)
GRV98NLO+EMC	1239.80/831
GRV98NLO+EMC+HT	1179.10/831
CTEQ5NLO+EMC	1310.91/831
CTEQ5NLO+EMC+HT	1230.77/831

Table 6.10: η^+ χ^2 for HT comparison

Model	χ^2/dof	
	ν	$\overline{\nu}$
GRV98NLO+EMC+HT	1114.51/860	979.65/831
GRV98NLO+EMC+HT+DRAD	1111.08/860	972.51/831
CTEQ5NLO+EMC+HT	1186.28/860	1003.37/831
CTEQ5NLO+EMC+HT+DRAD	1161.28/860	984.47/831

Table 6.11: Model χ^2 for radiative correction comparison

6.2.7 GEANT Flux

Section 4.1.1 discussed the two approaches to flux generation in the NuTeV monte carlo: a beam-optical calculation, known as DECAY TURTLE and a more rigorous GEANT calculation. As the former had no way of accounting for beam impurities and scraping, an auxiliary GEANT flux was added to it in order to provide these interaction sources. The NuTeV wrong sign muon analysis [31] used a fully GEANT based flux. Table 6.13 shows χ^2 values for the reference model (GRV98NLO+HT+DRAD) using both the GEANT and the augmented TURTLE flux. Although switching from a TURTLE based flux to a GEANT based flux can reasonably be included along with the other model comparisons, it might also be viewed as a systematic error which, as can be seen in Table 6.13, is small.

6.2.8 Summary

The model comparisons shown in the previous sections lead to the following conclusions:

- The NLO cross-section model is a better description of the NuTeV data than the LO model.
- GRV98 parton distributions provide better agreement than CTEQ5 parton distributions.
- The EMC effect is necessary at NLO.

Model	χ^2/dof	
	ν	$\overline{\nu}$
GRV98NLO+EMC+HT+DRAD	1111.08/860	972.51/831
GRV98NLO+EMC+HT+DRAD+SCALE	1108.35/860	974.50/831

Table 6.12: Model χ^2 for factorization scale comparison

Model	χ^2/dof	
	ν	$\overline{\nu}$
GRV98NLO+EMC+HT+DRAD	1111.08/860	972.51/831
GRV98NLO+EMC+HT+DRAD+GFLUX	1106.74/860	968.38/831

Table 6.13: Model χ^2 for flux comparison

- Use of the R_L inherent in the NLO hard-scattering coefficients gives better agreement than subsitution of the Whitlow parameterization of R_L.
- The data to monte carlo comparisons support the addition of higher twist effects as corrections to the structure functions.
- The EMC effect should be applied to both the singlet (F_2 and $2xF_1$) and non-singlet (xF_3) structure functions.
- Higher twist corrections are the same for both singlet and non-singlet structure functions.

Tables B.1, B.2, B.3, and B.4 contain the χ^2 results for all models in ν and $\overline{\nu}$ mode.

6.3 Charm Mass and Strange Sea Level

6.3.1 Sensitivity

Two ways to measure charm production parameters are:

1) Isolate a data sample that is highly sensitive to charm production (as in dimuon analyses).
2) Isolate a data sample that is moderately sensitive to charm production and which has extremely high statistics.

Treating the charm mass and strange sea level as systematic effects in the monte carlo, the sensitivity of the η distributions to m_c and ε_s can be seen graphically (in

Appendix D). In order to extract the charm mass and strange sea level, the QCD model GRV98NLO+EMC+HT was chosen for its good agreement with the data. All calibration systematics from the QCD region fits were incorporated into the model before fitting. Subsequently, a two parameter fit was performed by calculating the quantity $\chi^2_\nu + \chi^2_{\overline{\nu}}$ as m_c and $s(x,Q^2)$ were varied. The parameter extraction region was defined to be that within the kinematic limits $x < 0.7$ and $Q^2 > 5$ GeV^2. The results of this fit are shifts in the charm mass and strange sea level. To check model dependence, the fit was performed for CTEQ5NLO in addition to GRV98NLO and the results compared.

6.3.2 Results

Several fits for the parameters: χ^2_0, m_c, $s(x,Q^2)$, and associated correlation terms were performed. It is important to determine in exactly which kinematic region the sensitivity to a given parameter comes from for a given model. Therefore, Appendix D contains plots of η distributions with 33% m_c shifts (from the central value of 1.5 GeV) and 50% $s(x,Q^2)$ shifts (from the central value of 1) respectively. The sensitivity to both parameters is large at low x and high E_ν but dies off at high values of x and the fit is noticeably more sensitive to changes in the strange sea than to changes in m_c. For GRV98NLO+EMC+HT, the results of the two parameter fit, with statistical errors only, are:

$$m_c = 2.29 \pm 0.13 \text{ GeV}$$

$$s^{'}(x,Q^2) = (1.80 \pm 0.08) \times s_{GRV}(x,Q^2),$$

while CTEQ5NLO+EMC+HT yields:

$$m_c = 1.47 \pm 0.07 \text{ GeV}$$

$$s^{'}(x,Q^2) = (1.39 \pm 0.03) \times s_{CTEQ}(x,Q^2),$$

All statistical errors have been scaled by a factor of $\sqrt{\chi^2_0/N_{dof}}$ to account for the fact that the χ^2/dof for the GRV model is greater than 1. This number is about 1.2 for both GRV98NLO and CTEQ5NLO. The fitted values of m_c differ by approximately 7 statistical sigma and are inconsistent. Figure 6.5 shows that the initial levels of $s(x,Q^2)$ for GRV98NLO and CTEQ5NLO are radically different from each other. The values of $s(x,Q^2)$ after the fit are much closer together, suggesting that the sensitivity to the strange sea in the data is attempting to pull the model strange seas closer to their "true" values. The relative lack of sensitivity to the charm mass of the data sample (shown in Figs. 6.3 and 6.4) causes the charm masses associated with

each model to be pulled along with the strange sea level due to the high correlation ($\sim$90% in the case of GRV98) between the two parameters. The conclusion is that it is not possible, using a comparison of model χ^2's in the low x QCD region, to determine both m_c and the level of the strange sea. The values of ε_s can be measured , however, by fixing the charm mass parameter to an outside measurement, such as the result of the CCFR NLO analysis [6], $m_c = 1.70 \pm 0.19$ GeV. The high sensitivity of the data to the strange sea level (see Figs. 6.3 and 6.4) leads to consistent values for ε_s when m_c is set equal to the NLO CCFR value, found in Table 5.1. The central value of ε_s is defined to be the value of the shift in the strange sea when the charm mass parameter is set equal to the central value of the CCFR NLO charm mass fit. Errors on the sea associated with the charm mass are determined by shifting the charm mass up and down by its statistical errors and recalculating ε_s. The results of this procedure are:

$$\varepsilon_s^{grv98nlo} = 0.524 \pm 0.075^{+0.095}_{-0.101}$$
$$\varepsilon_s^{cteq5nlo} = 0.433 \pm 0.031^{+0.079}_{-0.042}$$

and the values are consistent to within 1σ. The first set of errors are statistical and the second set are the errors due to the charm mass. The corresponding values of κ are:

$$\kappa_{grv98nlo} = 0.623 \pm 0.031^{+0.039}_{-0.041}$$

and

$$\kappa_{cteq5nlo} = 0.921 \pm 0.013^{+0.051}_{-0.027}.$$

The astatistical discrepancy between the two model predictions of κ is due to the large difference in the relative sizes of the strange and non-strange seas provided by the GRV98 and CTEQ PDF sets (see Fig. 6.2). Although the size of the non-strange sea may differ widely from one parameterization to another, the valence distributions are well constrained from a large number of measurements. Therefore, it is interesting to look at the quantity η_s which has the values:

$$\eta_s^{grv98nlo} = 0.110 \pm 0.005 \pm 0.007$$

and

$$\eta_s^{cteq5nlo} = 0.145 \pm 0.003^{+0.008}_{-0.004}.$$

The statistical difference between the CTEQ5 and GRV98 predictions of η_s is less than that between the predictions for κ due to relatively small theoretical differences in the modeling of valence quark distributions in the nucleon between PDF sets.

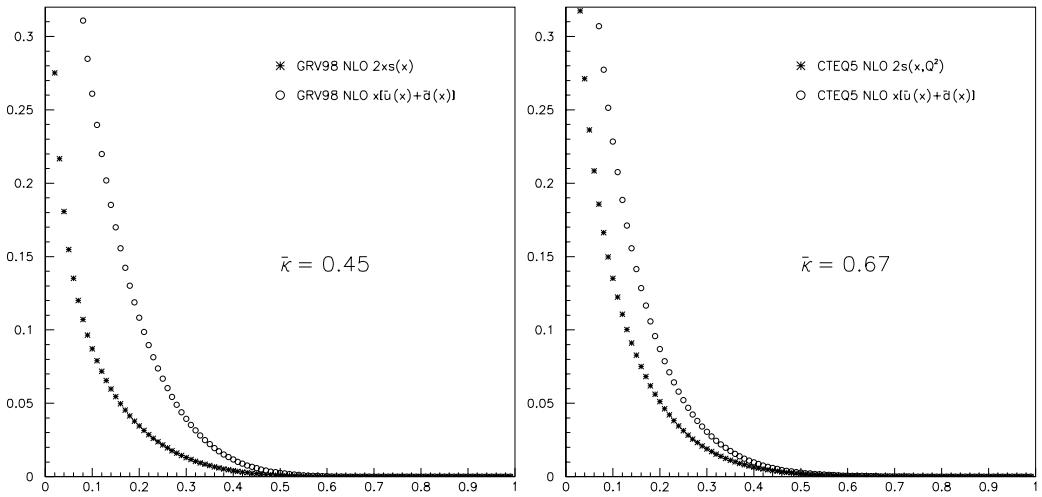

Figure 6.2: GRV98NLO and CTEQ5NLO strange and non-strange seas at $Q^2 = 16$ GeV^2

Systematic Effects

Calibration systematic errors on the $s(x, Q^2)$ level were calculated by independently shifting the individual calibration errors by one standard deviation and performing a $m_c/s(x, Q^2)$ fit corresponding to each shift (see Table 6.14). Only the shifts in the ε_s and κ are shown in the table, as the m_c parameter is no longer relevant. The deviation of the central values of the QCD parameters were added in quadrature to form the aggregate calibration error which is derived from Table 6.14 and applied to both the GRV98NLO and CTEQ5NLO results. Another systematic effect considered was that associated with the Q^2 kinematic cut used to define the parameter extraction region. This cut originally required that (refer to Sec. 6.1) Q^2 be greater than 5 GeV^2 in order to eliminate kinematic regions in which such effects as resonance production and shadowing are large. Of course, this cutoff is not known precisely and so, the lower bound on Q^2 was varied around its "optimal" value to determine the change produced in κ, ε_s and η_s. Fit values as a function of the lower bound on Q^2 can be found in Table 6.15. Contributions to GRV98NLO and CTEQ5NLO from these sources of systematic error are listed in Table 6.16.

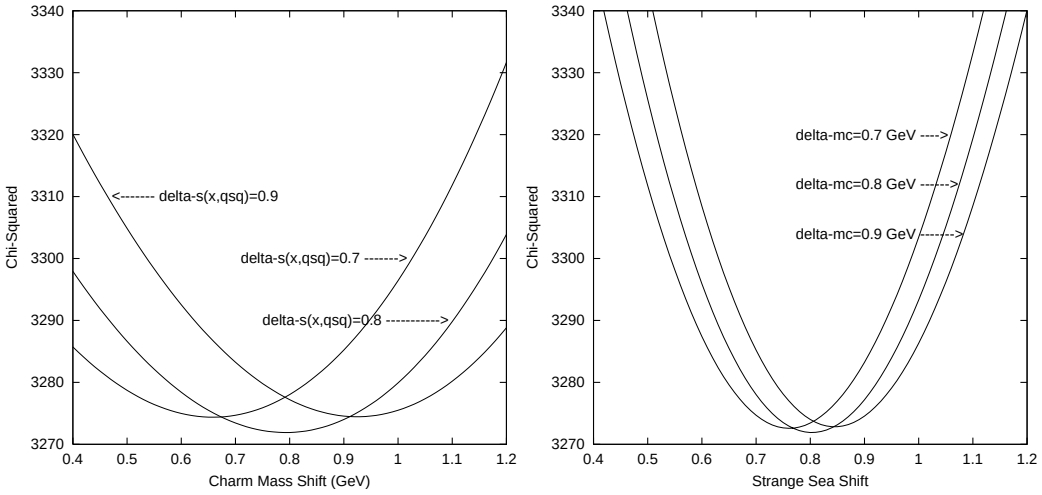

Figure 6.3: Sensitivity of GRV98NLO model to $\Delta s(x, Q^2)$ and Δm_c

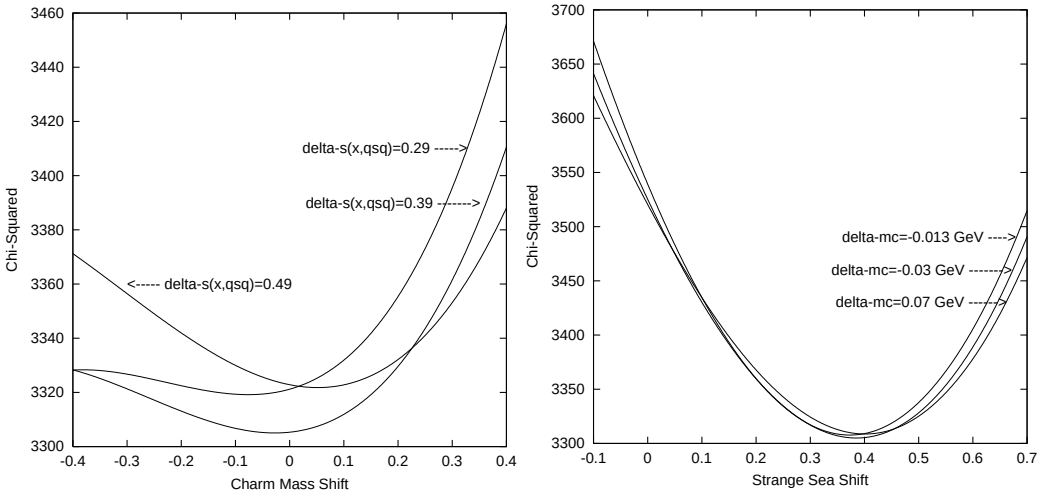

Figure 6.4: Sensitivity of CTEQ5NLO model to $\Delta s(x, Q^2)$ and Δm_c

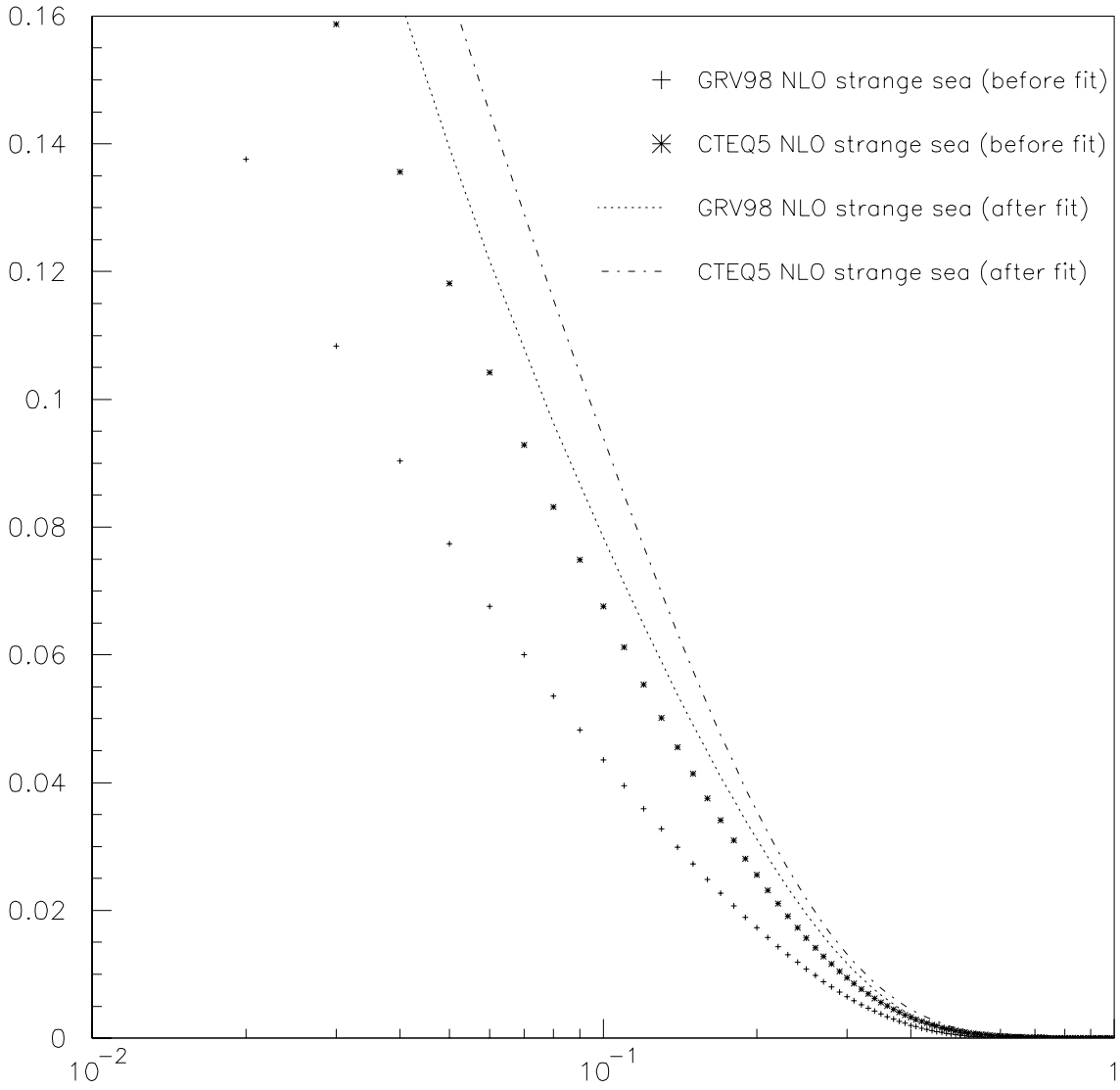

Figure 6.5: $xs(x)$ before and after fit ($Q^2 = 16$ Gev^2)

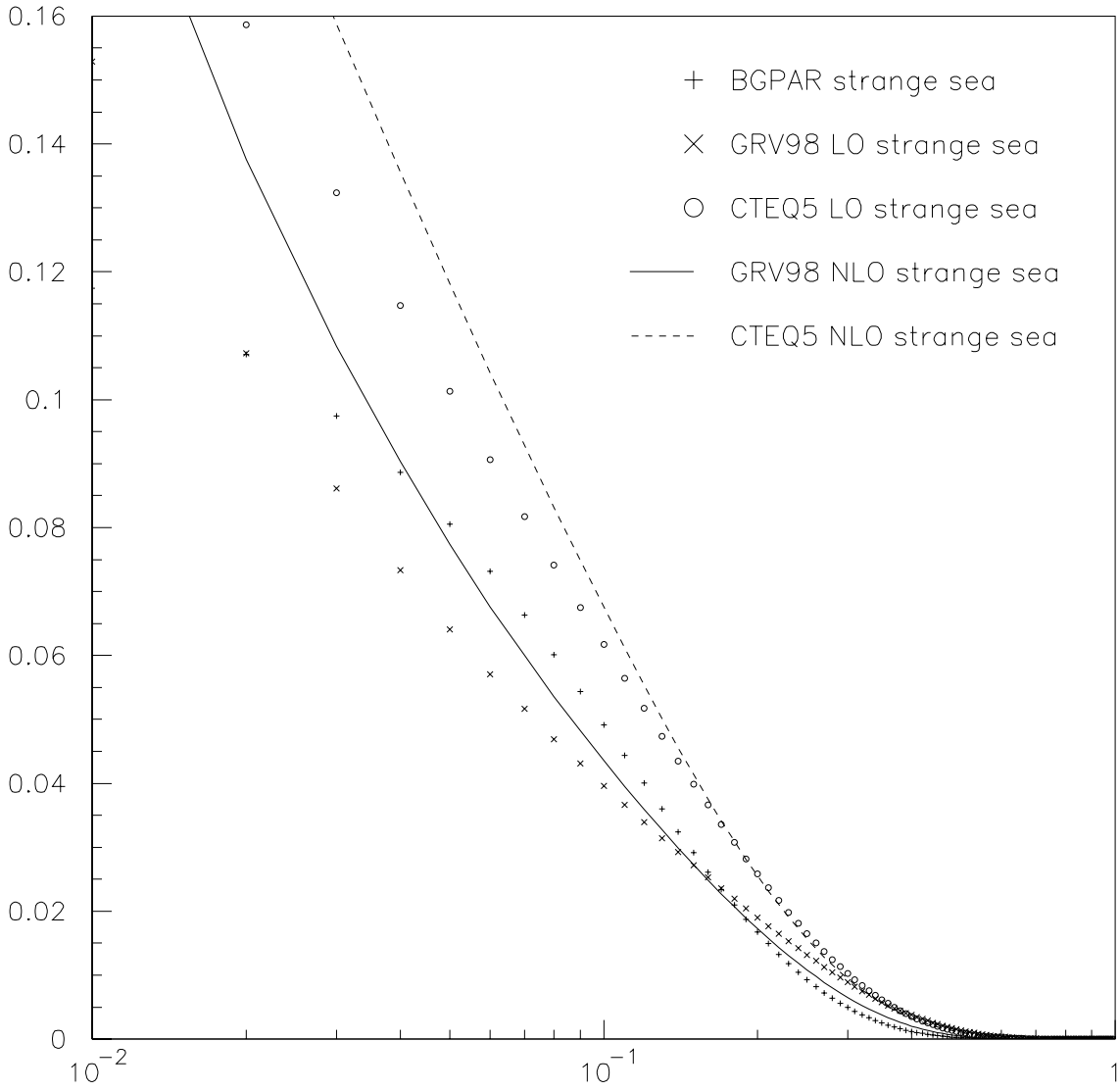

Figure 6.6: Comparison of $xs(x)$ for several different PDF sets ($Q^2 = 16$ GeV^2)

CTEQ5NLO	$s^{'}(x,Q^2)$	κ	η_s
Central	$(1.385\pm0.031)s(x,Q^2)$	0.891 ± 0.020	0.140 ± 0.003
$E_{had}^{scale}+$	$(1.368\pm0.033)s(x,Q^2)$	0.880 ± 0.021	0.138 ± 0.003
$E_{\mu}^{scale}+$	$(1.394\pm0.033)s(x,Q^2)$	0.896 ± 0.021	0.141 ± 0.003
$E_{had}^{lin}+$	$(1.370\pm0.033)s(x,Q^2)$	0.881 ± 0.021	0.138 ± 0.003
$E_{\mu}^{lin}+$	$(1.391\pm0.033)s(x,Q^2)$	0.894 ± 0.021	0.140 ± 0.003
$dE/dx+$	$(1.394\pm0.032)s(x,Q^2)$	0.896 ± 0.021	0.141 ± 0.003

Table 6.14: Calibration systematics

GRV98NLO	$s^{'}(x,Q^2)$	κ	η_s
Standard ($Q^2 > 5$ GeV^2)	$(1.524\pm0.075)s(x,Q^2)$	0.623 ± 0.031	0.110 ± 0.005
$Q^2 > 4$ GeV^2	$(1.509\pm0.082)s(x,Q^2)$	0.617 ± 0.034	0.109 ± 0.006
$Q^2 > 6$ GeV^2	$(1.530\pm0.071)s(x,Q^2)$	0.626 ± 0.029	0.110 ± 0.005
CTEQ5NLO	$s^{'}(x,Q^2)$	κ	η_s
Standard ($Q^2 > 5$ GeV^2)	$(1.433\pm0.033)s(x,Q^2)$	0.921 ± 0.021	0.145 ± 0.003
$Q^2 > 4$ GeV^2	$(1.420\pm0.034)s(x,Q^2)$	0.913 ± 0.022	0.143 ± 0.003
$Q^2 > 6$ GeV^2	$(1.410\pm0.032)s(x,Q^2)$	0.907 ± 0.021	0.142 ± 0.003

Table 6.15: Q^2 lower limit systematics

With calibration and Q^2 cutoff systematic errors included, the results of the strange sea measurement are:

$$\varepsilon_s^{grv98nlo} = 0.524\pm0.075^{+0.095}_{-0.101}\pm0.016,$$

$$\varepsilon_s^{cteq5nlo} = 0.433\pm0.031^{+0.079}_{-0.042}\pm0.017,$$

$$\kappa_{grv98nlo} = 0.623\pm0.033^{+0.039}_{-0.041}\pm0.009,$$

$$\kappa_{cteq5nlo} = 0.921\pm0.021^{+0.051}_{-0.027}\pm0.010,$$

$$\eta_s^{grv98nlo} = 0.110\pm0.005\pm0.007\pm0.001,$$

and

$$\eta_s^{cteq5nlo} = 0.145\pm0.003^{+0.008}_{-0.004}\pm0.002.$$

6.4 $|V_{cs}|^2$

Equation 5.14 contains, in principle, the precise relationship between V_{cs}^{exp} and the measured values of B_c, κ_{inc}, and $\kappa_{2\mu}$. However, V_{cs}^{exp} is sensitive to the other quantities to the extent that a straightforward numerical solution of the equation leads to an unphysical result. It is necessary, therefore, to perform a simultaneous χ^2 fit to

Model	*Calibration*	Q^2 *Scale*
GRV98NLO ($\varepsilon_s/\kappa/\eta_s$)	0.012/0.007/0.001	0.011/0.005/0.001
CTEQ5NLO ($\varepsilon_s/\kappa/\eta_s$)	0.012/0.007/0.001	0.012/0.007/0.002

Table 6.16: Systematic errors due to calibration and Q^2 scale

all relevant quantities using the constraints outlined in Sec. 5.2.4. In addition, the correlation between κ_{inc} and r_{cc} with the charm mass necessitates a linear expansion in both variables of the form:

$$\kappa_{inc} \rightarrow \kappa_{inc} + \frac{d\kappa_{inc}}{dm_c}\Delta m_c,$$

and

$$r_{cc} \rightarrow r_{cc} + \frac{dr_{cc}}{dm_c}\Delta m_c.$$

The quantity Δm_c must remain within the statistical error of the CCFR NLO measurement which is ± 0.19 GeV. This constraint is enforced by the addition of the final term to the χ^2 function in Eq. 6.1. The correlation terms $d\kappa_{inc}/dm_c$ for GRV98 and CTEQ5 result from the two parameter fits to m_c discussed in Sec. 6.3.2 while r_{cc} and dr_{cc}/dm_c are calculated by the monte carlo using the leading-order approximation in Eq 5.13. Numerical values can be found in Table 6.17.

$$\chi^2 = \frac{(B_c^{ext} - \overline{B}_c^{ext})^2}{\sigma^2_{B_c^{ext}}} + \frac{(B_c^{exp} - \overline{B}_c^{exp})^2}{\sigma^2_{B_c^{exp}}} + \frac{(\kappa_{inc} - \overline{\kappa}_{inc})^2}{\sigma^2_{\kappa_{inc}}} + \frac{(\kappa_{2\mu} - \overline{\kappa}_{2\mu})^2}{\sigma^2_{\kappa_{2\mu}}} + \frac{{\Delta m_c}^2}{(0.19\ \text{GeV})^2} \tag{6.1}$$

In the above equation, overlined quantities are the experimentally measured quantities, with errors, found in Table 6.21. Minimization is performed with respect to these variables subject to the constraints from Eqs. 5.10, 5.11, and 5.12 and the additional constraint that the theoretical value of the strange sea level, $\widetilde{\kappa}$, remain less than 1. This enforces the physical requirement that the strange sea remain smaller than the non-strange sea. It is through these constraints that a measurement of $|V_{cs}^{exp}|^2$ is possible. Note that the number $\kappa_{2\mu}$, like κ_{inc}, is somewhat model dependent and, for the case of the NuTeV dimuon analysis, was extracted with both LO GRV94 and CTEQ4 parton distributions. Before fitting, both CTEQ and GRV fits for $\kappa_{2\mu}$ were corrected so as to be consistent with the GRV98NLO and CTEQ5NLO models used to extract κ_{inc}. This was done via a simple multiplicative factor with the GRV case given as an example:

$$\kappa_{2\mu}^{grv98nlo} = \kappa_{2\mu}^{grv94lo} \left.\frac{\kappa^{grv98nlo}}{\kappa^{grv94lo}}\right|_{theory}. \tag{6.2}$$

The "theory" designation in Eq. 6.2 indicates a κ calculated from the appropriate PDF set at the average Q^2 value of the NuTeV experiment in inclusive case, and separately for neutrinos and anti-neutrinos in the dimuon case. The theoretical values of κ are shown in Table 6.19 and the experimental values from the dimuon analysis are contained in Table 6.20. This table also contains $\kappa_{2\mu}$ values corrected to the GRV98NLO and CTEQ5NLO models by use of the numbers in Table 6.19. For neutrino mode $\langle Q^2 \rangle = 20.61$ GeV^2 and, for anti-neutrino mode, $\langle Q^2 \rangle = 12.86$ GeV^2. The average over modes gives $\langle Q^2 \rangle = 16.74$ GeV^2. Average values for the kinematic variables x, E_ν, and Q^2 are listed in Table 6.18. Treating $\kappa_{2\mu}^{\nu}$ and $\kappa_{2\mu}^{\overline{\nu}}$ as the results of independent experiments and averaging yields:

$$\kappa_{2\mu}^{grv98nlo} = 0.42 \pm 0.07,$$

$$\kappa_{2\mu}^{cteq5nlo} = 0.54 \pm 0.09.$$

From Secs. 6.3.2 and 6.3.2, the values of κ_{inc} are:

$$\kappa_{grv98nlo} = 0.623 \pm 0.031^{+0.039}_{-0.041}$$

and

$$\kappa_{cteq5nlo} = 0.921 \pm 0.021^{+0.051}_{-0.027}$$

which, along with the experimental values of $\kappa_{2\mu}$ and B_c are contained in Table 6.21. These number are used in the χ^2 fit described at the beginning of this section (they are equal to the overlined quantities) which results in values for $|V_{cs}^{exp}|^2$ of:

$$|V_{cs}^{exp}|^2_{grv98nlo} = 0.72^{+0.30}_{-0.04} \pm 0.03 \pm 0.01$$

and

$$|V_{cs}^{exp}|^2_{cteq5nlo} = 0.92^{+0.15+0.03}_{-0.02-0.02} \pm 0.01.$$

As usual, the first set of errors is statistical, the second is the error due to the CCFR charm mass and the final set is the total systematic error. Note that the constraint $\widetilde{\kappa} < 1$ is responsible for the stringent lower limits on V_{cs} seen above.

6.5 Conclusions

6.5.1 QCD Model Comparisons

This analysis was divided into two parts. The first of these was a comparison of different QCD-based theoretical models with the NuTeV charged current data

sample using a model χ^2 as the basis. These comparisons revealed that, within the kinematic cuts designed to select out regions most sensitive to QCD, next-to-leading-order models, as exemplified by GRV98NLO and CTEQ5NLO, were in much better agreement with the data than their leading order counterparts and, strikingly, showed better agreement than the leading-order Buras-Gaemers (BG-PAR) parameterization extracted from NuTeV data. Within the group of models designated as NLO and, to a lesser extent, within the LO models as well, a number of different corrections were applied to the base model to determine what the effect would be on the χ^2 comparison. Among these corrections were: application of the EMC effect, application of higher-twist corrections, substitution of the longitudinal structure function implicit in the base QCD model (R_{QCD} in the NLO case and $R_{Callan-Gross}$ in the LO case) with a parameterization of world data ($R_{whitlow}$), inclusion of electroweak radiative corrections by Bardin or Derujula, and alteration of the QCD factorization scale in the NLO charm production cross-section. These comparisons indicate that the GRV98NLO PDF set is in best agreement with the data and that application of the EMC and higher twist corrections result in substantial improvement of this agreement. In addition, the data slightly favor Derujula radiative corrections over those provided by Bardin although the improvement in the χ^2 value is not large enough to be conclusive. Similarly, the QCD factorization scale choice of $\mu^2 = Q^2 + m_c^2$ in the charm production part of the cross-section leads to a χ^2 value that is almost indistinguishable from that resulting from the choice $\mu^2 = Q^2$. Use of the $R_{whitlow}$ parameterization of the longitudinal structure function is contraindicated by the χ^2 comparisons. This conclusion is of some importance as it confirms that, at this stage, use of a consistent QCD based calculation of R_{long} is vital in NLO cross-section calculations. It is also important to note here again that the substitution of $R_{whitlow}$ for $R_{Callan-Gross}$ in the LO cross-section model leads to a *substantial* worsening of agreement between the model and the data as demonstrated by a factor of 2 increase in the χ^2 (see Tables B.3 and B.4). It is currently not uncommon practice to "improve" LO cross-section model calculations by artifically imposing the constraint $F_2 = 2xF_1(R_{long}+1)/(1+(2M_px)/(Ey))$ in an attempt to account for gluon and other NLO parton effects in a leading order framework. This is theoretically unwarranted and introduces an inconsistency between the cross-section model (which, with the R_{long} correction, effectively becomes a $1\frac{1}{2}$ order calculation) and the PDF sets, which are extracted under the assumption that $F_2 = 2xF_1$ and that there are no gluons in the nucleon. It is clear from the results in Sec. 6.2.3 that inclusion of the longitudinal structure function in a leading order cross-section model could, depending on the particulars of the analysis, lead to unexpected and/or incorrect results. Beyond the model comparisons mentioned above, three additional questions were addressed:

1) Should the EMC correction be applied to xF_3?

2) Are the higher twist corrections for F_2 and xF_3 equal?

3) Does substitution of a GEANT flux for the DECAY TURTLE flux improve the model?

The first two questions made use of the variable η^- which is sensitive to the xF_3 component of the cross-section. Comparisons using these variables indicate both that the EMC correction should be applied to xF_3 and that higher twist corrections for both singlet and non-singlet structure functions are the same. Use of the GEANT flux leads to a slight ($\sim$8 unit) improvement in χ^2 over the TURTLE flux.

6.5.2 κ, η_s, and $|V_{cs}|^2$

In addition to QCD model studies, the χ^2 comparison technique was also used to extract QCD and electroweak model parameters related to NLO charm production. As mentioned in Sec 6.1, the kinematic cuts were altered from those used for the QCD model comparisons to include regions of x phase space that are sensitive to charm production and the strange sea level. Performing joint fits to m_c and the shift in the strange sea level, ε_s, leads to two conclusions. The first is that, due to large differences in the strange and non-strange seas provided by the GRV98 and CTEQ5 NLO PDF sets, the values of the fit parameters differ by a margin far outside what would be expected from statistical error. The second is that the fits show much greater sensitivity to ε_s than to m_c. The solution to the problem posed by the first conclusion was to abandon the independent measurement of the charm quark mass and, instead, to constrain it to the recent [6] NLO CCFR measured value of $m_c = 1.70 \pm 0.19$ GeV, effectively converting the fit into a one parameter determination of ε_s. This procedure results in the following values of ε_s for GRV98 and CTEQ5.

$$\varepsilon_s^{grv98nlo} = 0.524 \pm 0.075^{+0.095}_{-0.101} \pm 0.016$$

$$\varepsilon_s^{cteq5nlo} = 0.433 \pm 0.031^{+0.079}_{-0.042} \pm 0.017$$

which can be converted to the standard strange sea level parameters, κ and η_s, via Eqs. 4.21 and 4.22, yielding:

$$\kappa_{grv98nlo} = 0.623 \pm 0.031^{+0.039}_{-0.041} \pm 0.009,$$

$$\kappa_{cteq5nlo} = 0.921 \pm 0.021^{+0.051}_{-0.027} \pm 0.010,$$

$$\eta_s^{grv98nlo} = 0.110 \pm 0.005 \pm 0.007 \pm 0.001,$$

and

$$\eta_s^{cteq5nlo} = 0.145 \pm 0.003^{+0.008}_{-0.004} \pm 0.002.$$

The large disparity between the calculation of $\kappa_{grv98nlo}$ and $\kappa_{cteq5nlo}$ is due to the relatively small difference between the CTEQ5NLO strange and non-strange seas. Because this analysis is performed with an inclusive charged current data sample, the quantity "κ_{inc}" is technically $\kappa_{inc}(|V_{cs}|^2 + |V_{us}|^2)$, as diagrams associated with both c and u quark production from the strange sea contribute to the total cross-section. The dimuon analysis, by contrast, is sensitive mainly to charm production leading to a second muon, which means that the measured quantity $\kappa_{2\mu}$ is actually $\kappa_{2\mu}|V_{cs}|^2 B_c$. Using this information in conjunction with both NuTeV dimuon and external measurements of B_c and performing a χ^2 fit results in measurements of the CKM matrix element $|V_{cs}^{exp}|^2_{grv98nlo} = 0.72^{+0.30}_{-0.04} \pm 0.03 \pm 0.01$ and $|V_{cs}^{exp}|^2_{cteq5nlo} = 0.92^{+0.15+0.03}_{-0.02-0.02} \pm 0.01$.

Fit Parameter	*GRV98NLO*	*CTEQ5NLO*
r_{cc}	0.348	0.334
$d\kappa_{inc}/dm_c$	0.145	0.125
dr_{cc}/dm_c	-0.283	-0.290

Table 6.17: V_{cs} fit correlation and charm suppression parameters

Kinematic Variable	ν	$\overline{\nu}$
$\langle x \rangle$	0.204	0.187
$\langle E_\nu \rangle$	140.7 GeV	120.6 GeV
$\langle Q^2 \rangle$	20.61 GeV^2	12.86 GeV^2

Table 6.18: Average x, E_ν, and Q^2 of the CC data sample

Model	κ_ν	$\kappa_{\overline{\nu}}$	$\overline{\kappa}$
GRV98NLO	0.42	0.40	0.41
CTEQ5NLO	0.65	0.63	0.64
GRV94LO	0.42	0.40	0.41
CTEQ4LO	0.60	0.58	0.59

Table 6.19: Theoretical κ

Model κ	χ^2/dof	
	ν	$\overline{\nu}$
$\kappa_{2\mu}^{grv94lo}$	0.42±0.09	0.41±0.10
$\kappa_{2\mu}^{cteq4lo}$	0.50±0.11	0.49±0.12
$\kappa_{2\mu}^{grv98nlo}$	0.42±0.09	0.41±0.10
$\kappa_{2\mu}^{cteq5nlo}$	0.54±0.12	0.53±0.13

Table 6.20: Dimuon measured κ

Parameter	*Value*
B_c^{ext}	(9.1±0.9)%
B_c^{exp}	(9.4±1.8)%
$\kappa_{inc}^{grv98nlo}$	$0.623^{+0.039}_{-0.041}$
$\kappa_{inc}^{cteq5nlo}$	$0.921^{+0.051}_{-0.027}$
$\kappa_{2\mu}^{grv98nlo}$	0.42±0.07
$\kappa_{2\mu}^{cteq5nlo}$	0.54±0.09

Table 6.21: Measured quantities used in $|V_{cs}|^2$/ $|V_{cd}|^2$ χ^2 fit

Appendix A

Positive Definite Integrals

The calculation of the structure functions F_1, F_2, and F_3 involves a convolution integral of the form:

$$F^j(x,Q^2) = \sum_i \int_x^1 \frac{dy}{y} \mathcal{C}^j(y, \overline{g}(Q^2)) p_i(x/y) \tag{A.1}$$

with

$$\mathcal{C}(y) = \delta(1-y) + \frac{g^2}{16\pi^2}\mathcal{C}^i(y).$$

In general, the distribution $\mathcal{C}^i(y)$ may be expressed as a product of two functions, $F(y)_+$ and $f(y)$. To calculate the structure functions, then, it is eventually necessary to perform an integral of the form:

$$I = \int_x^1 F(y)_+ f(y) dy$$

By definition of a positive definite function:

$$\int_0^1 F(y)_+ f(y) dy = \int_0^1 F(y)[f(y) - f(1)] dy$$

This is more useful if rearranged as follows:

$$I = \int_x^1 F(y)_+ f(y) dy = \int_0^1 F(y)_+ f(y) dy - \int_0^x F(y)_+ f(y) dy$$

$$I = \int_0^1 F(y)[f(y) - f(1)]dy - \int_0^x F(y)_+ f(y)dy$$

Positive definiteness is important only if there is a discontinuity at any point along the interval. Clearly, there is a discontinuity when x is equal to y. Since this condition does not occur in the integral bounded by 0 and x, the positive definite sign is no longer necessary and the integral may be performed without modification. This leaves:

$$I = \int_0^1 F(y)[f(y) - f(1)]dy - \int_0^x F(y)f(y)dy$$

and, combining the first term of the first integral with the last integral:

$$I = \int_x^1 F(y)f(y)dy - \int_0^1 F(y)f(1)dy$$

Numerical integration packages such as `ADZINT` (ACOT) or `DGAUSS` (CERNLIB) can be used with the preceding forumulas to calculate structure functions from Eq. A.1. Outlines of the calculations for light and heavy quark structure functions follow.

A.1 Light Quark Structure Function Calculation

Recalling Eq. 3.23 and inserting the definitions for the $\mathcal{C}$ functions from Ref. 4:

$$\mathcal{C}_Q^1 = (c_F/2)\,[F_q(x) - 4x] \tag{A.2}$$

$$\mathcal{C}_Q^2 = c_F F_q(x) \tag{A.3}$$

$$\mathcal{C}_Q^3 = c_F[F_q(x) - 2 - 2x] \tag{A.4}$$

gives the following expression for the light quark structure functions with the up quark as an example.

$$F_1^u(x,Q^2) = \frac{u(x,Q^2)}{2} + \frac{c_F g^2}{32\pi^2}\int_x^1 \frac{dy}{y}[F_q(y) - 4y]u(x/y,Q^2) \tag{A.5}$$

$$F_2^u(x,Q^2)/x = u(x,Q^2) + \frac{c_F g^2}{16\pi^2}\int_x^1 \frac{dy}{y} F_q(y) u(x/y,Q^2) \tag{A.6}$$

$$F_3^u(x,Q^2) = u(x,Q^2) + \frac{c_F g^2}{16\pi^2}\int_x^1 \frac{dy}{y} [F_q(y) - 2 - 2y] u(x/y,Q^2) \tag{A.7}$$

The term $u(x,Q^2)$, common to all three of the structure functions, is just the NLO up quark PDF and corresponds to the "LO" or α_s^0 piece of the NLO structure function. The factor of $\frac{1}{2}$ in the expression for F_1^u is necessary to enforce the Callan-Gross relation at LO. The function $F_q(y)$ contains positive definite pieces and must be evaluated according to the rules outlined at the beginning of this appendix. Structure functions for the gluons can be calculated in a similar way. The $\mathcal{C}^i$ function for gluons in the massless formalism does not have an α_s^0 term and does not exist for the singlet (xF_3) case.

$$\mathcal{C}_G^1 = 2T_R\left[F_G(x) - 4x(1-x)\right] \tag{A.8}$$

$$\mathcal{C}_G^2 = 4T_R F_G(x) \tag{A.9}$$

The function $F_G(x)$ can be found together with its equivalent for quarks in Ref. 4. The final gluon structure functions are calculated according to the same mathematical prescription as their quark counterparts:

$$F_1^g(x,Q^2) = \frac{T_R g^2}{8\pi^2}\int_x^1 \frac{dy}{y}[F_G(y) - 4y(1-y)] g(x/y,Q^2) \tag{A.10}$$

$$F_2^g(x,Q^2)/x = \frac{T_R g^2}{4\pi^2}\int_x^1 \frac{dy}{y} F_G(y) g(x/y,Q^2) \tag{A.11}$$

A way to check the NLO massless quark structure functions is to determine whether they obey the Gross-Llewellyn Smith Sum Rule [41]:

$$\int_0^1 \frac{xF_3}{x}dx = 3\left[1 - \frac{\alpha_s}{\pi} - a(n_f)\left(\frac{\alpha_s}{\pi}\right)^2\right] \tag{A.12}$$

where, $a(n_f = 3) = -(67/12)$ for the three flavor case (see Ref. 42). Figure A.1 contains comparisons of the integrated values for the LHS of Eq. A.12 with the RHS, $\mathcal{F}[\alpha_s(Q^2)]$ as functions of Q^2.

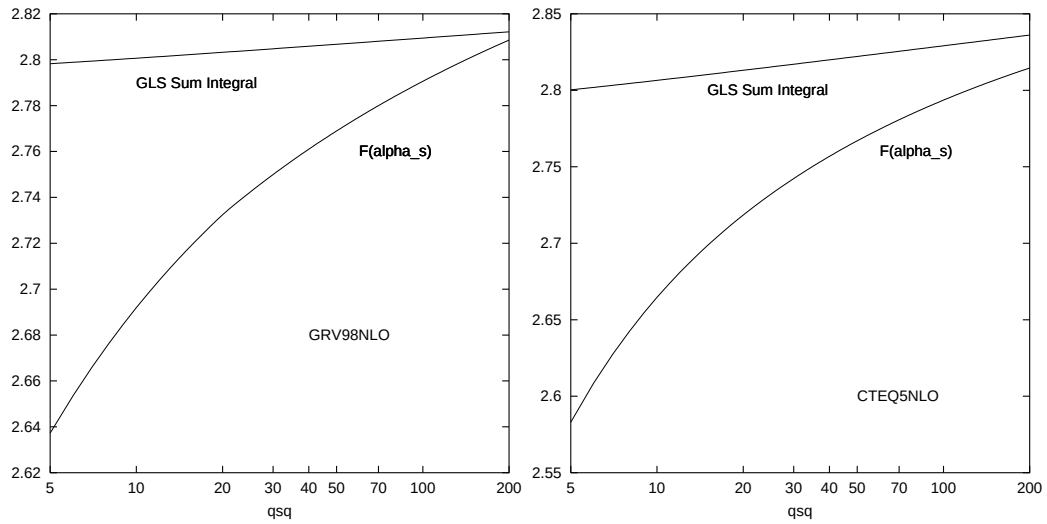

Figure A.1: Comparison of GLS integral and $\mathcal{F}[\alpha_s(Q^2)]$ for GR98NLO and CTEQ5NLO

A.2 Heavy Quark Structure Function Calculation

Heavy quark structure functions are calculated, in principle, in a similar manner to their light quark counterparts. The difference lies in the use of massive quark evolution and the explicit incorporation of slow rescaling (see Sec. 4.1.3) into the factorization equations. The general formula for heavy quark structure functions in the GKR scheme is:

$$\mathcal{F}_i^c(x,Q^2) = s^{'}(\xi,\mu^2) + \frac{\alpha_s(\mu^2)}{2\pi}\left\{\int_\xi^1 \frac{d\xi^{'}}{\xi^{'}}\left[H_i^q(\xi^{'},\mu^2,\lambda)s^{'}(\frac{\xi}{\xi^{'}},\mu^2) + H_i^g(\xi^{'},\mu^2,\lambda)g(\frac{\xi}{\xi^{'}},\mu^2)\right]\right\} \tag{A.13}$$

In the expression above, the variable i runs over the partons $u, \overline{u}, d, \overline{d}, s$, and g. Of particular importance in heavy quark charm production is the form of the strange sea parameterized here by:

$$s^{'} \equiv |V_{cs}|^2 \, s + |V_{cd}|^2 \, \frac{d+u}{2}$$

$$\xi = x\left(1 + \frac{m_c^2}{Q^2}\right)$$

The H functions for quarks and gluons in Eq. A.13 are written [8]:

$$H_i^q(y,\mu^2,\lambda) = \left[P_{qq}^{(0)}(y)\ln\frac{Q^2+m_c^2}{\mu^2} + h_i^q(y,\lambda)\right]$$

$$H^{g}_{i=\frac{1,2}{3}}(y,\mu^2,\lambda) = \left[P^{(0)}_{qg}(y)\left(\pm L_\lambda + \ln\frac{Q^2+m_c^2}{\mu^2}\right) + h^g_i(y,\lambda)\right]$$

where,

$$\lambda = \frac{Q^2}{Q^2+m_c^2},$$

$$L_\lambda = \ln\frac{1-\lambda y}{(1-\lambda)y},$$

and h^q_i contains positive definite elements (h^g_i does not). The H functions and the strange sea may now be inserted into Eq. A.13 and the heavy quark structure functions can be calculated. As the calculation of the integrals both for light and heavy quarks is extremely time consuming, quark structure function values were written out as tables in x, Q^2, and m_c bins and subsequently, interpolated as needed by the cross-section code.

Appendix B

χ^2 Tables

This appendix contains several different kinds of χ^2 tables. The first set contains χ^2's relevant to the model comparisons discussed in the results section. That is to say, χ^2 values calculated in the "QCD Region" of Sec. 6.1. The second set of tables contains the χ^2's for the "Low x/Q^2 Region", the third set refers to the "High x" region, and the fourth and final set of tables displays χ^2 values for the "Parameter Extraction" region shown in Fig. 6.1.

B.1 QCD χ^2 Comparisons

(χ^2/dof)	*grv98nlo*	*cteq5nlo*
no EMC	1617.38/860	1267.47/860
+EMC	1168.80/860	1253.85/860
+EMC+HT	1114.51/860	1186.28/860
+EMC+HT+DRAD	1111.08/860	1161.28/860
+EMC+HT+DRAD+GFLUX	1106.74/860	N/A
+EMC+HT+DRAD+SCALE	1108.35/860	N/A
F2EMC+HT+DRAD	1148.91/860	N/A
EMC+$HT_{F_3F_2}$+DRAD	1121.33/860	N/A
+EMC+R_{whit}	1270.55/860	1377.47/860
+EMC+R_{whit}+HT	1259.03/860	1566.74/860
+EMC+R_{whit}+HT+DRAD	1285.41/860	1604.16/860

Table B.1: χ^2 comparison of NLO models to data (ν)

(χ^2/dof)	*grv98nlo*	*cteq5nlo*
no EMC	1146.11/831	1035.42/831
+EMC	974.48/831	1006.37/831
+EMC+HT	979.65/831	1003.37/831
+EMC+HT+DRAD	972.51/831	984.47/831
+EMC+HT+DRAD+GFLUX	968.38/831	N/A
+EMC+HT+DRAD+SCALE	974.50/831	N/A
+F2EMC+HT+DRAD	1033.04/831	N/A
EMC+$HT_{F_3F_2}$+DRAD	963.96/831	N/A
+EMC+R_{whit}	1016.40/831	1046.86/831
+EMC+R_{whit}+HT	993.93/831	1072.84/831
+EMC+R_{whit}+HT+DRAD	1002.01/831	1077.24/831

Table B.2: χ^2 comparison of NLO models to data ($\overline{\nu}$)

(χ^2/dof)	*bgpar*	*grv98lo*	*cteq5lo*
+EMC	1797.68/860	1646.59/860	1741.58/860
+EMC+R_{whit}	N/A	3867.65/860	3965.32/860

Table B.3: χ^2 comparison of LO models to data (ν)

(χ^2/dof)	*bgpar*	*grv98lo*	*cteq5lo*
+EMC	1124.08/831	1100.22/831	1177.40/831
+EMC+R_{whit}	N/A	1607.04/831	1636.65/831

Table B.4: χ^2 comparison of LO models to data ($\overline{\nu}$)

B.2 High x χ^2 Comparisons

(χ^2/dof)	*grv98nlo*	*cteq5nlo*
no EMC	639.13/185	429.24/185
+EMC	287.90/185	329.86/185
+EMC+HT	281.24/185	289.46/185
+EMC+HT+DRAD	293.03/185	270.97/185
+EMC+HT+DRAD+GFLUX	293.83/185	N/A
+EMC+HT+DRAD+SCALE	286.31/185	N/A
F2EMC+HT+DRAD	314.83/185	N/A
EMC+$HT_{F_3F_2}$+DRAD	286.91/185	N/A
+EMC+R_{whit}	312.60/185	329.04/185
+EMC+R_{whit}+HT	299.94/185	276.78/185
+EMC+R_{whit}+HT+DRAD	316.25/185	284.75/185

Table B.5: High x χ^2 comparison of NLO models to data (ν)

(χ^2/dof)	*grv98nlo*	*cteq5nlo*
no EMC	233.33/171	186.18/171
+EMC	186.35/171	227.64/171
+EMC+HT	172.82/171	209.21/171
+EMC+HT+DRAD	170.88/171	208.78/171
+EMC+HT+DRAD+GFLUX	172.89/171	N/A
+EMC+HT+DRAD+SCALE	172.52/171	N/A
F2EMC+HT+DRAD	180.23/171	N/A
EMC+$HT_{F_3F_2}$+DRAD	174.48/171	N/A
+EMC+R_{whit}	185.97/171	218.62/171
+EMC+R_{whit}+HT	179.09/171	195.55/171
+EMC+R_{whit}+HT+DRAD	177.34/171	188.90/171

Table B.6: High x χ^2 comparison of NLO models to data ($\overline{\nu}$)

(χ^2/dof)	*bgpar*	*grv98lo*	*cteq5lo*
+EMC	753.31/185	495.13/185	514.09/185
+EMC+R_{whit}	N/A	2245.85/185	2241.67/185

Table B.7: High x χ^2 comparison of LO models to data (ν)

(χ^2/dof)	*bgpar*	*grv98lo*	*cteq5lo*
+EMC	337.05/171	259.12/171	271.02/171
+EMC+R_{whit}	N/A	568.12/171	569.35/171

Table B.8: High x χ^2 comparison of LO models to data ($\overline{\nu}$)

B.3 Low x/Q^2 χ^2 Comparisons

(χ^2/dof)	*grv98nlo*	*cteq5nlo*
no EMC	4545.32/1160	2842.13/1160
+EMC	2866.63/1160	2377.63/1160
+EMC+HT	2700.60/1160	2214.70/1160
+EMC+HT+DRAD	2555.82/1160	2125.29/1160
+EMC+HT+DRAD+GFLUX	2530.93/1160	N/A
+EMC+HT+DRAD+SCALE	2568.45/1160	N/A
F2EMC+HT+DRAD	2583.65/1160	N/A
EMC+$HT_{F_3F_2}$+DRAD	2672.98/1160	N/A
+EMC+R_{whit}	3289.08/1160	2971.32/1160
+EMC+R_{whit}+HT	2305.24/1160	2984.91/1160
+EMC+R_{whit}+HT+DRAD	2186.77/1160	2887.35/1160

Table B.9: Low x/Q^2 χ^2 comparison of NLO models to data (ν)

(χ^2/dof)	*grv98nlo*	*cteq5nlo*
no EMC	2910.21/1106	2160.68/1106
+EMC	1909.20/1106	1532.39/1106
+EMC+HT	1882.54/1106	1511.61/1106
+EMC+HT+DRAD	1796.74/1106	1448.30/1106
+EMC+HT+DRAD+GFLUX	1780.71/1106	N/A
+EMC+HT+DRAD+SCALE	1805.85/1106	N/A
F2EMC+HT+DRAD	1843.59/1106	N/A
EMC+$HT_{F_3F_2}$+DRAD	1740.96/1106	N/A
+EMC+R_{whit}	2157.66/1106	1582.12/1106
+EMC+R_{whit}+HT	1594.14/1106	1425.62/1106
+EMC+R_{whit}+HT+DRAD	1515.77/1106	1391.32/1106

Table B.10: Low x/Q^2 χ^2 comparison of NLO models to data ($\overline{\nu}$)

(χ^2/dof)	*bgpar*	*grv98lo*	*cteq5lo*
+EMC	2129.76/1160	3289.46/1160	3006.93/1160
+EMC+R_{whit}	N/A	4929.81/1160	3947.23/1160

Table B.11: χ^2 comparison of LO models to data (ν)

(χ^2/dof)	*bgpar*	*grv98lo*	*cteq5lo*
+EMC	1405.72/1106	1928.58/1106	1655.10/1106
+EMC+R_{whit}	N/A	2814.39/1106	2248.48/1106

Table B.12: χ^2 comparison of LO models to data ($\overline{\nu}$)

Appendix C

η With Systematic Error Bands

This appendix contains plots showing the best model (GRV98NLO with EMC correction, higher twist, and Derujula radiative corrections applied) with calibration systematic error bands. All x, Q^2, and E_ν bins are shown. The error contributions, E_{had} and E_μ scale, E_{had} and E_μ linearity, and muon dE/dx, are added in quadrature. Upward and downward shifts of the errors in each bin are averaged and displayed as a single error of equal width on both sides of the central model.

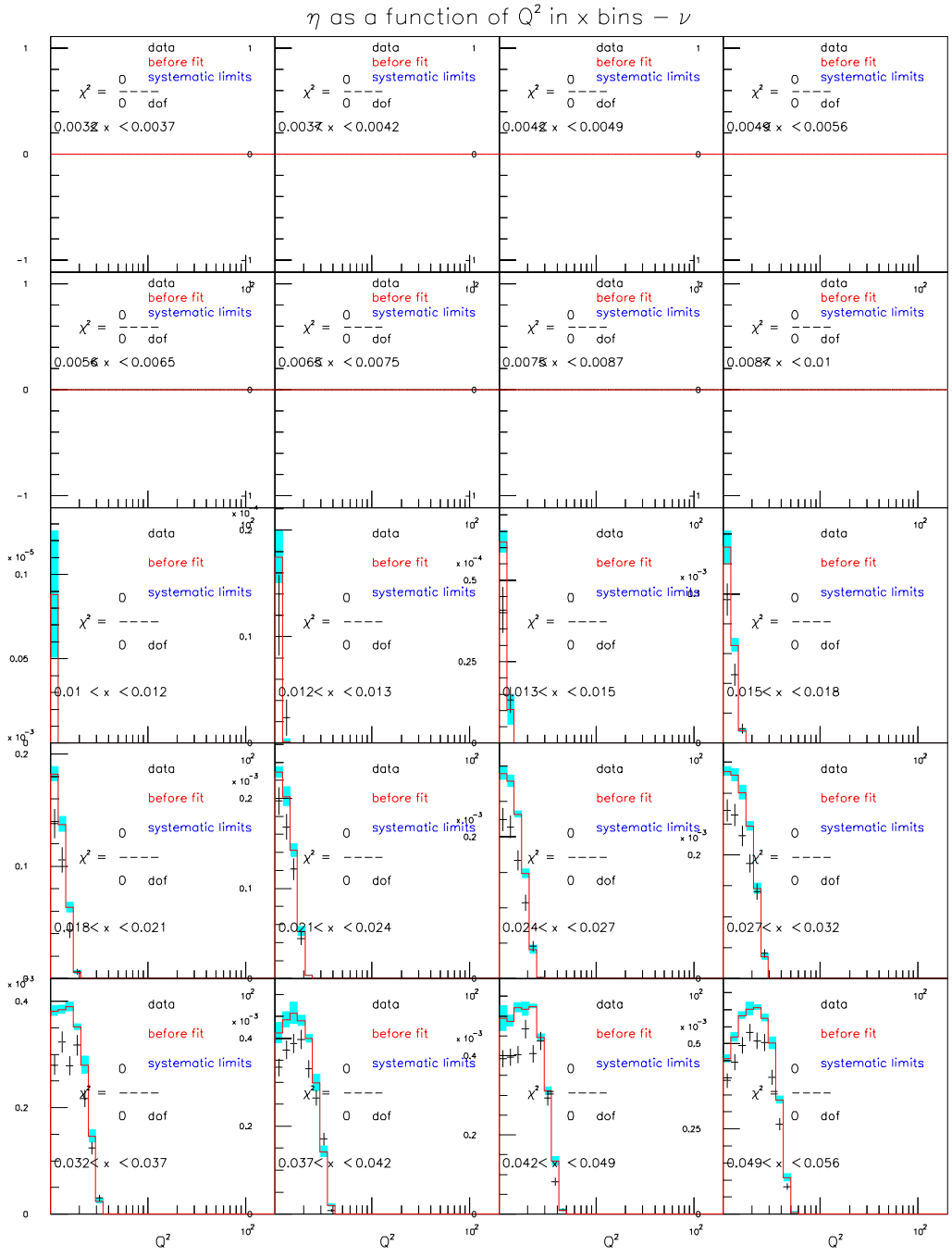

Figure C.1: GRV98NLO+EMC+HT+DRAD for $20 < E_\nu < 62$ GeV (ν mode)

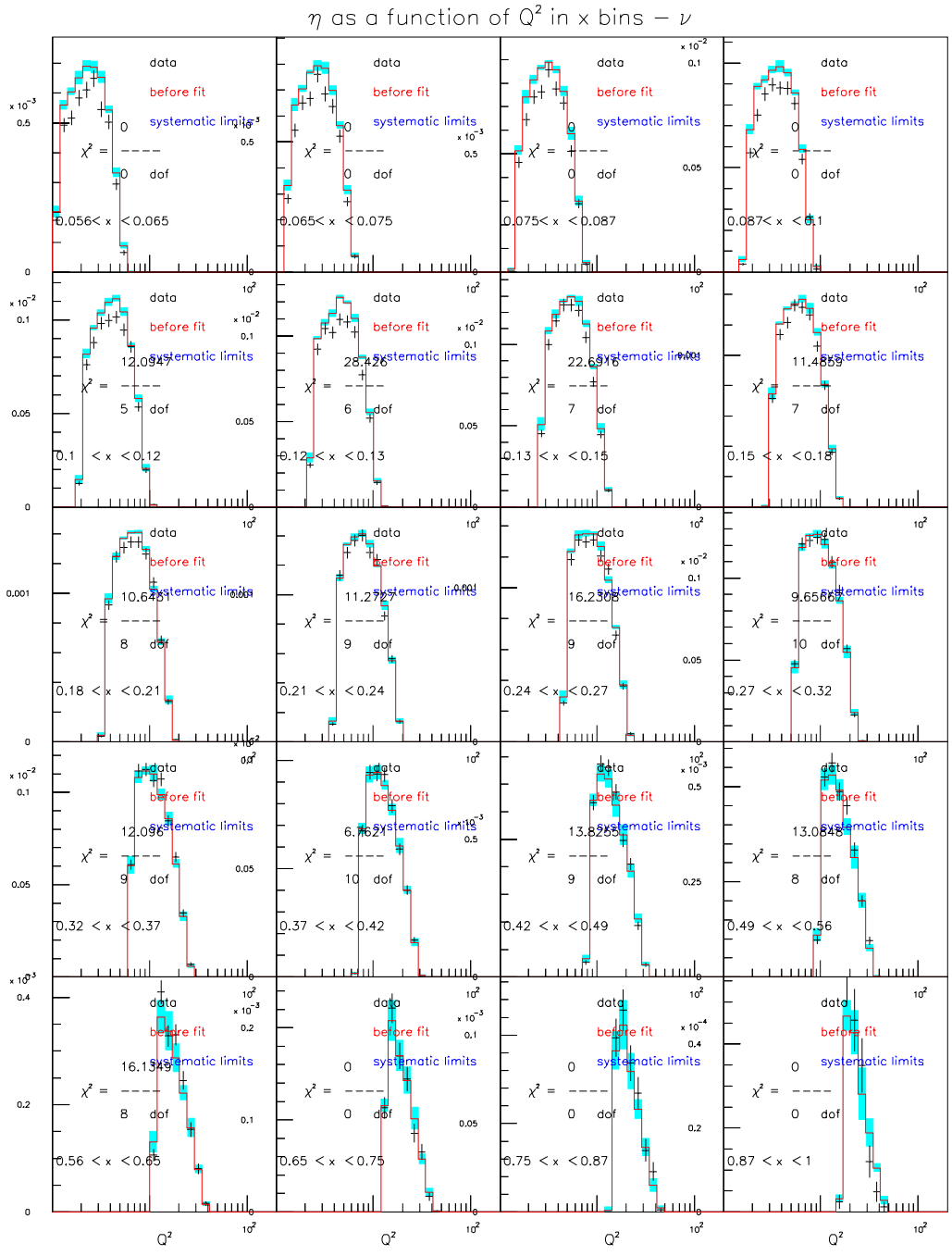

Figure C.2: GRV98NLO+EMC+HT+DRAD for $20 < E_\nu < 62$ GeV (ν mode)

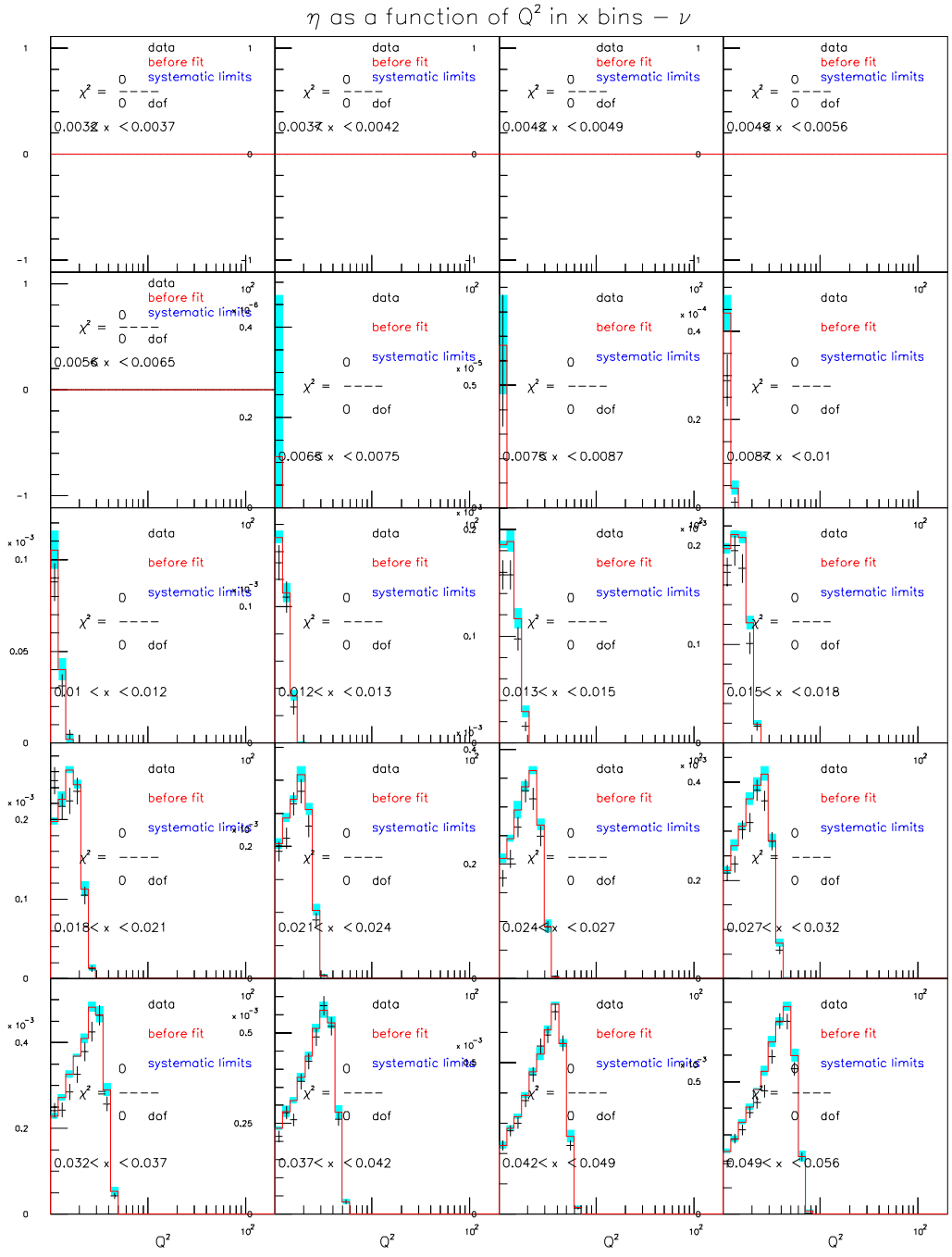

Figure C.3: GRV98NLO+EMC+HT+DRAD for $62 < E_\nu < 85$ GeV (ν mode)

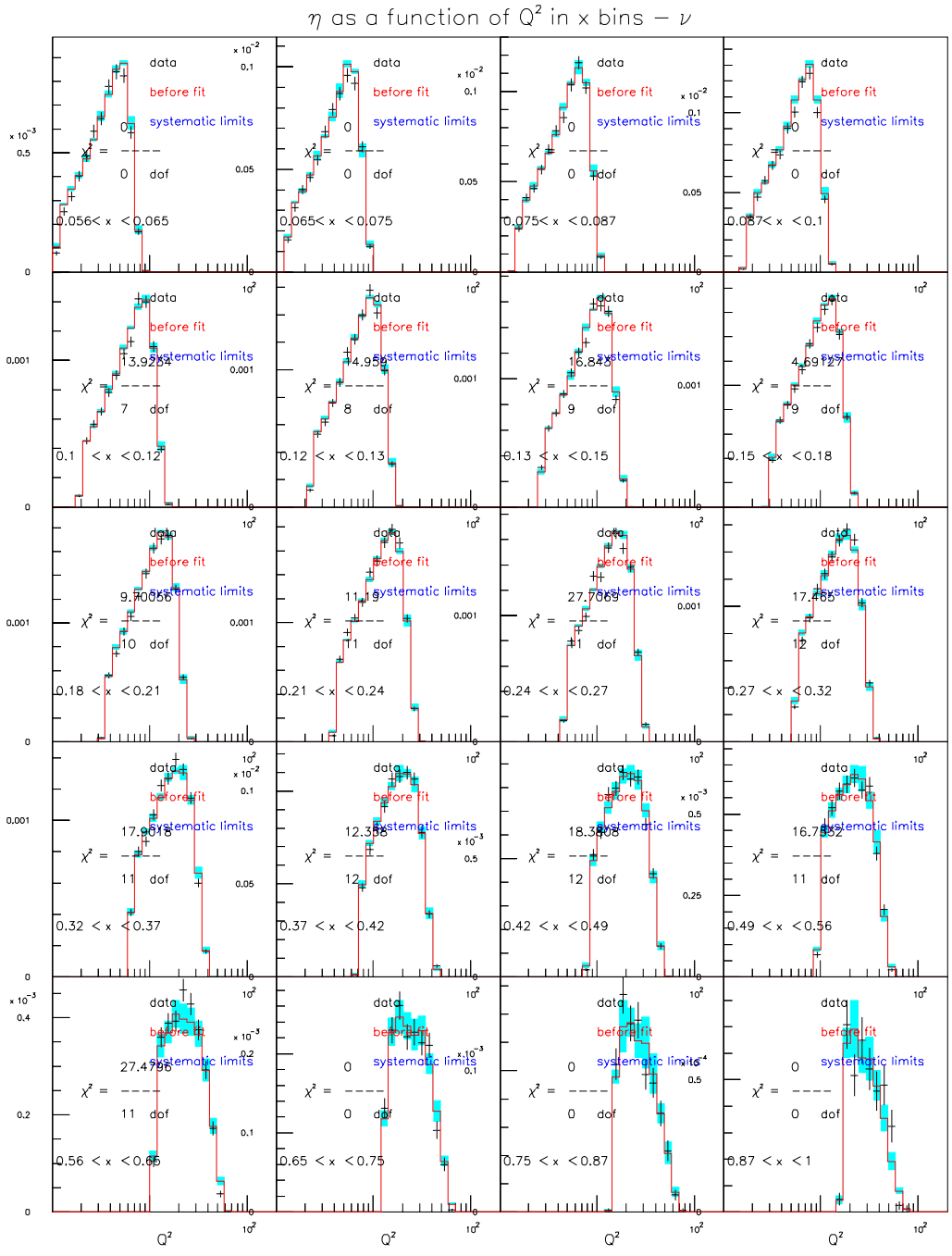

Figure C.4: GRV98NLO+EMC+HT+DRAD for $62 < E_\nu < 85$ GeV (ν mode)

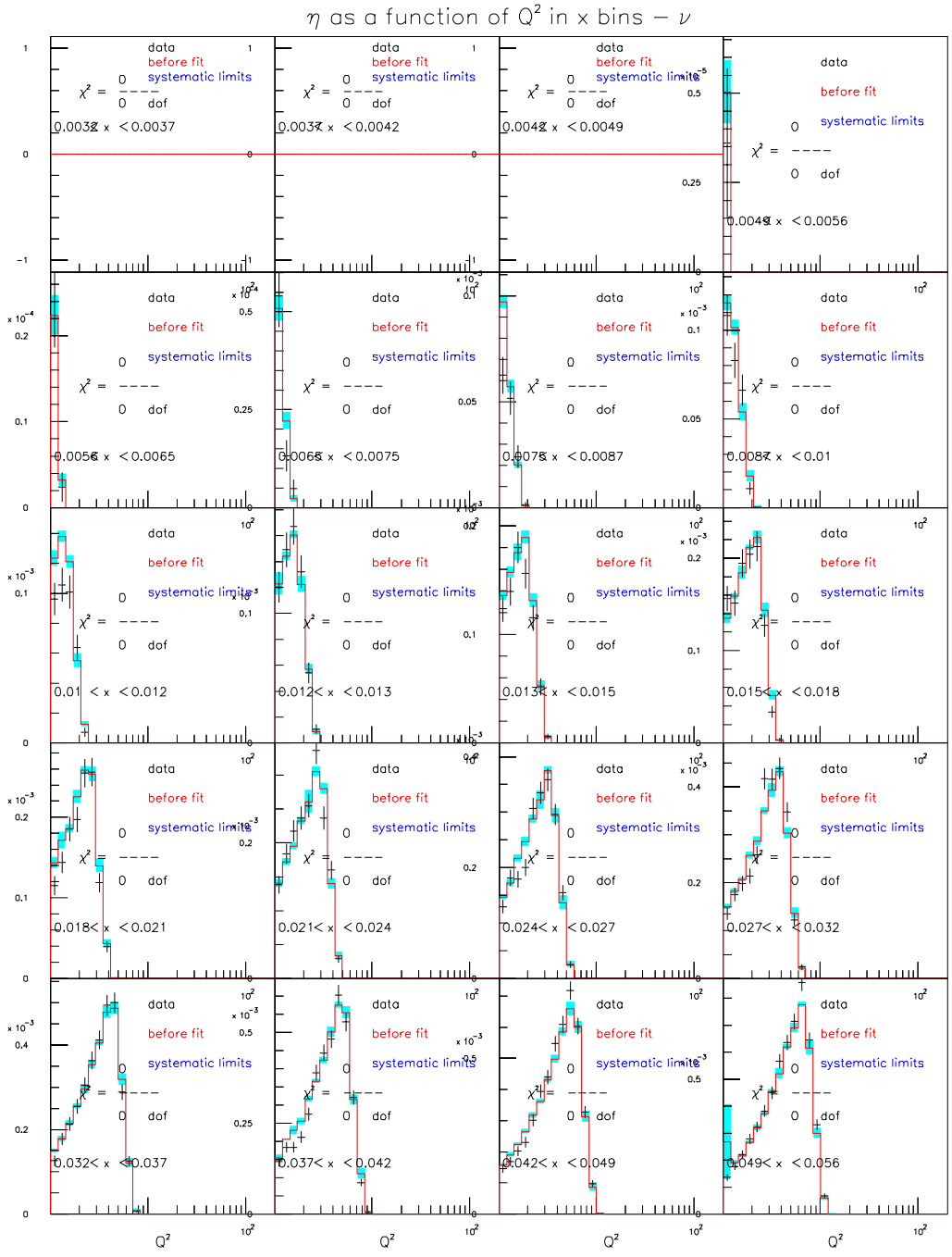

Figure C.5: GRV98NLO+EMC+HT+DRAD for $85 < E_\nu < 129$ GeV (ν mode)

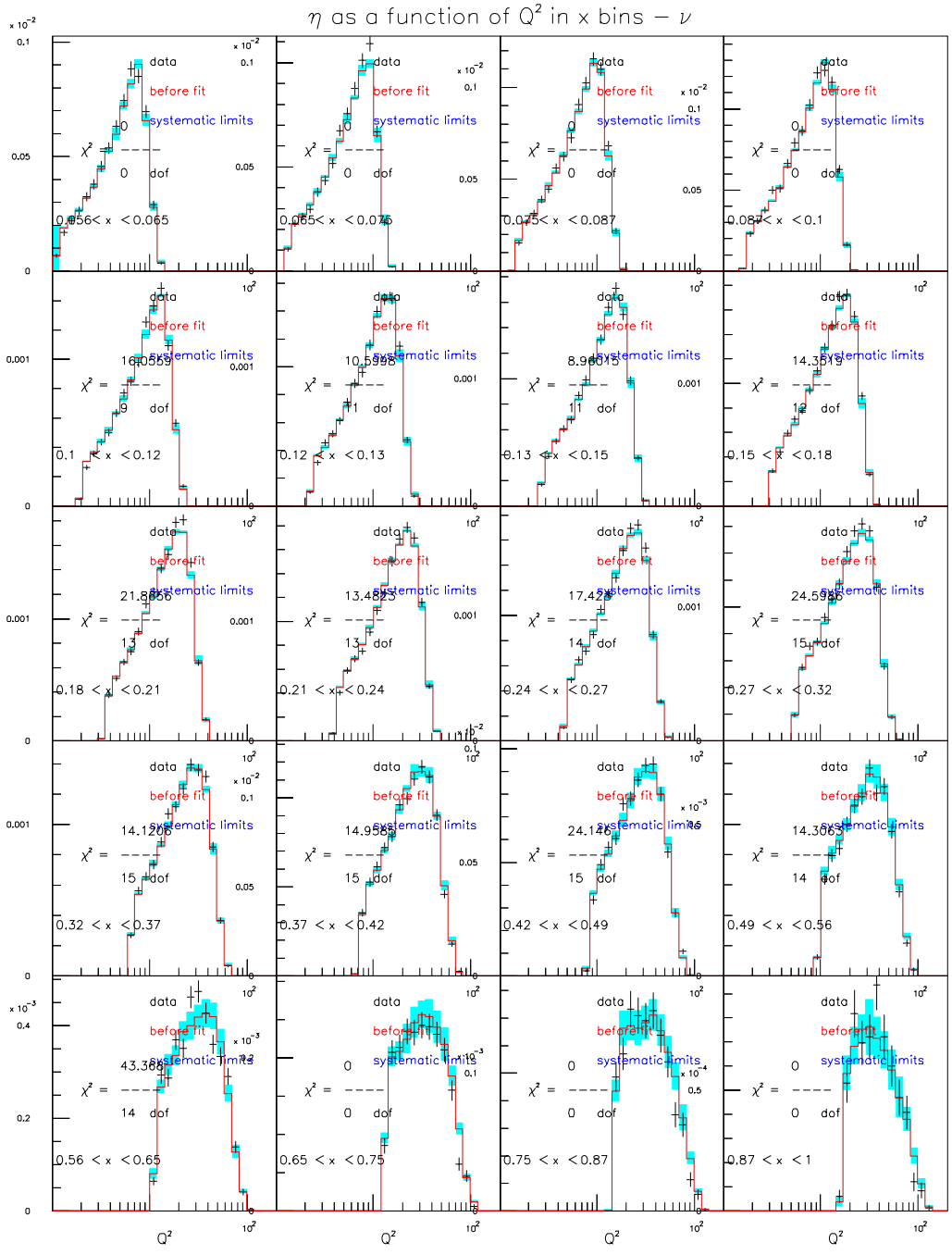

Figure C.6: GRV98NLO+EMC+HT+DRAD for $85 < E_\nu < 129$ GeV (ν mode)

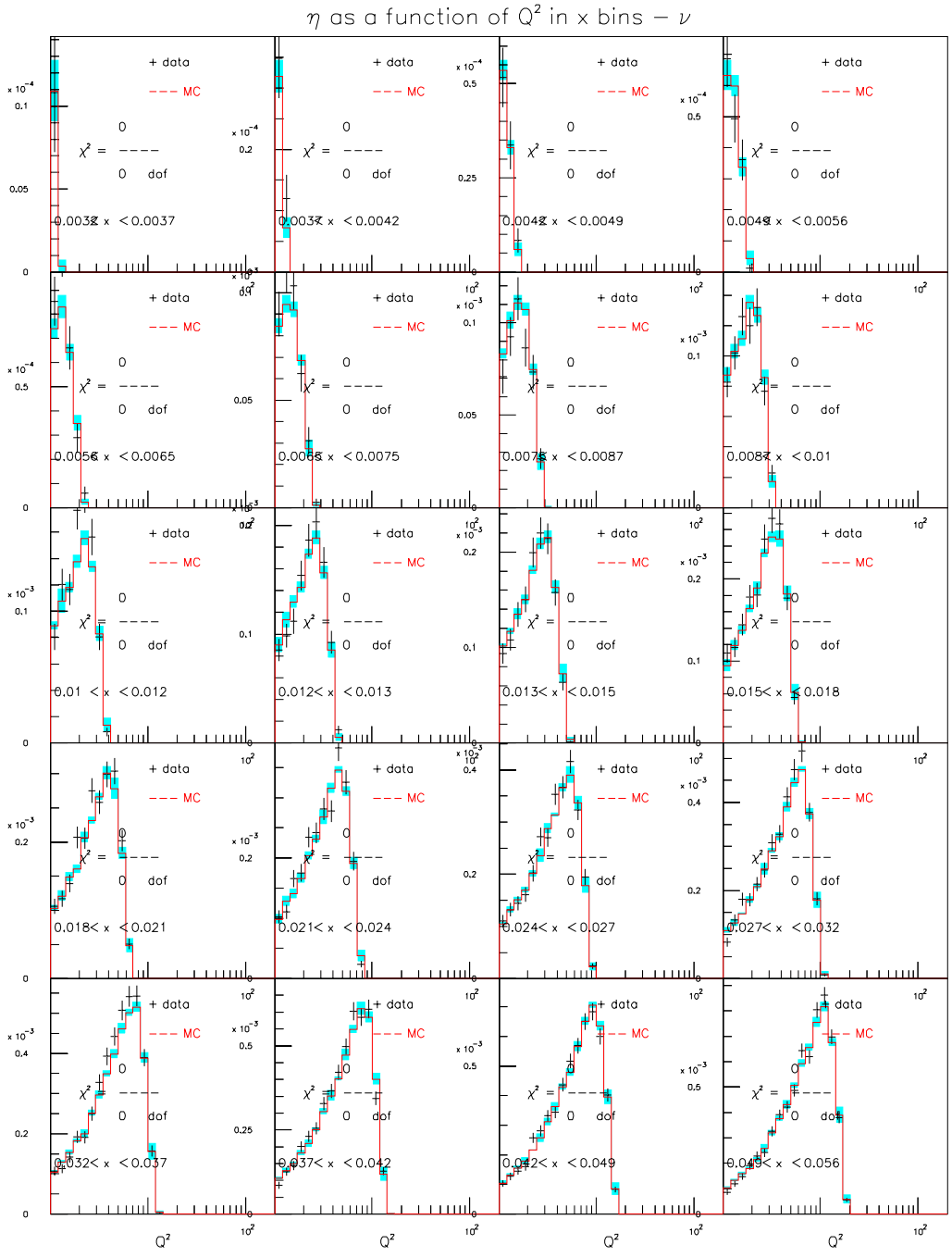

Figure C.7: GRV98NLO+EMC+HT+DRAD for $129 < E_\nu < 201$ GeV (ν mode)

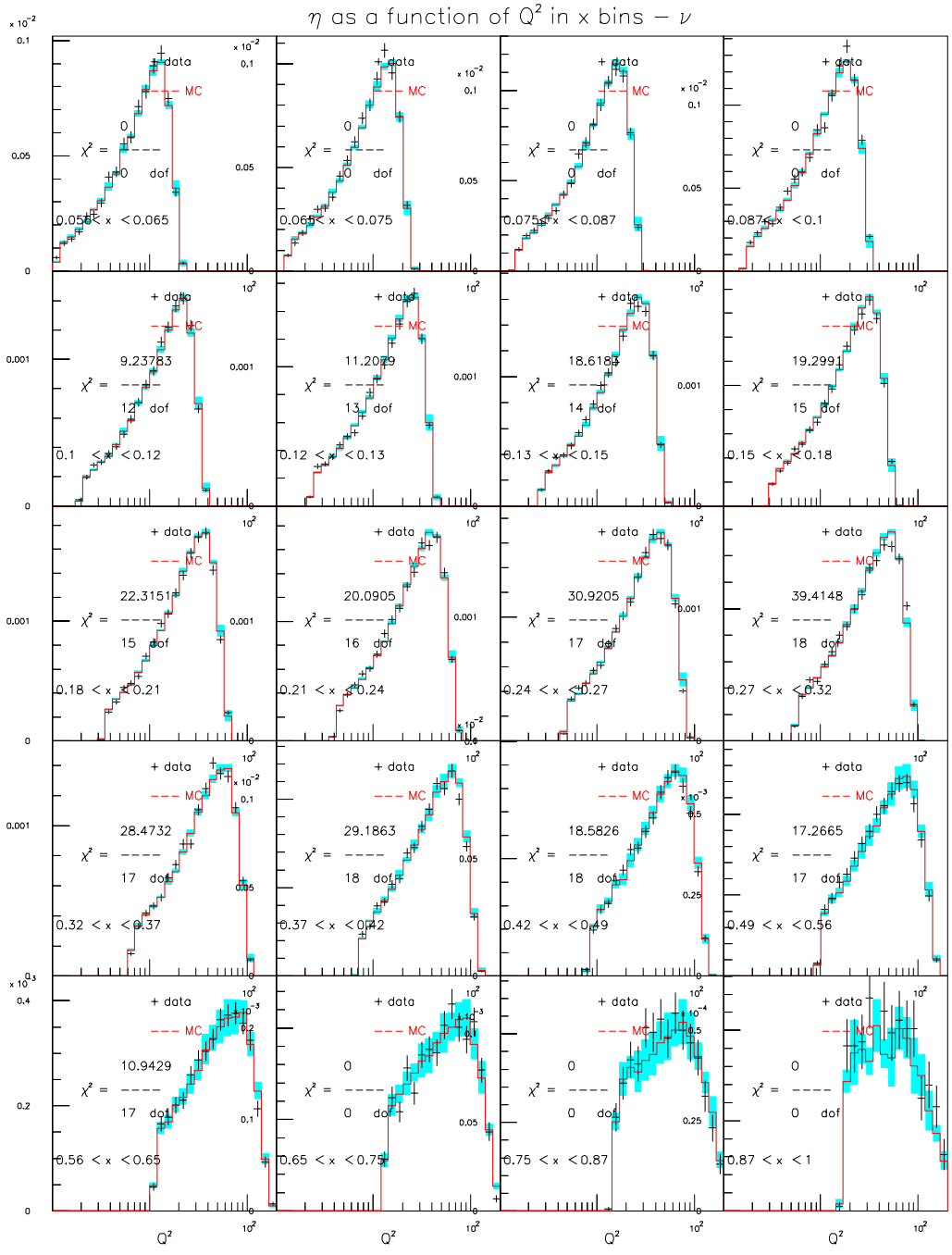

Figure C.8: GRV98NLO+EMC+HT+DRAD for $129 < E_\nu < 201$ GeV (ν mode)

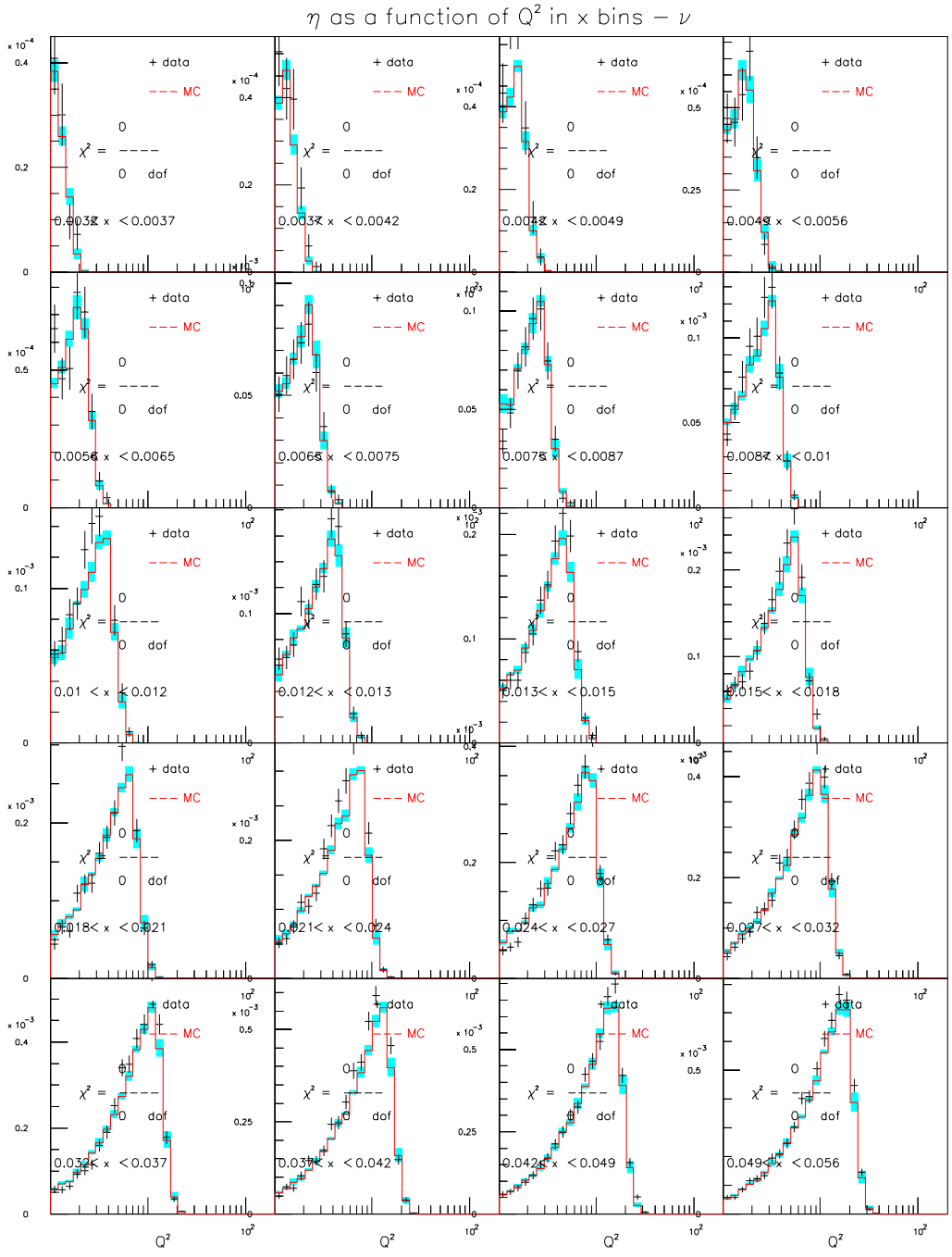

Figure C.9: GRV98NLO+EMC+HT+DRAD for $201 < E_\nu < 400$ GeV (ν mode)

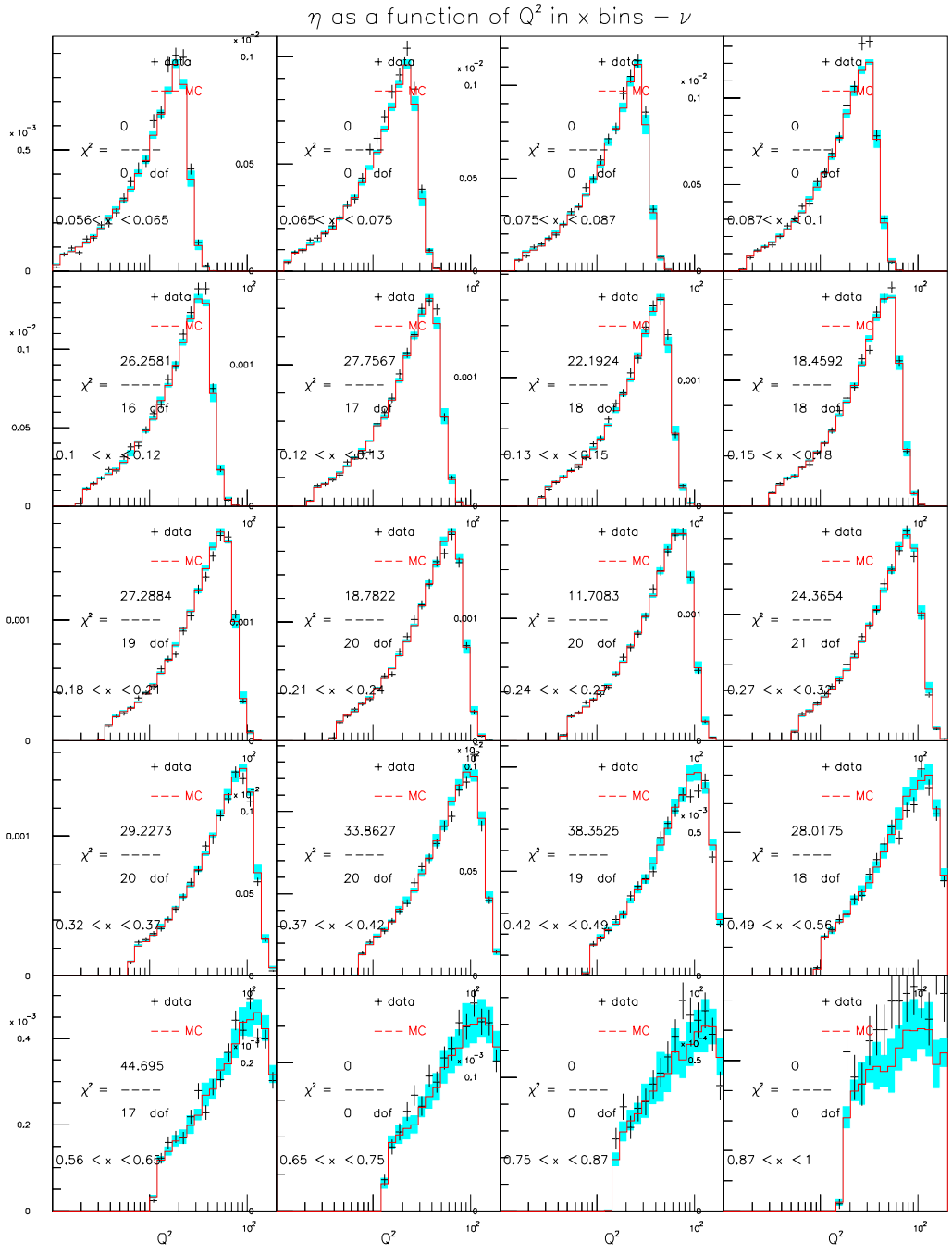

Figure C.10: GRV98NLO+EMC+HT+DRAD for $201 < E_\nu < 400$ GeV (ν mode)

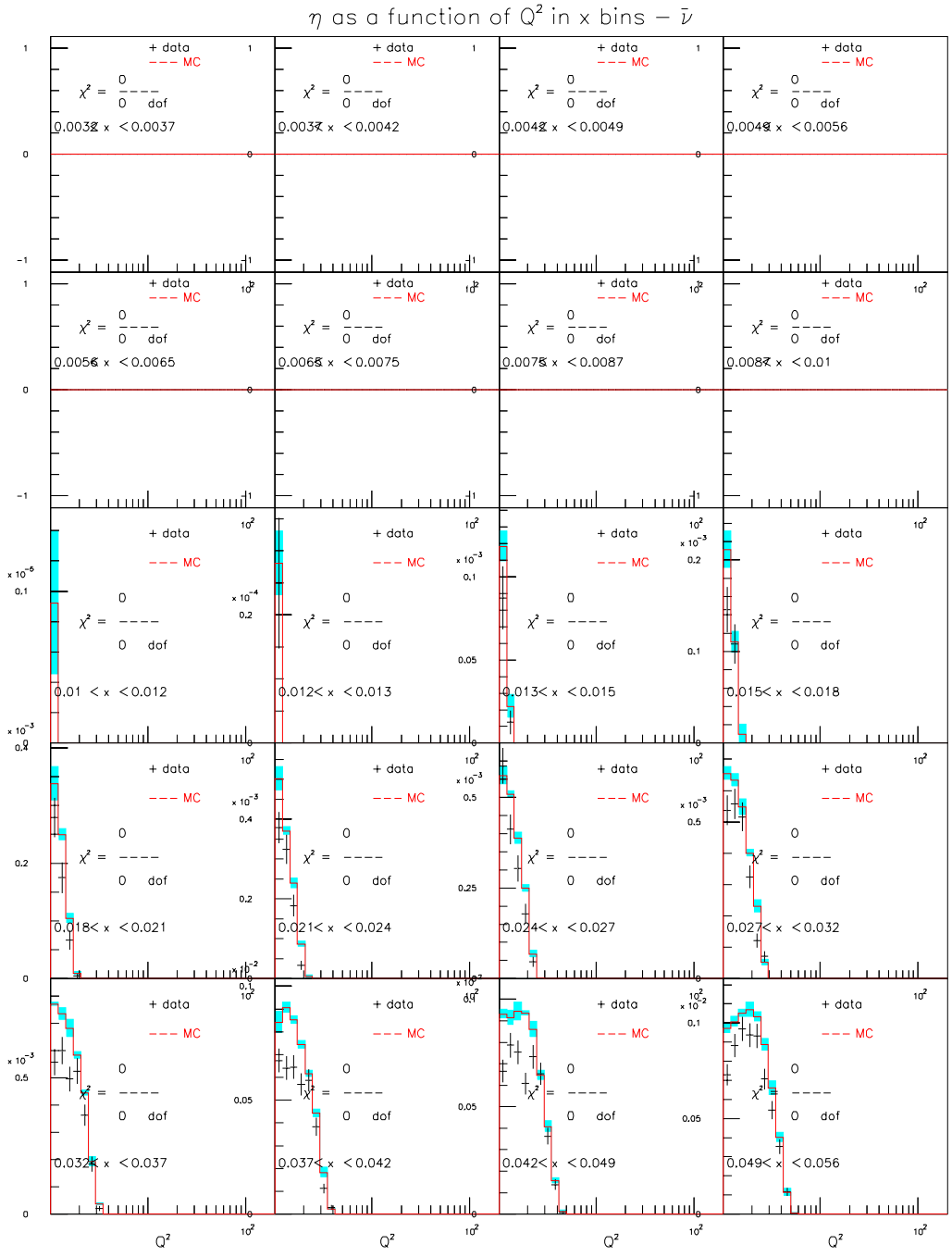

Figure C.11: GRV98NLO+EMC+HT+DRAD for $20 < E_\nu < 62$ GeV ($\overline{\nu}$ mode)

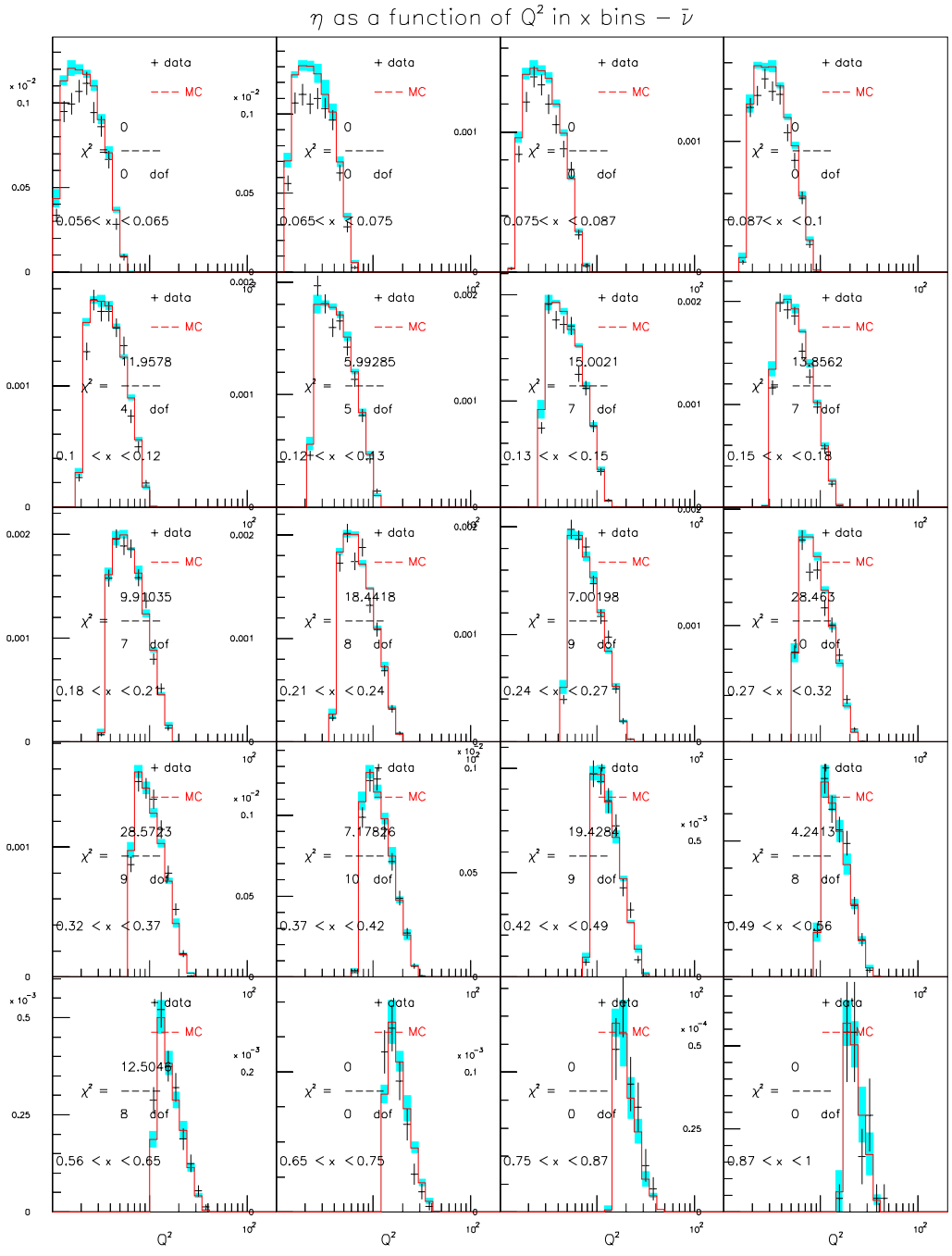

Figure C.12: GRV98NLO+EMC+HT+DRAD for $20 < E_\nu < 62$ GeV ($\overline{\nu}$ mode)

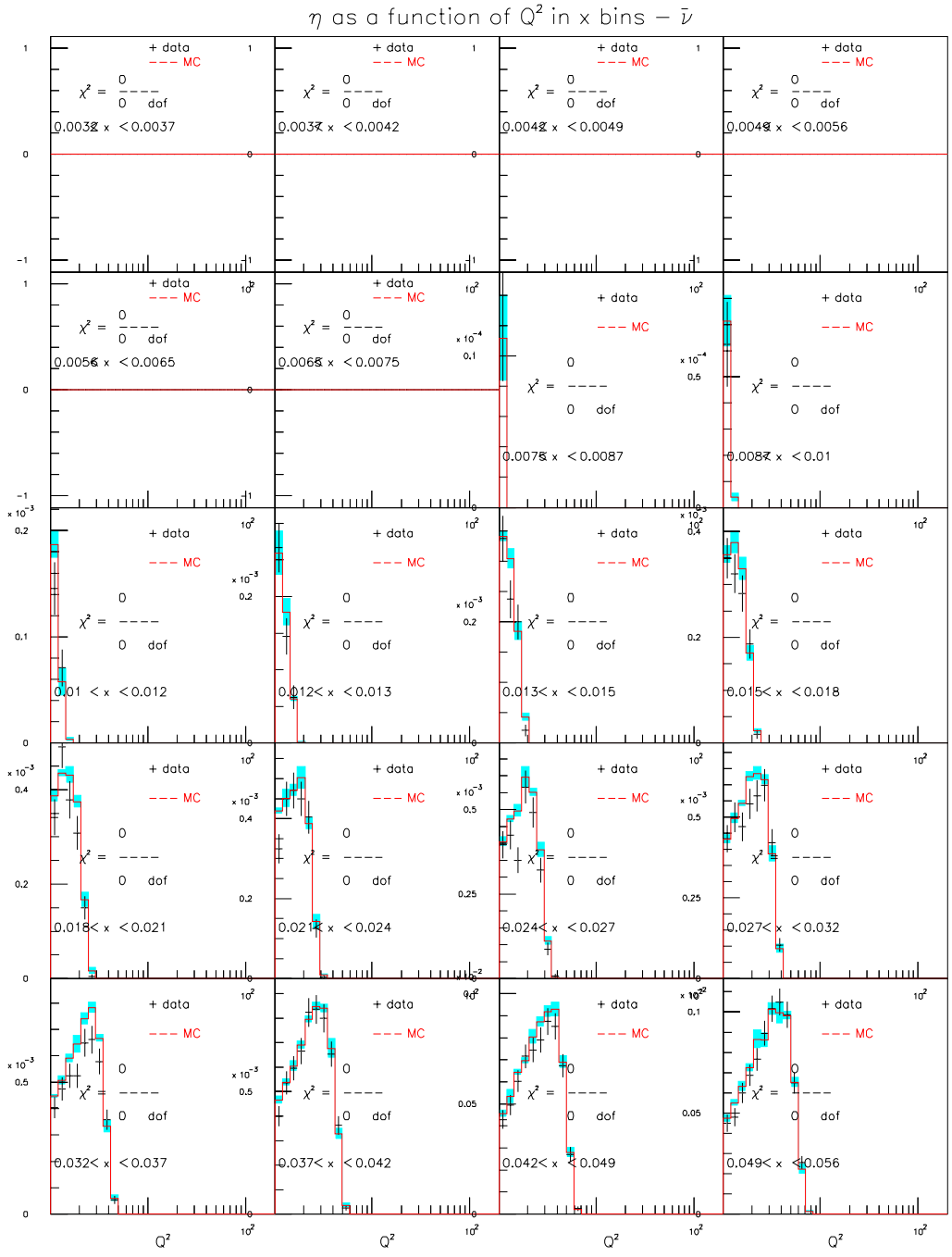

Figure C.13: GRV98NLO+EMC+HT+DRAD for $62 < E_\nu < 85$ GeV ($\overline{\nu}$ mode)

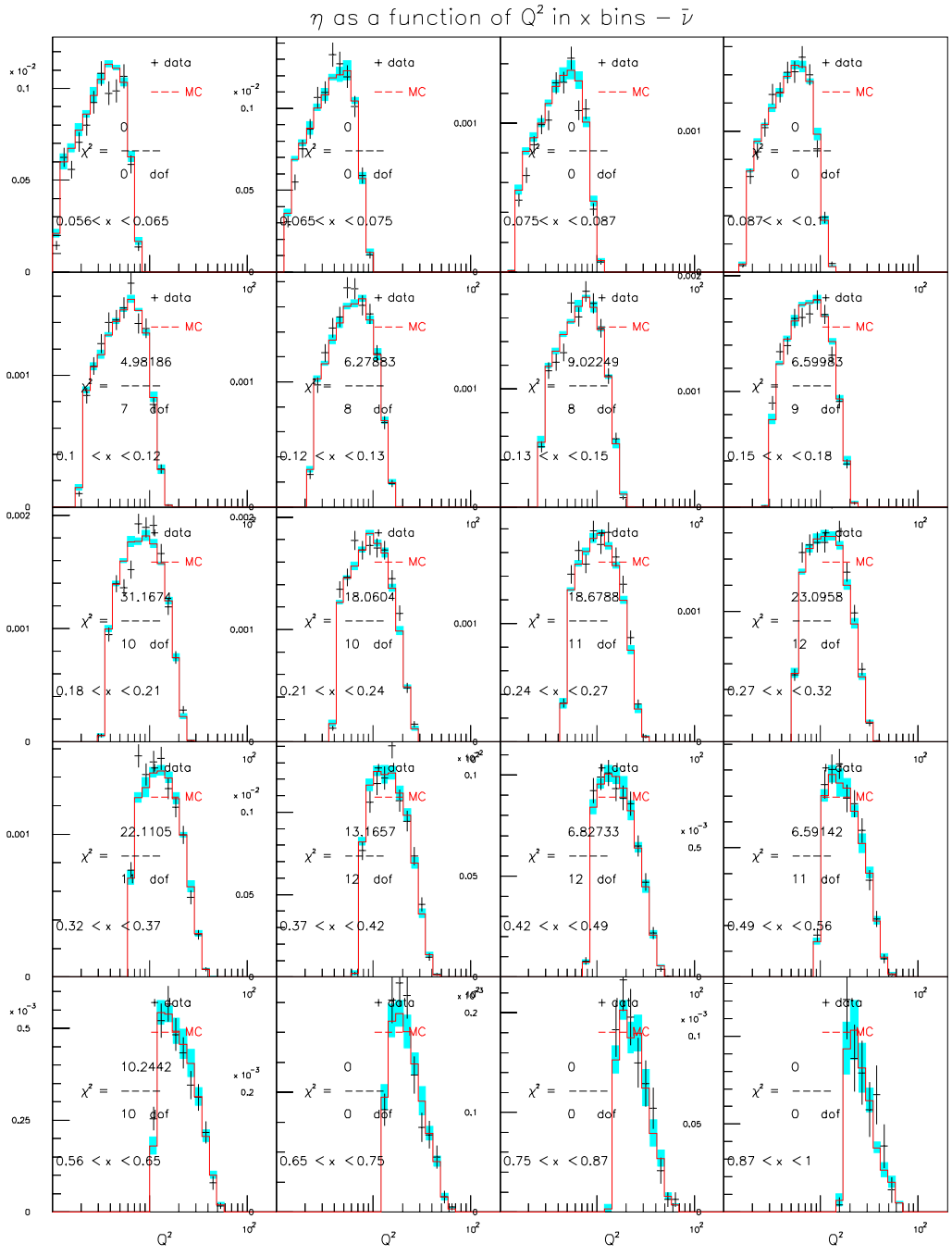

Figure C.14: GRV98NLO+EMC+HT+DRAD for $62 < E_\nu < 85$ GeV ($\overline{\nu}$ mode)

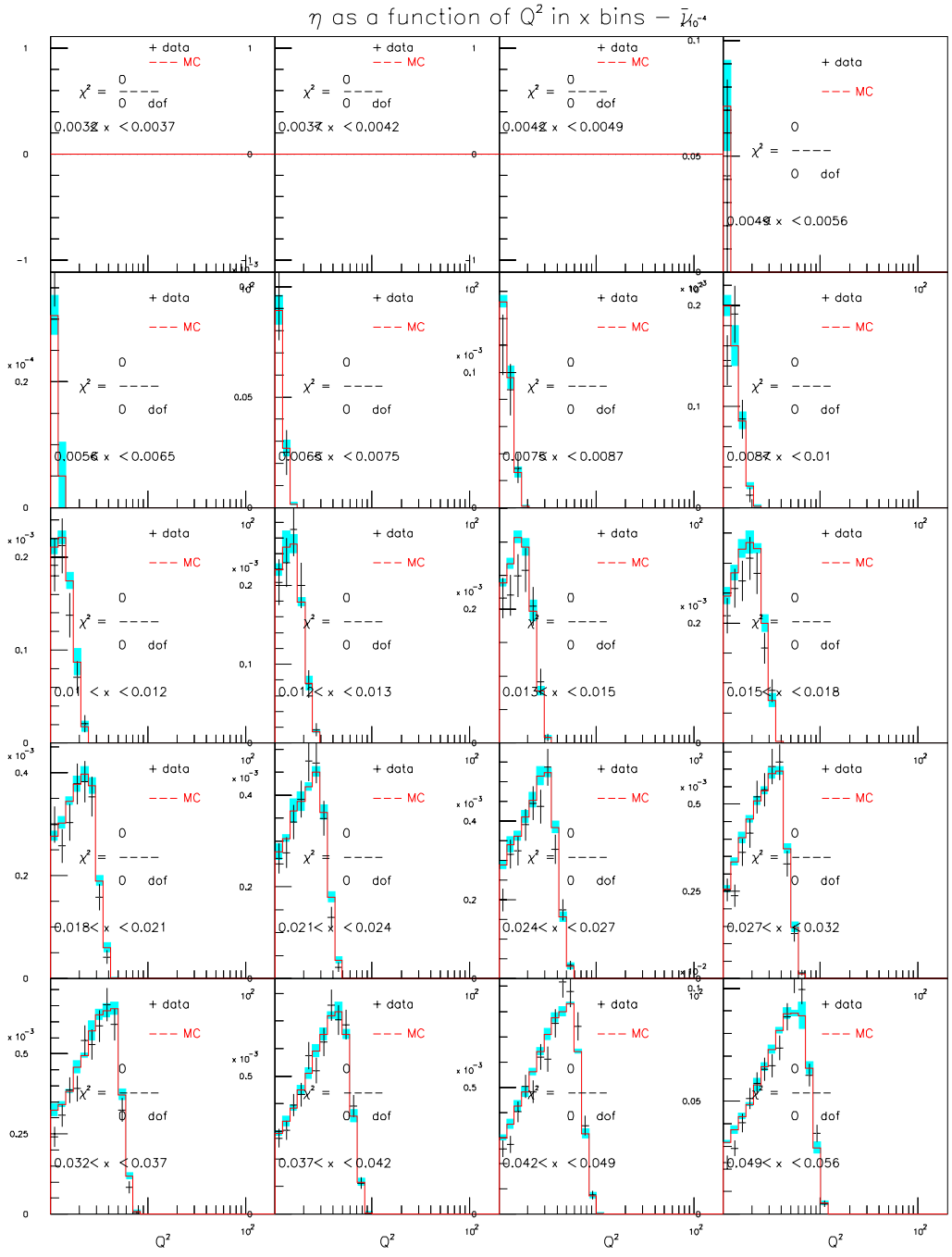

Figure C.15: GRV98NLO+EMC+HT+DRAD for $85 < E_\nu < 129$ GeV ($\overline{\nu}$ mode)

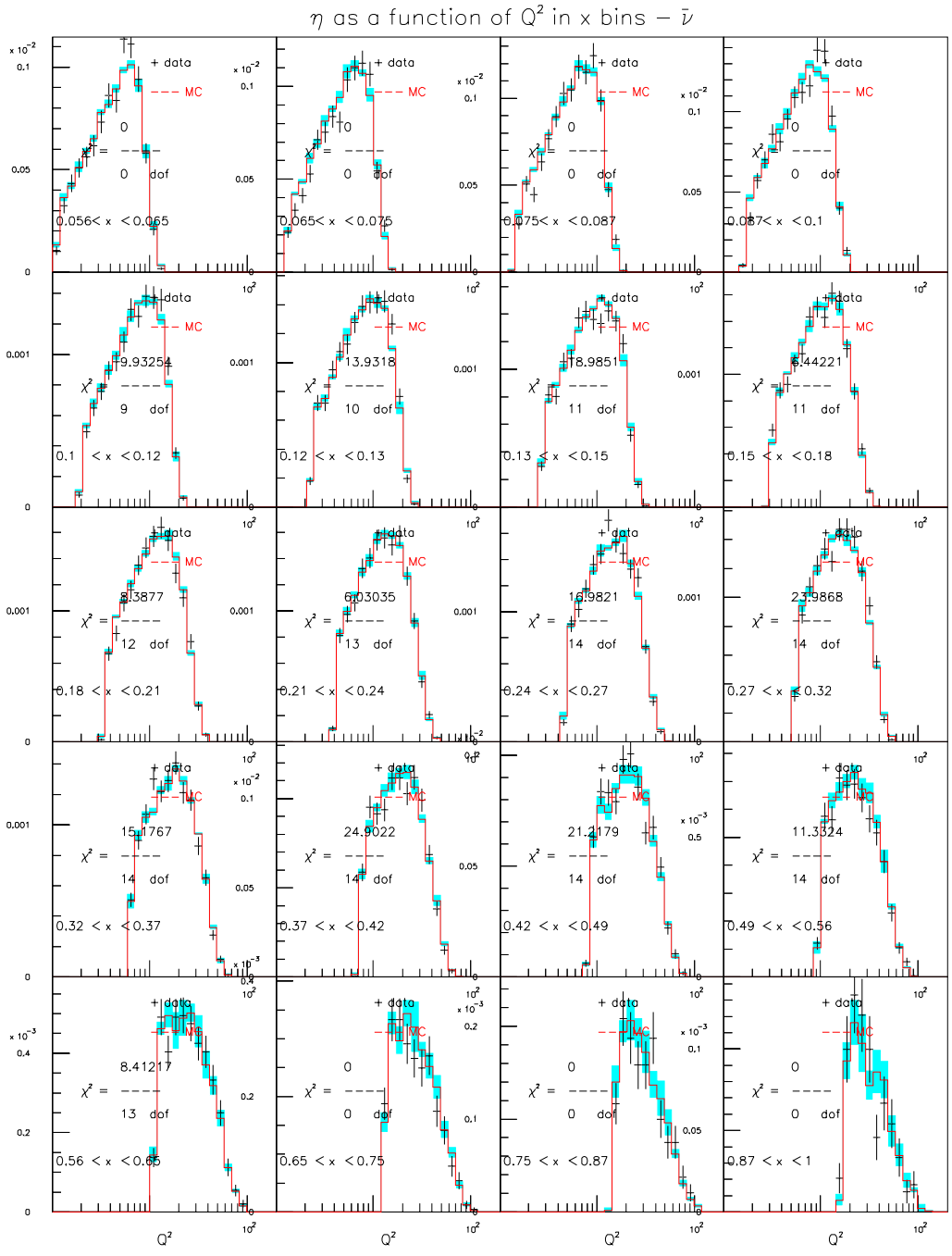

Figure C.16: GRV98NLO+EMC+HT+DRAD for $85 < E_\nu < 129$ GeV ($\overline{\nu}$ mode)

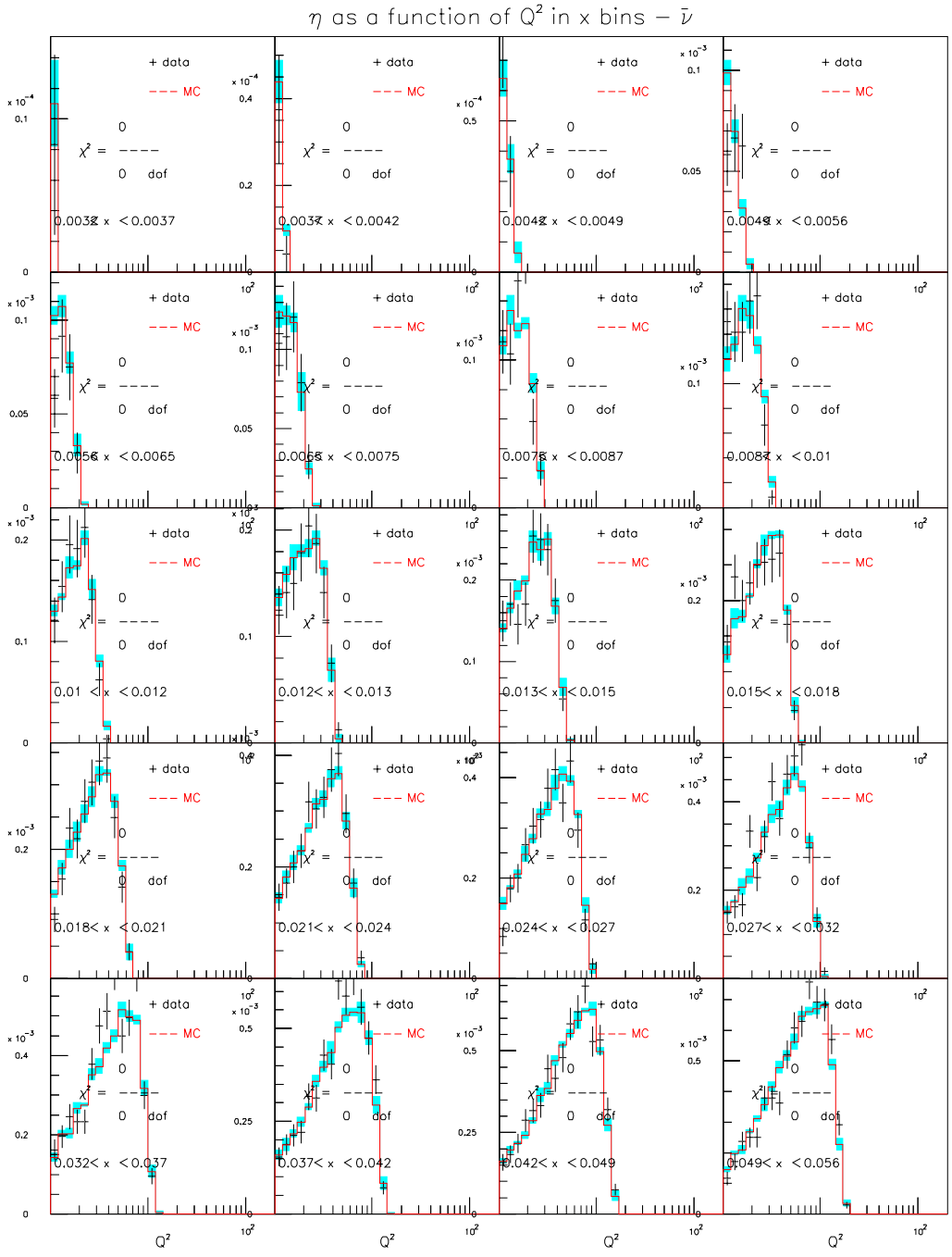

Figure C.17: GRV98NLO+EMC+HT+DRAD for $129 < E_\nu < 201$ GeV ($\overline{\nu}$ mode)

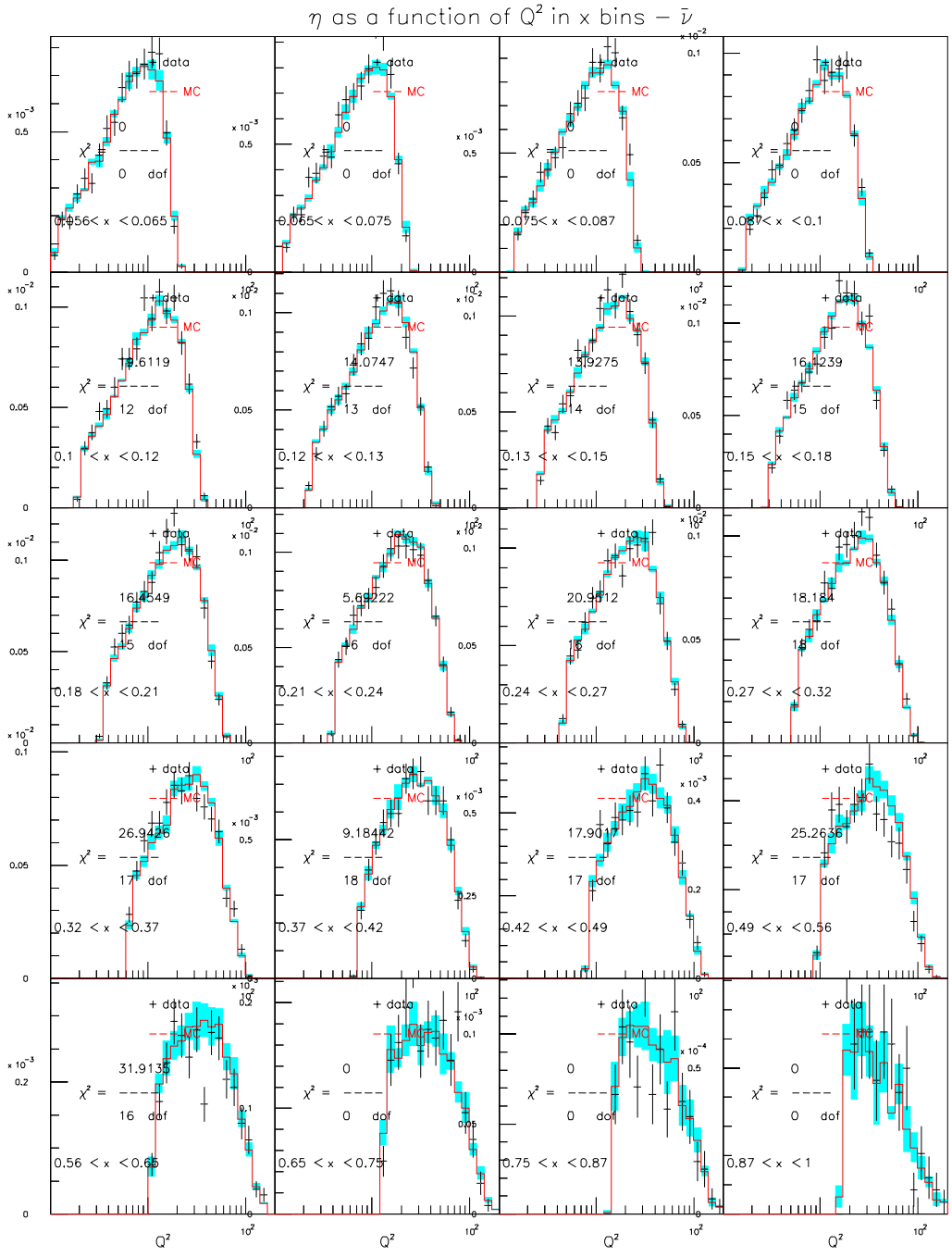

Figure C.18: GRV98NLO+EMC+HT+DRAD for $129 < E_\nu < 201$ GeV ($\overline{\nu}$ mode)

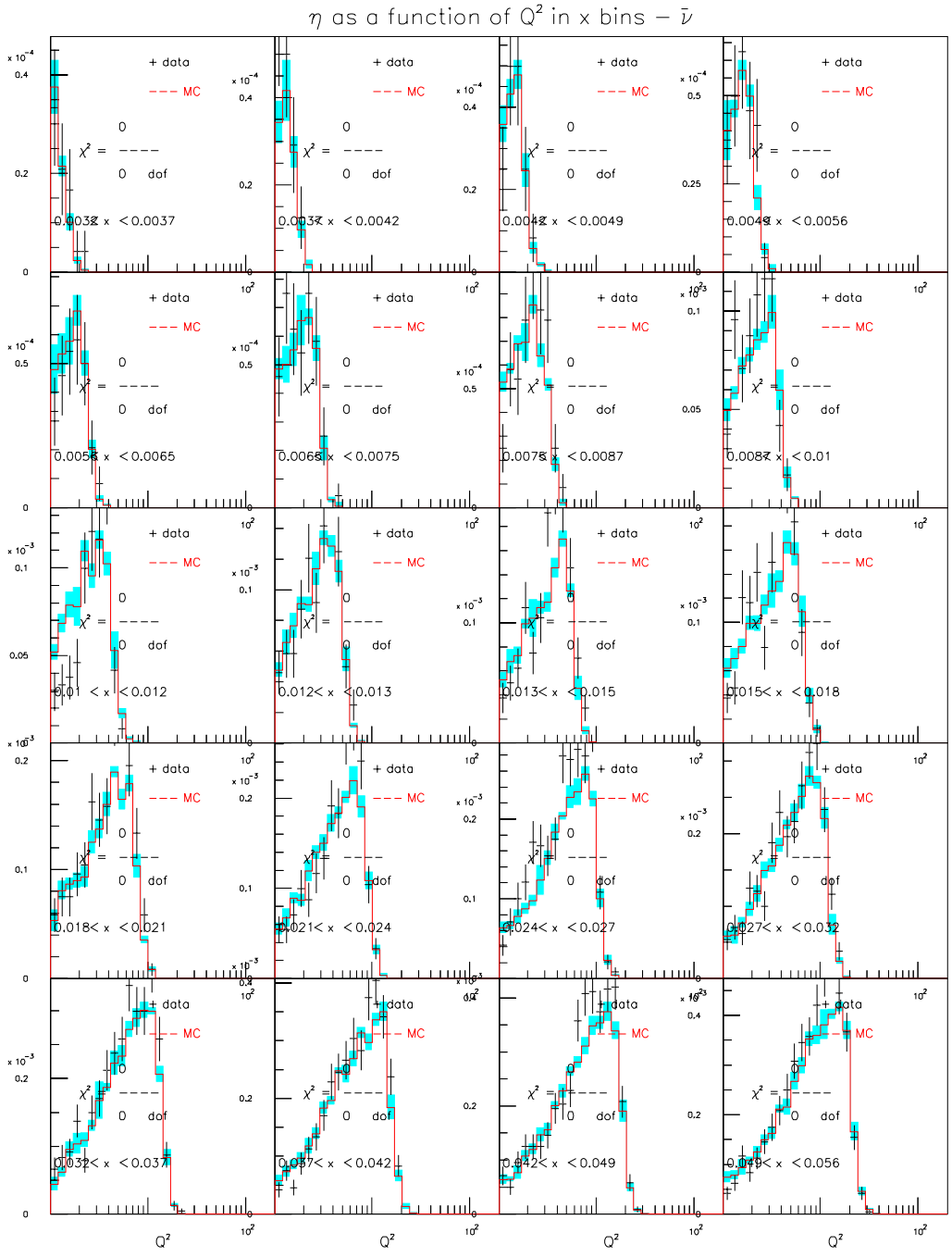

Figure C.19: GRV98NLO+EMC+HT+DRAD for $201 < E_\nu < 400$ GeV ($\overline{\nu}$ mode)

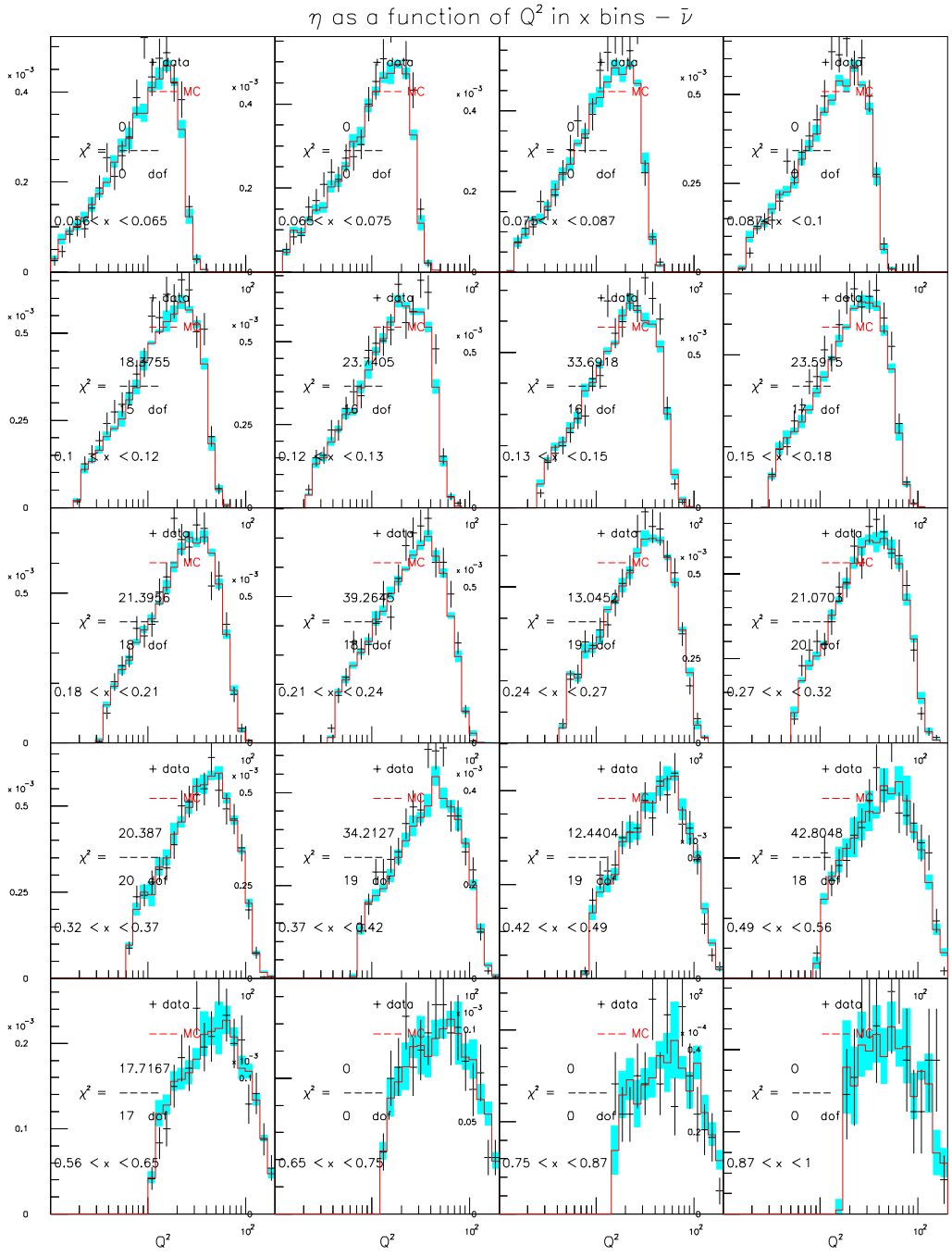

Figure C.20: GRV98NLO+EMC+HT+DRAD for $201 < E_\nu < 400$ GeV ($\overline{\nu}$ mode)

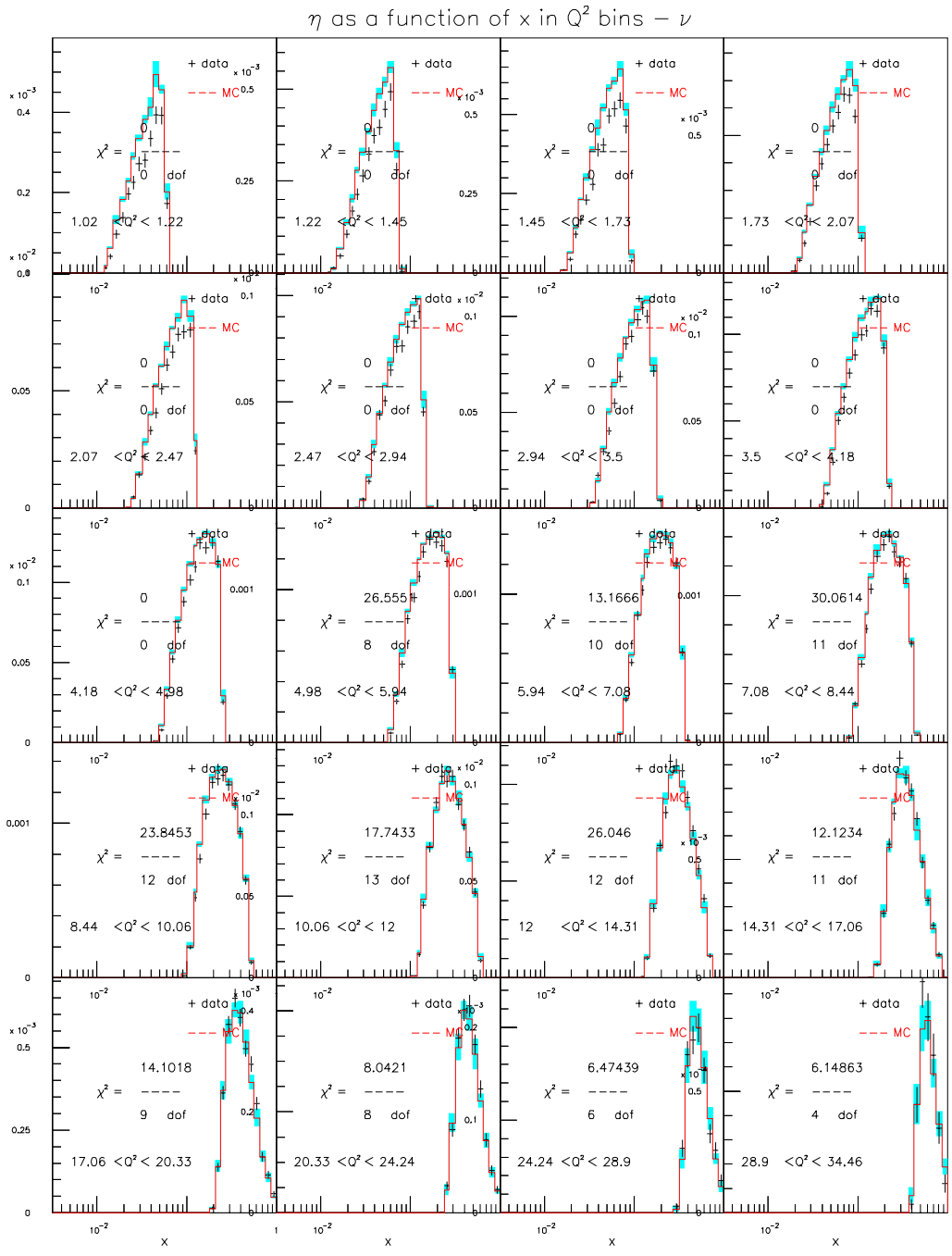

Figure C.21: GRV98NLO+EMC+HT+DRAD for $20 < E_\nu < 62$ GeV (ν mode)

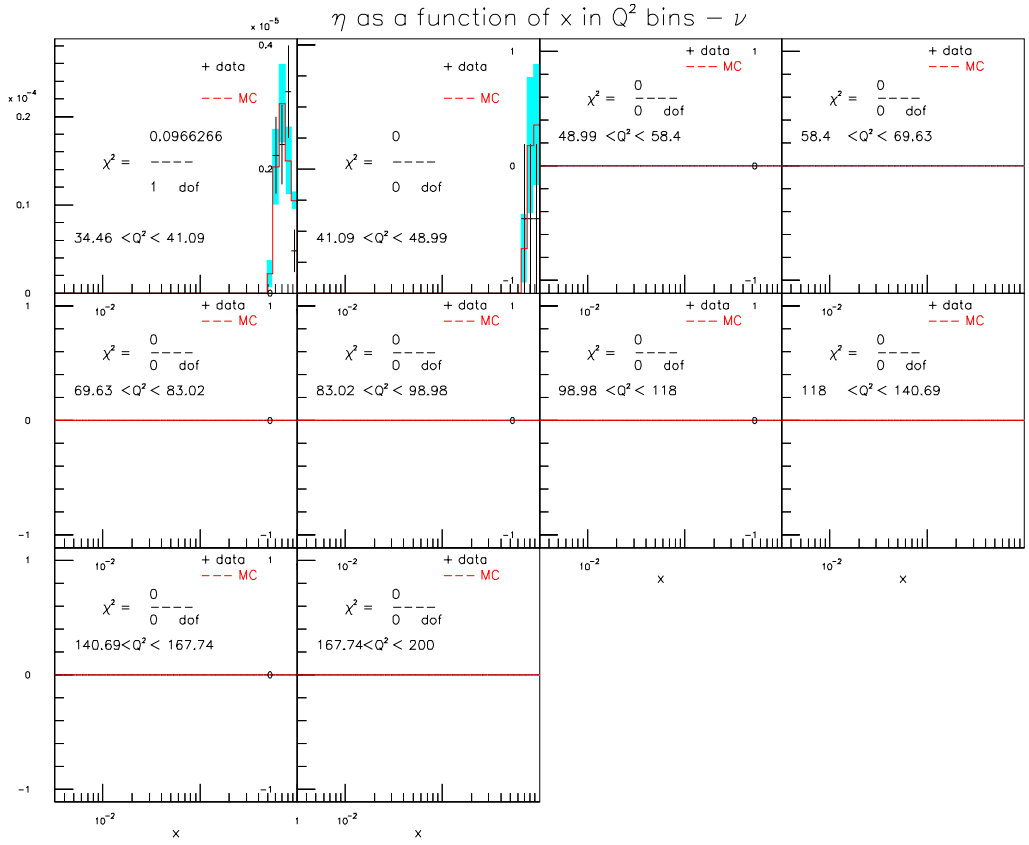

Figure C.22: GRV98NLO+EMC+HT+DRAD for $20 < E_\nu < 62$ GeV (ν mode)

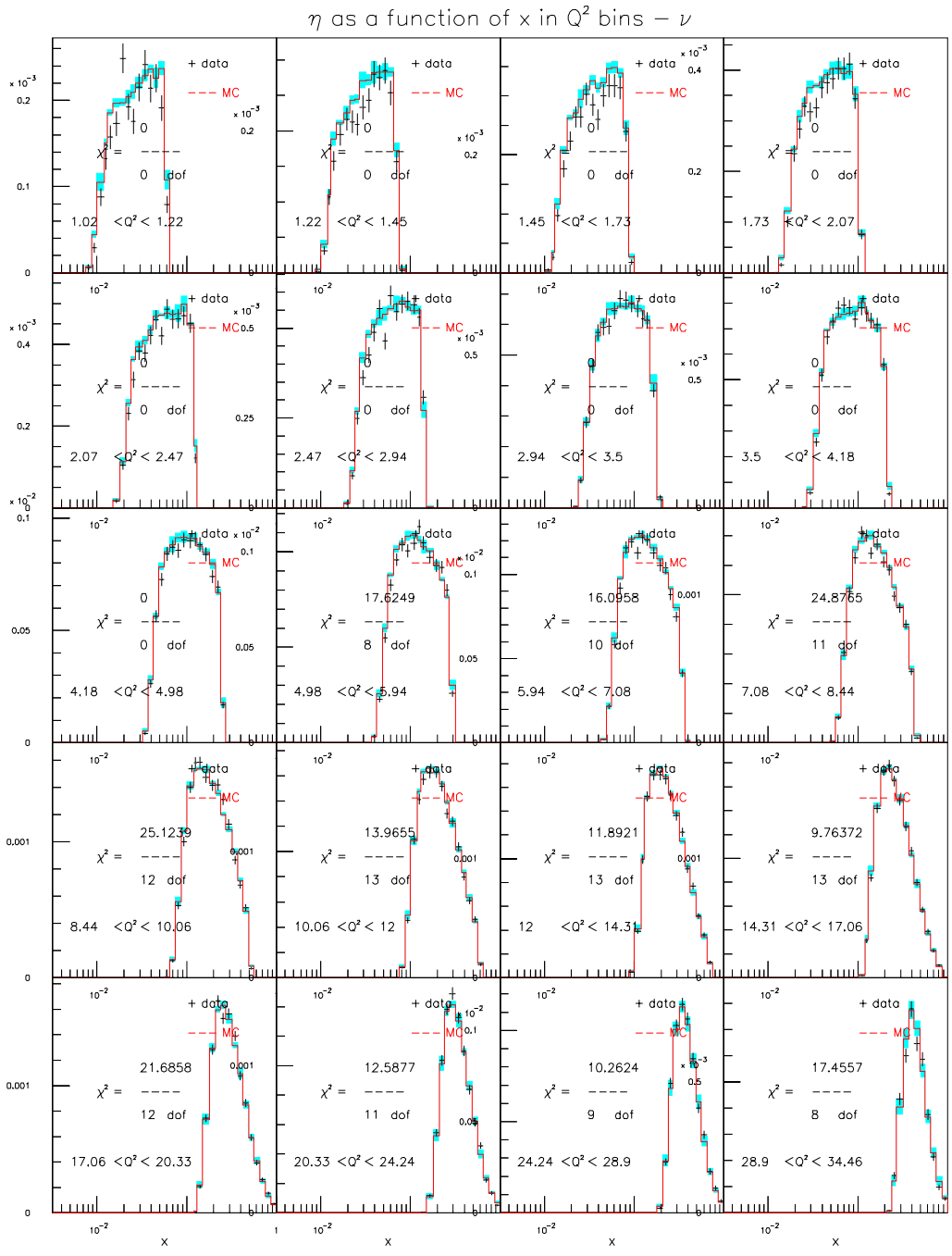

Figure C.23: GRV98NLO+EMC+HT+DRAD for $62 < E_\nu < 85$ GeV (ν mode)

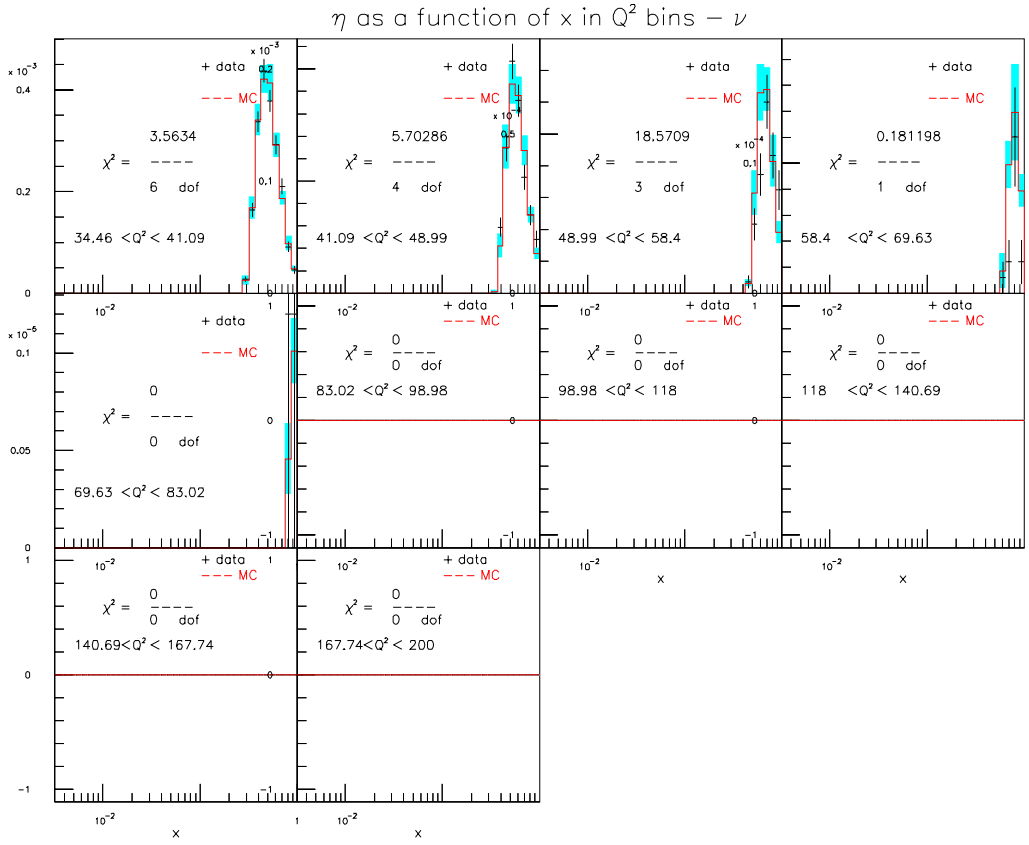

Figure C.24: GRV98NLO+EMC+HT+DRAD for $62 < E_\nu < 85$ GeV (ν mode)

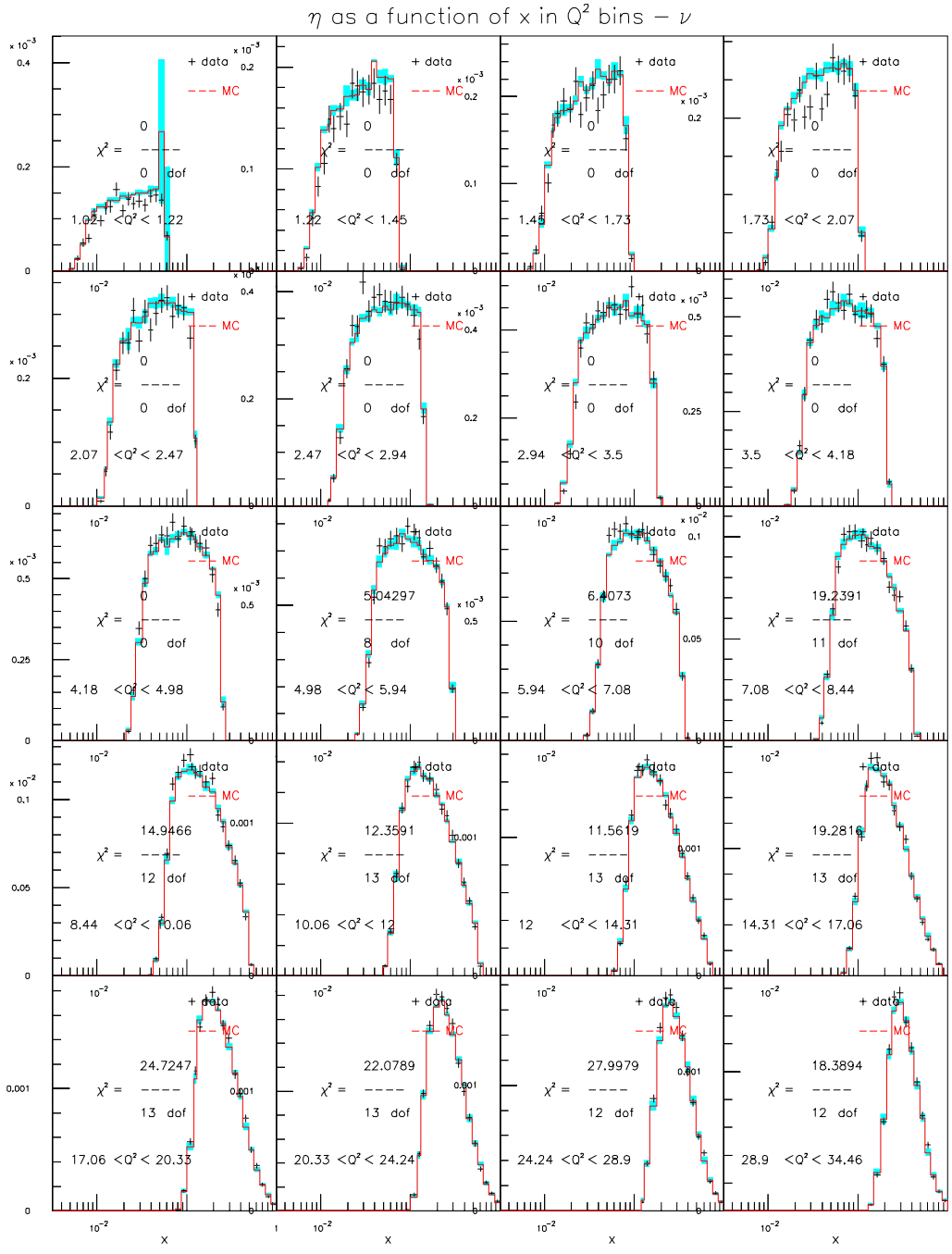

Figure C.25: GRV98NLO+EMC+HT+DRAD for $85 < E_\nu < 129$ GeV (ν mode)

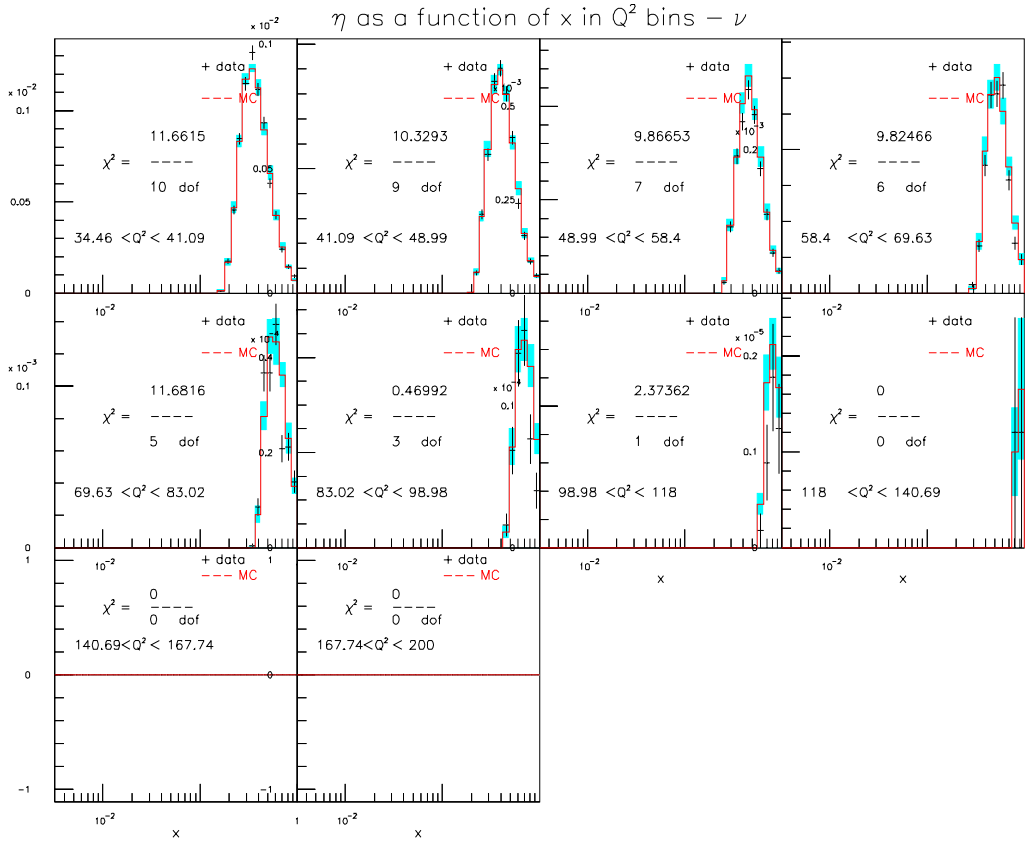

Figure C.26: GRV98NLO+EMC+HT+DRAD for $85 < E_\nu < 129$ GeV (ν mode)

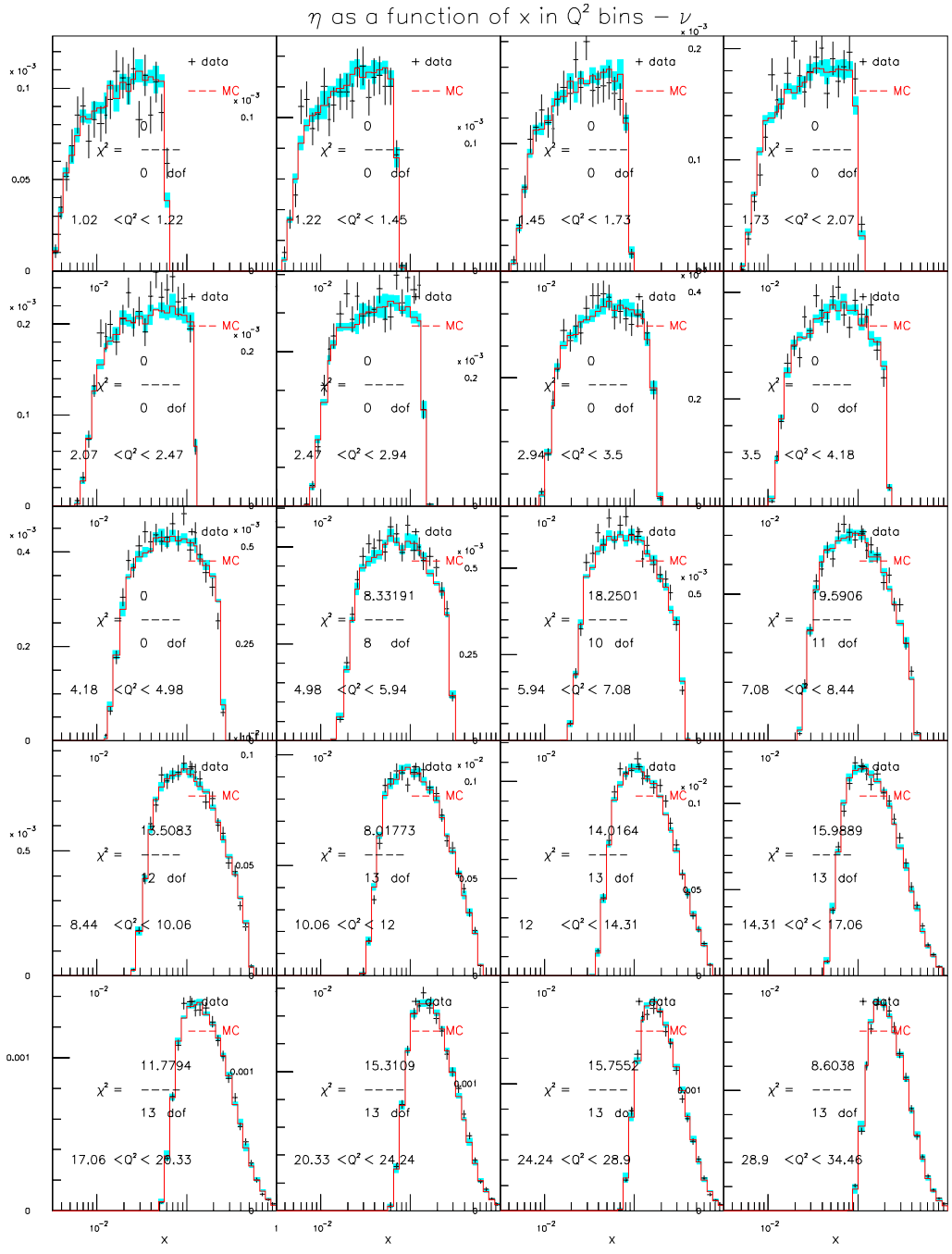

Figure C.27: GRV98NLO+EMC+HT+DRAD for $129 < E_\nu < 201$ GeV (ν mode)

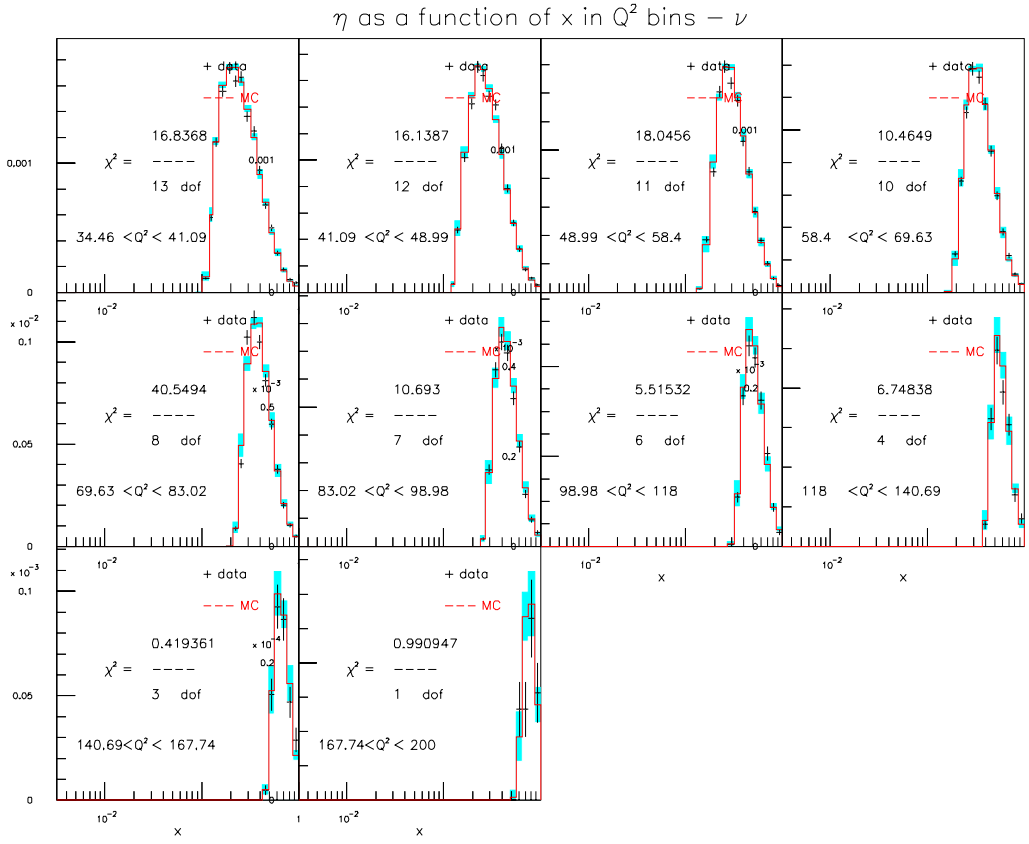

Figure C.28: GRV98NLO+EMC+HT+DRAD for $129 < E_\nu < 201$ GeV (ν mode)

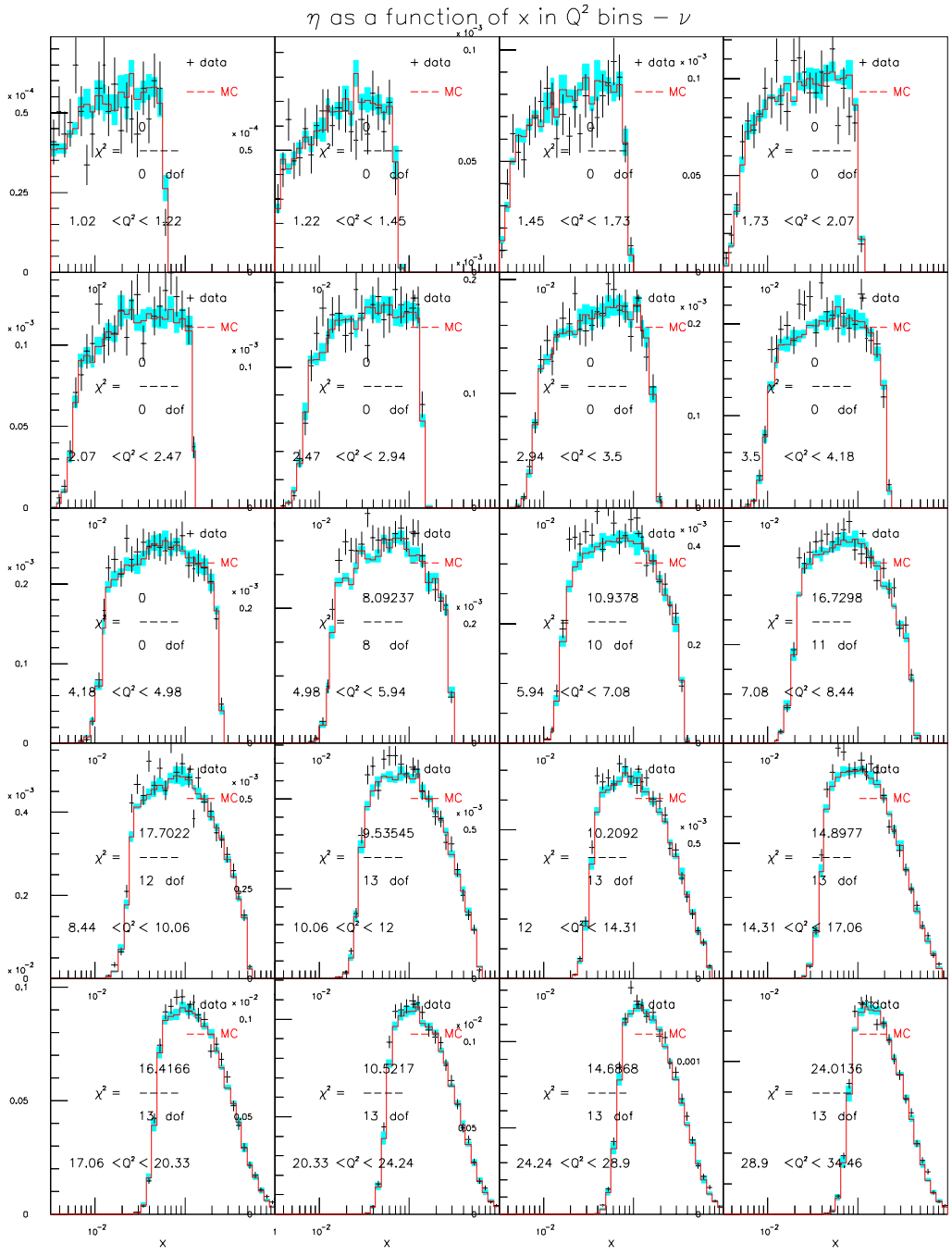

Figure C.29: GRV98NLO+EMC+HT+DRAD for $201 < E_\nu < 400$ GeV (ν mode)

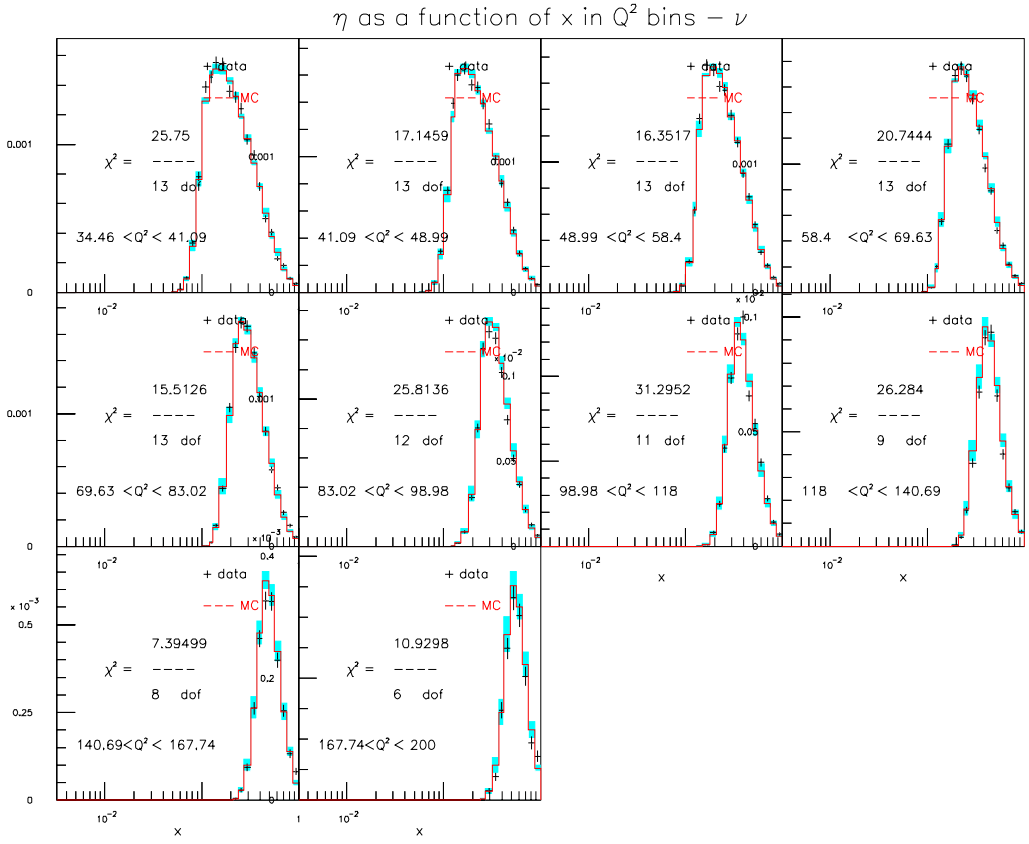

Figure C.30: GRV98NLO+EMC+HT+DRAD for $201 < E_\nu < 400$ GeV (ν mode)

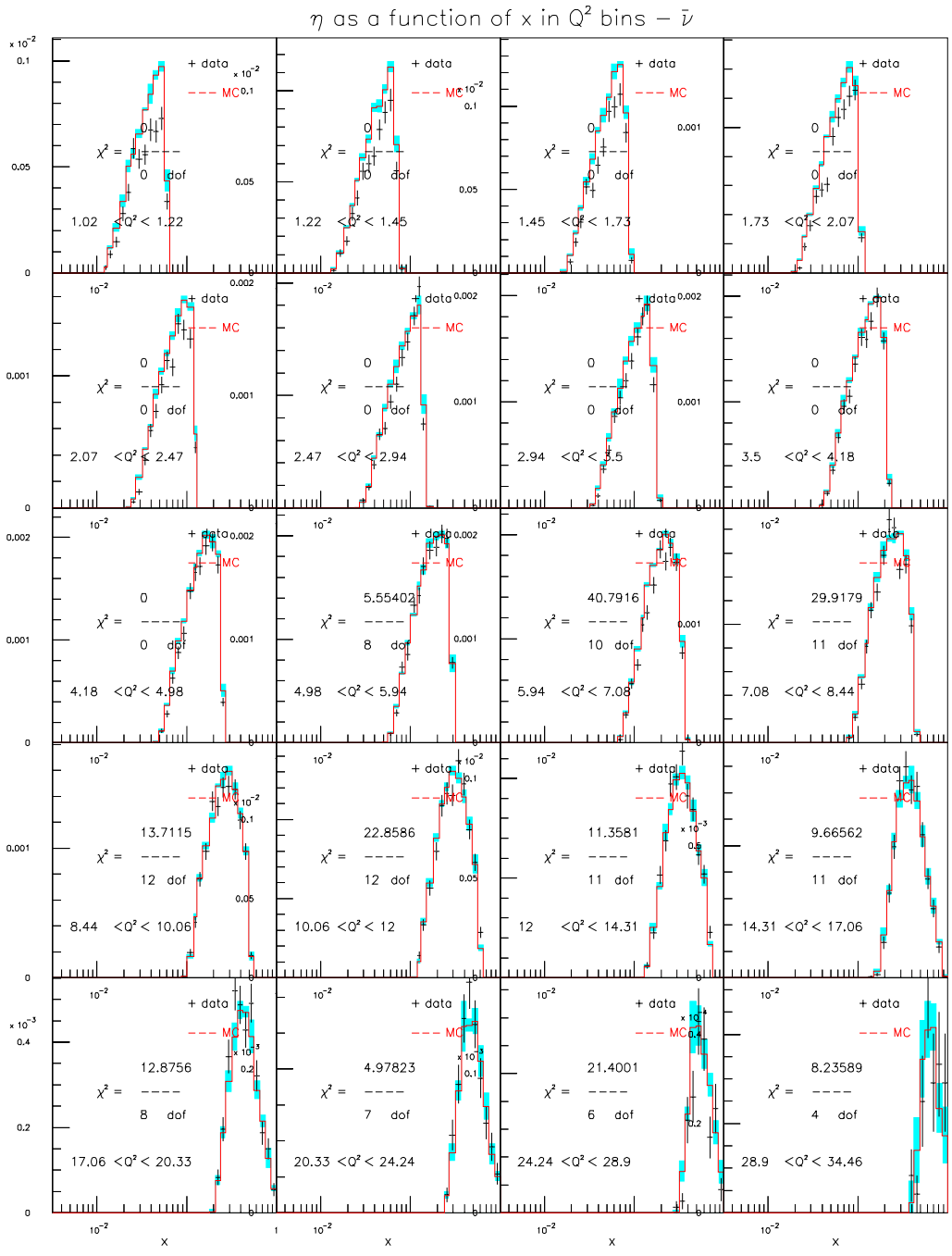

Figure C.31: GRV98NLO+EMC+HT+DRAD for $20 < E_\nu < 62$ GeV ($\overline{\nu}$ mode)

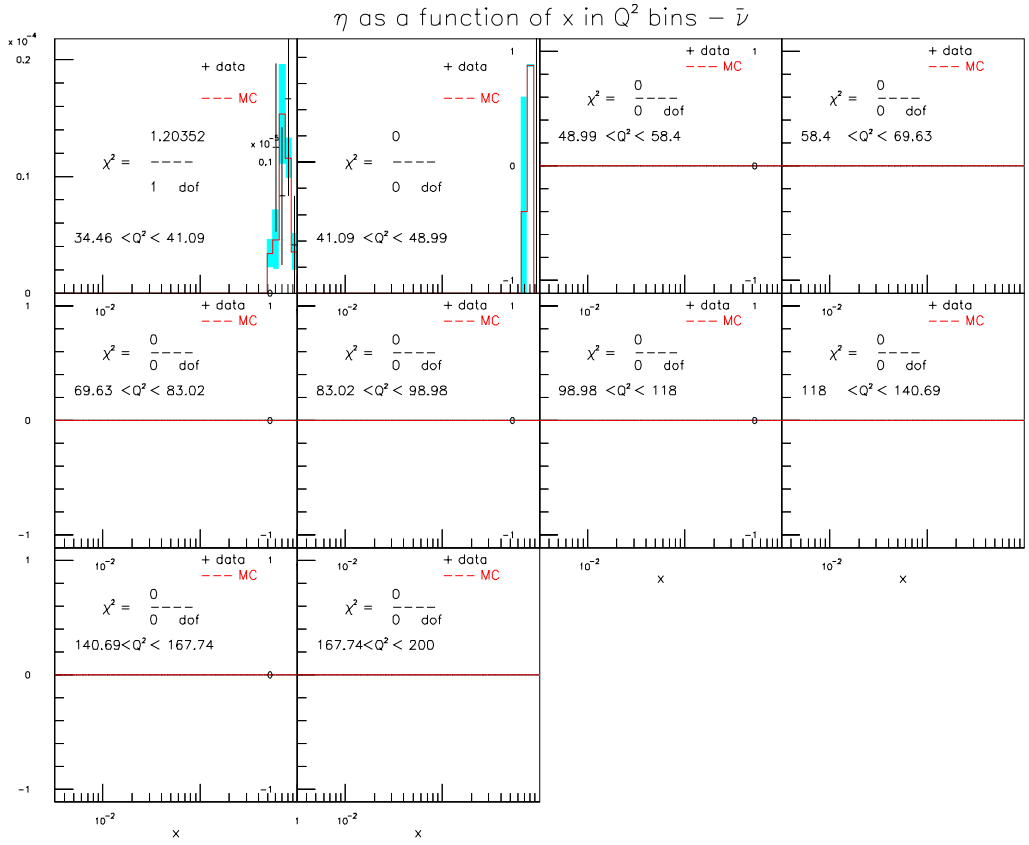

Figure C.32: GRV98NLO+EMC+HT+DRAD for $20 < E_\nu < 62$ GeV ($\overline{\nu}$ mode)

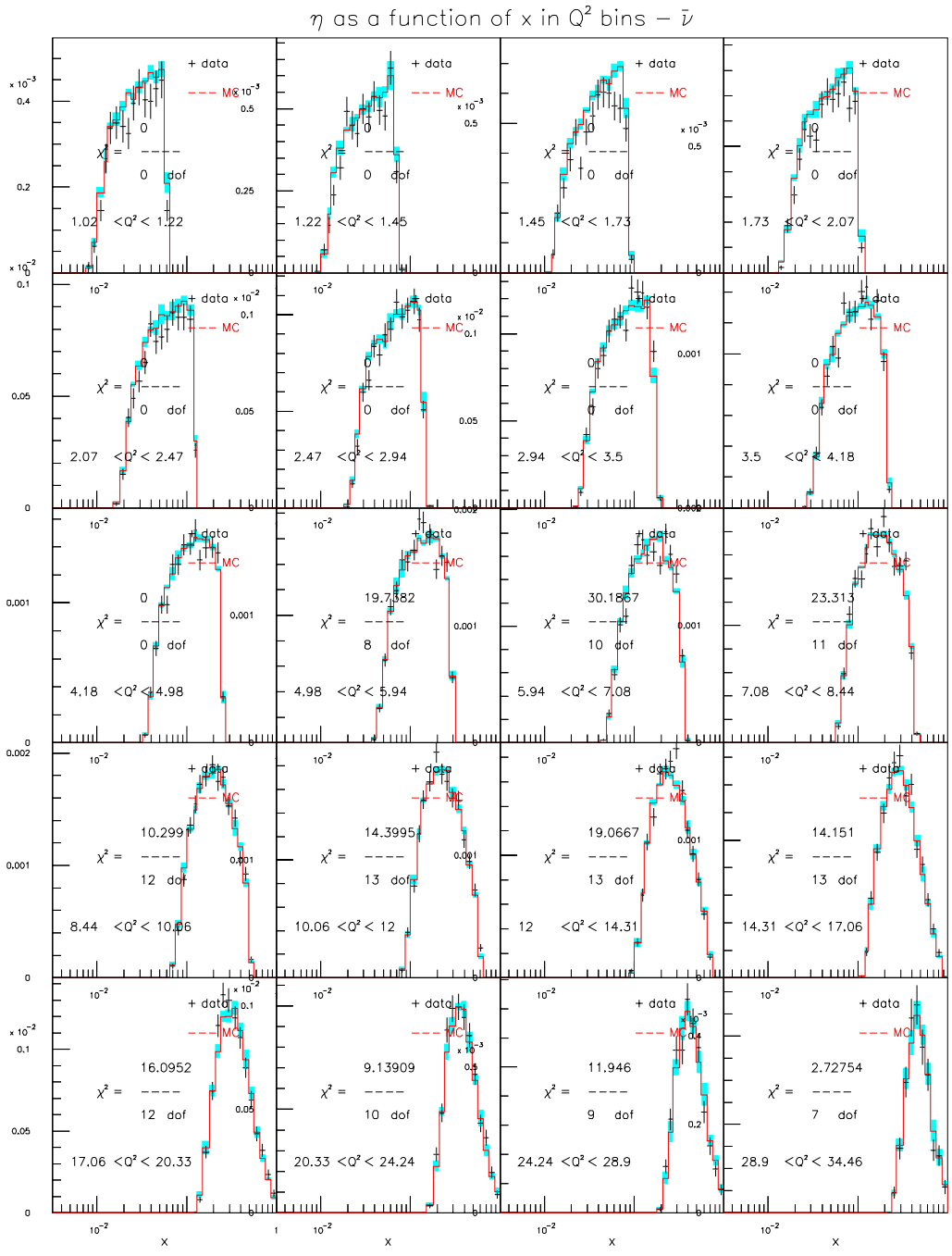

Figure C.33: GRV98NLO+EMC+HT+DRAD for $62 < E_\nu < 85$ GeV ($\overline{\nu}$ mode)

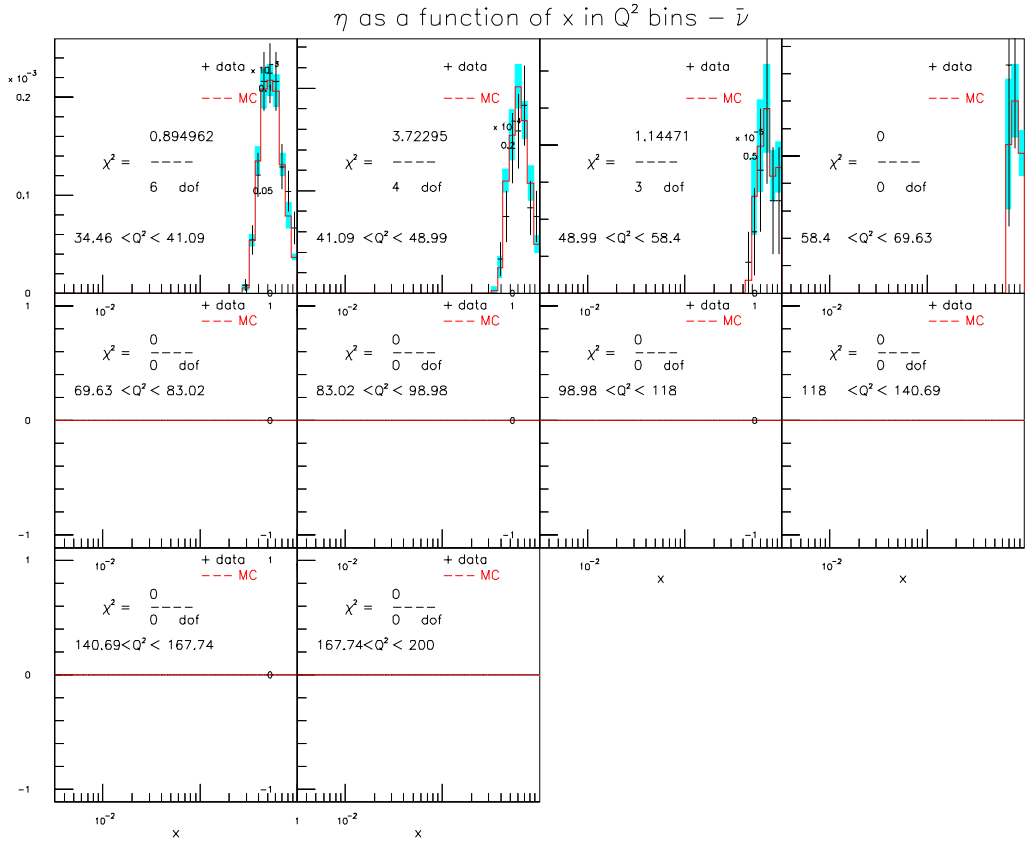

Figure C.34: GRV98NLO+EMC+HT+DRAD for $62 < E_\nu < 85$ GeV ($\overline{\nu}$ mode)

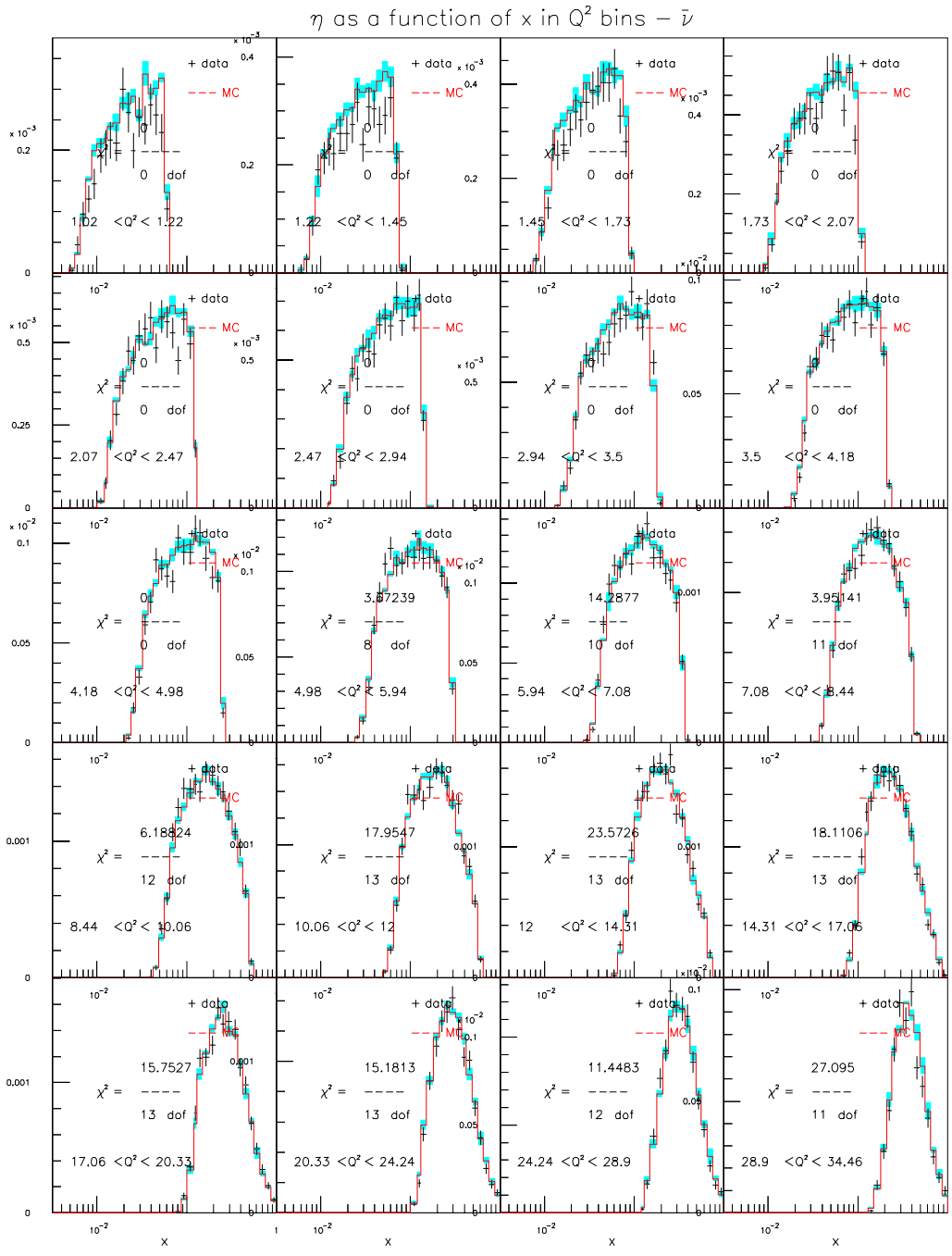

Figure C.35: GRV98NLO+EMC+HT+DRAD for $85 < E_\nu < 129$ GeV ($\overline{\nu}$ mode)

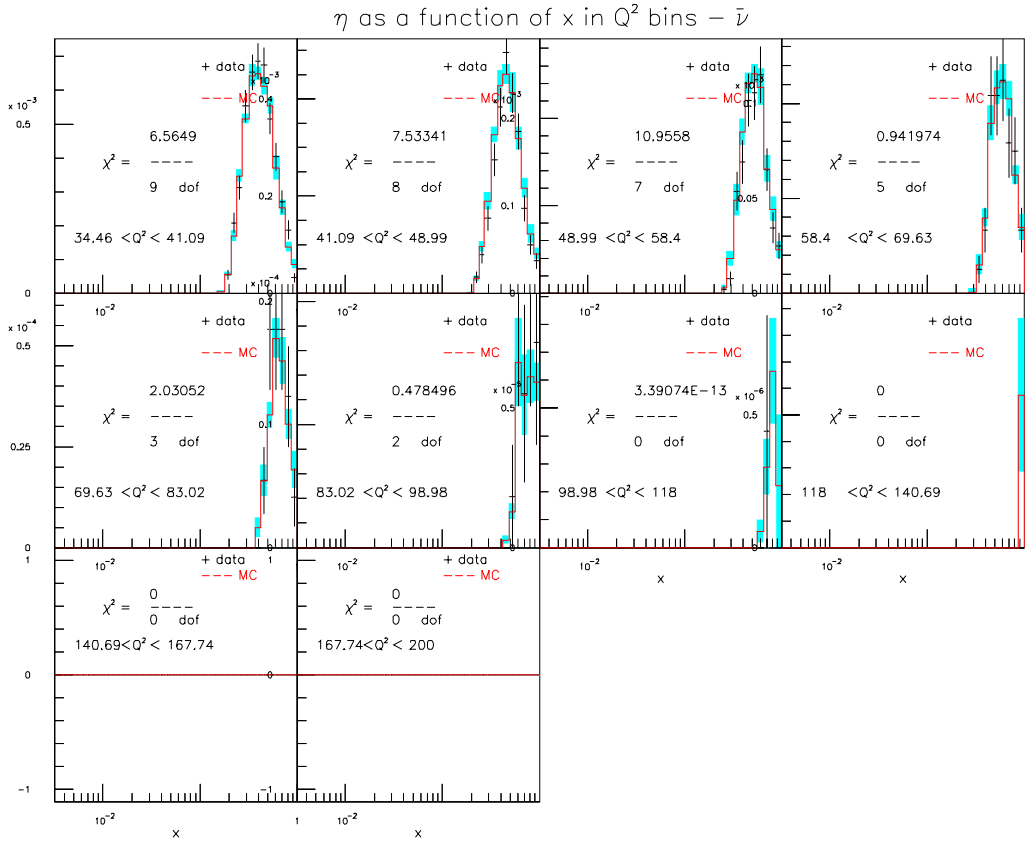

Figure C.36: GRV98NLO+EMC+HT+DRAD for $85 < E_\nu < 129$ GeV ($\overline{\nu}$ mode)

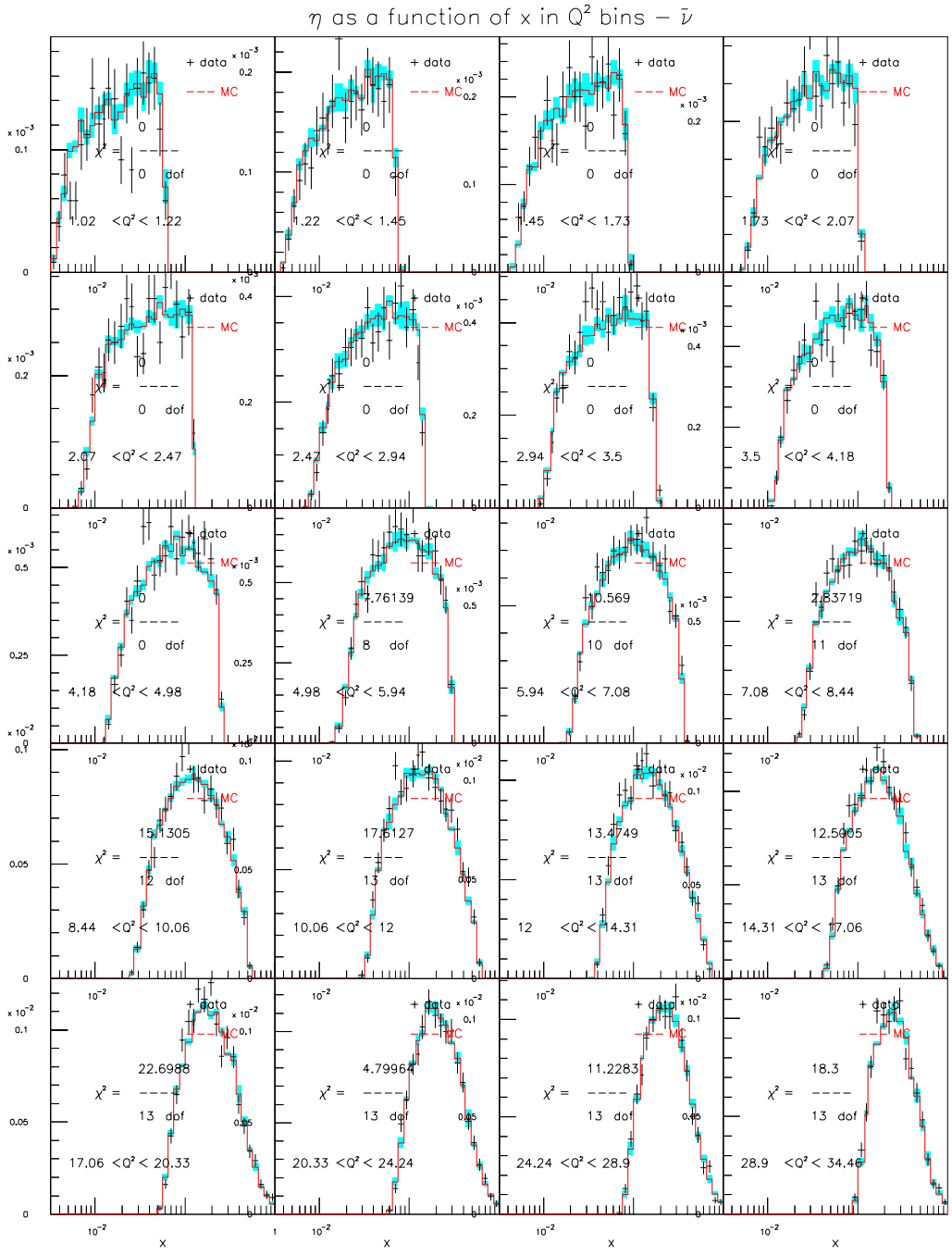

Figure C.37: GRV98NLO+EMC+HT+DRAD for $129 < E_\nu < 201$ GeV ($\overline{\nu}$ mode)

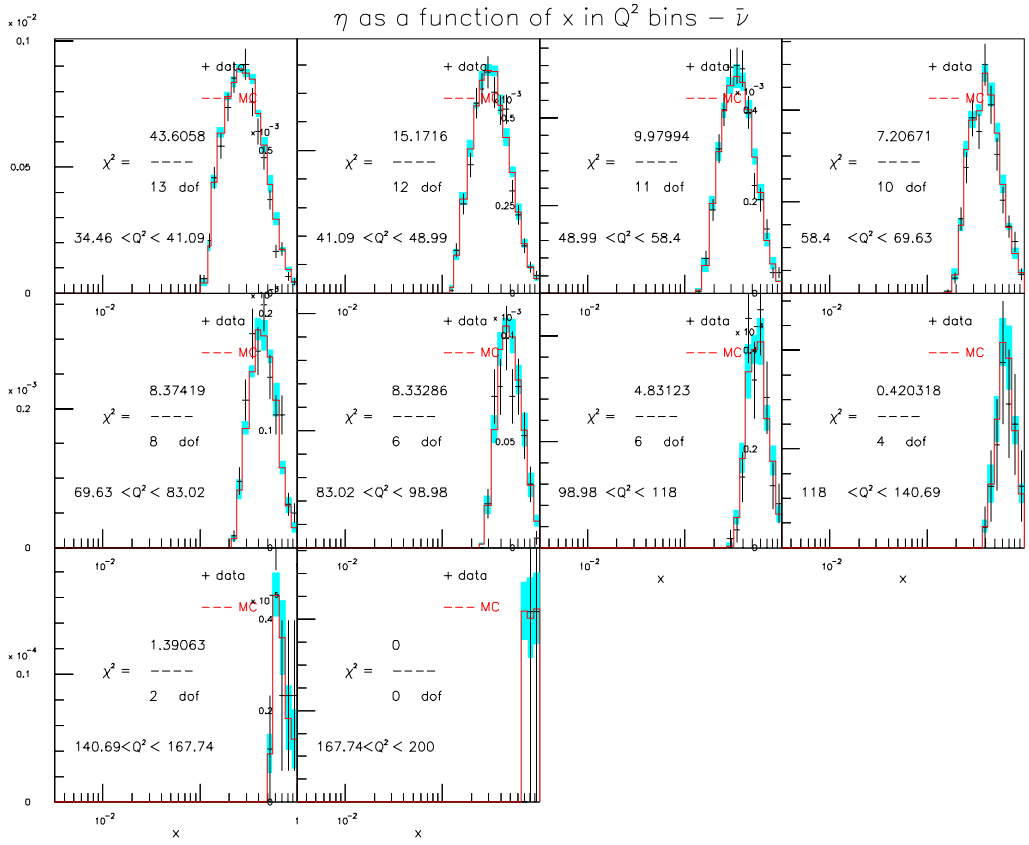

Figure C.38: GRV98NLO+EMC+HT+DRAD for $129 < E_\nu < 201$ GeV ($\overline{\nu}$ mode)

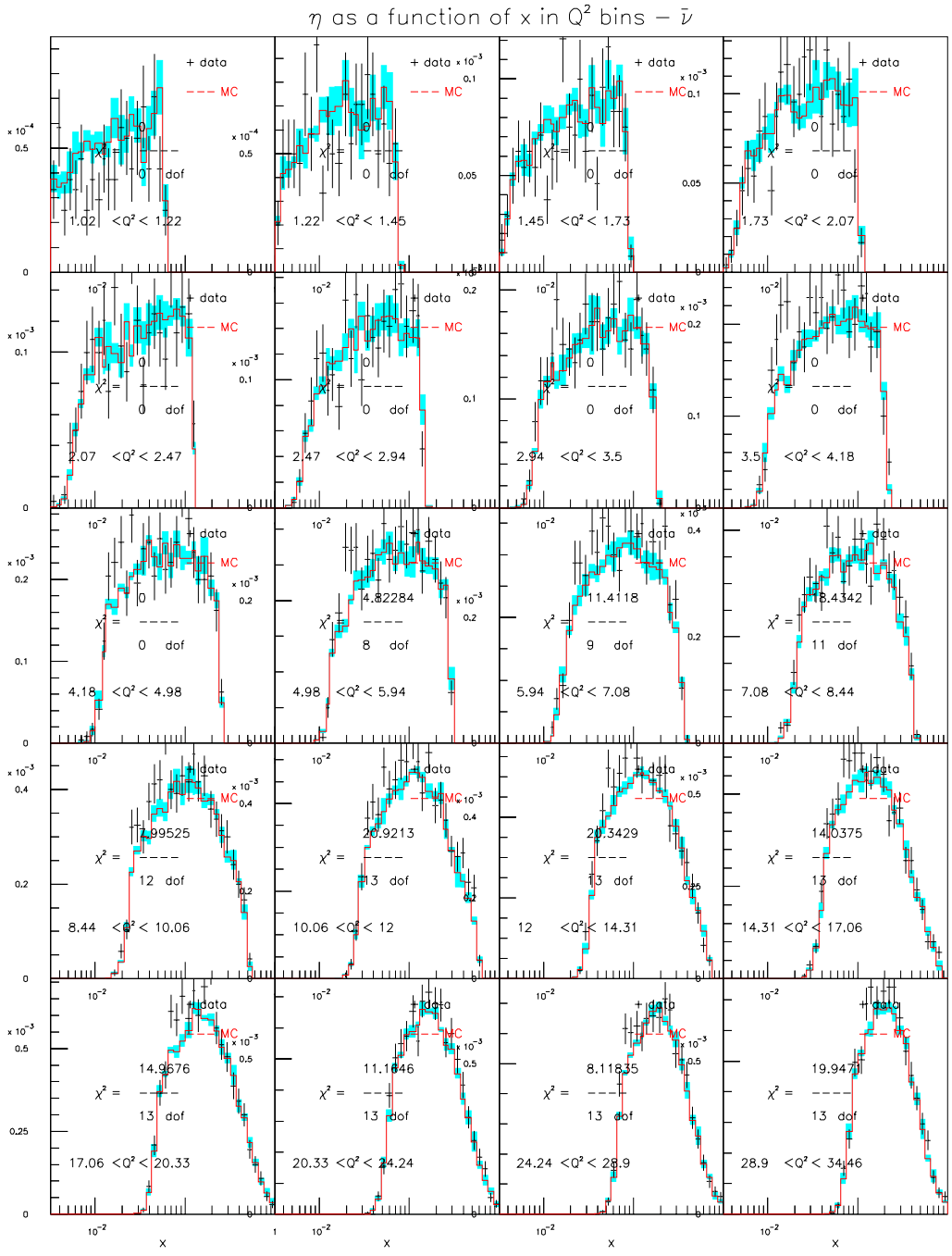

Figure C.39: GRV98NLO+EMC+HT+DRAD for $201 < E_\nu < 400$ GeV ($\overline{\nu}$ mode)

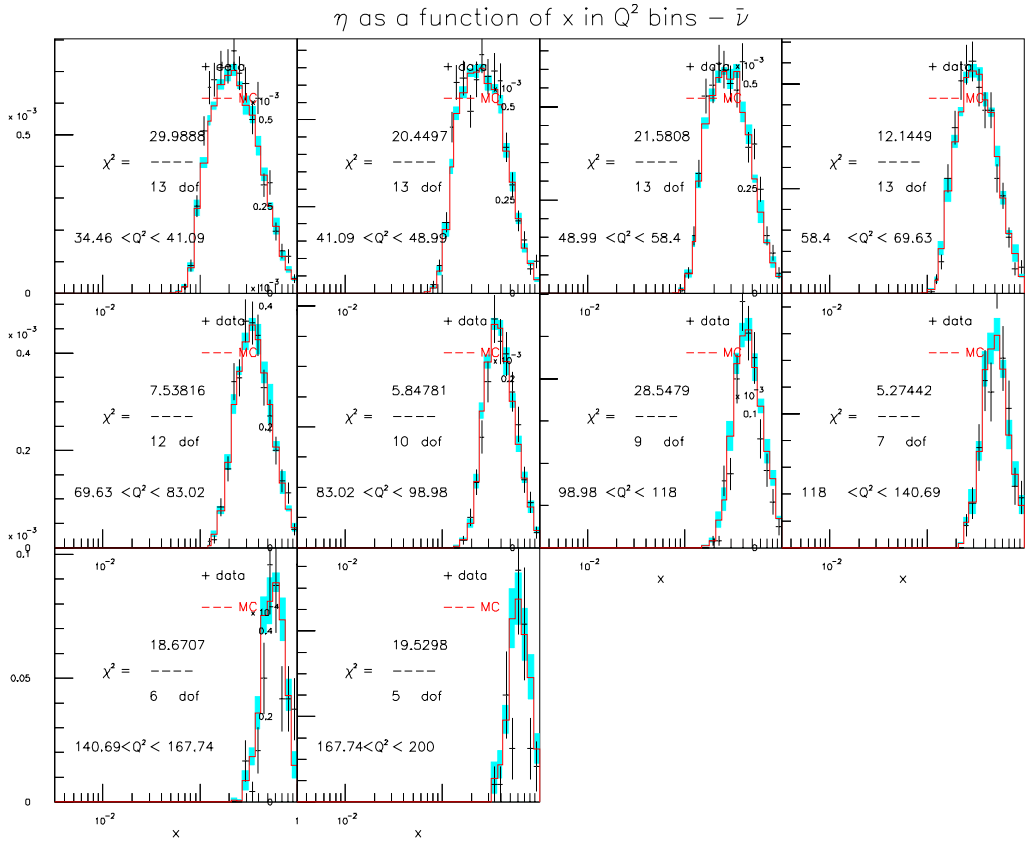

Figure C.40: GRV98NLO+EMC+HT+DRAD for $201 < E_\nu < 400$ GeV ($\overline{\nu}$ mode)

Appendix D

m_C and $s(x, Q^2)$ Sensitivity

This appendix contains plots showing $\eta^{\nu/\overline{\nu}}(Q^2)$ for x and E_ν bins with bands indicating the sensitivity of η, in that particular bin, to the parameters m_c and $s(x, Q^2)$. The models shown are GRV98NLO+EMC+HT and CTEQ5NLO+EMC+HT, which were used for parameter extraction. In the following plots, m_c has been shifted by 0.5 GeV from its nominal value of 1.5 GeV and $s(x, Q^2)$ has been shifted by half of its nominal value of 1.

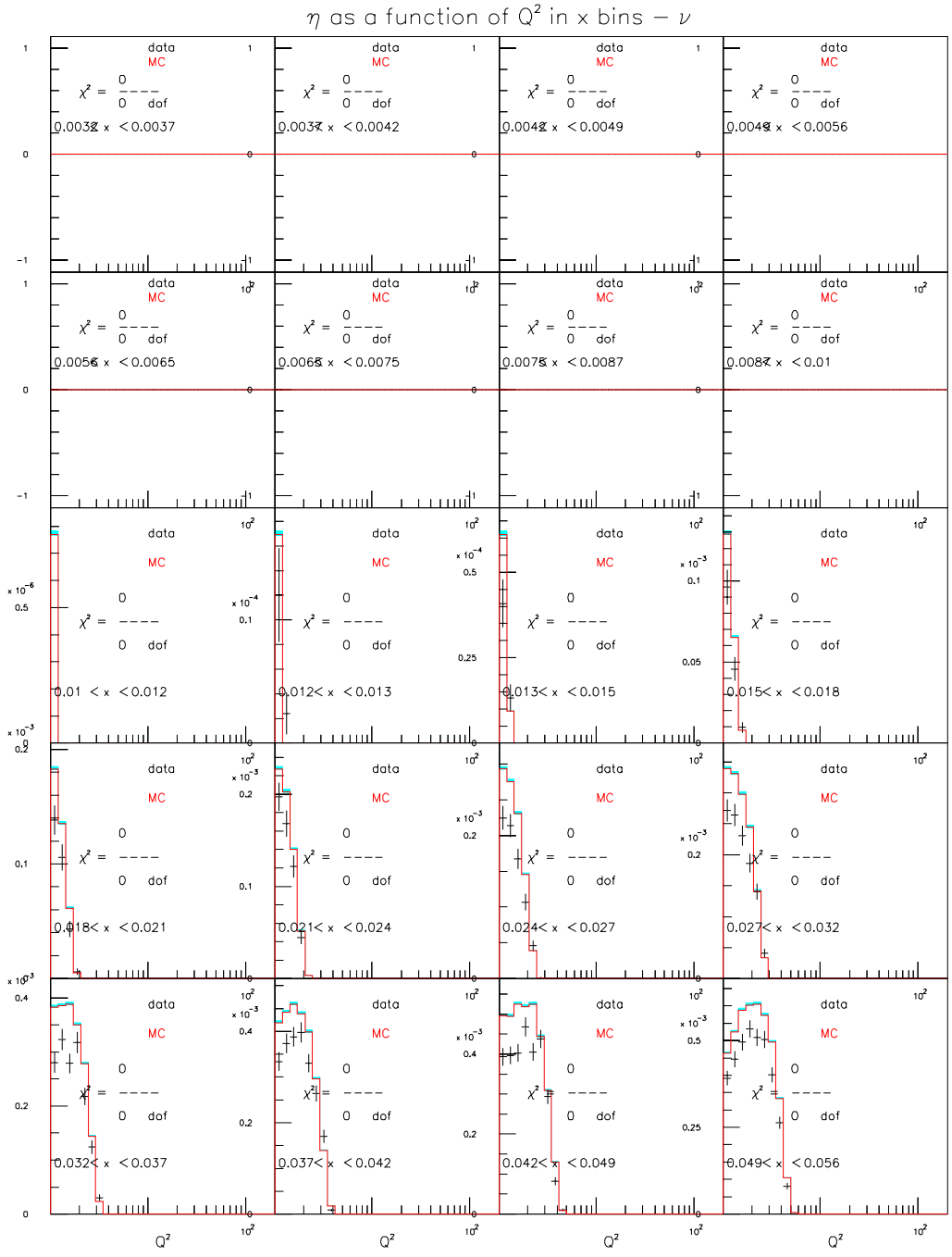

Figure D.1: GRV98NLO $\eta(Q^2)$ – ν mode m_c sensitivity $(20 < E_\nu < 62)$

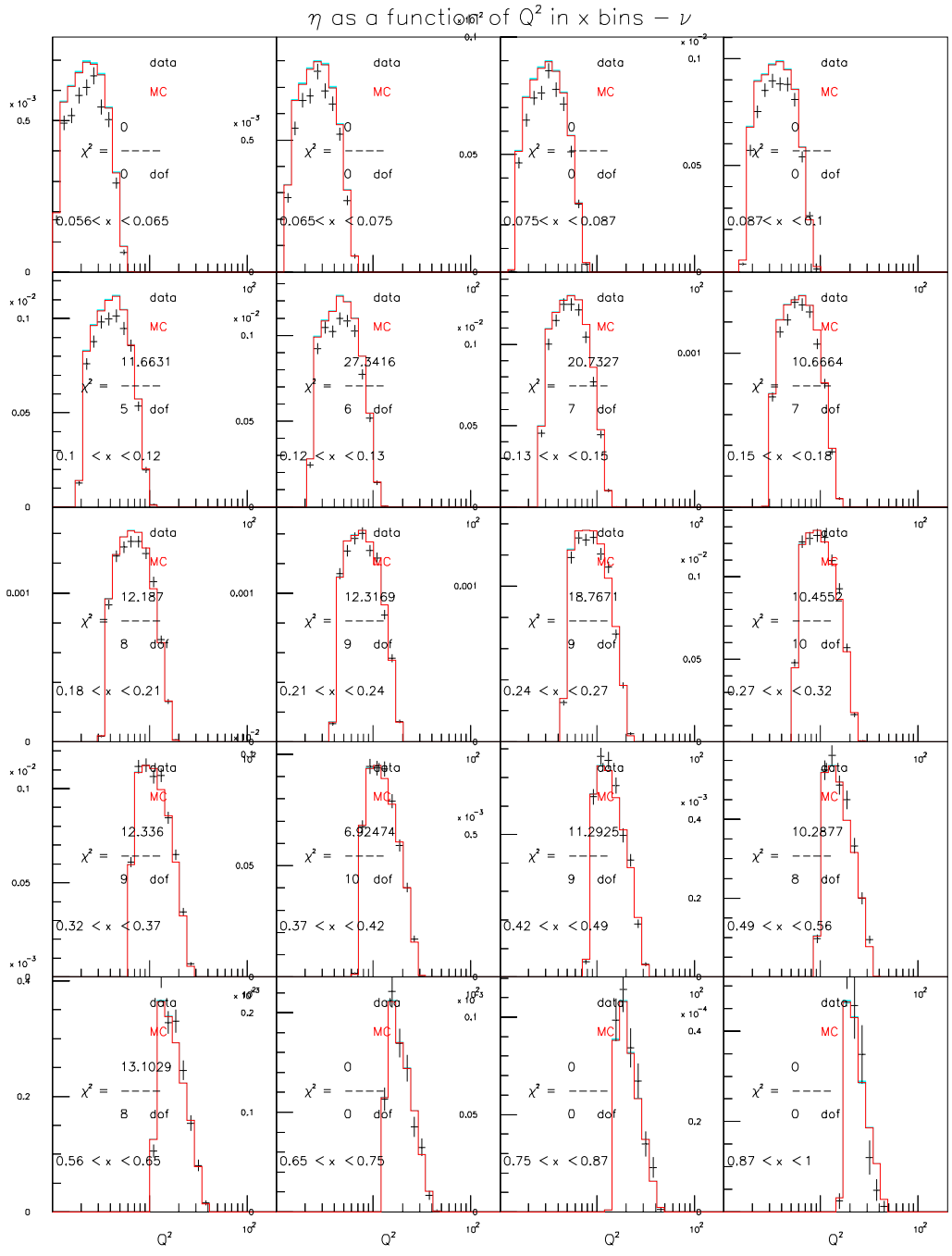

Figure D.2: GRV98NLO $\eta(Q^2)$ – ν mode m_c sensitivity $(20 < E_\nu < 62)$

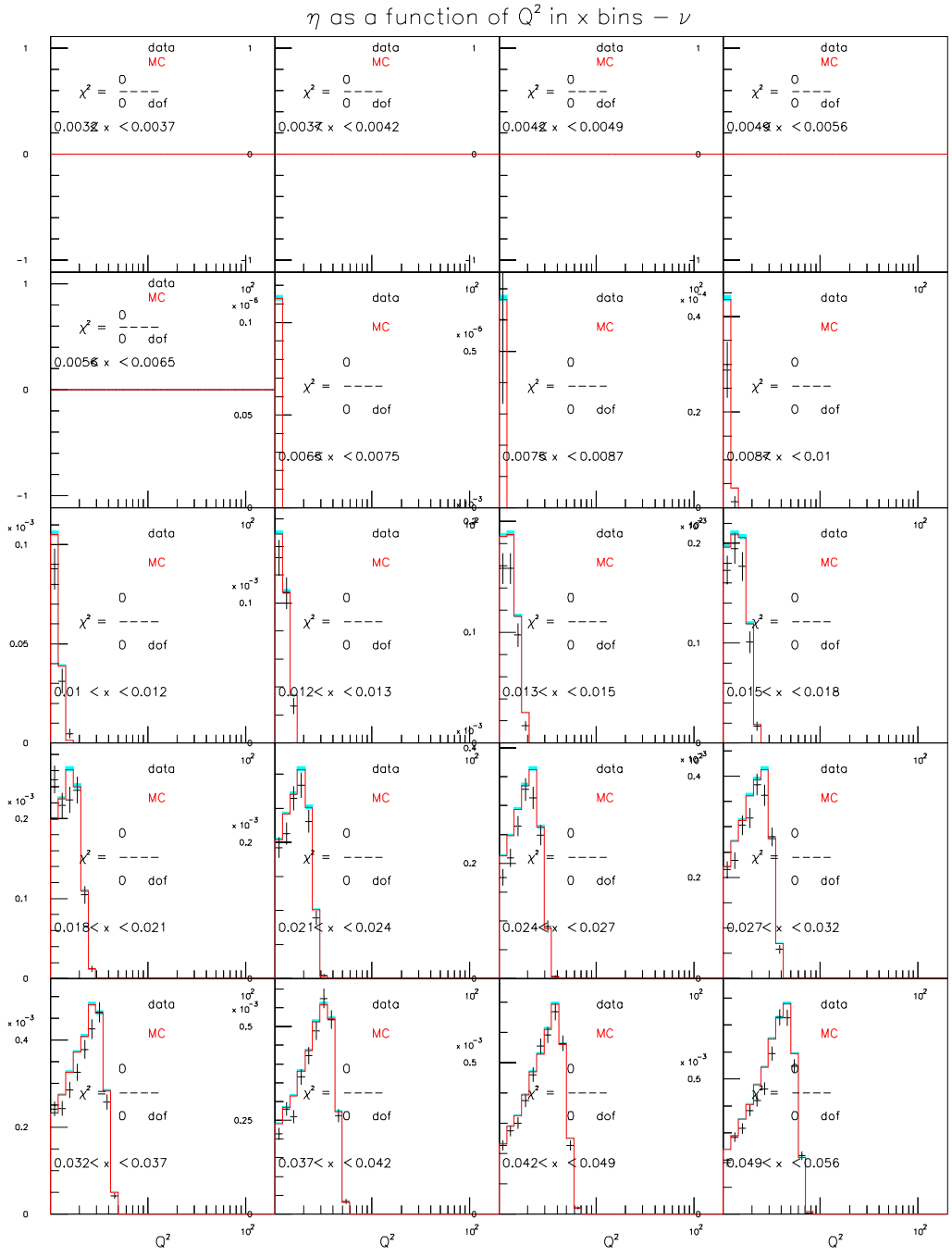

Figure D.3: GRV98NLO $\eta(Q^2)$ – ν mode m_c sensitivity $(62 < E_\nu < 85)$

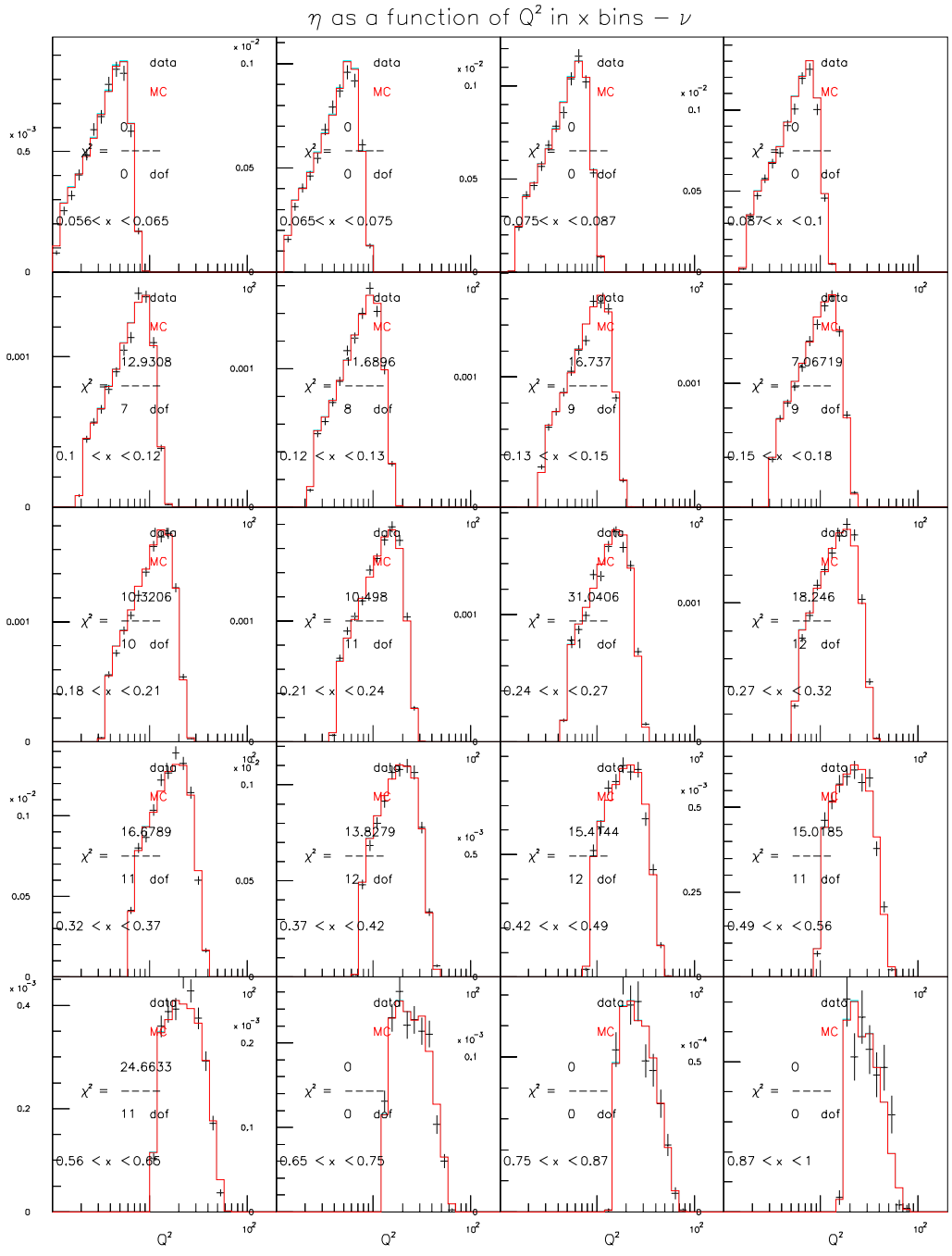

Figure D.4: GRV98NLO $\eta(Q^2)$ – ν mode m_c sensitivity ($62 < E_\nu < 85$)

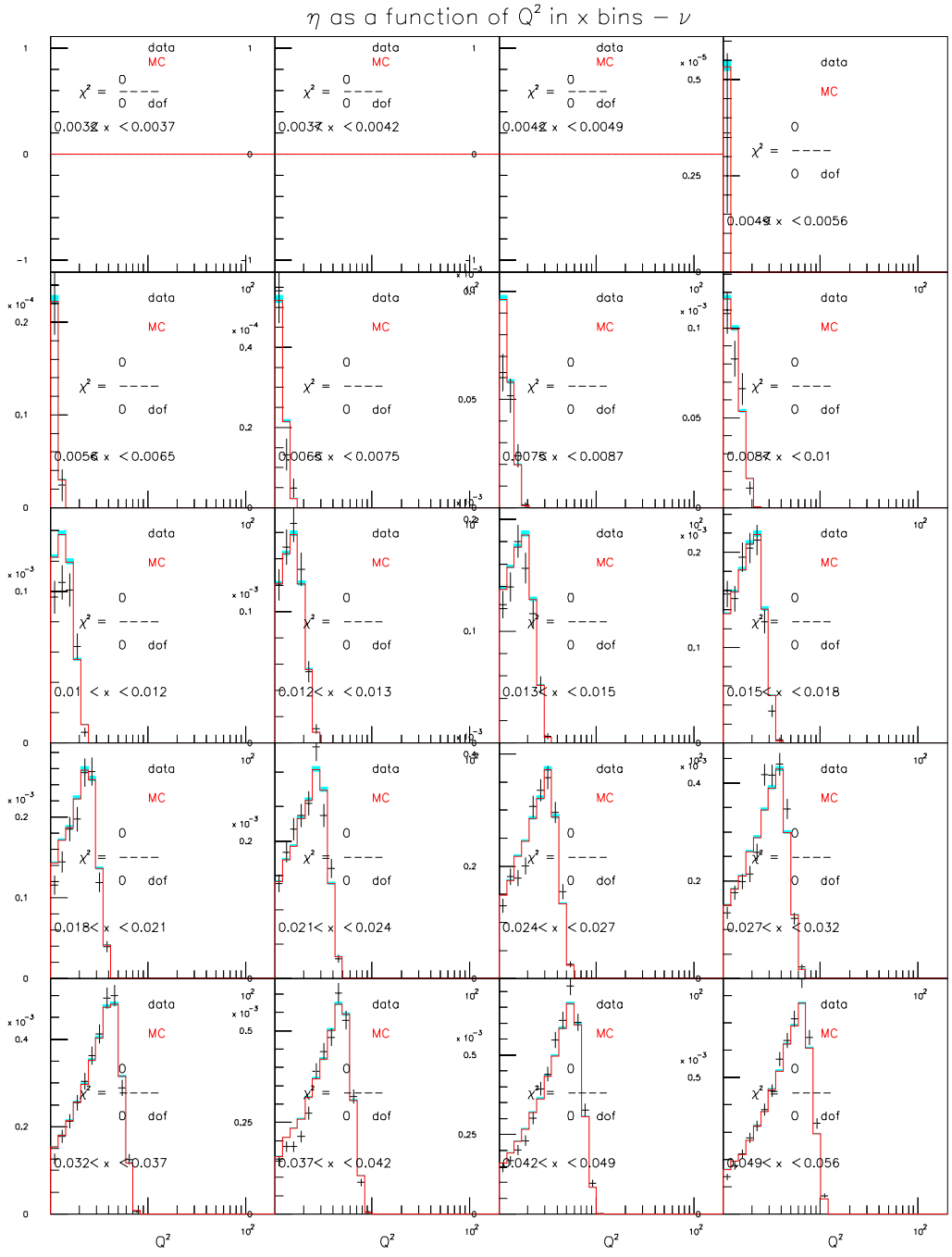

Figure D.5: GRV98NLO $\eta(Q^2)$ – ν mode m_c sensitivity ($85 < E_\nu < 129$)

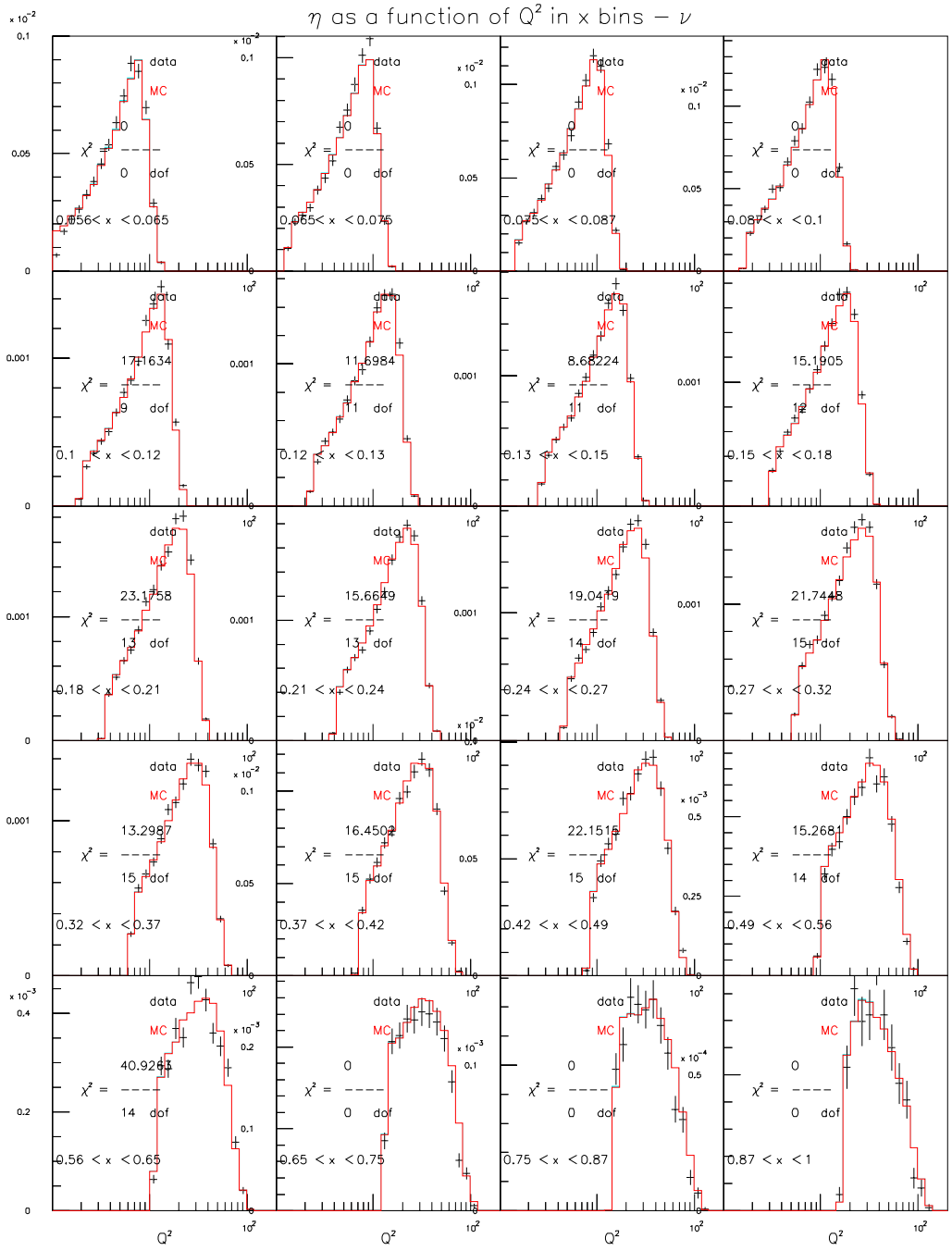

Figure D.6: GRV98NLO $\eta(Q^2)$ – ν mode m_c sensitivity ($85 < E_\nu < 129$)

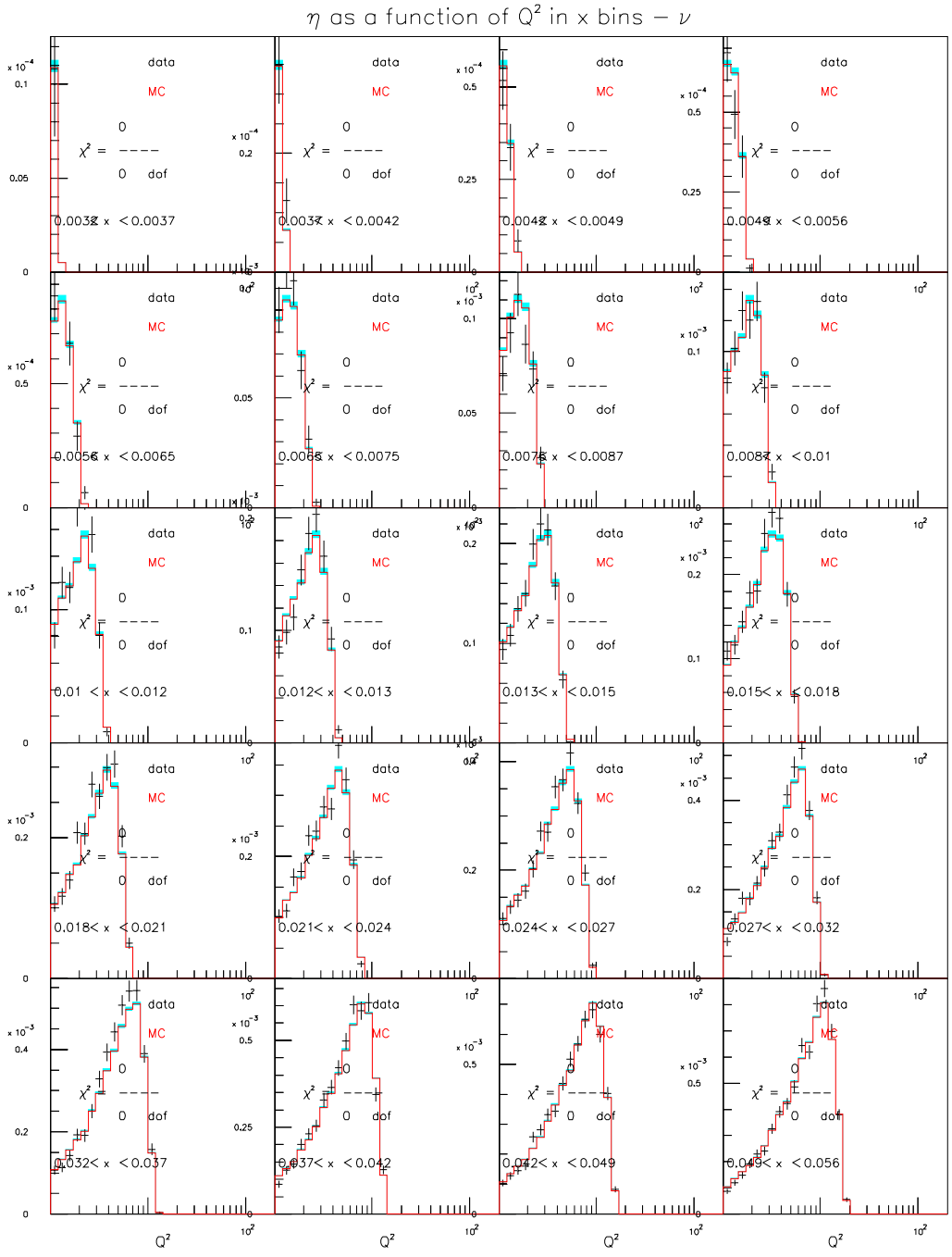

Figure D.7: GRV98NLO $\eta(Q^2)$ – ν mode m_c sensitivity ($129 < E_\nu < 201$)

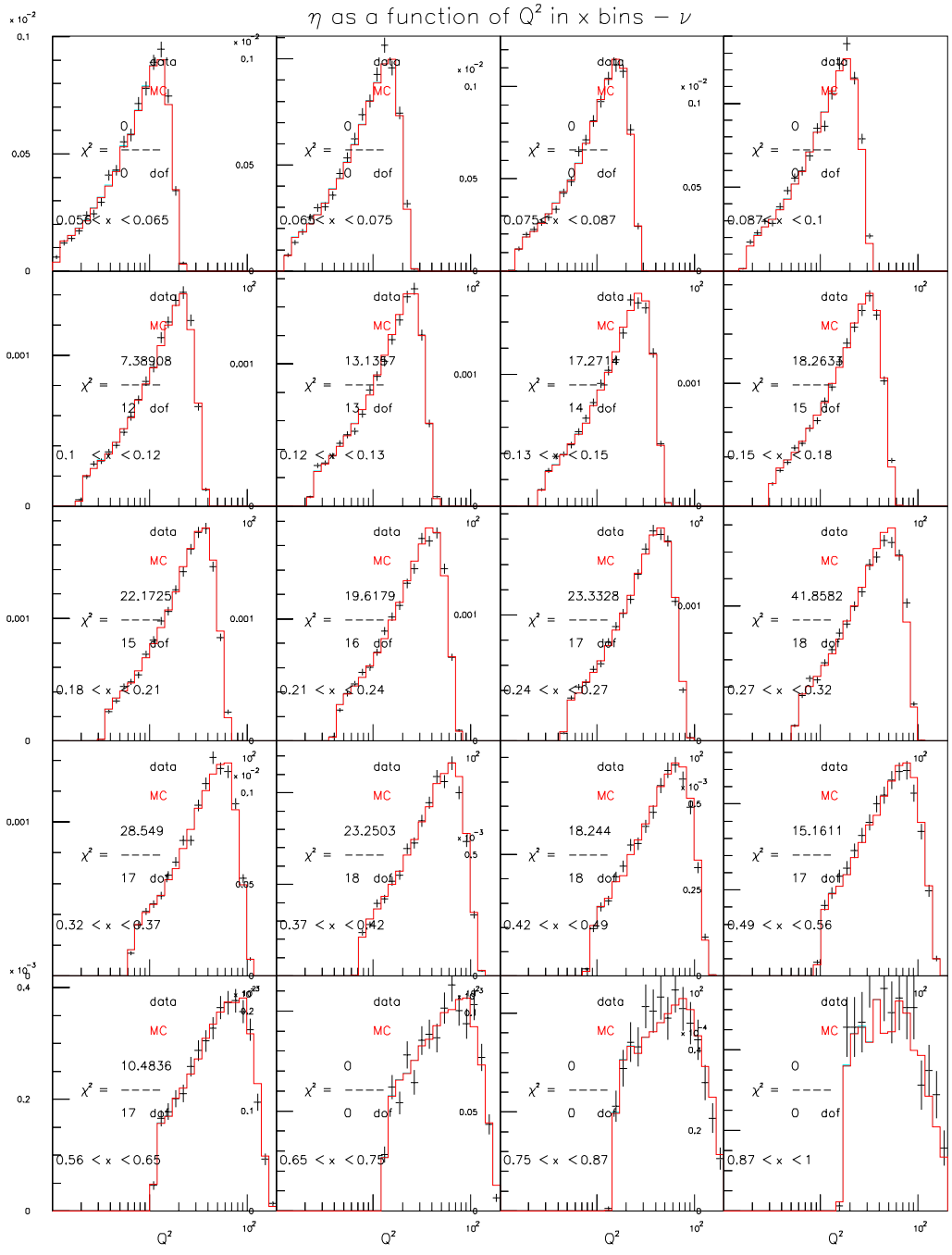

Figure D.8: GRV98NLO $\eta(Q^2)$ – ν mode m_c sensitivity ($129 < E_\nu < 201$)

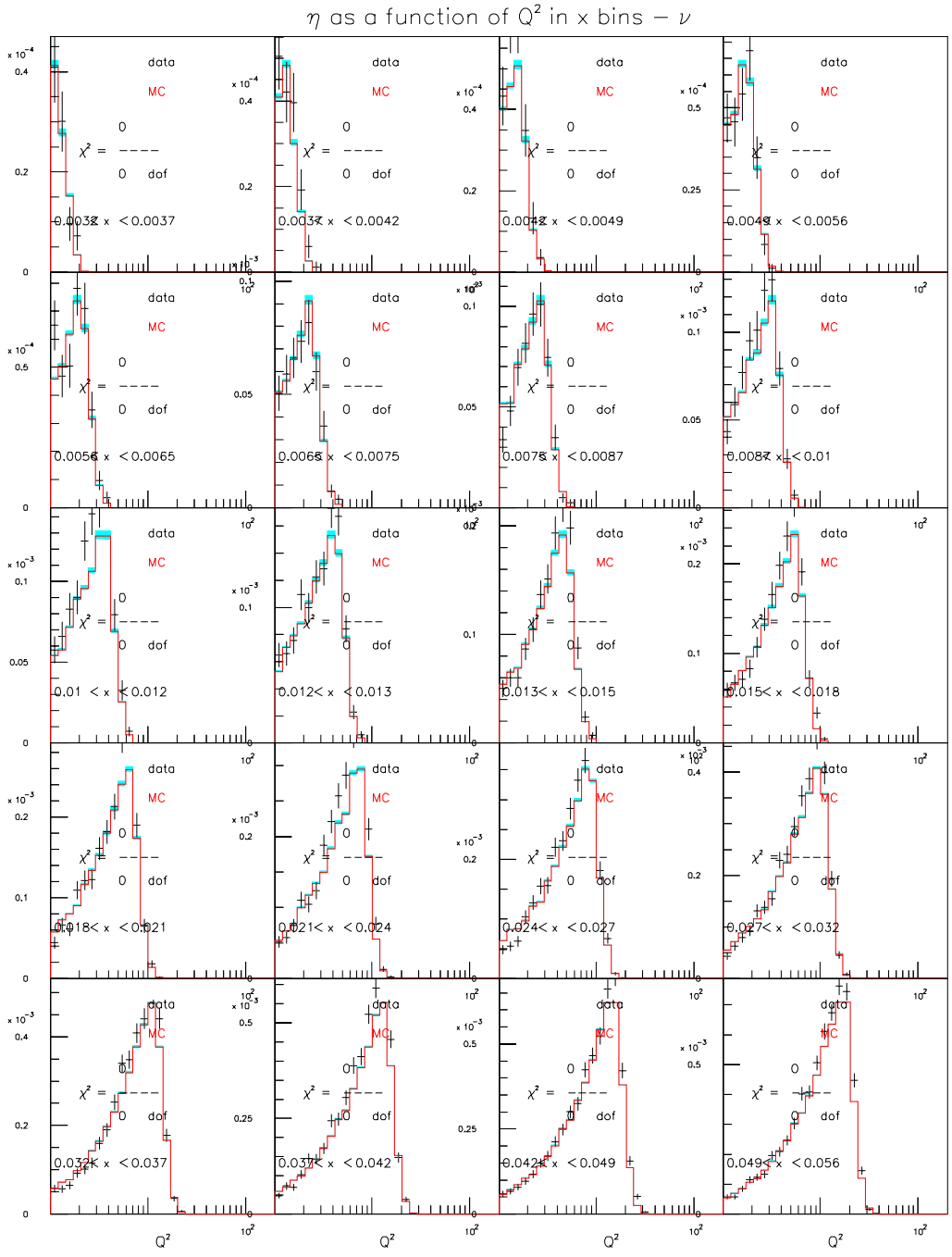

Figure D.9: GRV98NLO $\eta(Q^2)$ – ν mode m_c sensitivity ($201 < E_\nu < 400$)

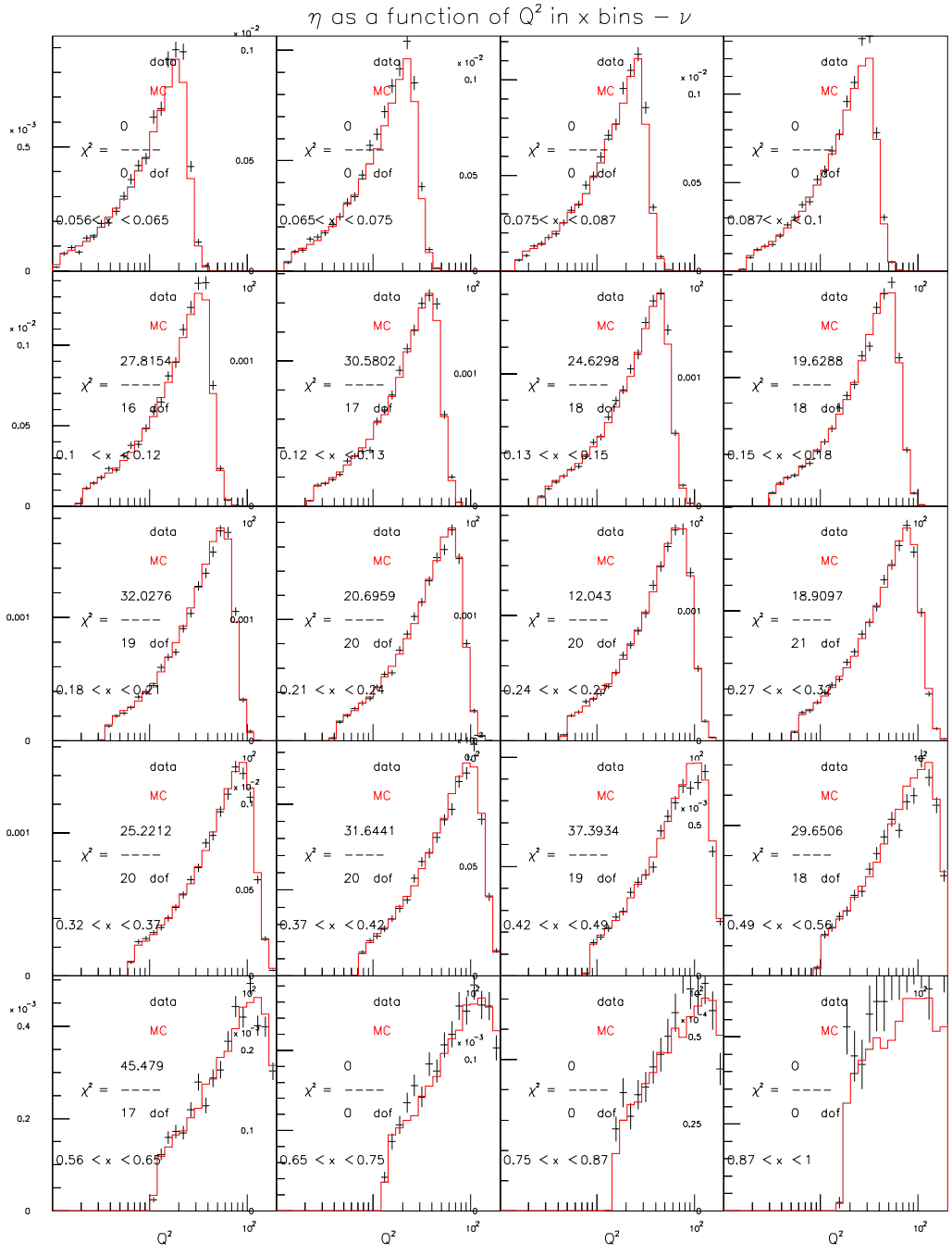

Figure D.10: GRV98NLO $\eta(Q^2)$ – ν mode m_c sensitivity ($201 < E_\nu < 400$)

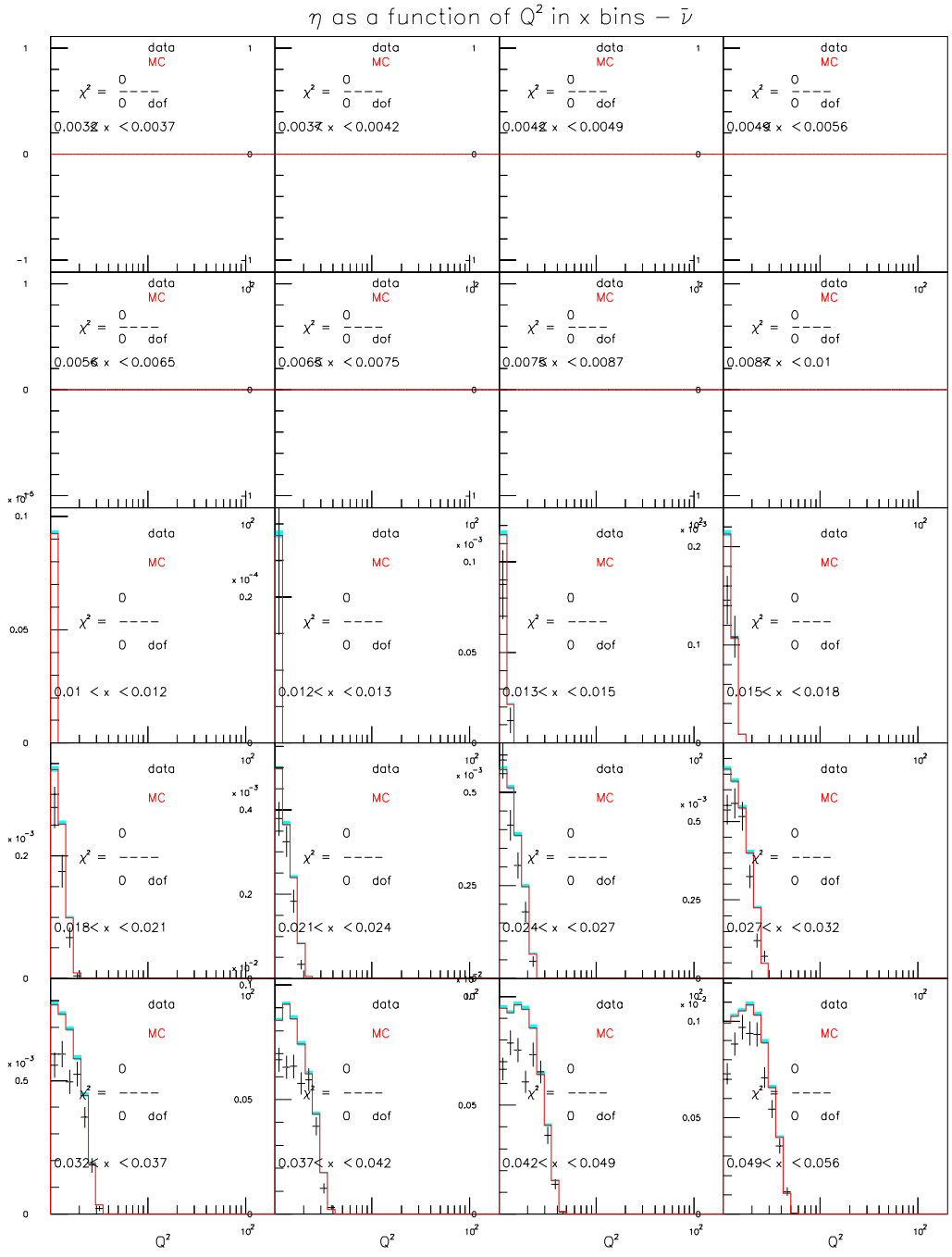

Figure D.11: GRV98NLO $\eta(Q^2)$ – $\overline{\nu}$ mode m_c sensitivity ($20 < E_\nu < 62$)

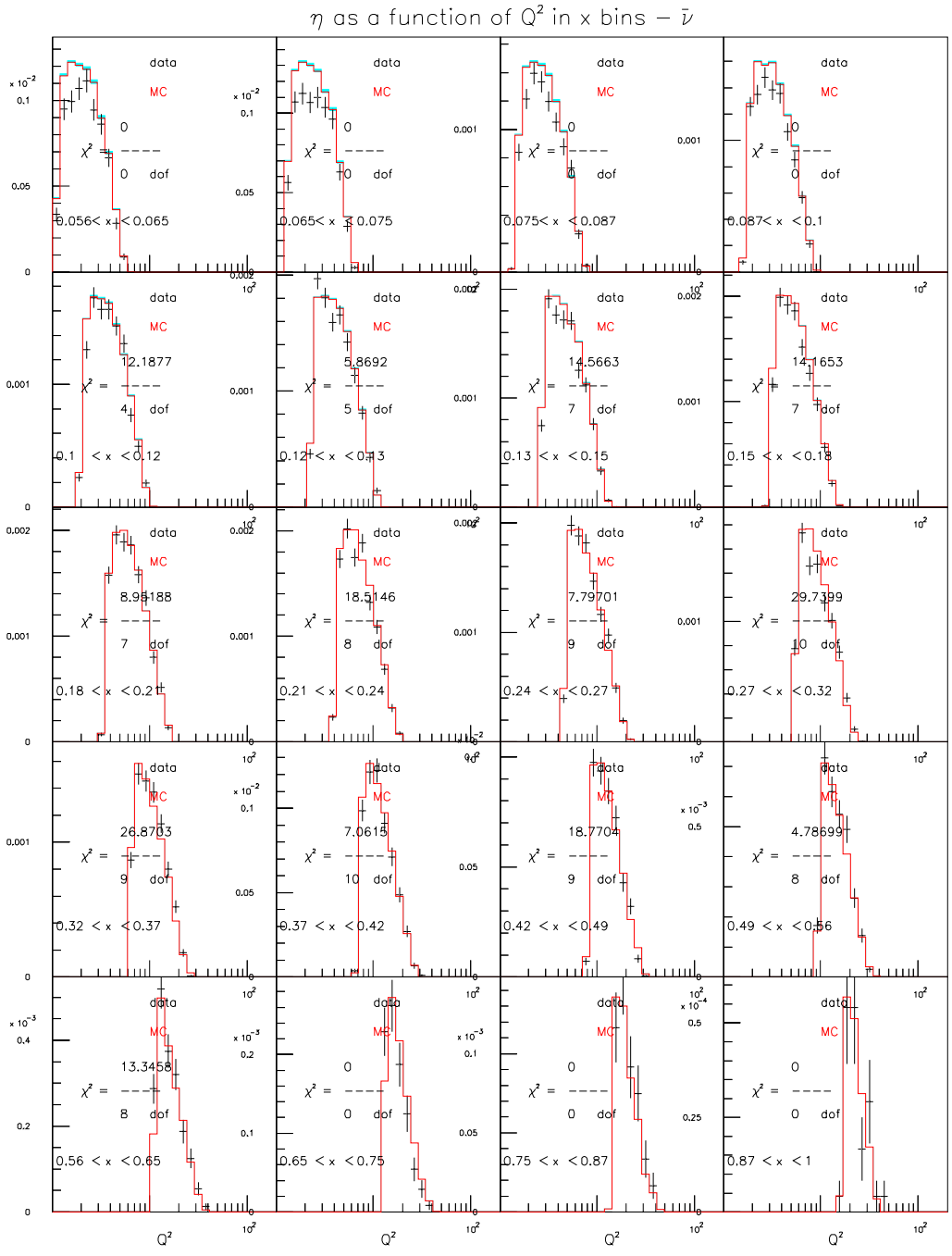

Figure D.12: GRV98NLO $\eta(Q^2)$ – $\overline{\nu}$ mode m_c sensitivity ($20 < E_\nu < 62$)

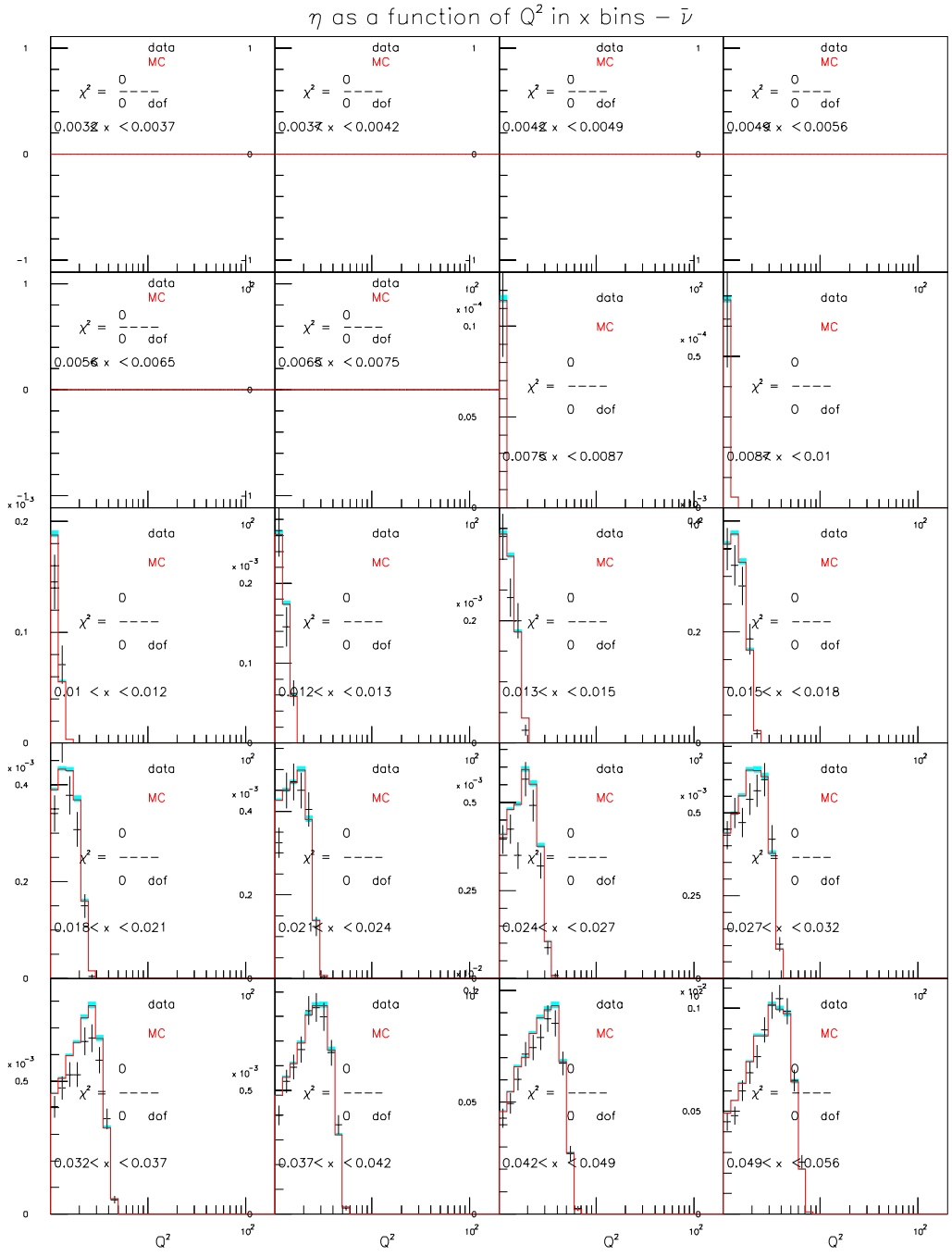

Figure D.13: GRV98NLO $\eta(Q^2)$ – $\overline{\nu}$ mode m_c sensitivity ($62 < E_\nu < 85$)

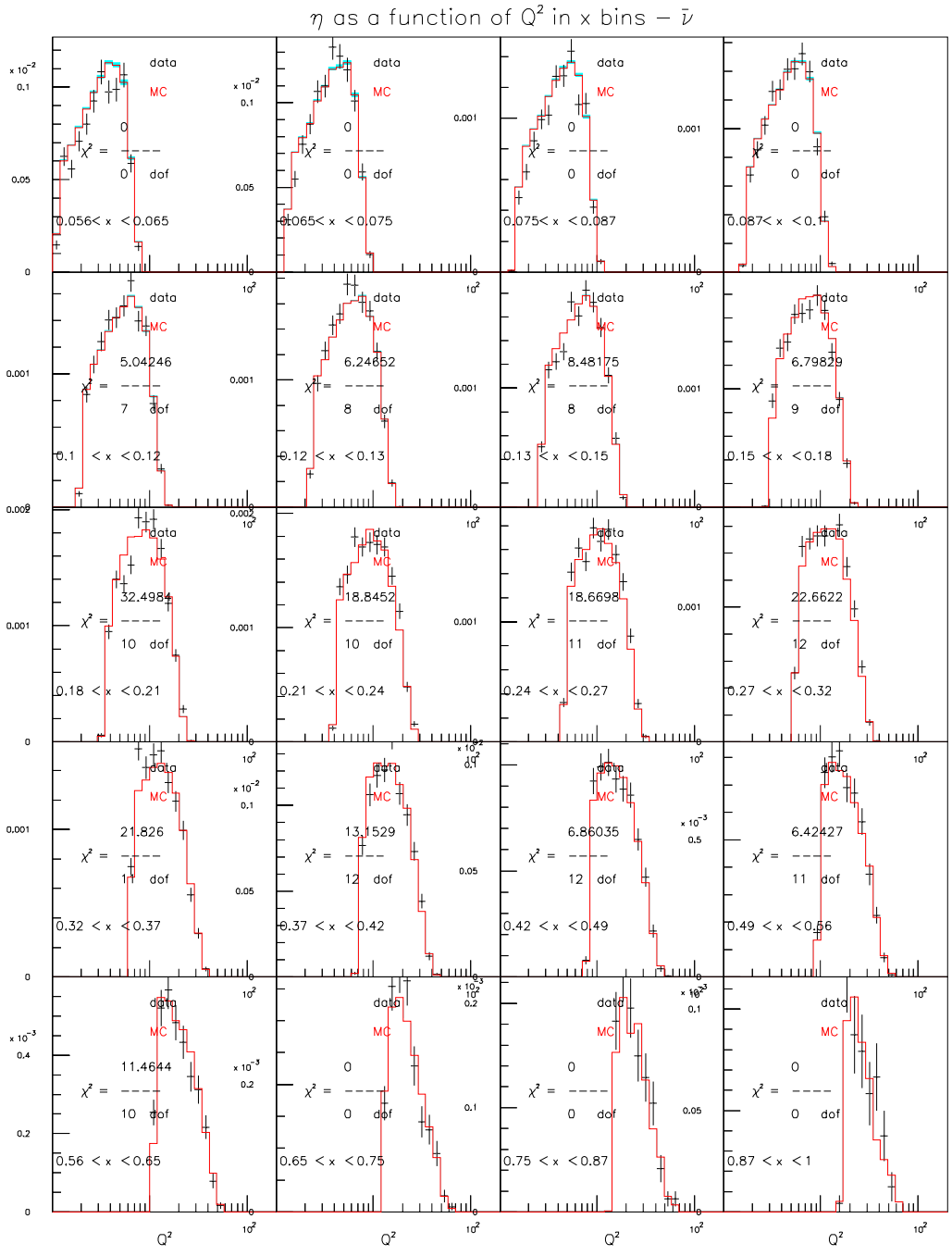

Figure D.14: GRV98NLO $\eta(Q^2)$ – $\overline{\nu}$ mode m_c sensitivity ($62 < E_\nu < 85$)

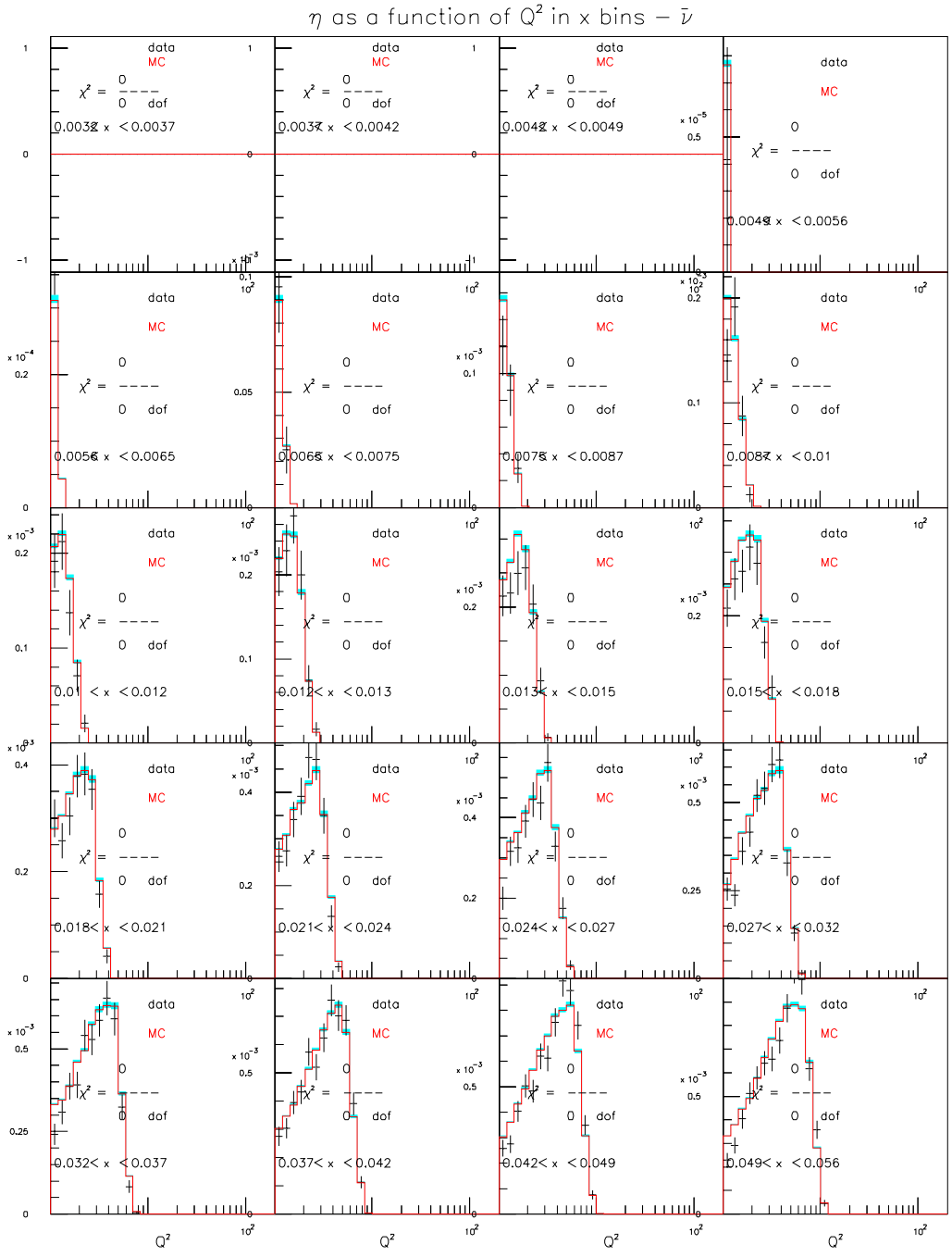

Figure D.15: GRV98NLO $\eta(Q^2)$ – $\overline{\nu}$ mode m_c sensitivity ($85 < E_\nu < 129$)

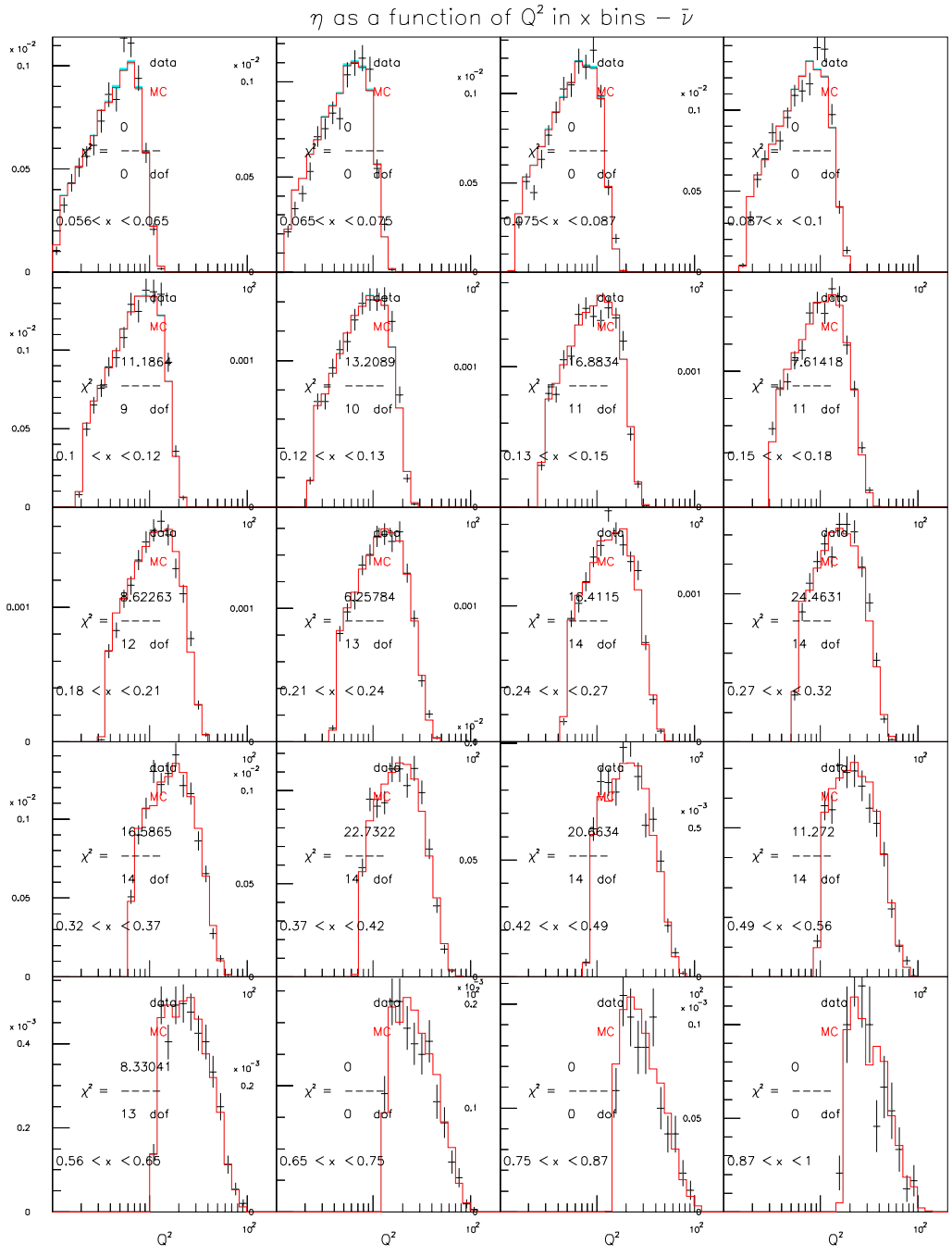

Figure D.16: GRV98NLO $\eta(Q^2)$ – $\overline{\nu}$ mode m_c sensitivity ($85 < E_\nu < 129$)

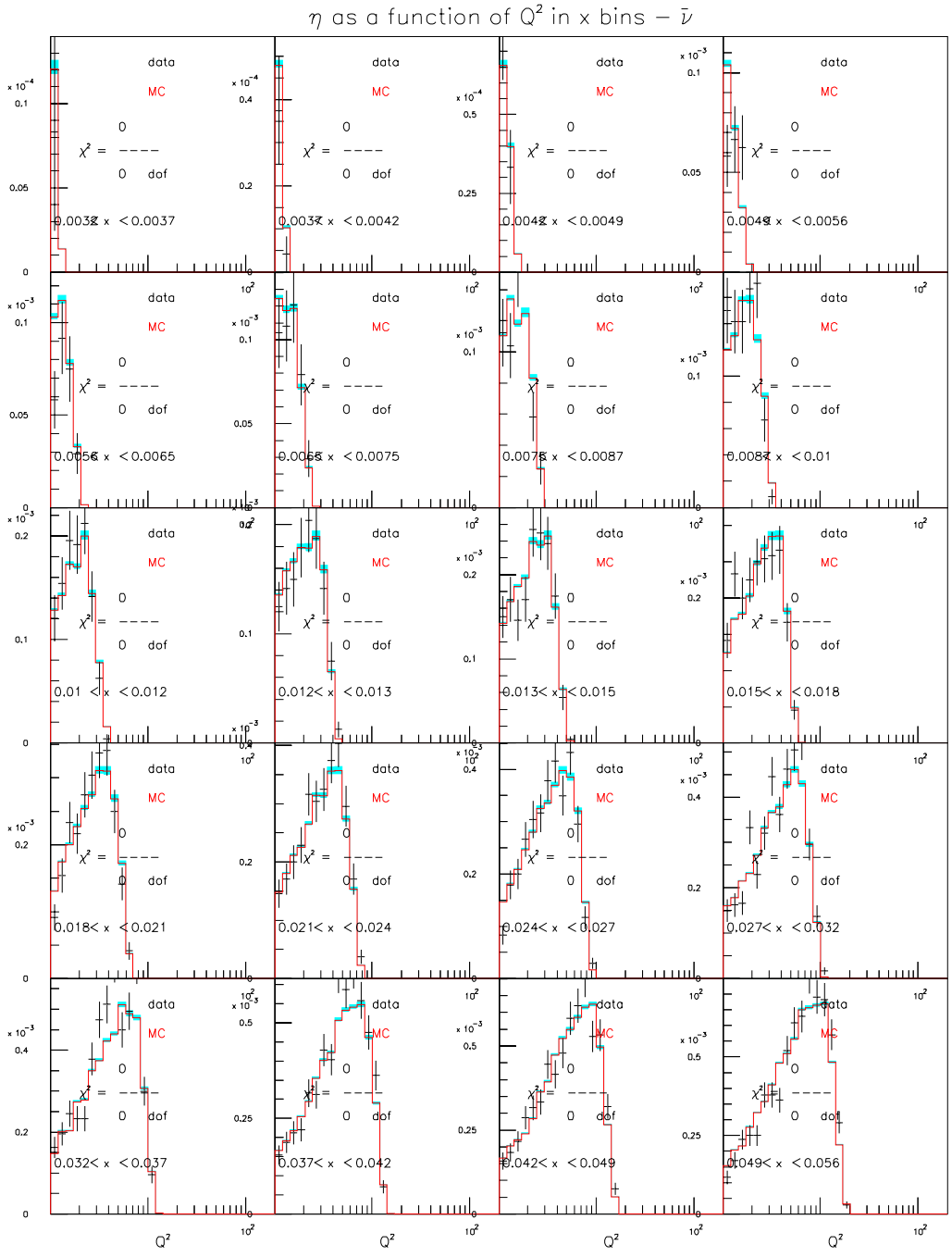

Figure D.17: GRV98NLO $\eta(Q^2)$ – $\overline{\nu}$ mode m_c sensitivity ($129 < E_\nu < 201$)

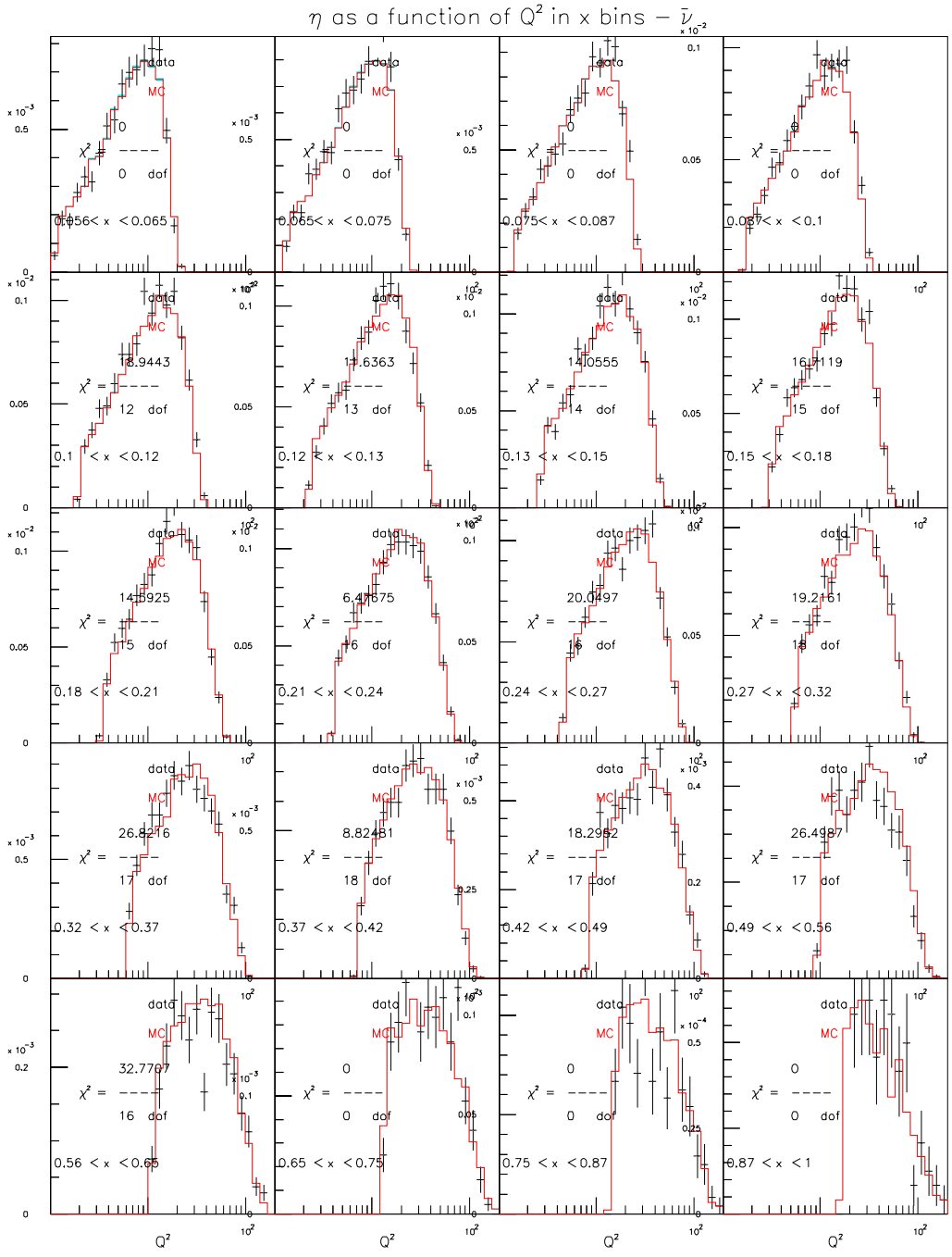

Figure D.18: GRV98NLO $\eta(Q^2)$ – $\overline{\nu}$ mode m_c sensitivity ($129 < E_\nu < 201$)

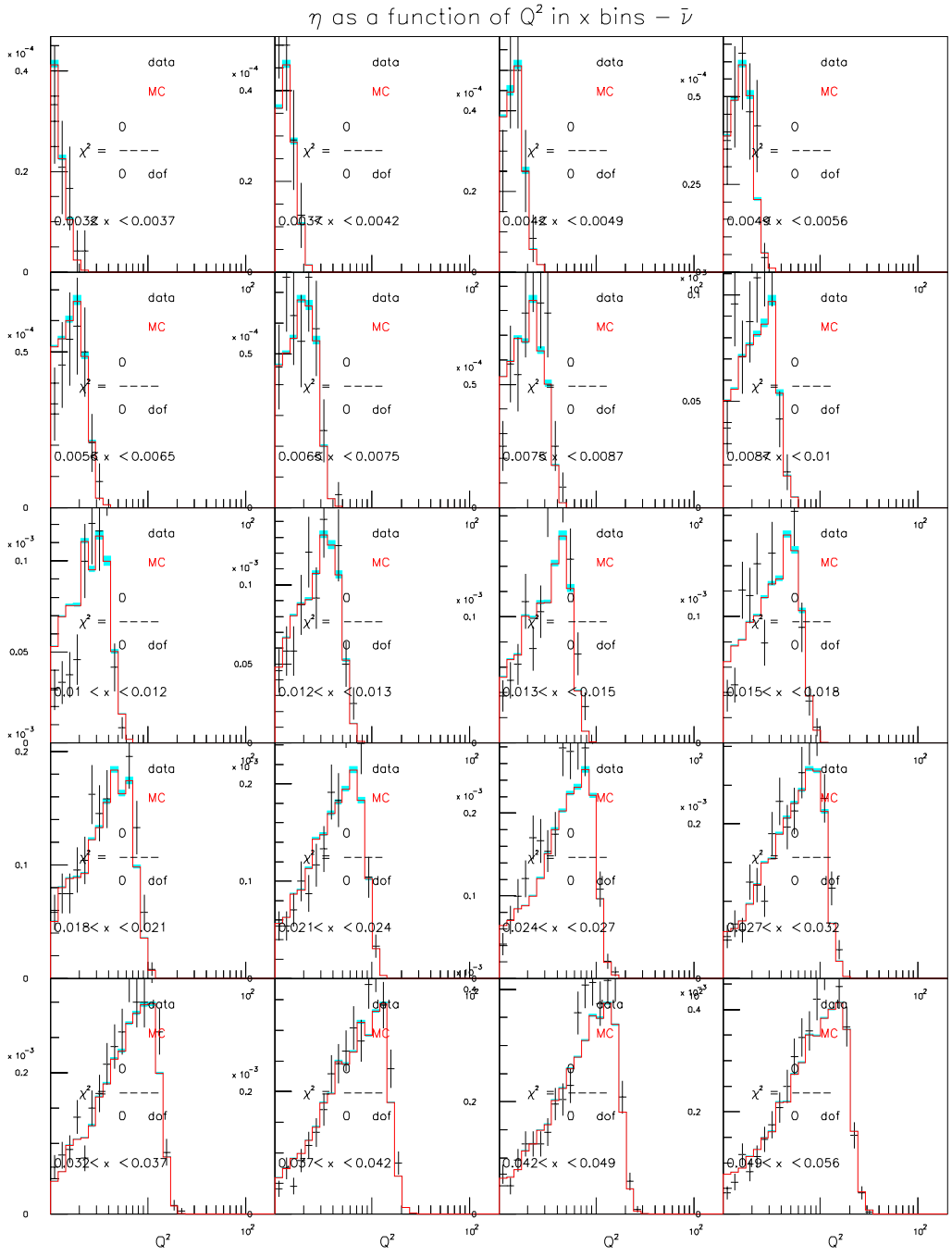

Figure D.19: GRV98NLO $\eta(Q^2)$ – $\overline{\nu}$ mode m_c sensitivity ($201 < E_\nu < 400$)

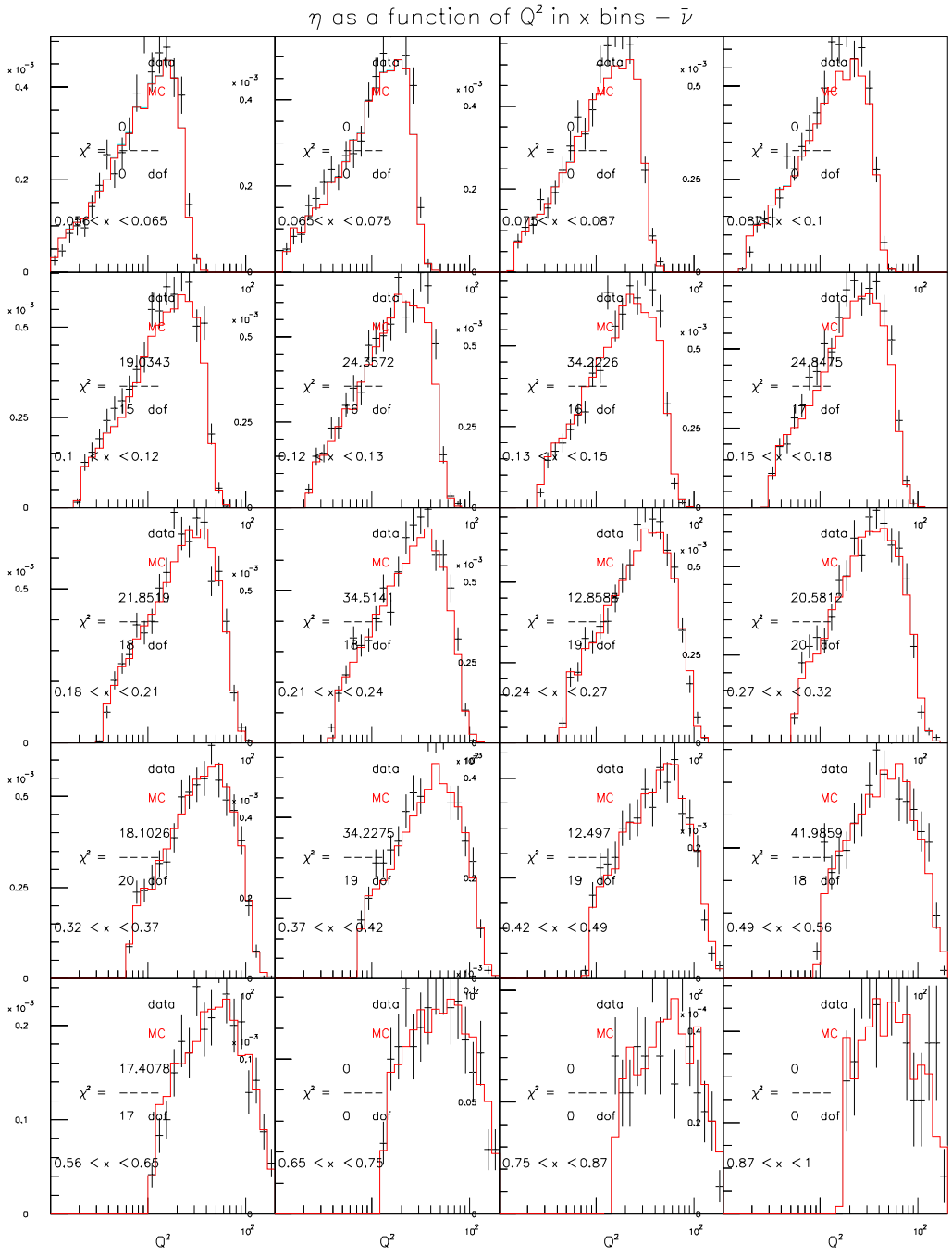

Figure D.20: GRV98NLO $\eta(Q^2)$ – $\overline{\nu}$ mode m_c sensitivity ($201 < E_\nu < 400$)

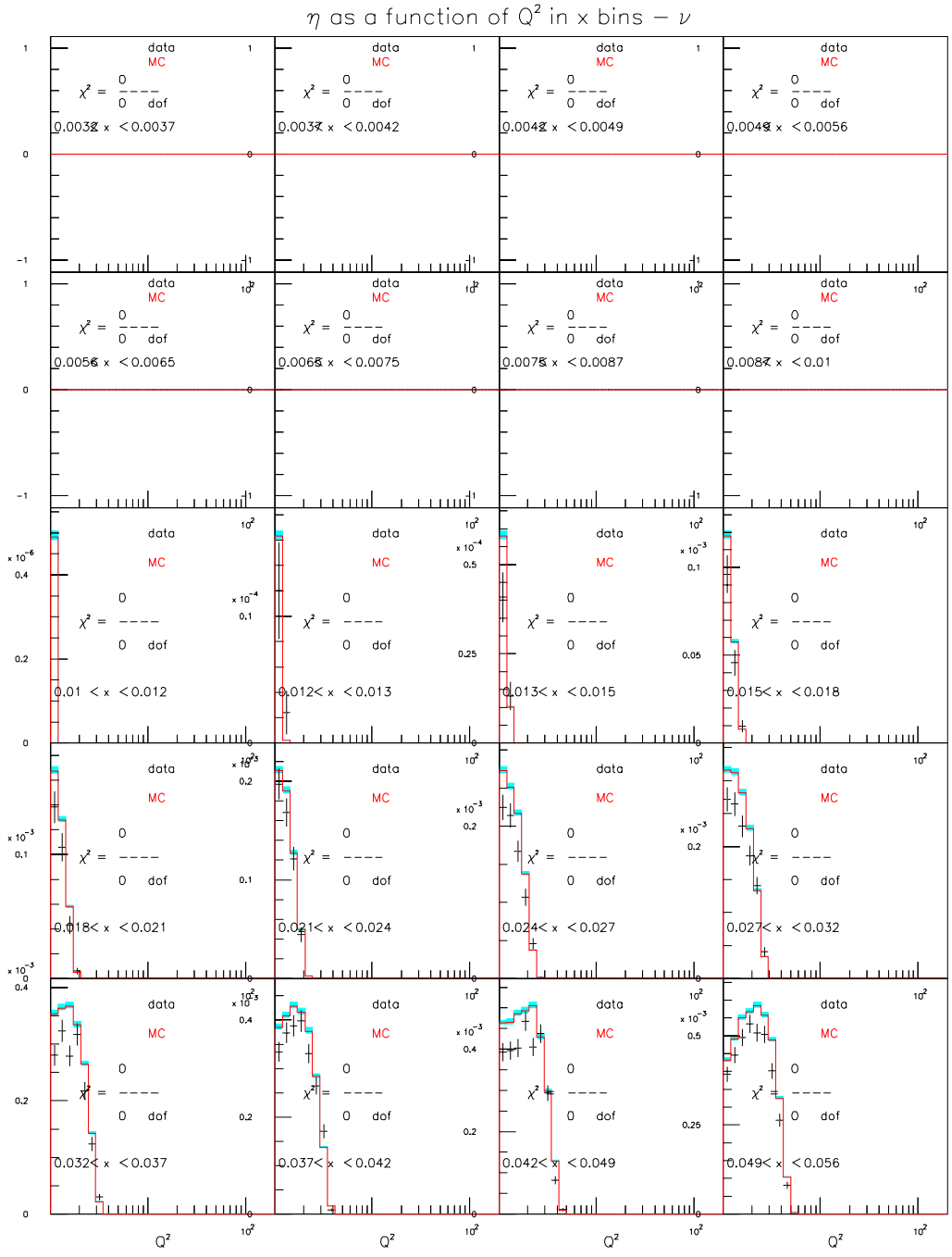

Figure D.21: CTEQ5NLO $\eta(Q^2)$ – ν mode m_c sensitivity ($20 < E_\nu < 62$)

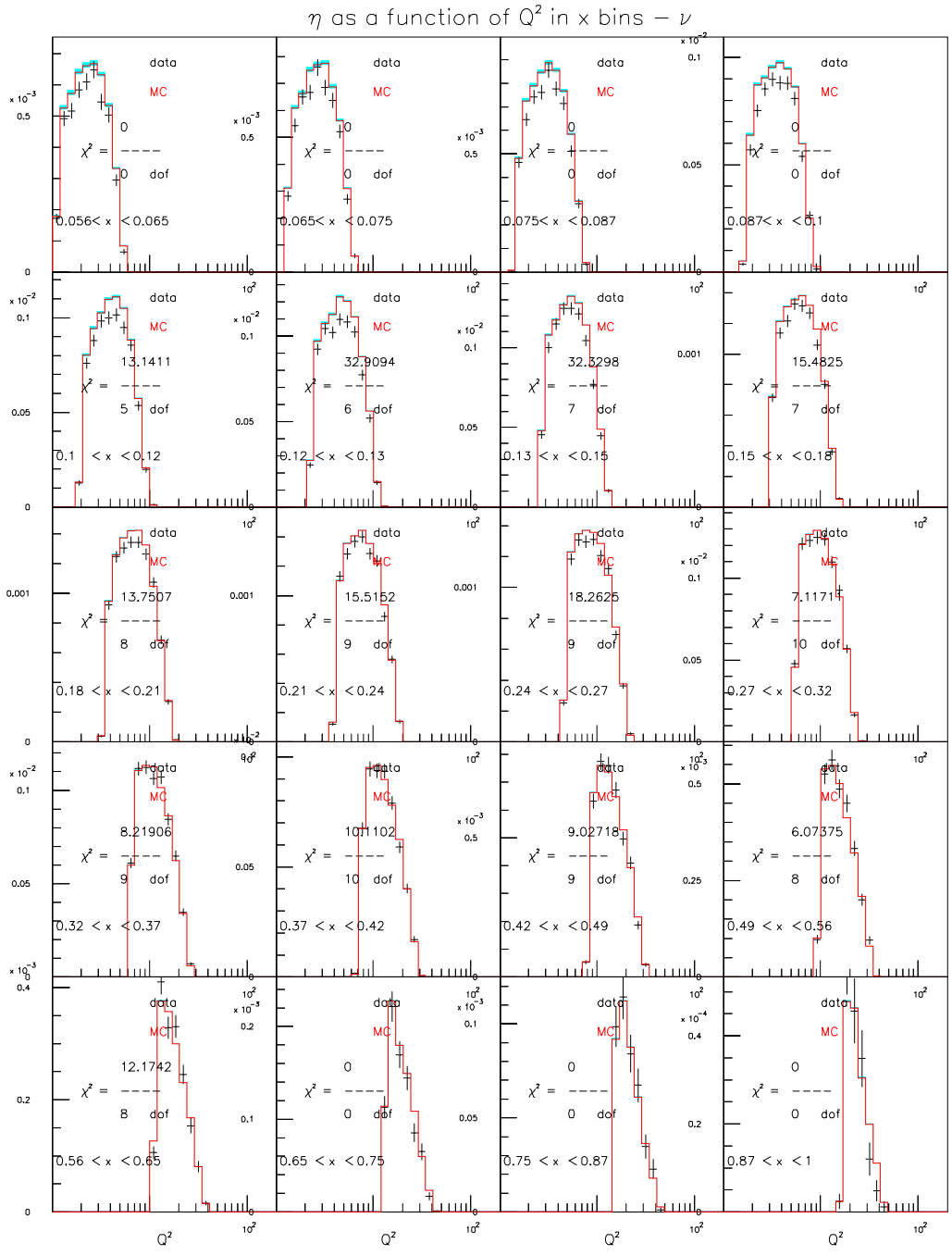

Figure D.22: CTEQ5NLO $\eta(Q^2)$ – ν mode m_c sensitivity ($20 < E_\nu < 62$)

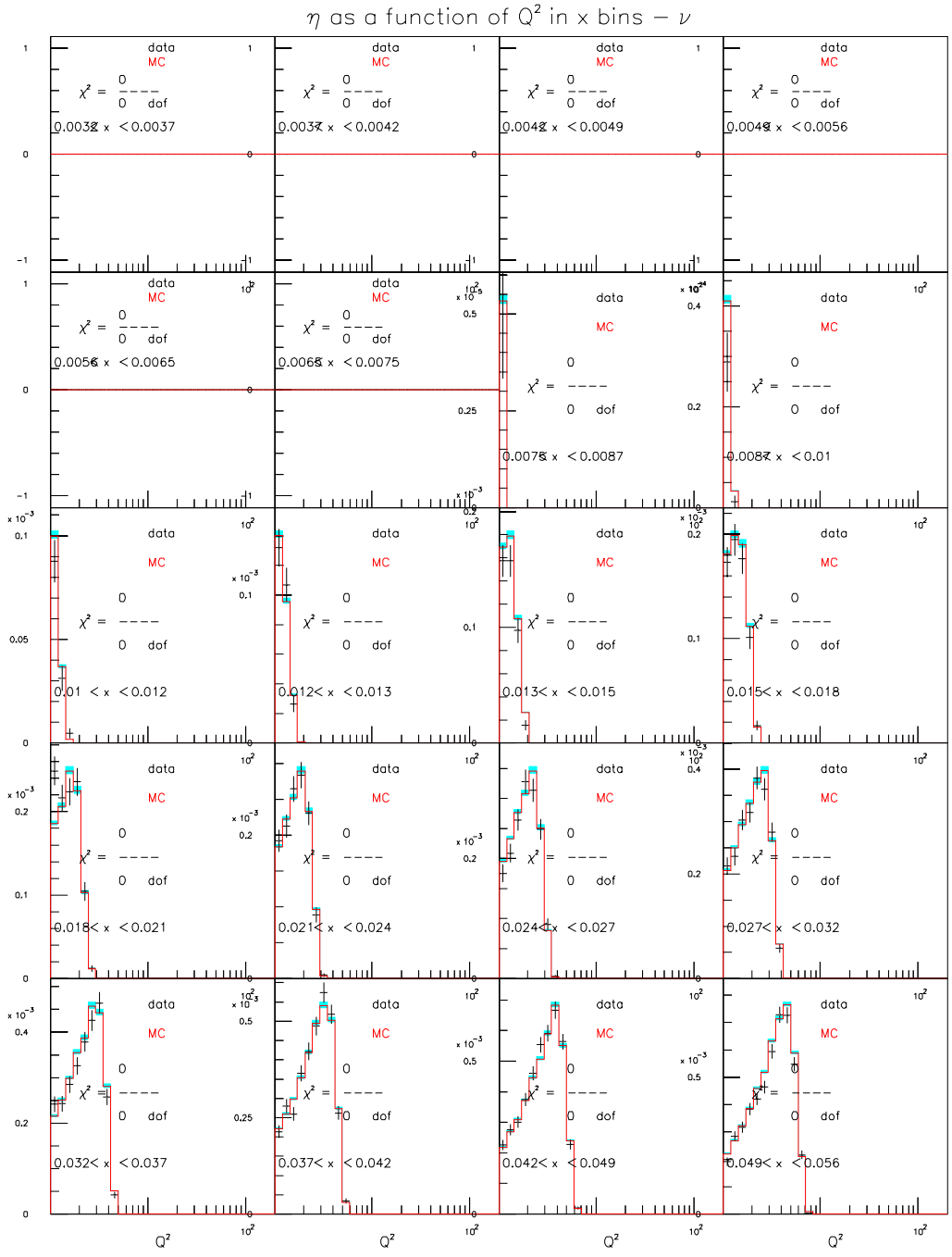

Figure D.23: CTEQ5NLO $\eta(Q^2)$ – ν mode m_c sensitivity ($62 < E_\nu < 85$)

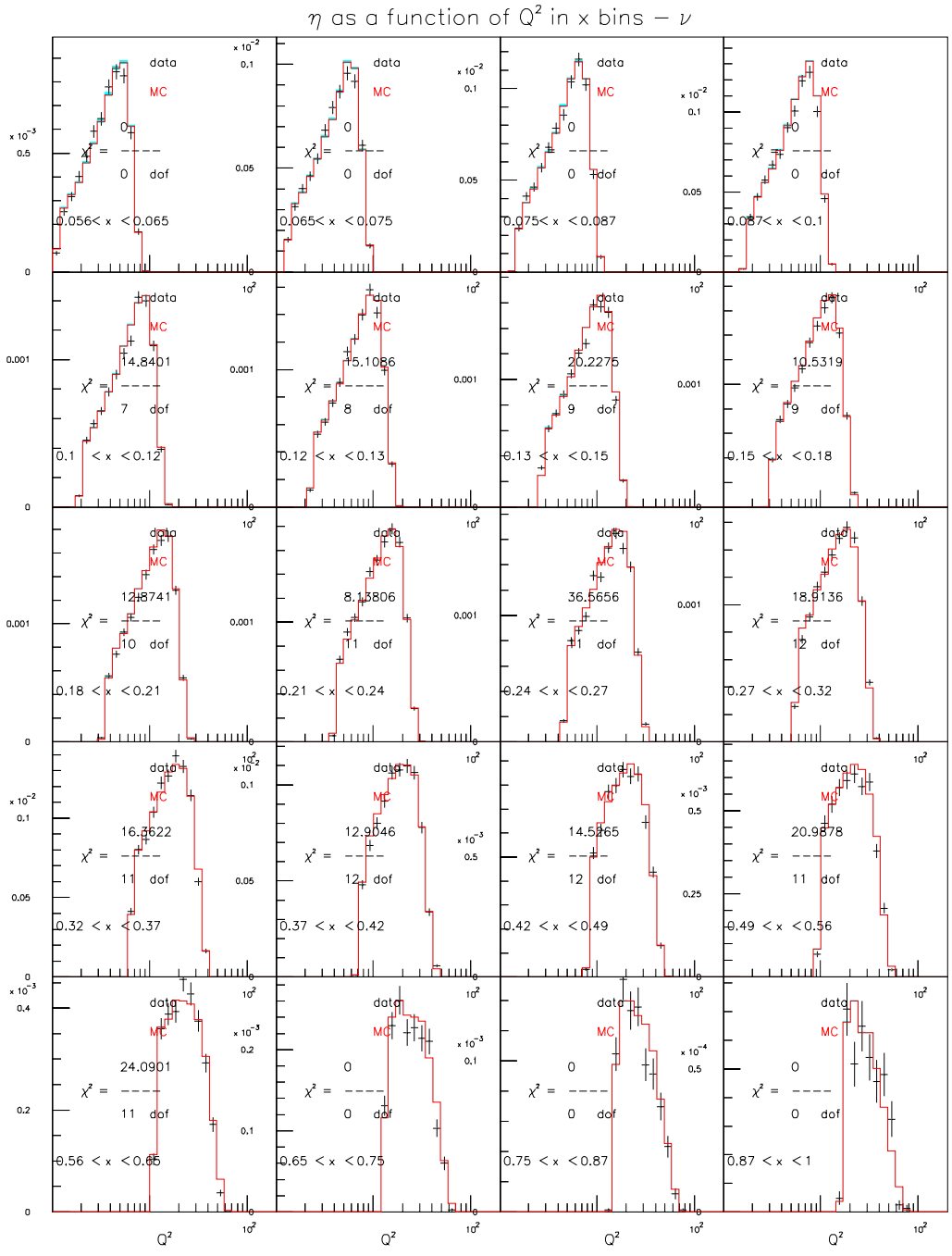

Figure D.24: CTEQ5NLO $\eta(Q^2)$ – ν mode m_c sensitivity ($62 < E_\nu < 85$)

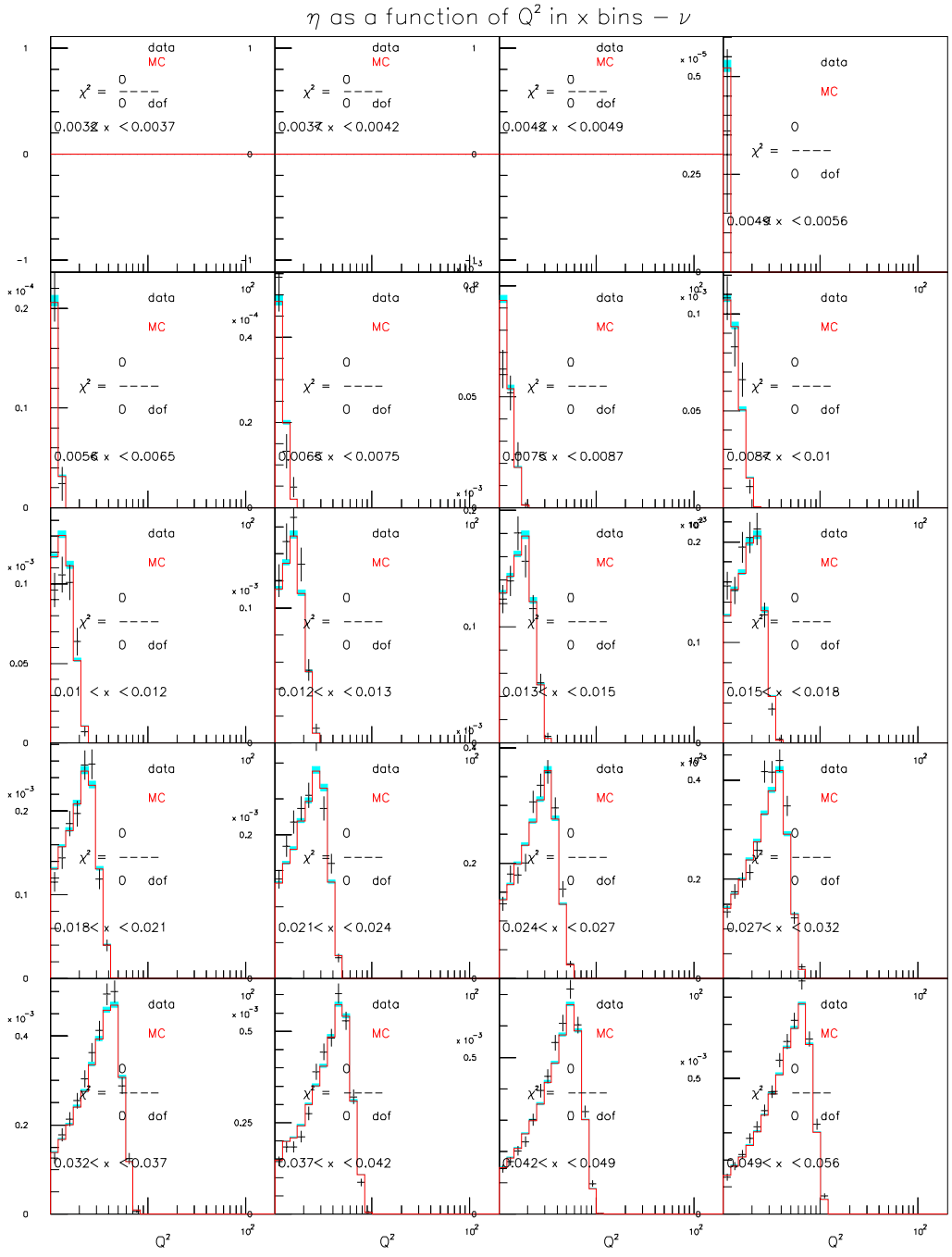

Figure D.25: CTEQ5NLO $\eta(Q^2)$ – ν mode m_c sensitivity ($85 < E_\nu < 129$)

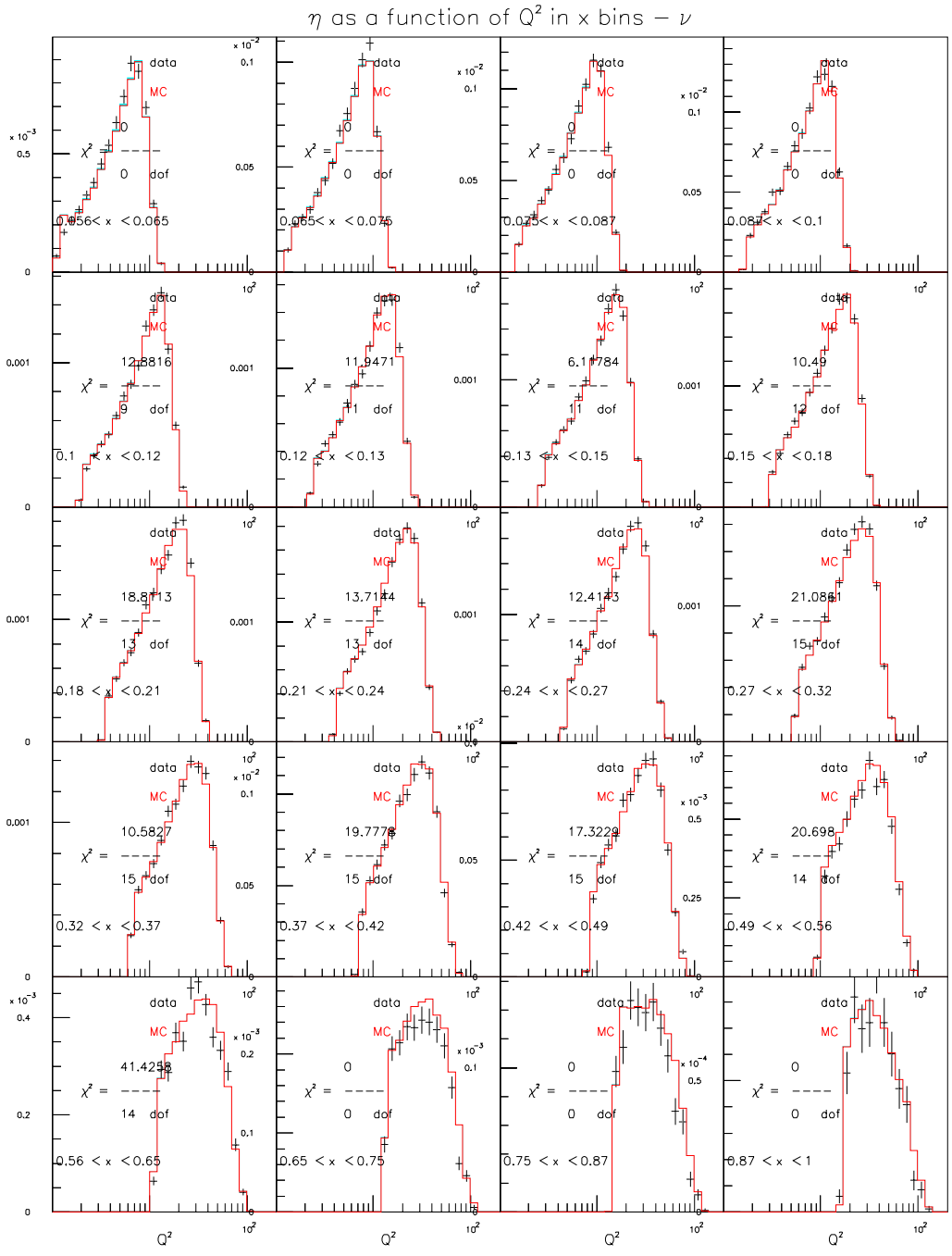

Figure D.26: CTEQ5NLO $\eta(Q^2)$ – ν mode m_c sensitivity ($85 < E_\nu < 129$)

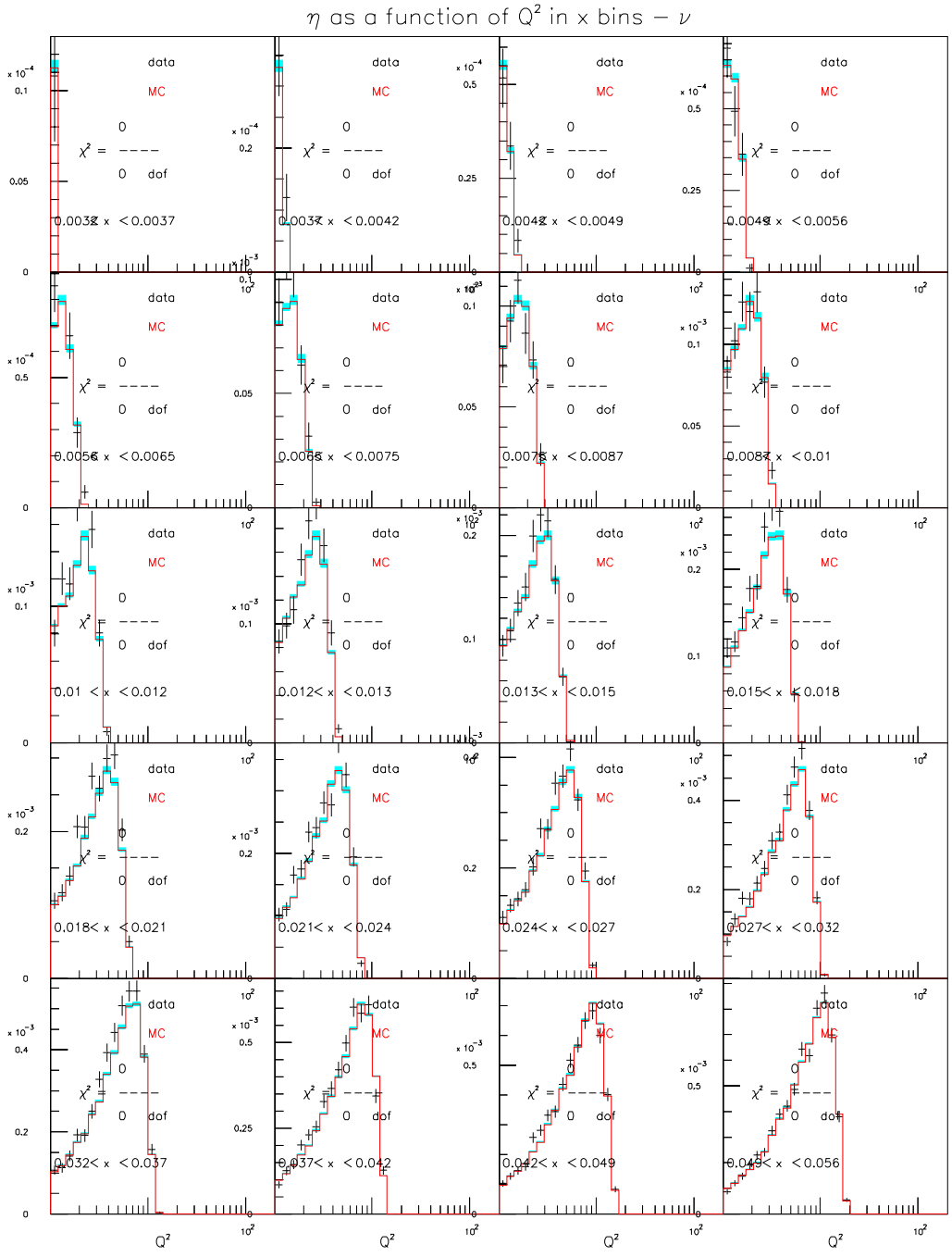

Figure D.27: CTEQ5NLO $\eta(Q^2)$ – ν mode m_c sensitivity ($129 < E_\nu < 201$)

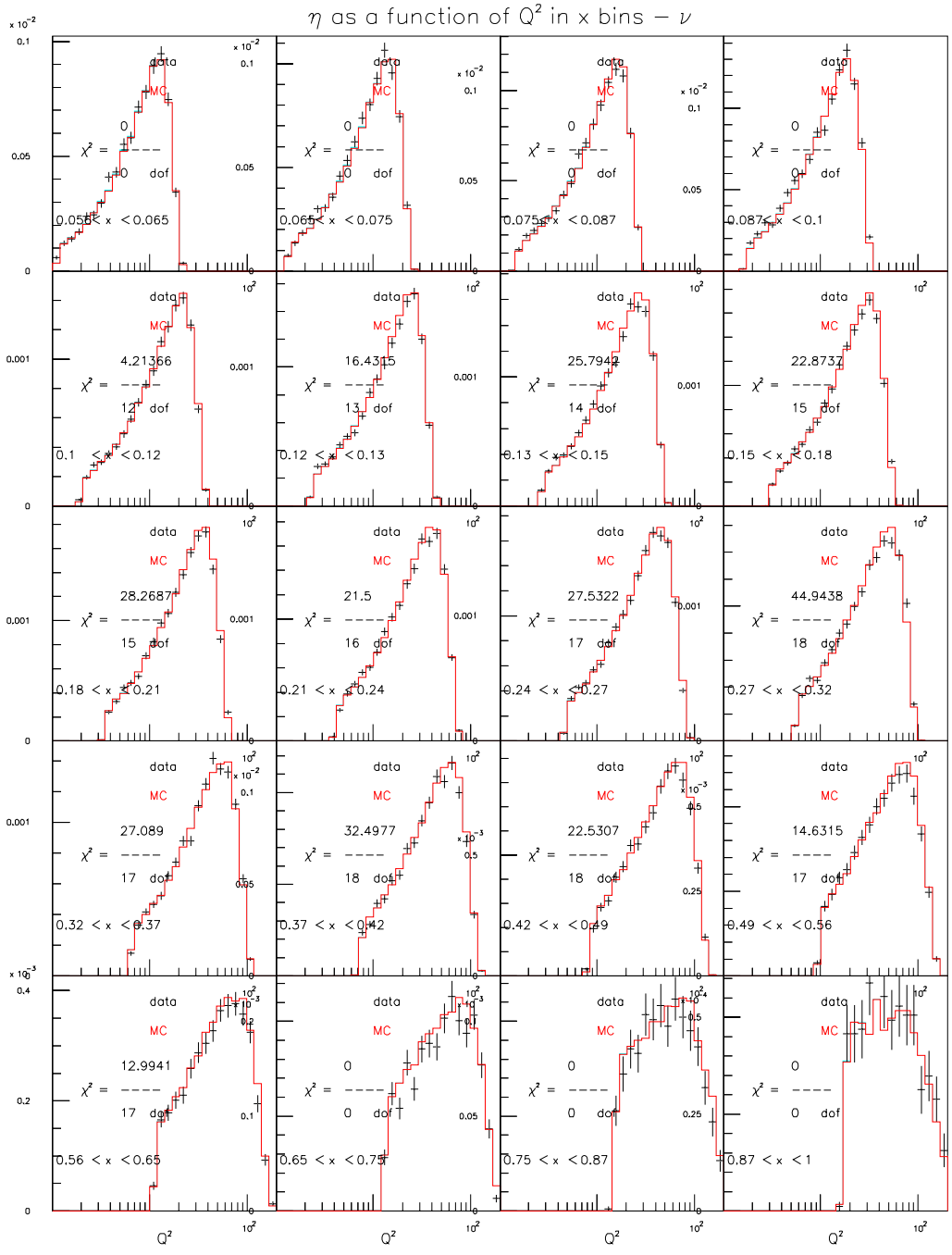

Figure D.28: CTEQ5NLO $\eta(Q^2)$ – ν mode m_c sensitivity ($129 < E_\nu < 201$)

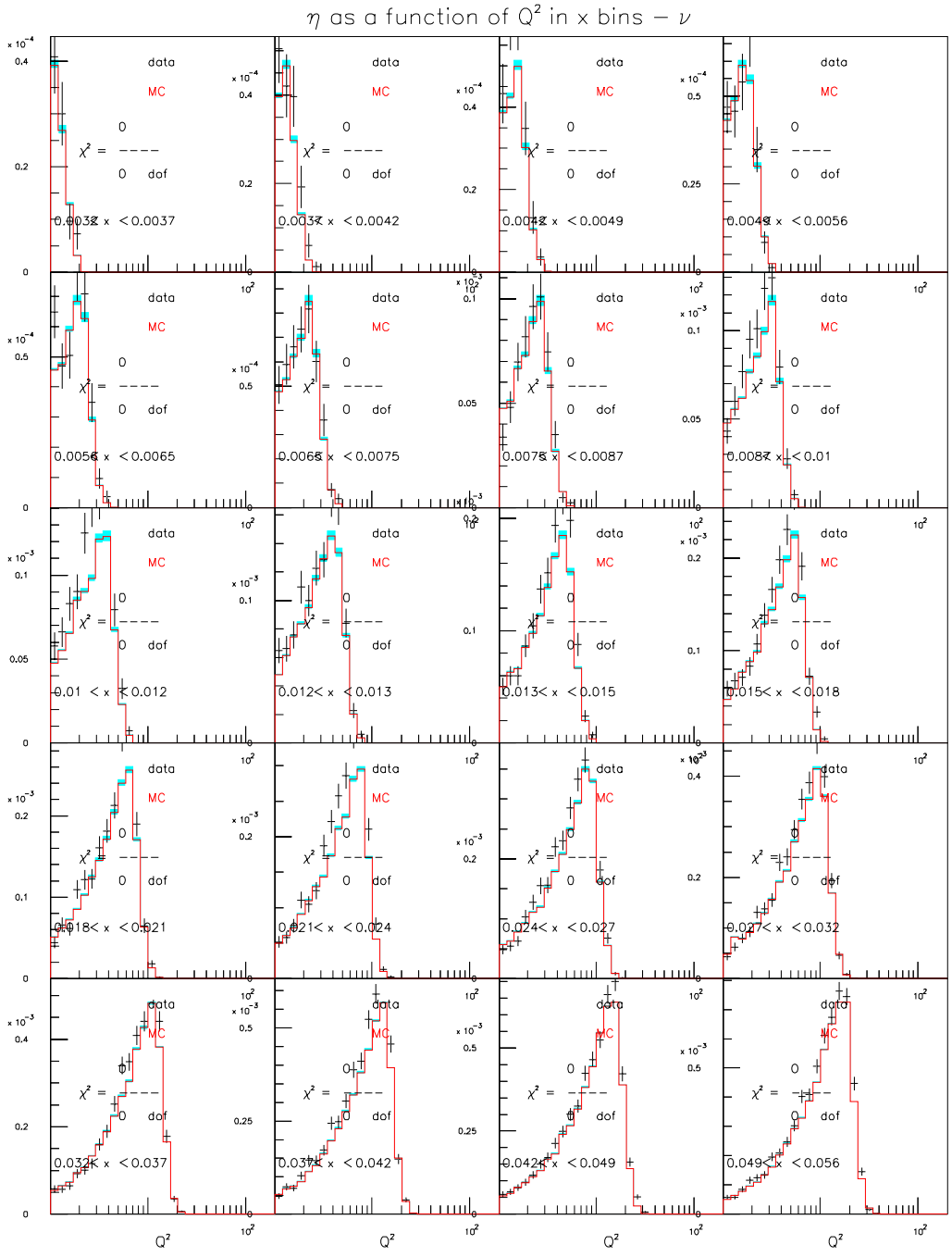

Figure D.29: CTEQ5NLO $\eta(Q^2)$ – ν mode m_c sensitivity ($201 < E_\nu < 400$)

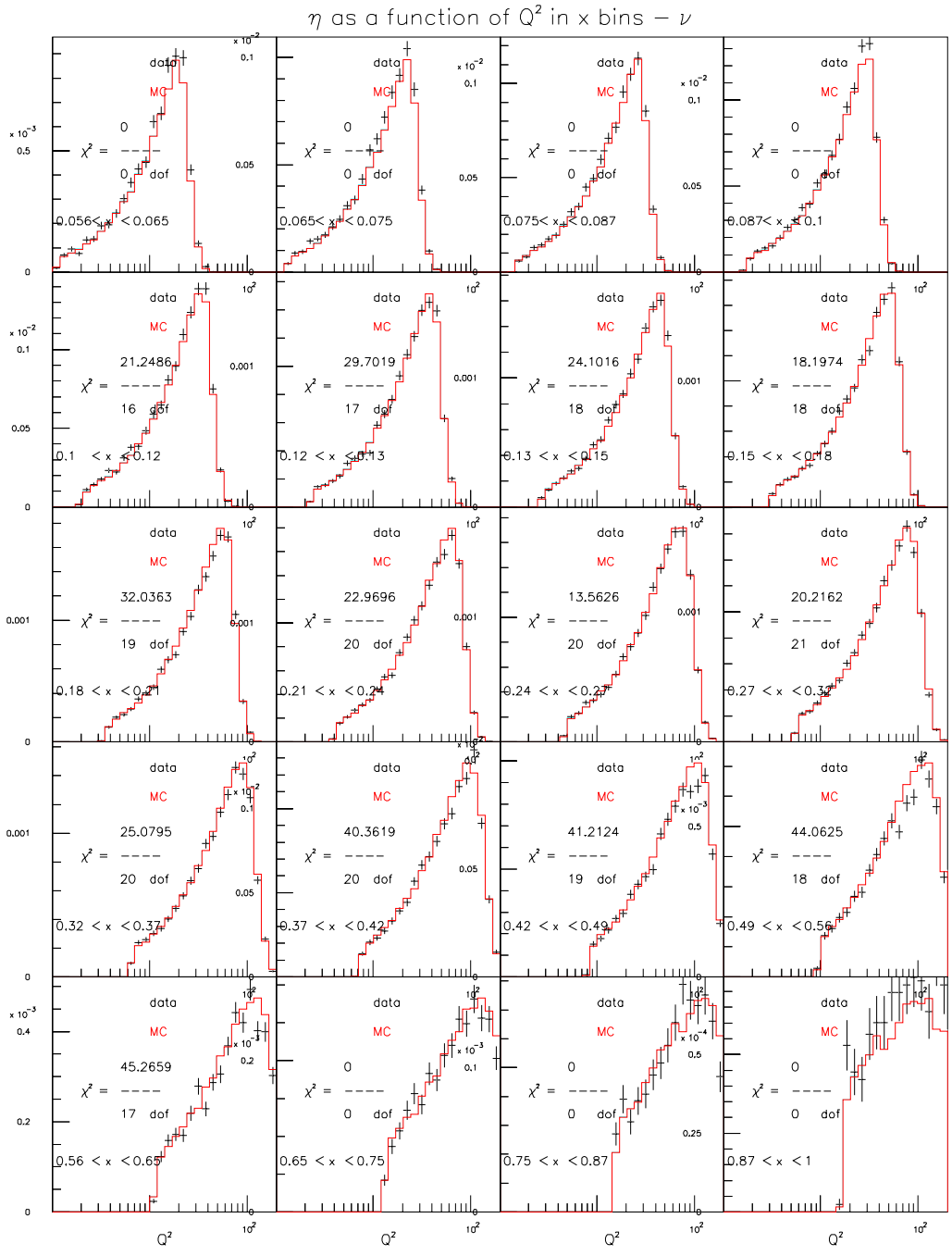

Figure D.30: CTEQ5NLO $\eta(Q^2)$ – ν mode m_c sensitivity ($201 < E_\nu < 400$)

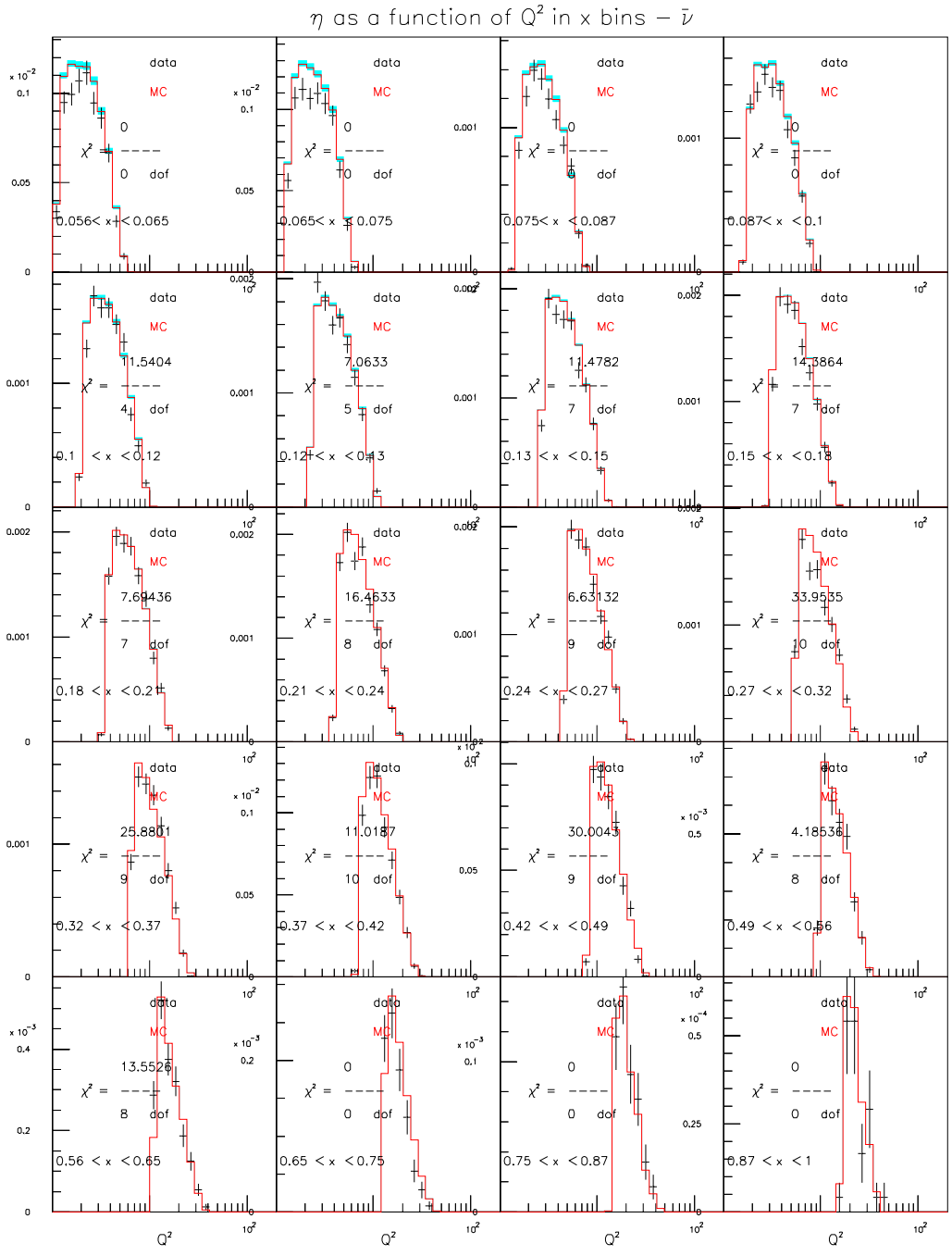

Figure D.31: CTEQ5NLO $\eta(Q^2)$ – $\overline{\nu}$ mode m_c sensitivity ($20 < E_\nu < 62$)

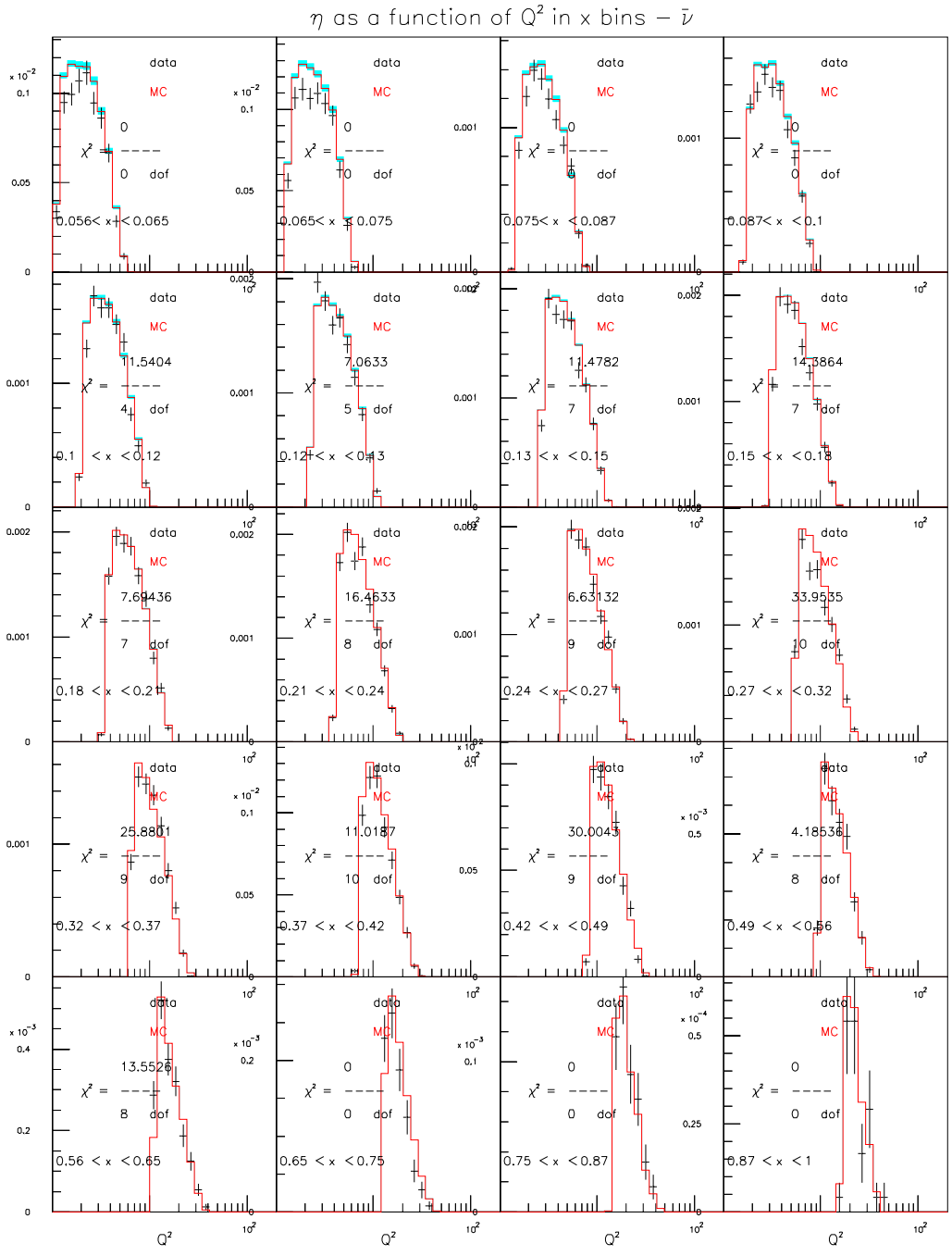

Figure D.32: CTEQ5NLO $\eta(Q^2)$ – $\overline{\nu}$ mode m_c sensitivity ($20 < E_\nu < 62$)

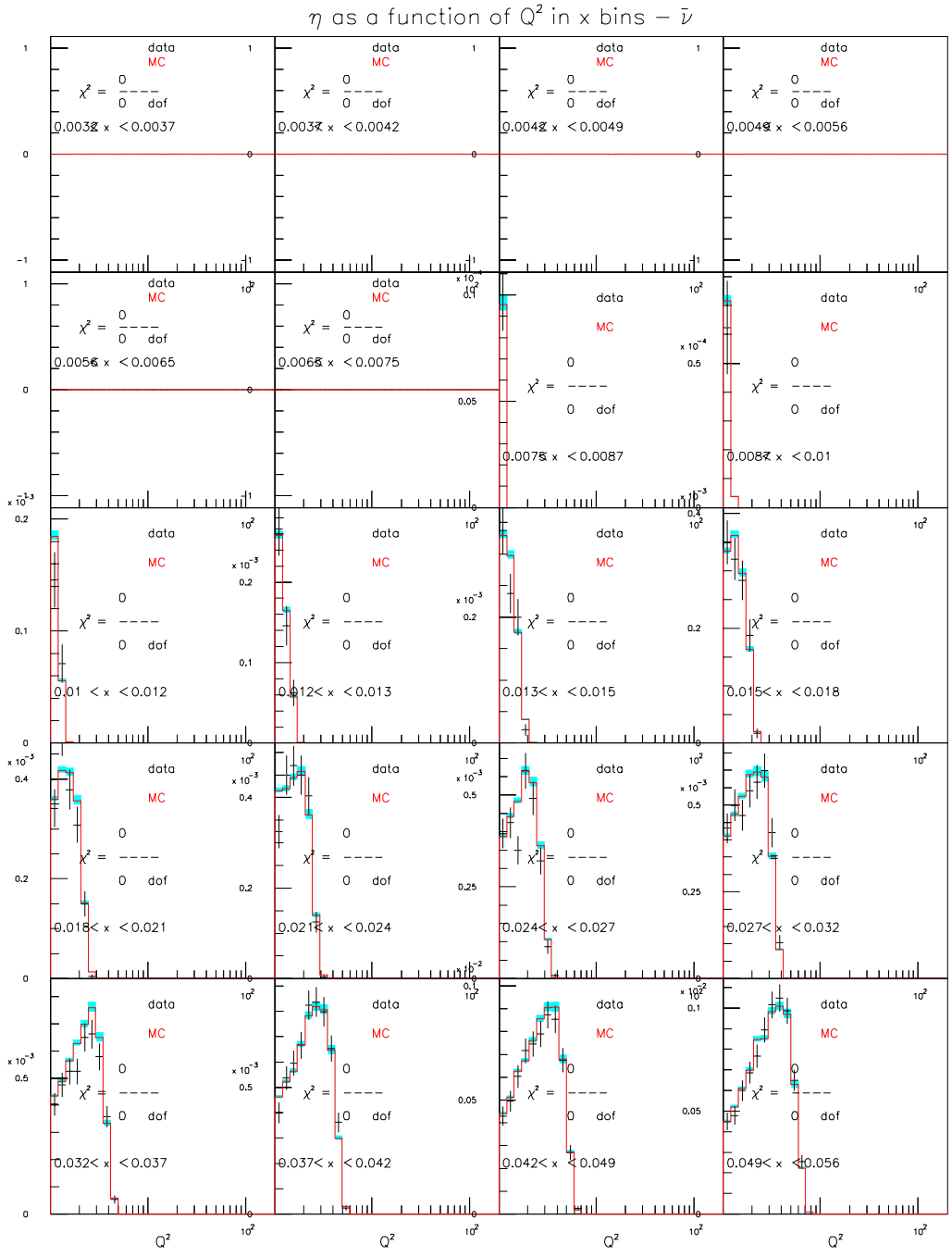

Figure D.33: CTEQ5NLO $\eta(Q^2)$ – $\overline{\nu}$ mode m_c sensitivity ($62 < E_\nu < 85$)

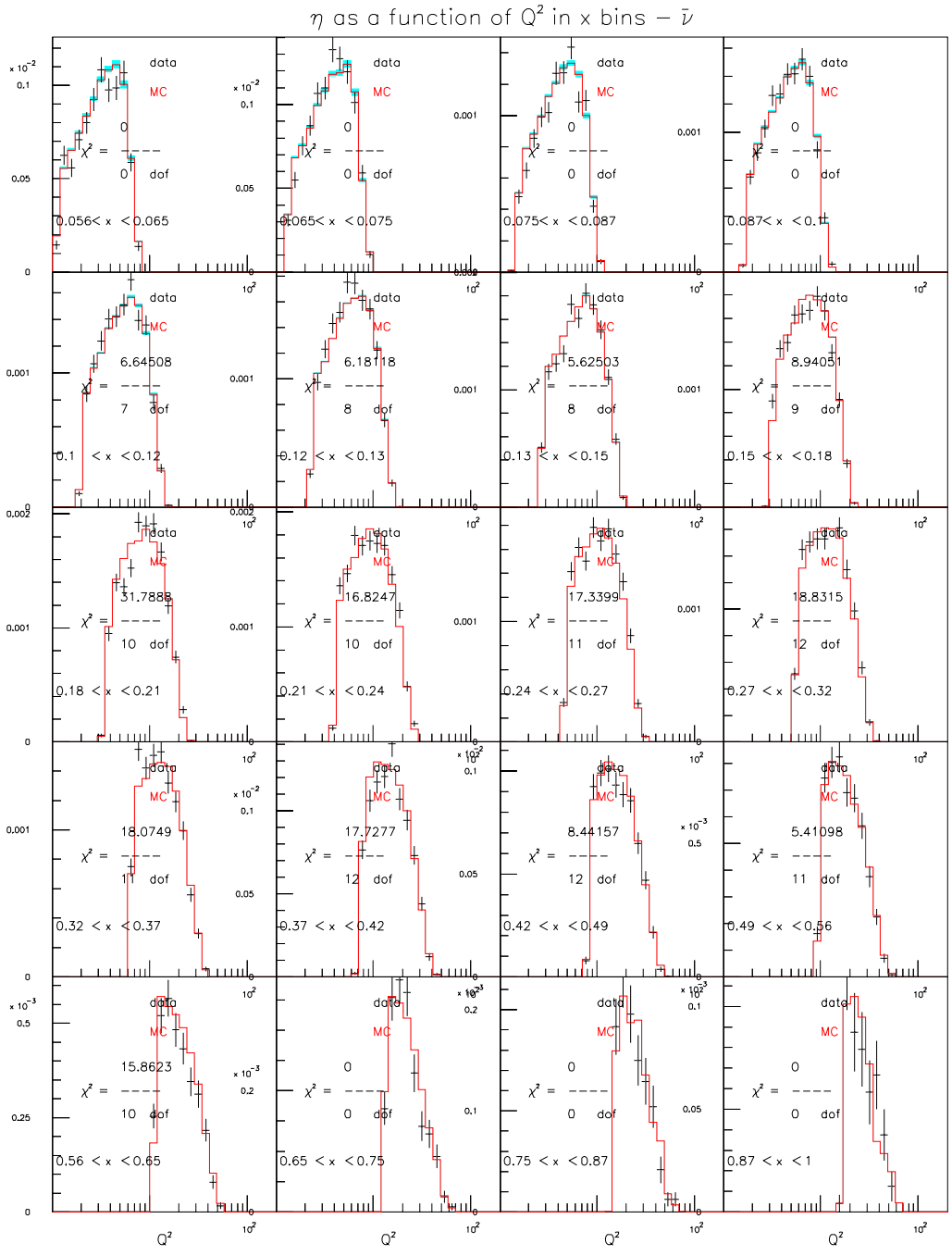

Figure D.34: CTEQ5NLO $\eta(Q^2)$ – $\overline{\nu}$ mode m_c sensitivity ($62 < E_\nu < 85$)

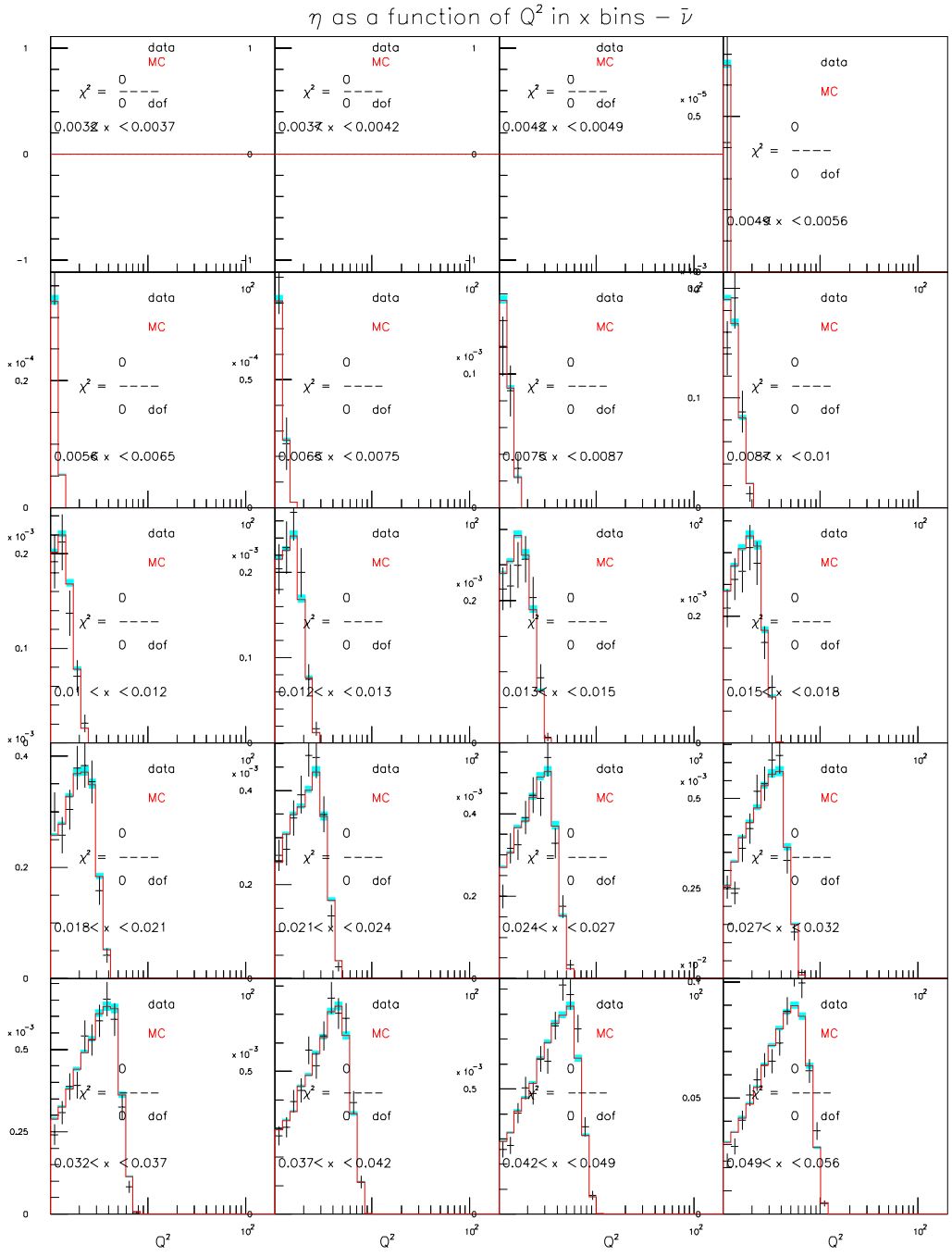

Figure D.35: CTEQ5NLO $\eta(Q^2)$ – $\overline{\nu}$ mode m_c sensitivity $(85 < E_\nu < 129)$

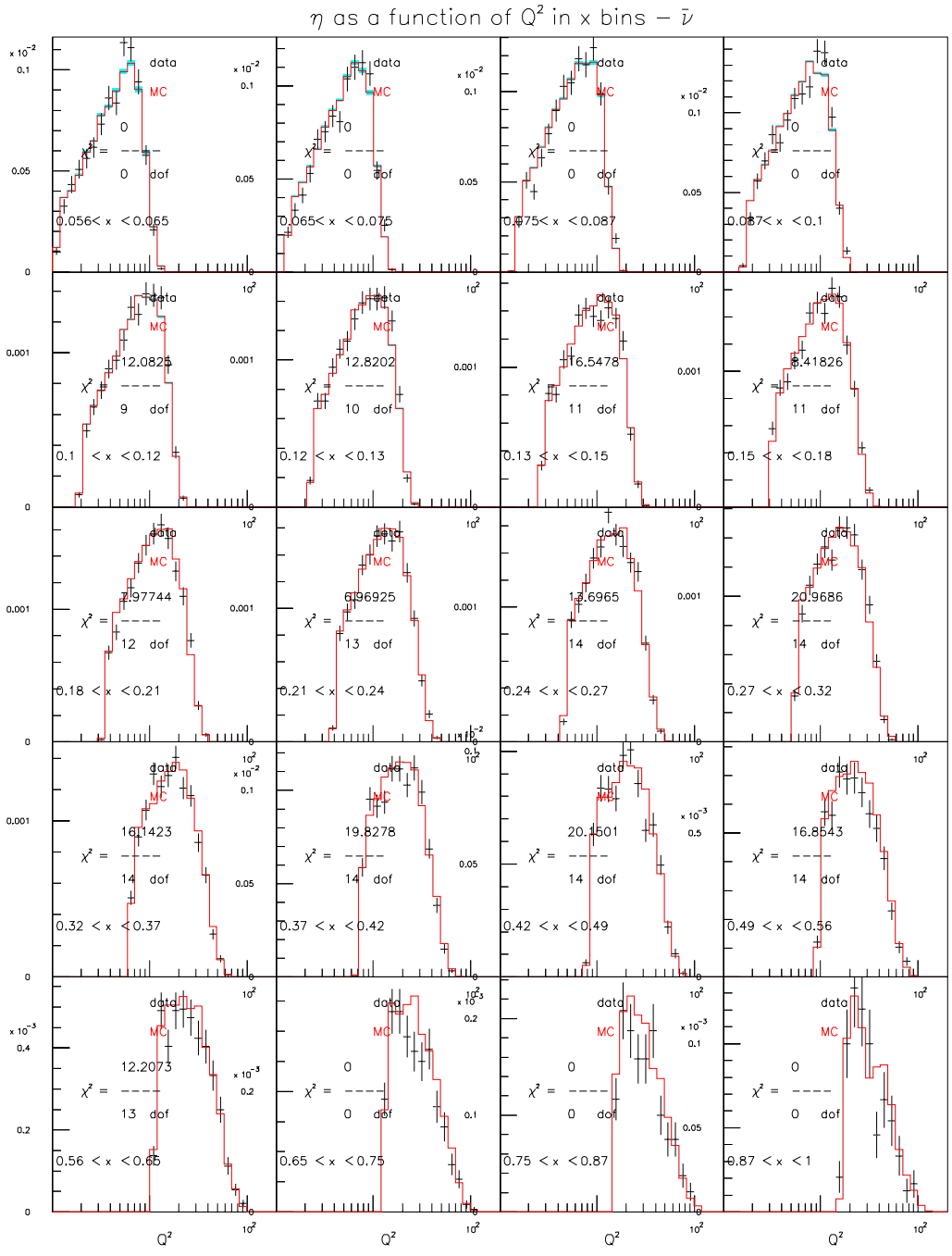

Figure D.36: CTEQ5NLO $\eta(Q^2)$ – $\overline{\nu}$ mode m_c sensitivity ($85 < E_\nu < 129$)

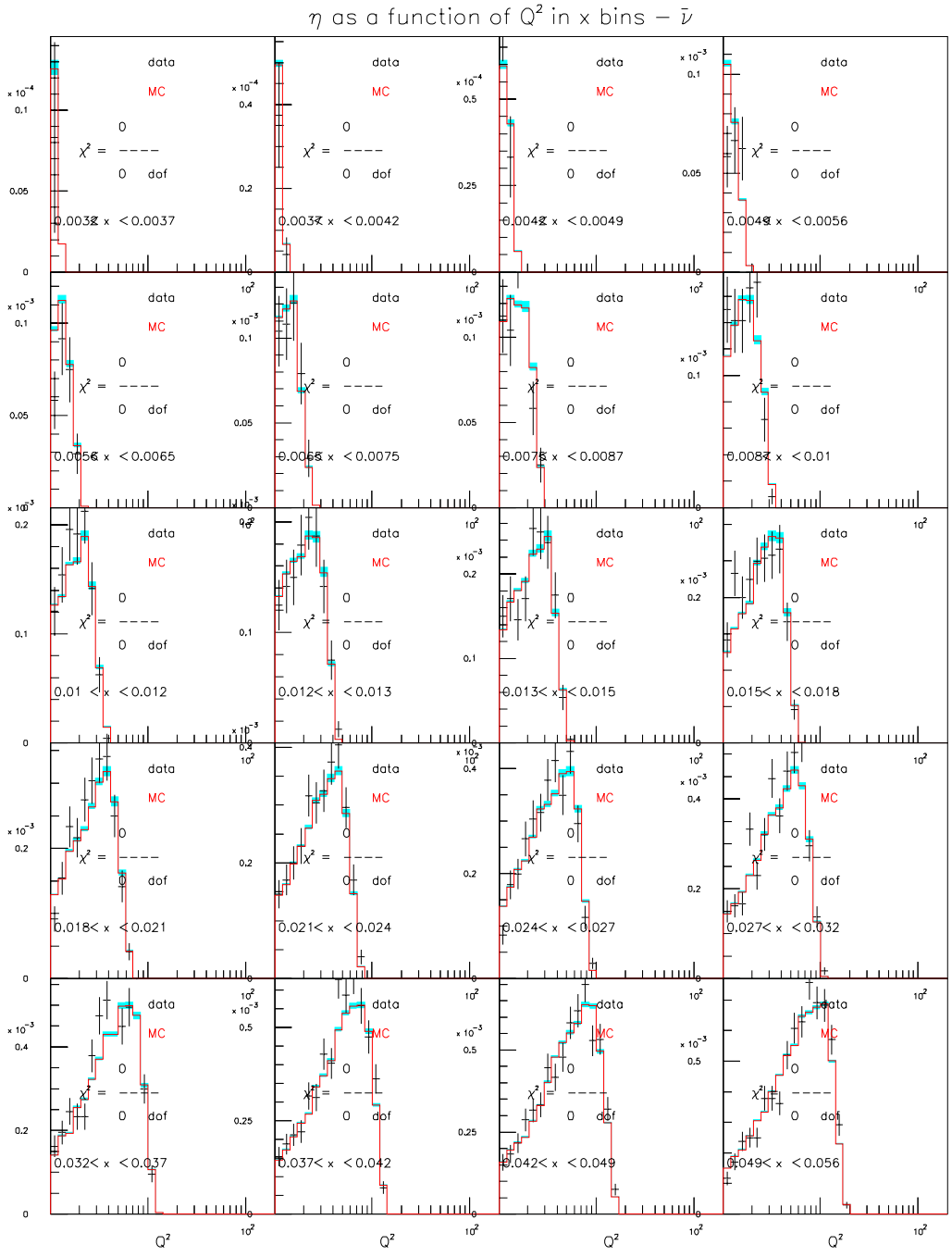

Figure D.37: CTEQ5NLO $\eta(Q^2)$ – $\overline{\nu}$ mode m_c sensitivity ($129 < E_\nu < 201$)

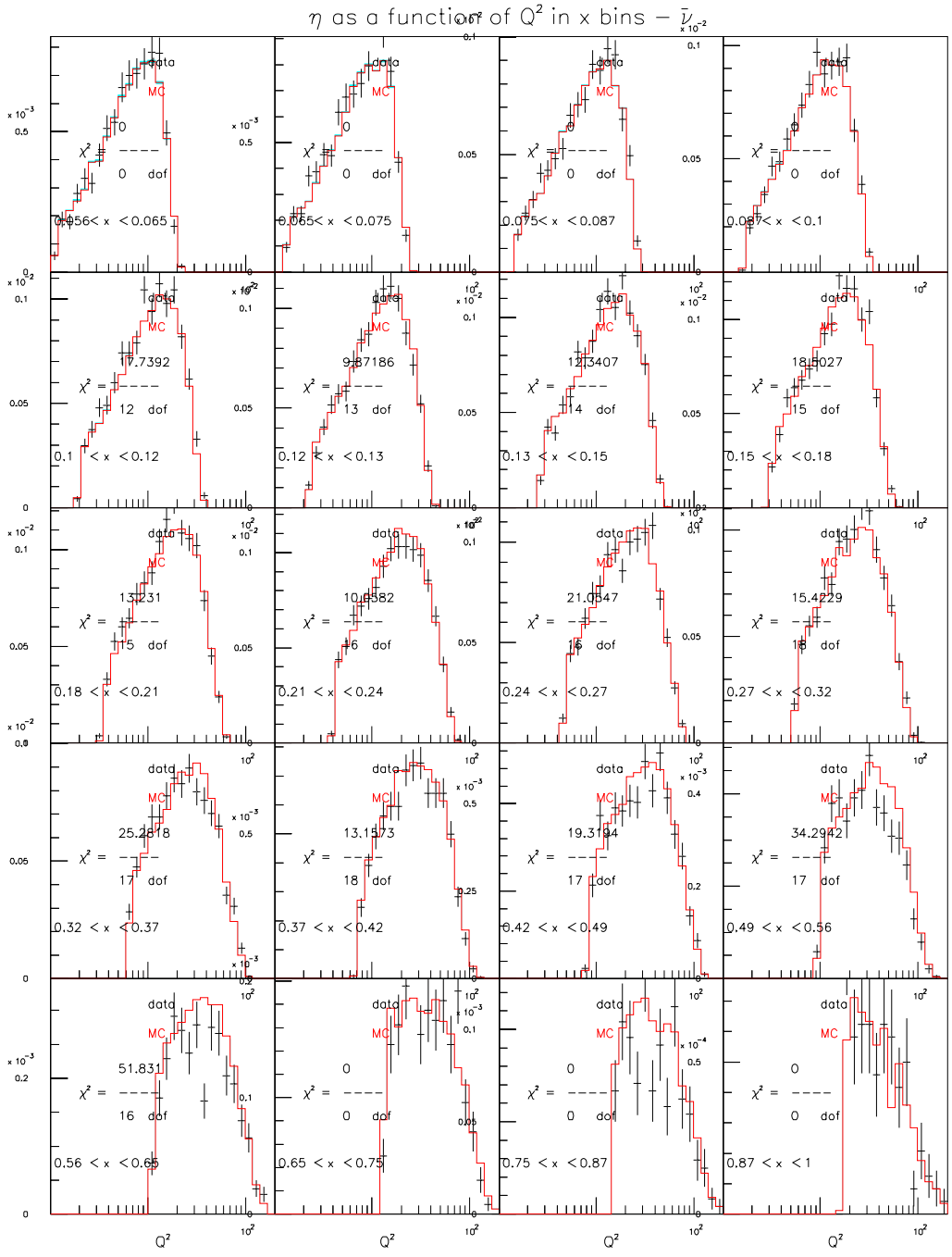

Figure D.38: CTEQ5NLO $\eta(Q^2)$ – $\overline{\nu}$ mode m_c sensitivity ($129 < E_\nu < 201$)

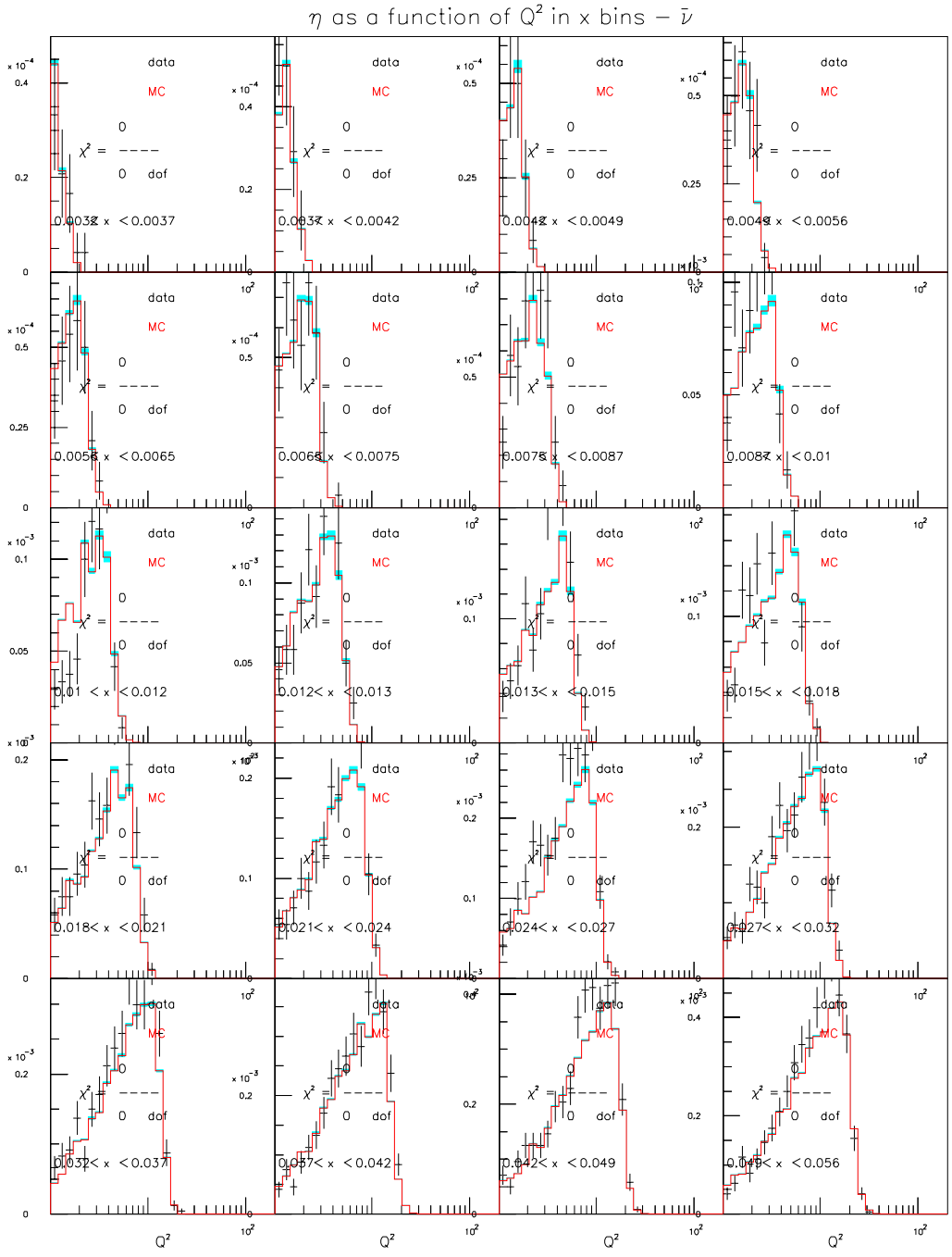

Figure D.39: CTEQ5NLO $\eta(Q^2)$ – $\overline{\nu}$ mode m_c sensitivity ($201 < E_\nu < 400$)

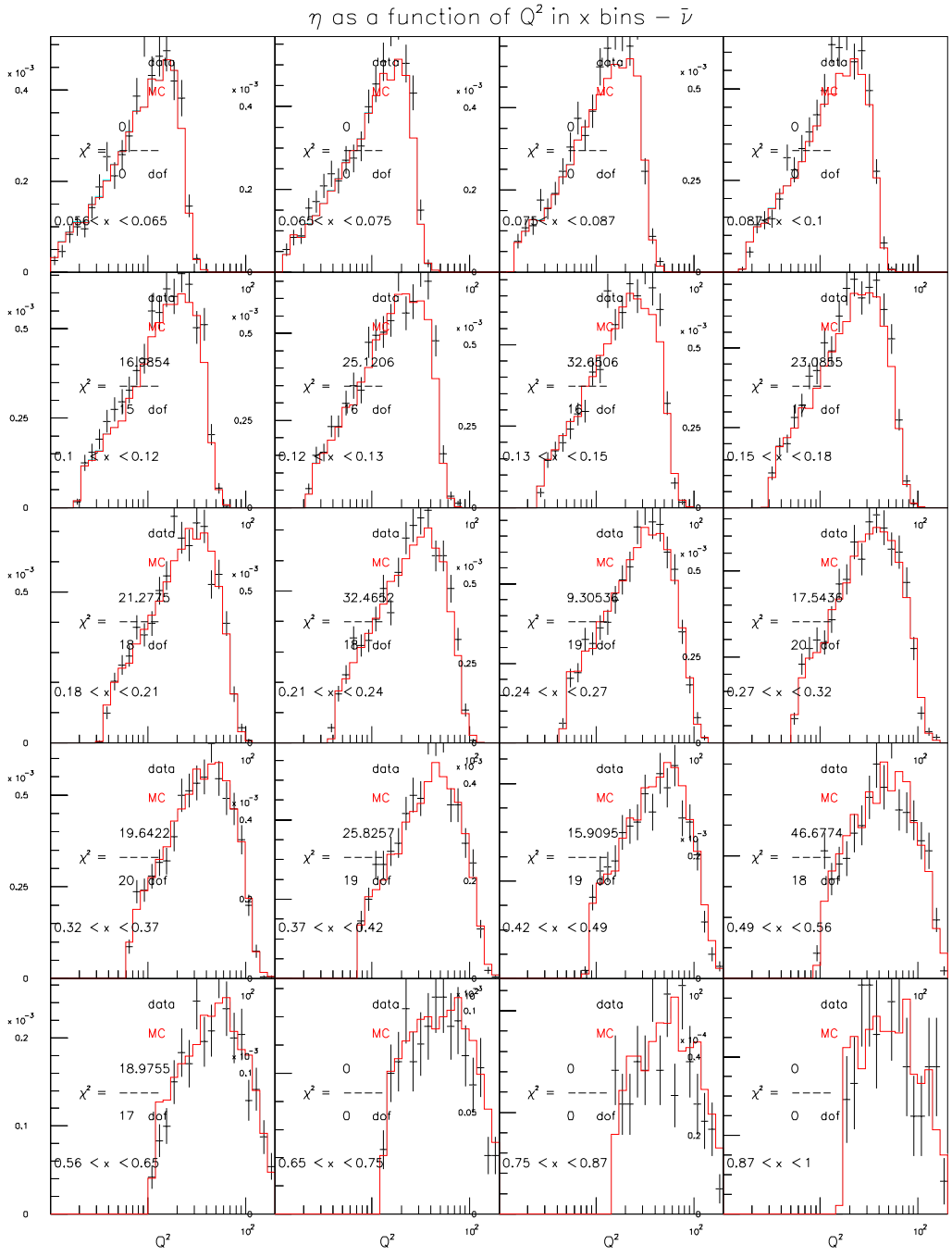

Figure D.40: CTEQ5NLO $\eta(Q^2)$ – $\overline{\nu}$ mode m_c sensitivity ($201 < E_\nu < 400$)

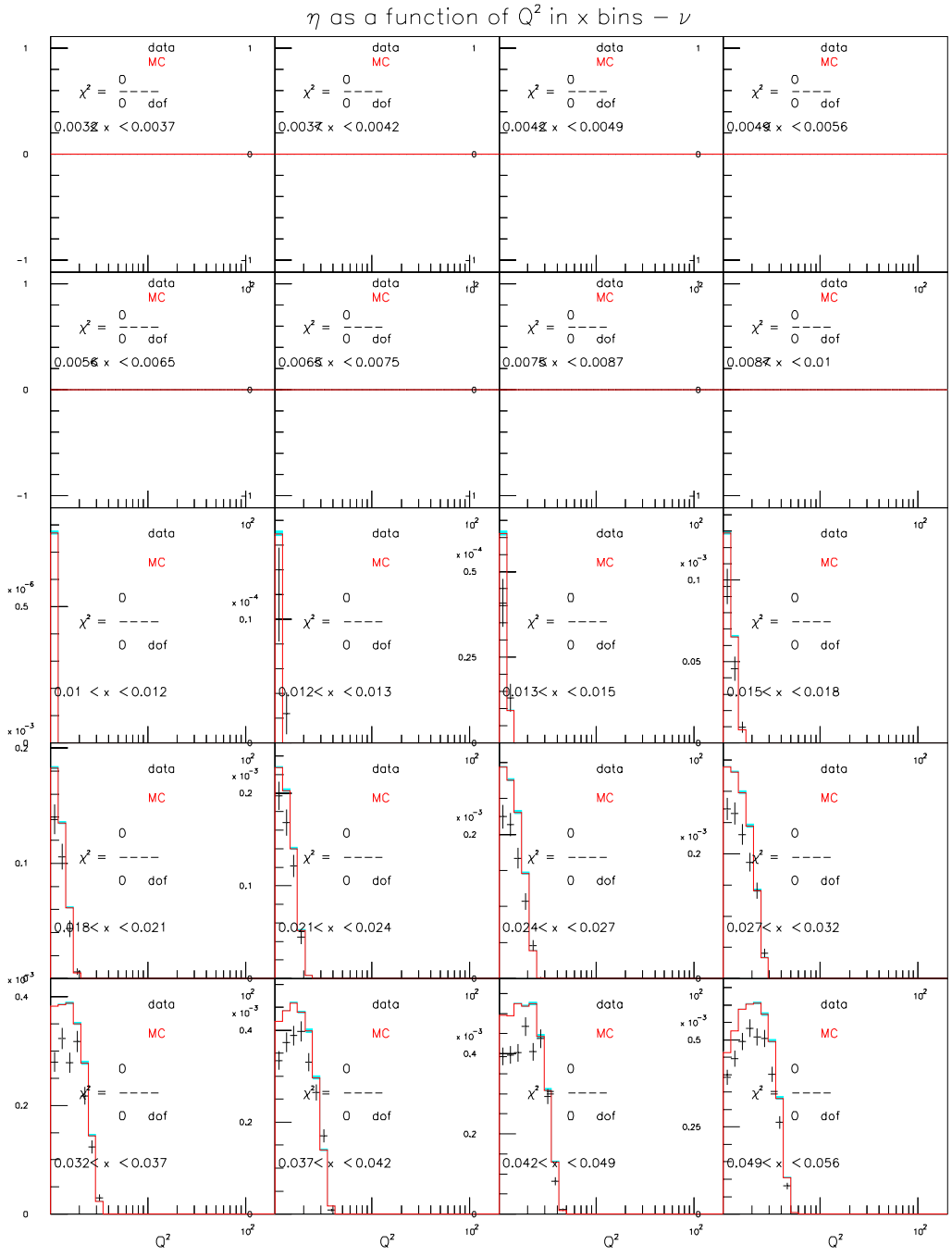

Figure D.41: GRV98NLO $\eta(Q^2)$ – ν mode $s(x,Q^2)$ sensitivity $(20 < E_\nu < 62)$

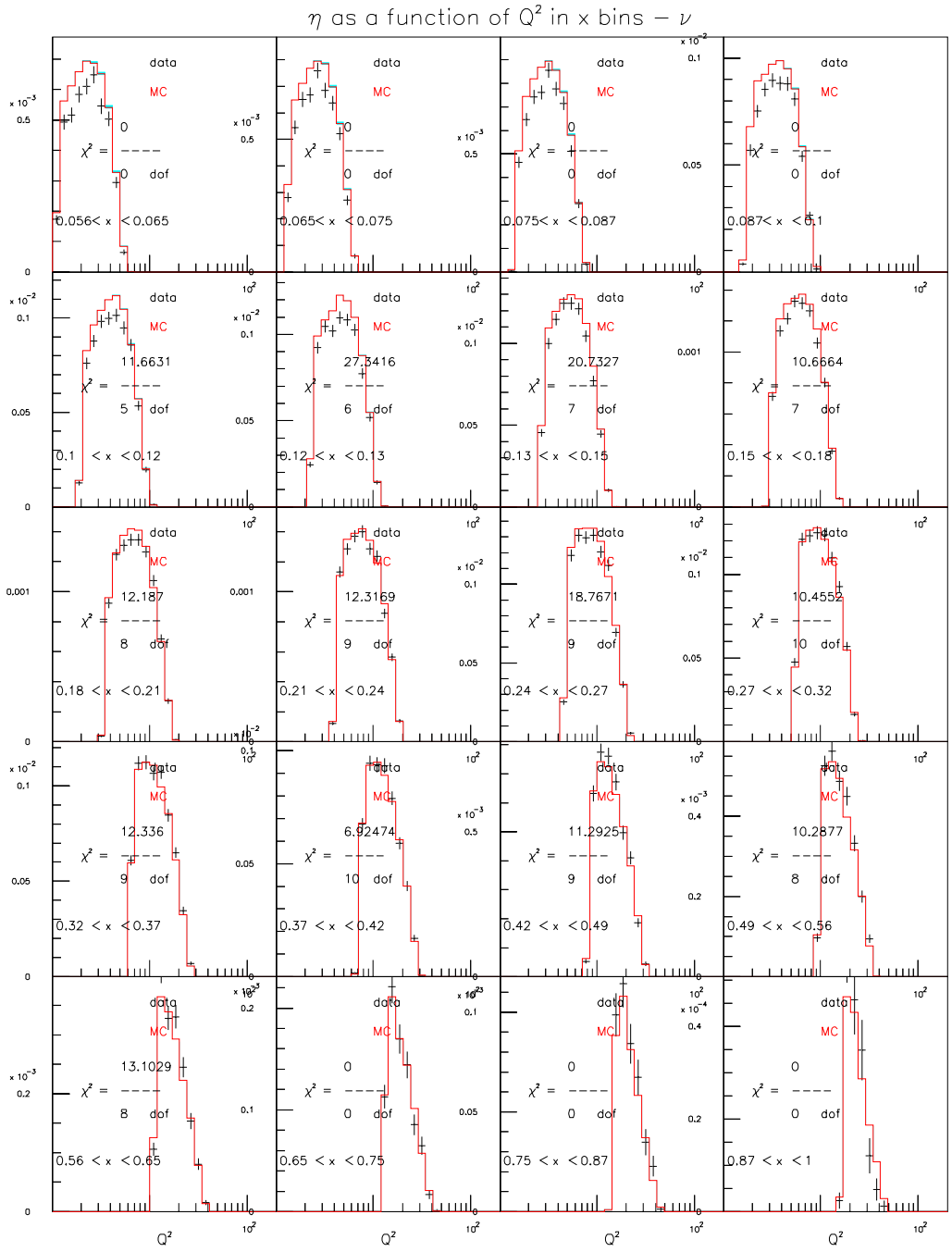

Figure D.42: GRV98NLO $\eta(Q^2)$ – ν mode $s(x, Q^2)$ sensitivity $(20 < E_\nu < 62)$

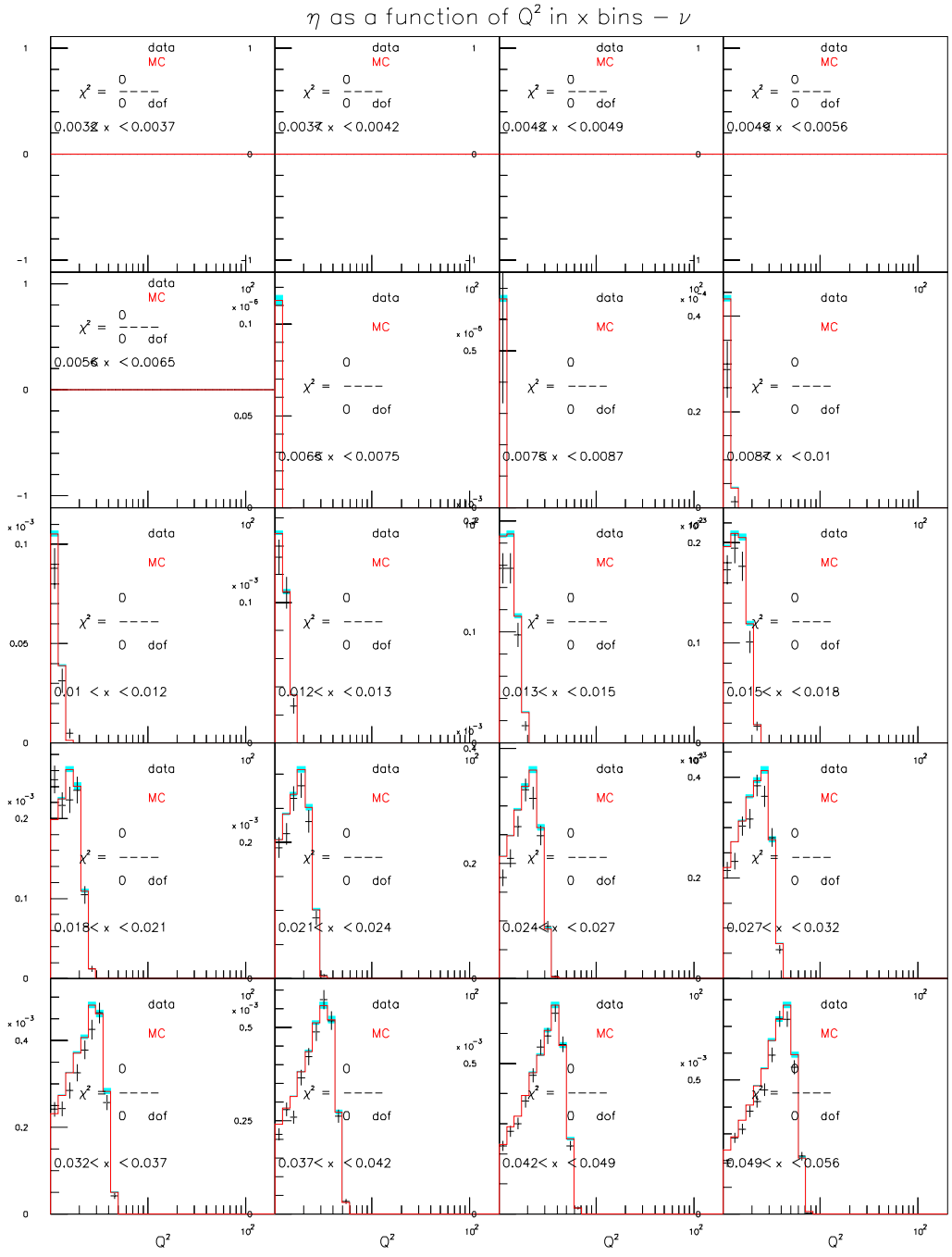

Figure D.43: GRV98NLO $\eta(Q^2)$ – ν mode $s(x, Q^2)$ sensitivity $(62 < E_\nu < 85)$

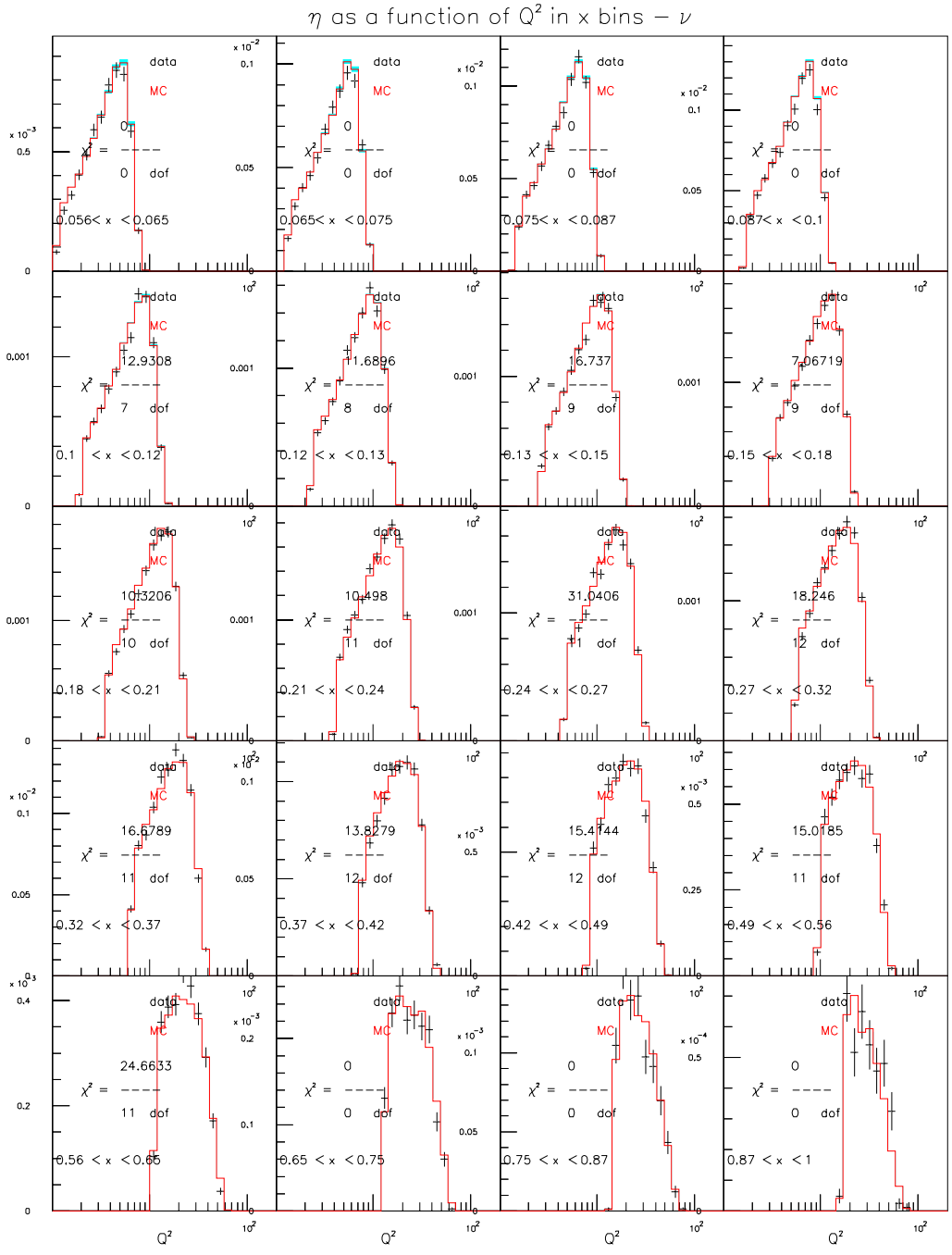

Figure D.44: GRV98NLO $\eta(Q^2)$ – ν mode $s(x, Q^2)$ sensitivity $(62 < E_\nu < 85)$

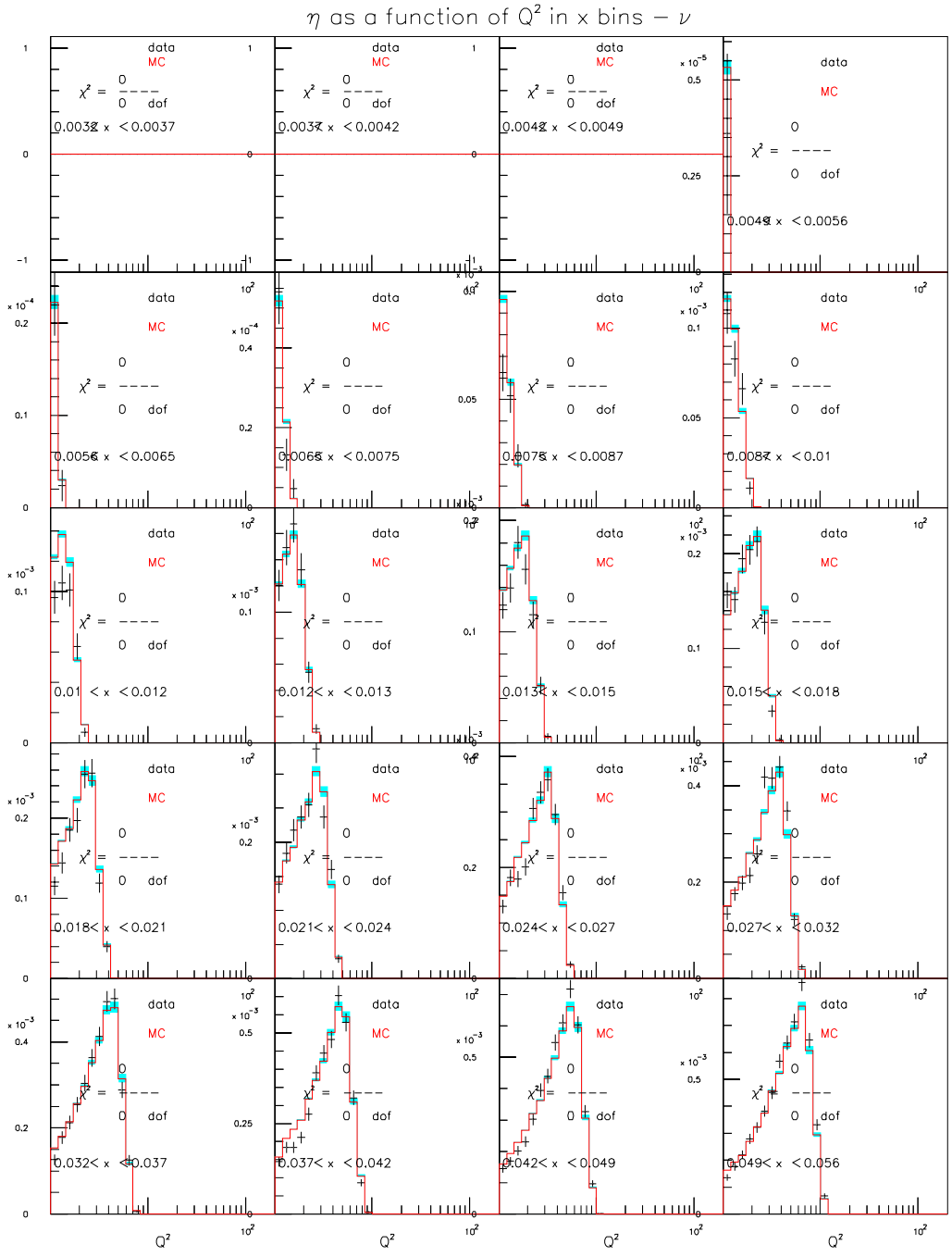

Figure D.45: GRV98NLO $\eta(Q^2)$ – ν mode $s(x, Q^2)$ sensitivity $(85 < E_\nu < 129)$

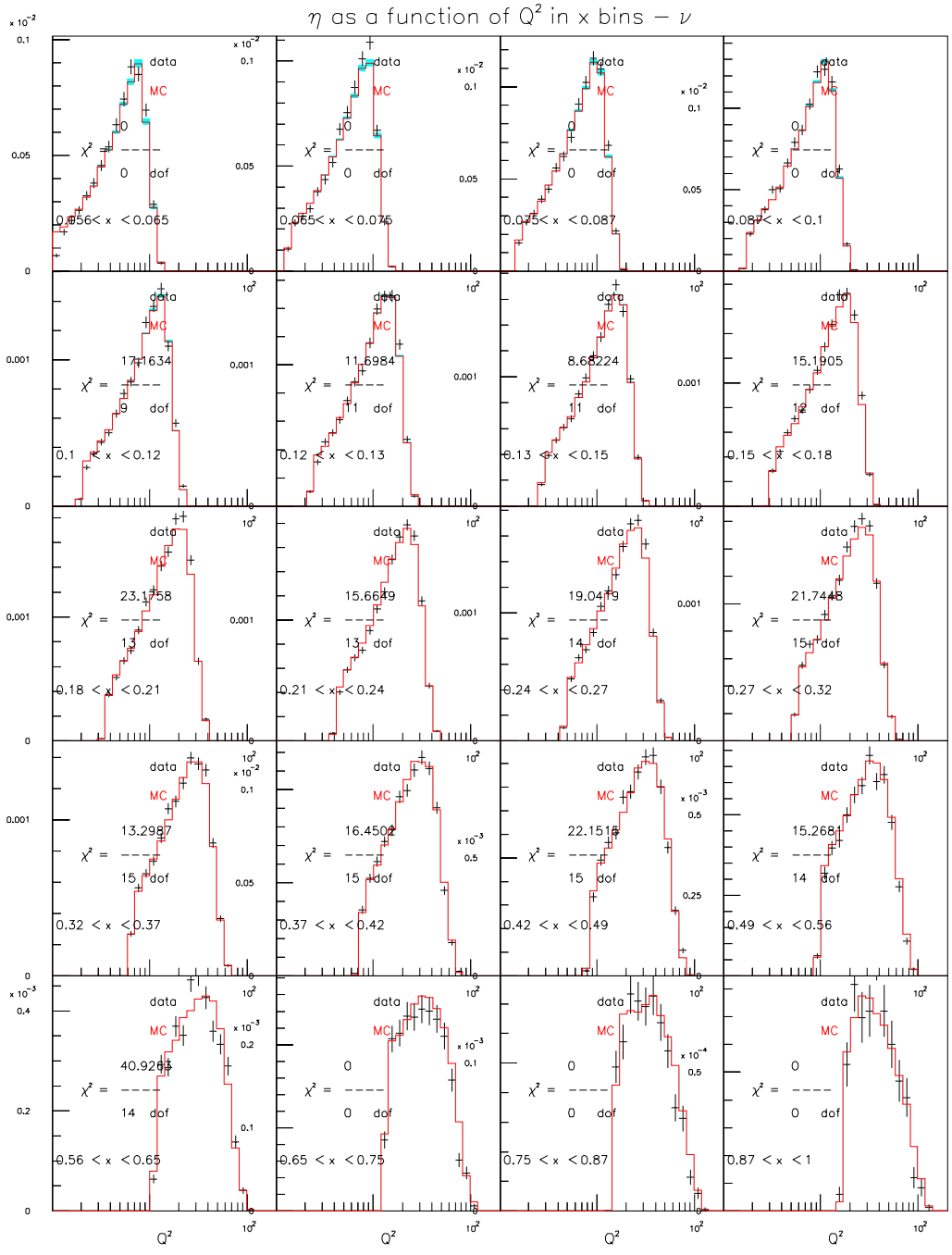

Figure D.46: GRV98NLO $\eta(Q^2)$ – ν mode $s(x, Q^2)$ sensitivity ($85 < E_\nu < 129$)

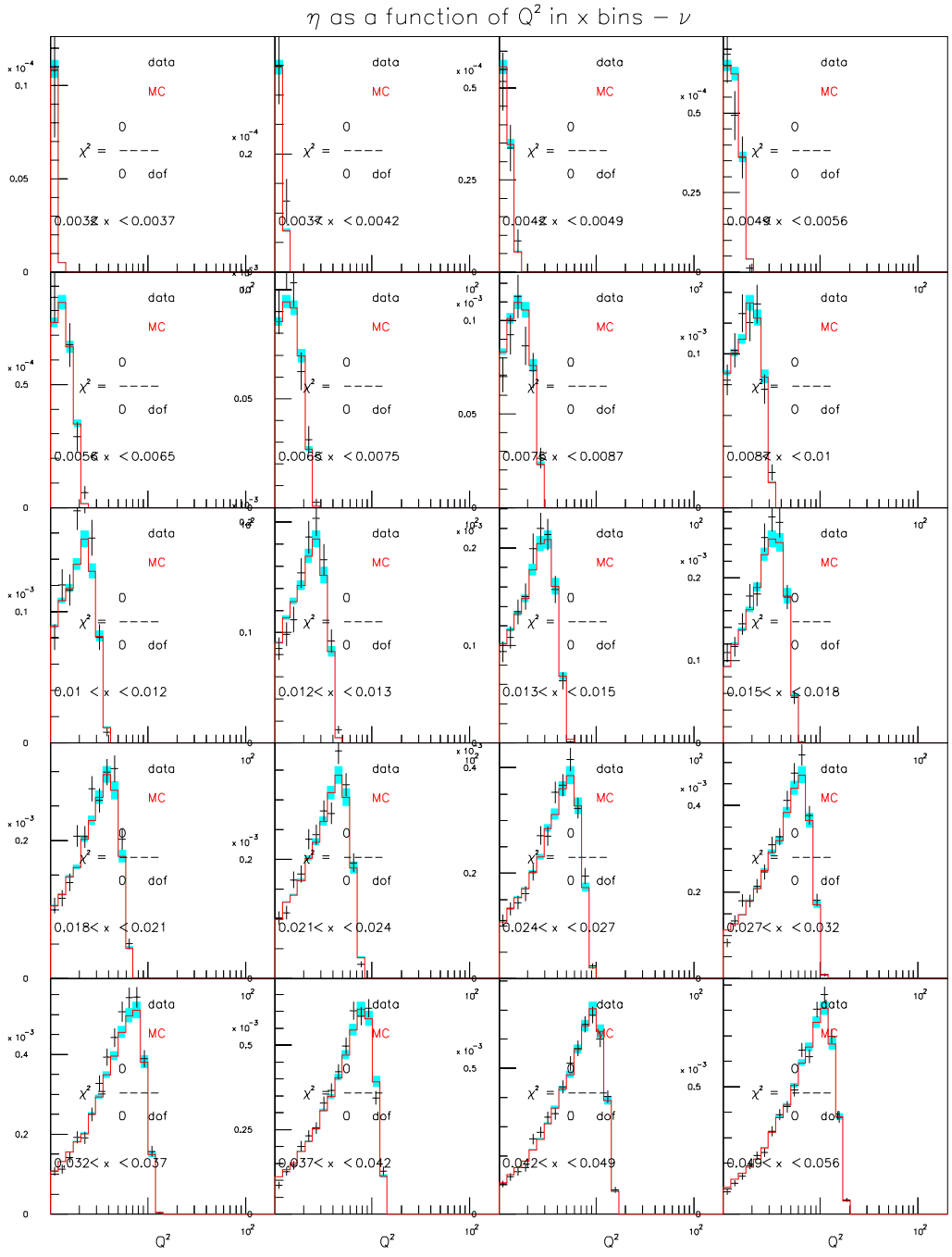

Figure D.47: GRV98NLO $\eta(Q^2)$ – ν mode $s(x, Q^2)$ sensitivity $(129 < E_\nu < 201)$

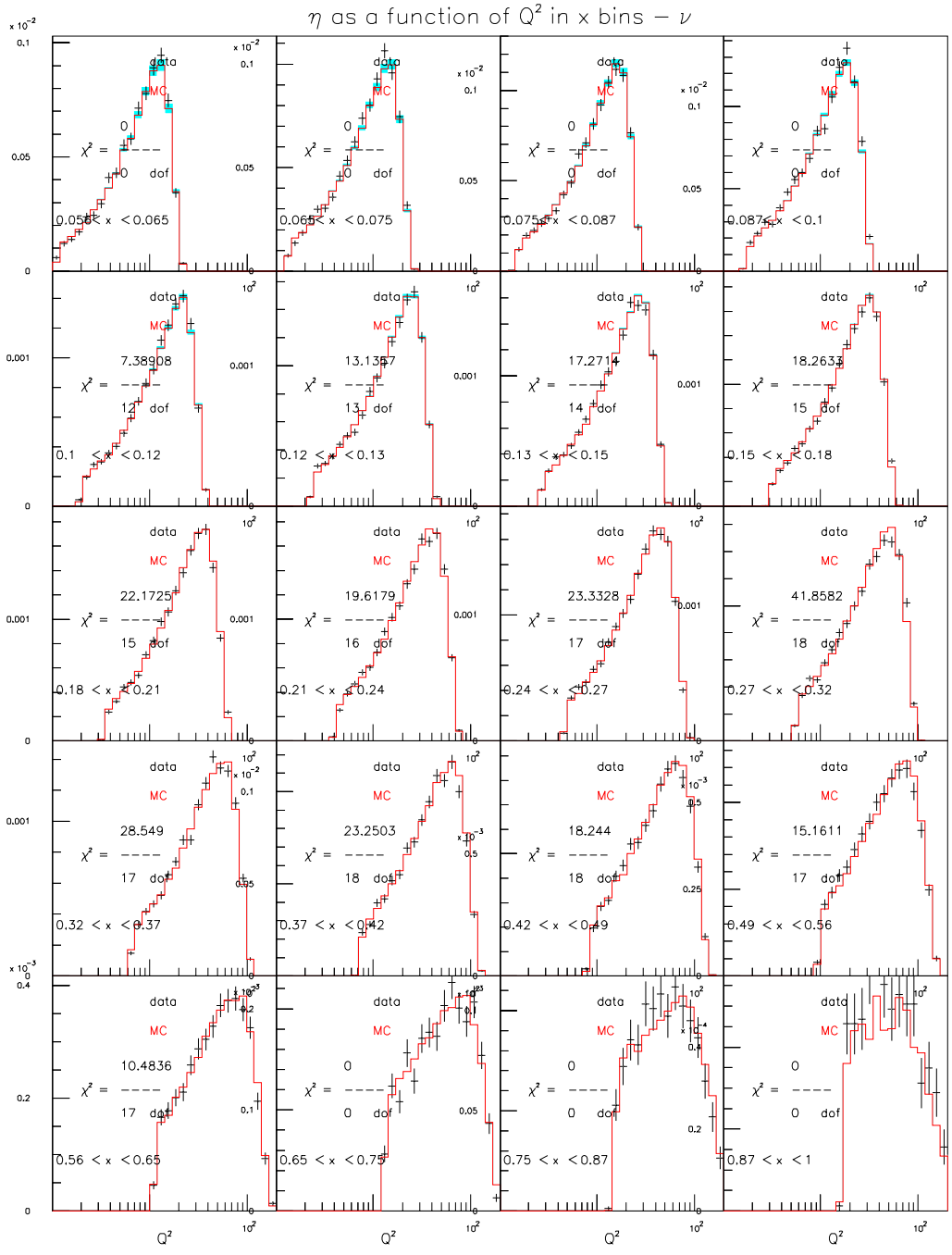

Figure D.48: GRV98NLO $\eta(Q^2)$ – ν mode $s(x, Q^2)$ sensitivity $(129 < E_\nu < 201)$

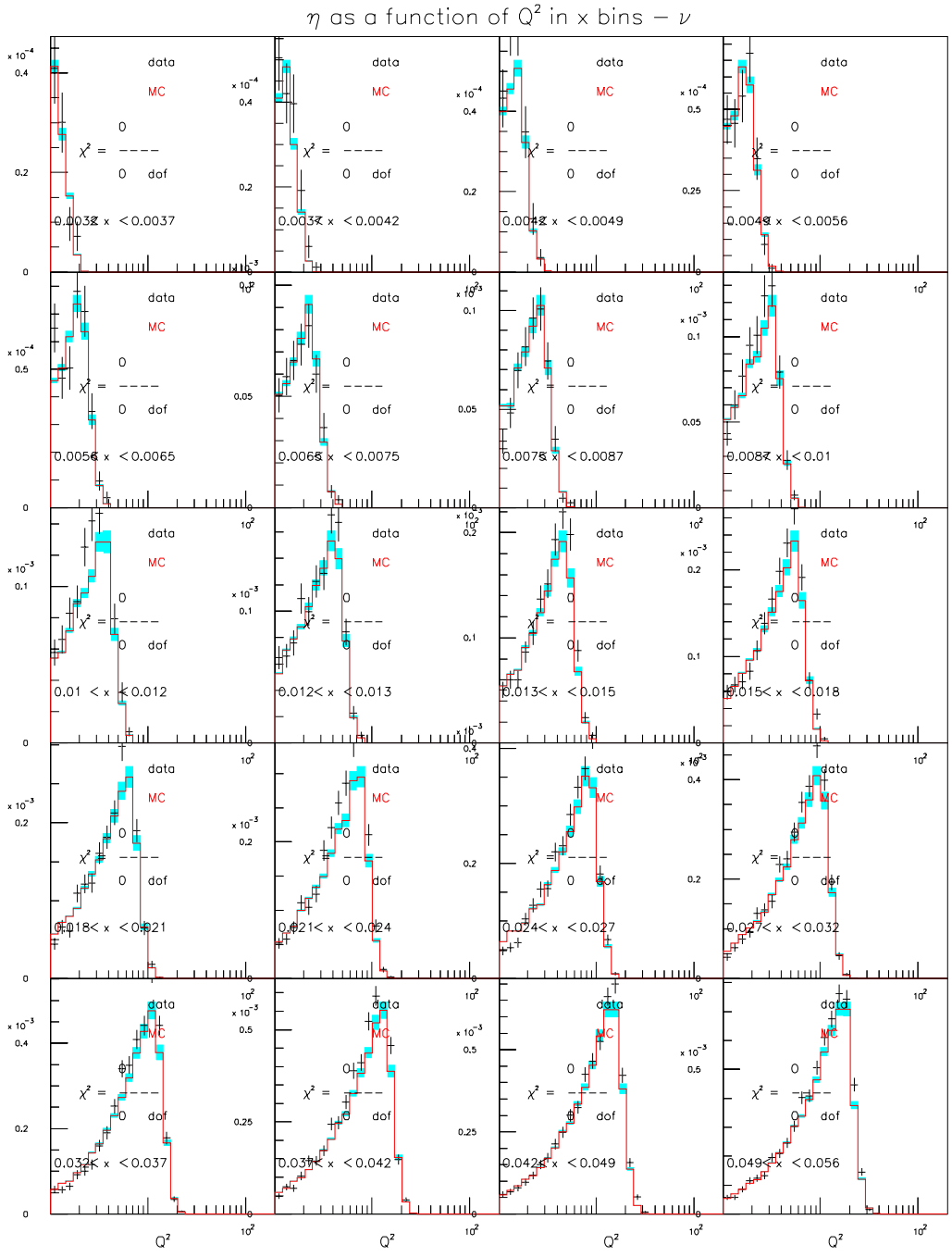

Figure D.49: GRV98NLO $\eta(Q^2)$ – ν mode $s(x, Q^2)$ sensitivity $(201 < E_\nu < 400)$

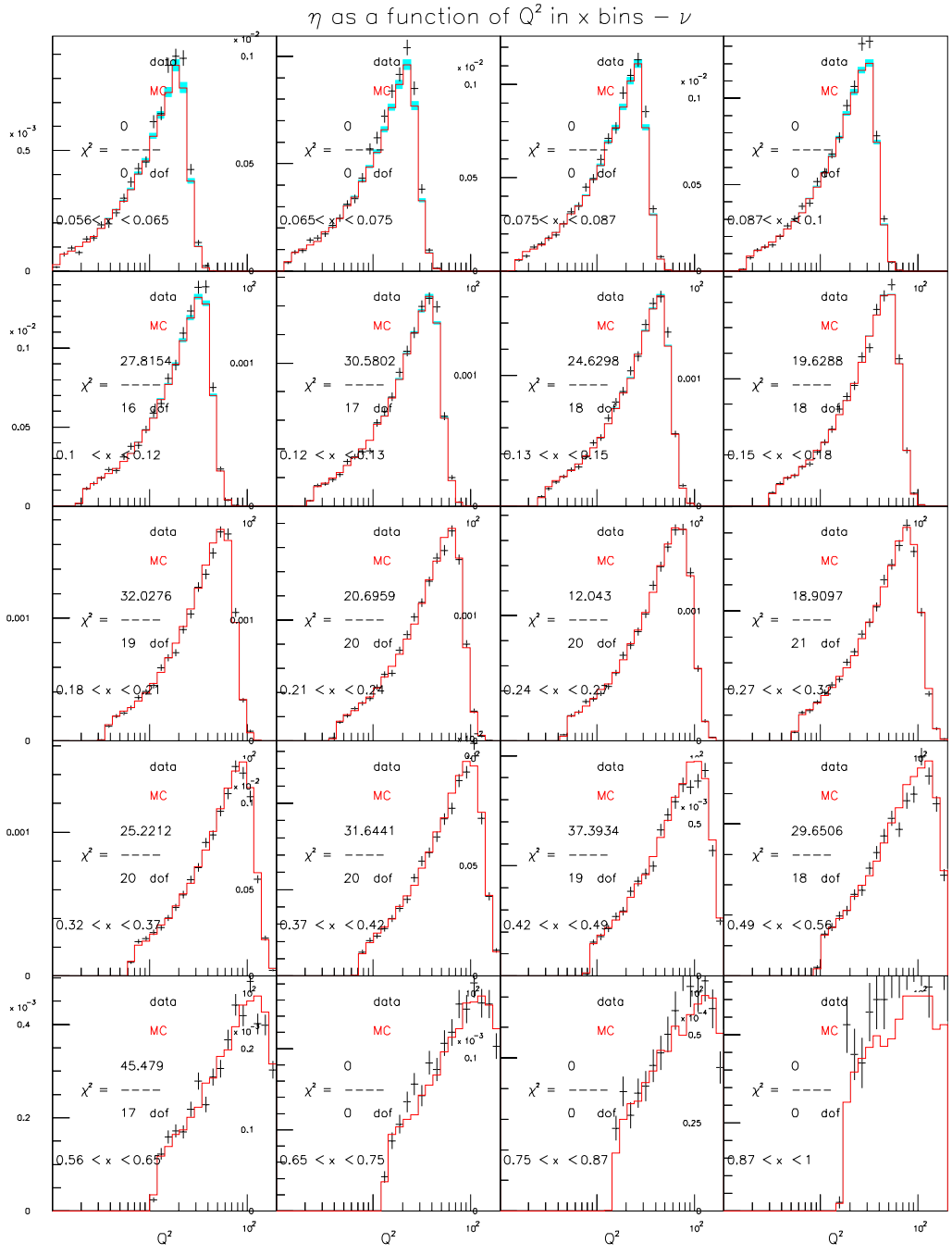

Figure D.50: GRV98NLO $\eta(Q^2)$ – ν mode $s(x, Q^2)$ sensitivity $(201 < E_\nu < 400)$

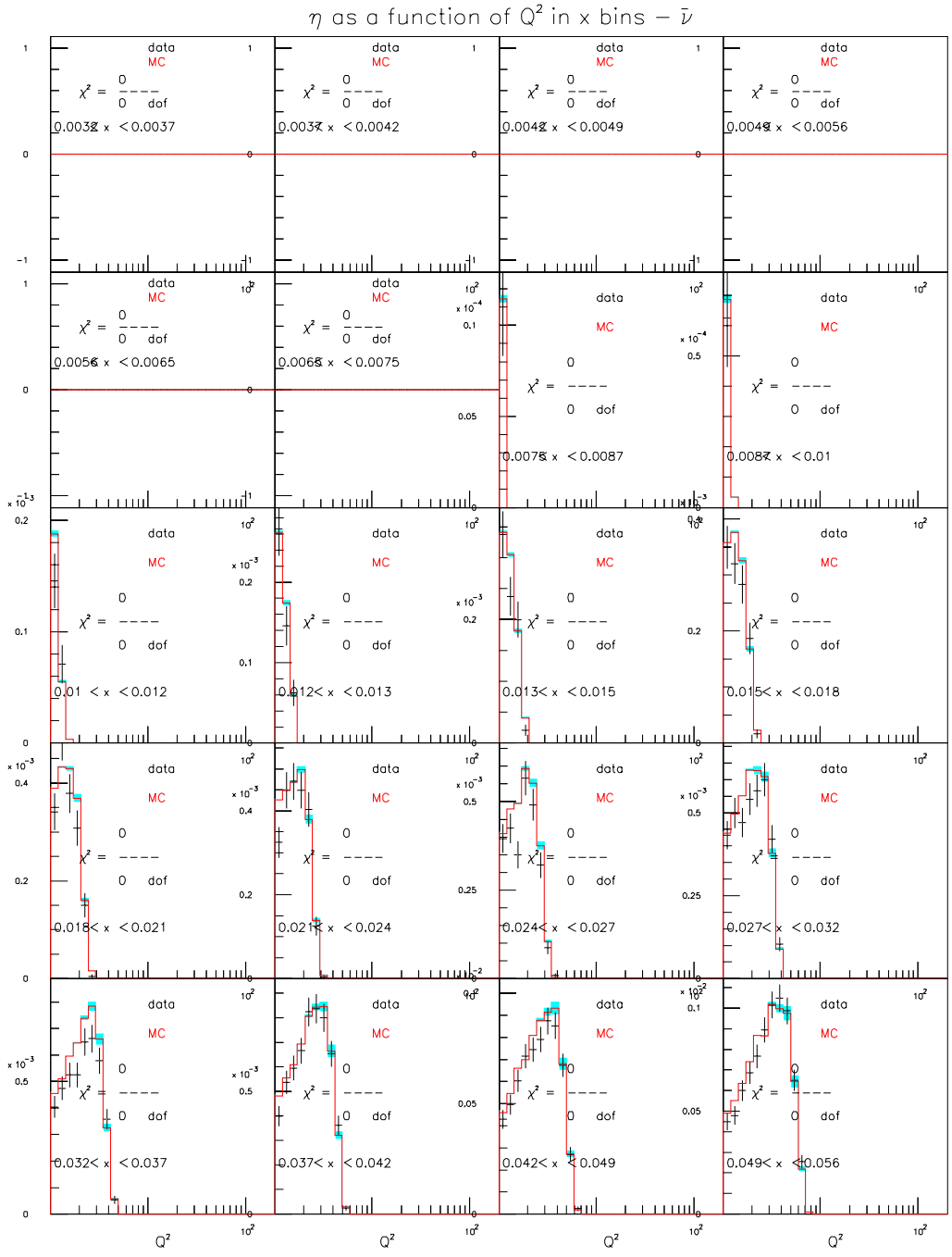

Figure D.51: GRV98NLO $\eta(Q^2)$ – $\overline{\nu}$ mode $s(x, Q^2)$ sensitivity $(20 < E_\nu < 62)$

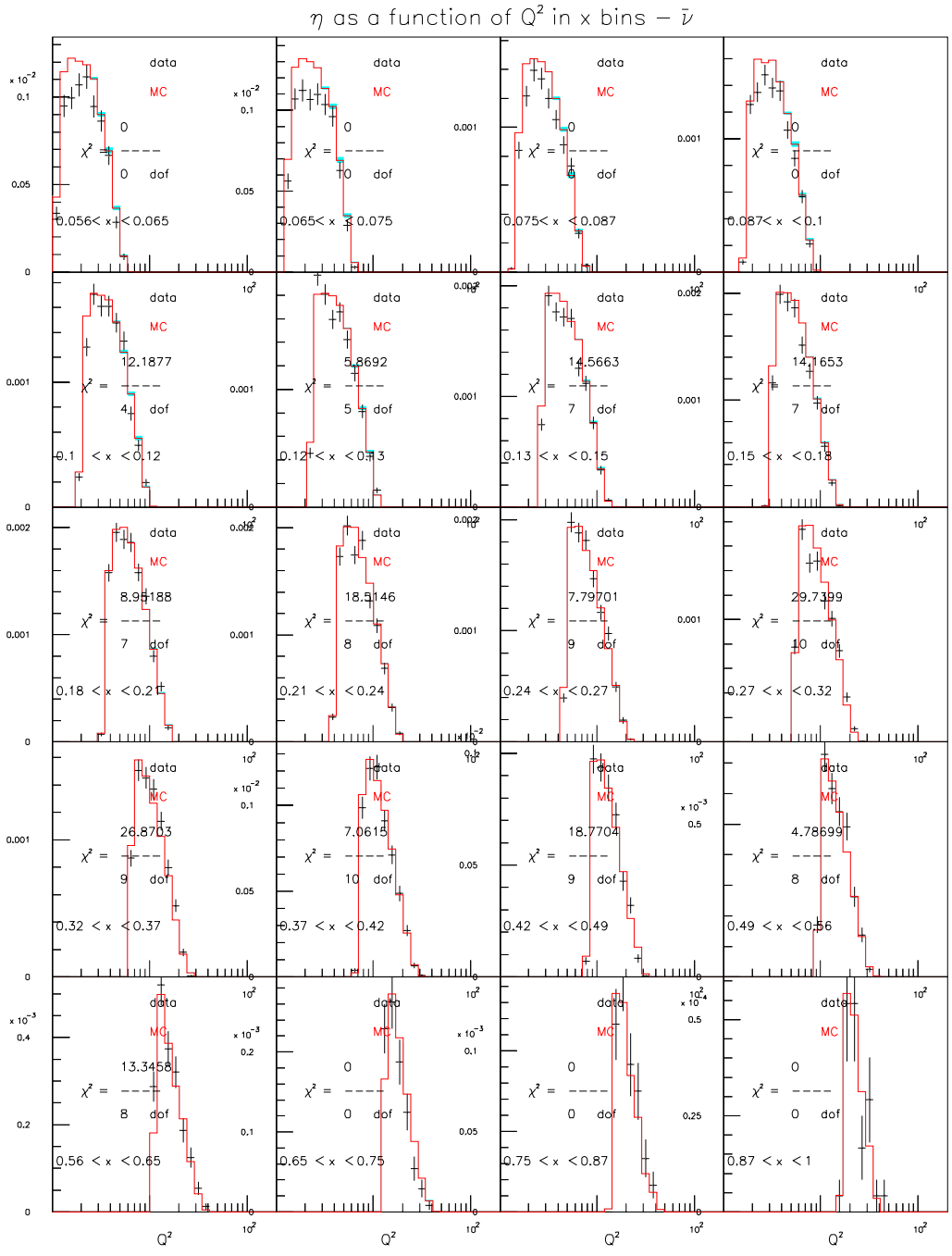

Figure D.52: GRV98NLO $\eta(Q^2)$ – $\overline{\nu}$ mode $s(x, Q^2)$ sensitivity $(20 < E_\nu < 62)$

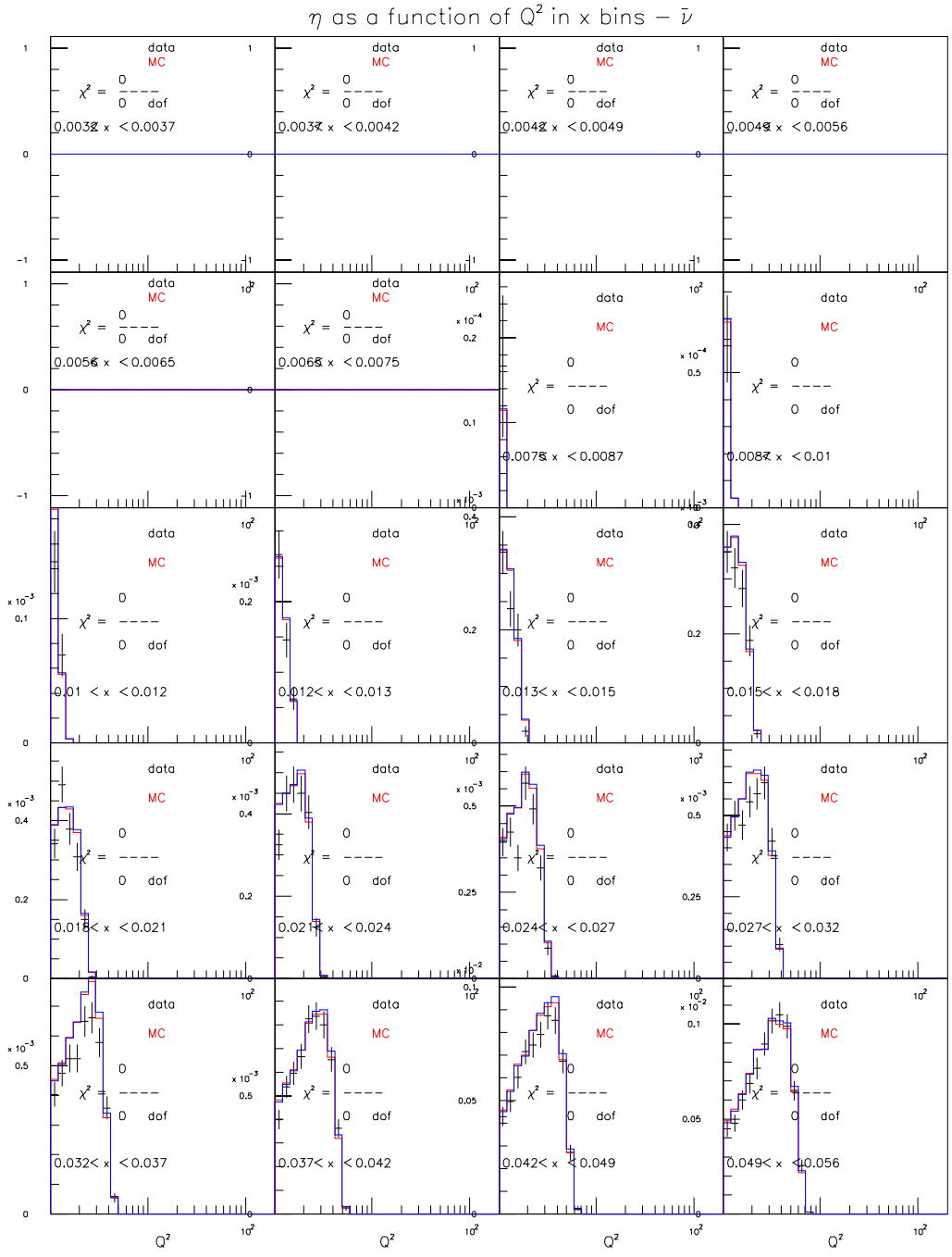

Figure D.53: GRV98NLO $\eta(Q^2)$ – $\overline{\nu}$ mode $s(x, Q^2)$ sensitivity $(62 < E_\nu < 85)$

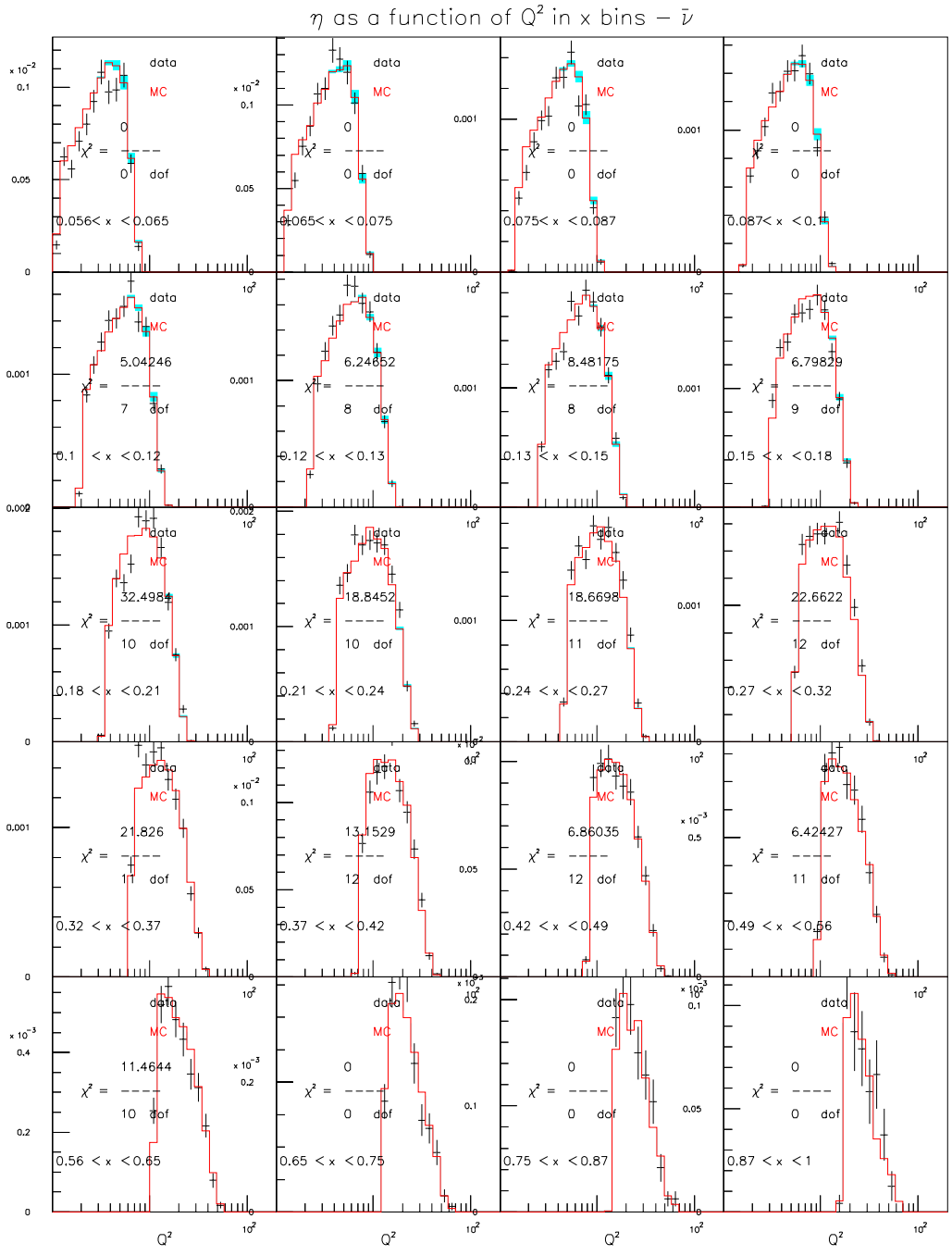

Figure D.54: GRV98NLO $\eta(Q^2)$ – $\overline{\nu}$ mode $s(x, Q^2)$ sensitivity $(62 < E_\nu < 85)$

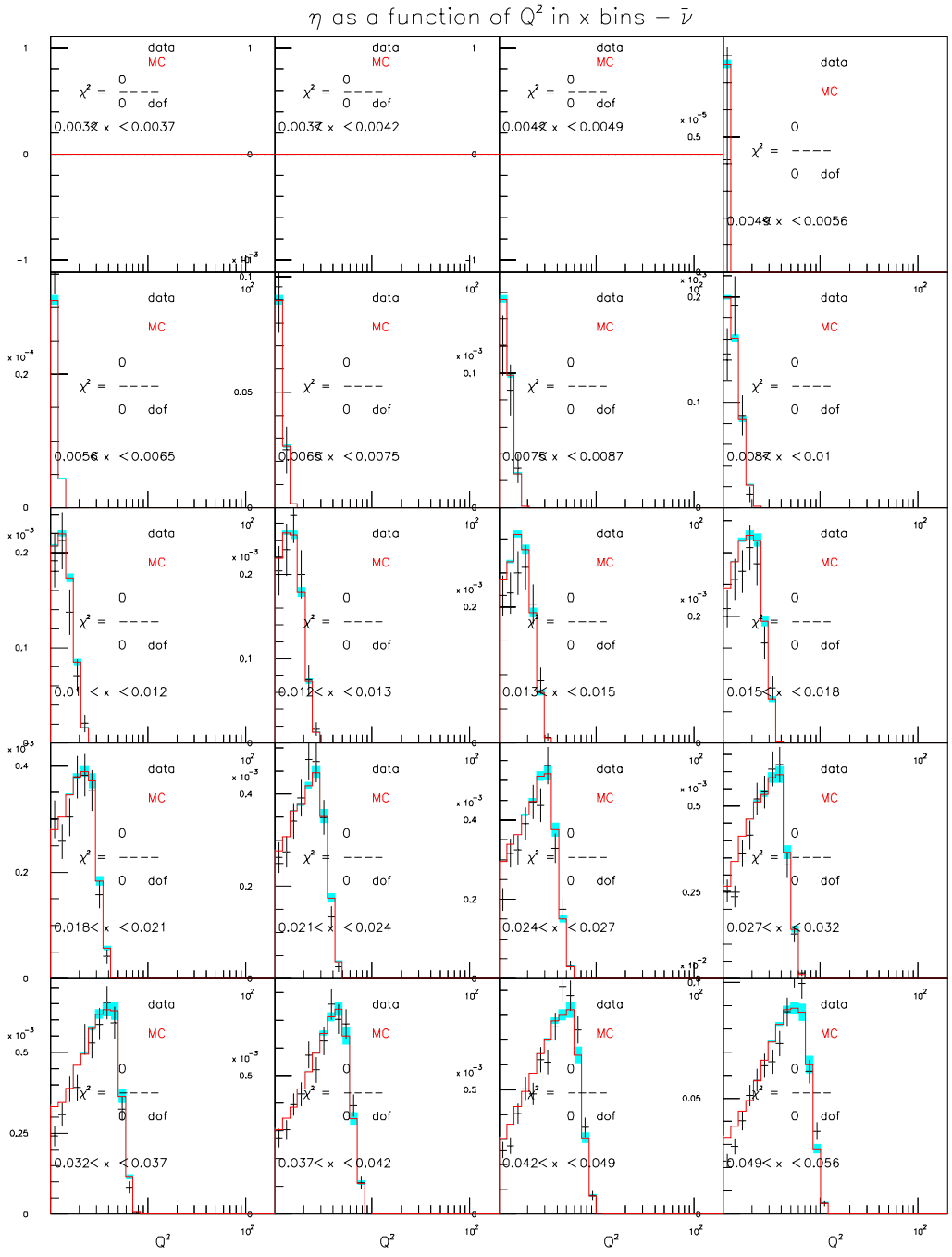

Figure D.55: GRV98NLO $\eta(Q^2)$ – $\overline{\nu}$ mode $s(x, Q^2)$ sensitivity $(85 < E_\nu < 129)$

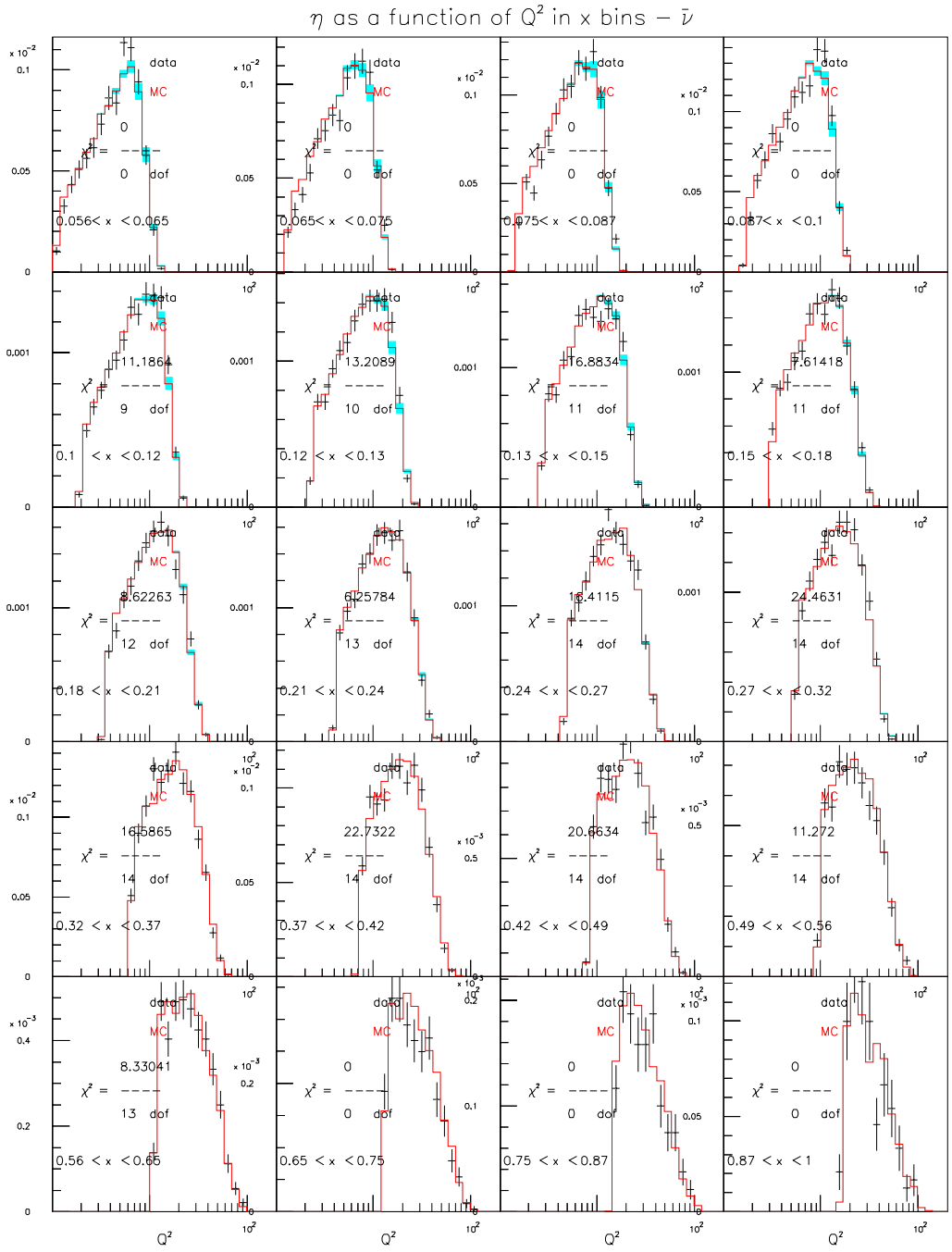

Figure D.56: GRV98NLO $\eta(Q^2)$ – $\overline{\nu}$ mode $s(x,Q^2)$ sensitivity $(85 < E_\nu < 129)$

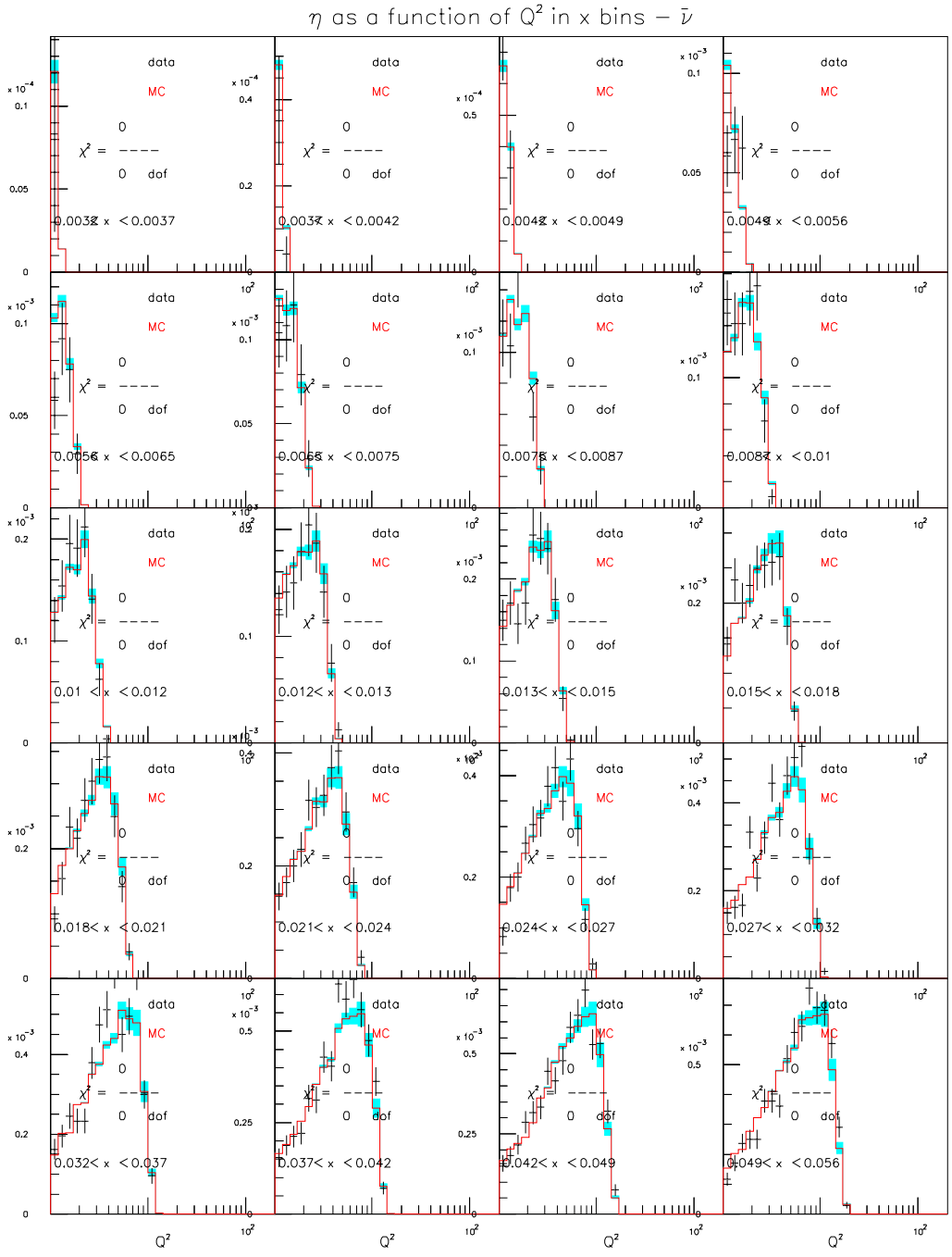

Figure D.57: GRV98NLO $\eta(Q^2) - \overline{\nu}$ mode $s(x, Q^2)$ sensitivity $(129 < E_\nu < 201)$

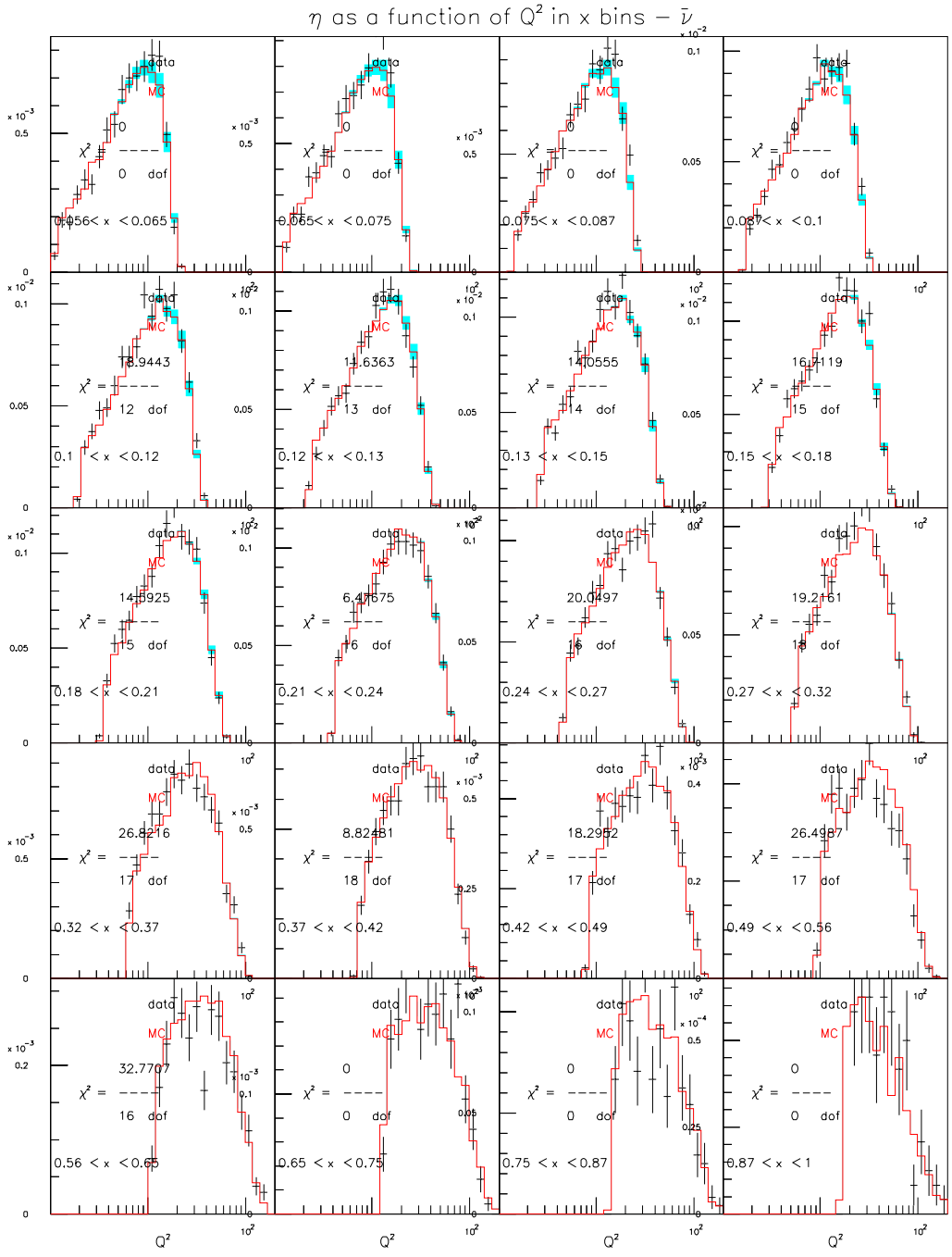

Figure D.58: GRV98NLO $\eta(Q^2) - \overline{\nu}$ mode $s(x, Q^2)$ sensitivity $(129 < E_\nu < 201)$

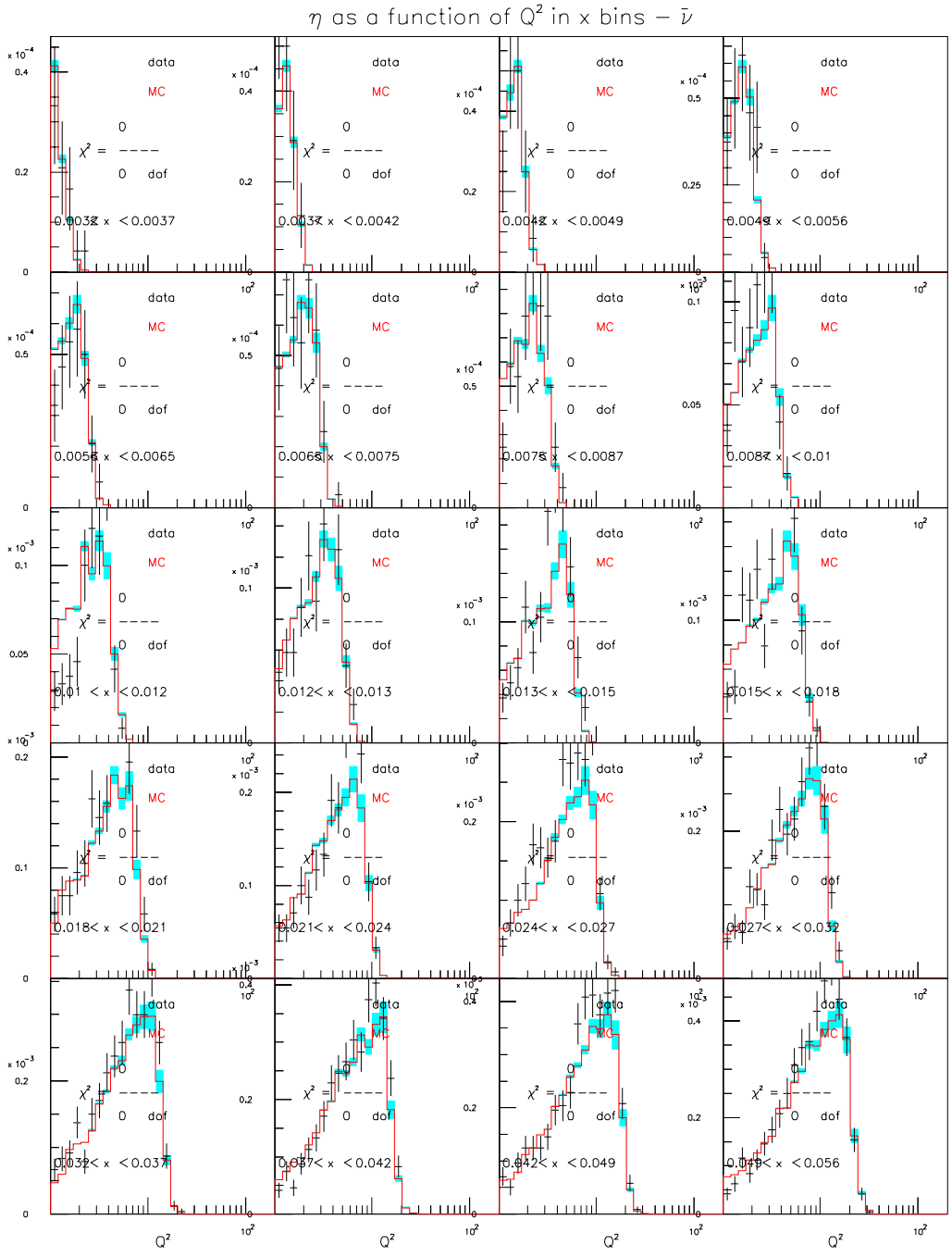

Figure D.59: GRV98NLO $\eta(Q^2) - \overline{\nu}$ mode $s(x, Q^2)$ sensitivity $(201 < E_\nu < 400)$

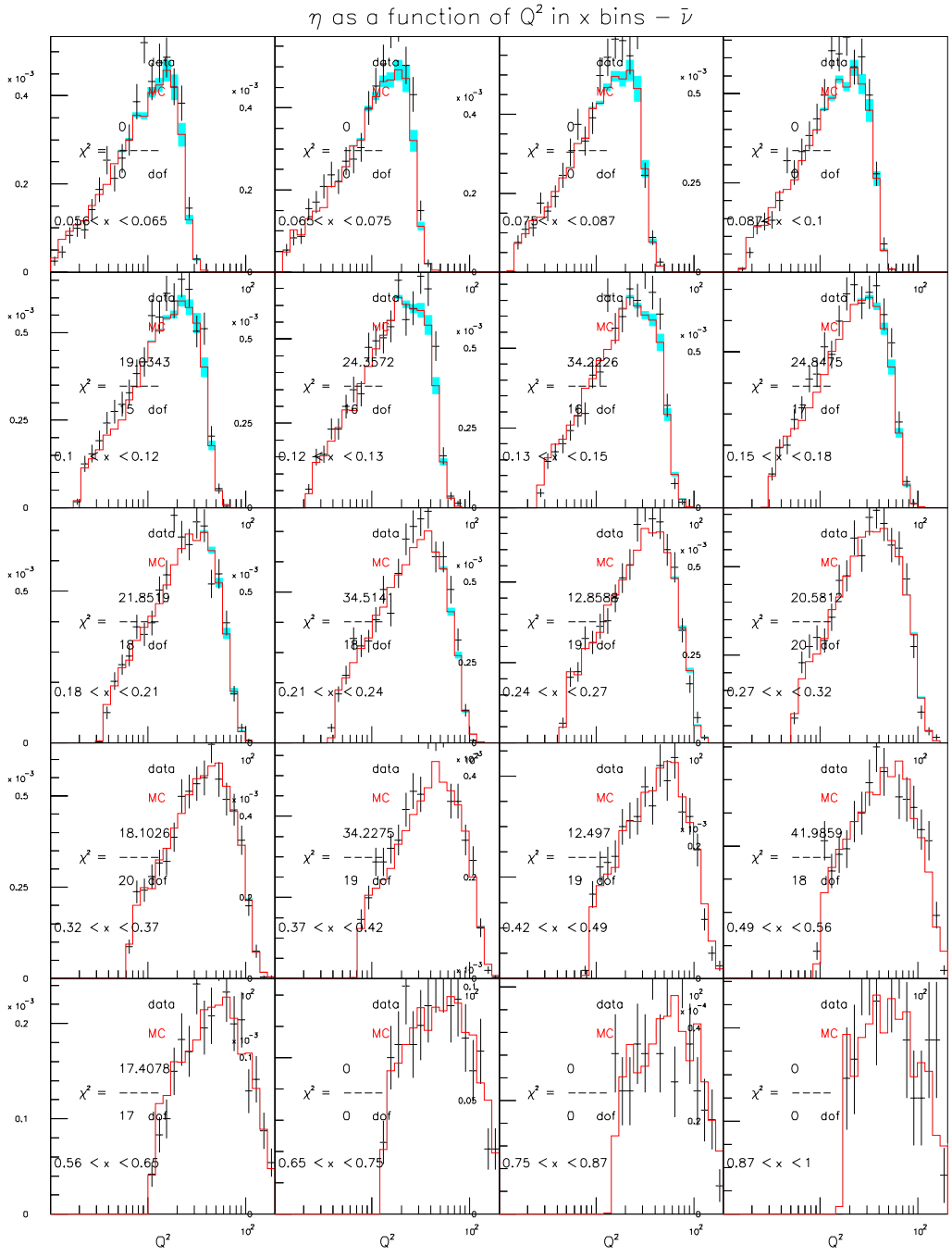

Figure D.60: GRV98NLO $\eta(Q^2)$ – $\overline{\nu}$ mode $s(x, Q^2)$ sensitivity $(201 < E_\nu < 400)$

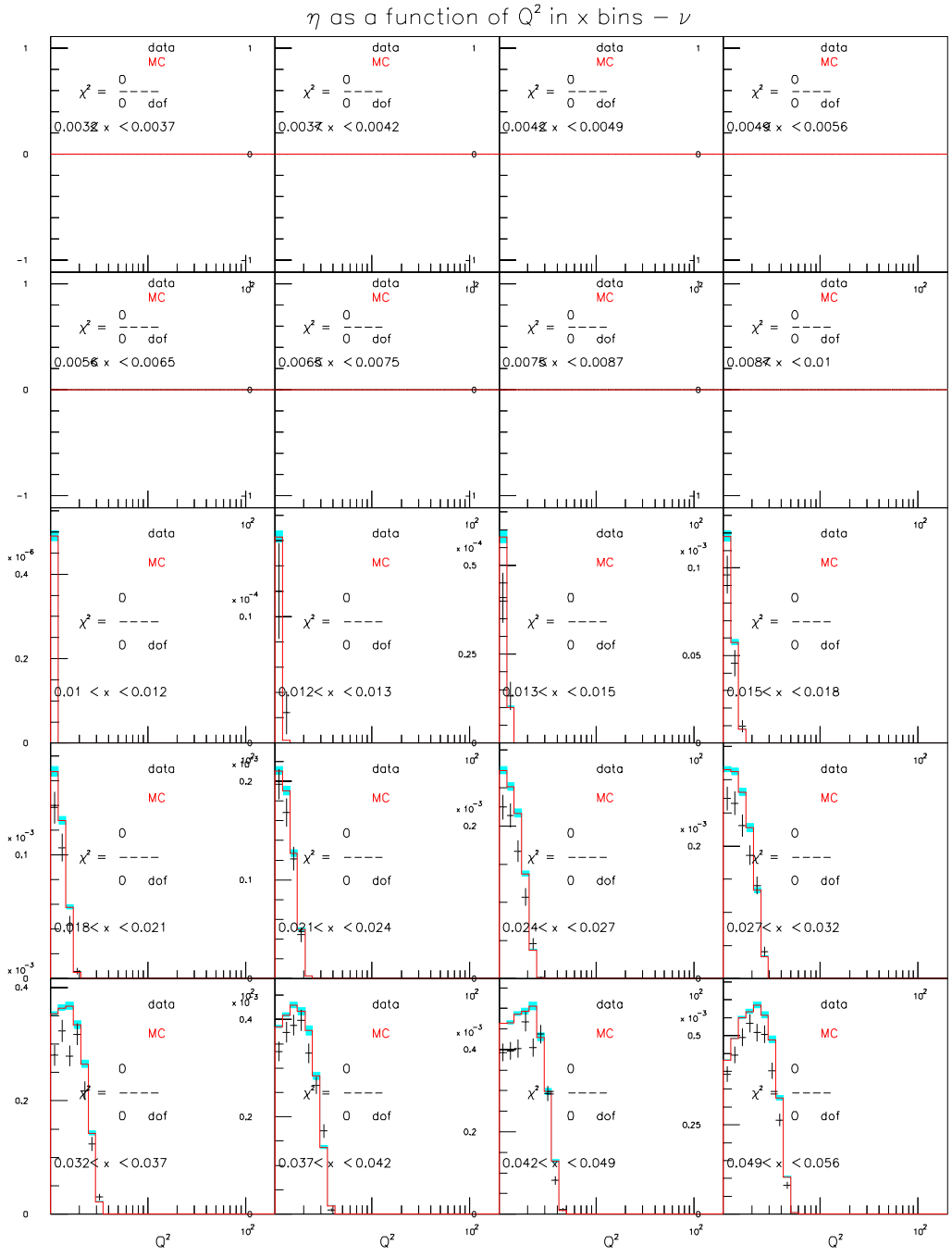

Figure D.61: CTEQ5NLO $\eta(Q^2)$ – ν mode $s(x, Q^2)$ sensitivity $(20 < E_\nu < 62)$

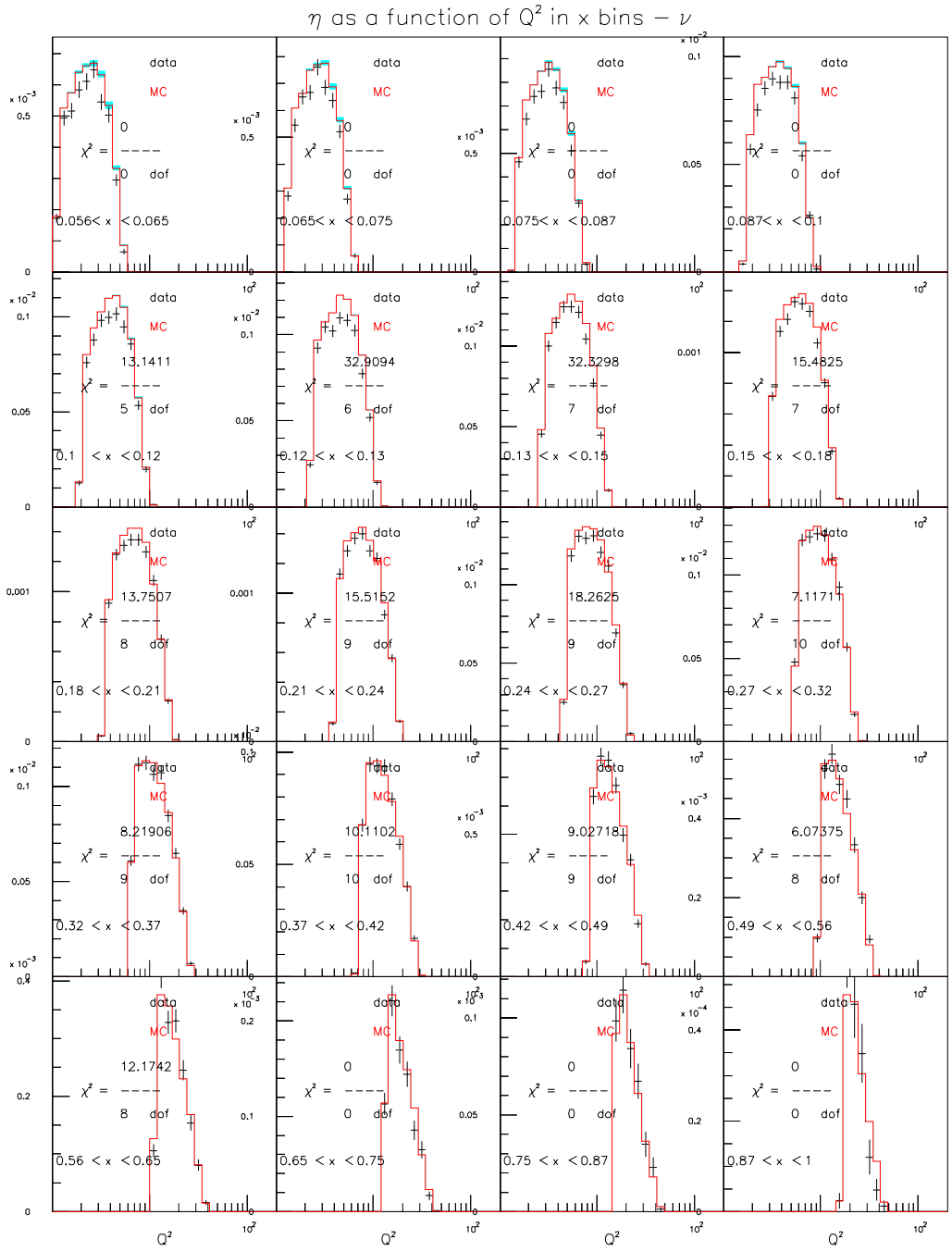

Figure D.62: CTEQ5NLO $\eta(Q^2)$ – ν mode $s(x, Q^2)$ sensitivity $(20 < E_\nu < 62)$

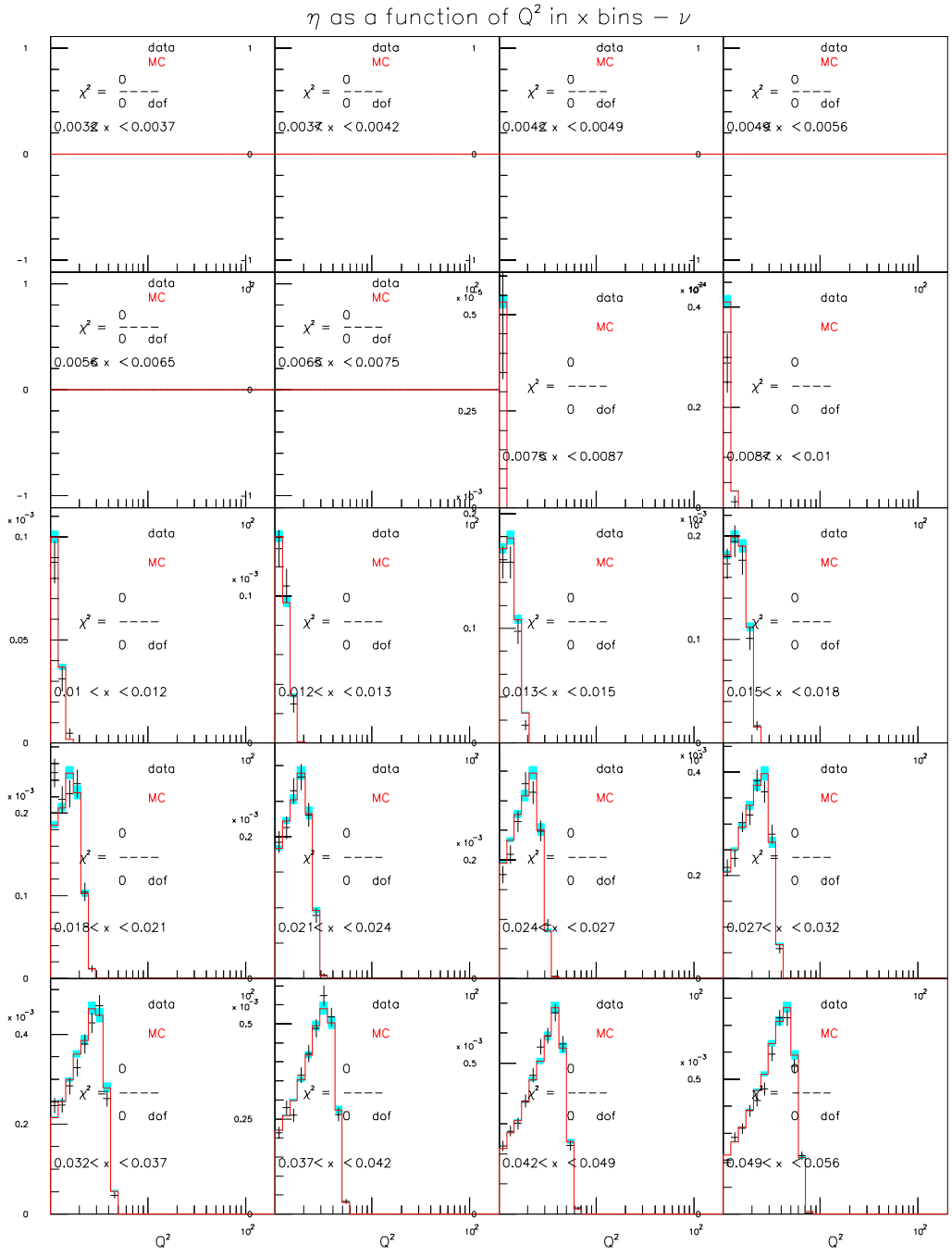

Figure D.63: CTEQ5NLO $\eta(Q^2)$ – ν mode $s(x, Q^2)$ sensitivity $(62 < E_\nu < 85)$

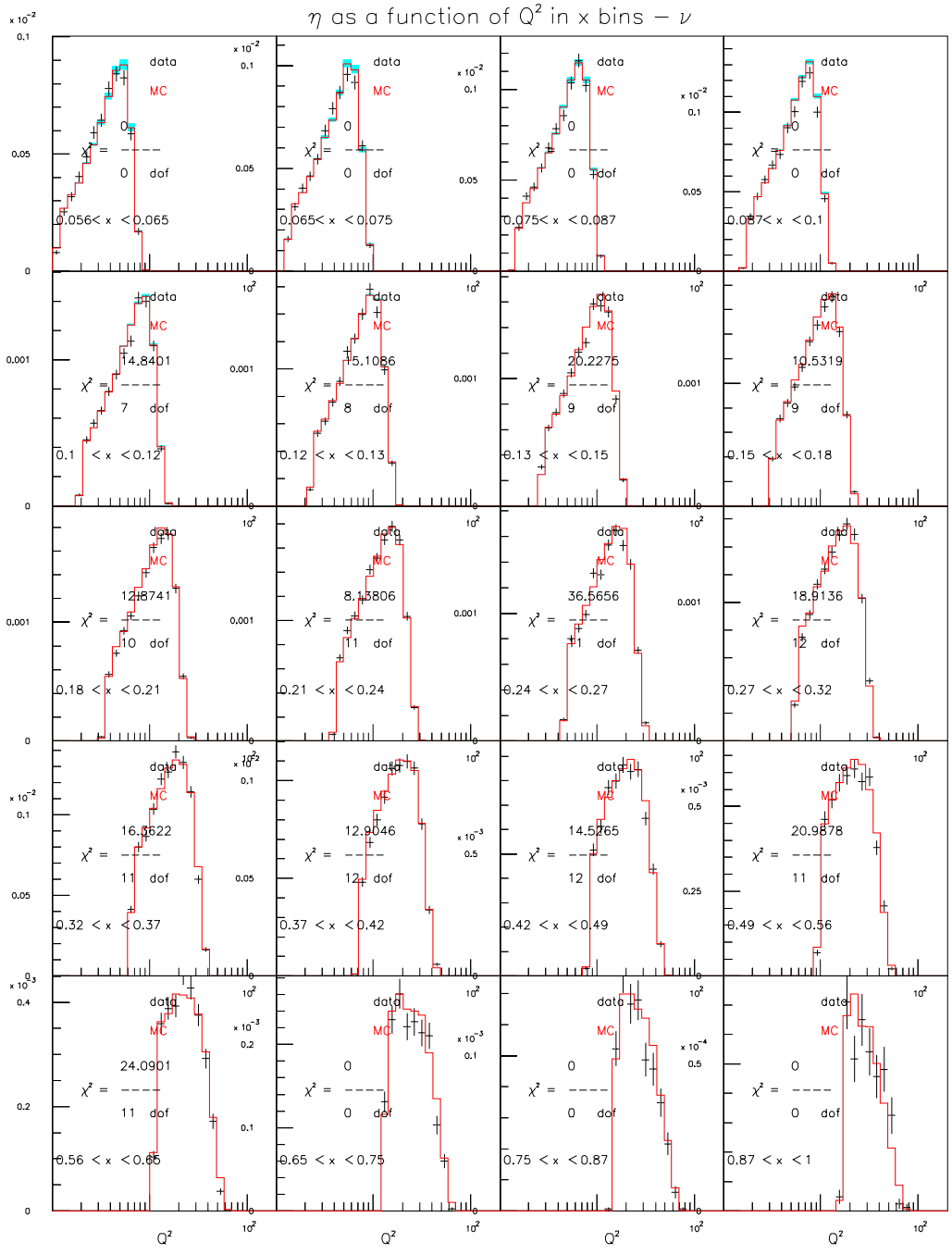

Figure D.64: CTEQ5NLO $\eta(Q^2)$ – ν mode $s(x, Q^2)$ sensitivity $(62 < E_\nu < 85)$

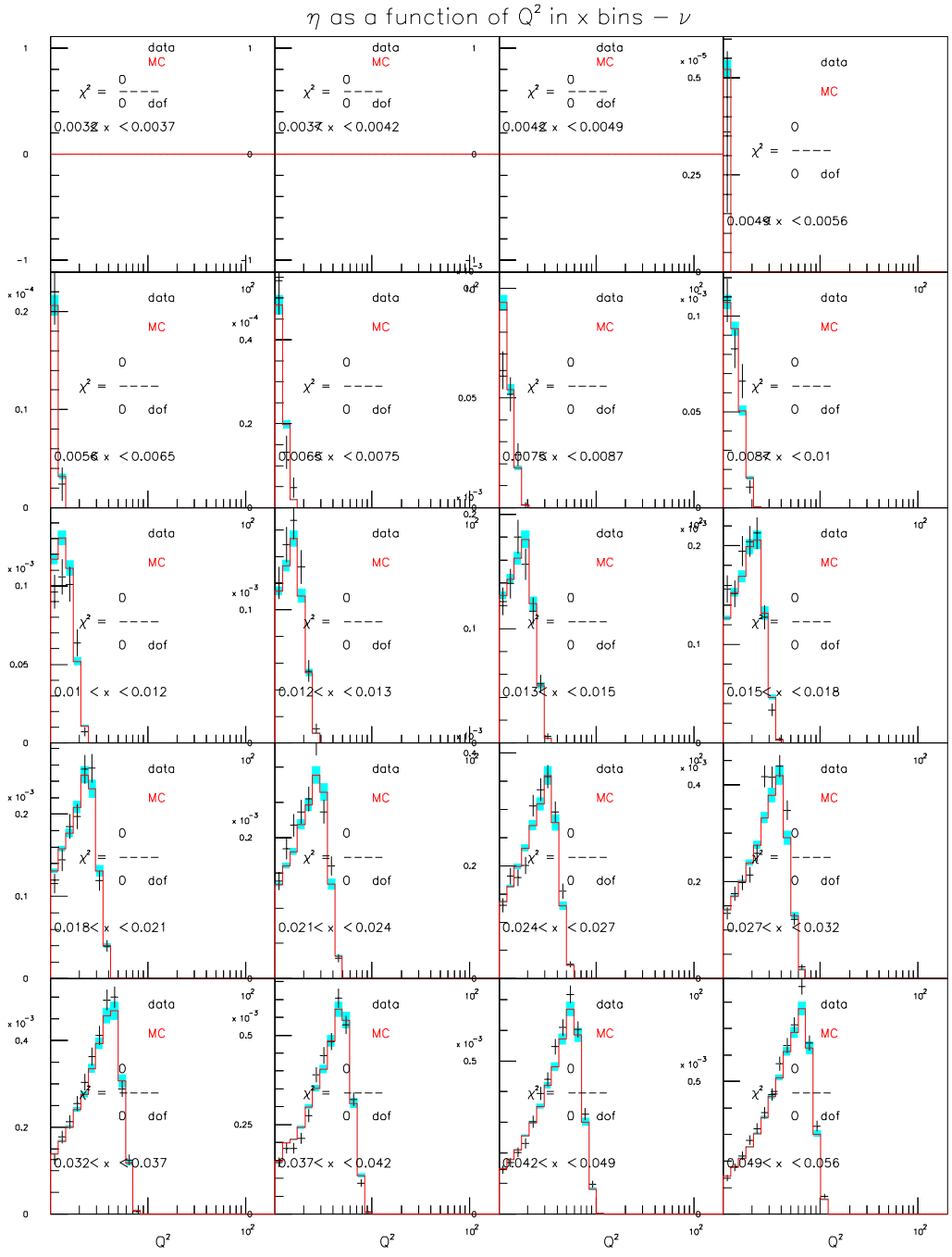

Figure D.65: CTEQ5NLO $\eta(Q^2)$ – ν mode $s(x, Q^2)$ sensitivity ($85 < E_\nu < 129$)

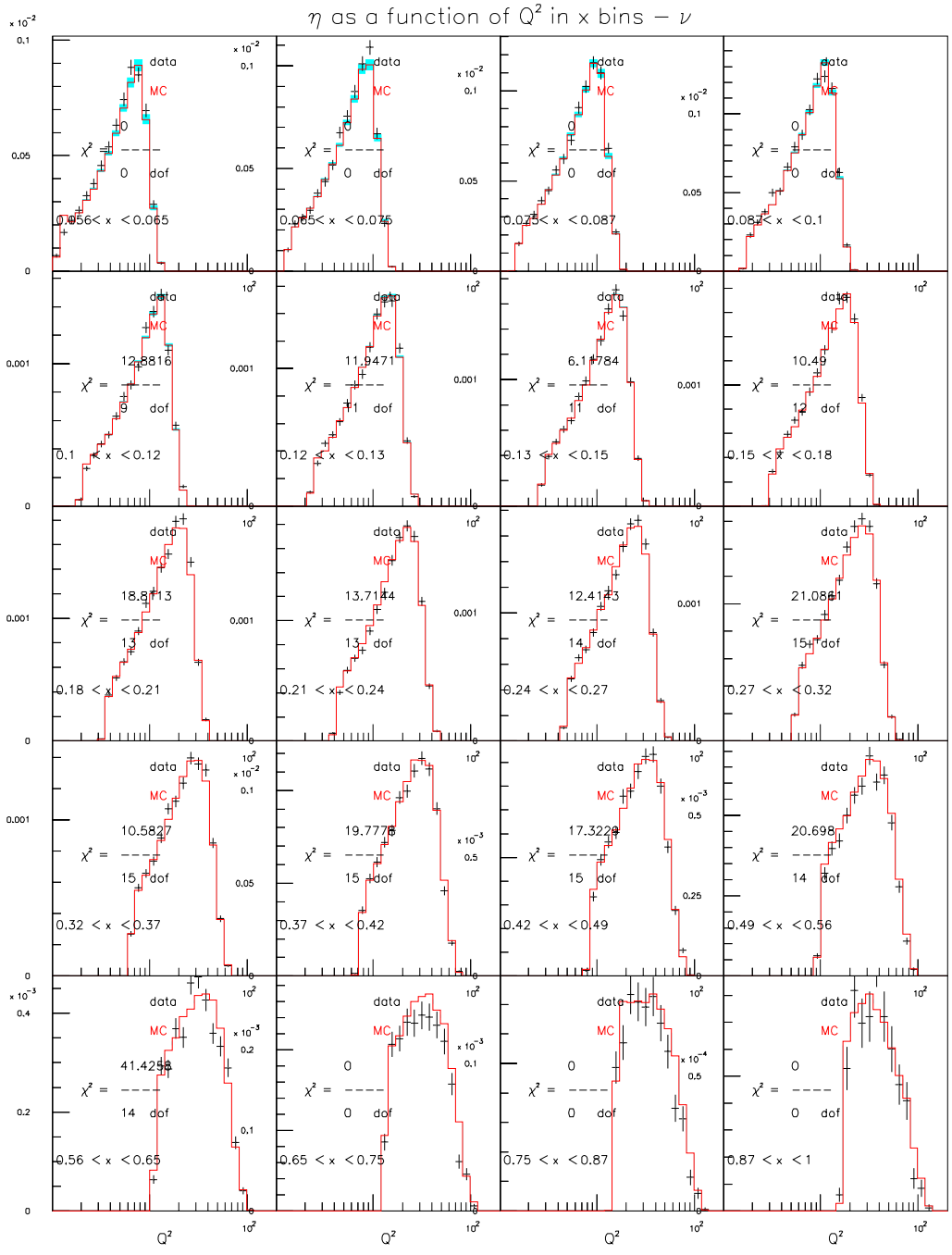

Figure D.66: CTEQ5NLO $\eta(Q^2)$ – ν mode $s(x, Q^2)$ sensitivity ($85 < E_\nu < 129$)

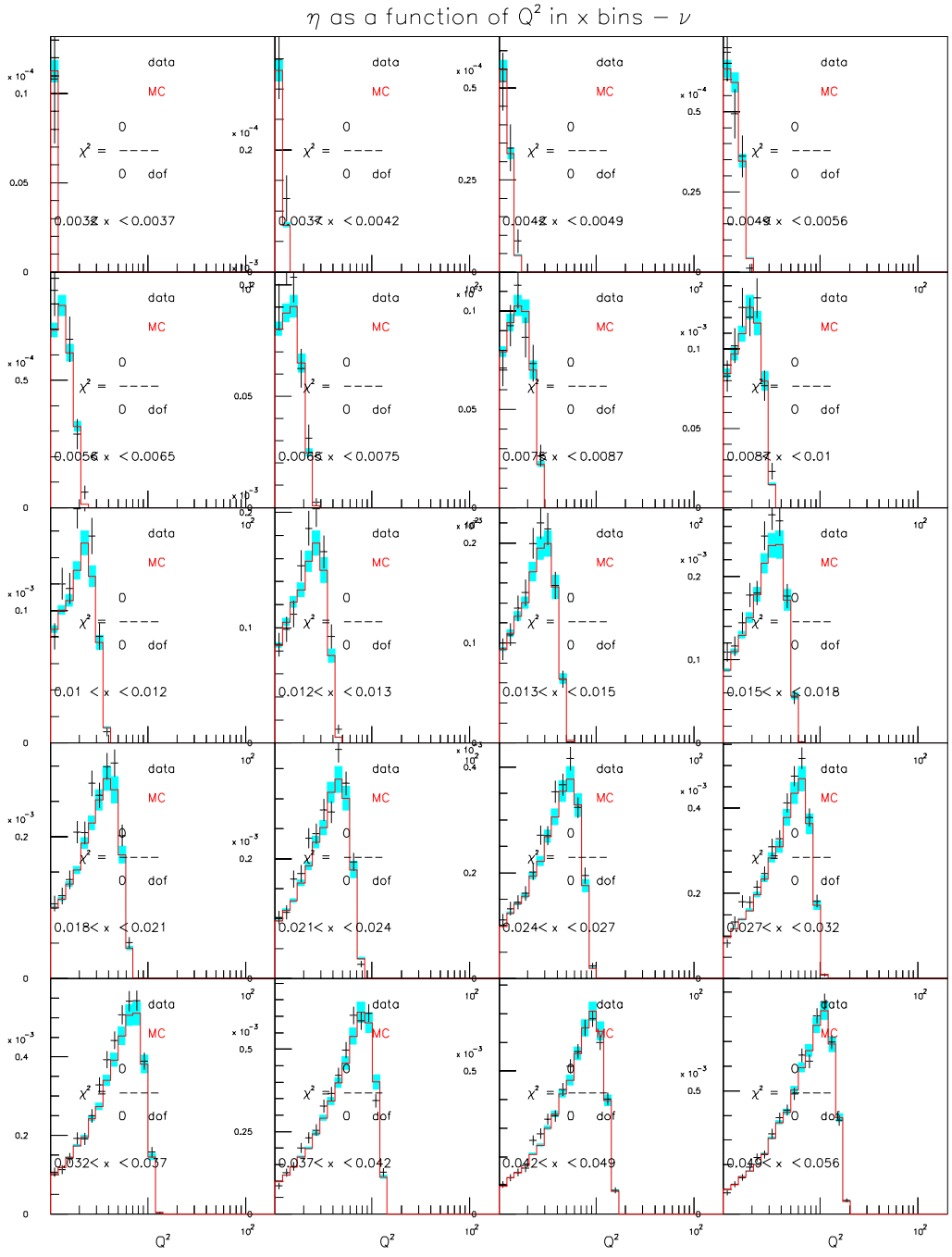

Figure D.67: CTEQ5NLO $\eta(Q^2)$ – ν mode $s(x, Q^2)$ sensitivity $(129 < E_\nu < 201)$

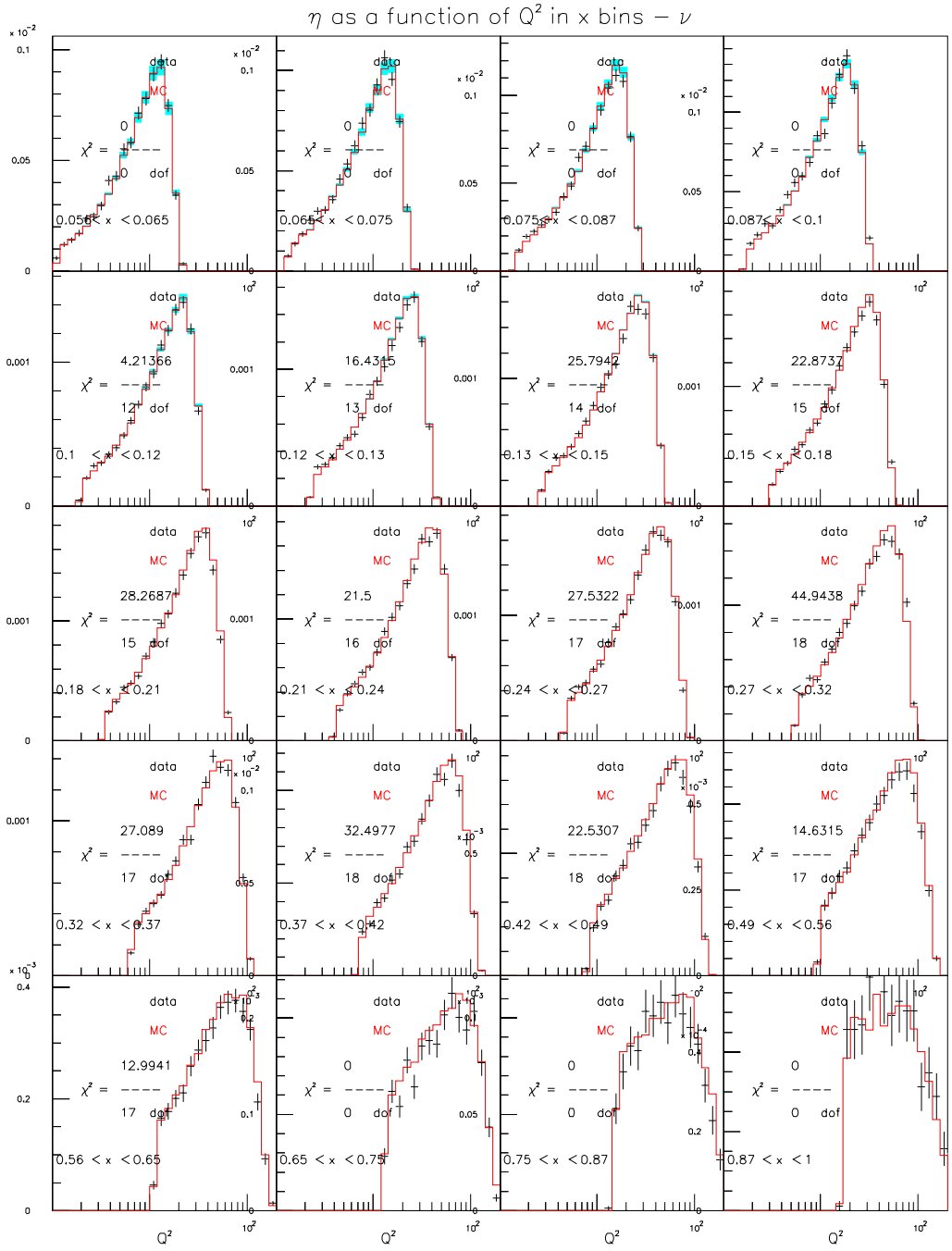

Figure D.68: CTEQ5NLO $\eta(Q^2)$ – ν mode $s(x, Q^2)$ sensitivity $(129 < E_\nu < 201)$

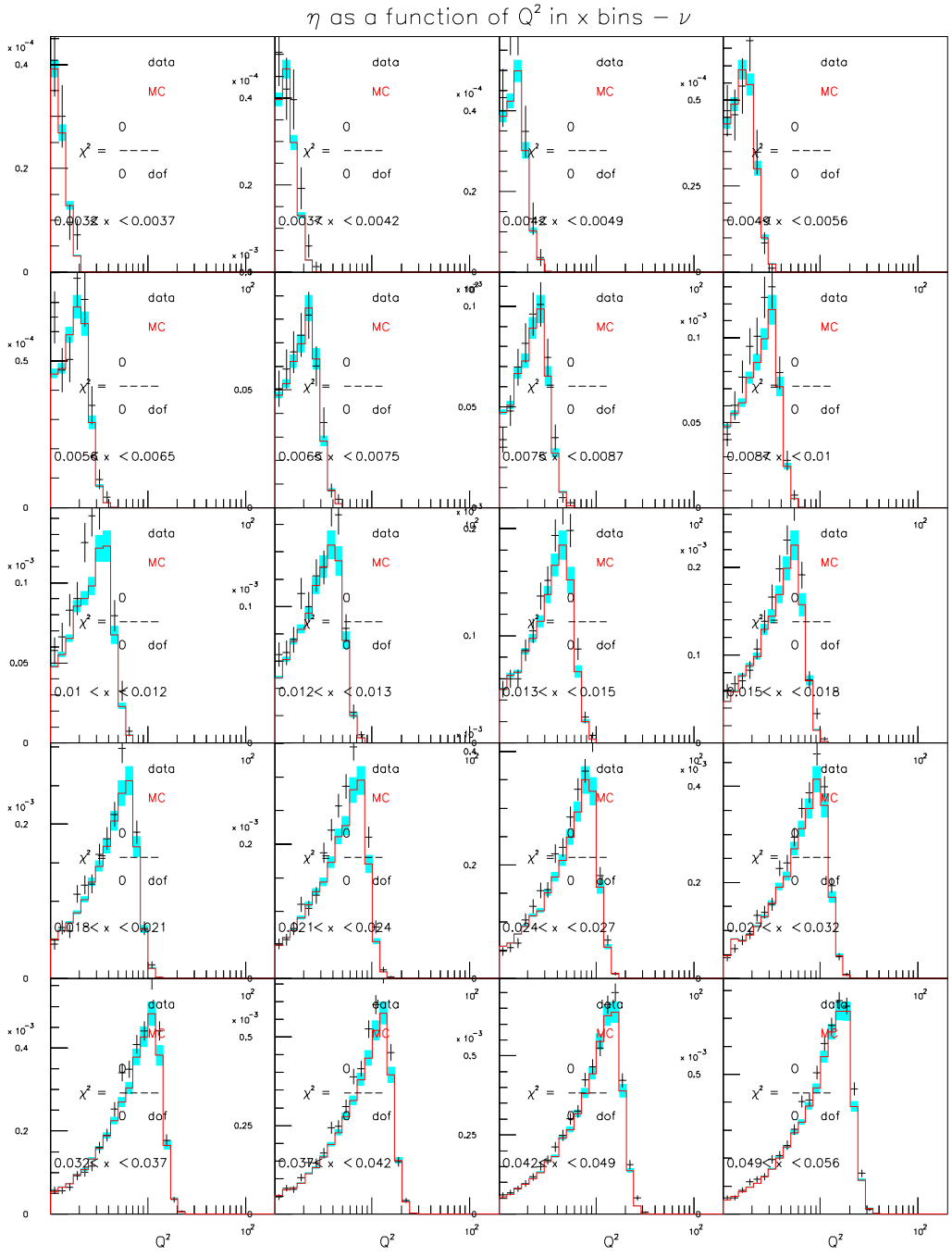

Figure D.69: CTEQ5NLO $\eta(Q^2)$ – ν mode $s(x, Q^2)$ sensitivity $(201 < E_\nu < 400)$

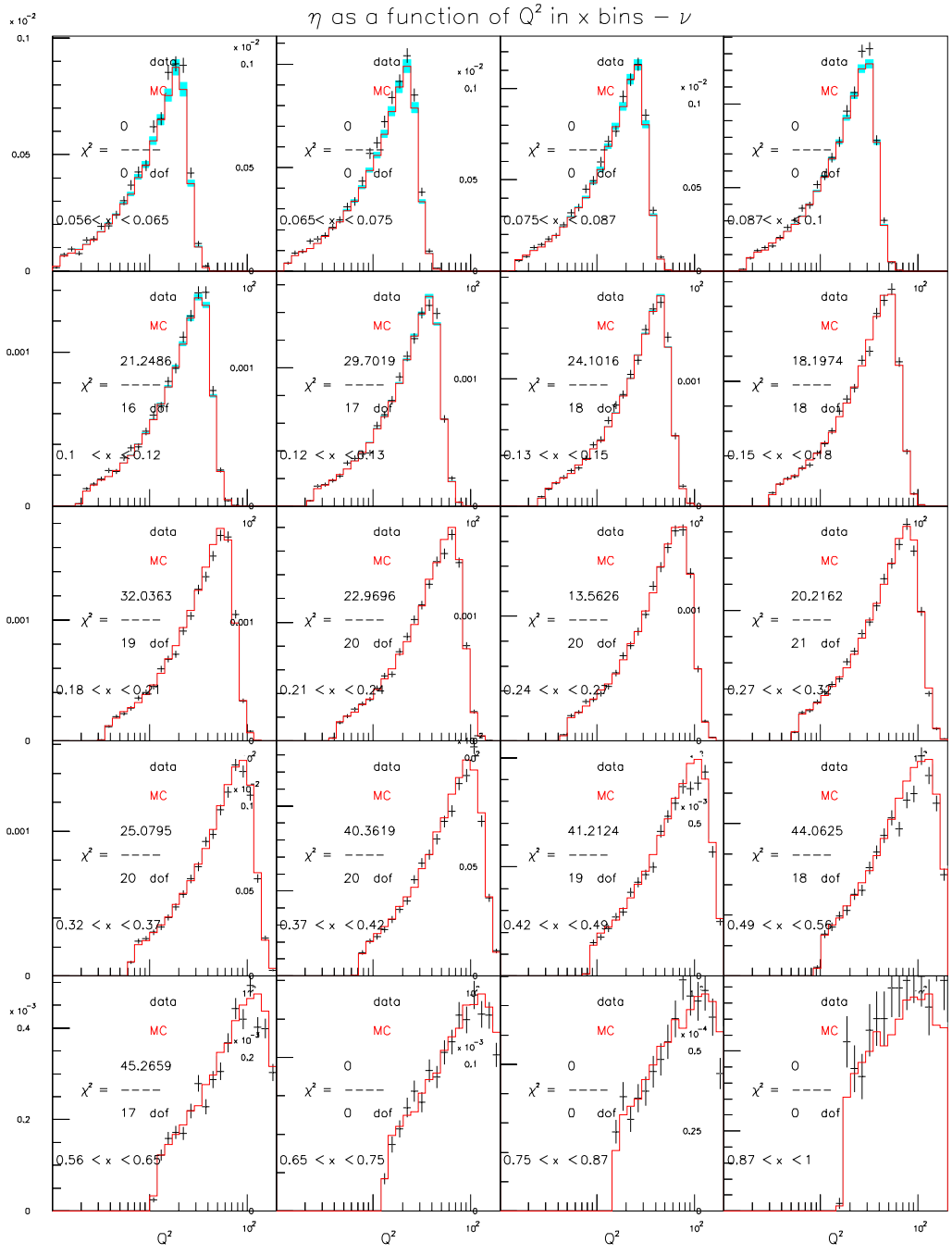

Figure D.70: CTEQ5NLO $\eta(Q^2)$ – ν mode $s(x, Q^2)$ sensitivity $(201 < E_\nu < 400)$

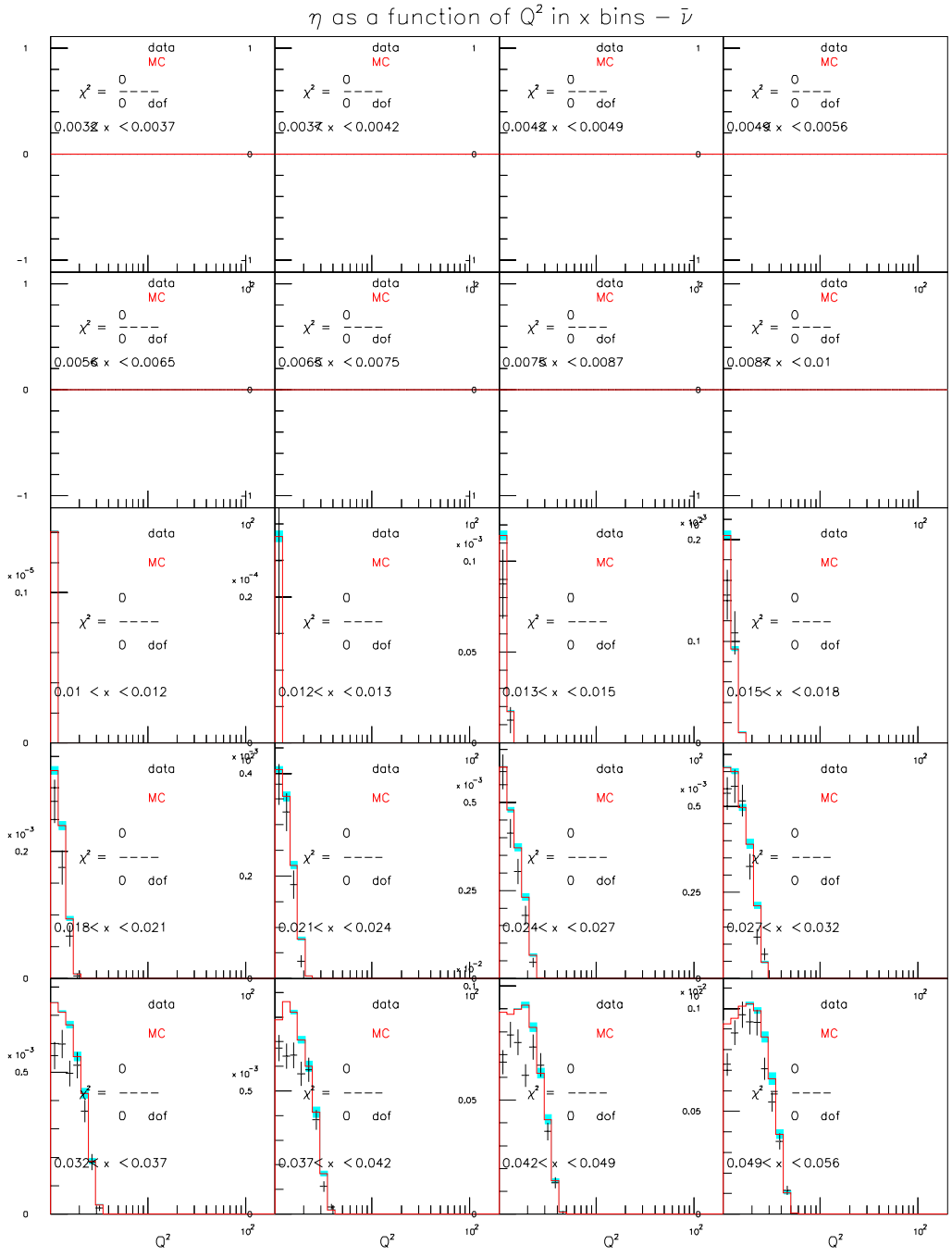

Figure D.71: CTEQ5NLO $\eta(Q^2) - \overline{\nu}$ mode $s(x, Q^2)$ sensitivity $(20 < E_\nu < 62)$

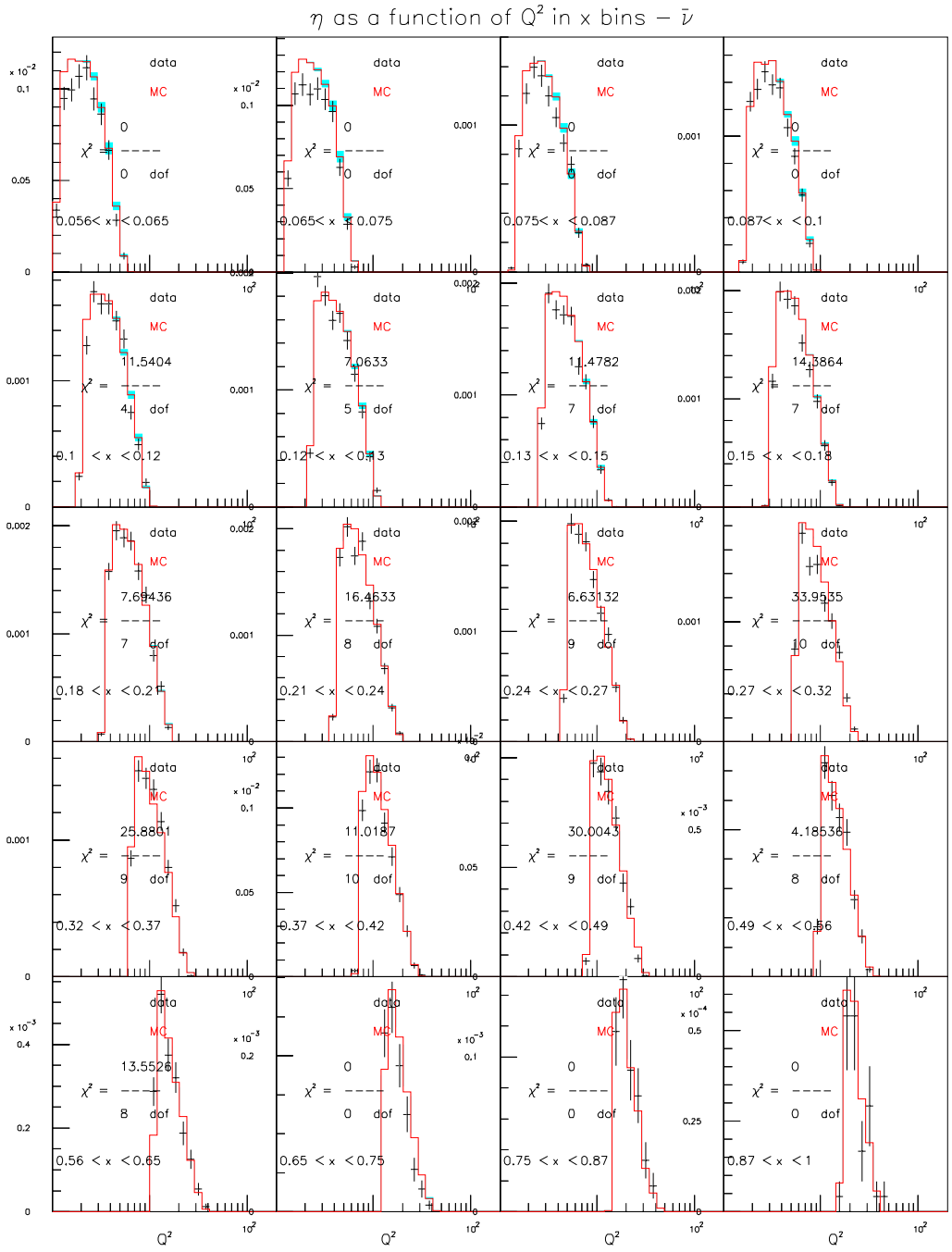

Figure D.72: CTEQ5NLO $\eta(Q^2)$ – $\overline{\nu}$ mode $s(x, Q^2)$ sensitivity $(20 < E_\nu < 62)$

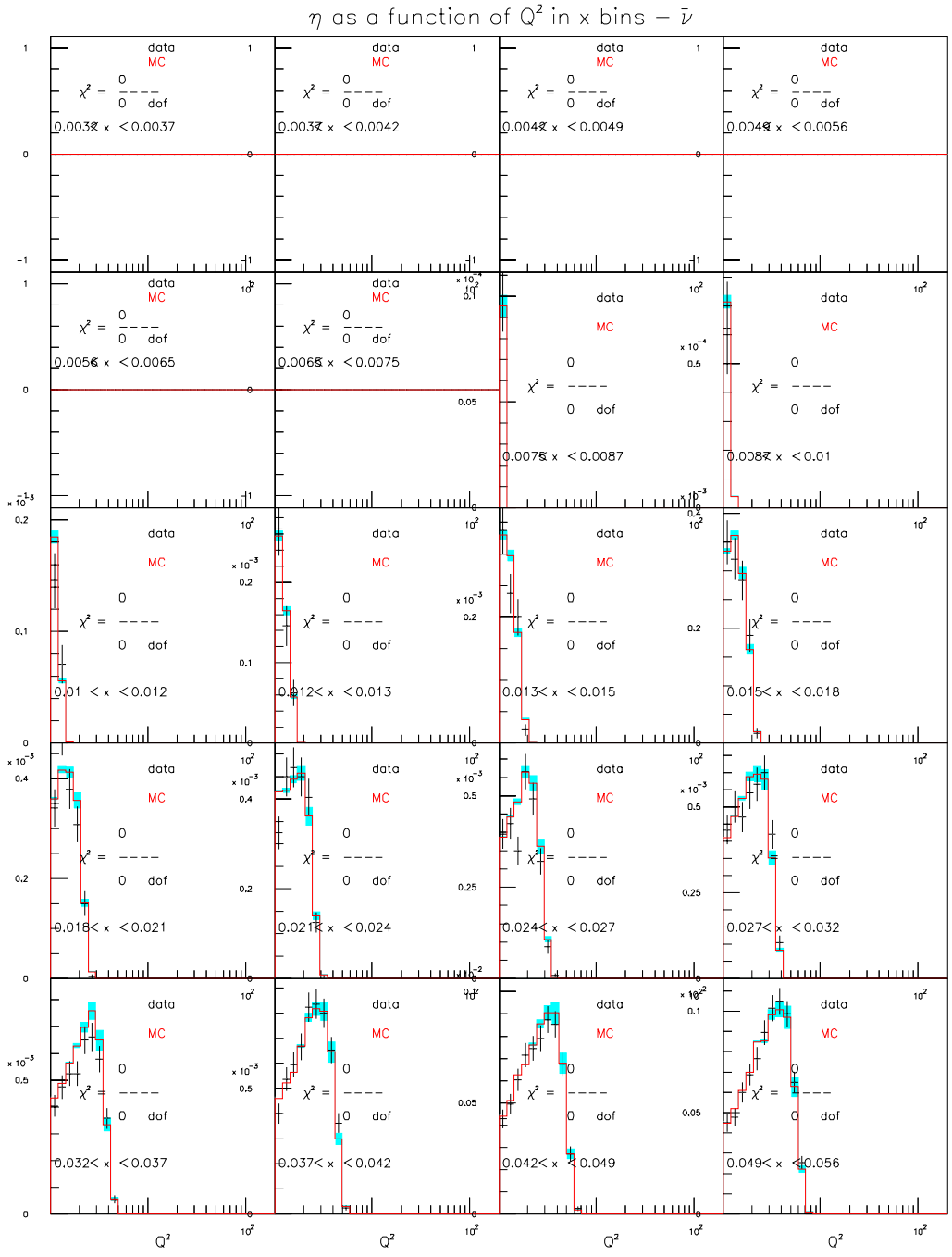

Figure D.73: CTEQ5NLO $\eta(Q^2) - \overline{\nu}$ mode $s(x, Q^2)$ sensitivity $(62 < E_\nu < 85)$

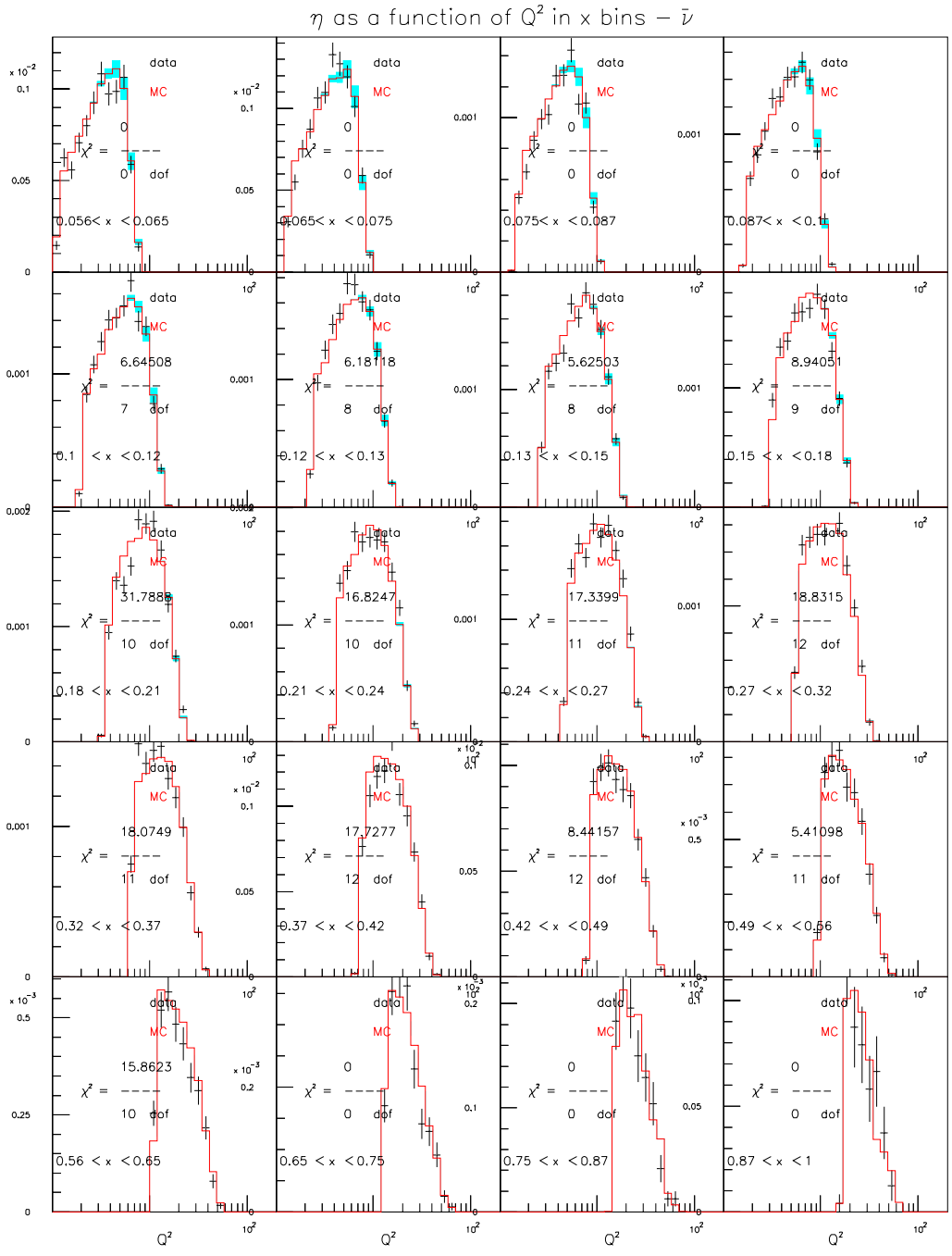

Figure D.74: CTEQ5NLO $\eta(Q^2)$ – $\overline{\nu}$ mode $s(x, Q^2)$ sensitivity $(62 < E_\nu < 85)$

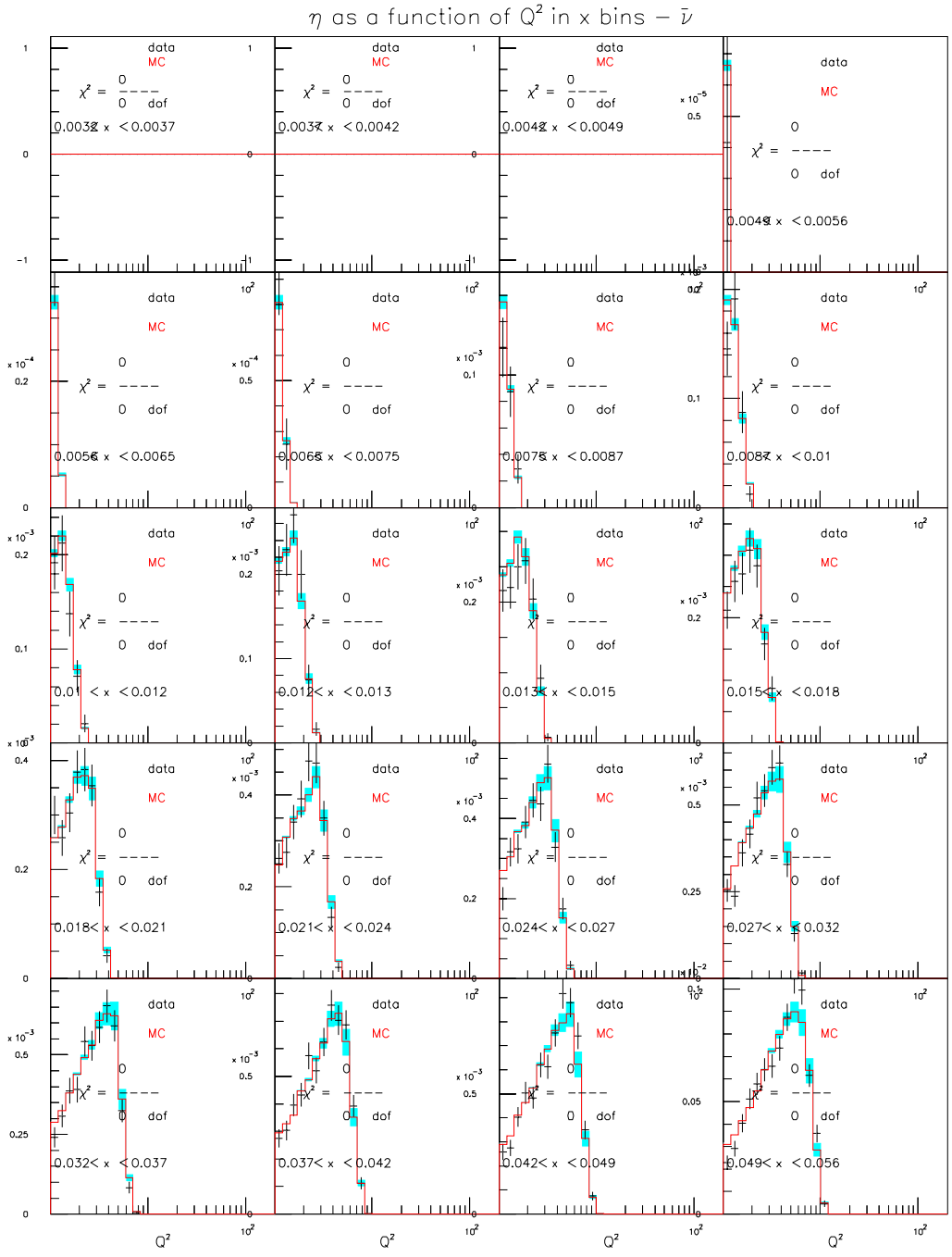

Figure D.75: CTEQ5NLO $\eta(Q^2)$ – $\overline{\nu}$ mode $s(x,Q^2)$ sensitivity ($85 < E_\nu < 129$)

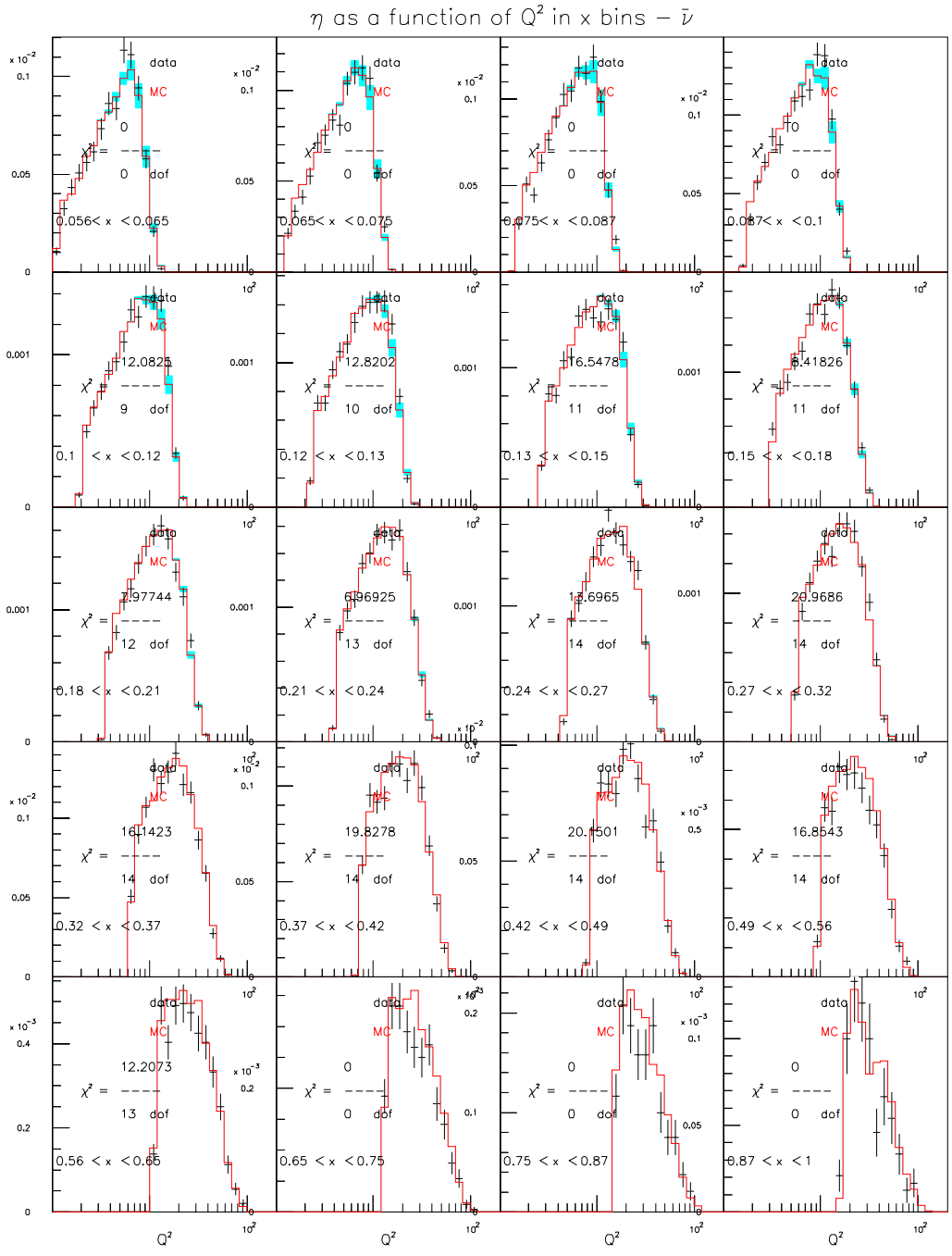

Figure D.76: CTEQ5NLO $\eta(Q^2)$ – $\overline{\nu}$ mode $s(x, Q^2)$ sensitivity ($85 < E_\nu < 129$)

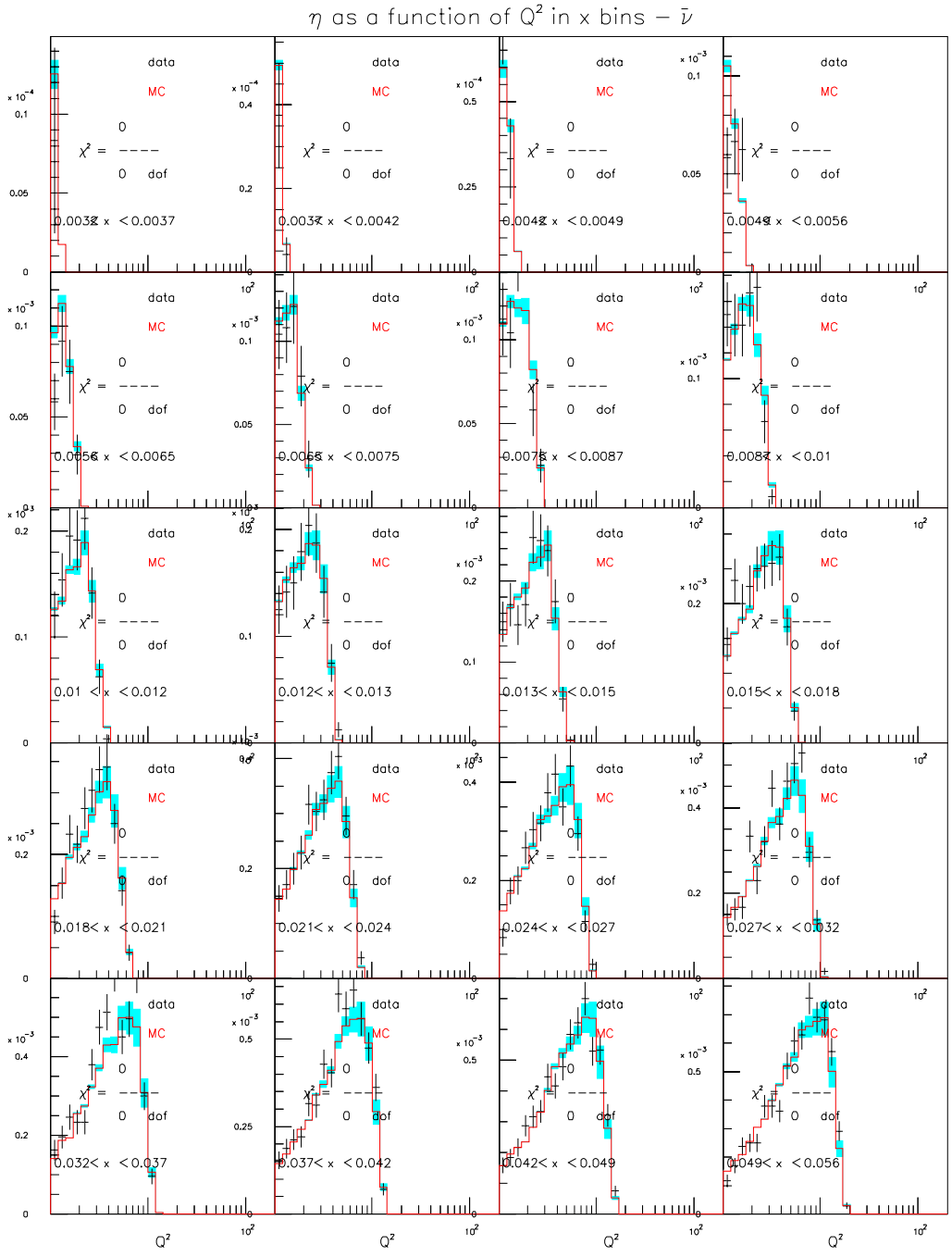

Figure D.77: CTEQ5NLO $\eta(Q^2) - \overline{\nu}$ mode $s(x, Q^2)$ sensitivity $(129 < E_\nu < 201)$

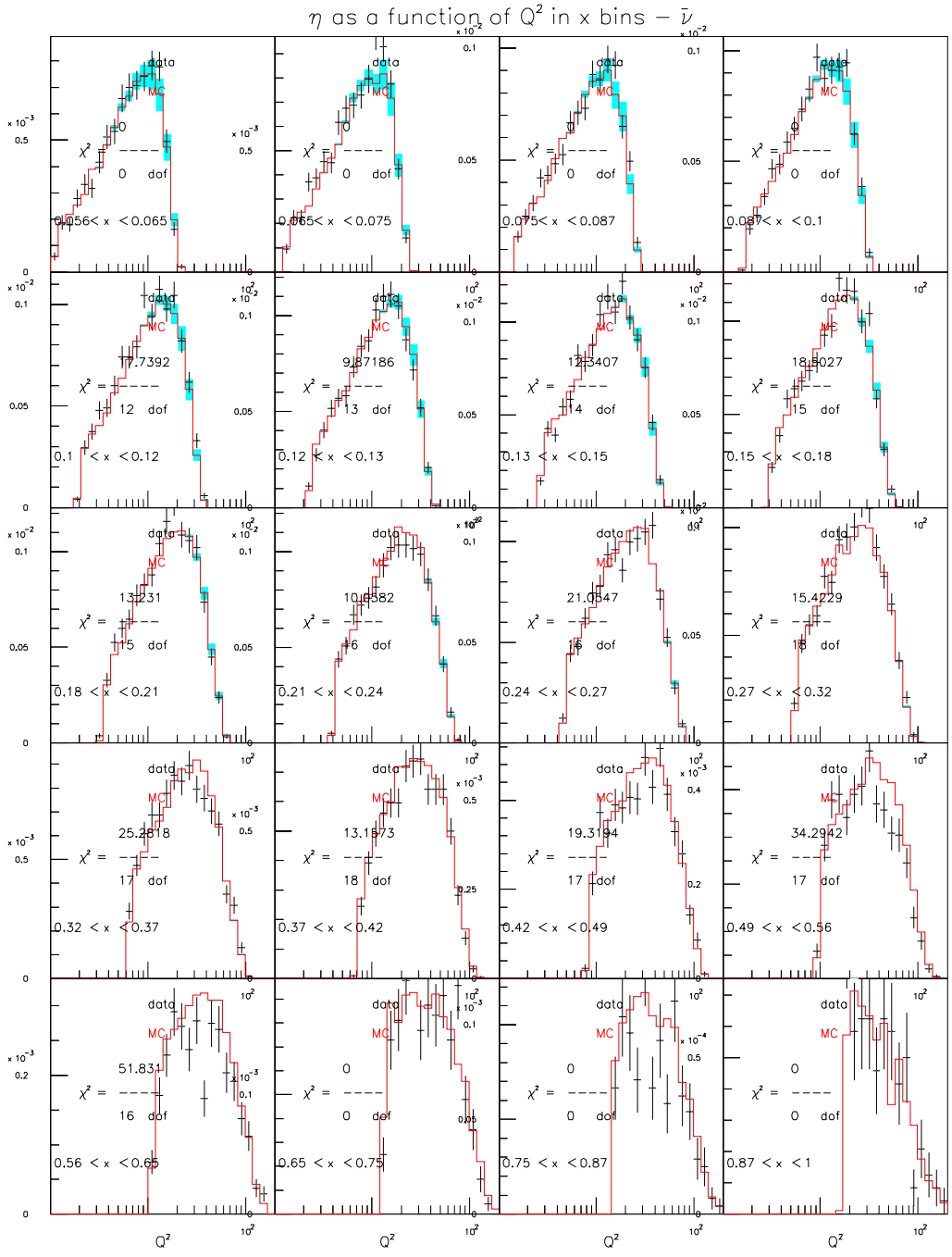

Figure D.78: CTEQ5NLO $\eta(Q^2) - \overline{\nu}$ mode $s(x, Q^2)$ sensitivity $(129 < E_\nu < 201)$

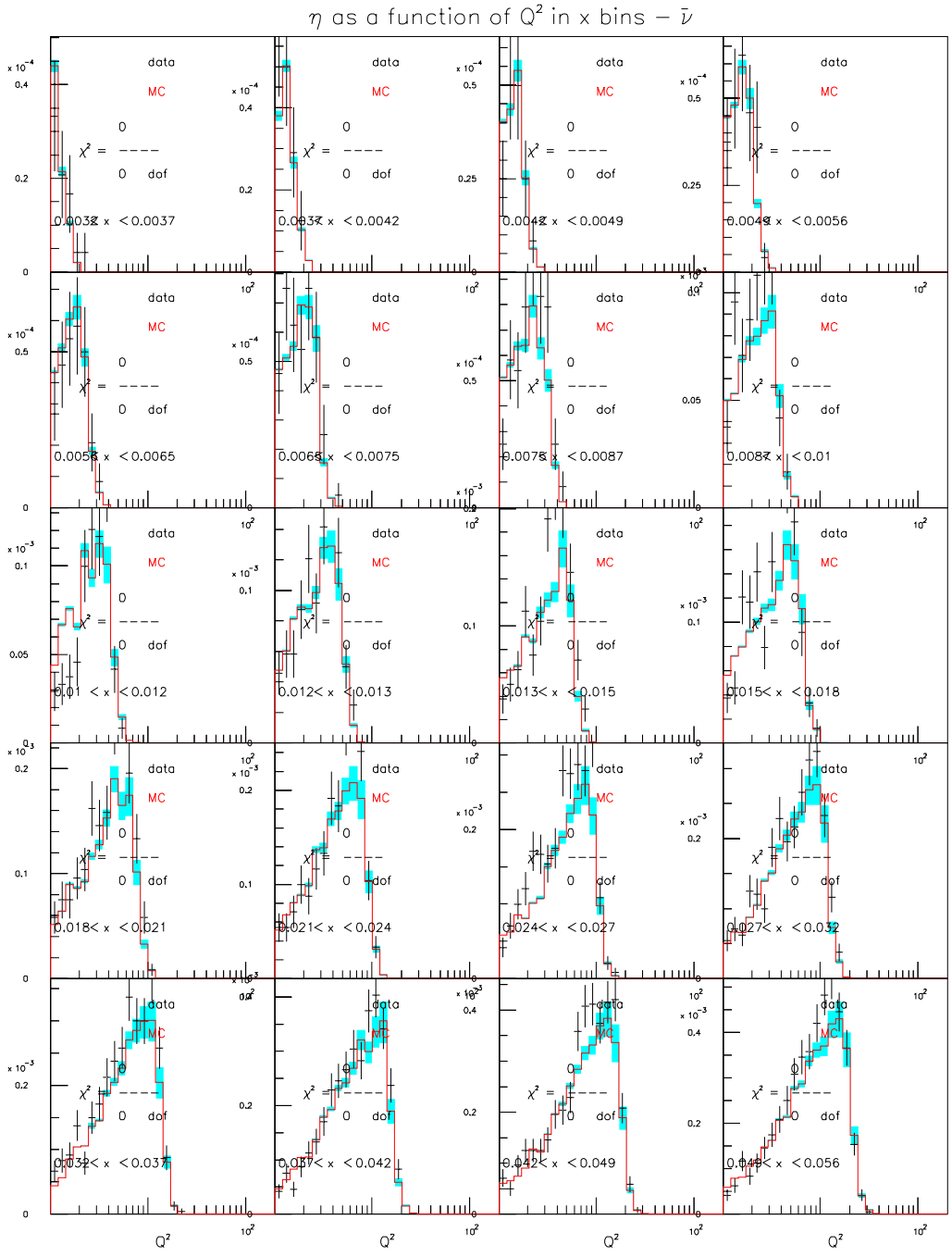

Figure D.79: CTEQ5NLO $\eta(Q^2) - \overline{\nu}$ mode $s(x, Q^2)$ sensitivity $(201 < E_\nu < 400)$

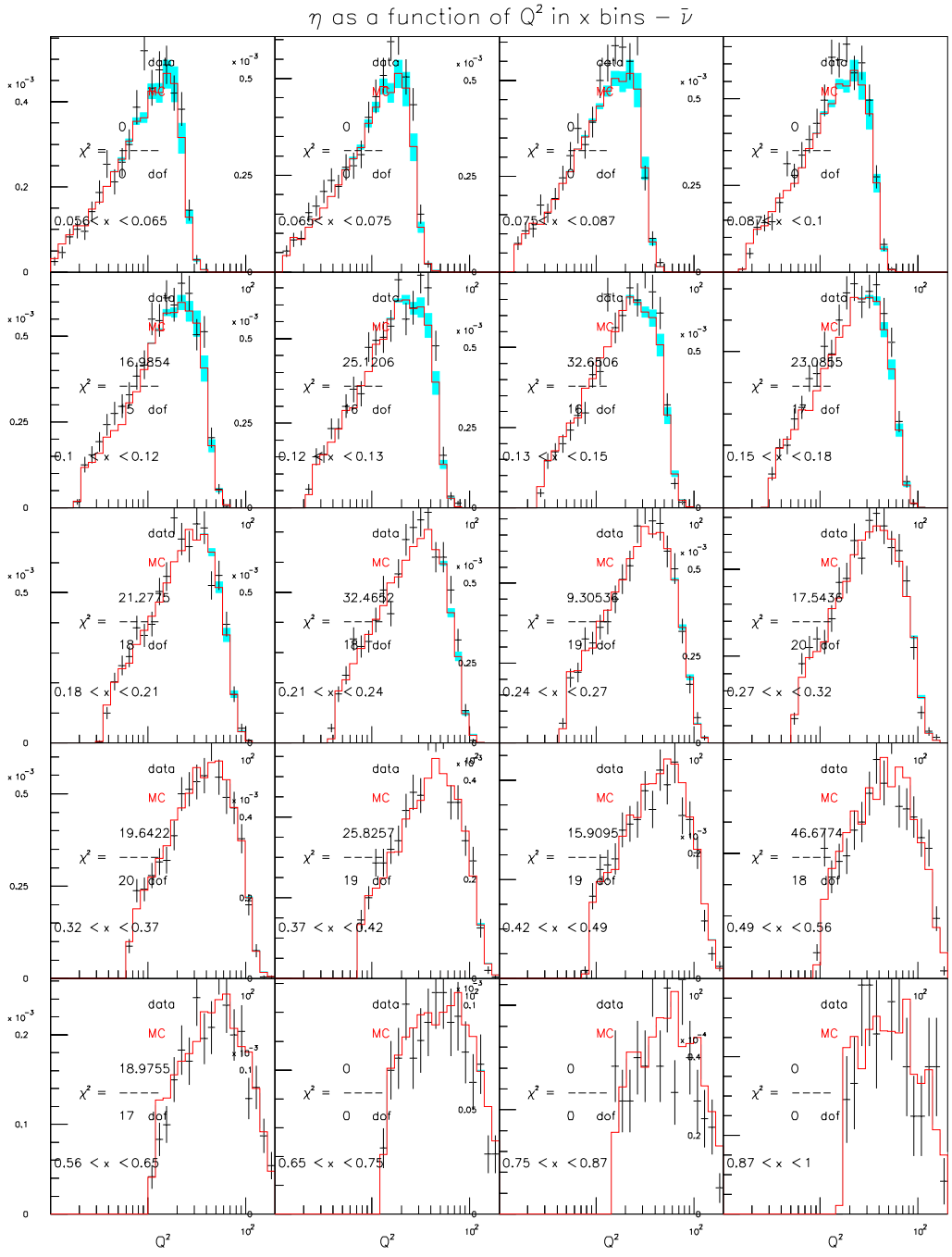

Figure D.80: CTEQ5NLO $\eta(Q^2) - \overline{\nu}$ mode $s(x, Q^2)$ sensitivity $(201 < E_\nu < 400)$

Appendix E

η Model Comparisons

Selected model comparisons are shown here via $\eta^{\nu/\overline{\nu}}(Q^2)$ in x and E_ν bins. These models include:

- GRV98NLO
- CTEQ5NLO
- GRV98NLO+EMC+HT
- CTEQ5NLO+EMC+HT
- GRV98LO+EMC
- BGPAR

The models were chosen based on the relatively large difference in overall χ^2 that occurs between them. A comparison of the different models indicates the individual contribution of, for example, higher twist, to the improvement in overall χ^2.

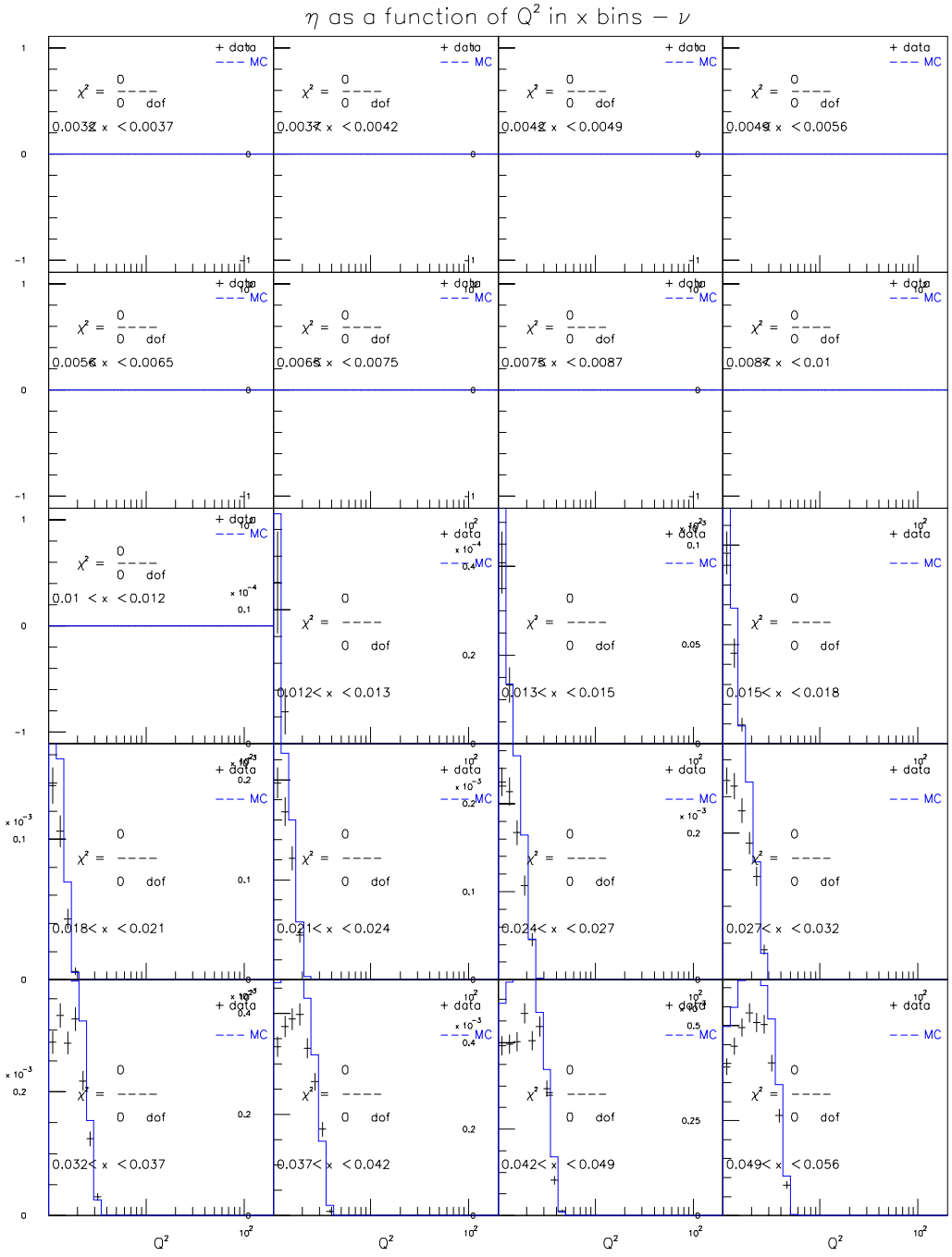

Figure E.1: GRV98NLO for $20 < E_\nu < 62$ GeV (ν mode)

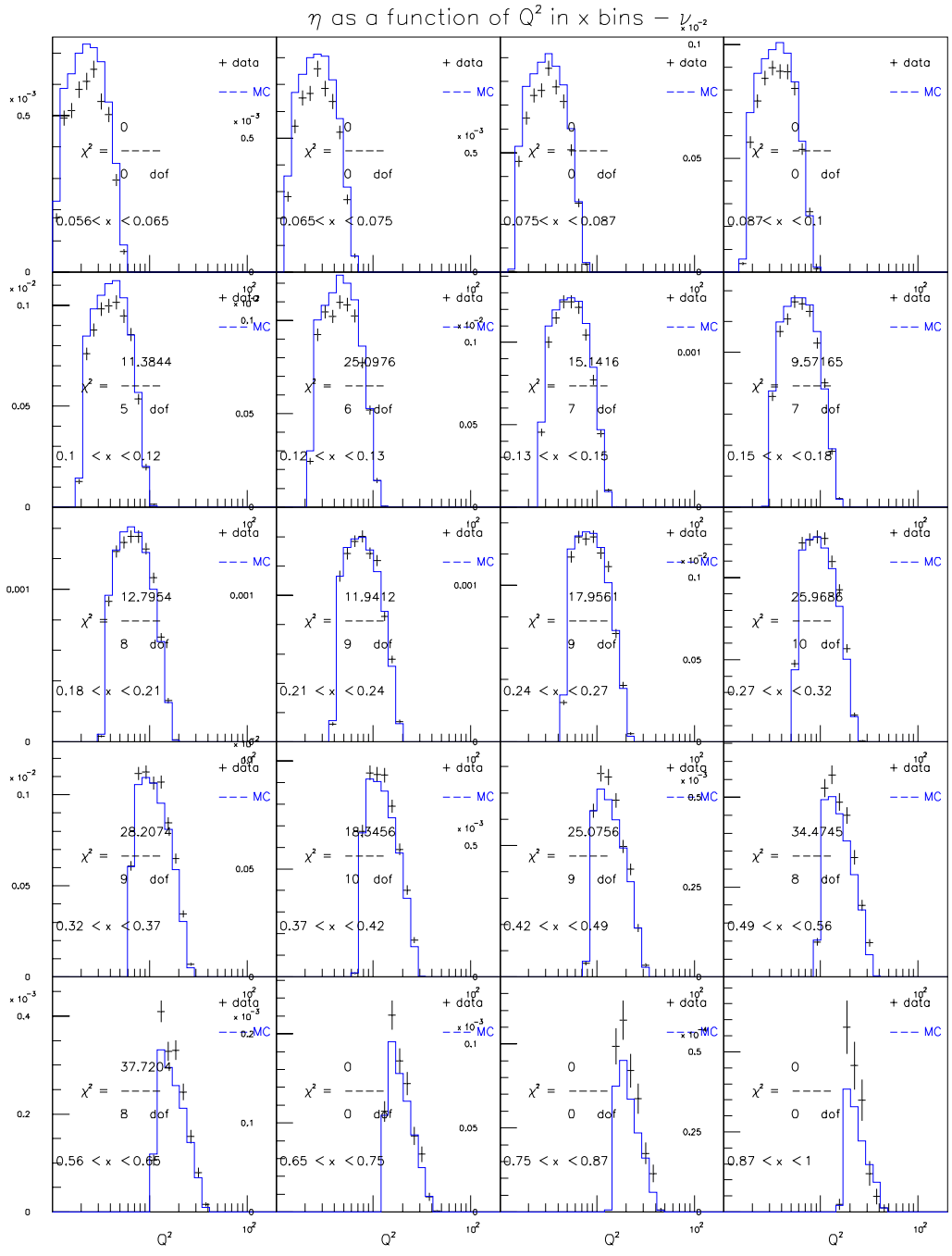

Figure E.2: GRV98NLO for $20 < E_\nu < 62$ GeV (ν mode)

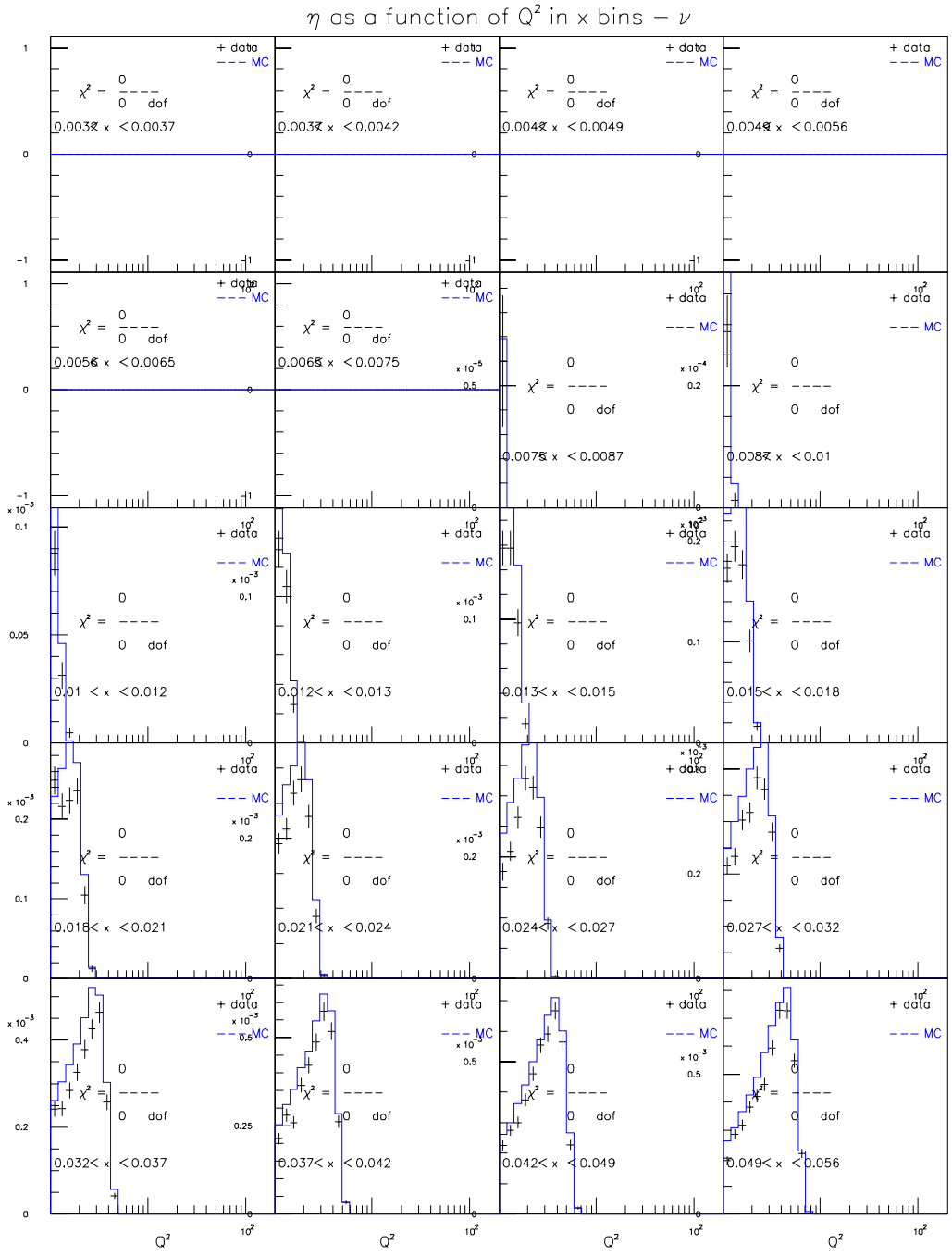

Figure E.3: GRV98NLO for $62 < E_\nu < 85$ GeV (ν mode)

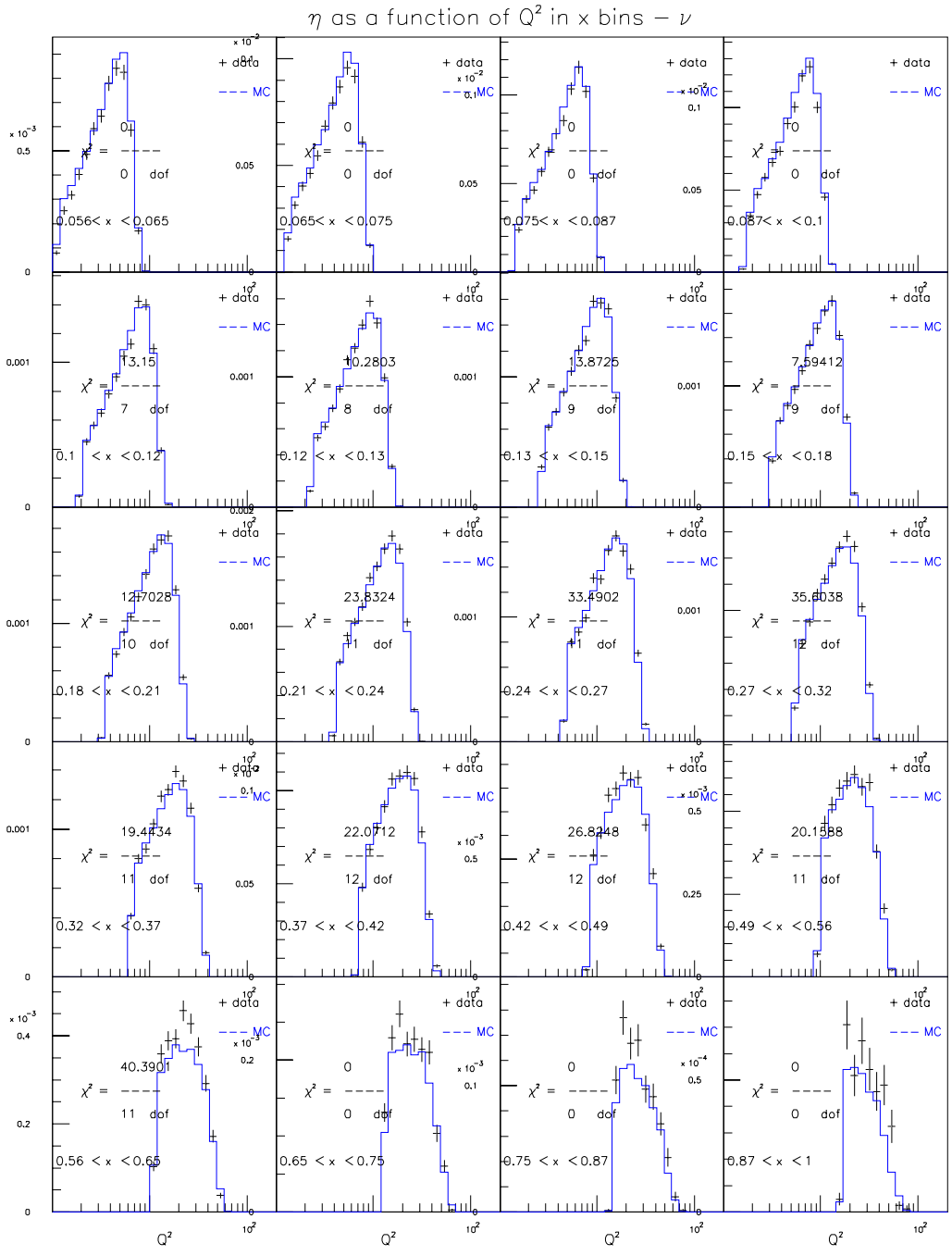

Figure E.4: GRV98NLO for $62 < E_\nu < 85$ GeV (ν mode)

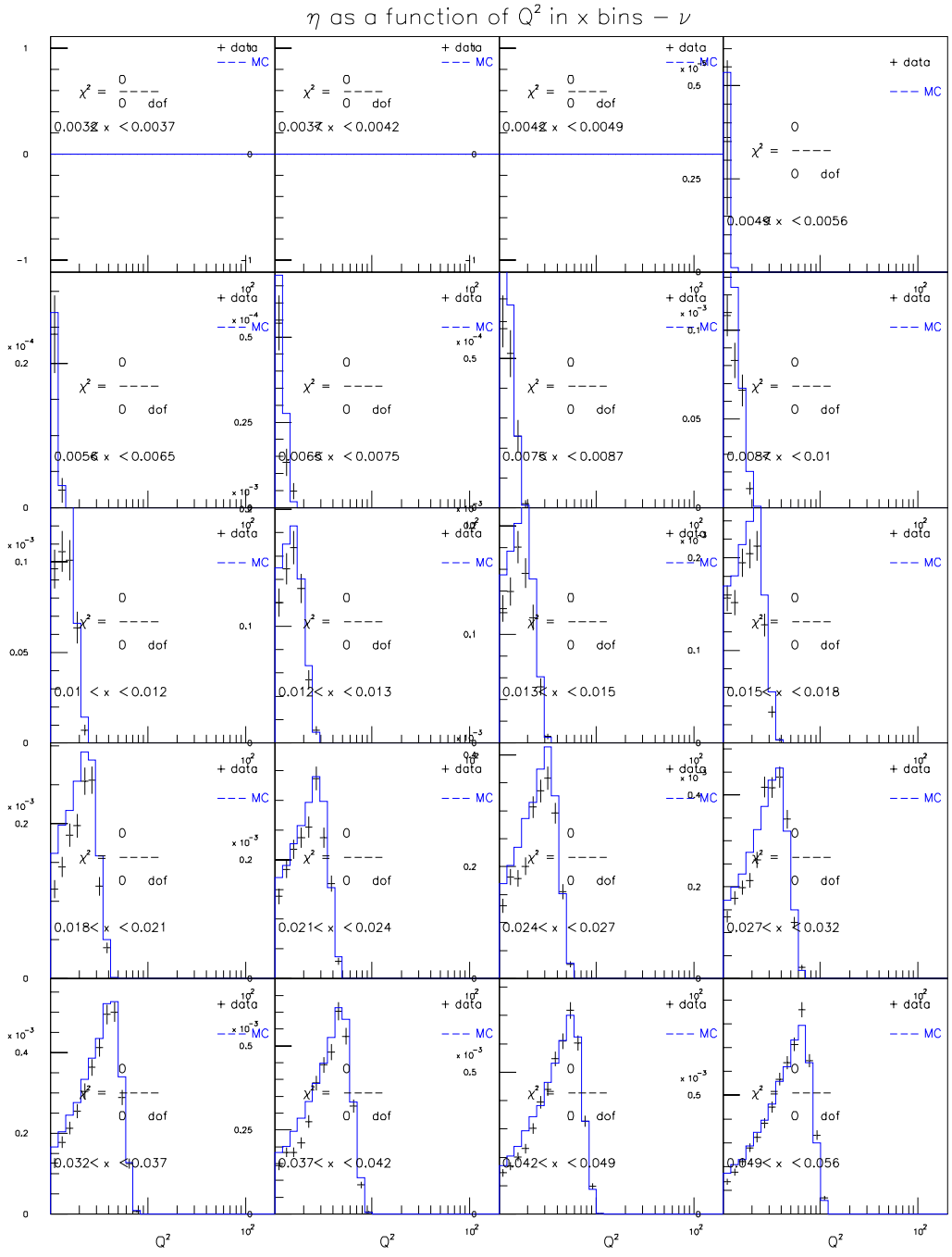

Figure E.5: GRV98NLO for $85 < E_\nu < 129$ GeV (ν mode)

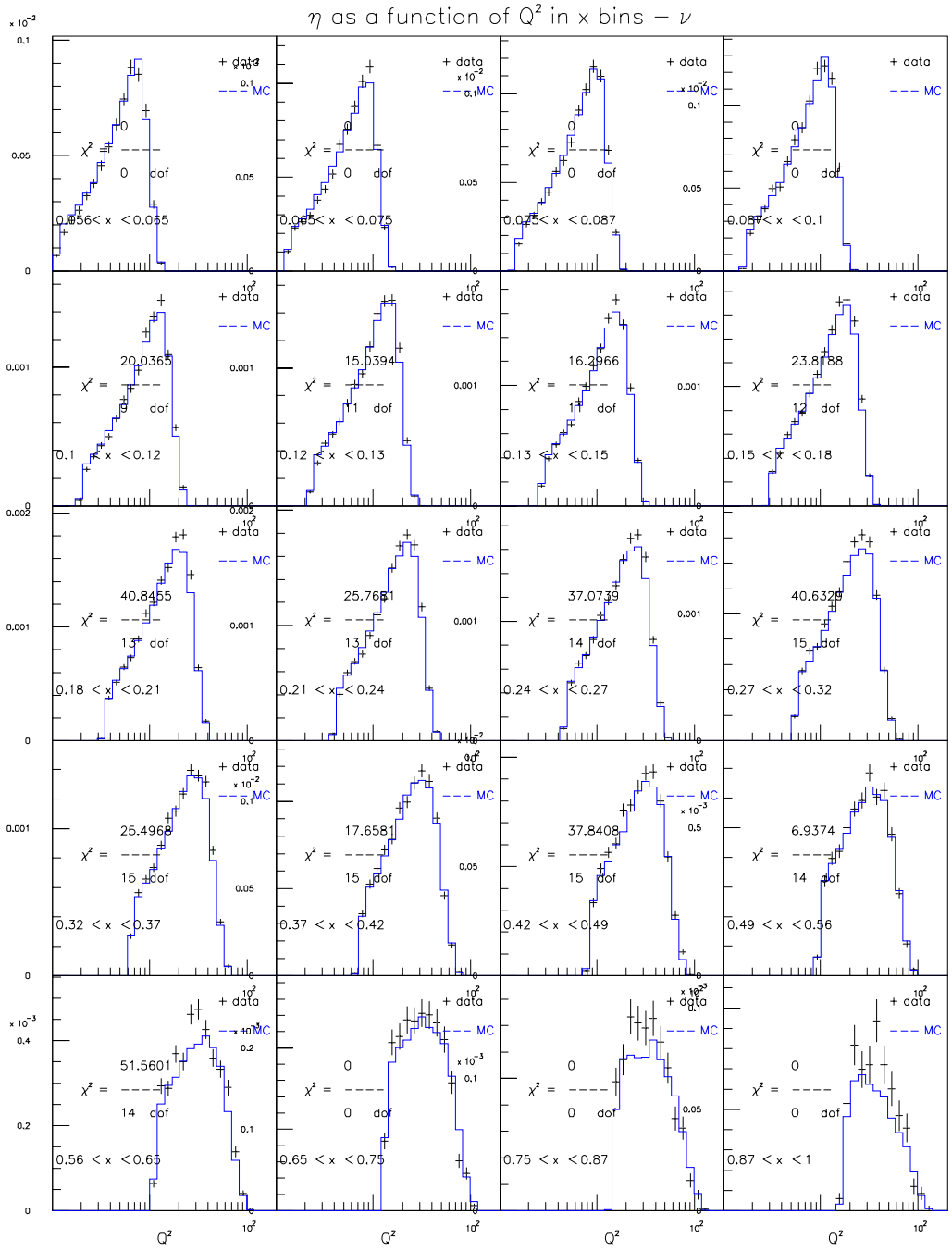

Figure E.6: GRV98NLO for $85 < E_\nu < 129$ GeV (ν mode)

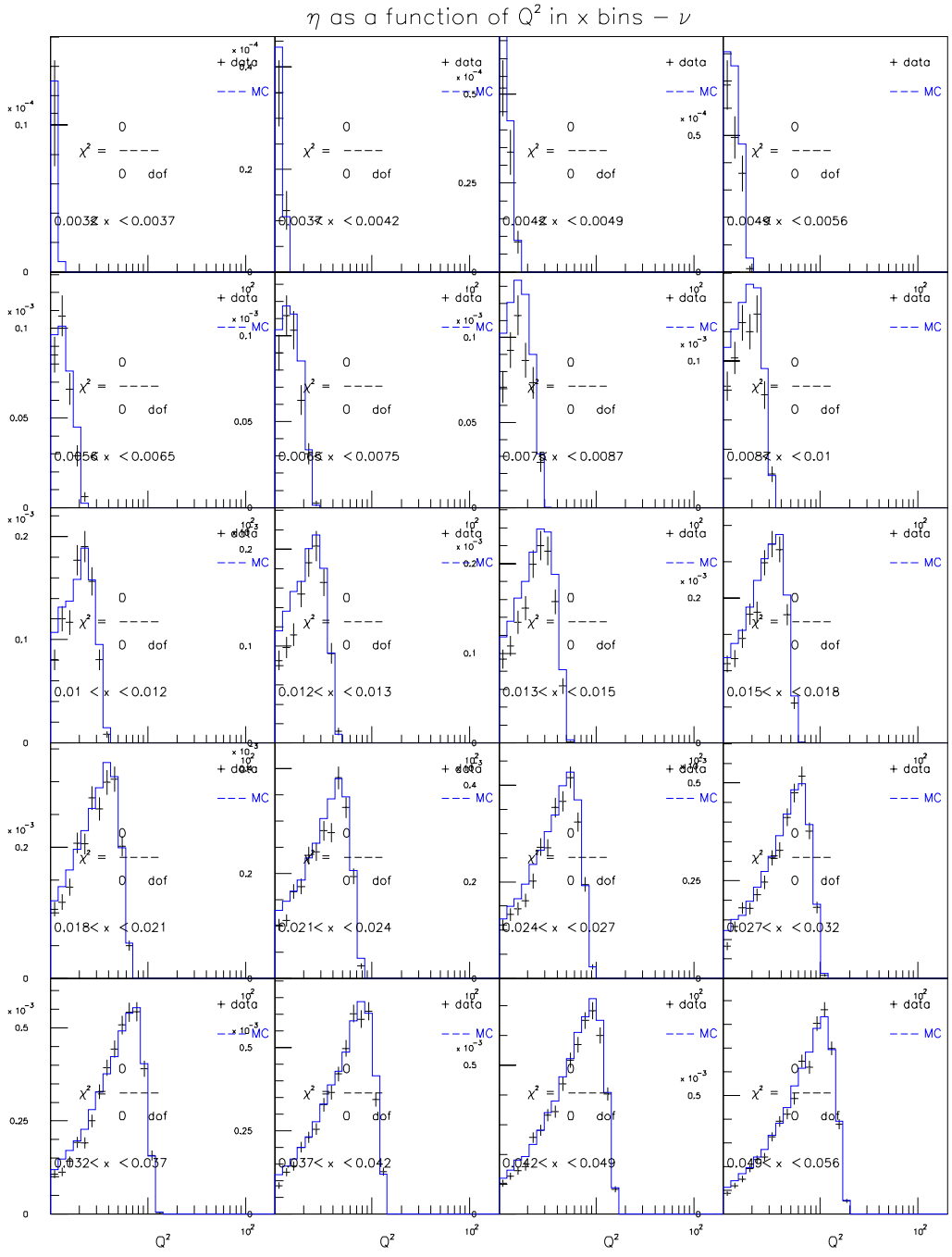

Figure E.7: GRV98NLO for $129 < E_\nu < 201$ GeV (ν mode)

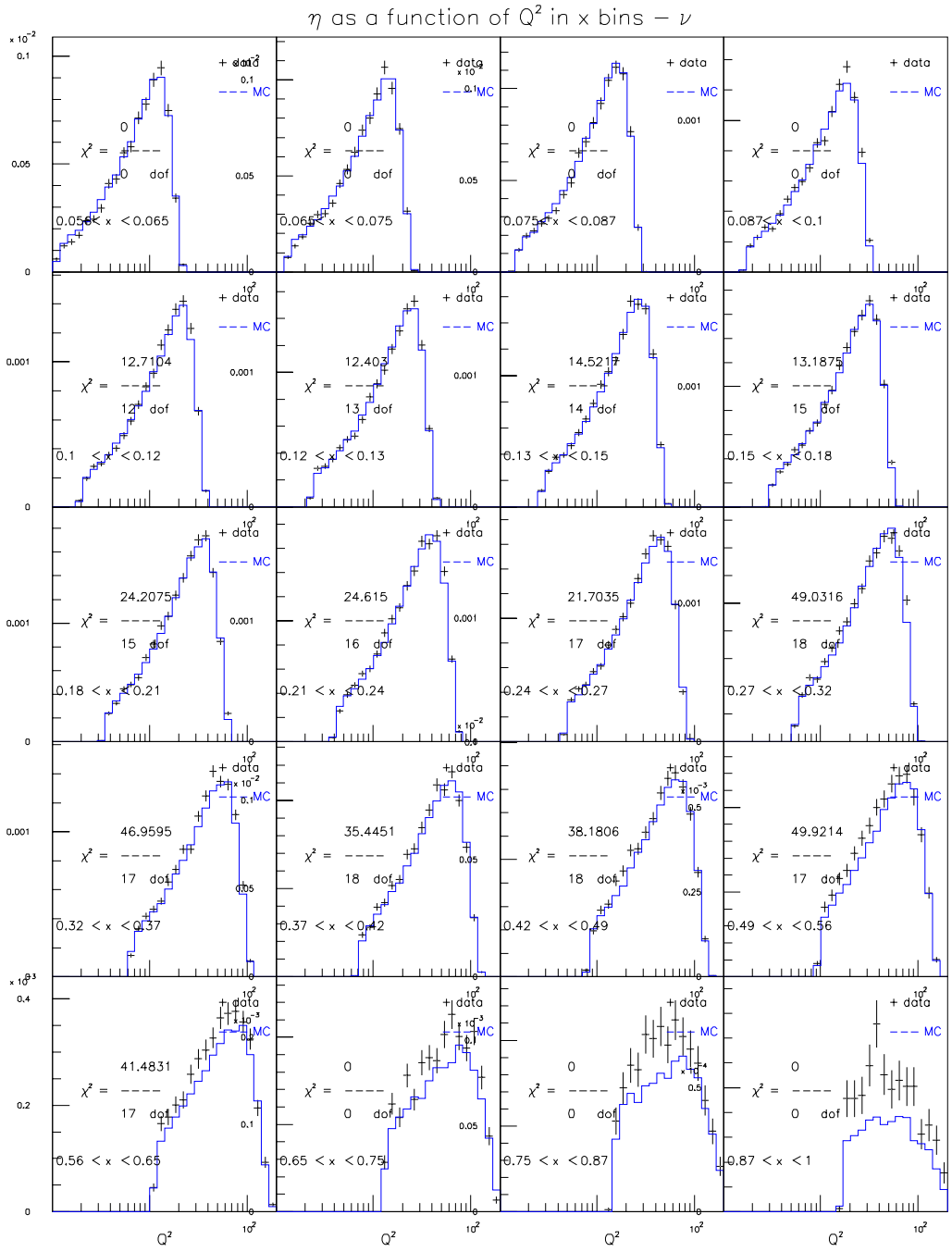

Figure E.8: GRV98NLO for $129 < E_\nu < 201$ GeV (ν mode)

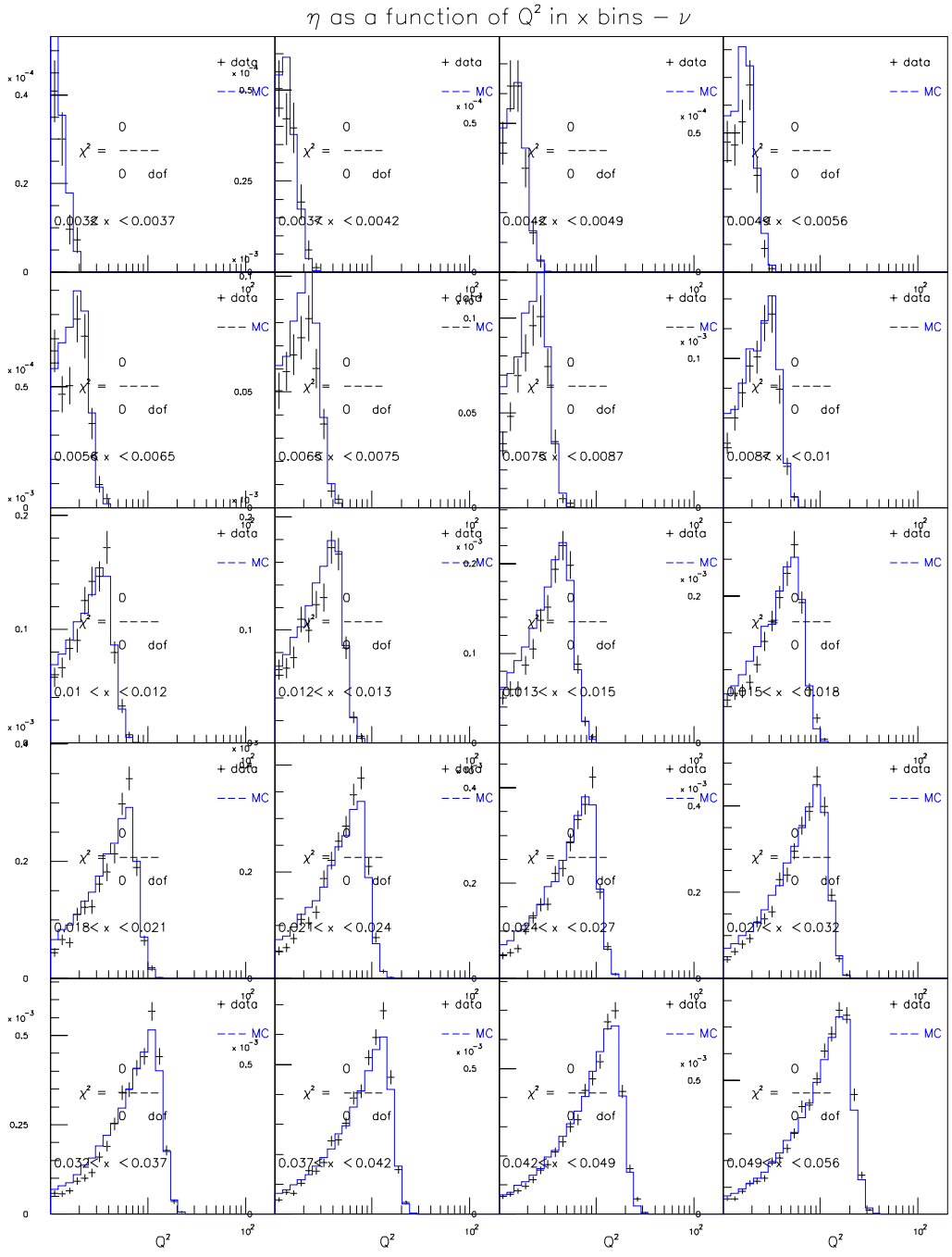

Figure E.9: GRV98NLO for $201 < E_\nu < 400$ GeV (ν mode)

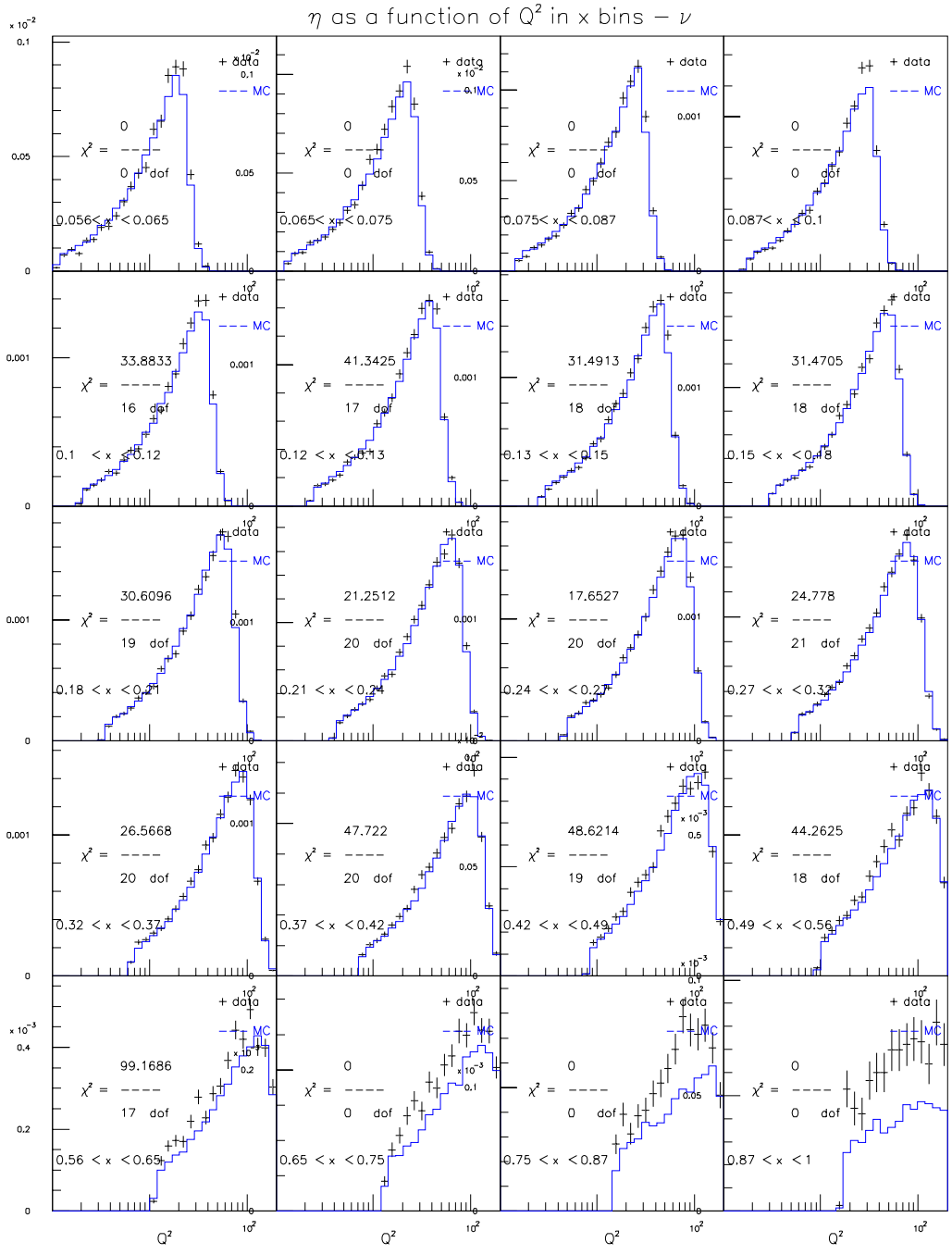

Figure E.10: GRV98NLO for $201 < E_\nu < 400$ GeV (ν mode)

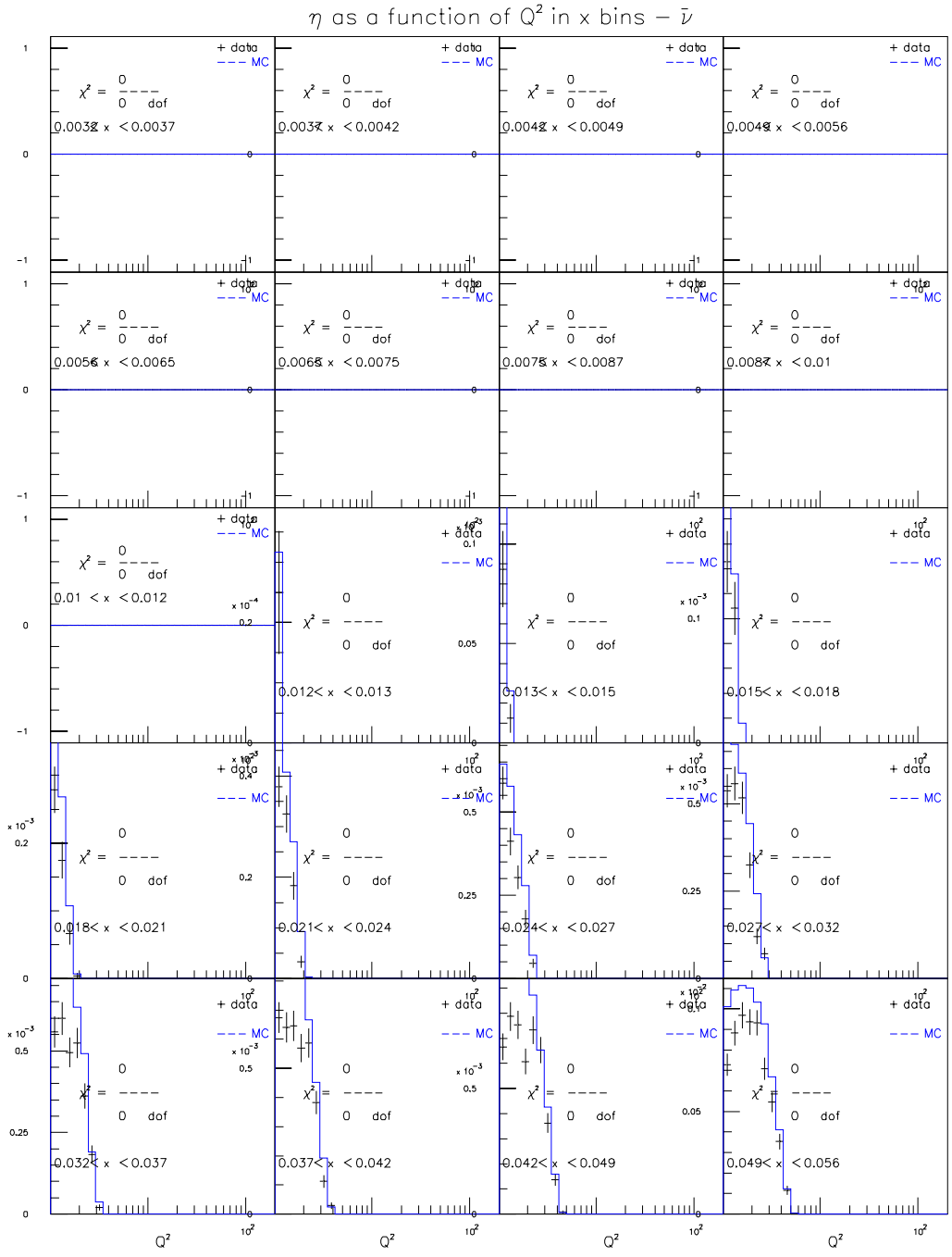

Figure E.11: GRV98NLO for $20 < E_\nu < 62$ GeV ($\overline{\nu}$ mode)

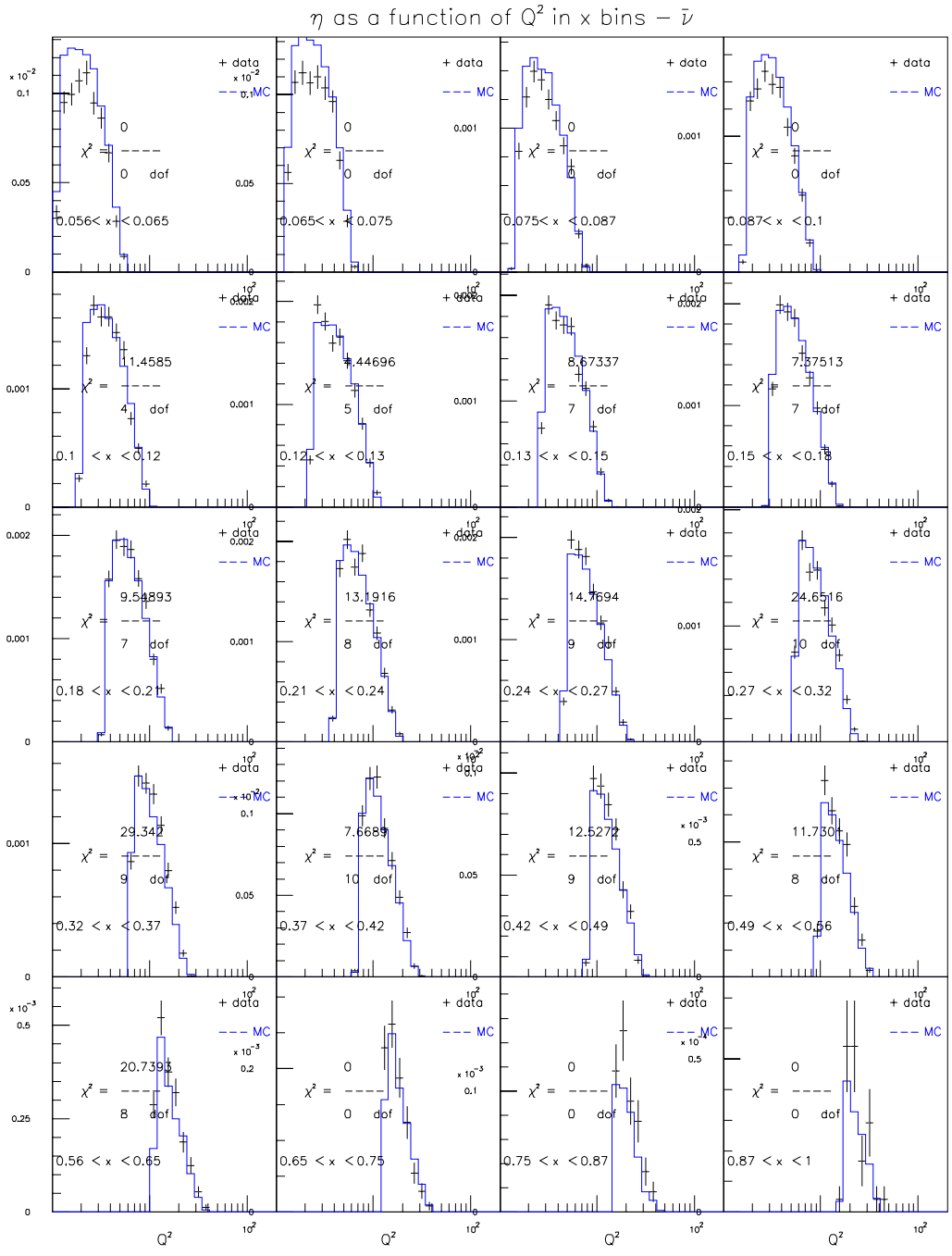

Figure E.12: GRV98NLO for $20 < E_\nu < 62$ GeV ($\overline{\nu}$ mode)

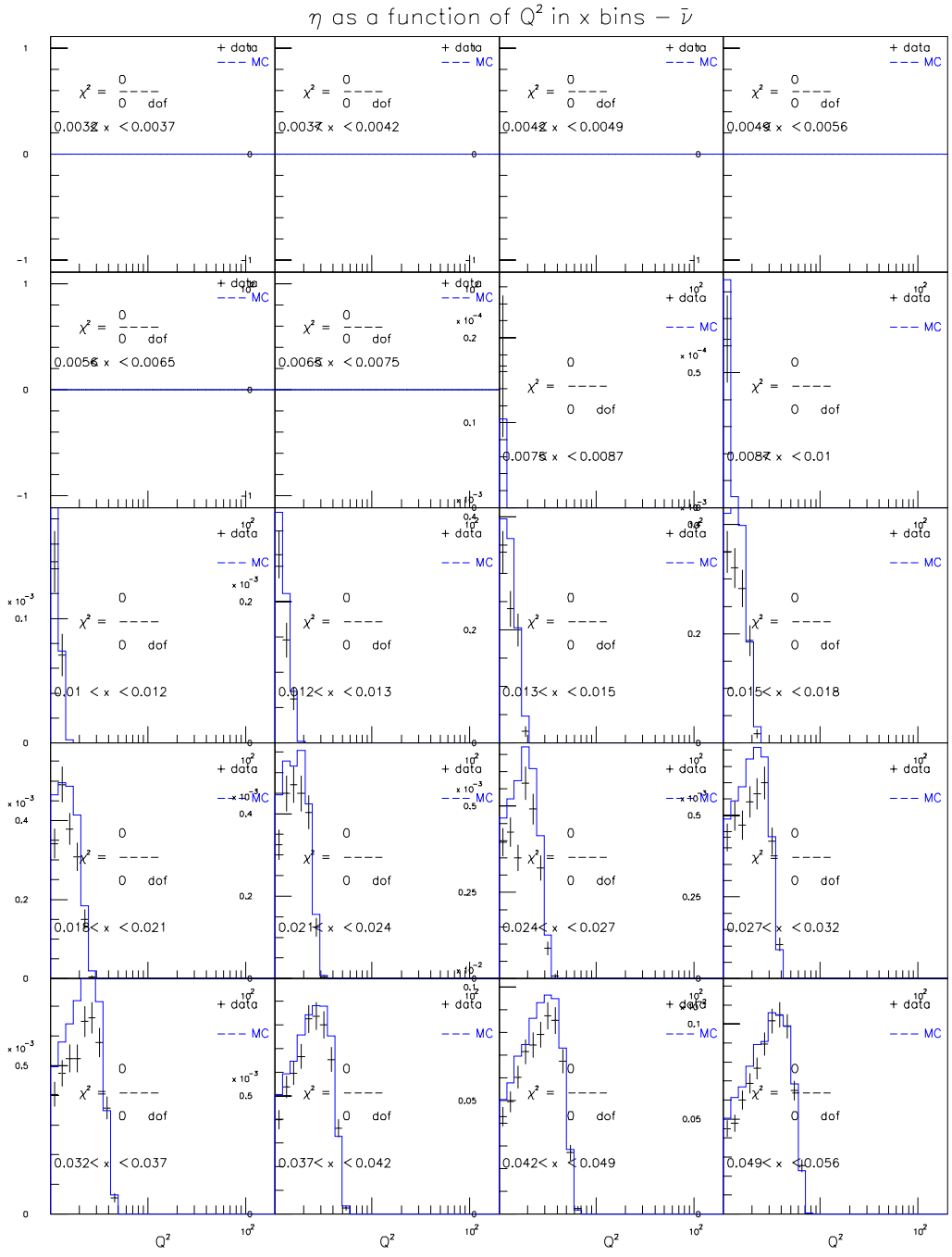

Figure E.13: GRV98NLO for $62 < E_\nu < 85$ GeV ($\overline{\nu}$ mode)

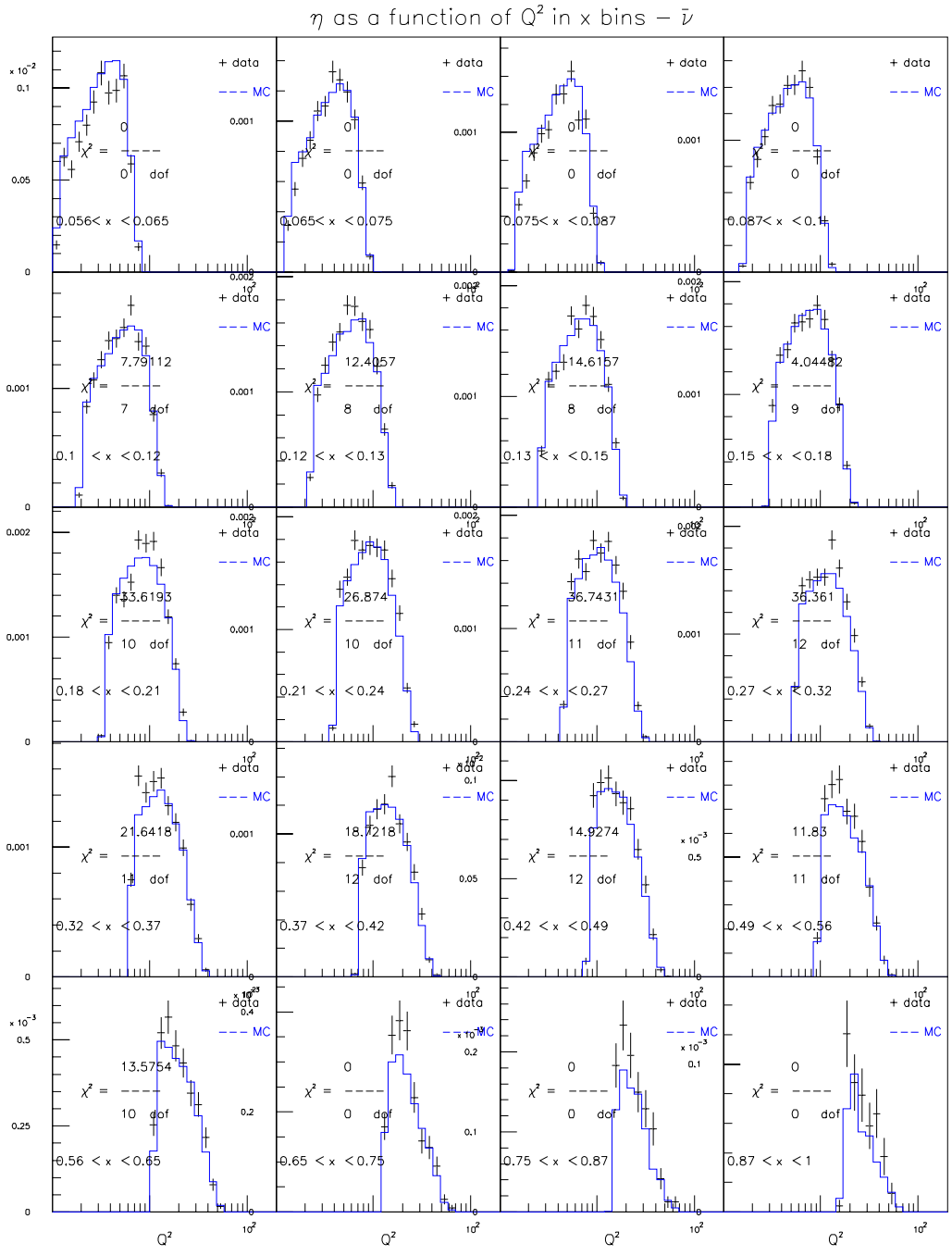

Figure E.14: GRV98NLO for $62 < E_\nu < 85$ GeV ($\overline{\nu}$ mode)

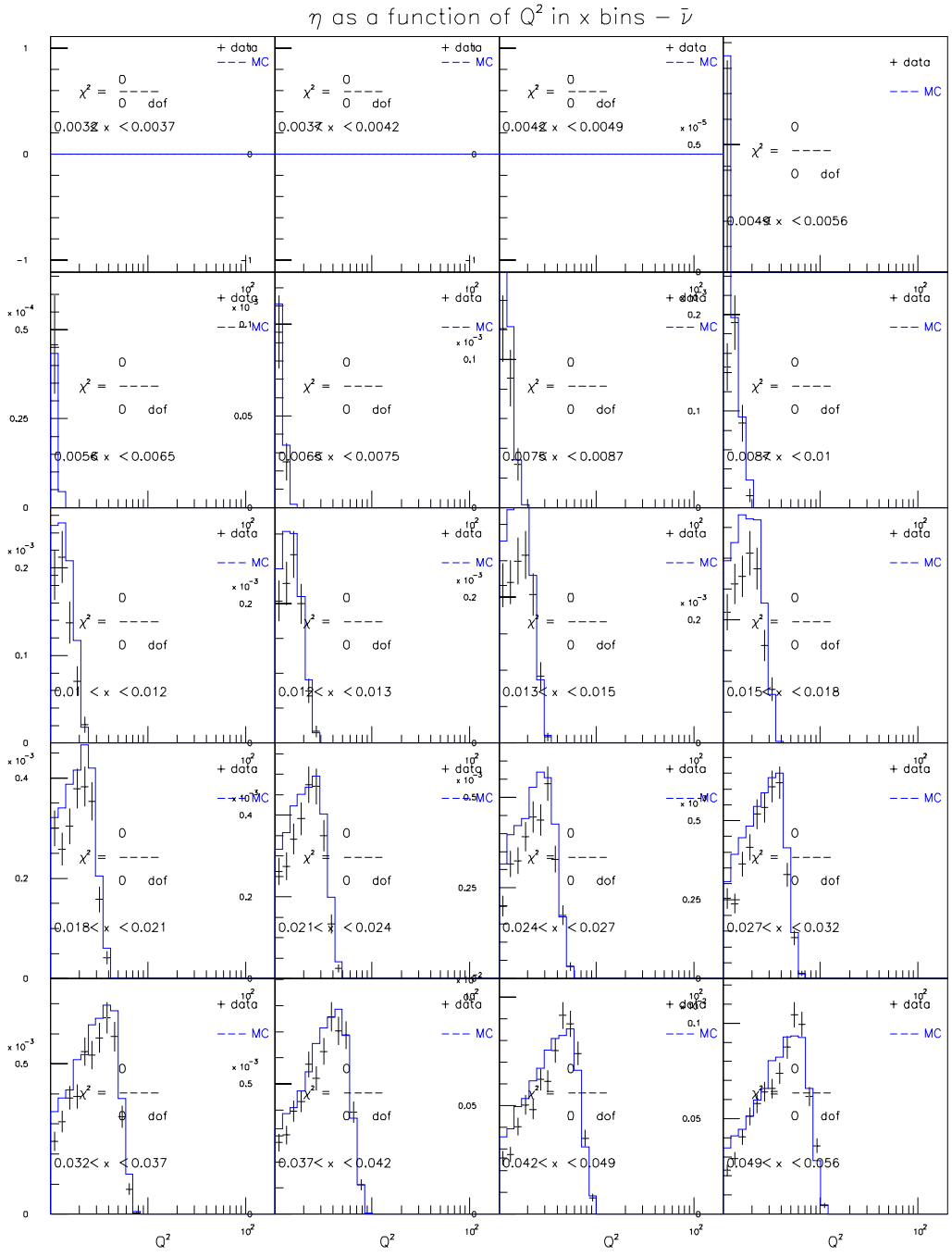

Figure E.15: GRV98NLO for $85 < E_\nu < 129$ GeV ($\overline{\nu}$ mode)

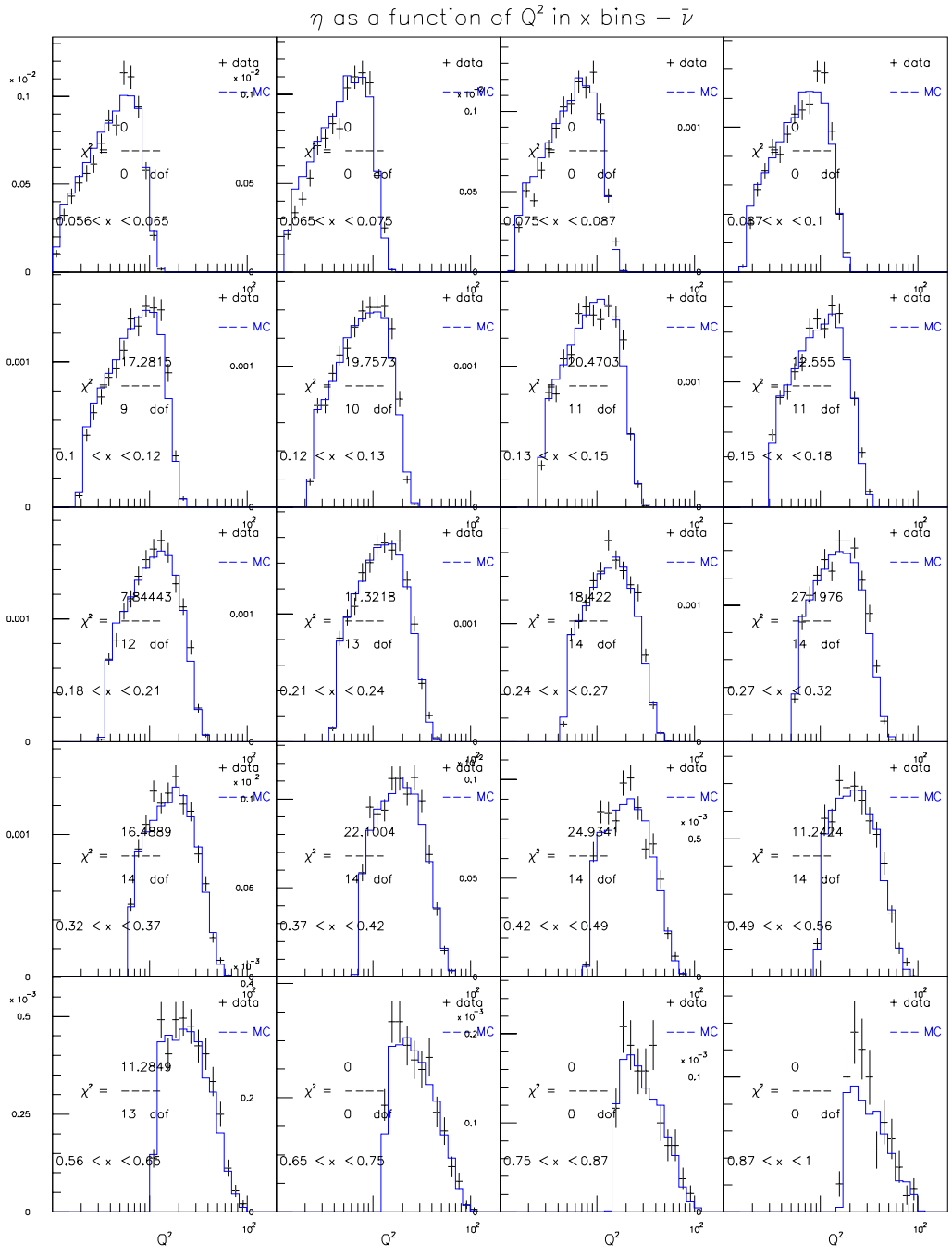

Figure E.16: GRV98NLO for $85 < E_\nu < 129$ GeV ($\overline{\nu}$ mode)

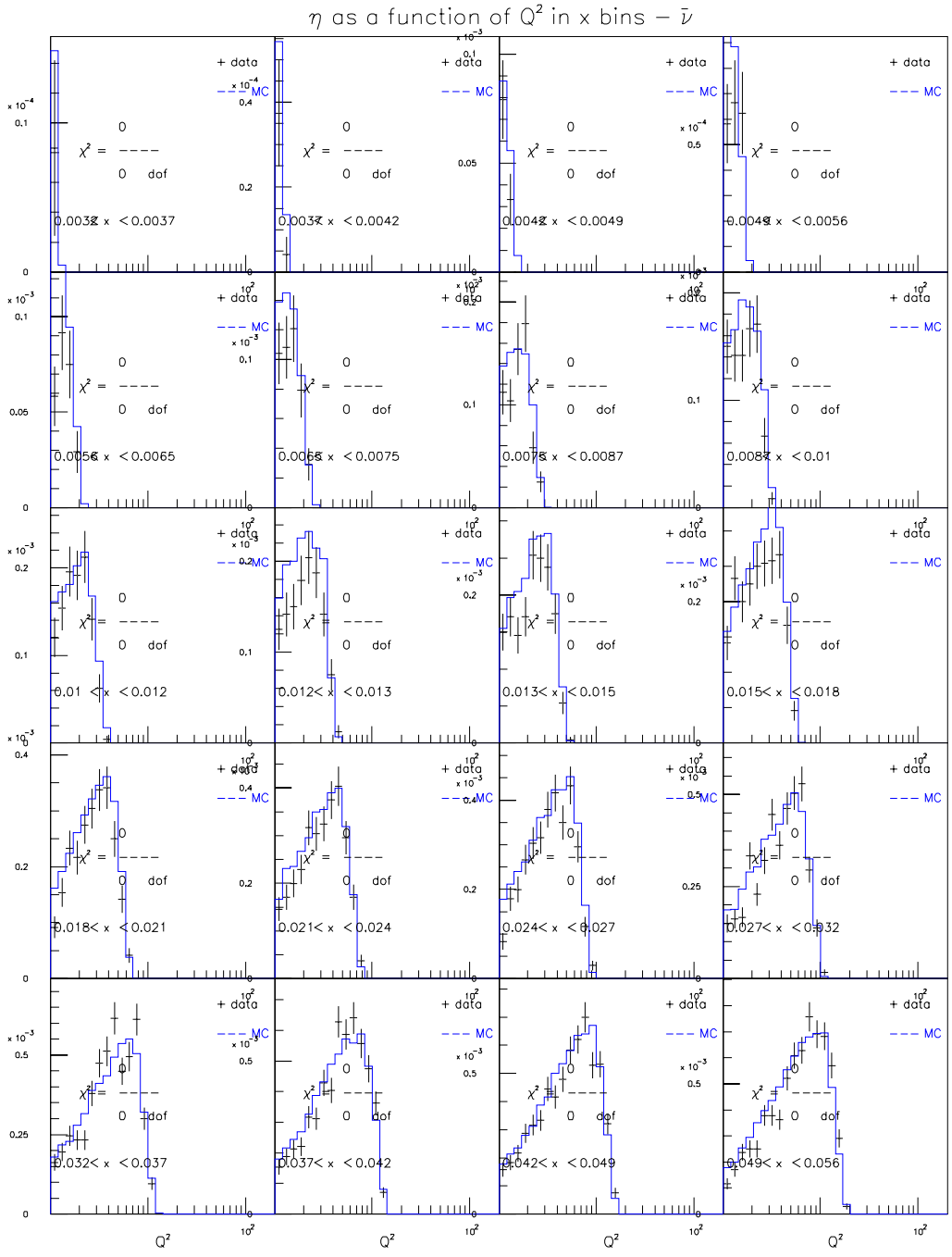

Figure E.17: GRV98NLO for $129 < E_\nu < 201$ GeV ($\overline{\nu}$ mode)

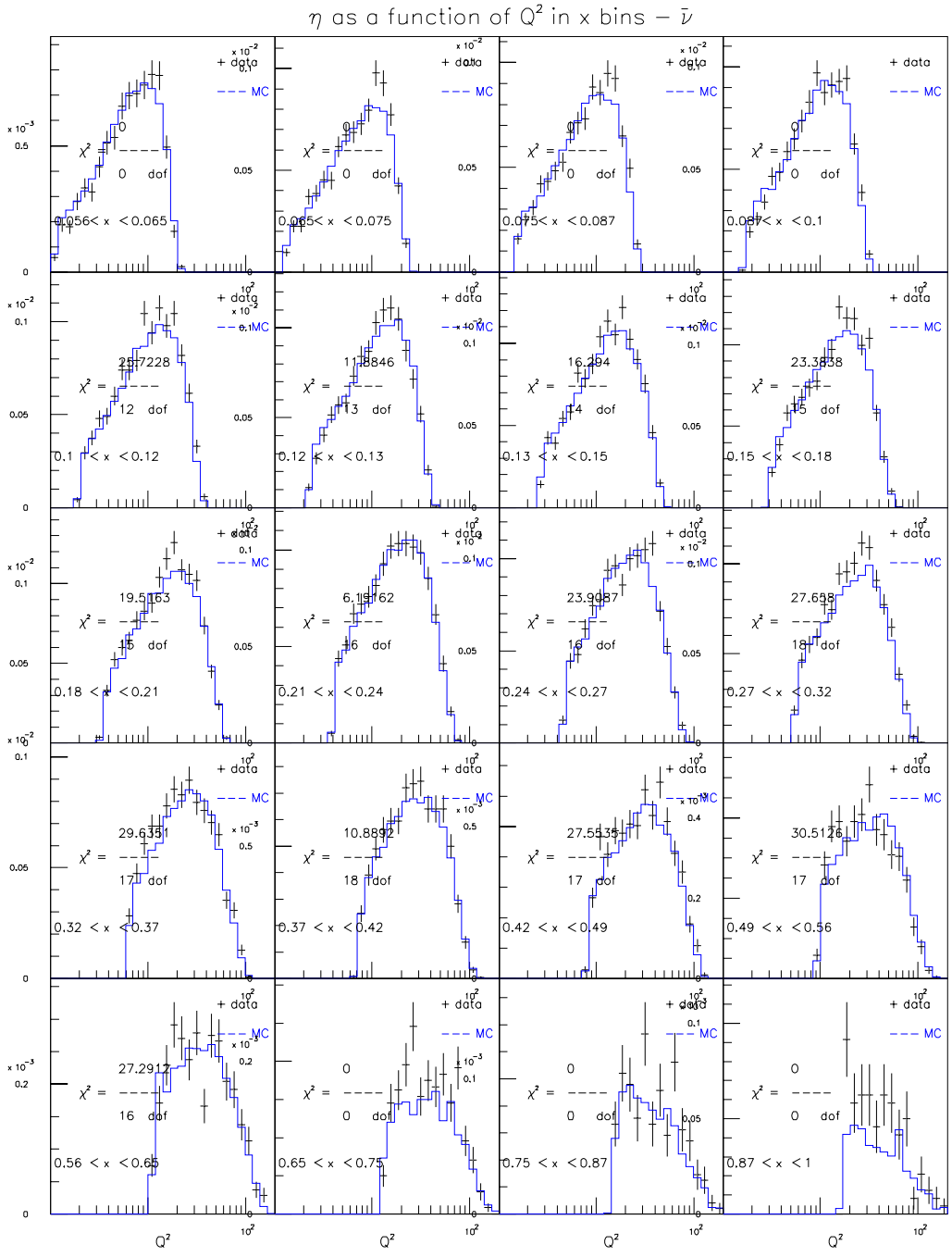

Figure E.18: GRV98NLO for $129 < E_\nu < 201$ GeV ($\overline{\nu}$ mode)

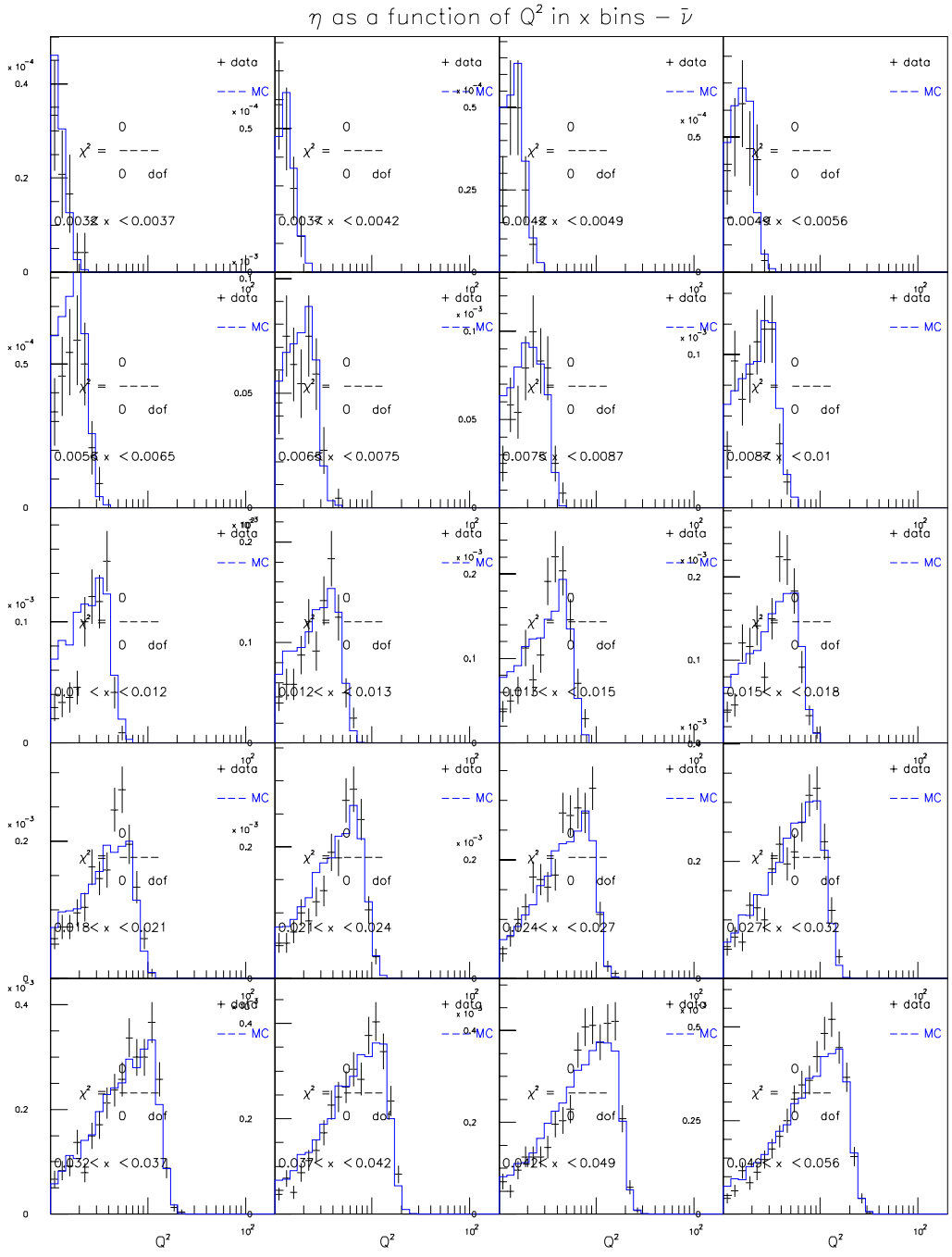

Figure E.19: GRV98NLO for $201 < E_\nu < 400$ GeV ($\overline{\nu}$ mode)

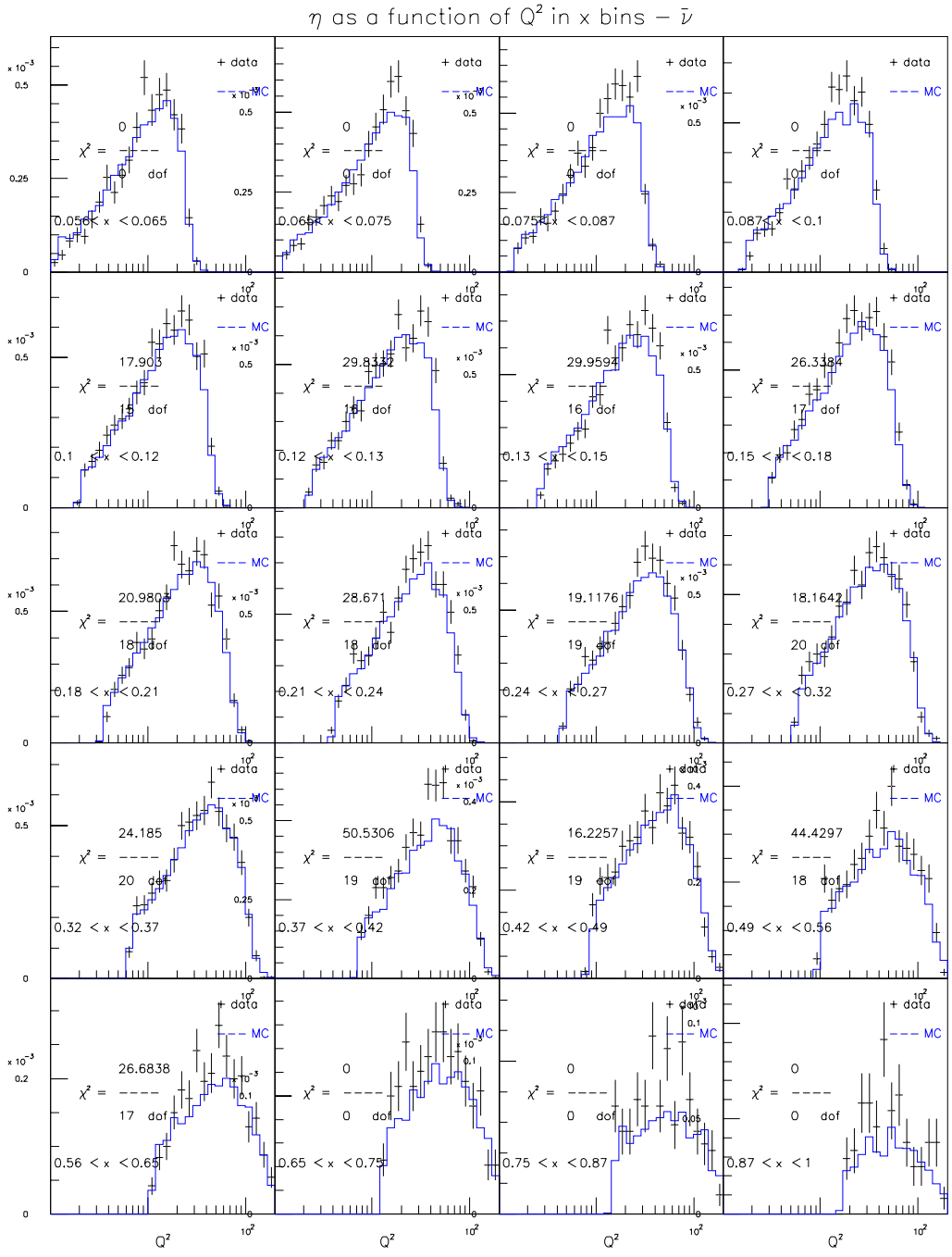

Figure E.20: GRV98NLO for $201 < E_\nu < 400$ GeV ($\overline{\nu}$ mode)

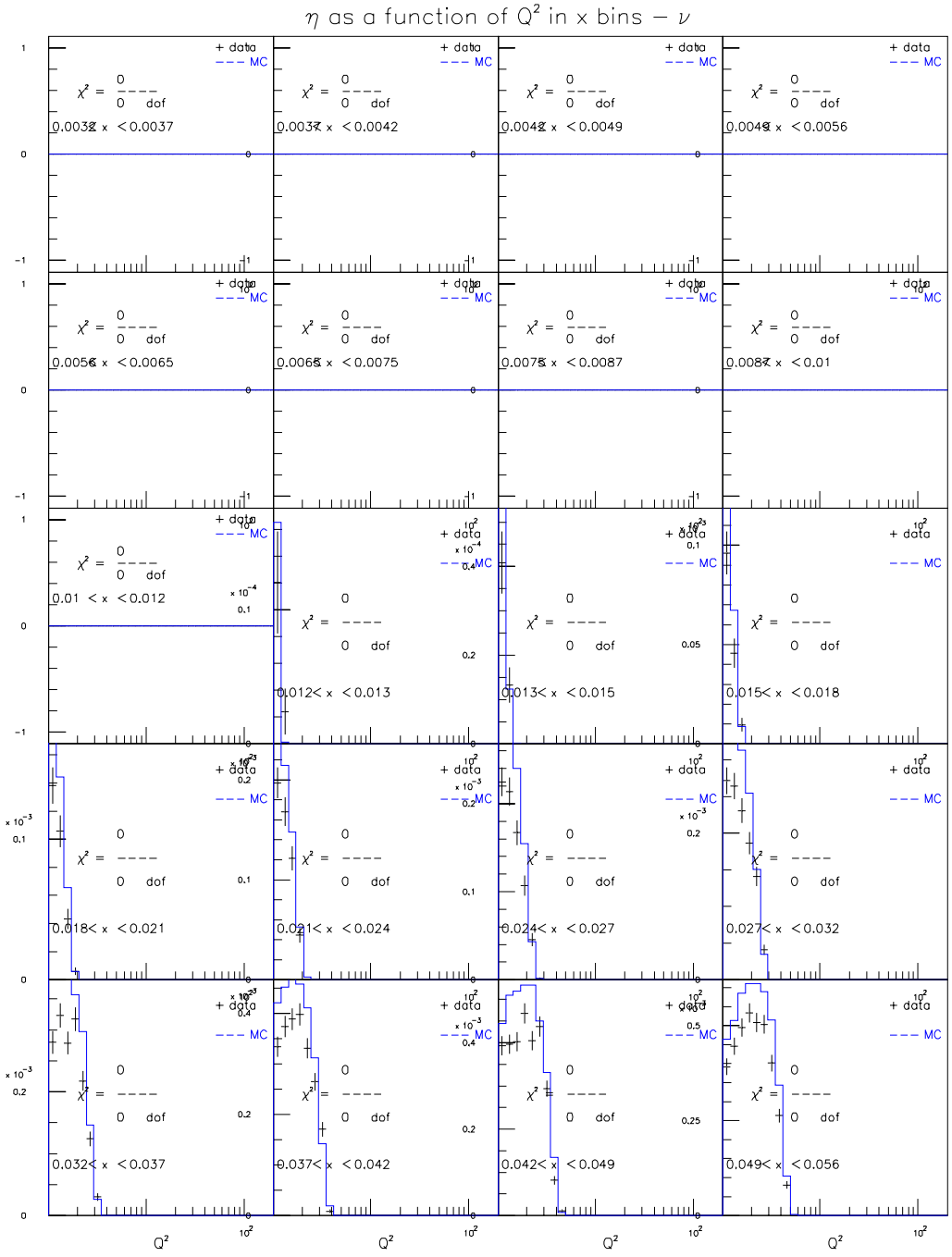

Figure E.21: CTEQ5NLO for $20 < E_\nu < 62$ GeV (ν mode)

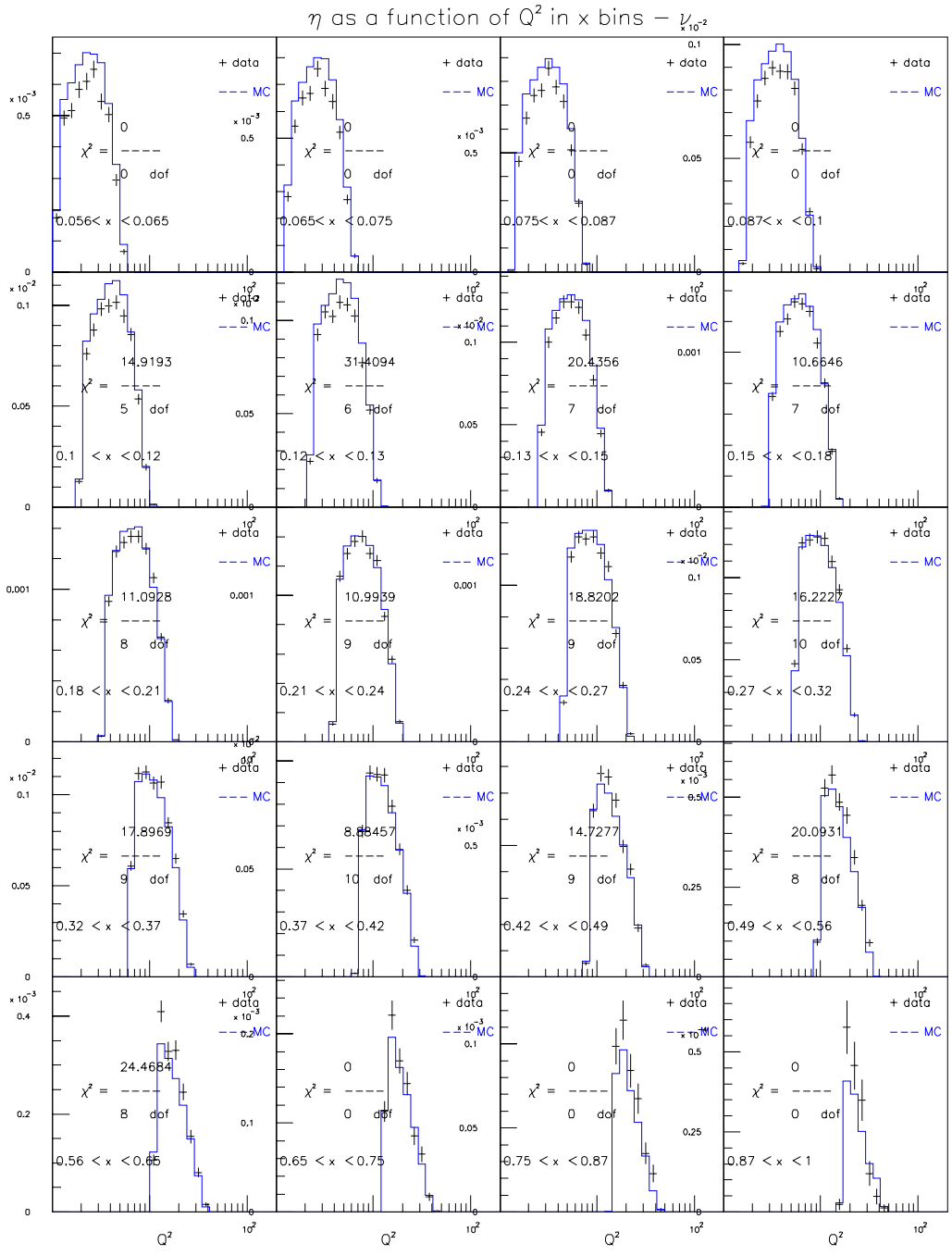

Figure E.22: CTEQ5NLO for $20 < E_\nu < 62$ GeV (ν mode)

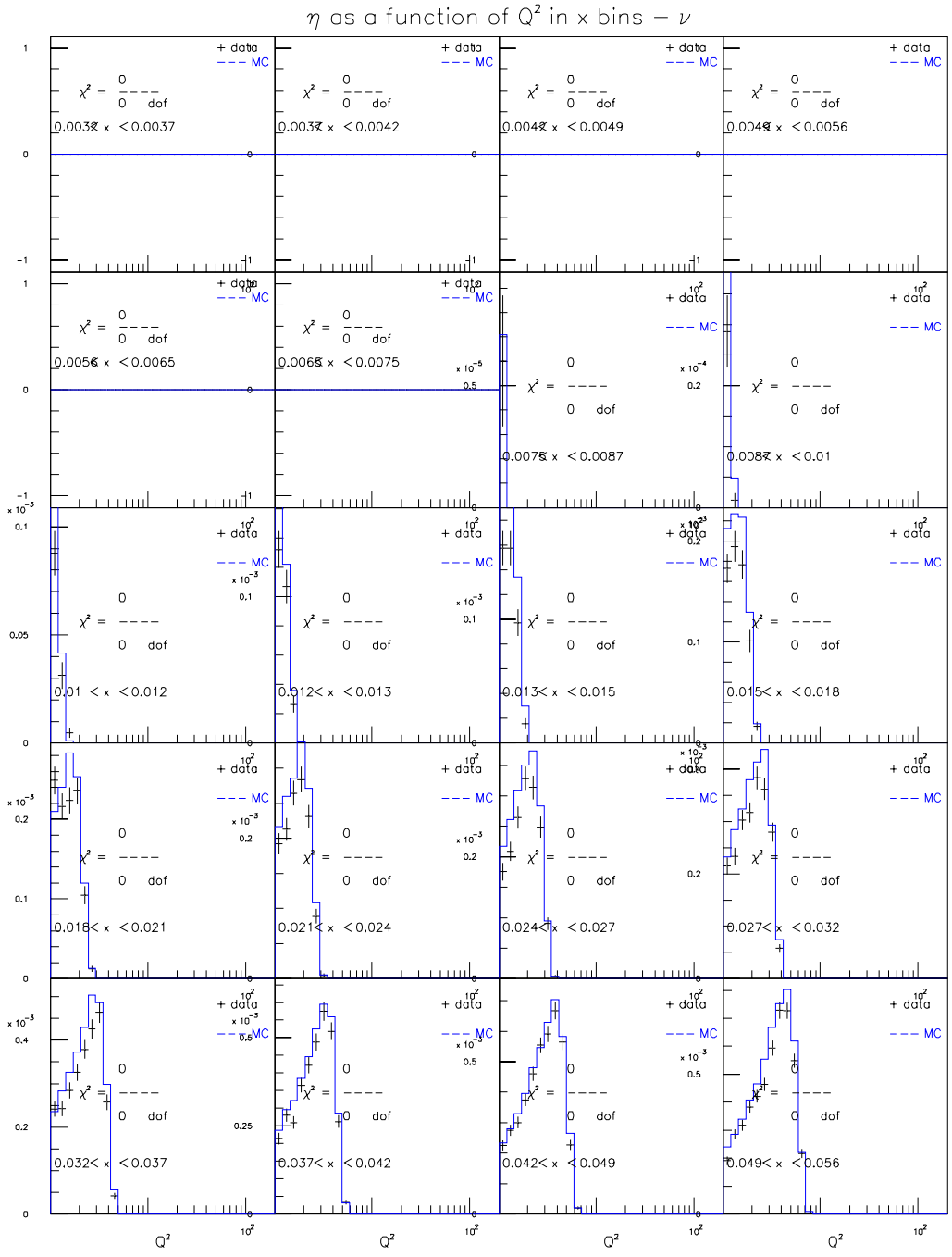

Figure E.23: CTEQ5NLO for $62 < E_\nu < 85$ GeV (ν mode)

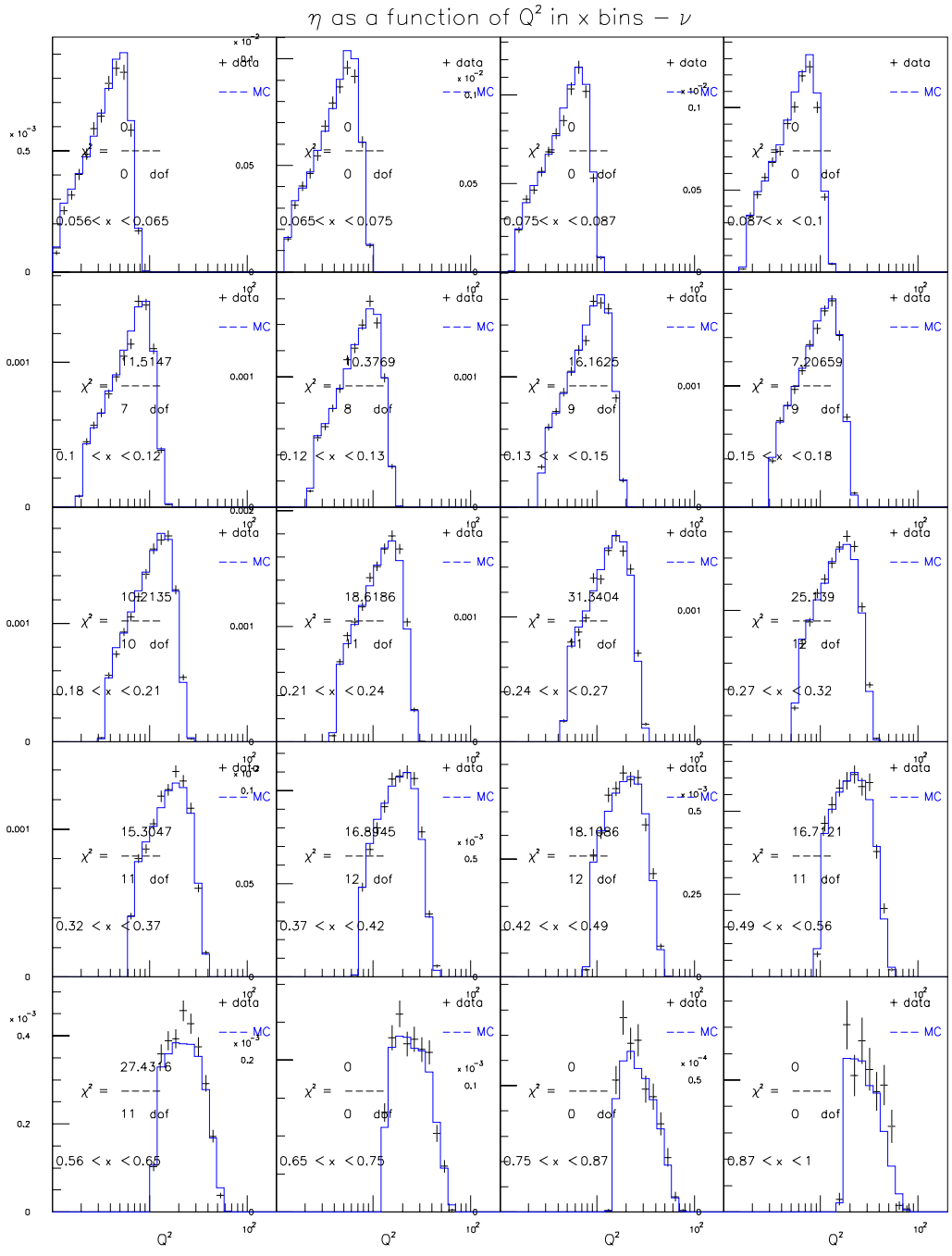

Figure E.24: CTEQ5NLO for $62 < E_\nu < 85$ GeV (ν mode)

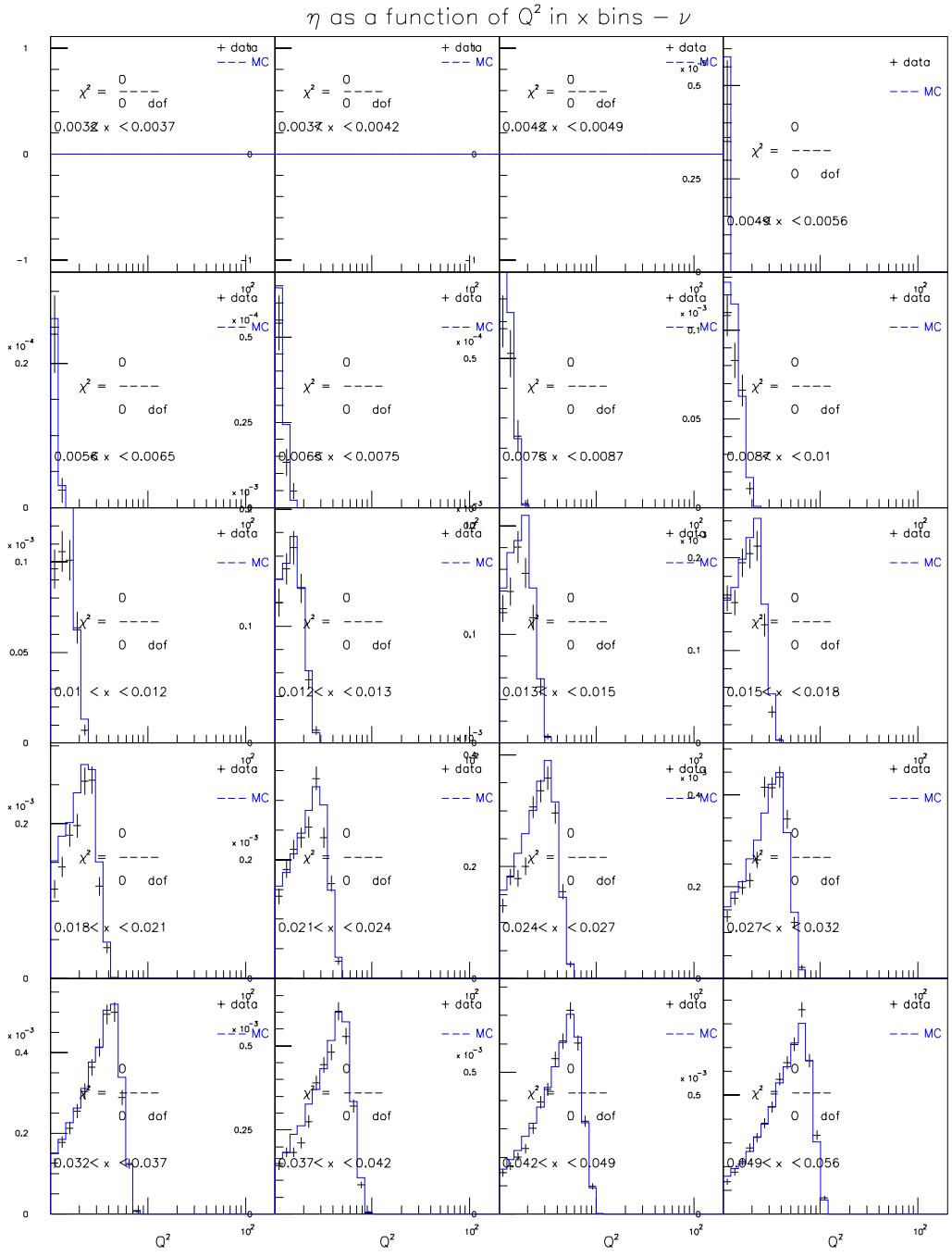

Figure E.25: CTEQ5NLO for $85 < E_\nu < 129$ GeV (ν mode)

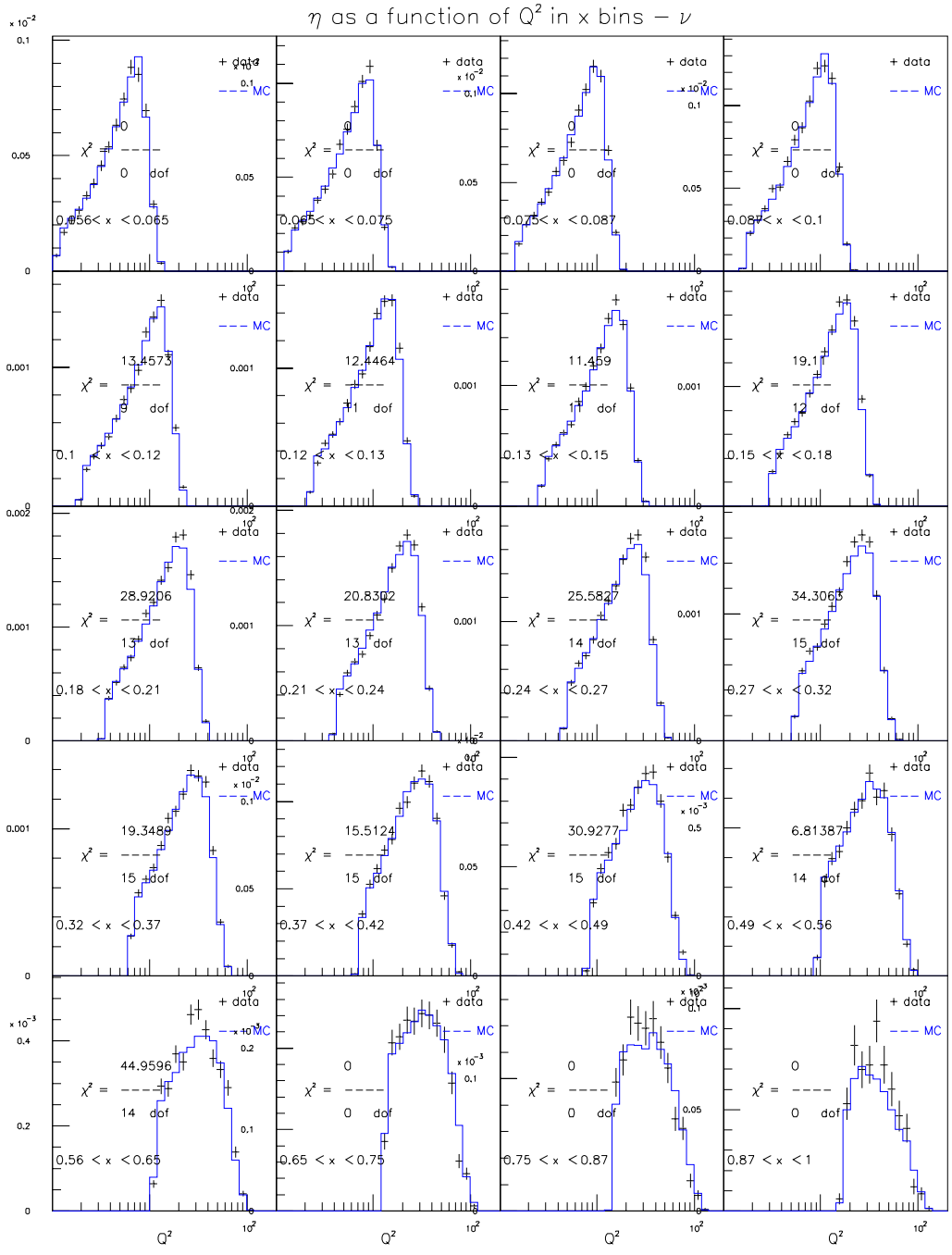

Figure E.26: CTEQ5NLO for $85 < E_\nu < 129$ GeV (ν mode)

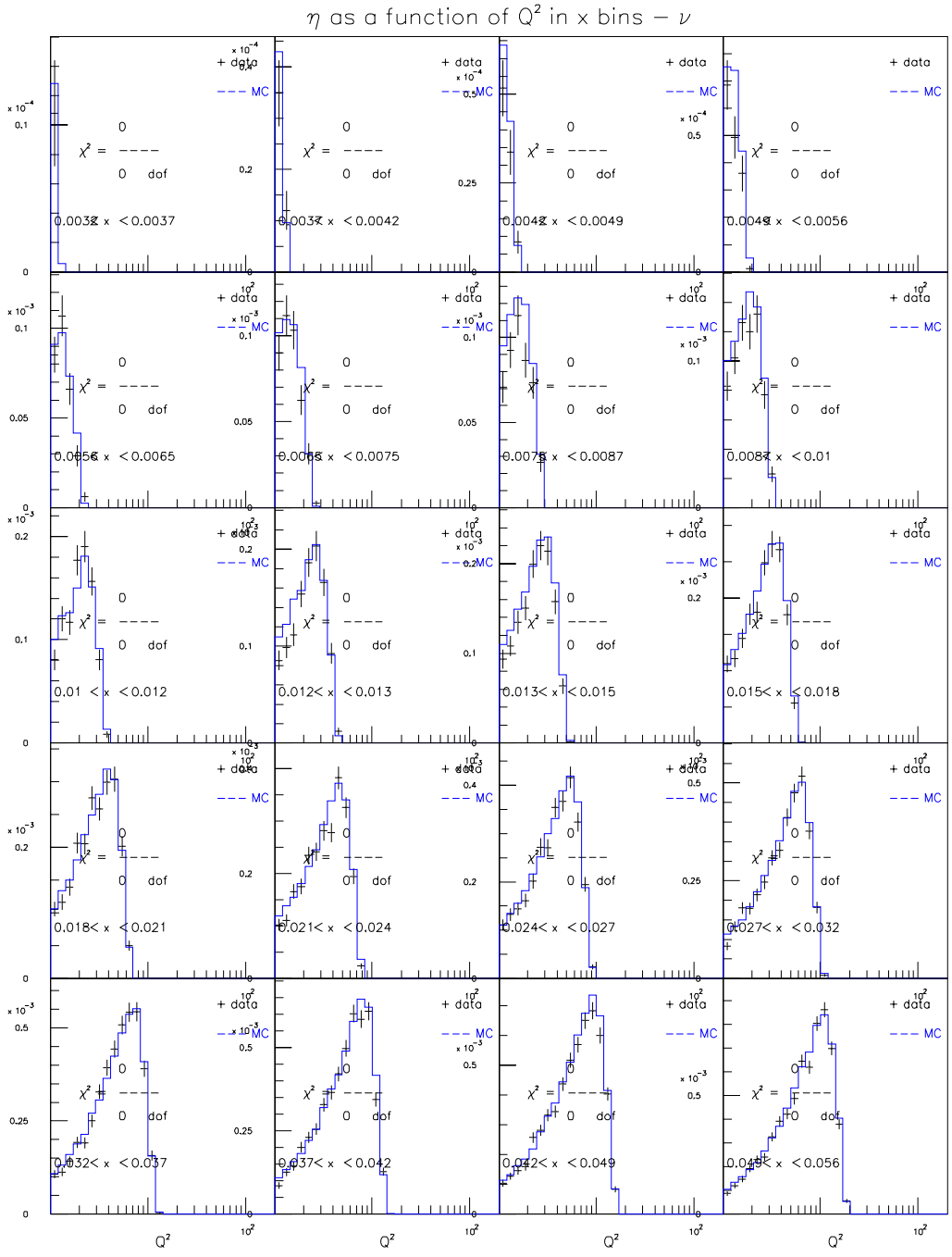

Figure E.27: CTEQ5NLO for $129 < E_\nu < 201$ GeV (ν mode)

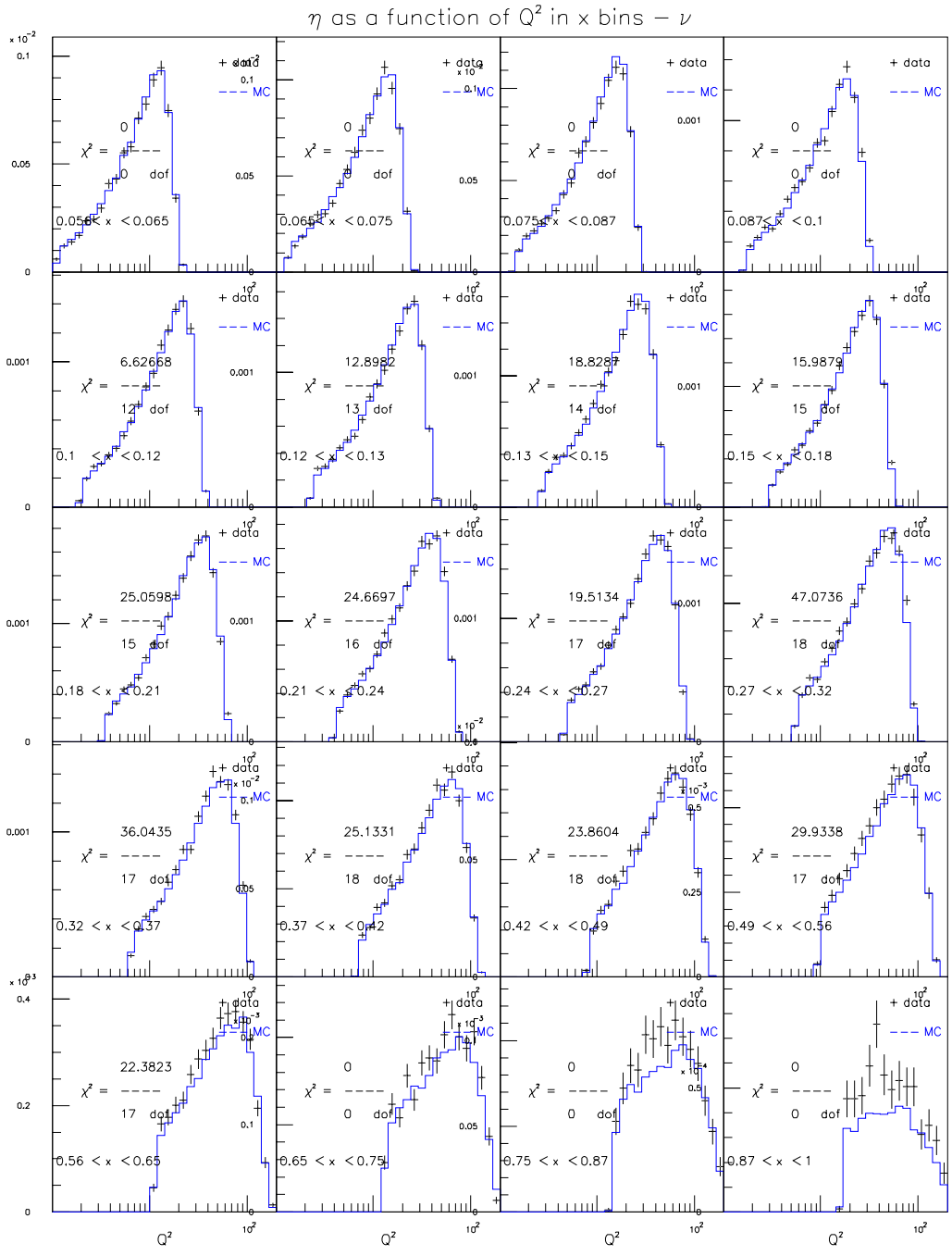

Figure E.28: CTEQ5NLO for $129 < E_\nu < 201$ GeV (ν mode)

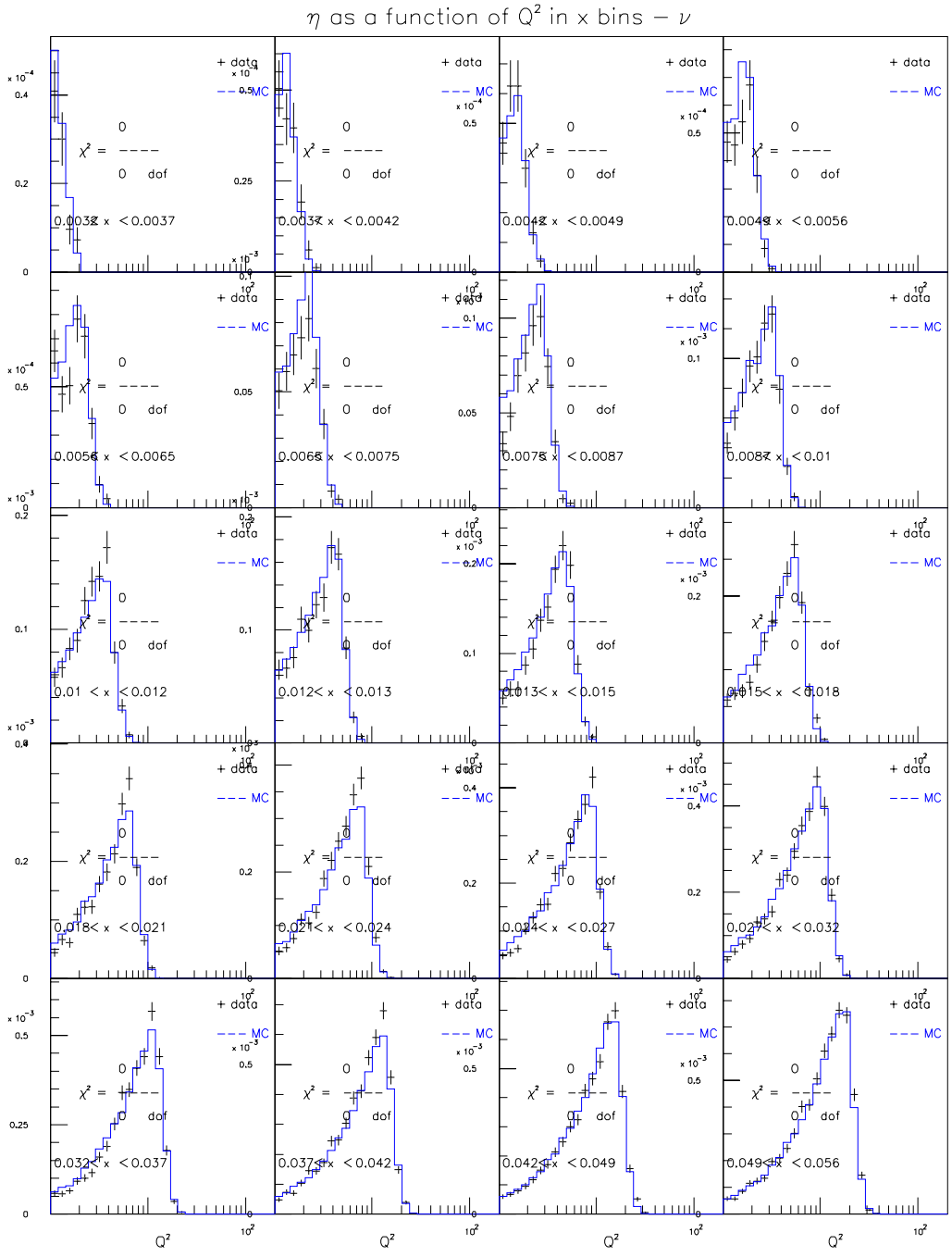

Figure E.29: CTEQ5NLO for $201 < E_\nu < 400$ GeV (ν mode)

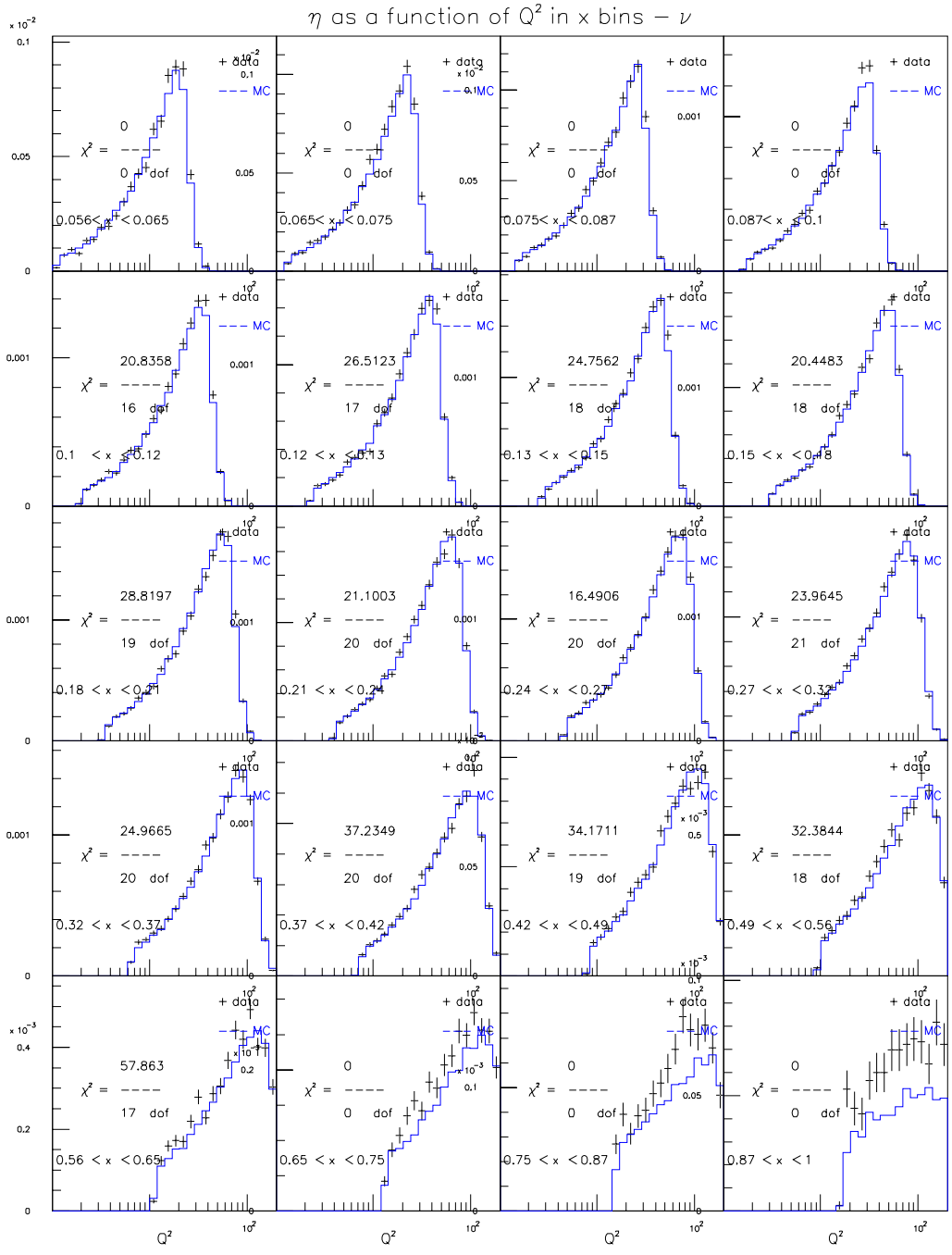

Figure E.30: CTEQ5NLO for $201 < E_\nu < 400$ GeV (ν mode)

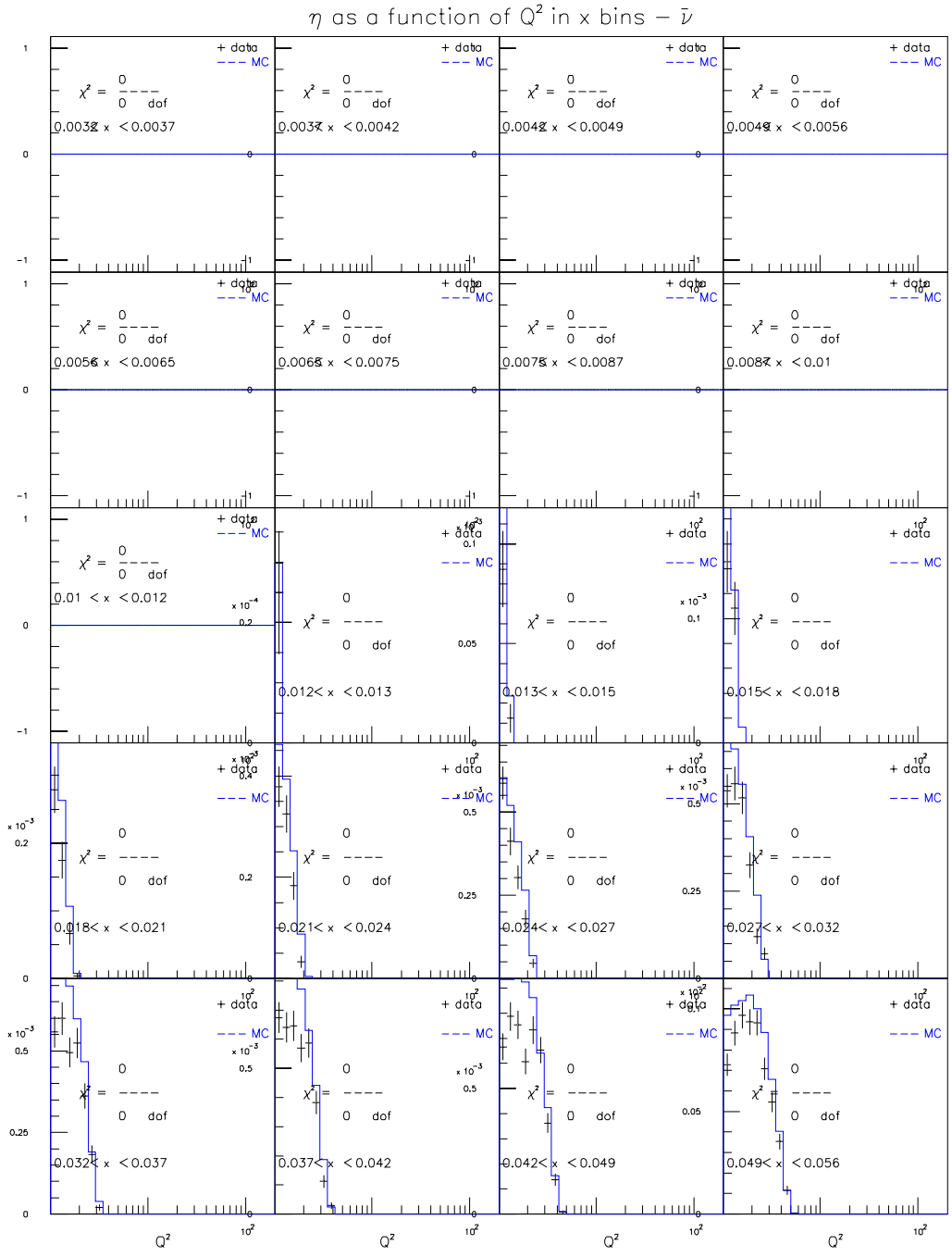

Figure E.31: CTEQ5NLO for $20 < E_\nu < 62$ GeV ($\overline{\nu}$ mode)

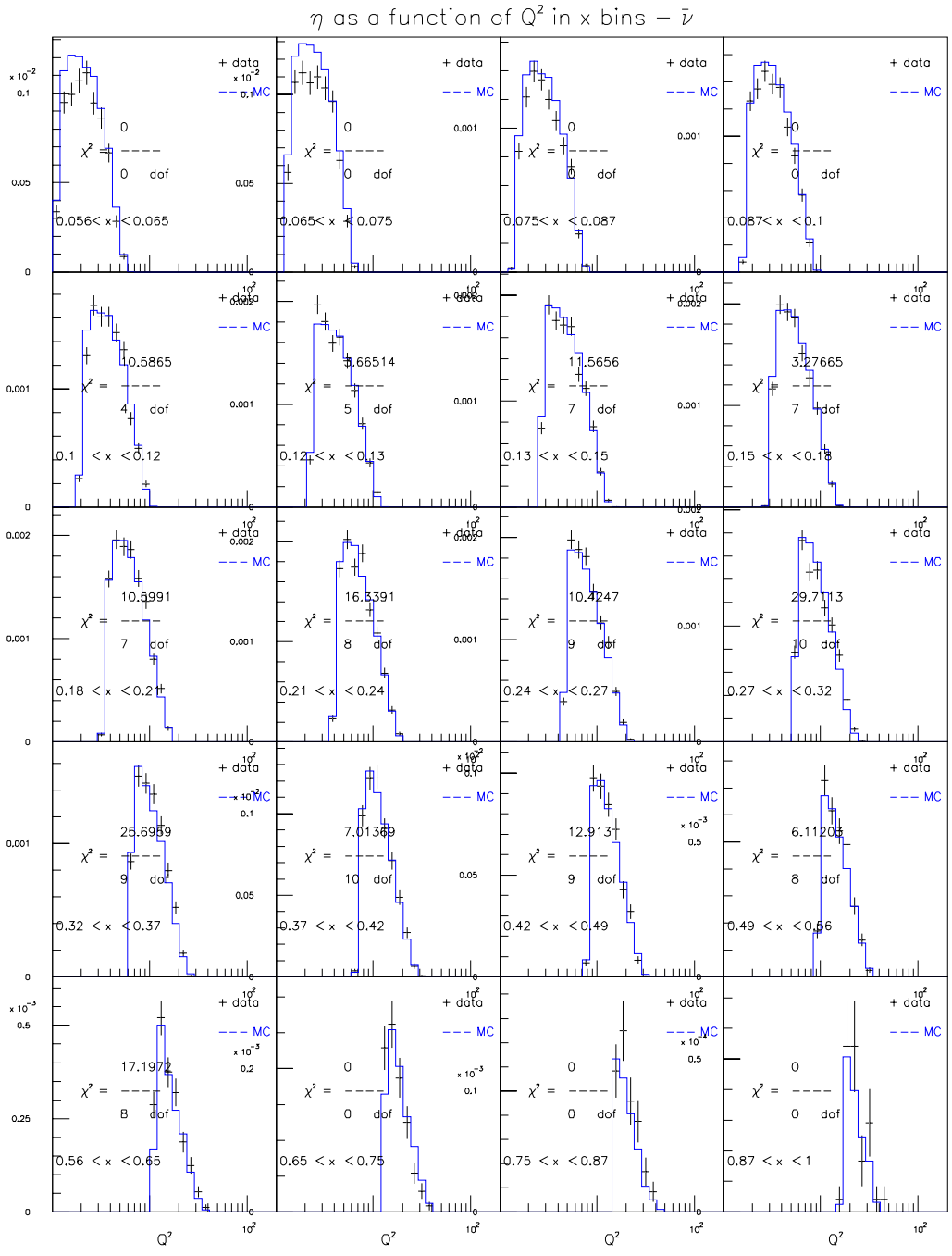

Figure E.32: CTEQ5NLO for $20 < E_\nu < 62$ GeV ($\overline{\nu}$ mode)

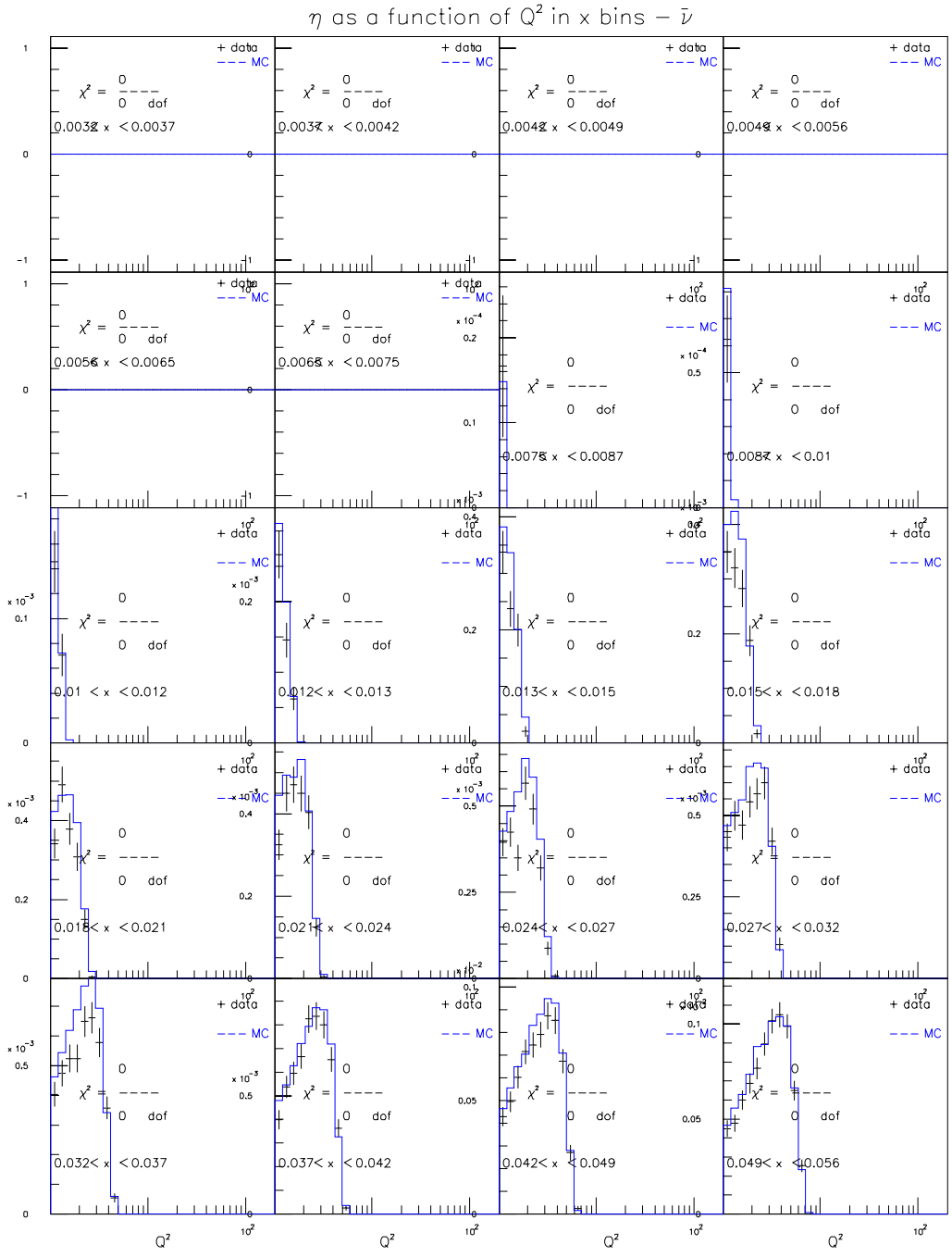

Figure E.33: CTEQ5NLO for $62 < E_\nu < 85$ GeV ($\overline{\nu}$ mode)

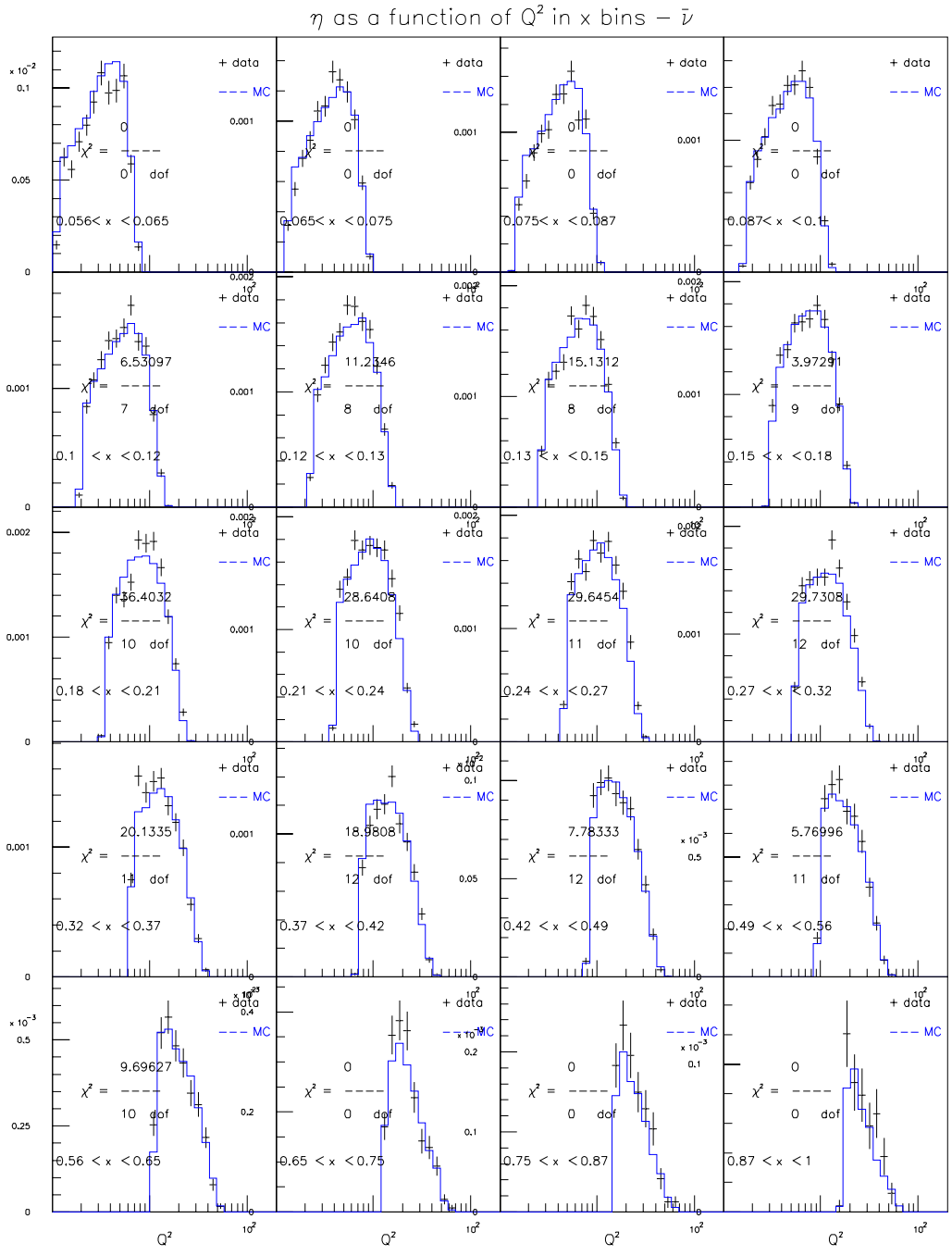

Figure E.34: CTEQ5NLO for $62 < E_\nu < 85$ GeV ($\overline{\nu}$ mode)

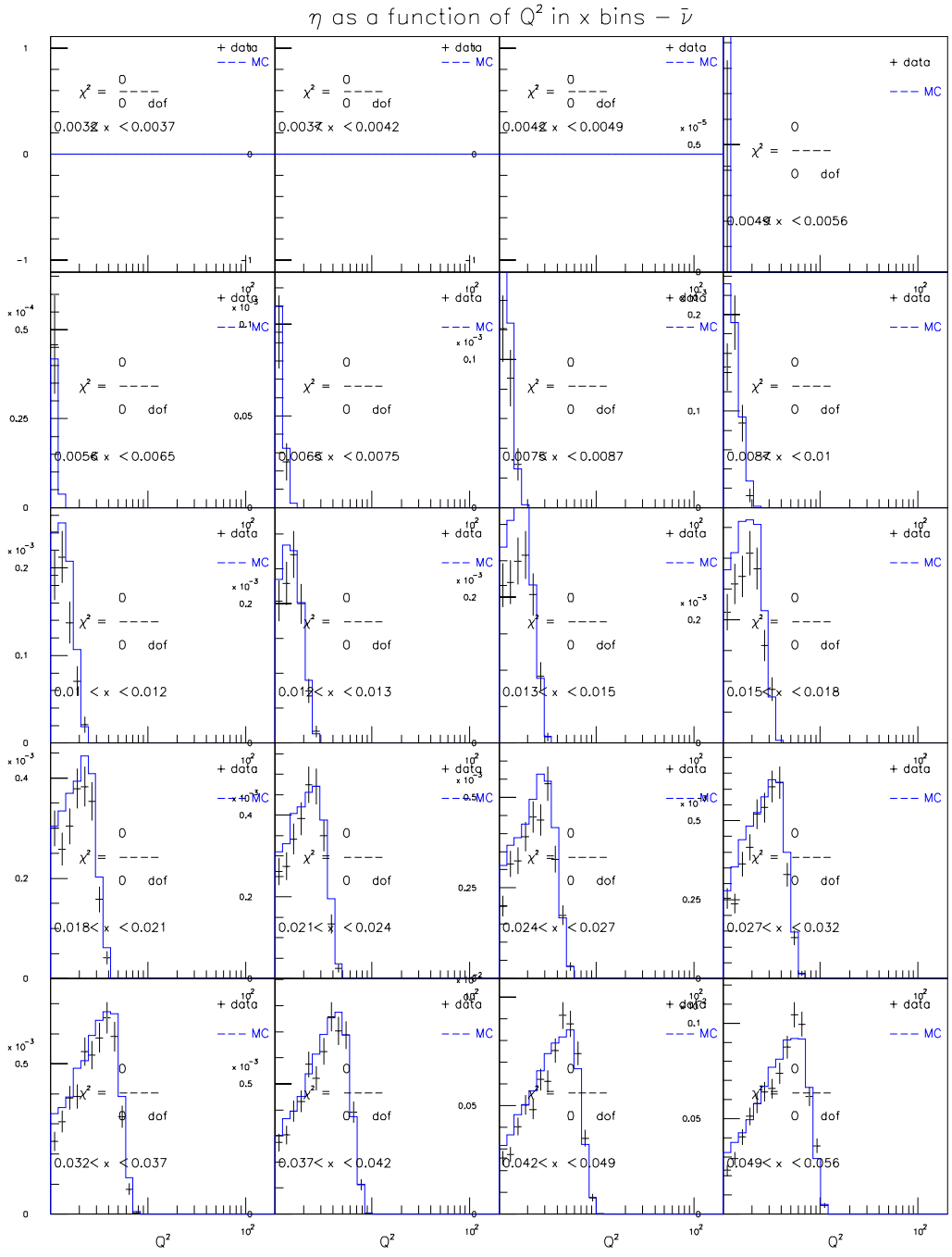

Figure E.35: CTEQ5NLO for $85 < E_\nu < 129$ GeV ($\overline{\nu}$ mode)

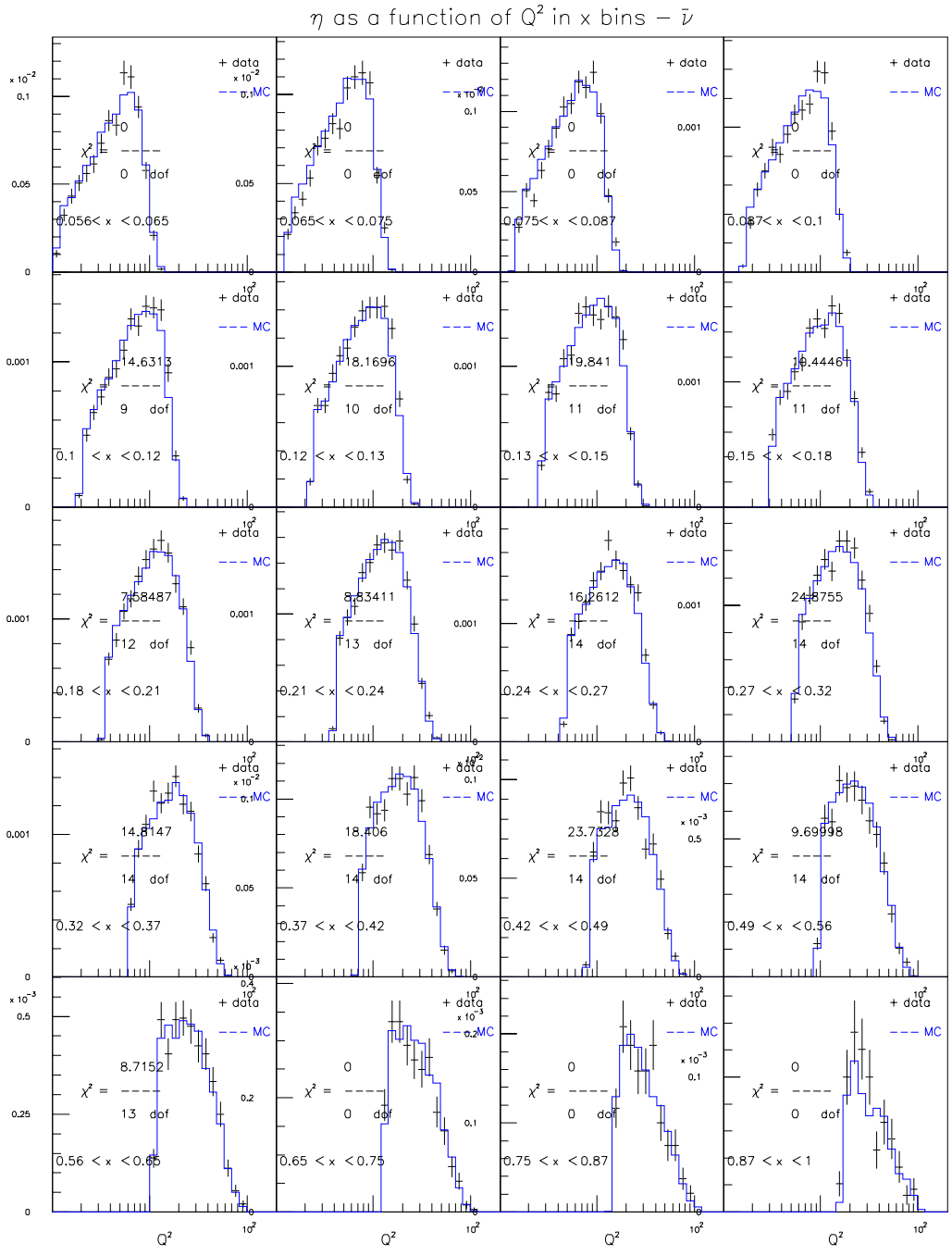

Figure E.36: CTEQ5NLO for $85 < E_\nu < 129$ GeV ($\overline{\nu}$ mode)

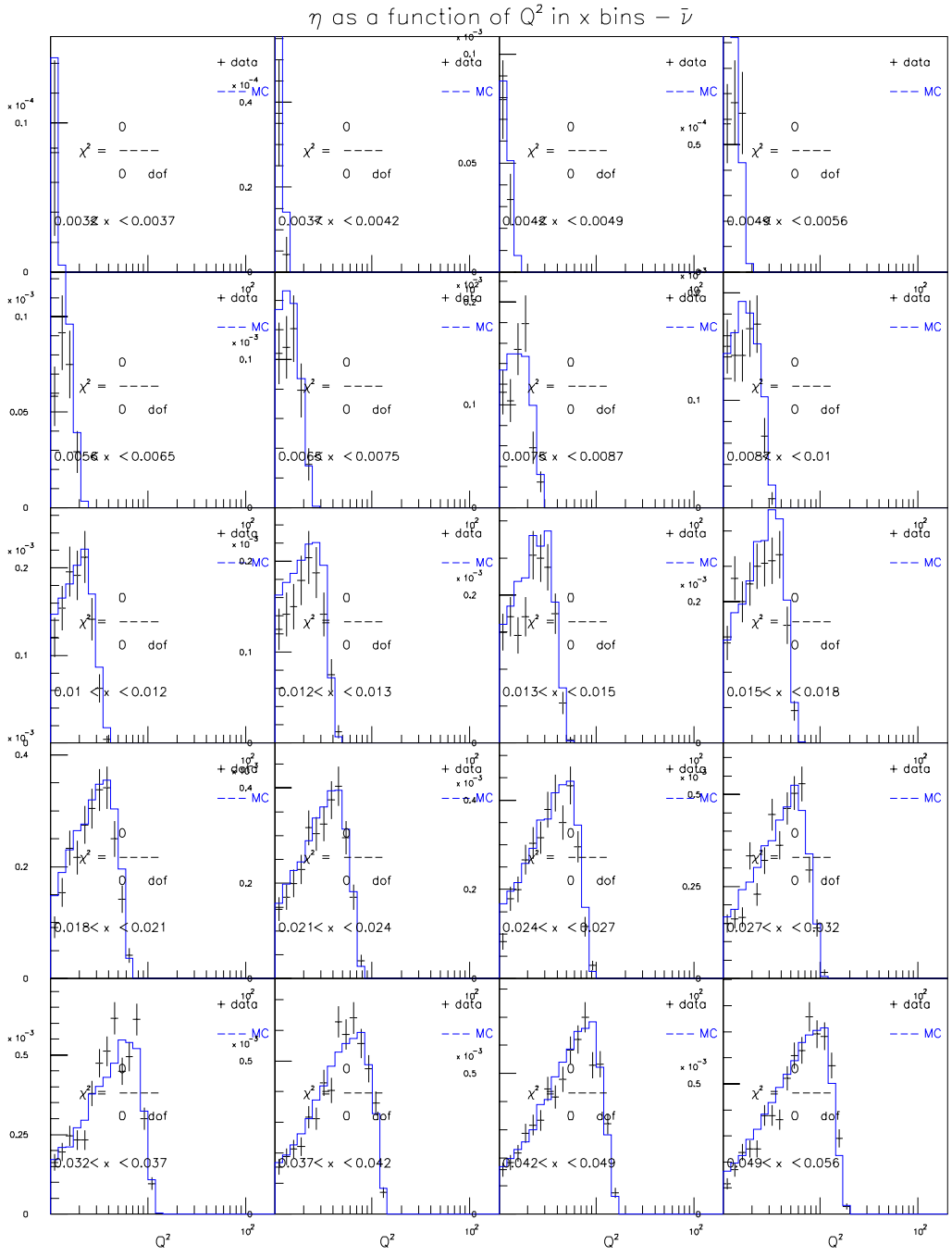

Figure E.37: CTEQ5NLO for $129 < E_\nu < 201$ GeV ($\overline{\nu}$ mode)

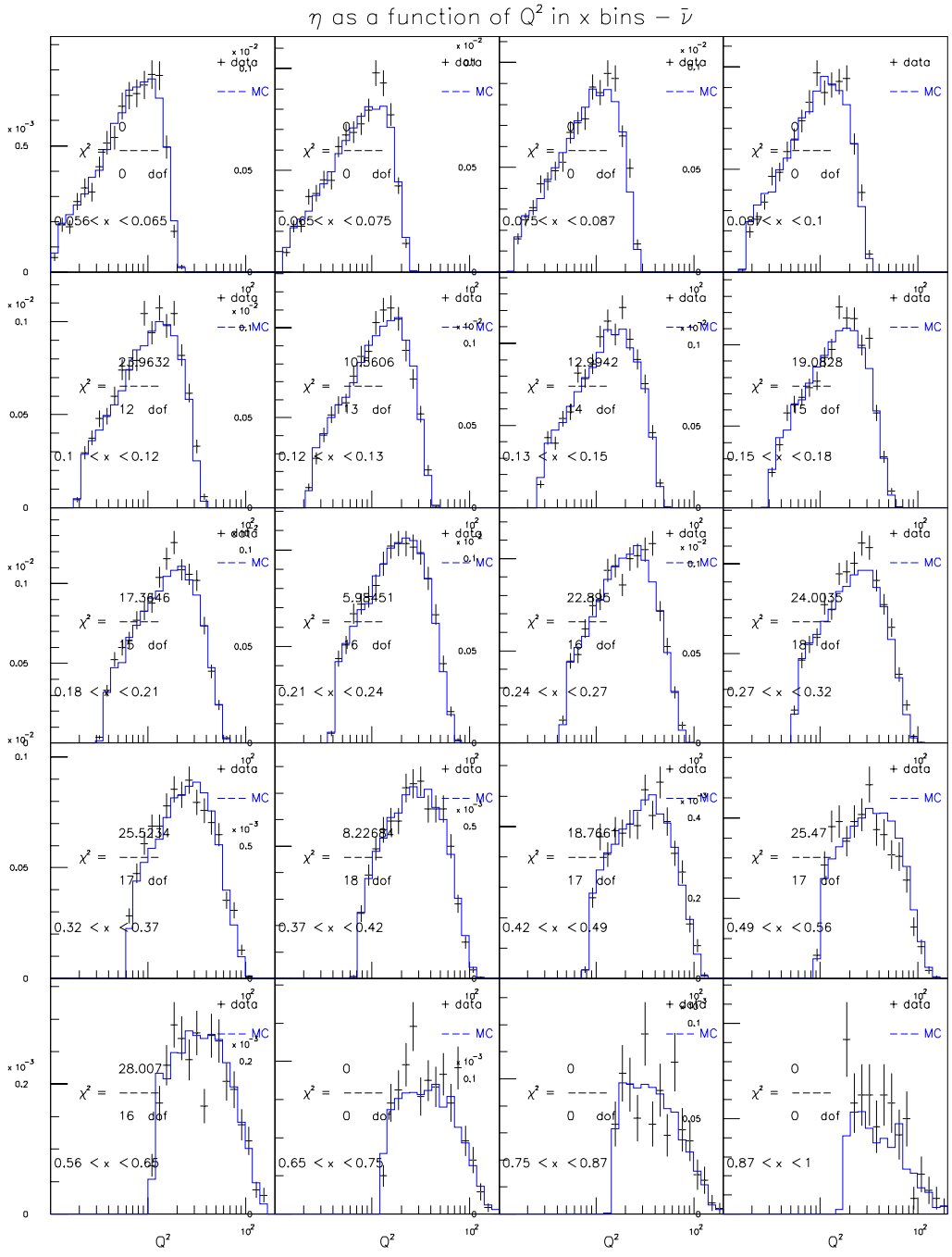

Figure E.38: CTEQ5NLO for $129 < E_\nu < 201$ GeV ($\overline{\nu}$ mode)

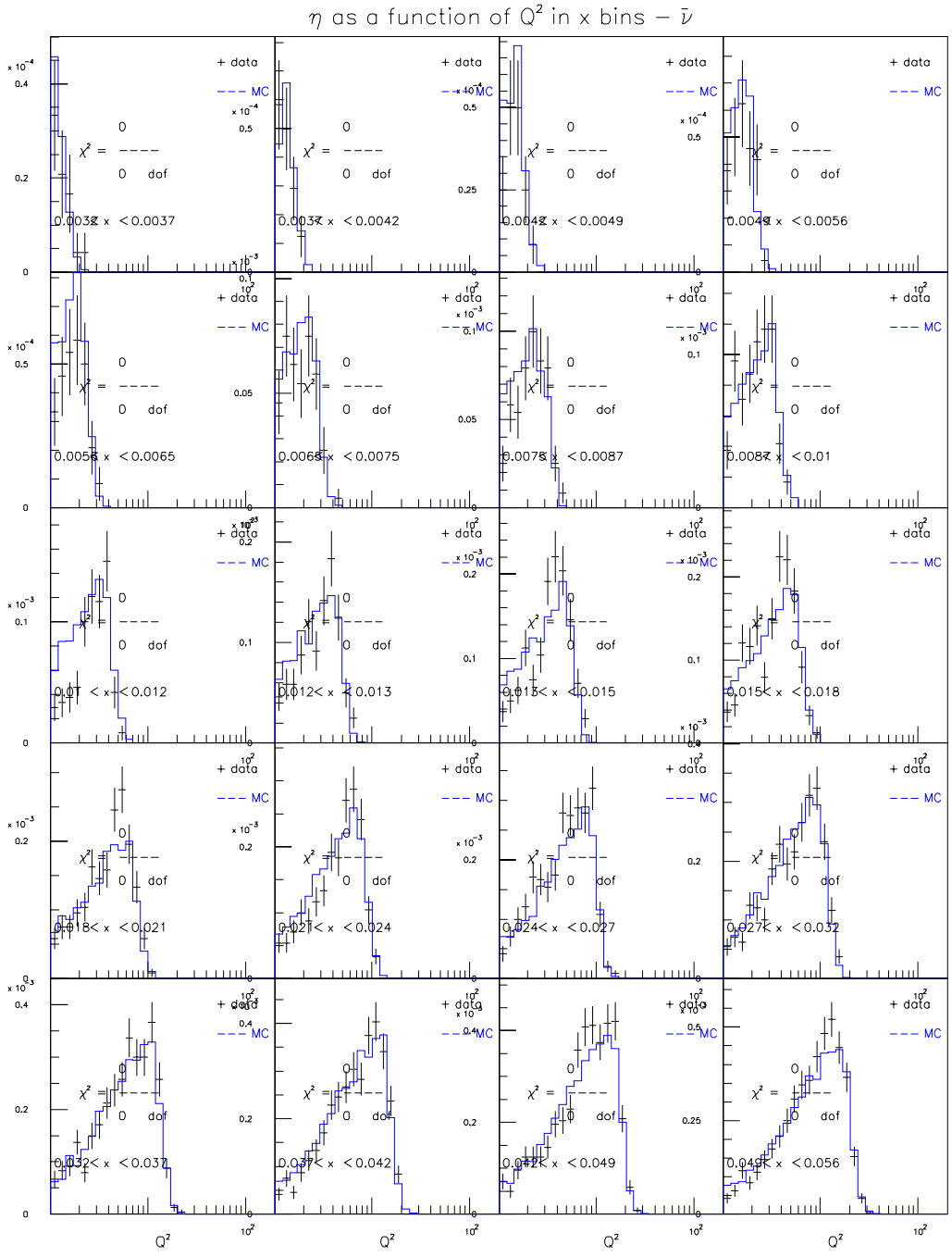

Figure E.39: CTEQ5NLO for $201 < E_\nu < 400$ GeV ($\overline{\nu}$ mode)

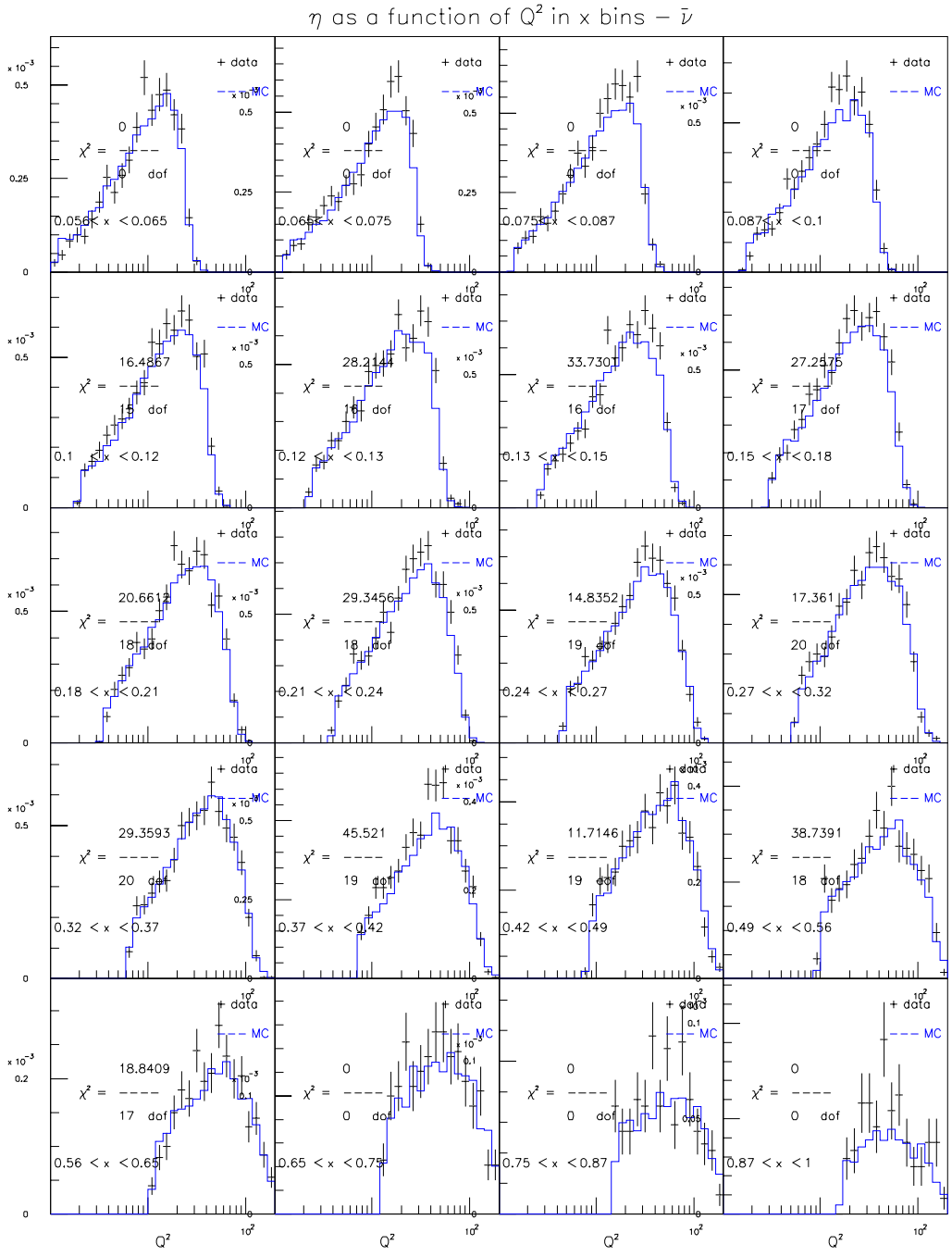

Figure E.40: CTEQ5NLO for $201 < E_\nu < 400$ GeV ($\overline{\nu}$ mode)

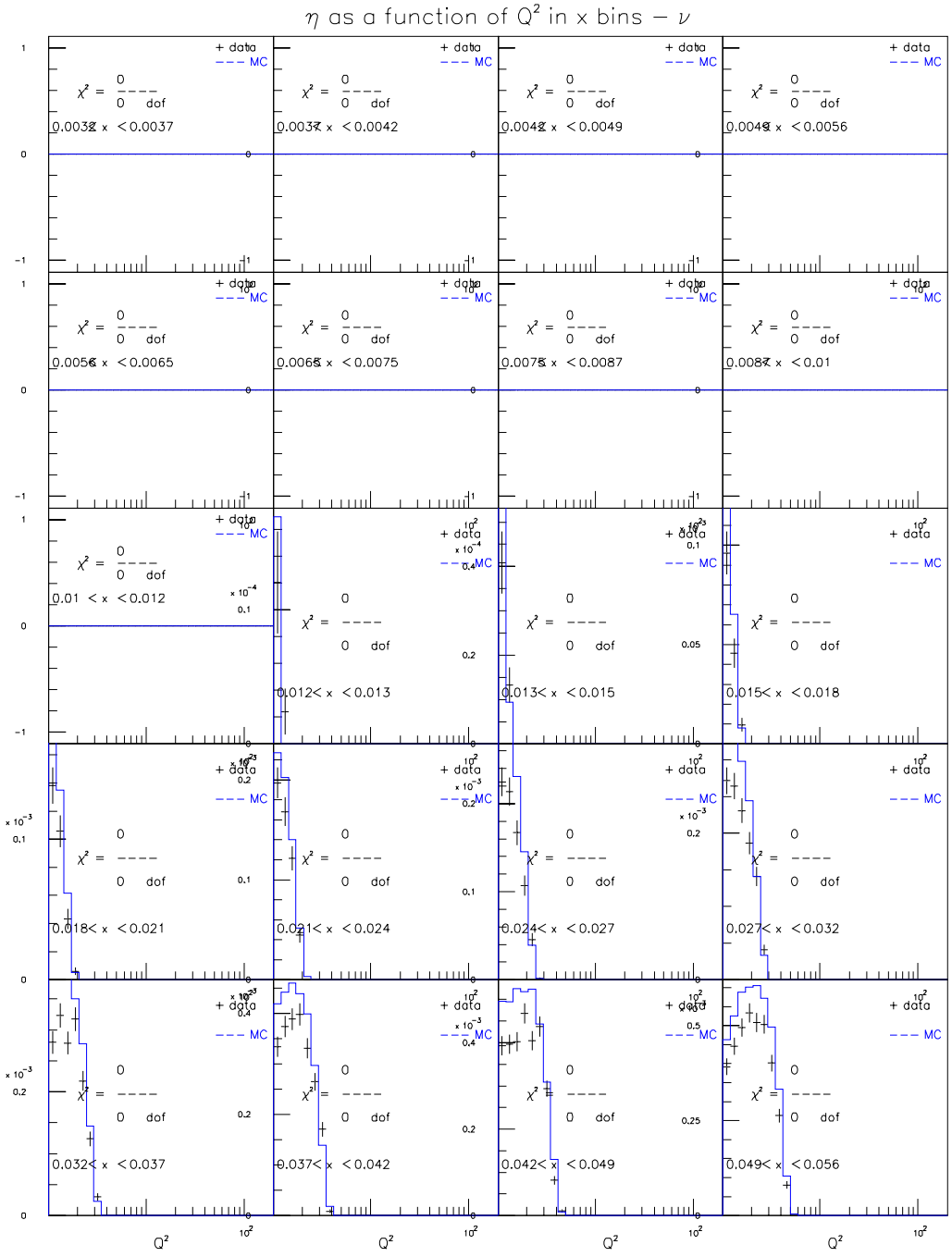

Figure E.41: GRV98NLO+EMC+HT for $20 < E_\nu < 62$ GeV (ν mode)

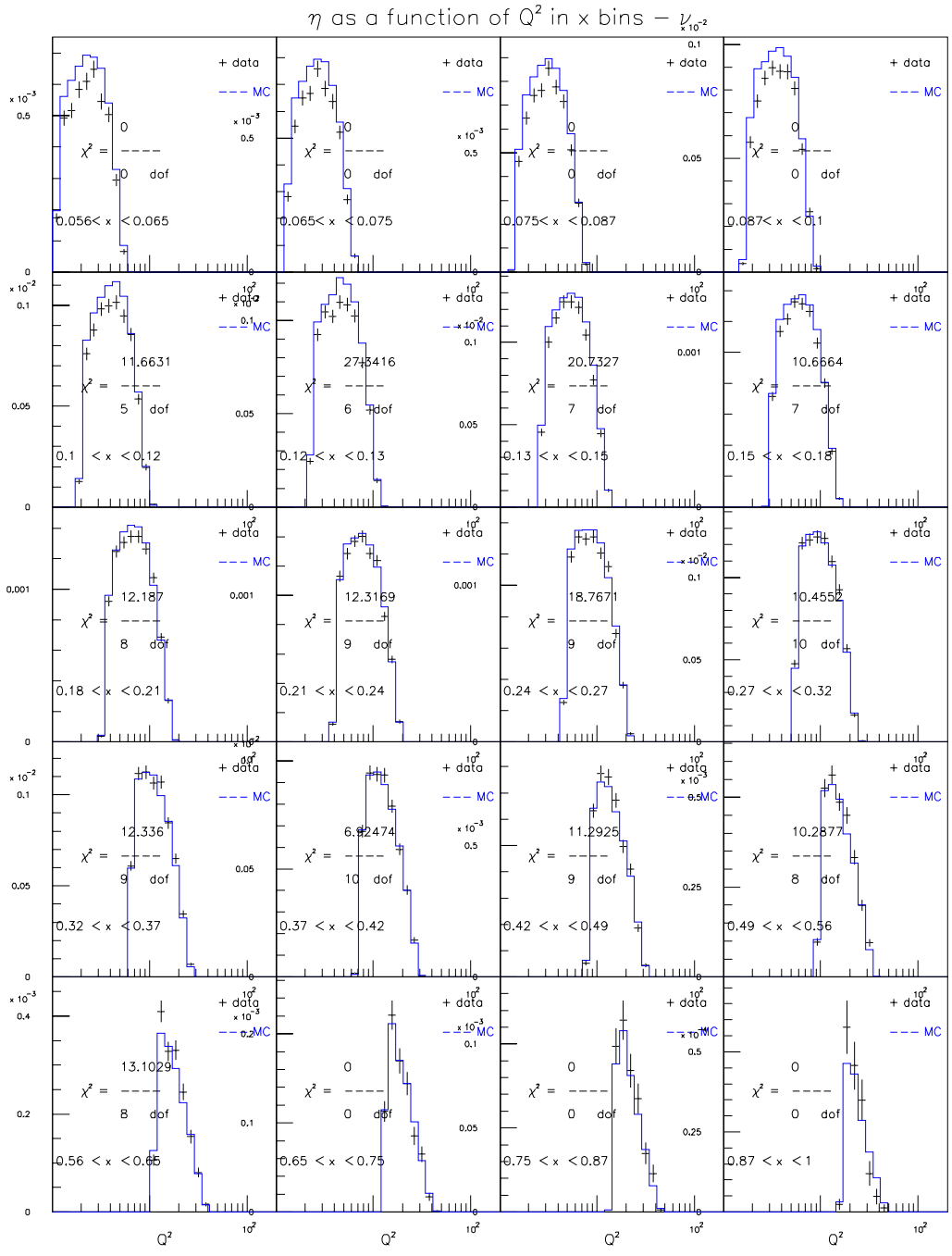

Figure E.42: GRV98NLO+EMC+HT for $20 < E_\nu < 62$ GeV (ν mode)

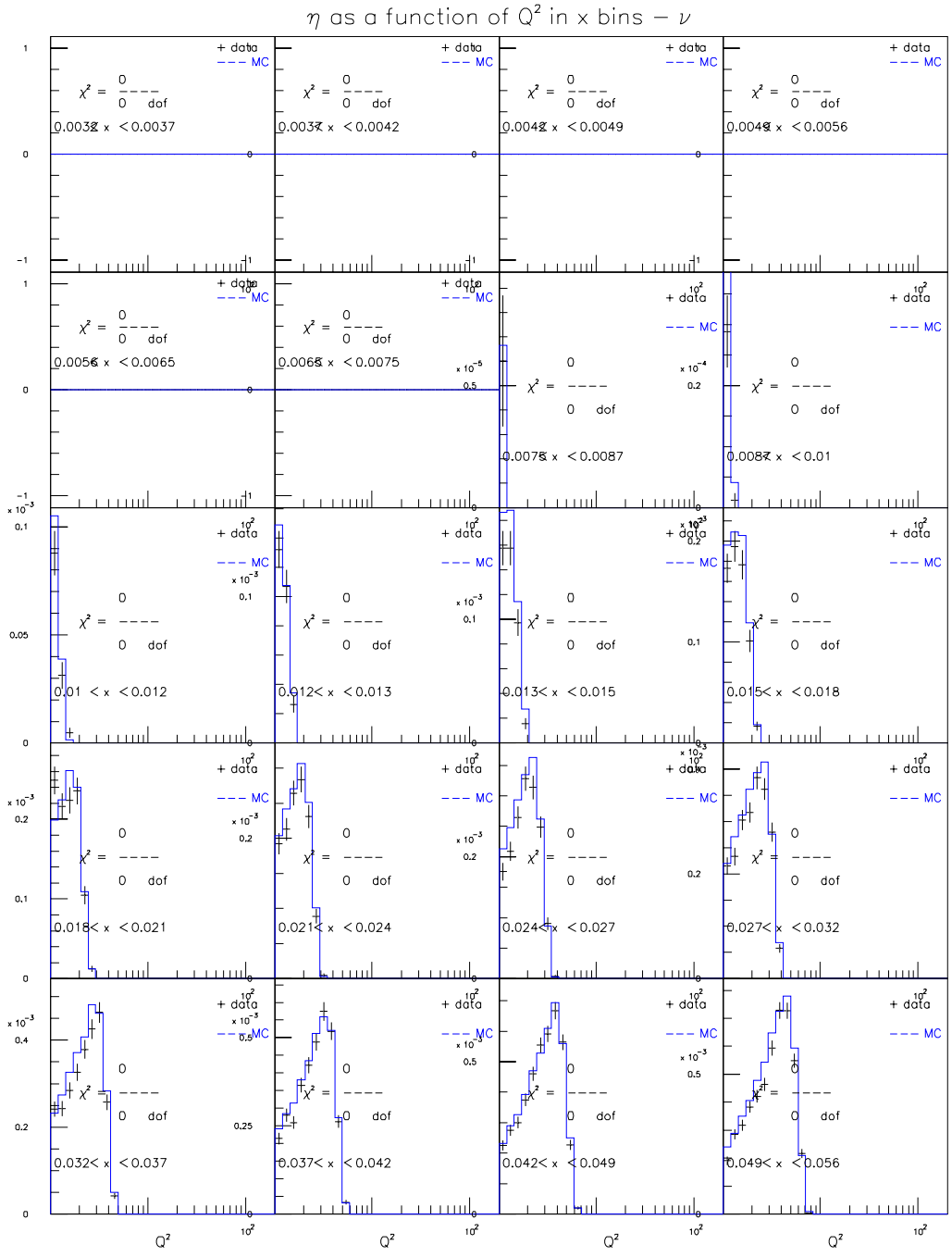

Figure E.43: GRV98NLO+EMC+HT for $62 < E_\nu < 85$ GeV (ν mode)

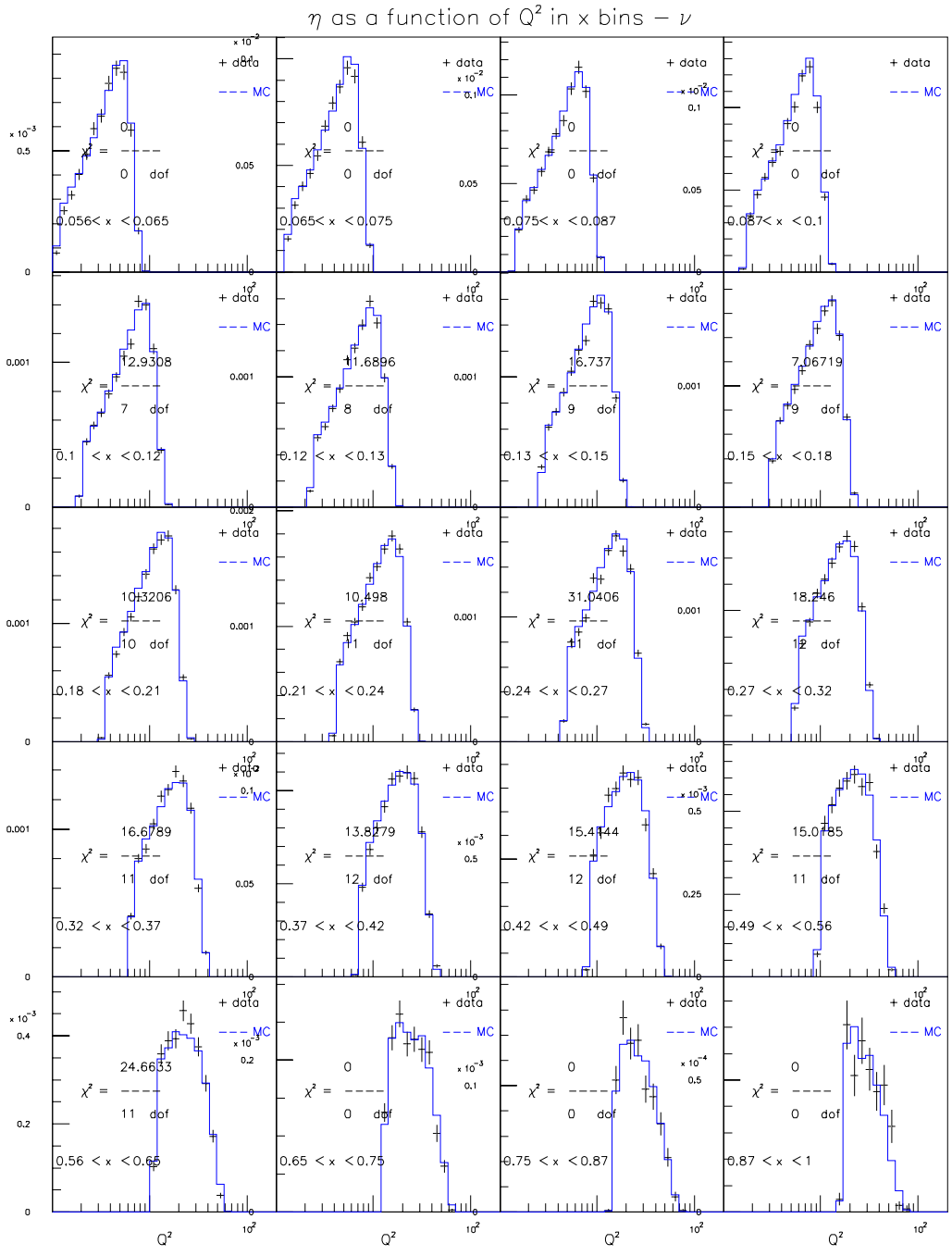

Figure E.44: GRV98NLO+EMC+HT for $62 < E_\nu < 85$ GeV (ν mode)

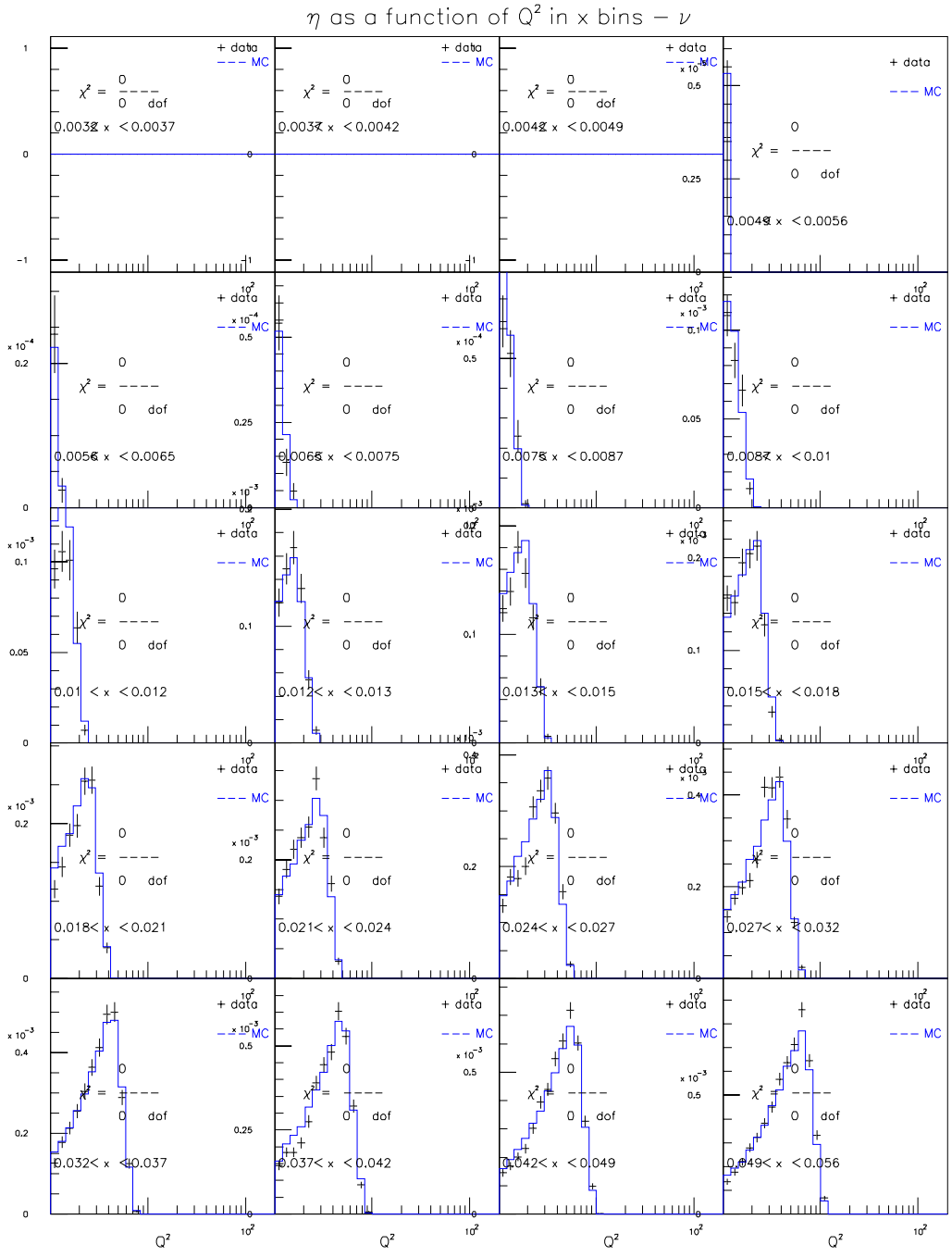

Figure E.45: GRV98NLO+EMC+HT for $85 < E_\nu < 129$ GeV (ν mode)

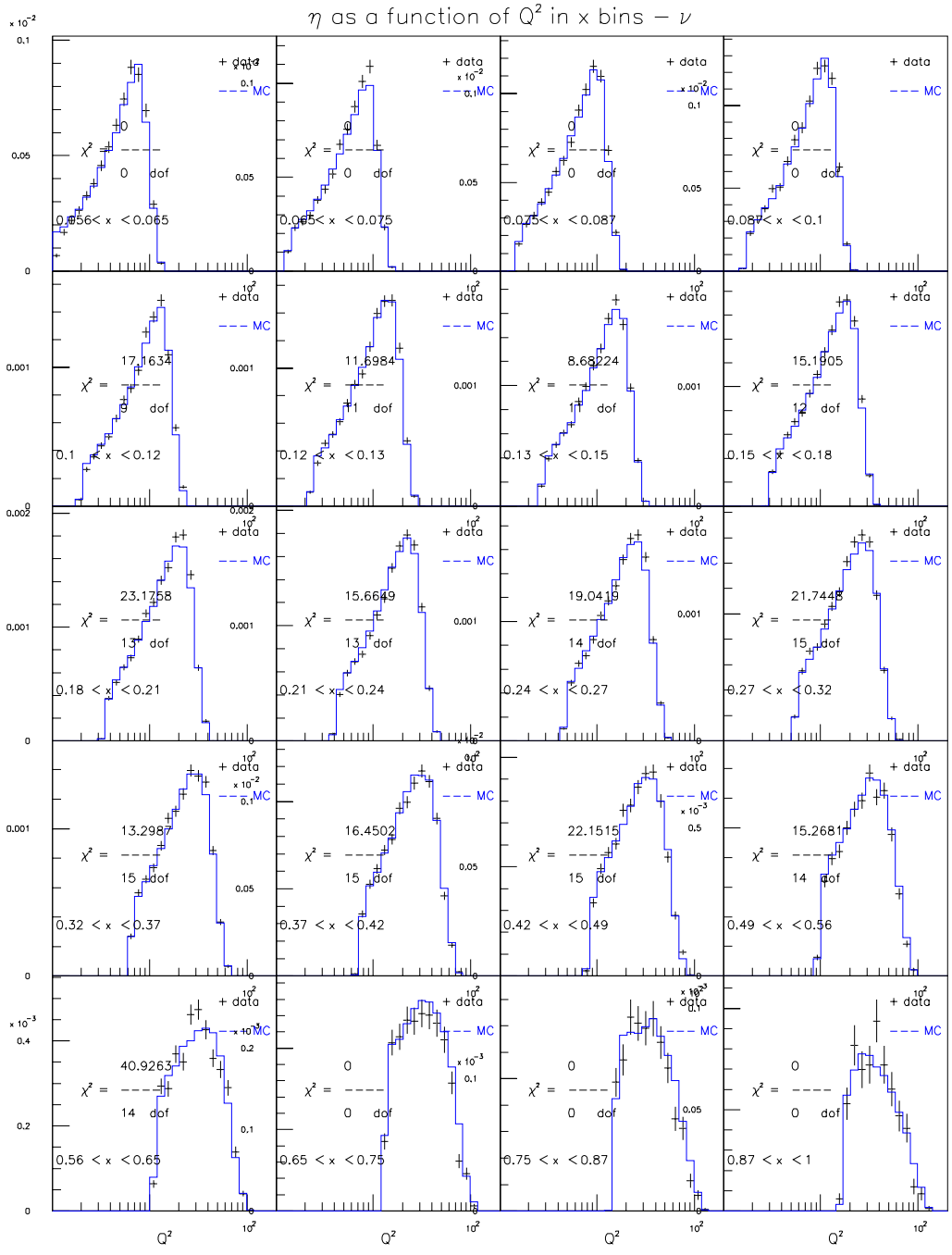

Figure E.46: GRV98NLO+EMC+HT for $85 < E_\nu < 129$ GeV (ν mode)

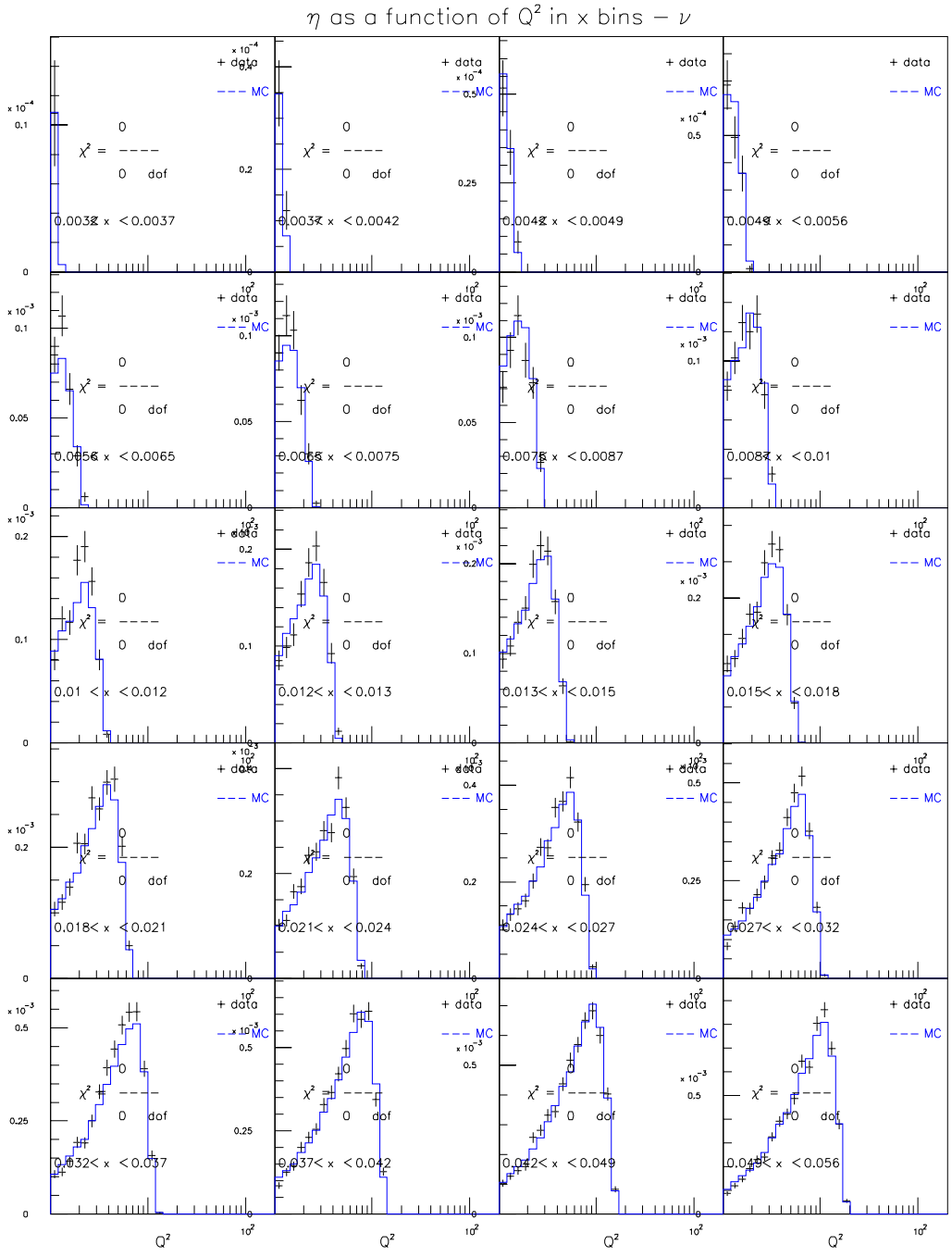

Figure E.47: GRV98NLO+EMC+HT for $129 < E_\nu < 201$ GeV (ν mode)

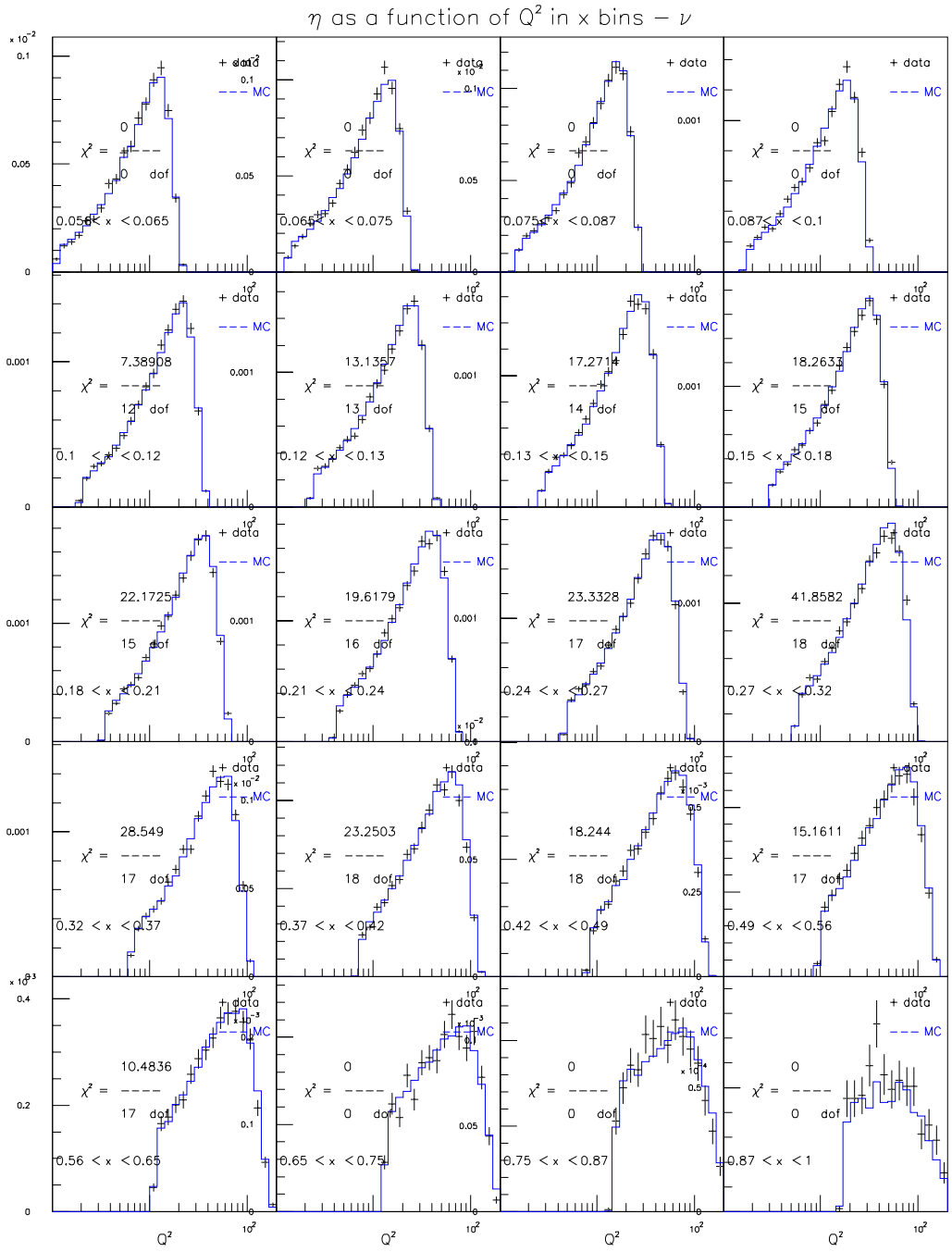

Figure E.48: GRV98NLO+EMC+HT for $129 < E_\nu < 201$ GeV (ν mode)

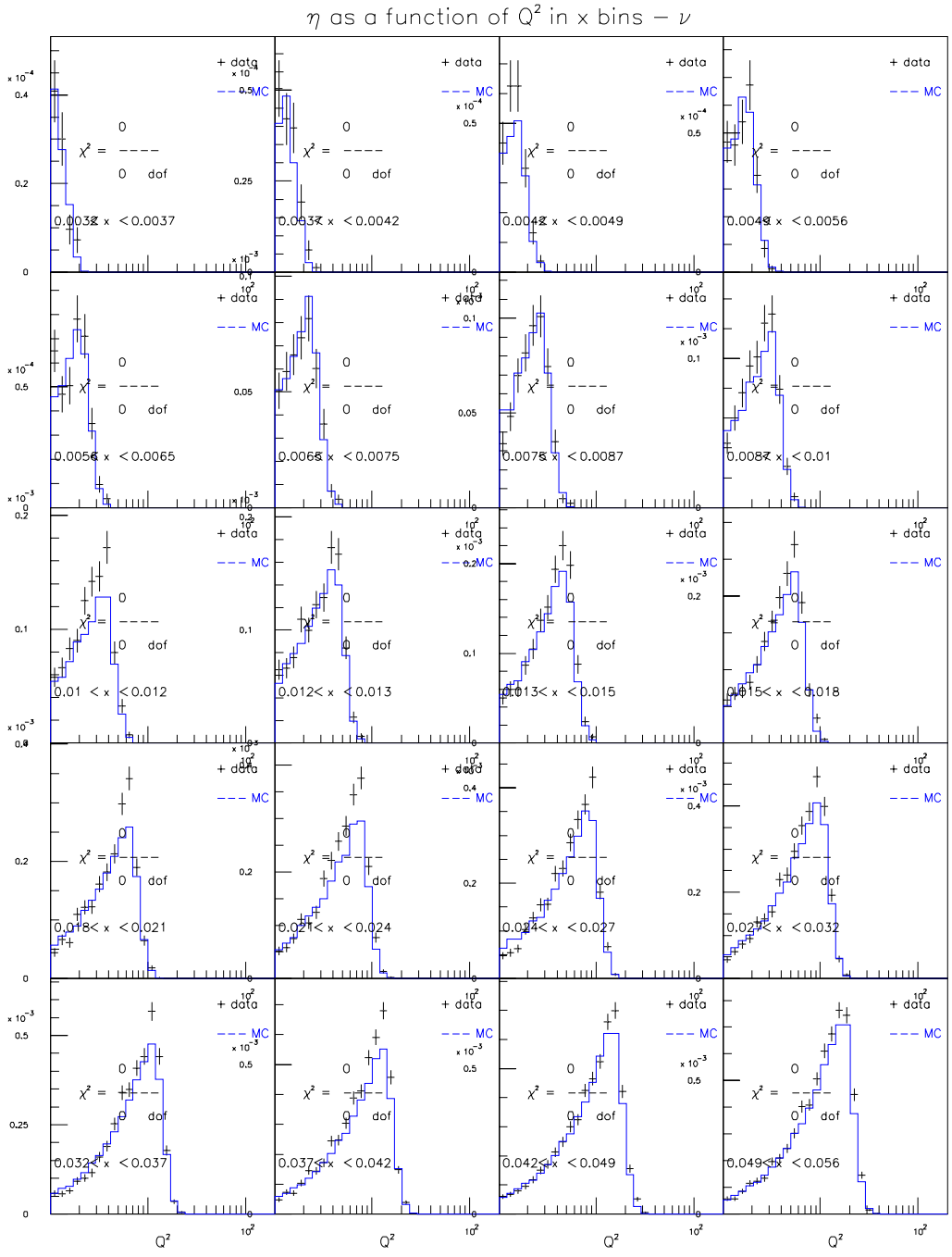

Figure E.49: GRV98NLO+EMC+HT for $201 < E_\nu < 400$ GeV (ν mode)

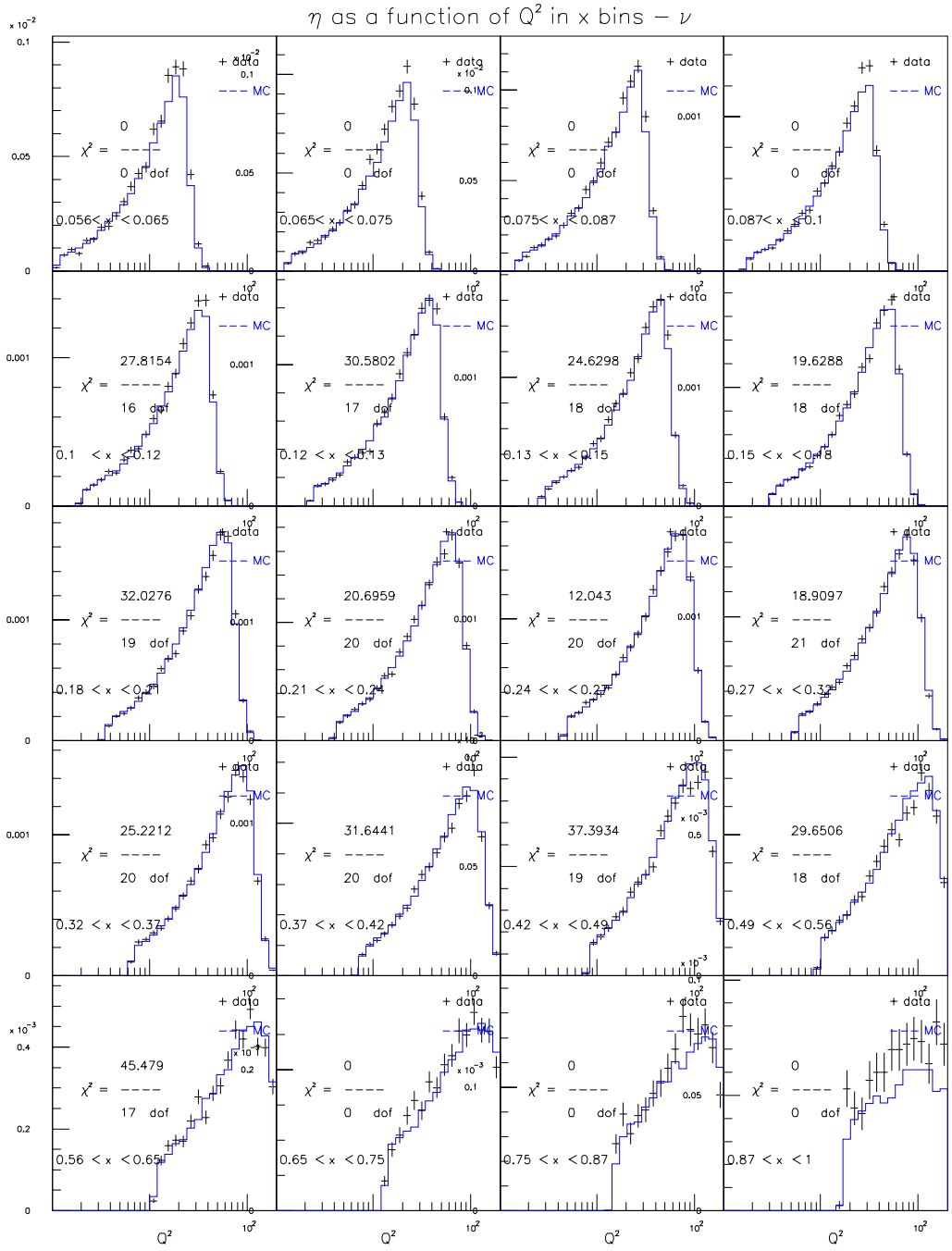

Figure E.50: GRV98NLO+EMC+HT for $201 < E_\nu < 400$ GeV (ν mode)

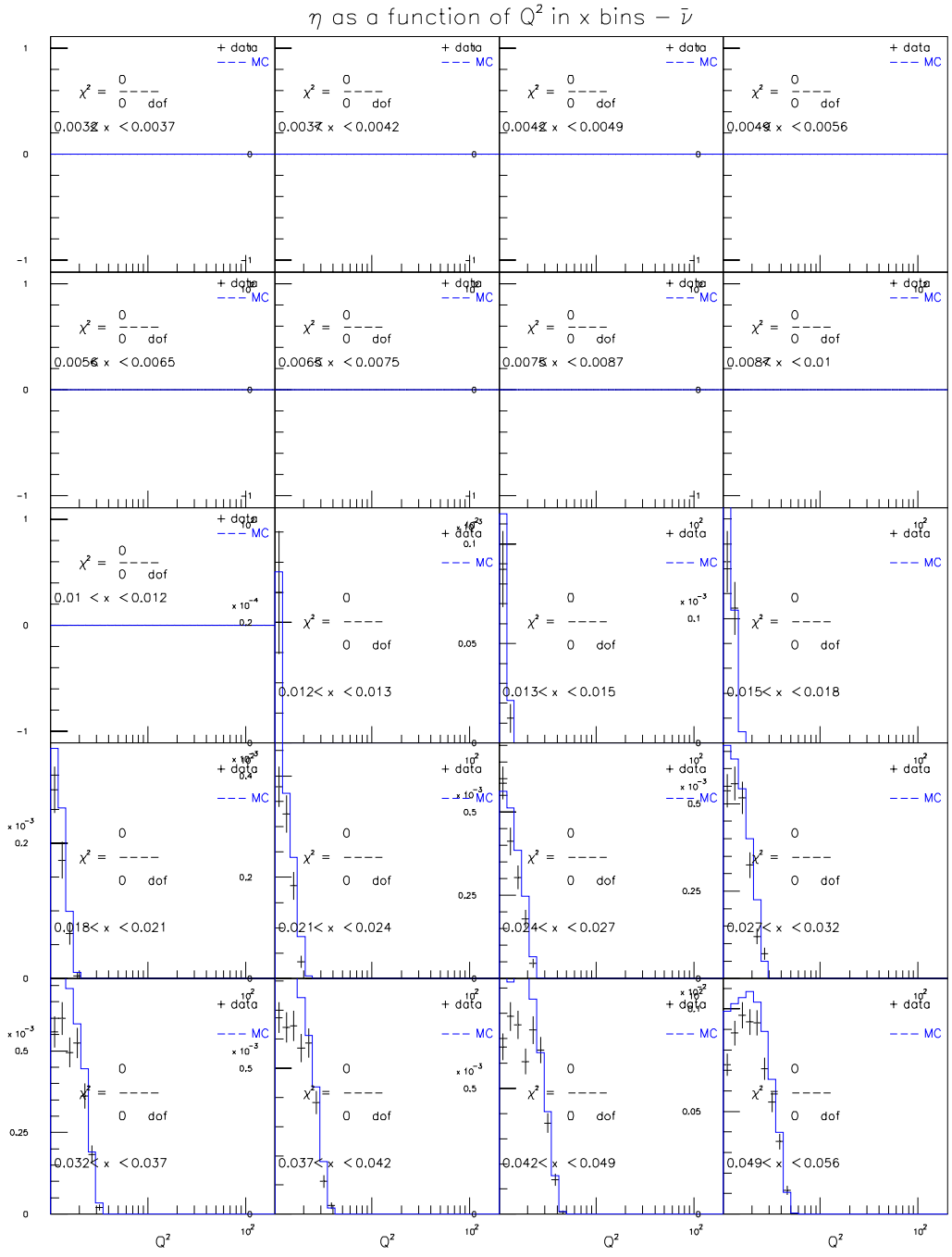

Figure E.51: GRV98NLO+EMC+HT for $20 < E_\nu < 62$ GeV ($\overline{\nu}$ mode)

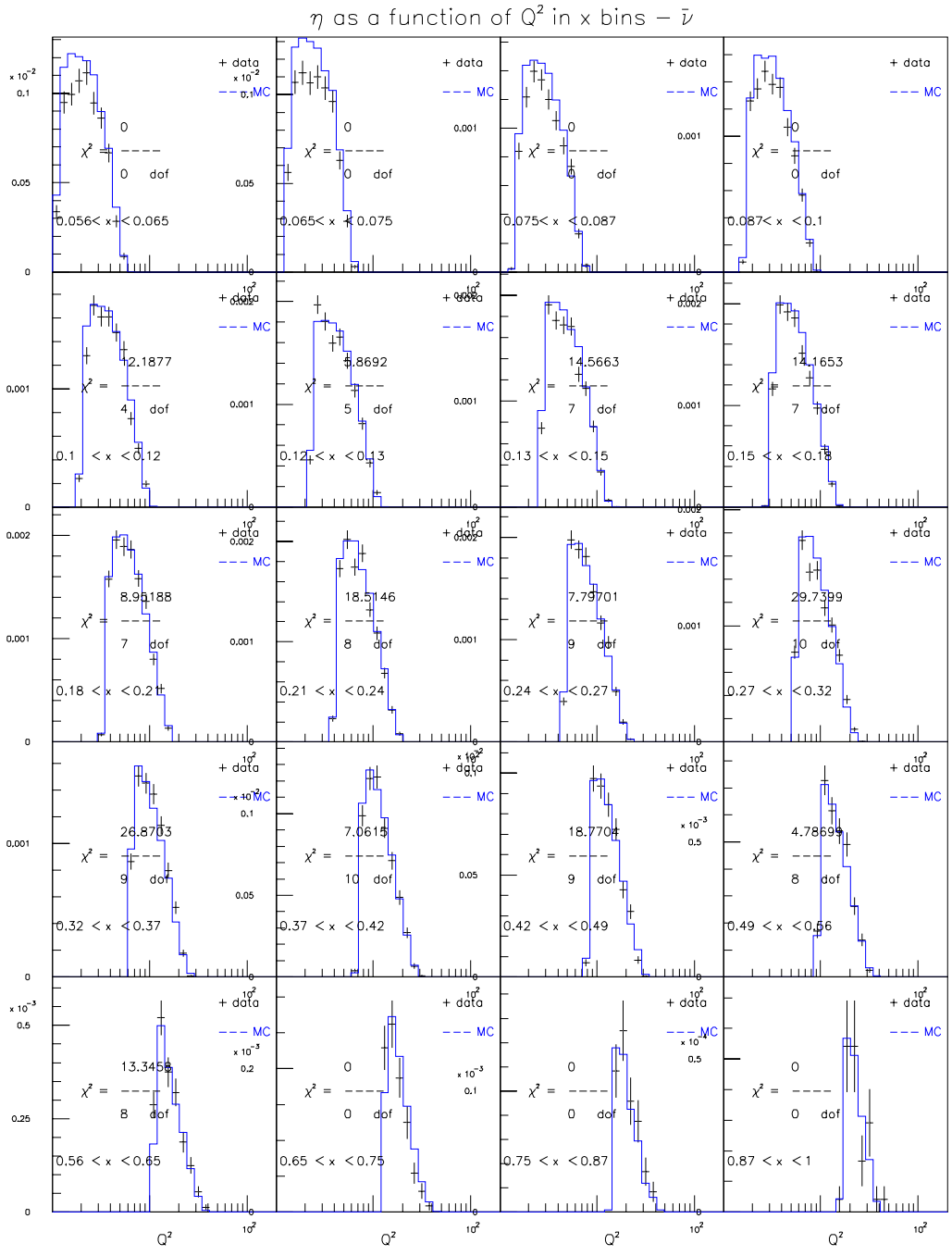

Figure E.52: GRV98NLO+EMC+HT for $20 < E_\nu < 62$ GeV ($\overline{\nu}$ mode)

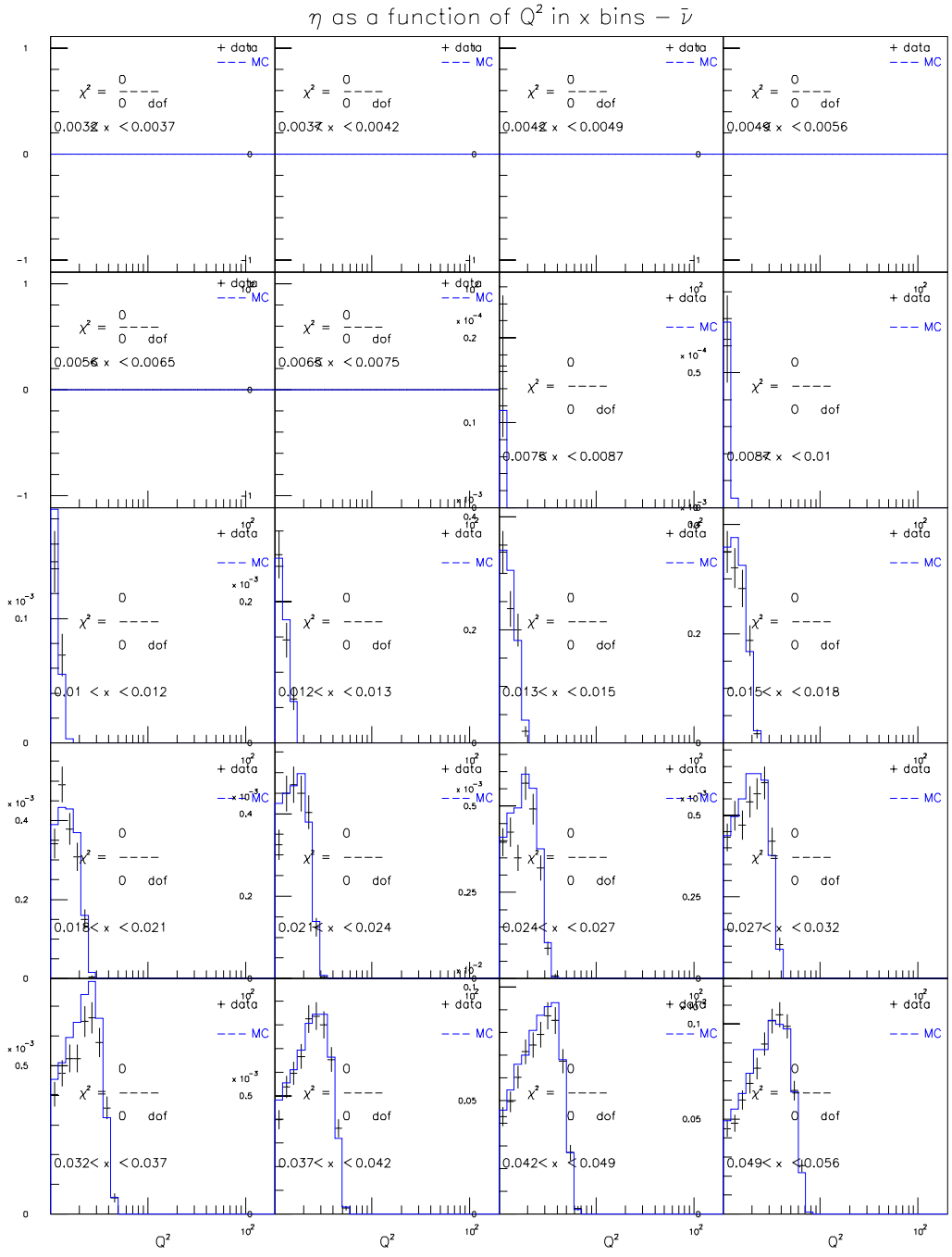

Figure E.53: GRV98NLO+EMC+HT for $62 < E_\nu < 85$ GeV ($\overline{\nu}$ mode)

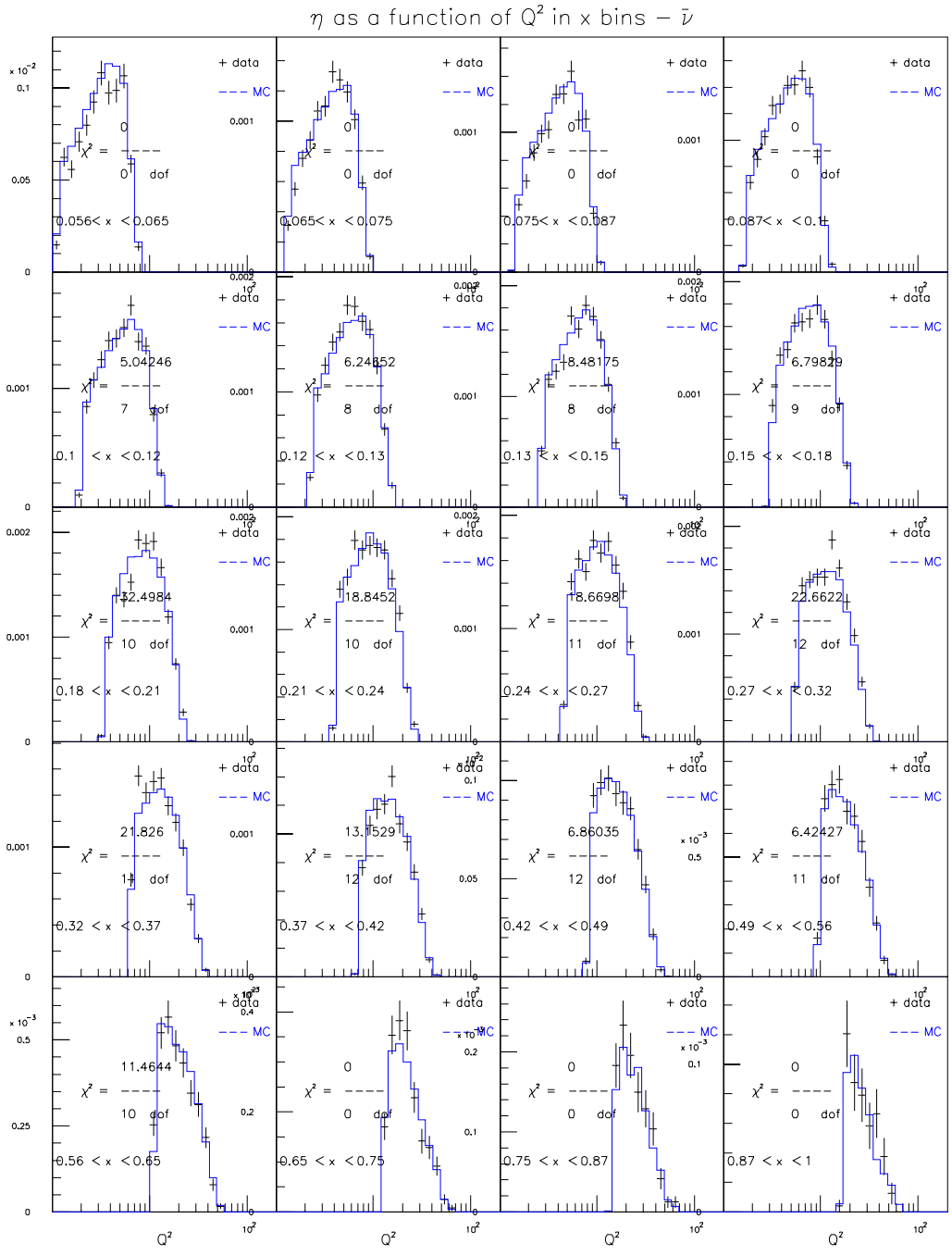

Figure E.54: GRV98NLO+EMC+HT for $62 < E_\nu < 85$ GeV ($\overline{\nu}$ mode)

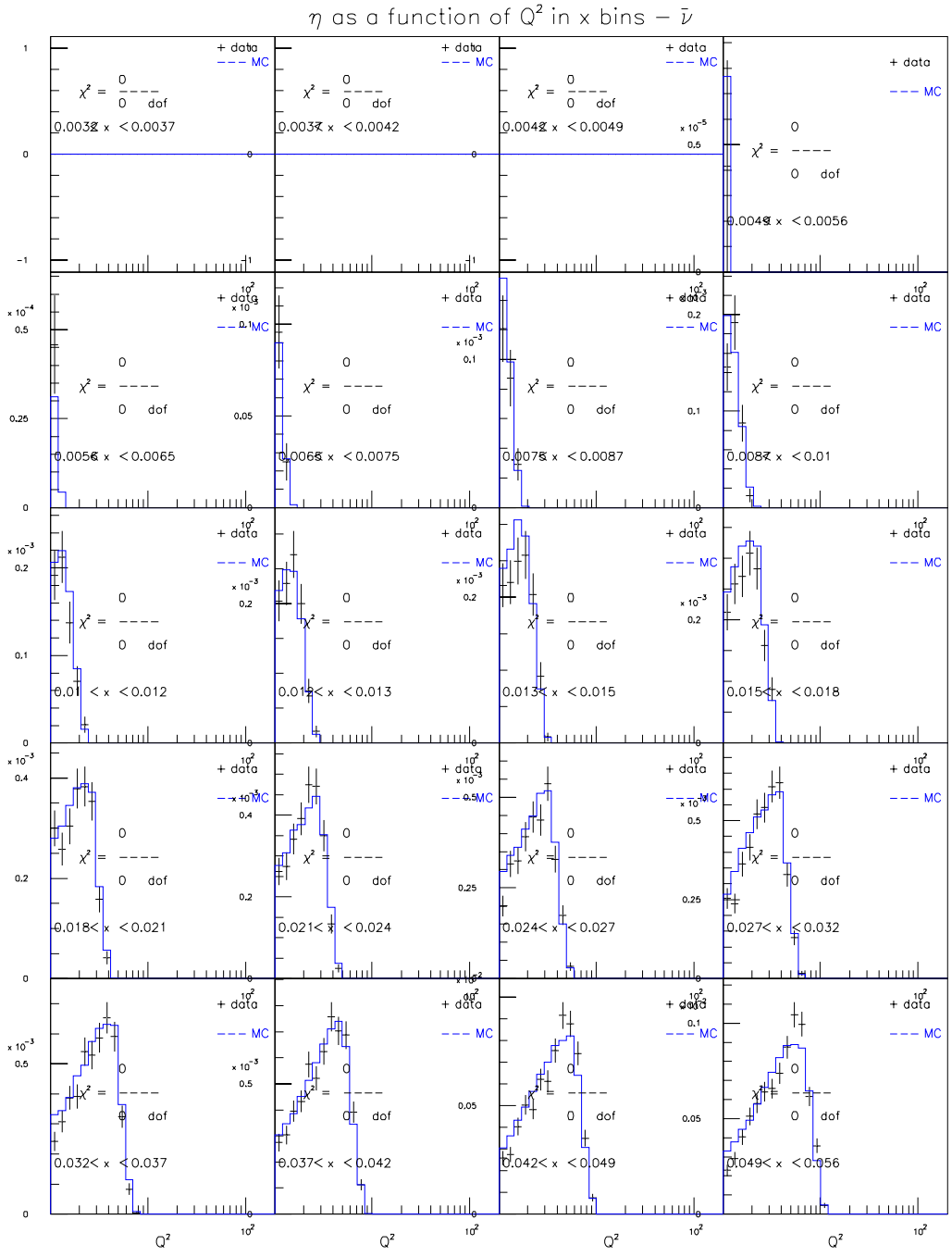

Figure E.55: GRV98NLO+EMC+HT for $85 < E_\nu < 129$ GeV ($\overline{\nu}$ mode)

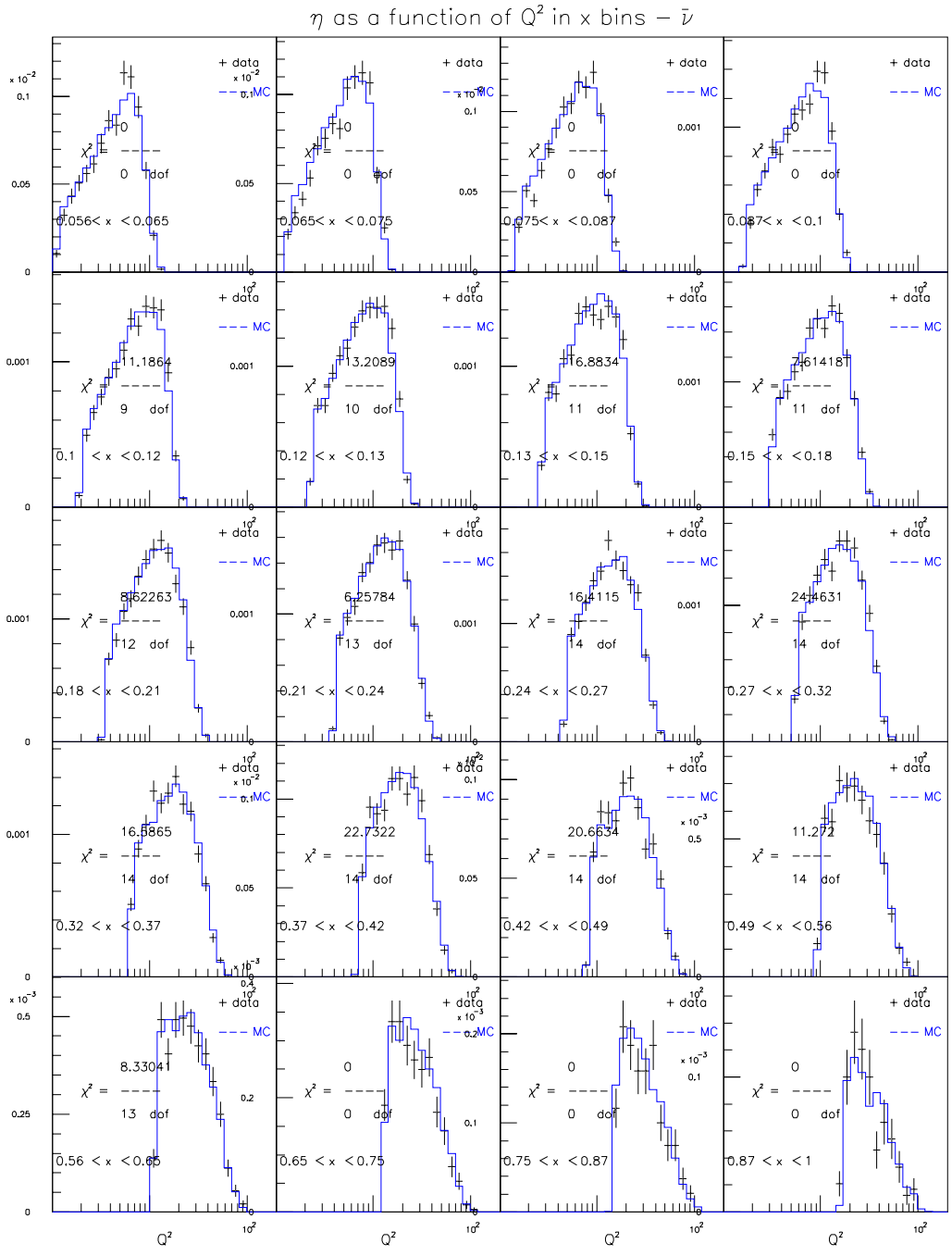

Figure E.56: GRV98NLO+EMC+HT for $85 < E_\nu < 129$ GeV ($\overline{\nu}$ mode)

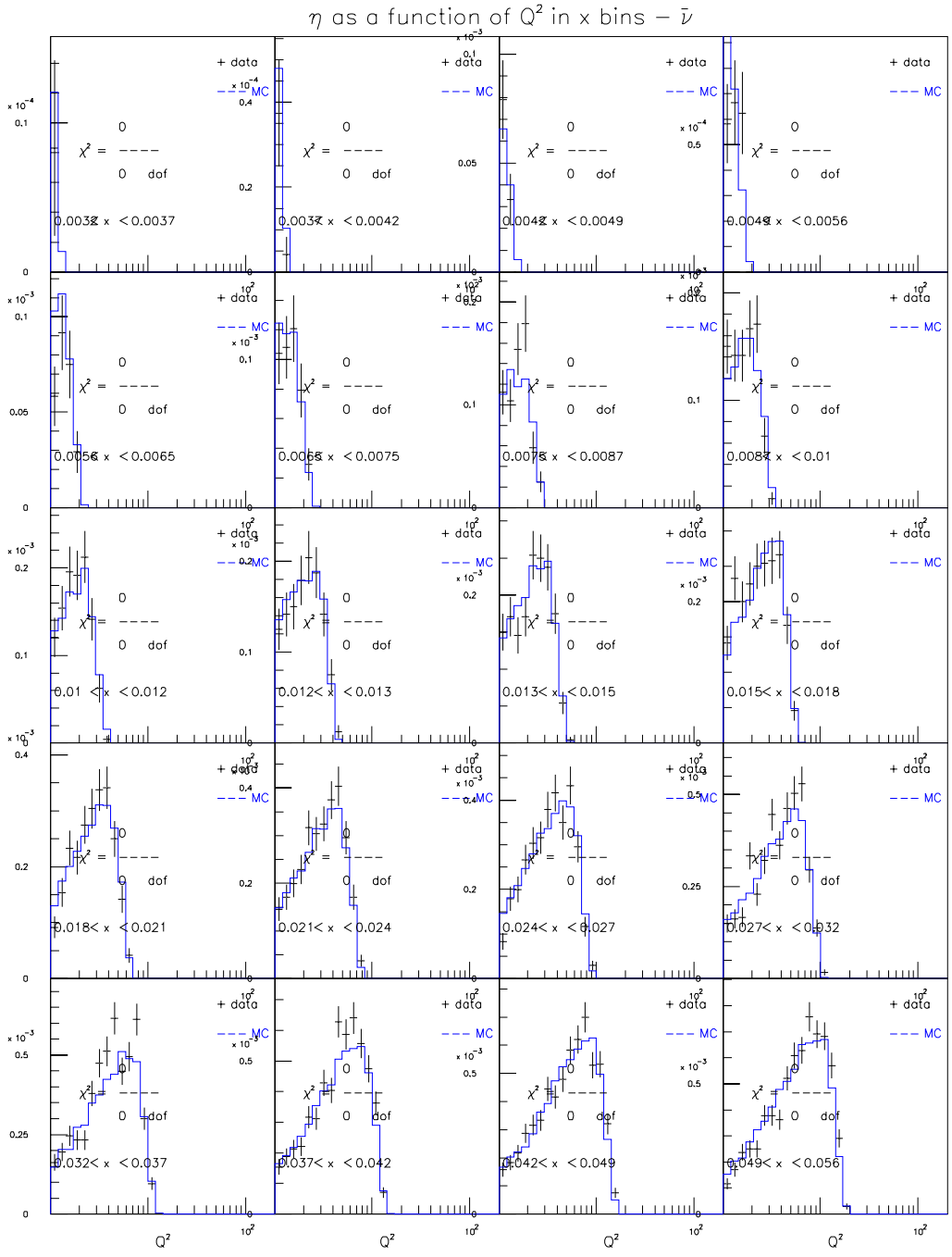

Figure E.57: GRV98NLO+EMC+HT for $129 < E_\nu < 201$ GeV ($\overline{\nu}$ mode)

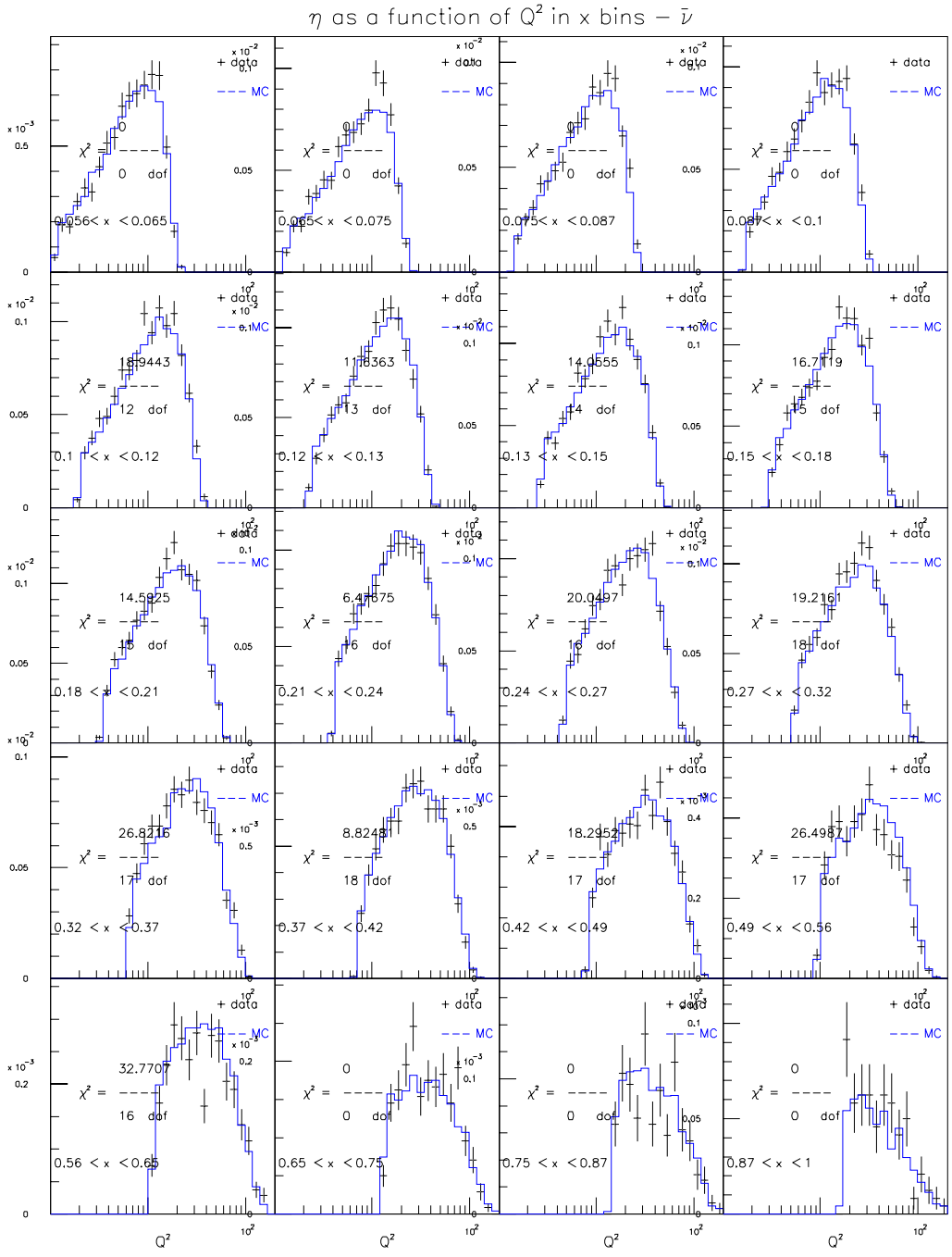

Figure E.58: GRV98NLO+EMC+HT for $129 < E_\nu < 201$ GeV ($\overline{\nu}$ mode)

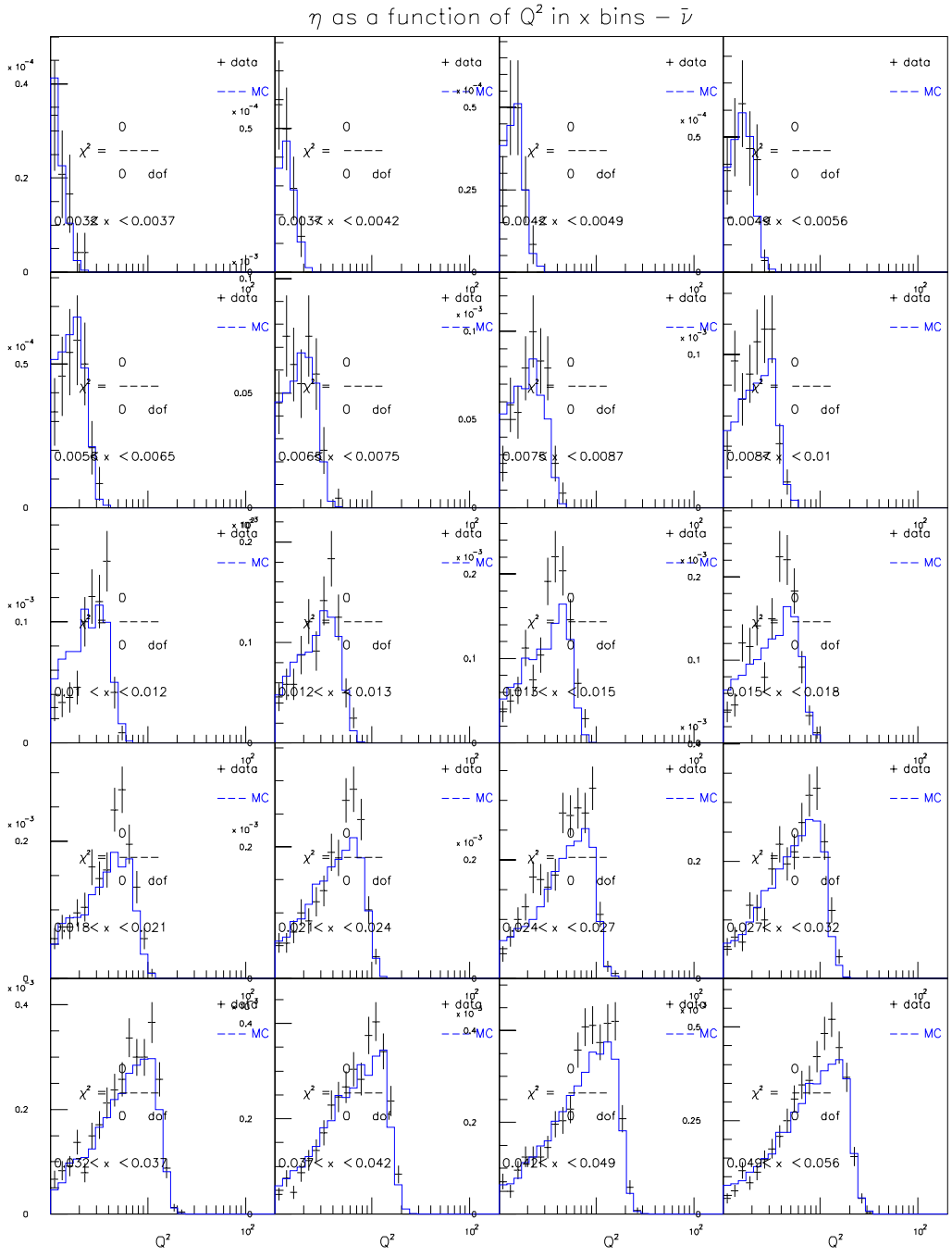

Figure E.59: GRV98NLO+EMC+HT for $201 < E_\nu < 400$ GeV ($\overline{\nu}$ mode)

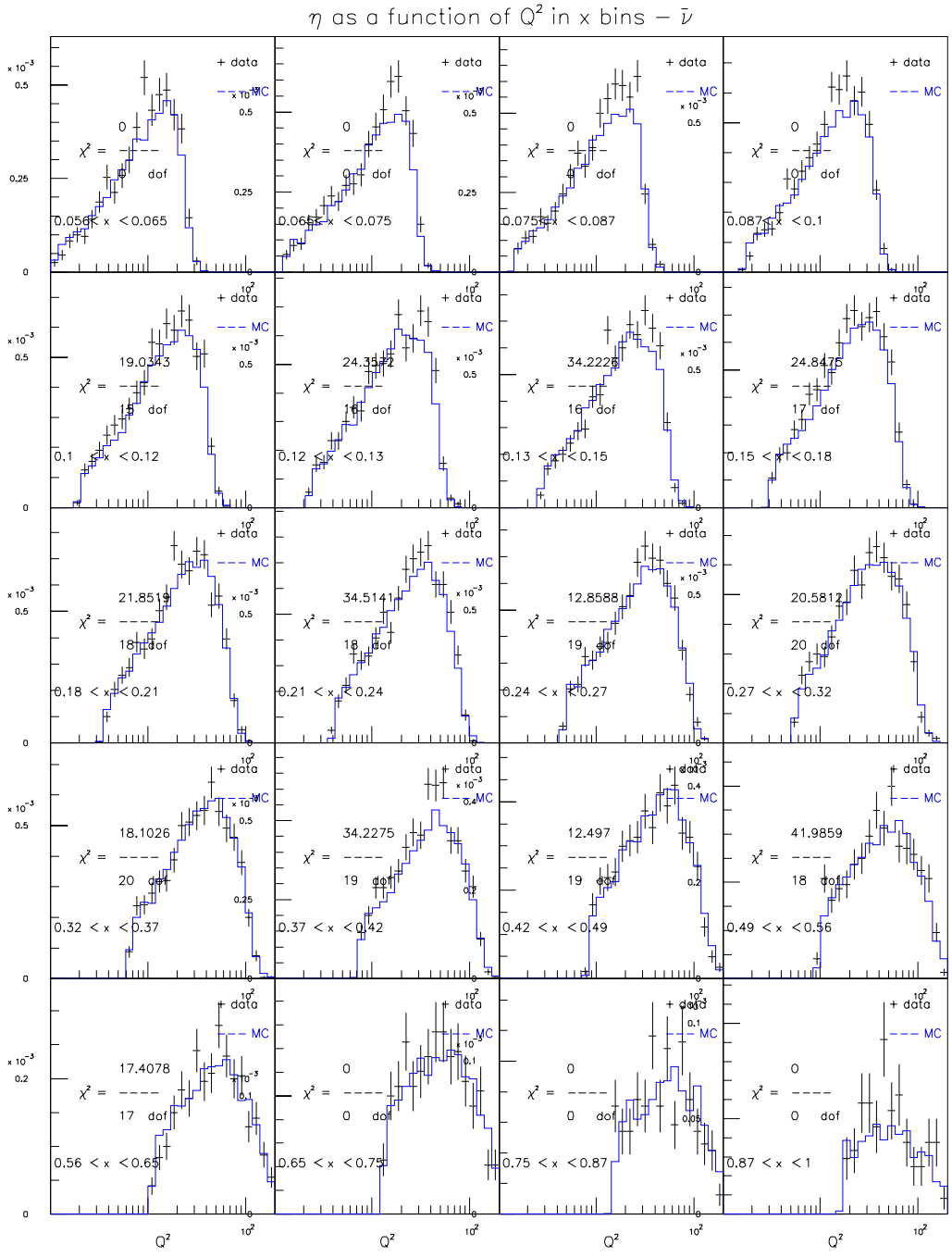

Figure E.60: GRV98NLO+EMC+HT for $201 < E_\nu < 400$ GeV ($\overline{\nu}$ mode)

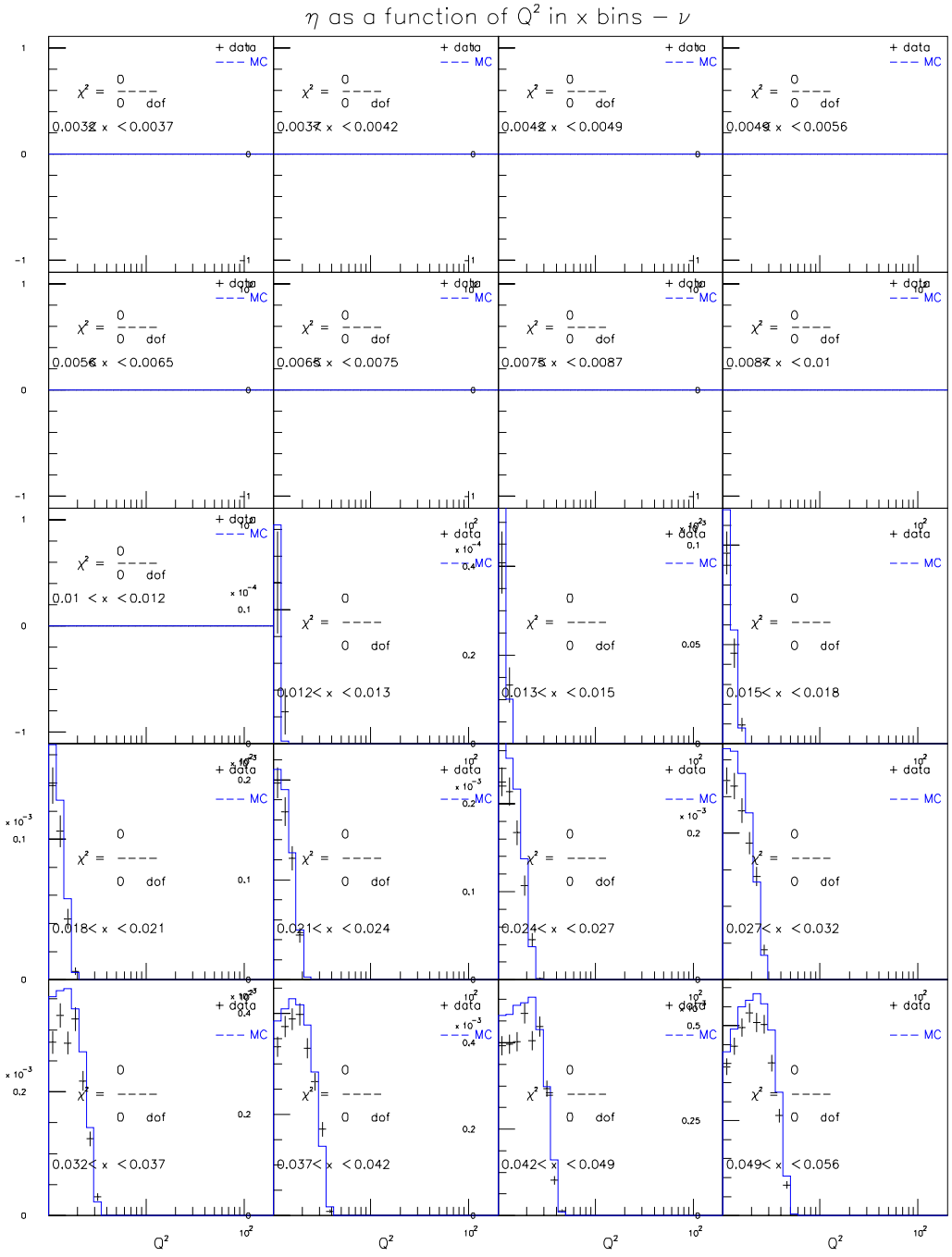

Figure E.61: CTEQ5NLO+EMC+HT for $20 < E_\nu < 62$ GeV (ν mode)

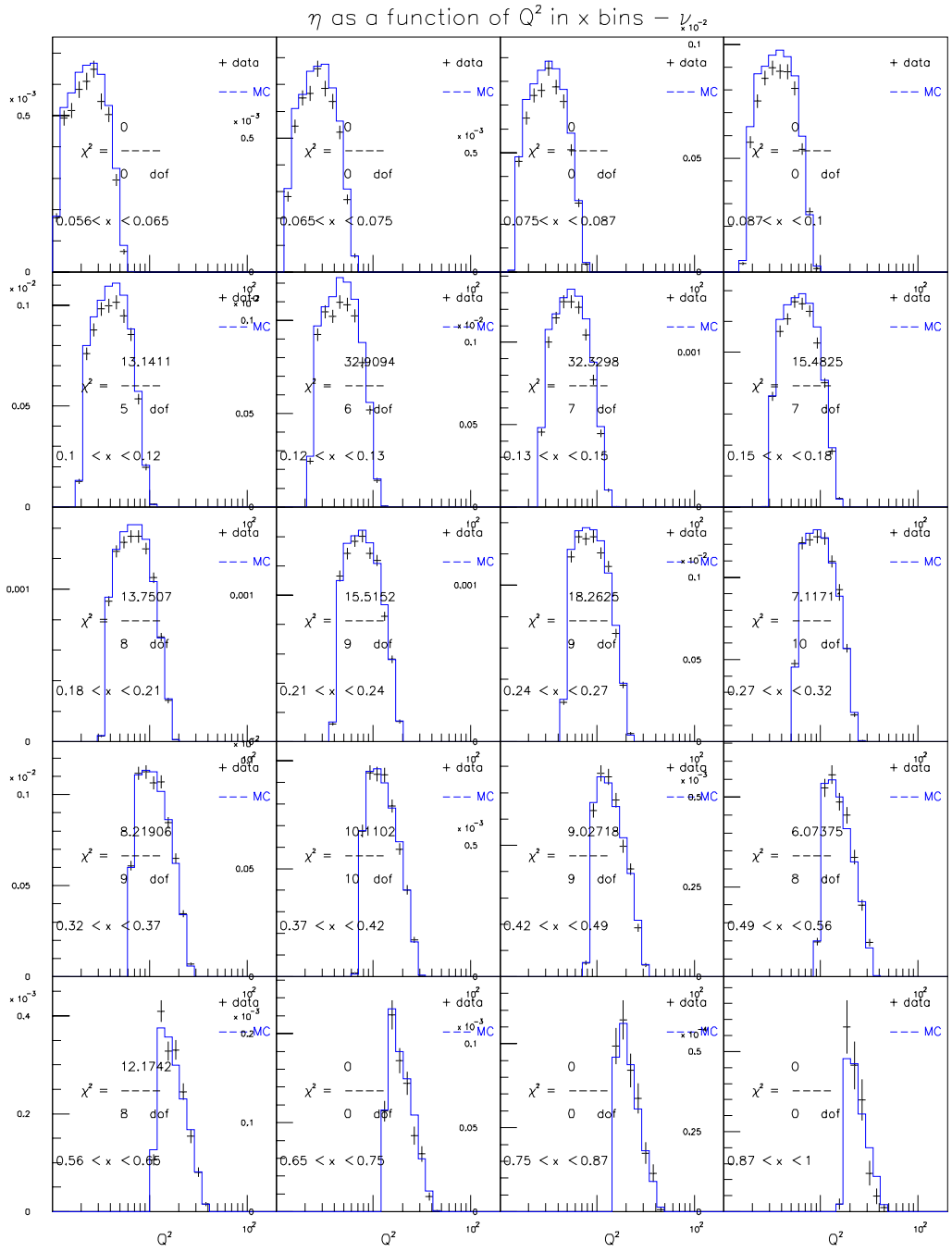

Figure E.62: CTEQ5NLO+EMC+HT for $20 < E_\nu < 62$ GeV (ν mode)

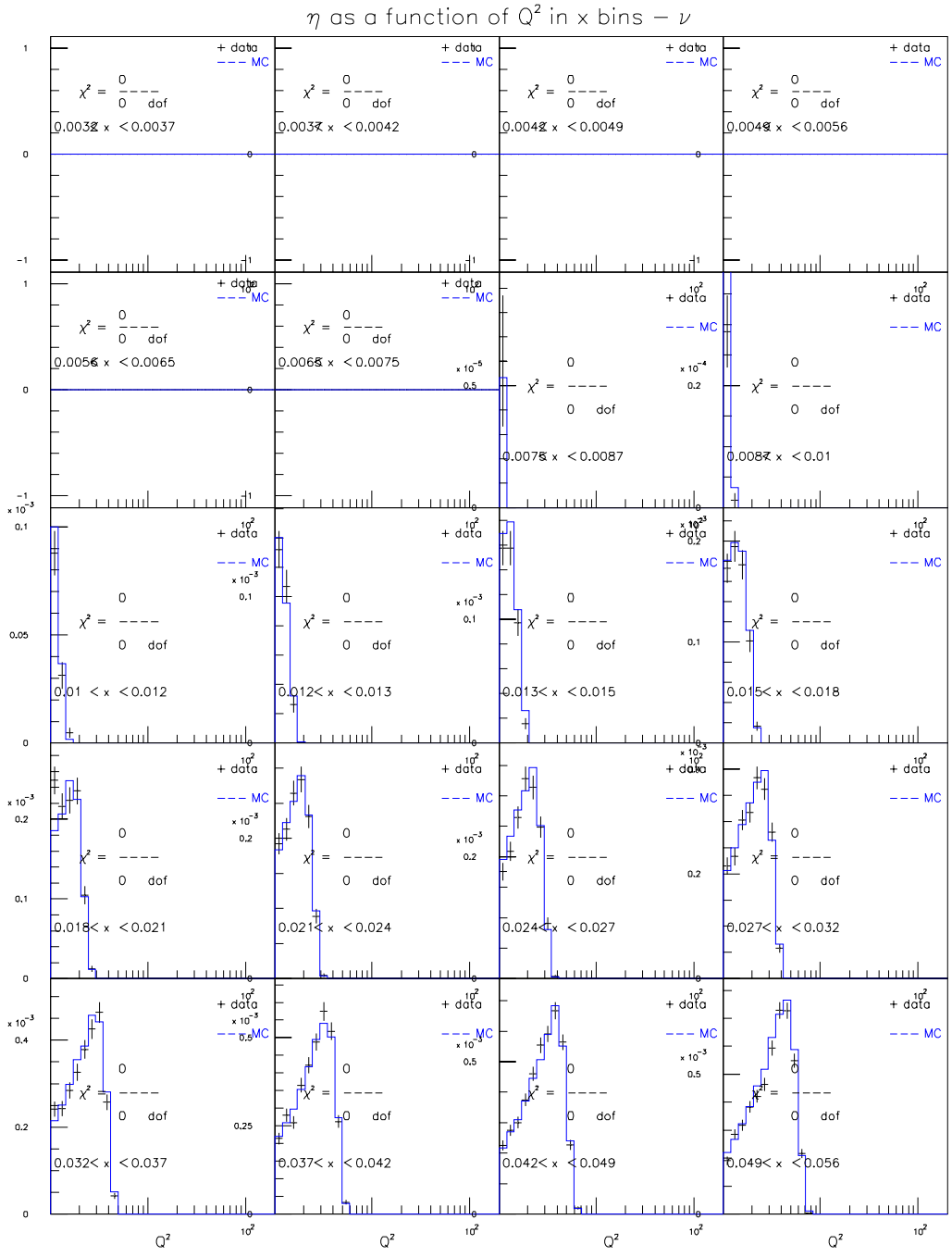

Figure E.63: CTEQ5NLO+EMC+HT for $62 < E_\nu < 85$ GeV (ν mode)

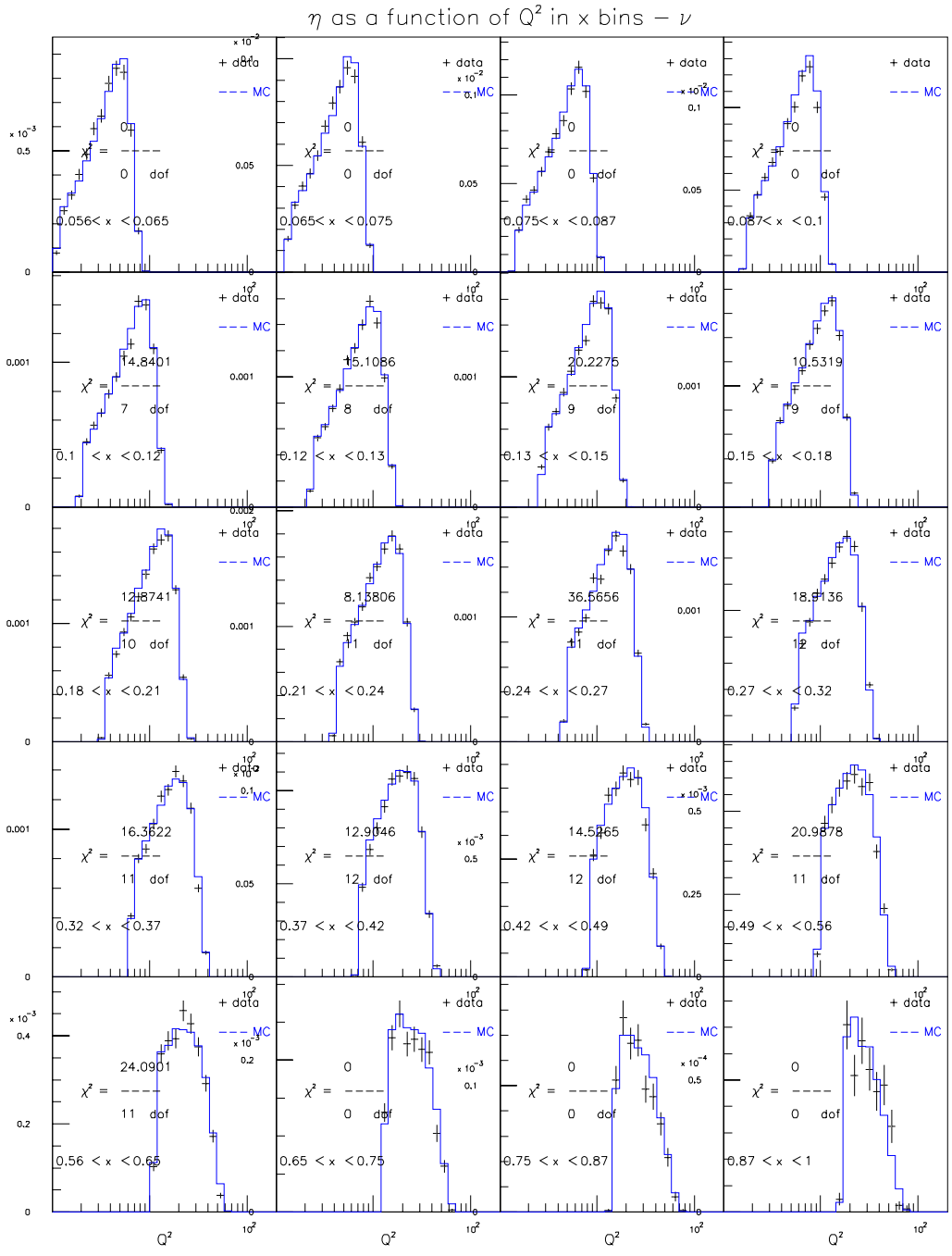

Figure E.64: CTEQ5NLO+EMC+HT for $62 < E_\nu < 85$ GeV (ν mode)

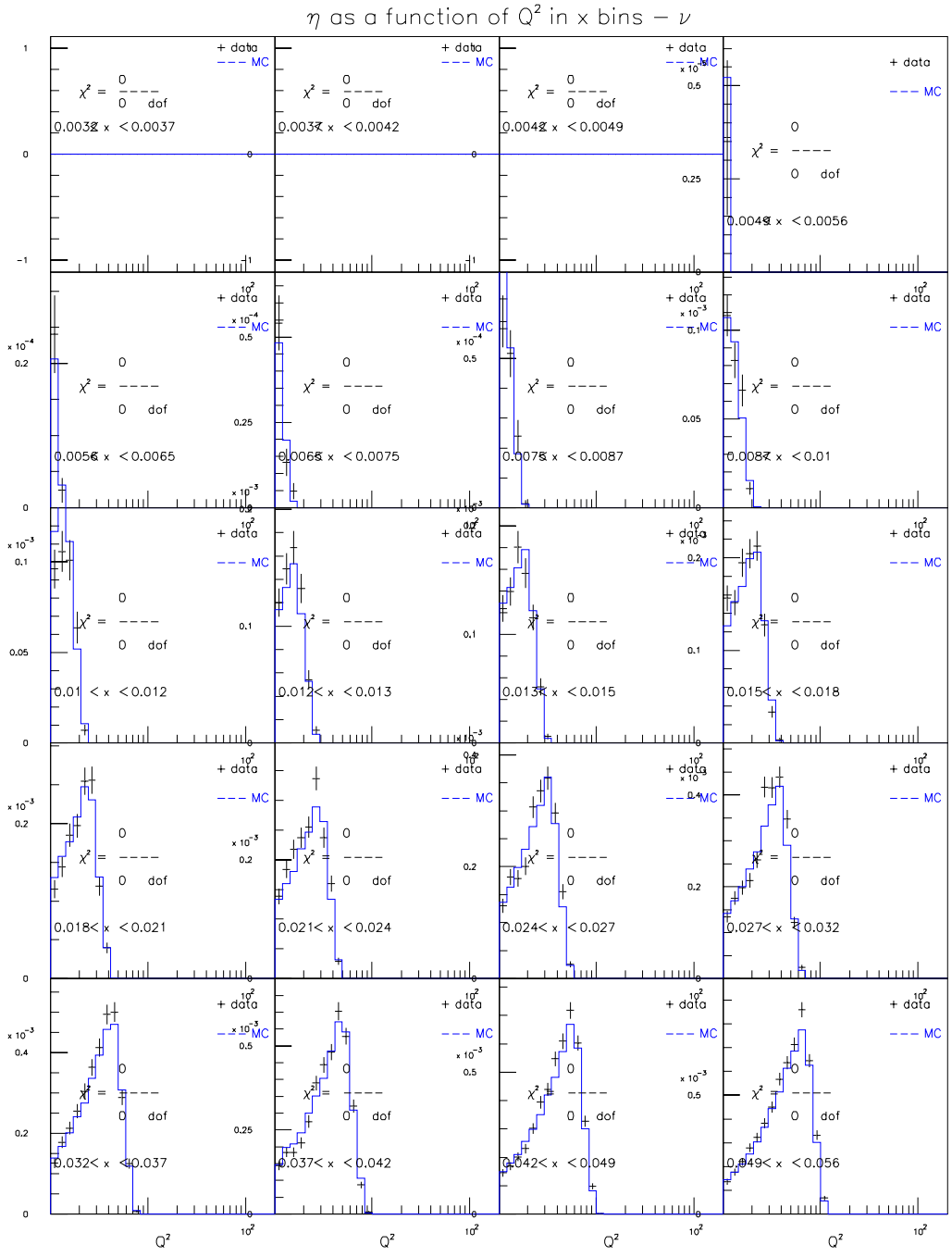

Figure E.65: CTEQ5NLO+EMC+HT for $85 < E_\nu < 129$ GeV (ν mode)

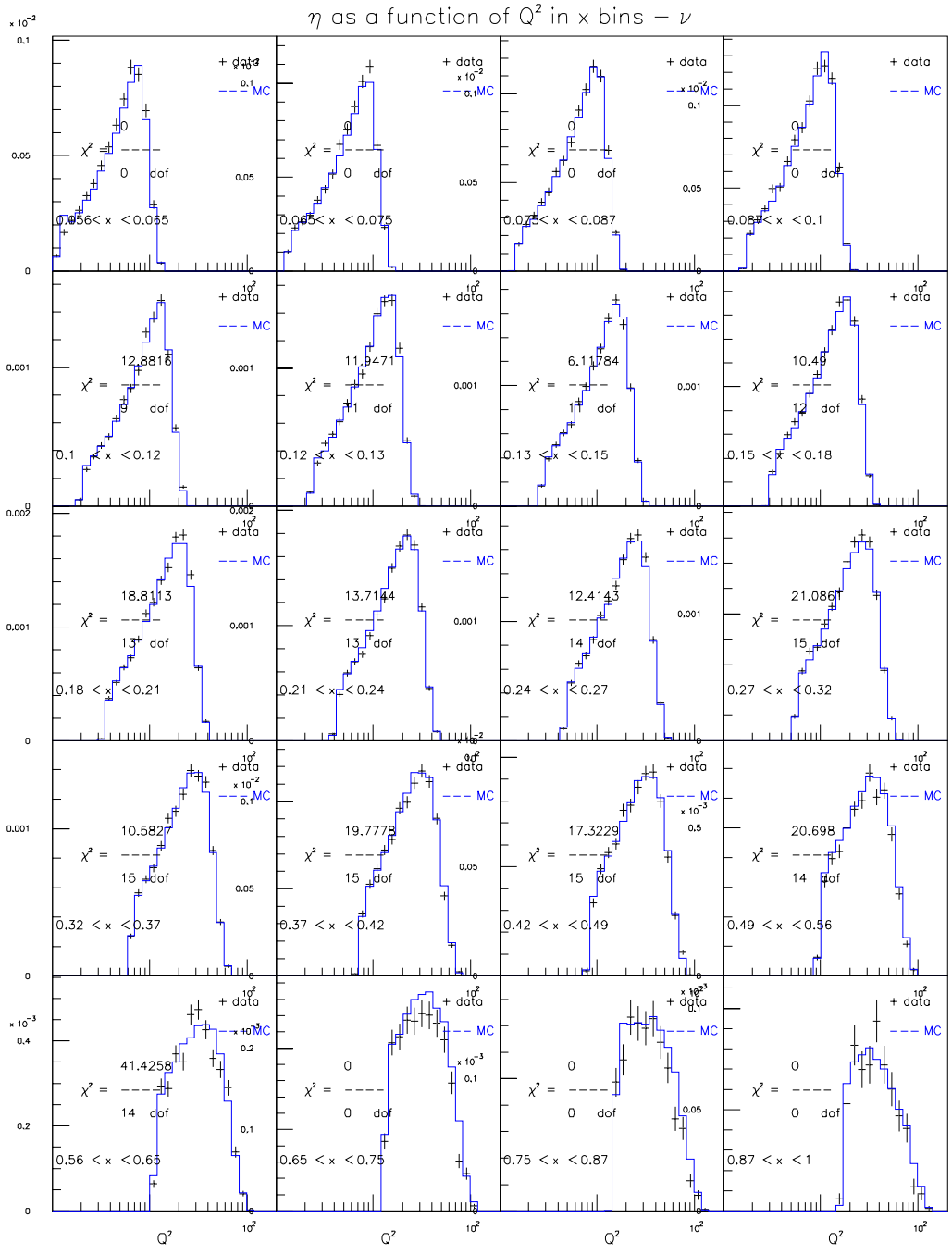

Figure E.66: CTEQ5NLO+EMC+HT for $85 < E_\nu < 129$ GeV (ν mode)

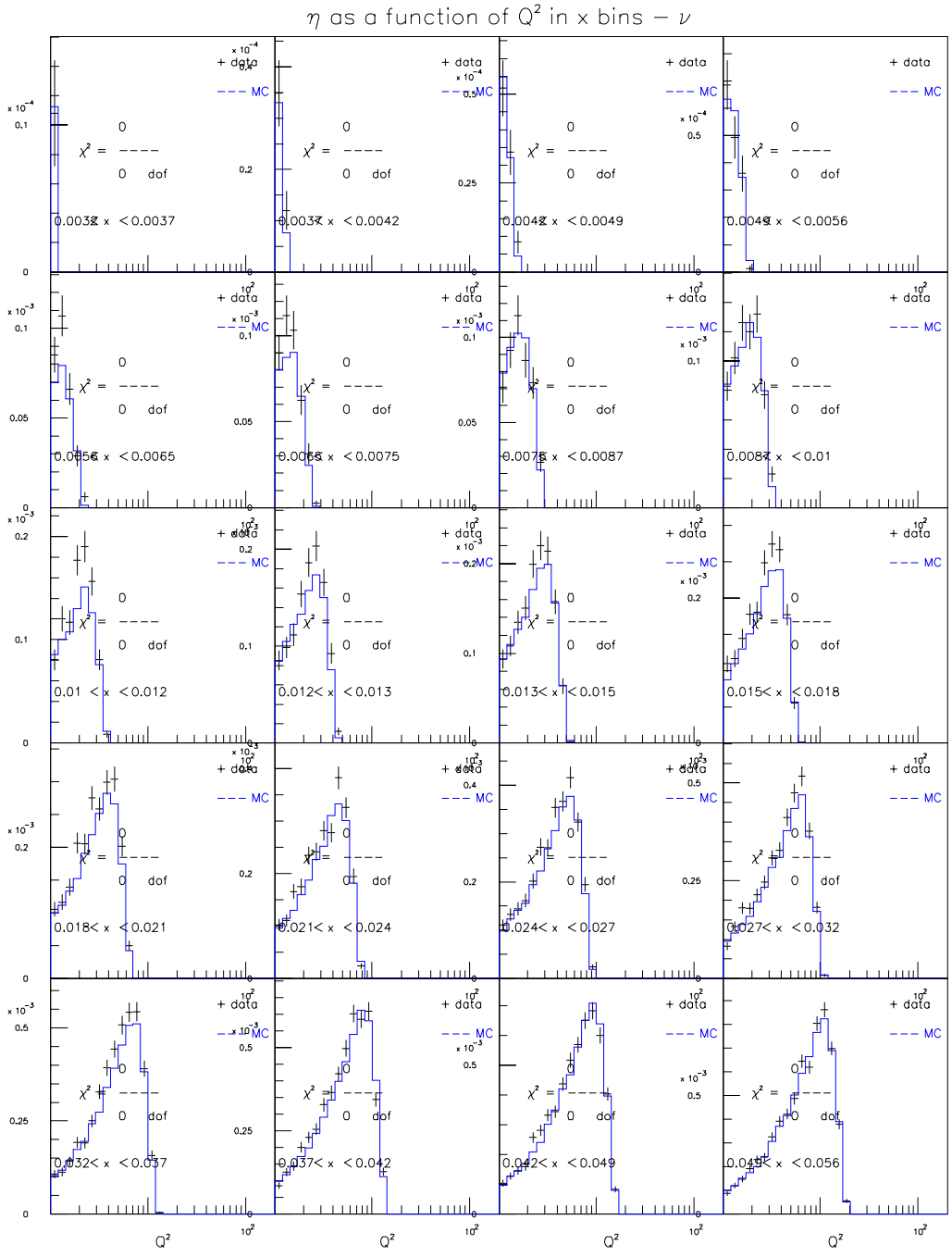

Figure E.67: CTEQ5NLO+EMC+HT for $129 < E_\nu < 201$ GeV (ν mode)

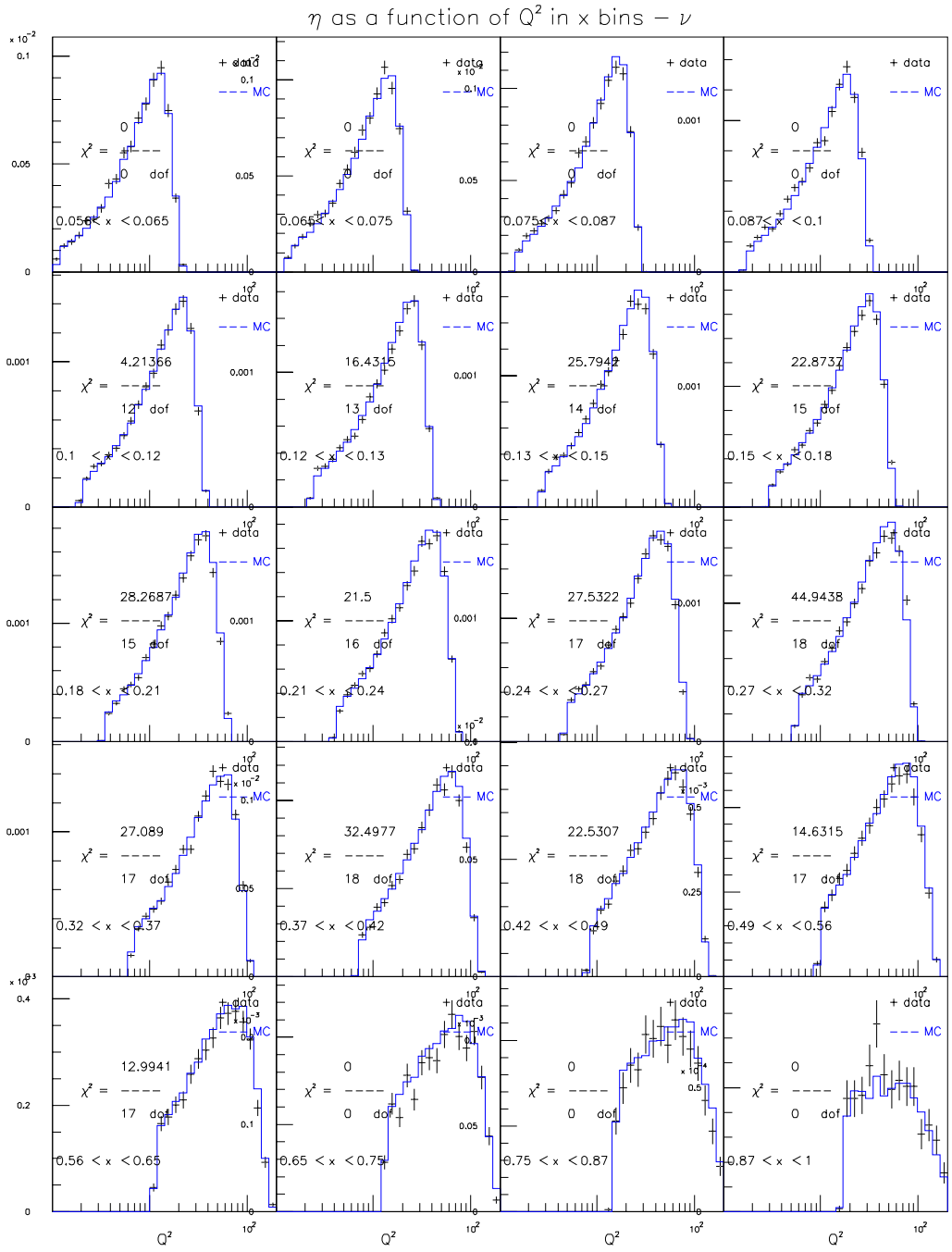

Figure E.68: CTEQ5NLO+EMC+HT for $129 < E_\nu < 201$ GeV (ν mode)

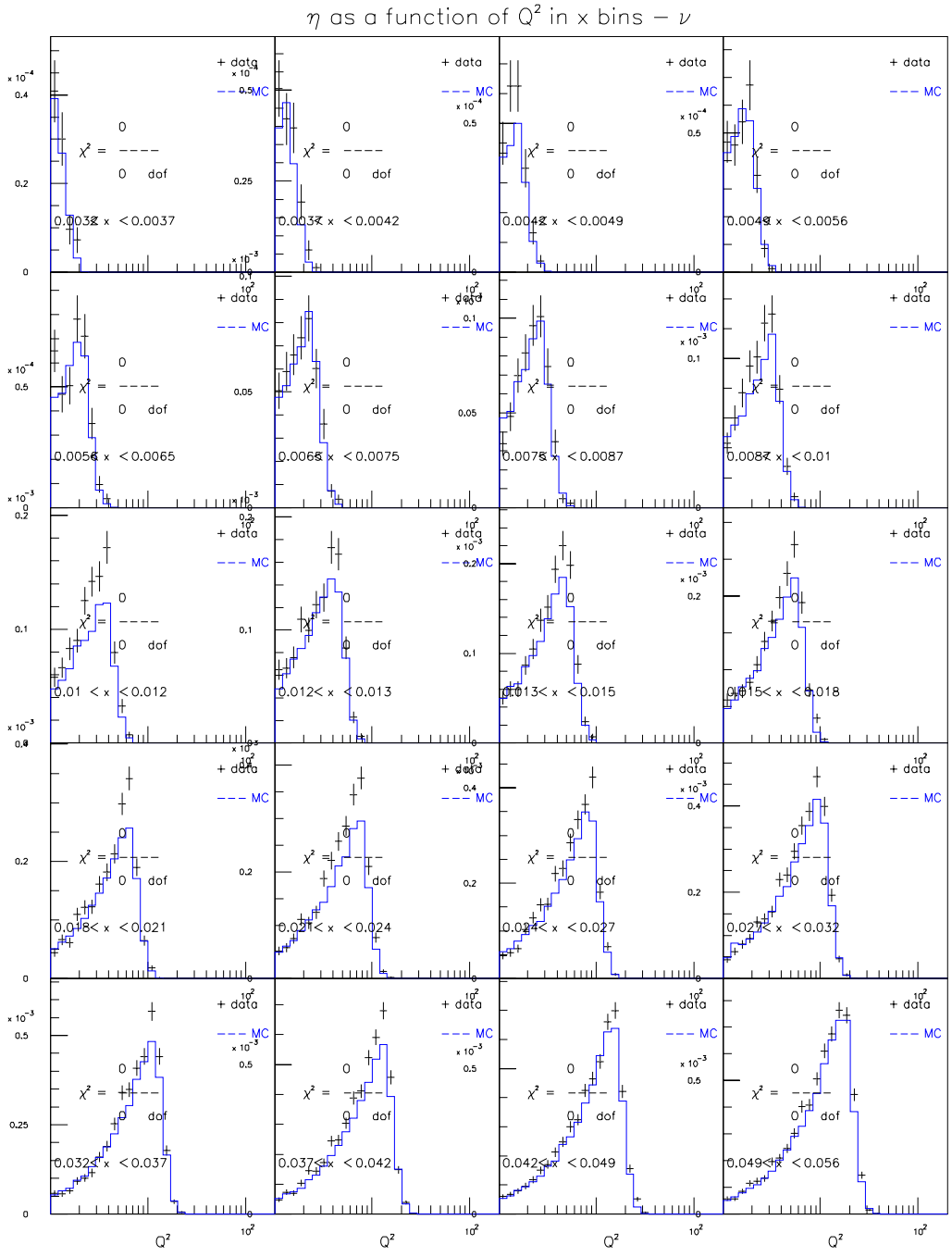

Figure E.69: CTEQ5NLO+EMC+HT for $201 < E_\nu < 400$ GeV (ν mode)

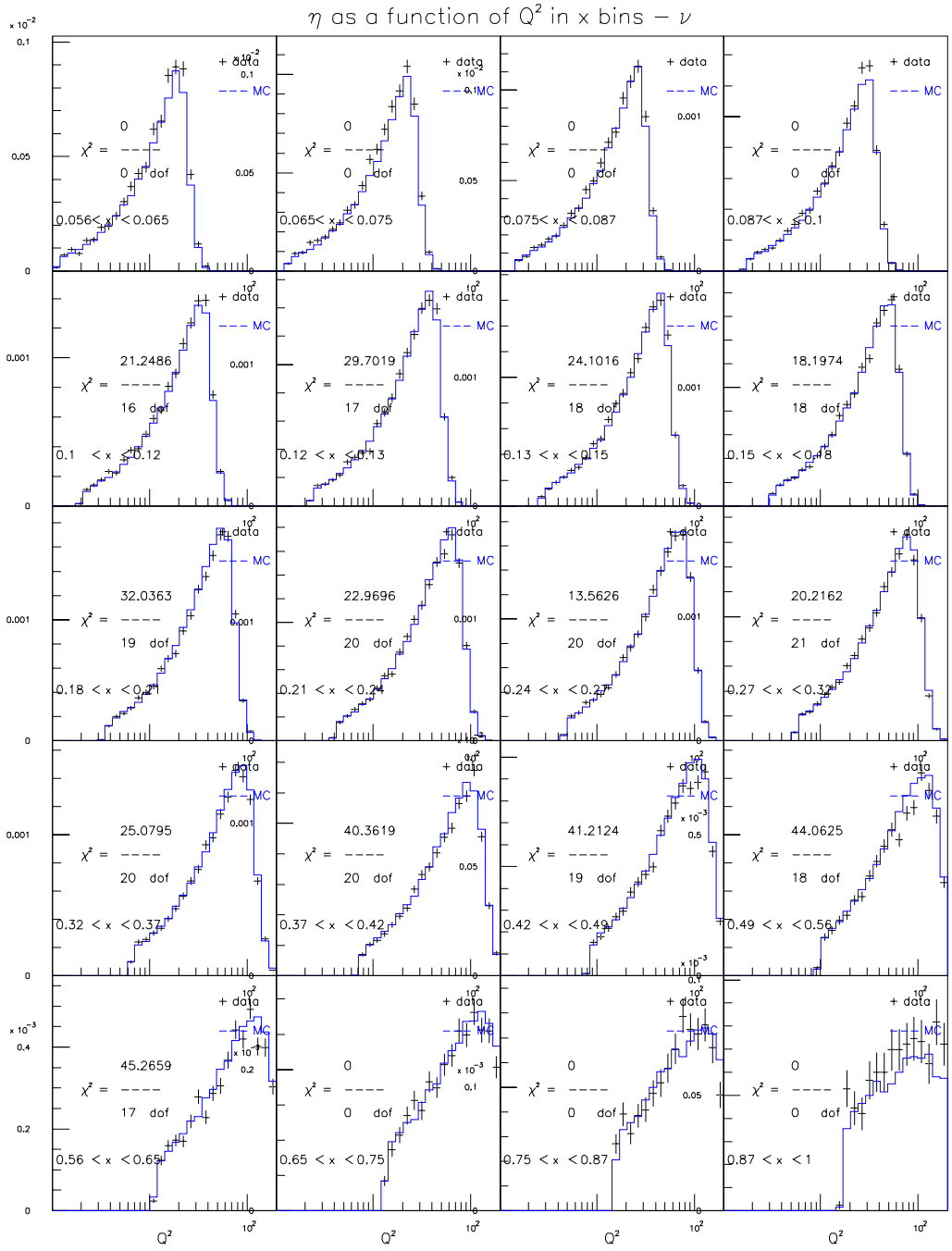

Figure E.70: CTEQ5NLO+EMC+HT for $201 < E_\nu < 400$ GeV (ν mode)

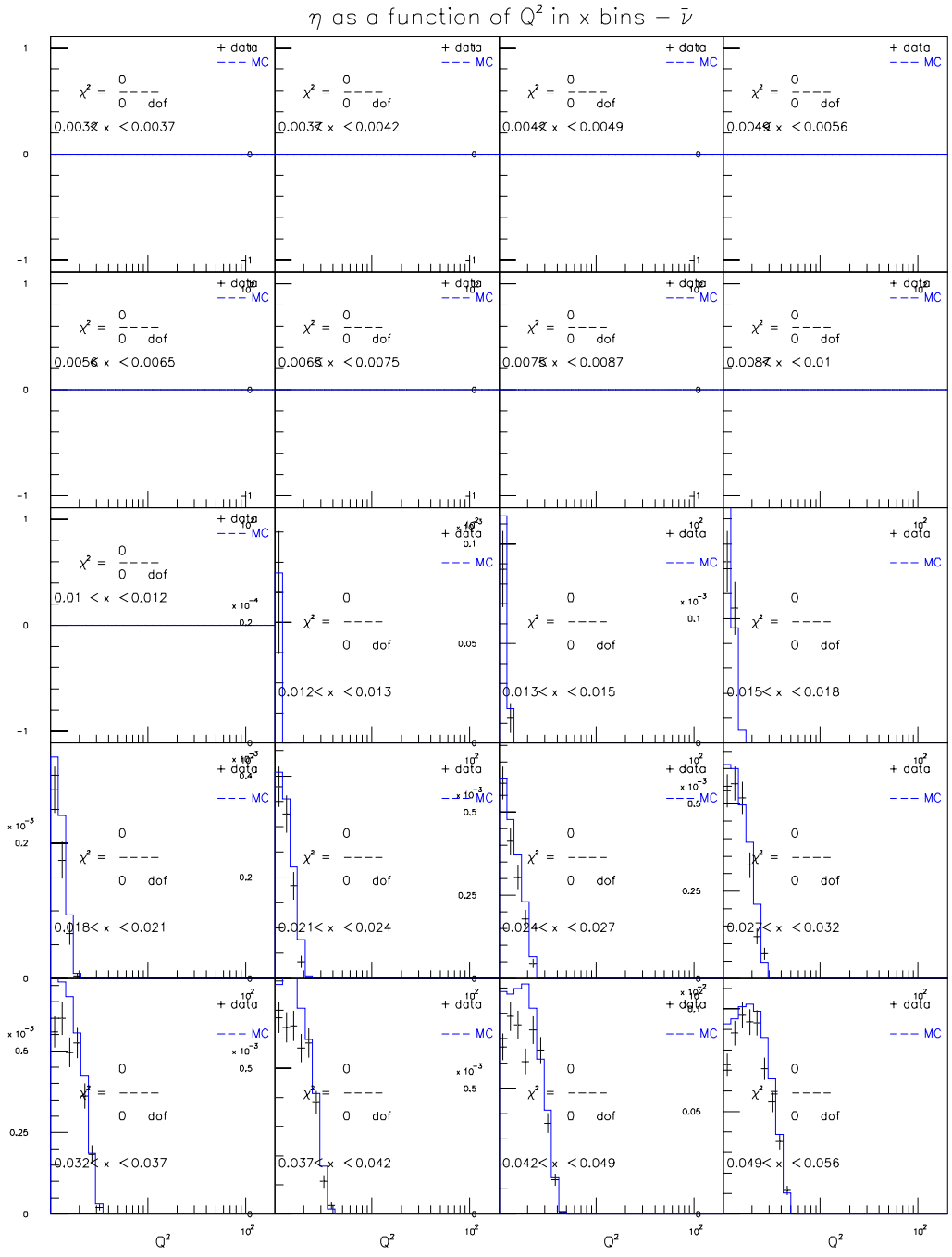

Figure E.71: CTEQ5NLO+EMC+HT for $20 < E_\nu < 62$ GeV ($\overline{\nu}$ mode)

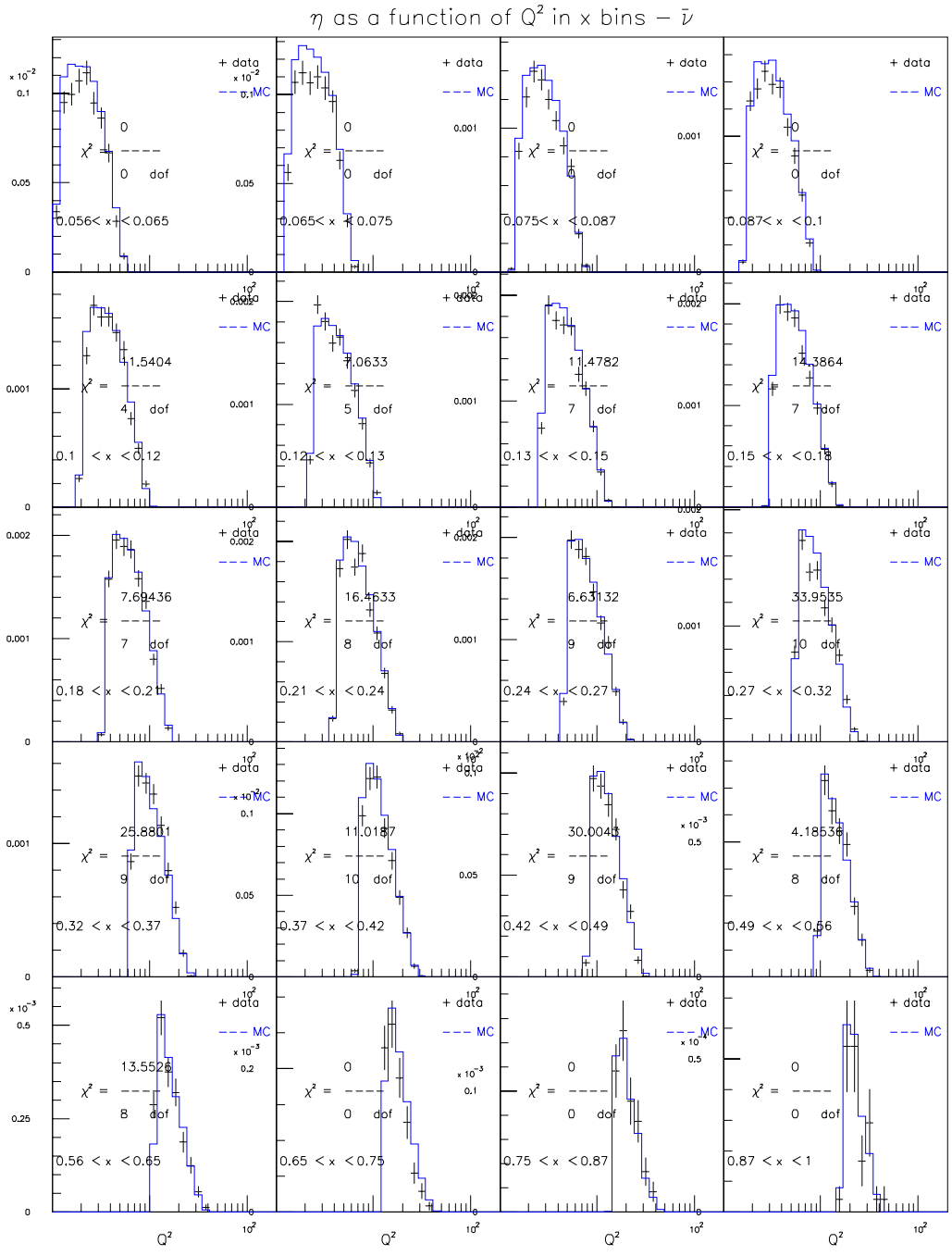

Figure E.72: CTEQ5NLO+EMC+HT for $20 < E_\nu < 62$ GeV ($\overline{\nu}$ mode)

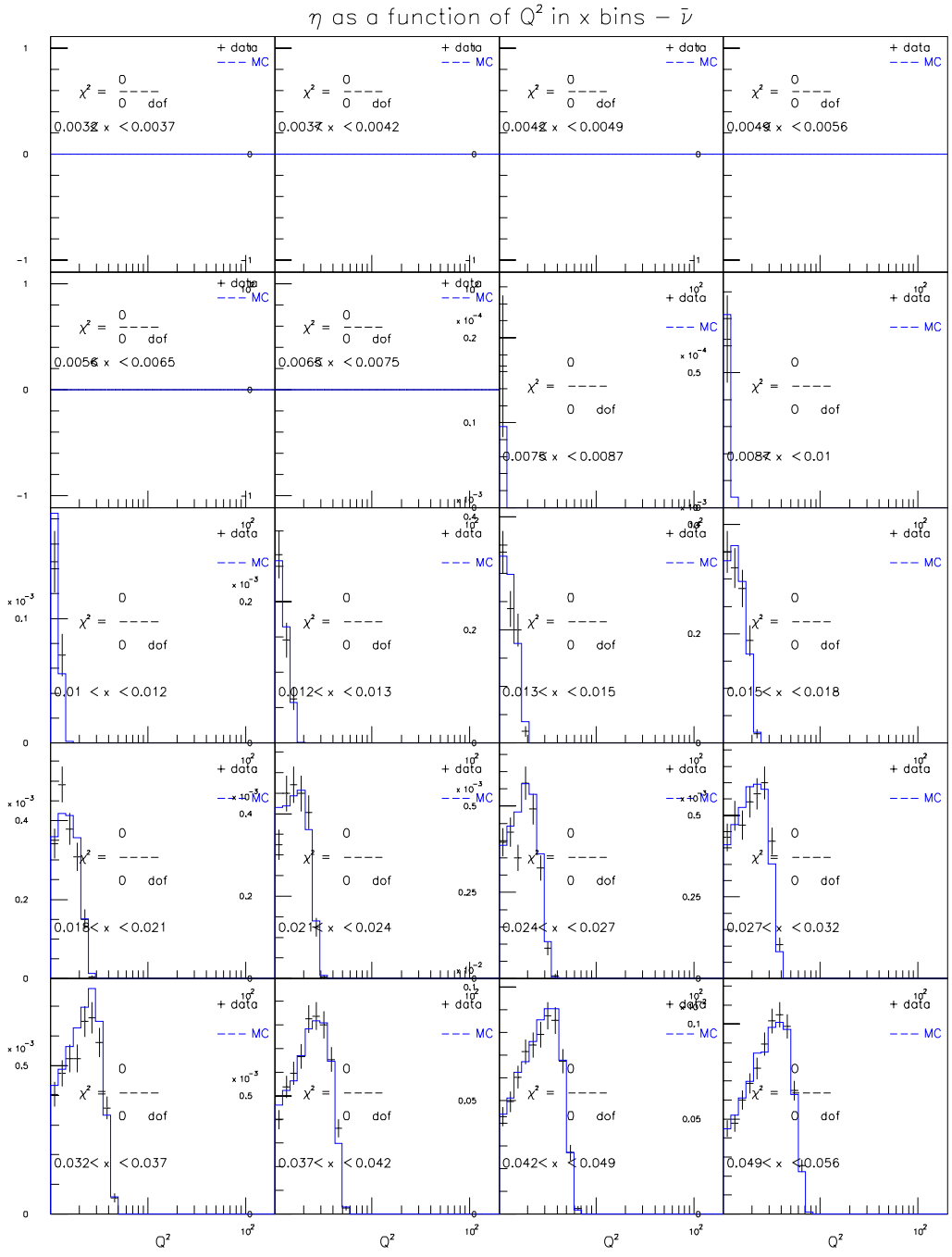

Figure E.73: CTEQ5NLO+EMC+HT for $62 < E_\nu < 85$ GeV ($\overline{\nu}$ mode)

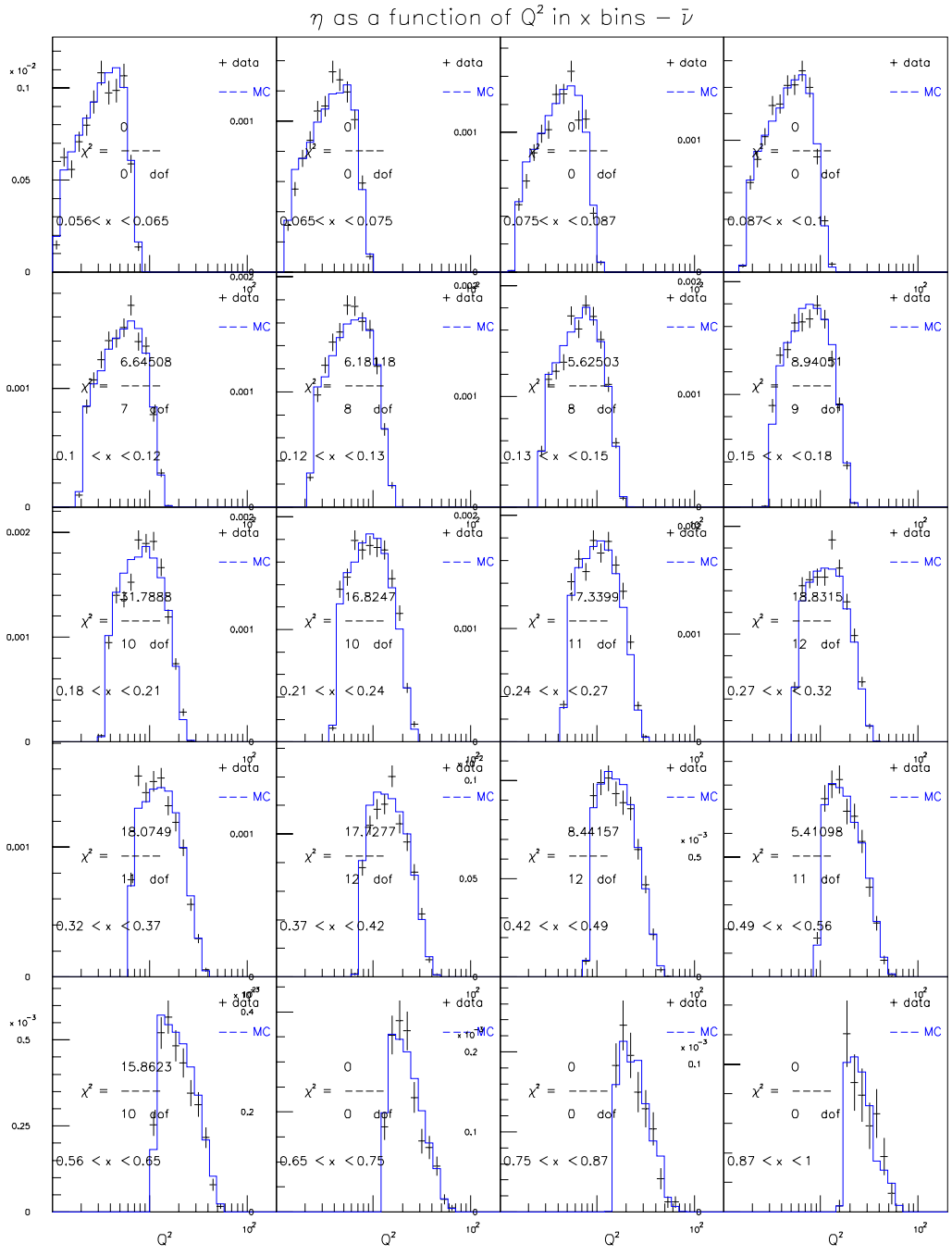

Figure E.74: CTEQ5NLO+EMC+HT for $62 < E_\nu < 85$ GeV ($\overline{\nu}$ mode)

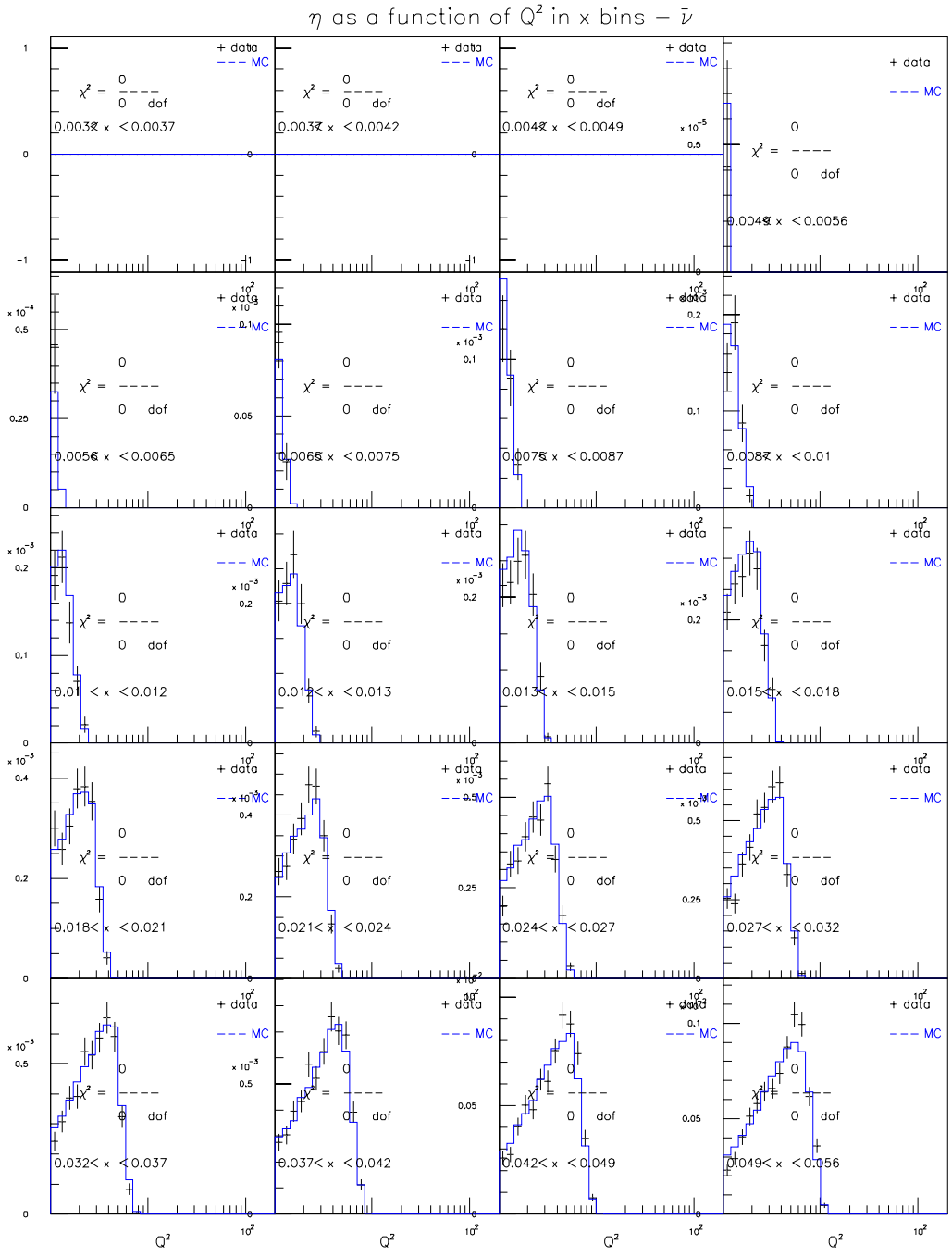

Figure E.75: CTEQ5NLO+EMC+HT for $85 < E_\nu < 129$ GeV ($\overline{\nu}$ mode)

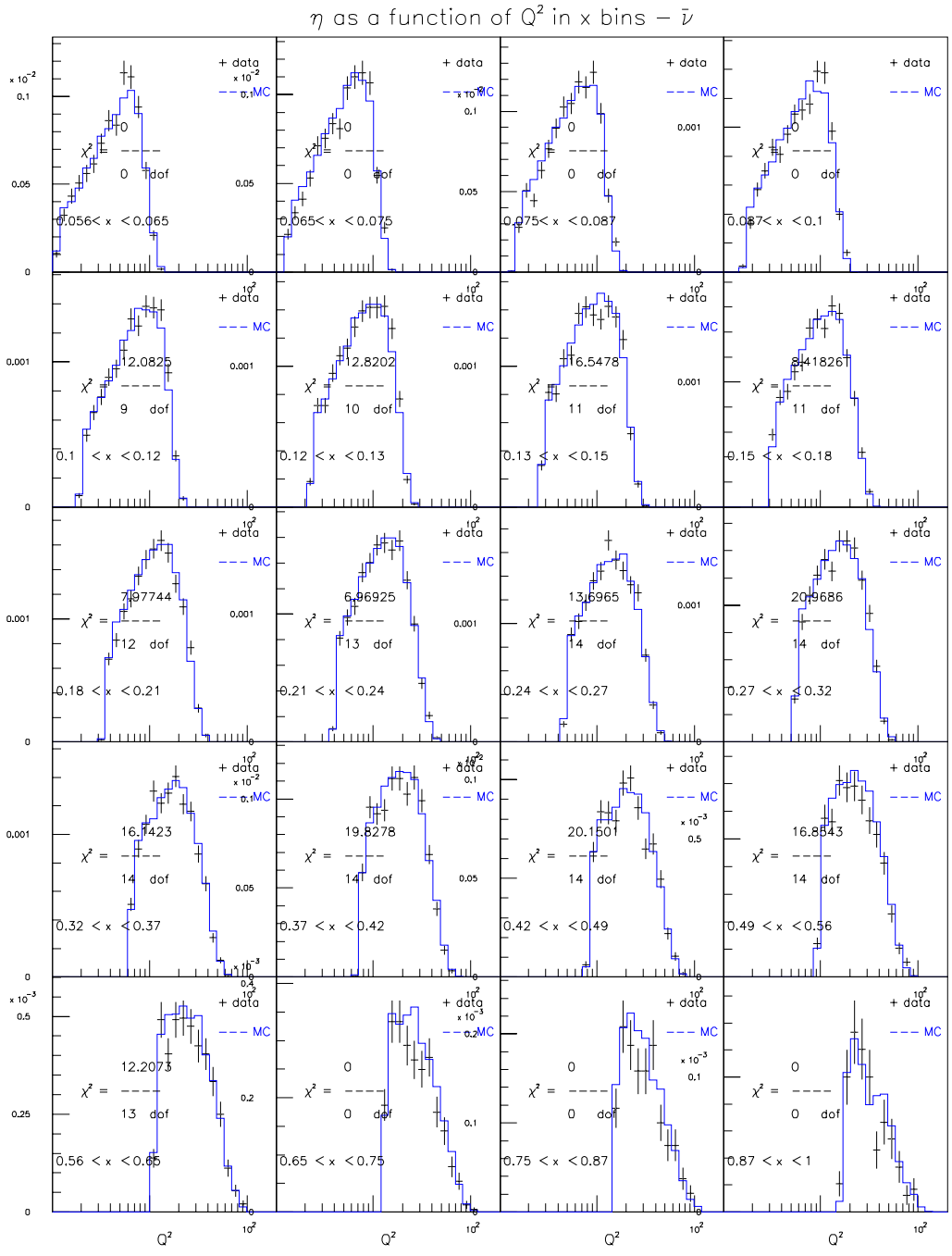

Figure E.76: CTEQ5NLO+EMC+HT for $85 < E_\nu < 129$ GeV ($\overline{\nu}$ mode)

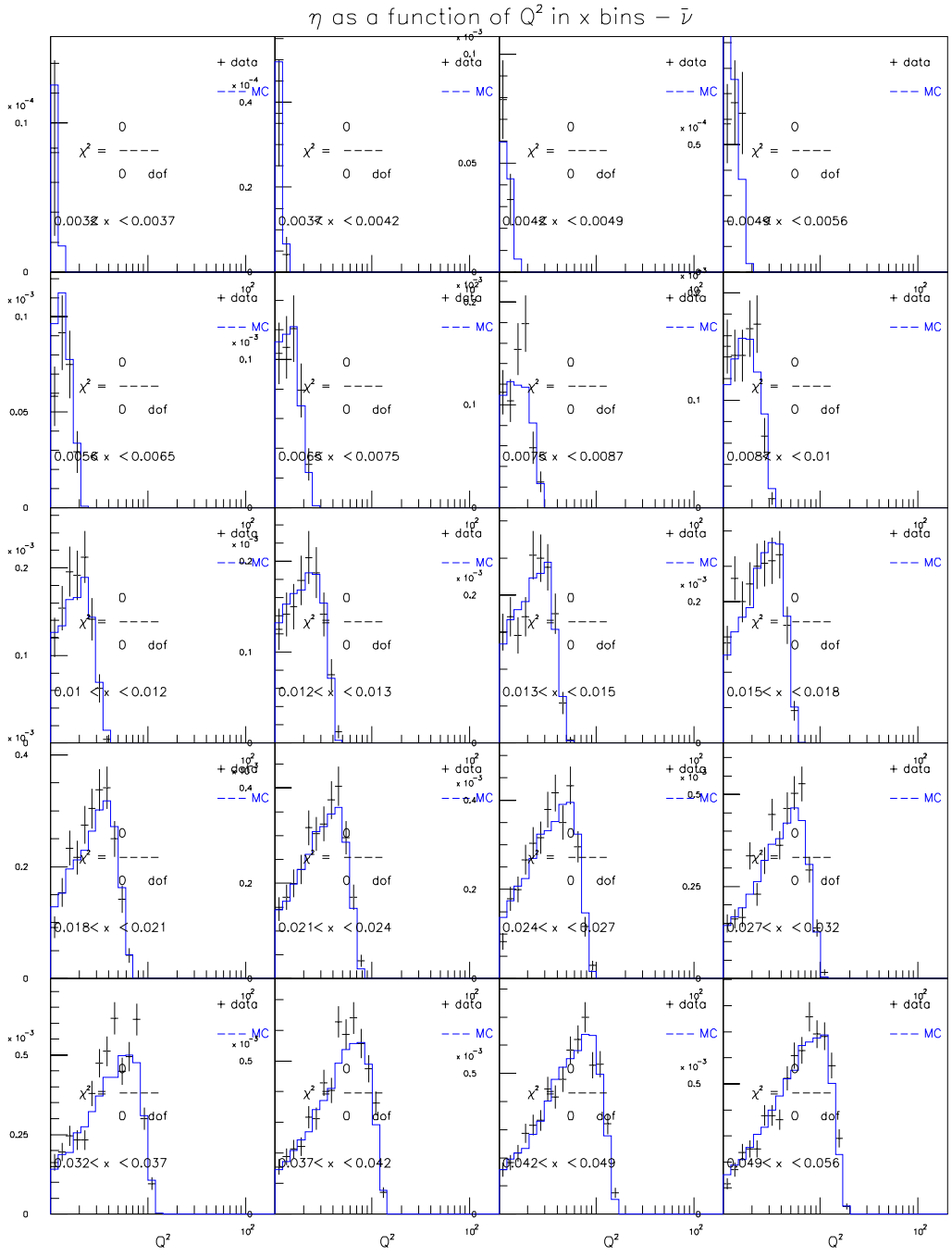

Figure E.77: CTEQ5NLO+EMC+HT for $129 < E_\nu < 201$ GeV ($\overline{\nu}$ mode)

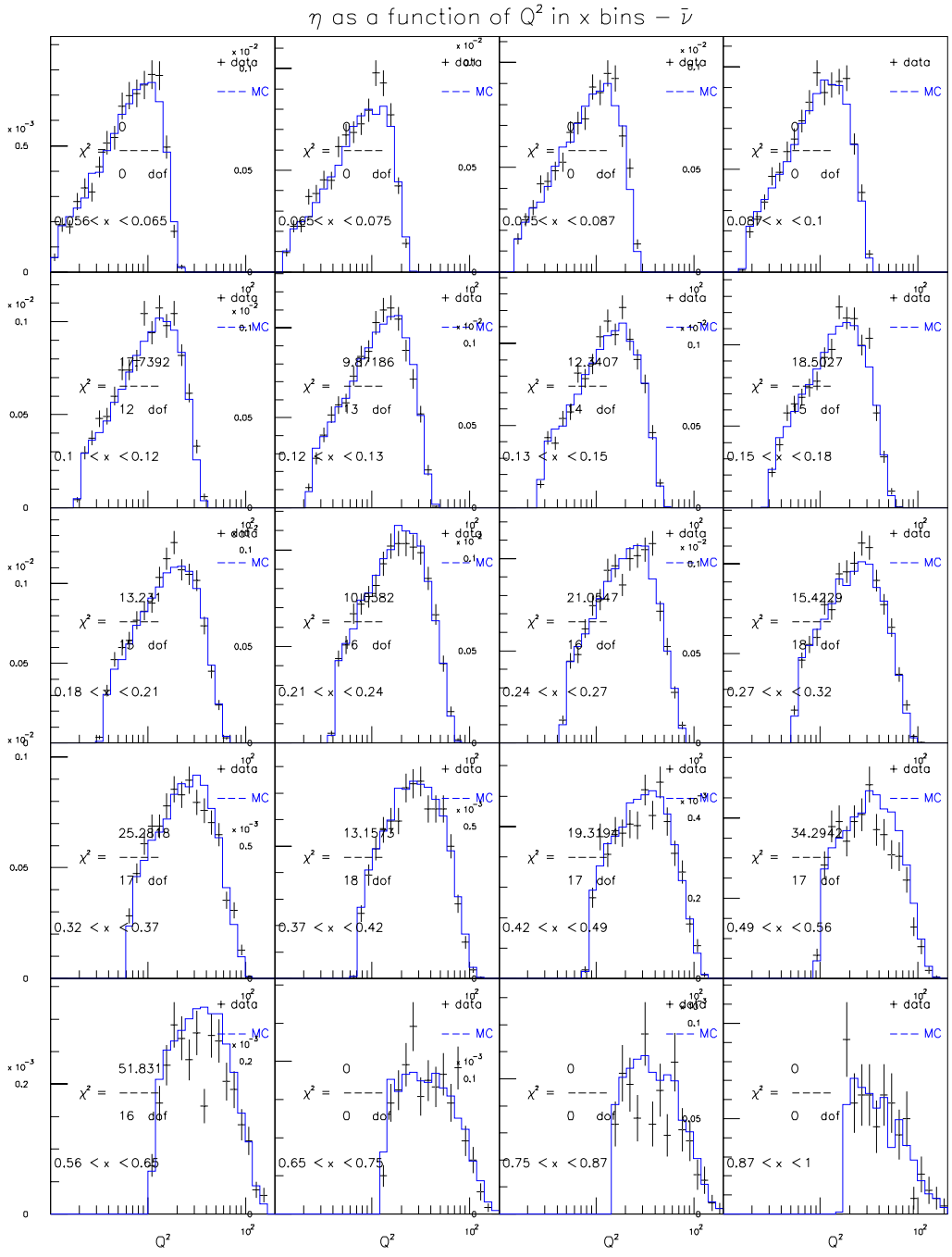

Figure E.78: CTEQ5NLO+EMC+HT for $129 < E_\nu < 201$ GeV ($\overline{\nu}$ mode)

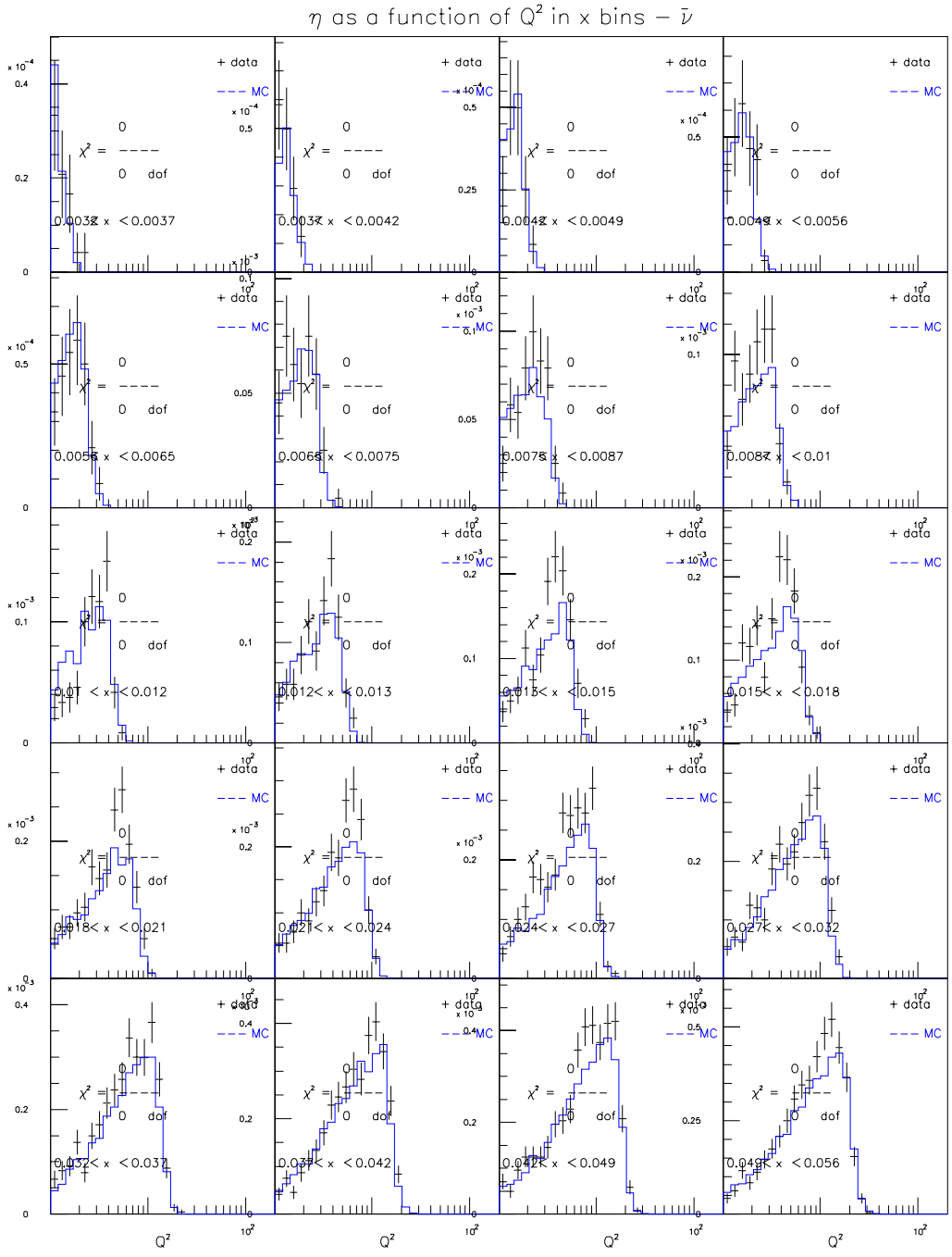

Figure E.79: CTEQ5NLO+EMC+HT for $201 < E_\nu < 400$ GeV ($\overline{\nu}$ mode)

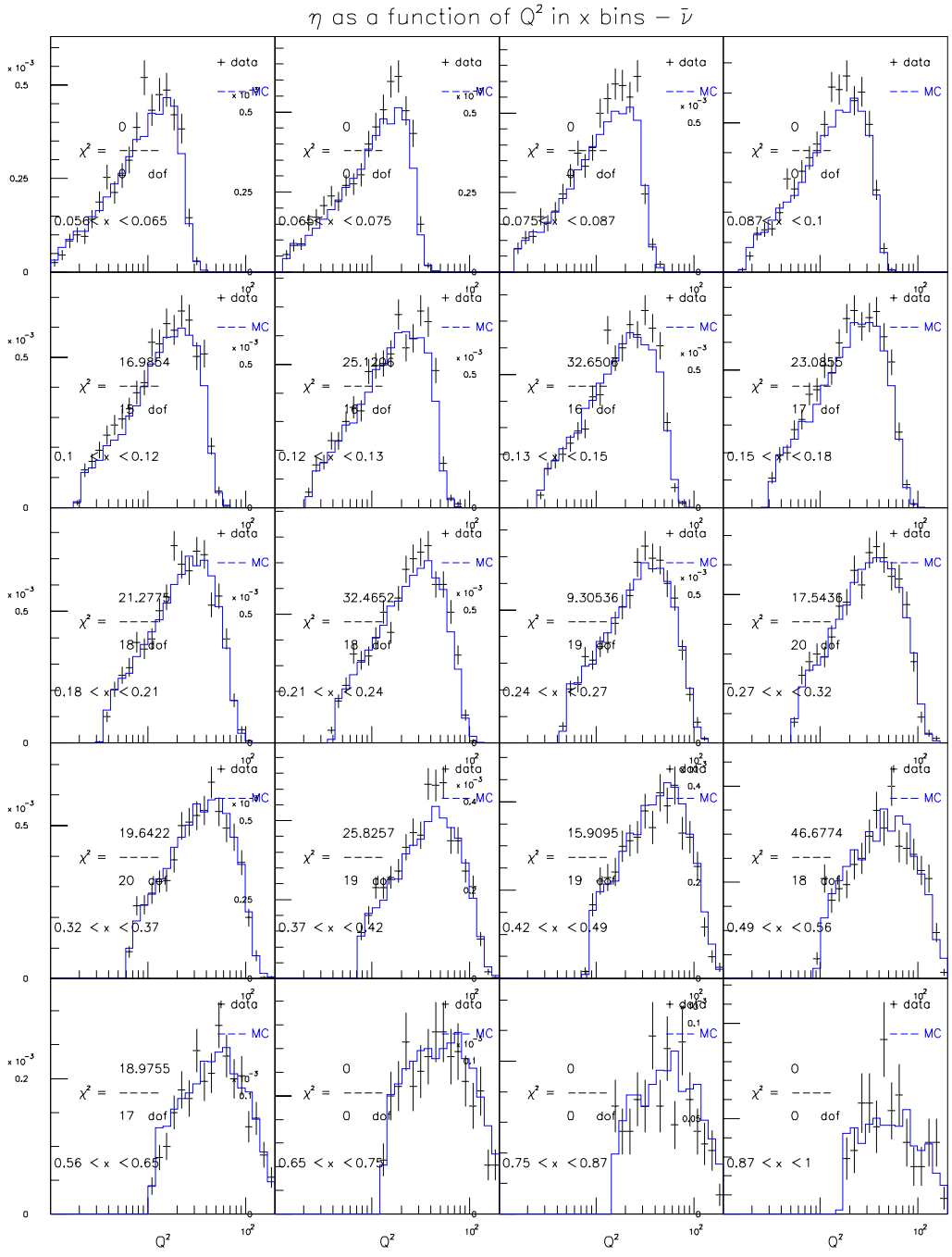

Figure E.80: CTEQ5NLO+EMC+HT for $201 < E_\nu < 400$ GeV ($\overline{\nu}$ mode)

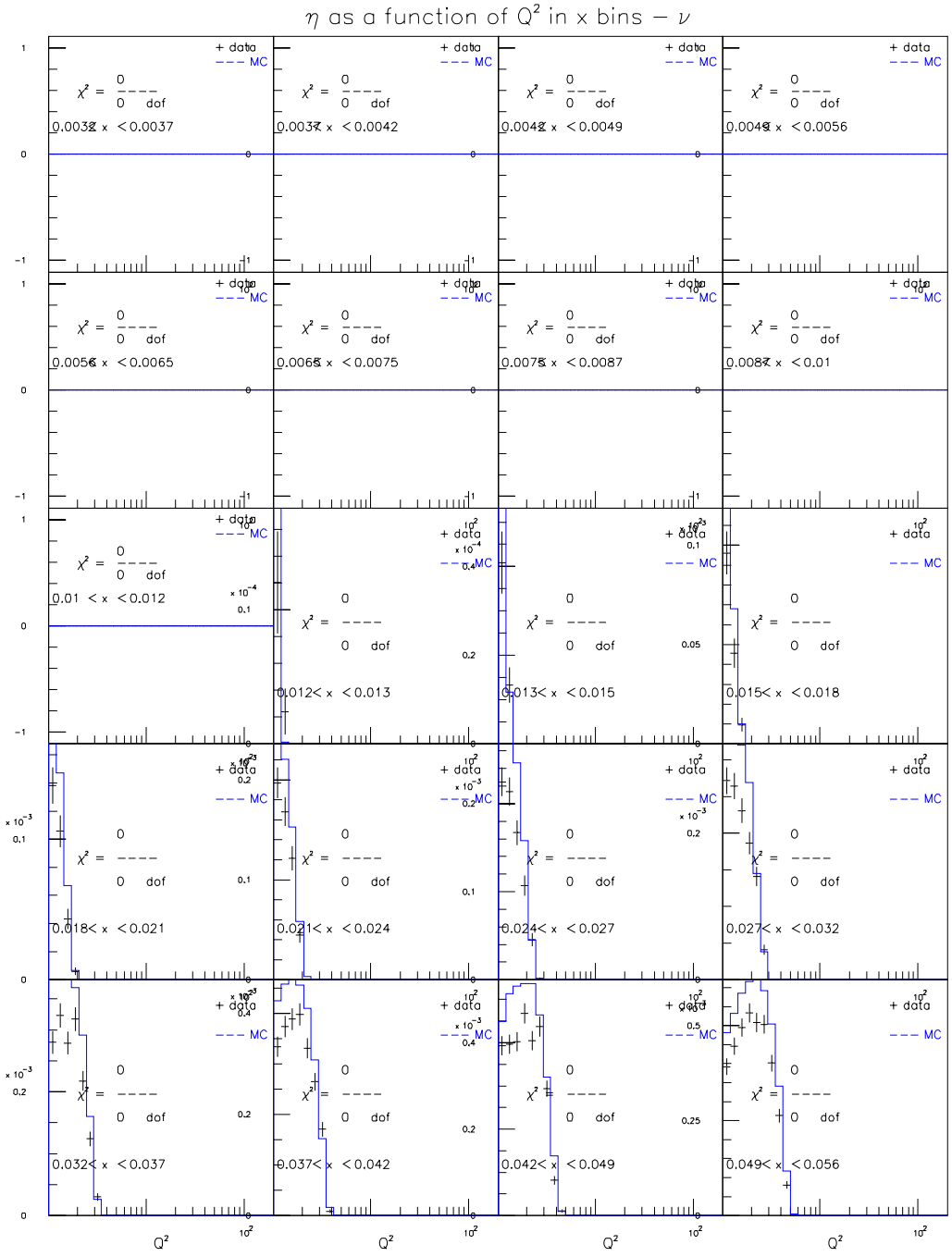

Figure E.81: GRV98LO+EMC for $20 < E_\nu < 62$ GeV (ν mode)

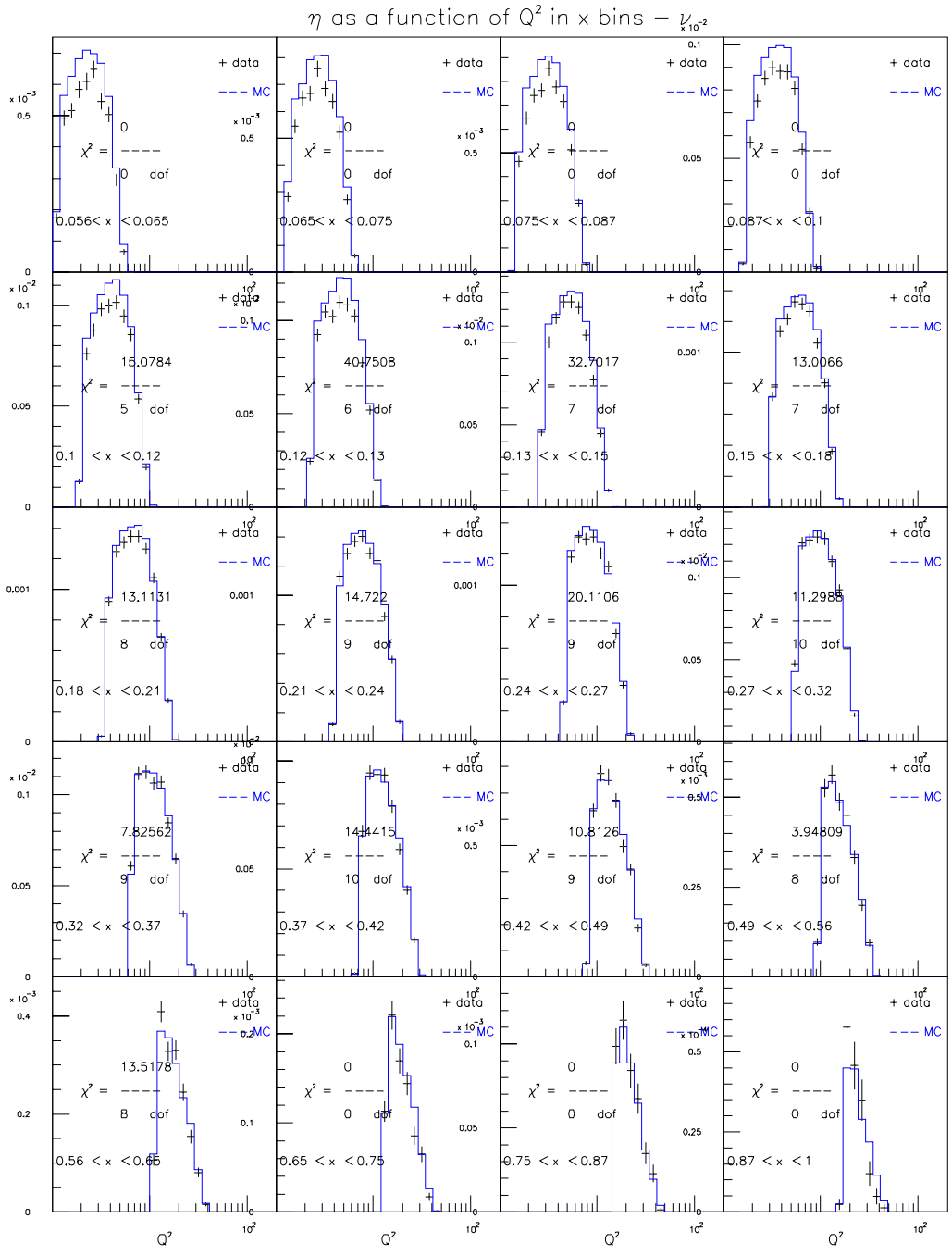

Figure E.82: GRV98LO+EMC for $20 < E_\nu < 62$ GeV (ν mode)

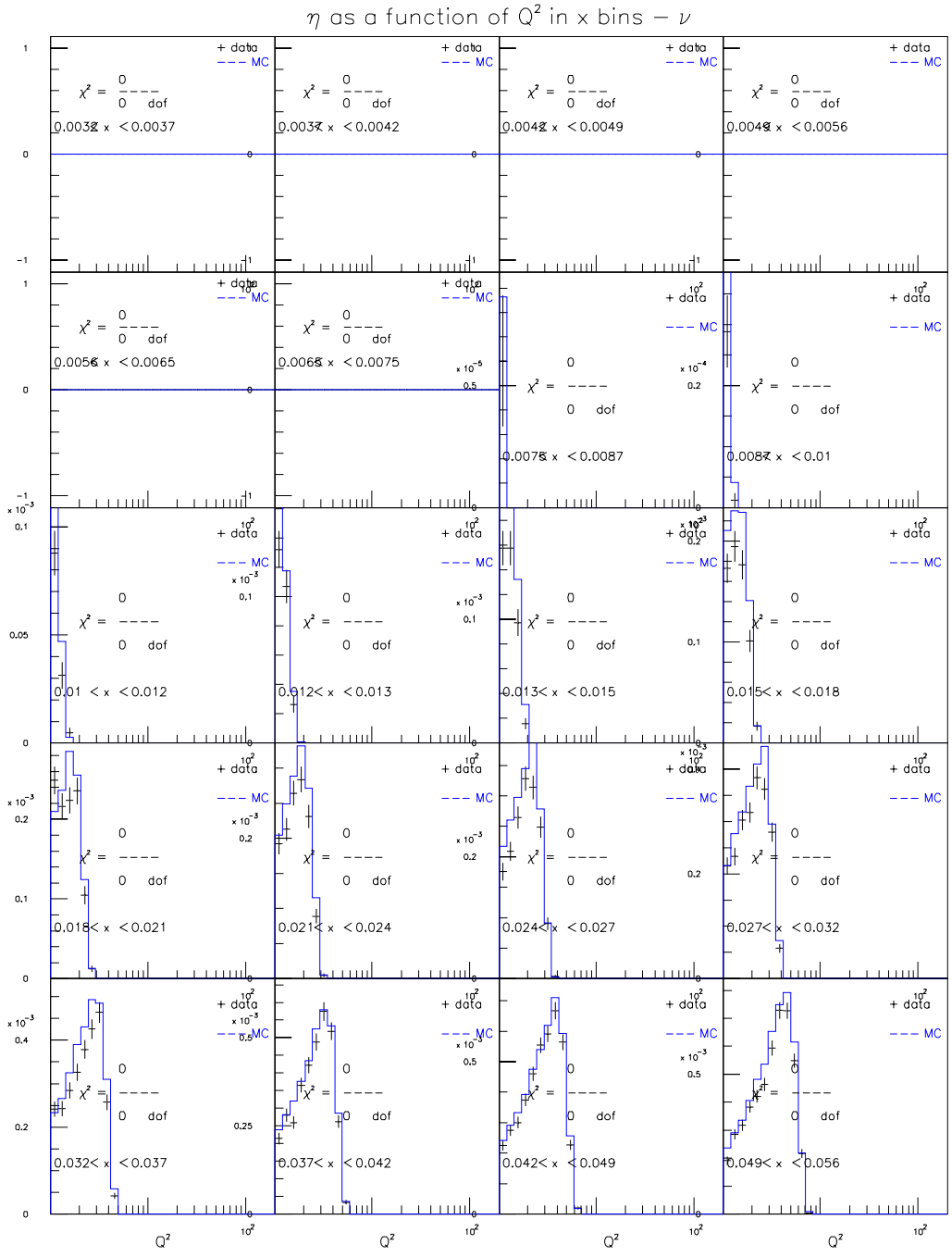

Figure E.83: GRV98LO+EMC for $62 < E_\nu < 85$ GeV (ν mode)

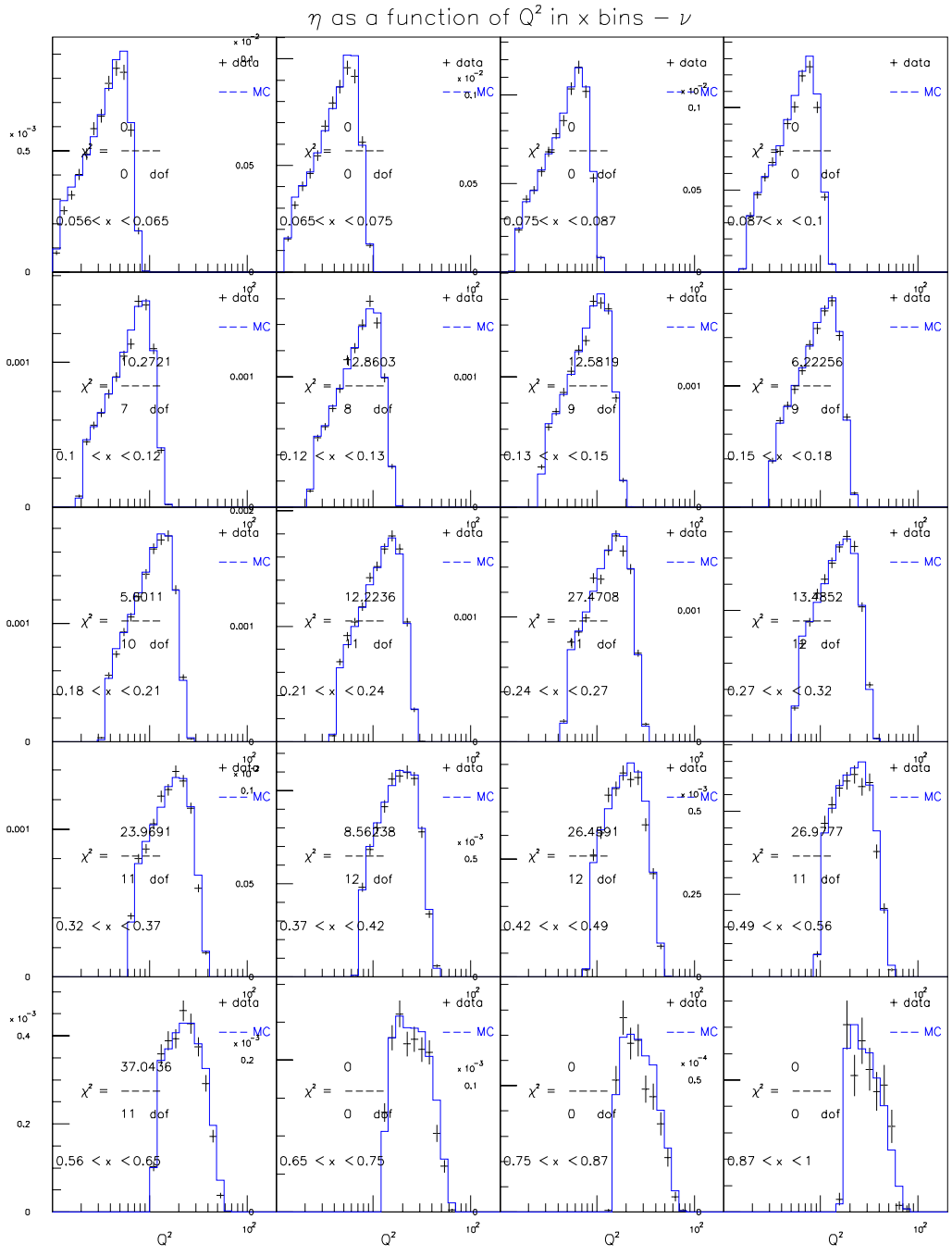

Figure E.84: GRV98LO+EMC for $62 < E_\nu < 85$ GeV (ν mode)

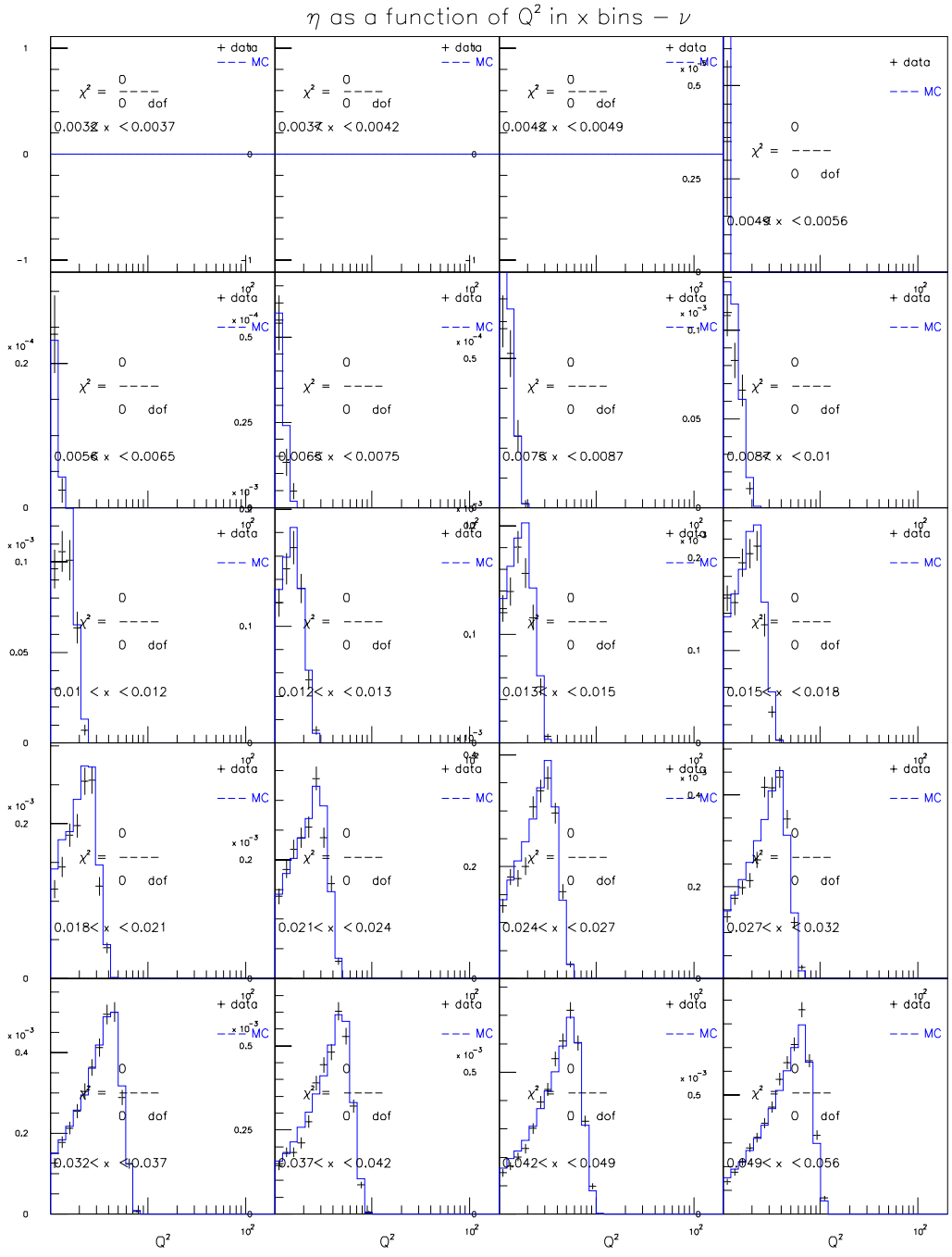

Figure E.85: GRV98LO+EMC for $85 < E_\nu < 129$ GeV (ν mode)

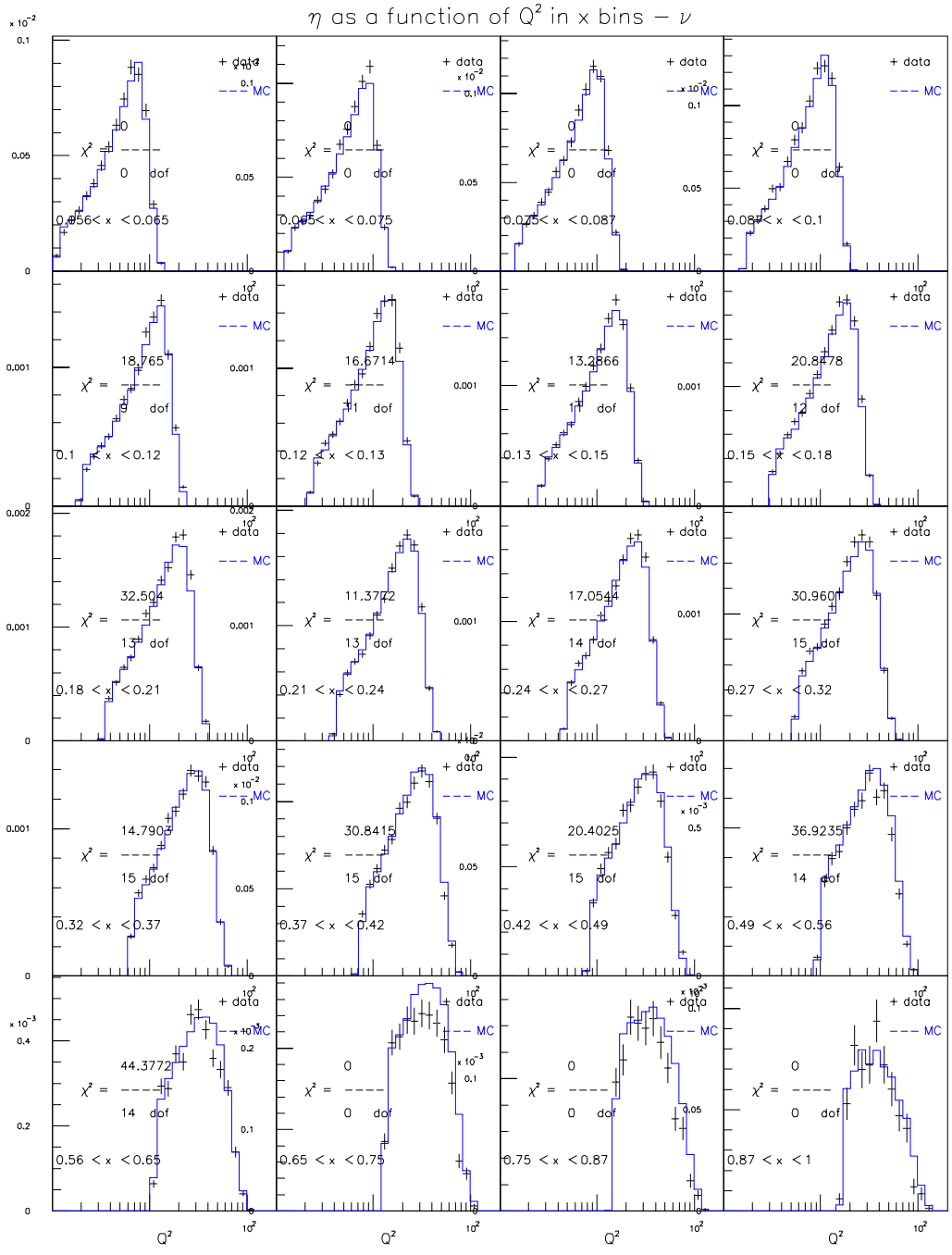

Figure E.86: GRV98LO+EMC for $85 < E_\nu < 129$ GeV (ν mode)

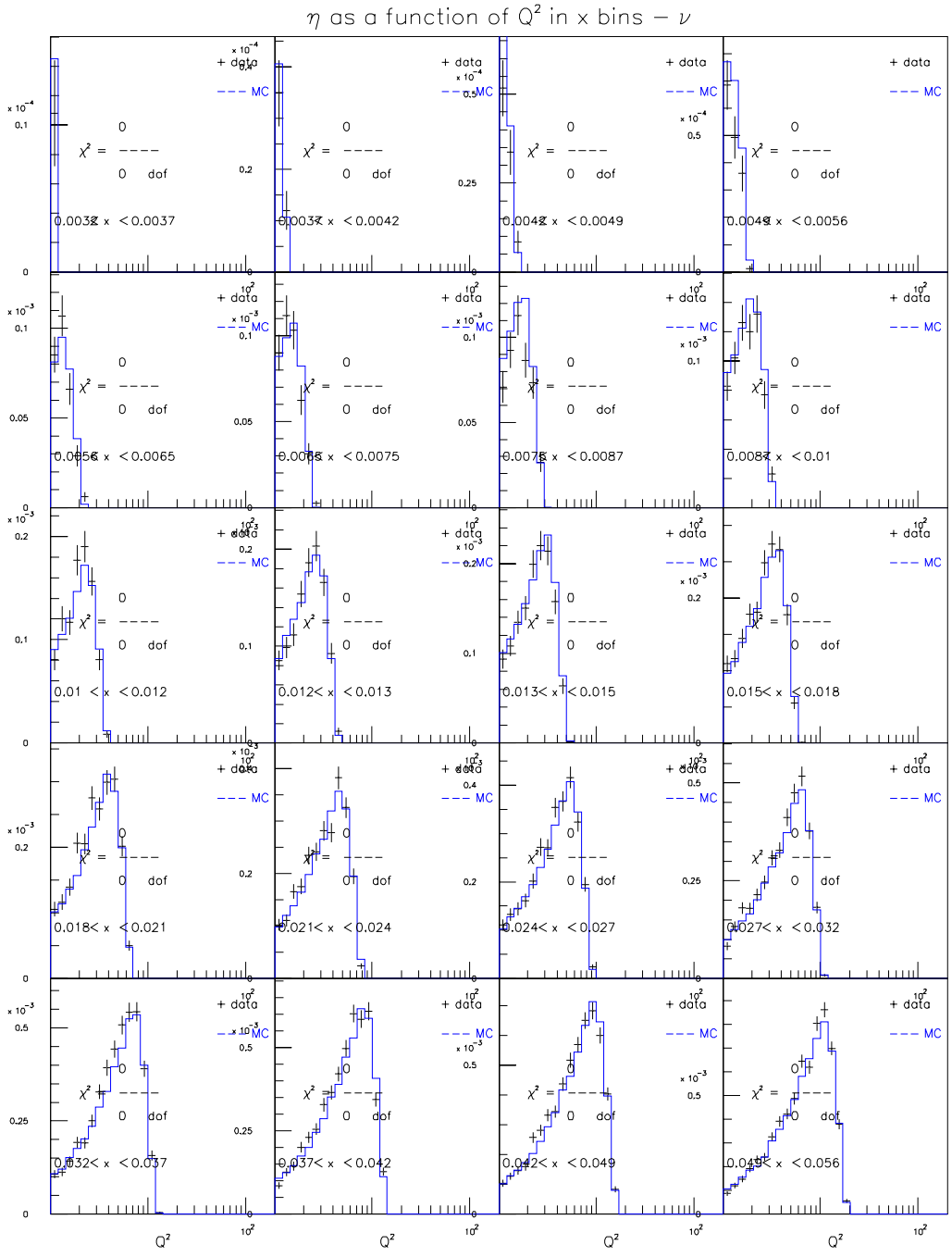

Figure E.87: GRV98LO+EMC for $129 < E_\nu < 201$ GeV (ν mode)

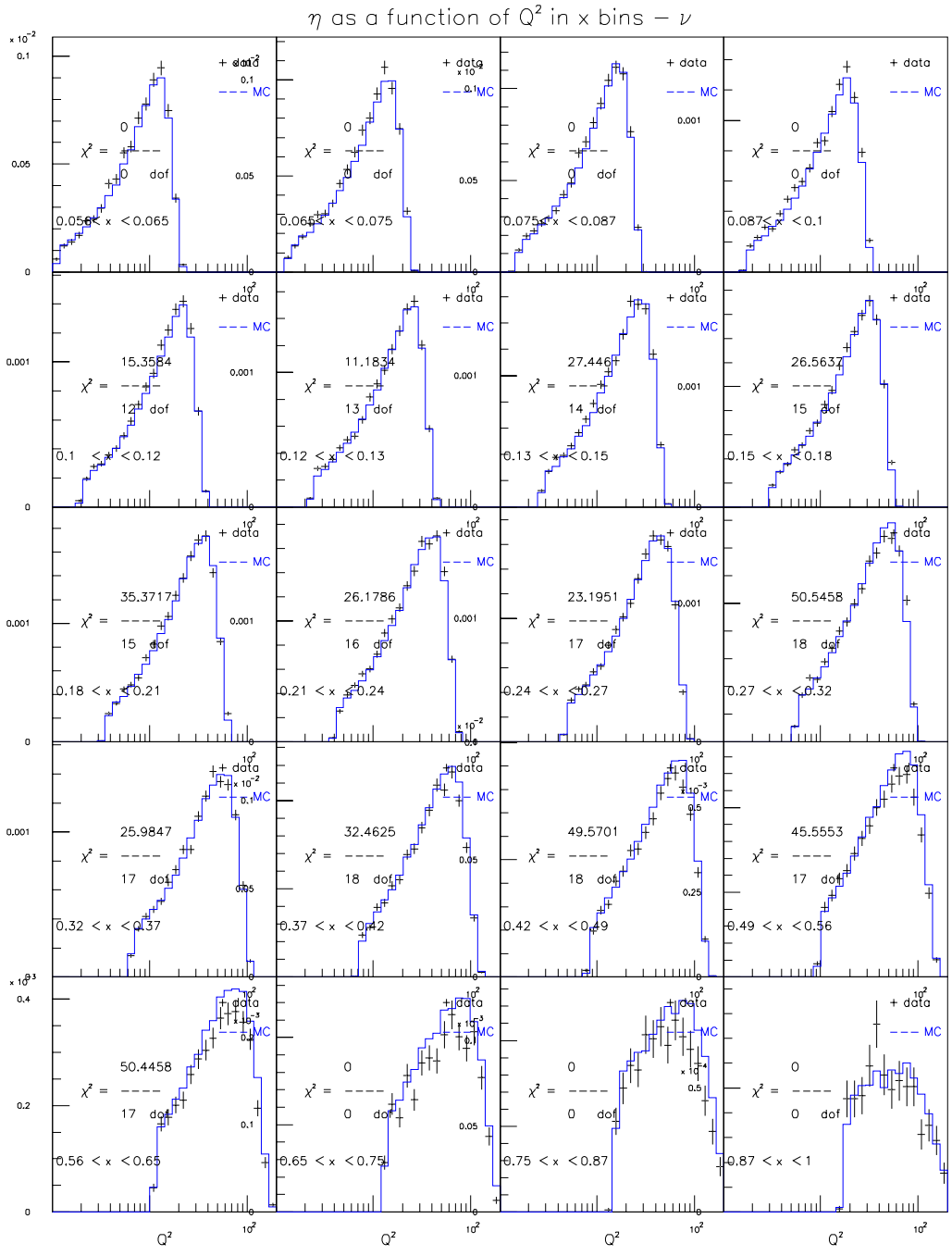

Figure E.88: GRV98LO+EMC for $129 < E_\nu < 201$ GeV (ν mode)

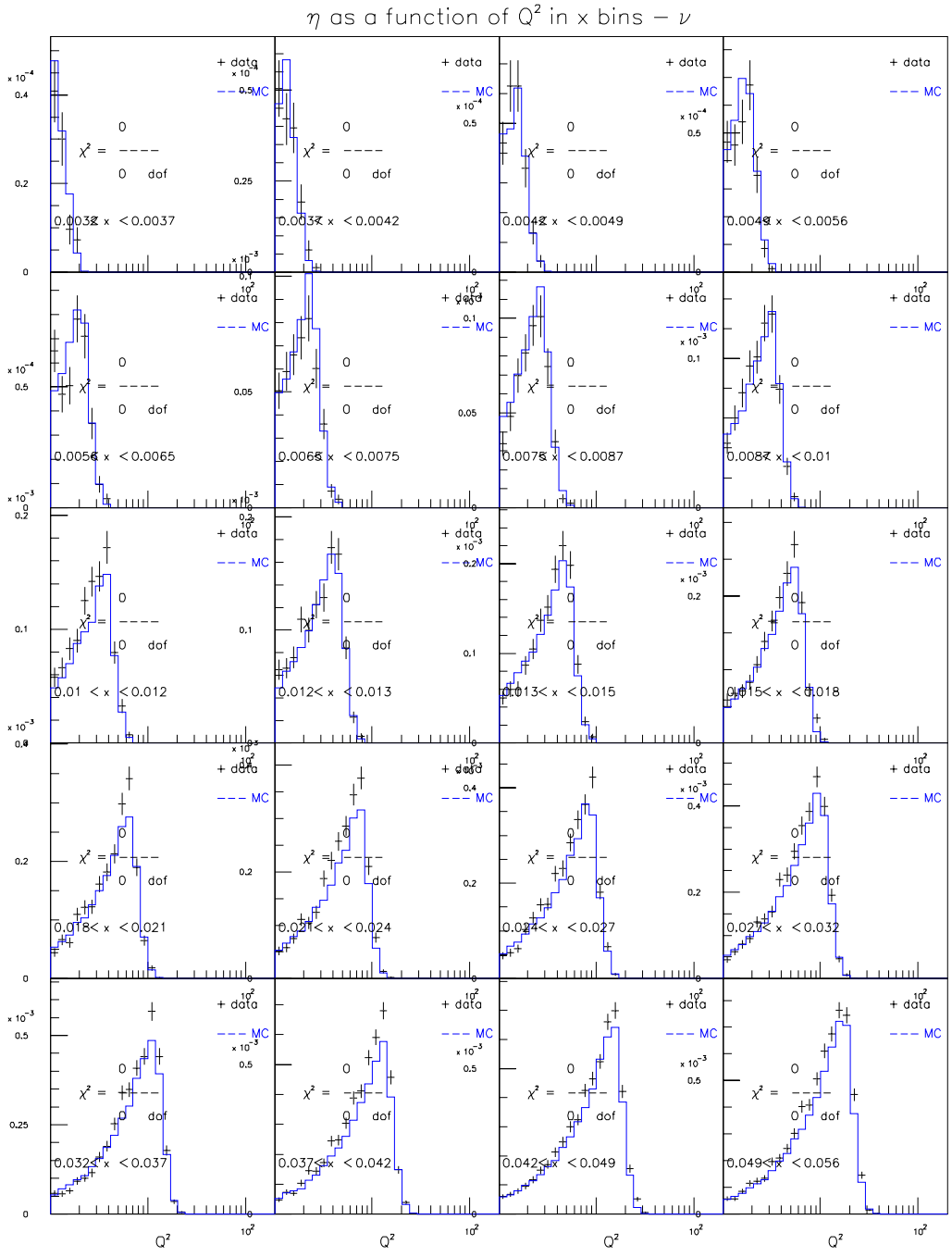

Figure E.89: GRV98LO+EMCfor $201 < E_\nu < 400$ GeV (ν mode)

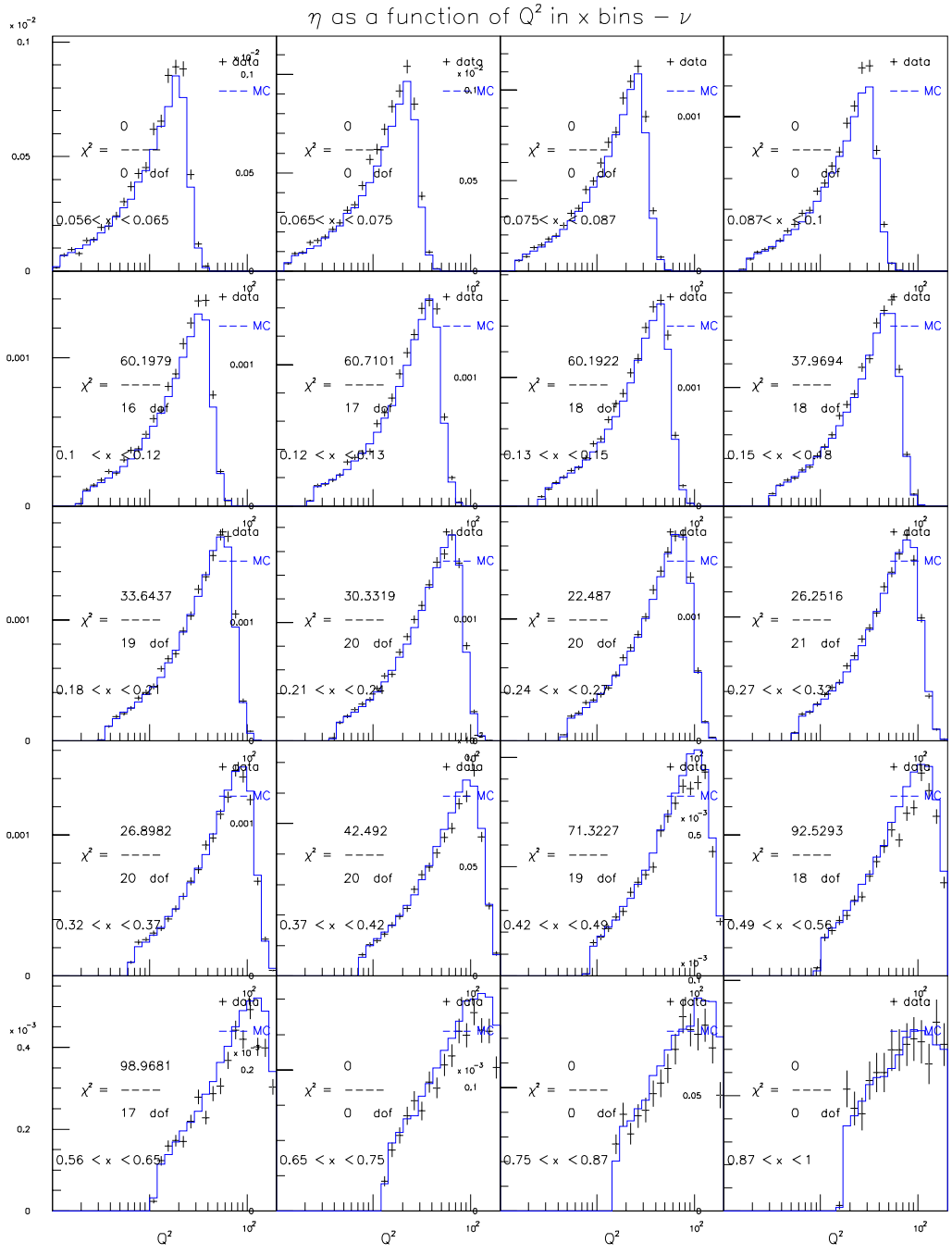

Figure E.90: GRV98LO+EMC for $201 < E_\nu < 400$ GeV (ν mode)

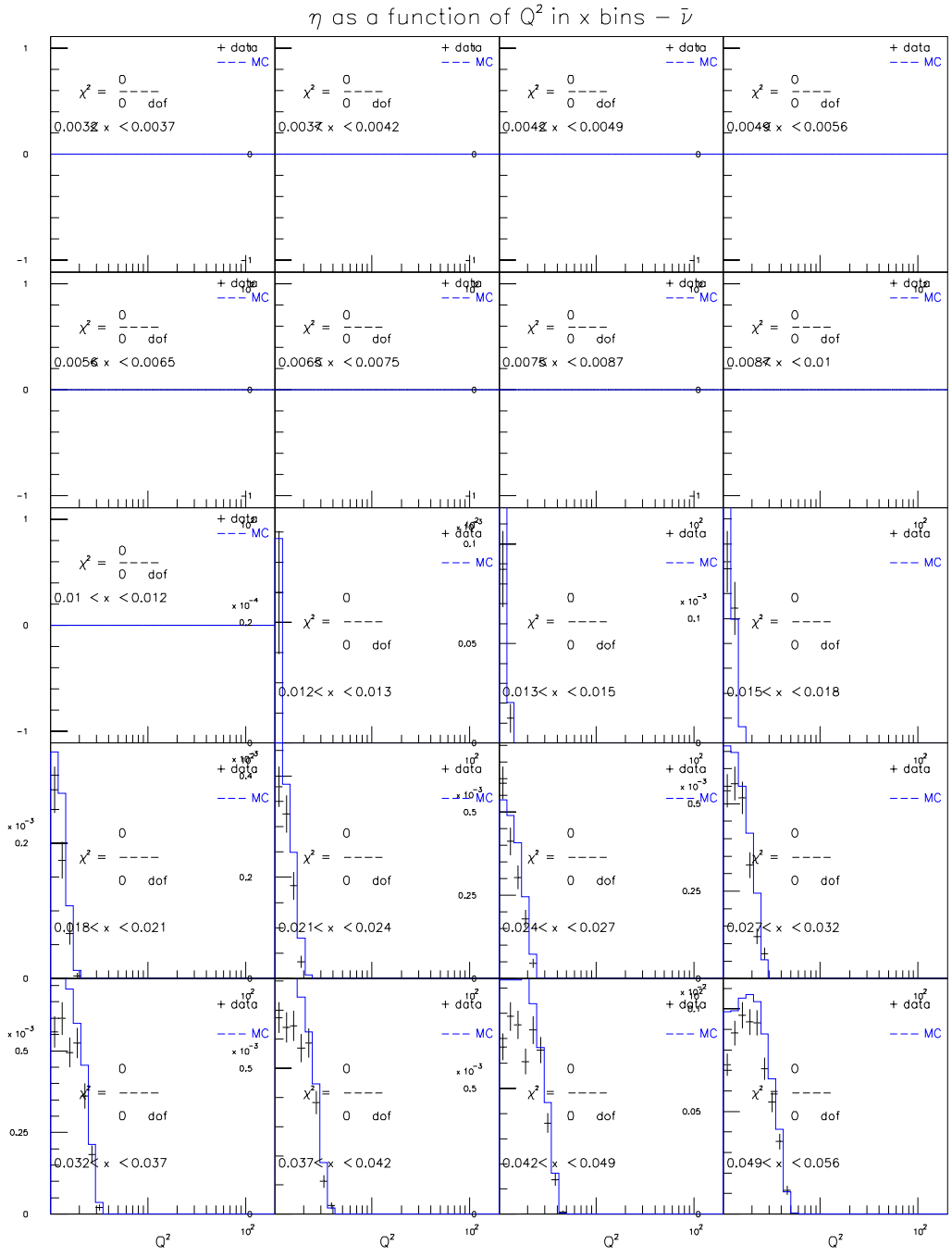

Figure E.91: GRV98LO+EMC for $20 < E_\nu < 62$ GeV ($\overline{\nu}$ mode)

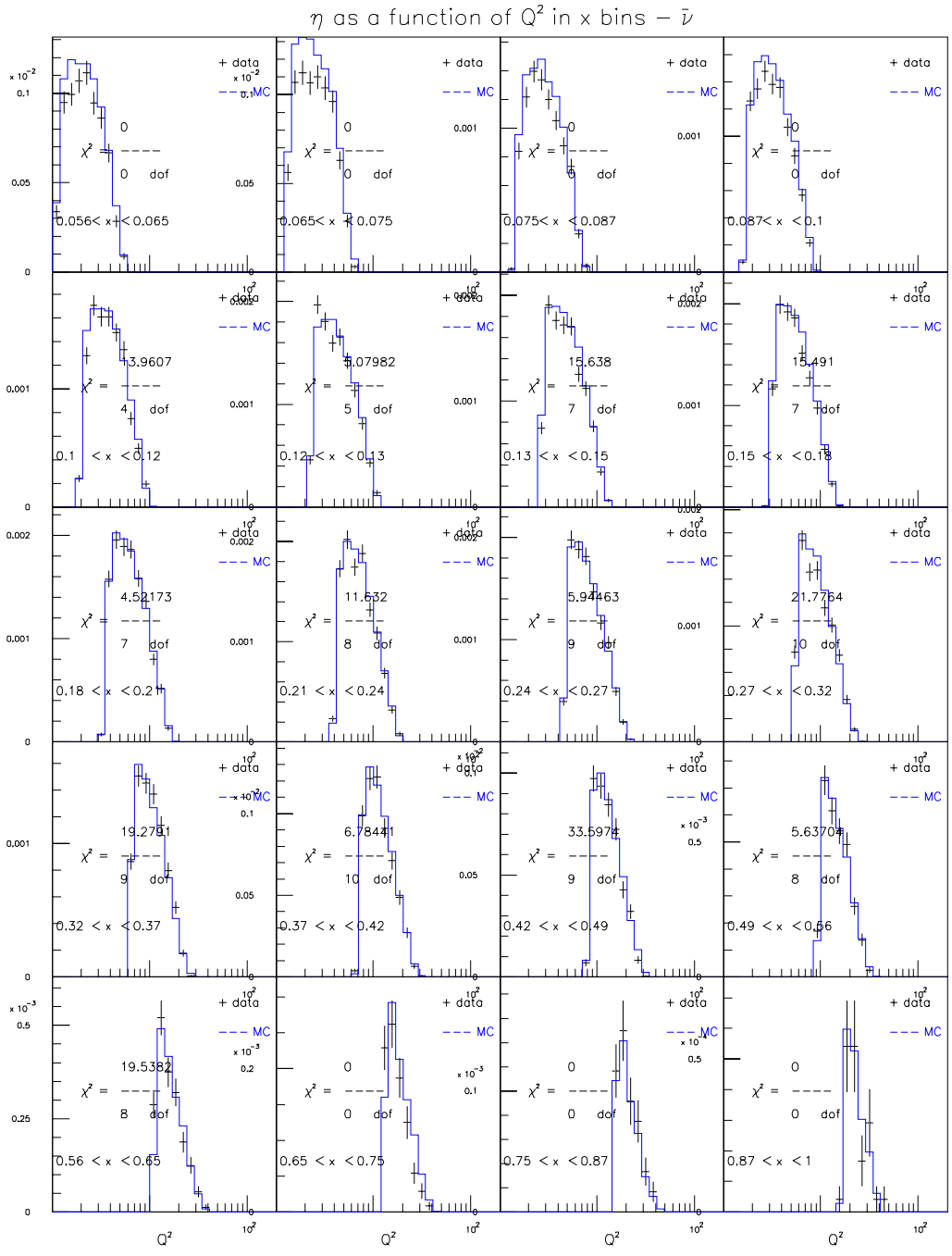

Figure E.92: GRV98LO+EMC for $20 < E_\nu < 62$ GeV ($\overline{\nu}$ mode)

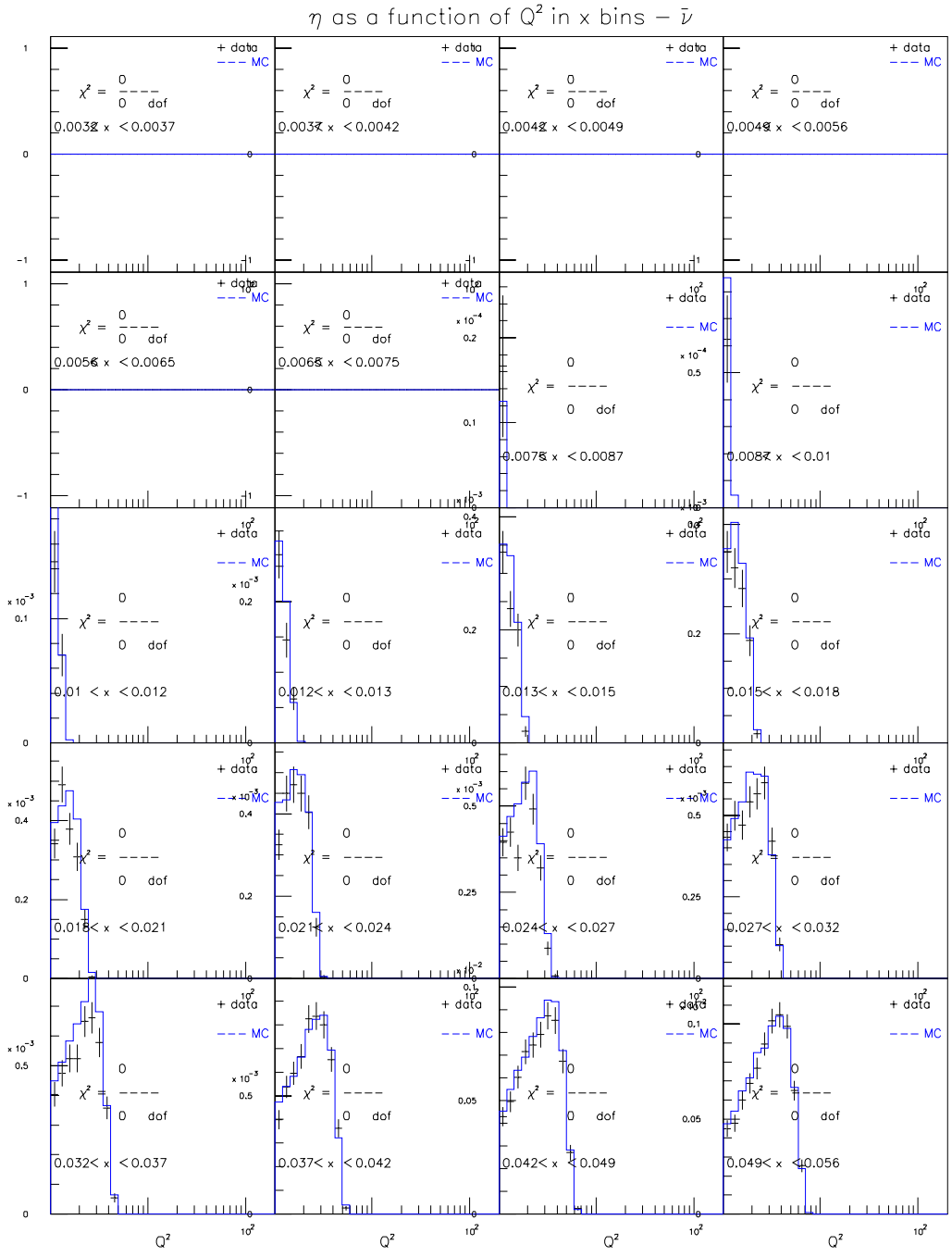

Figure E.93: GRV98LO+EMC for $62 < E_\nu < 85$ GeV ($\overline{\nu}$ mode)

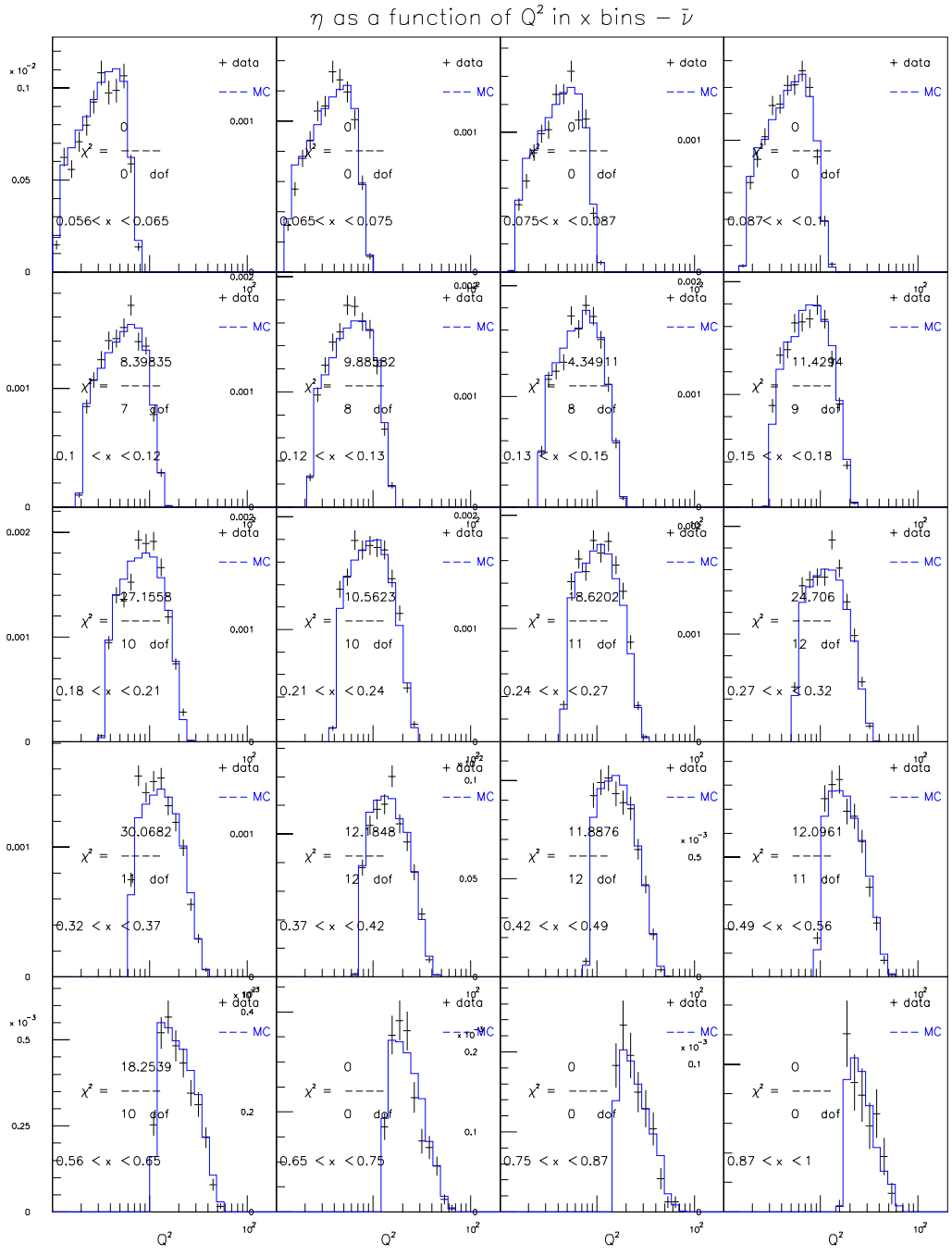

Figure E.94: GRV98LO+EMC for $62 < E_\nu < 85$ GeV ($\overline{\nu}$ mode)

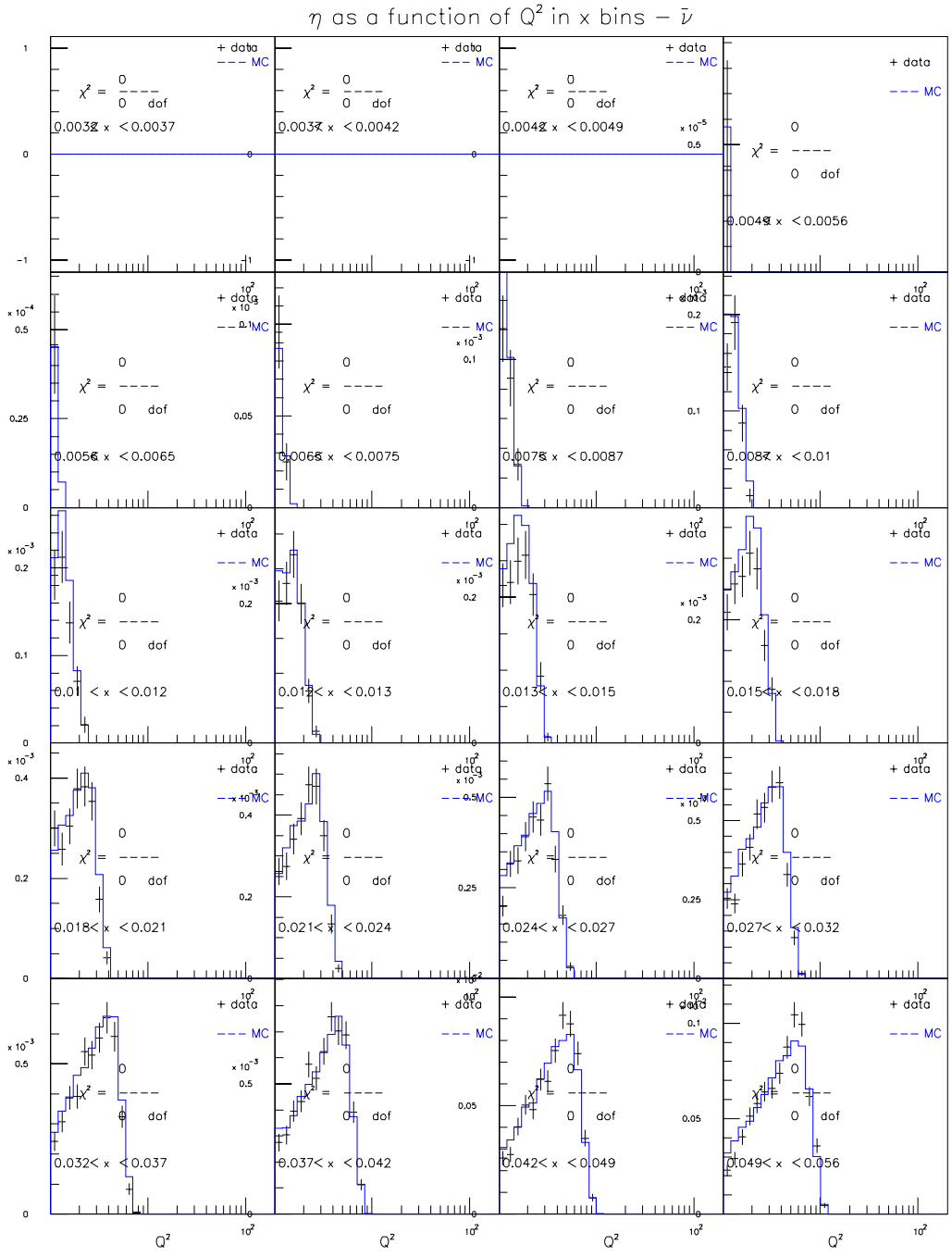

Figure E.95: GRV98LO+EMC for $85 < E_\nu < 129$ GeV ($\overline{\nu}$ mode)

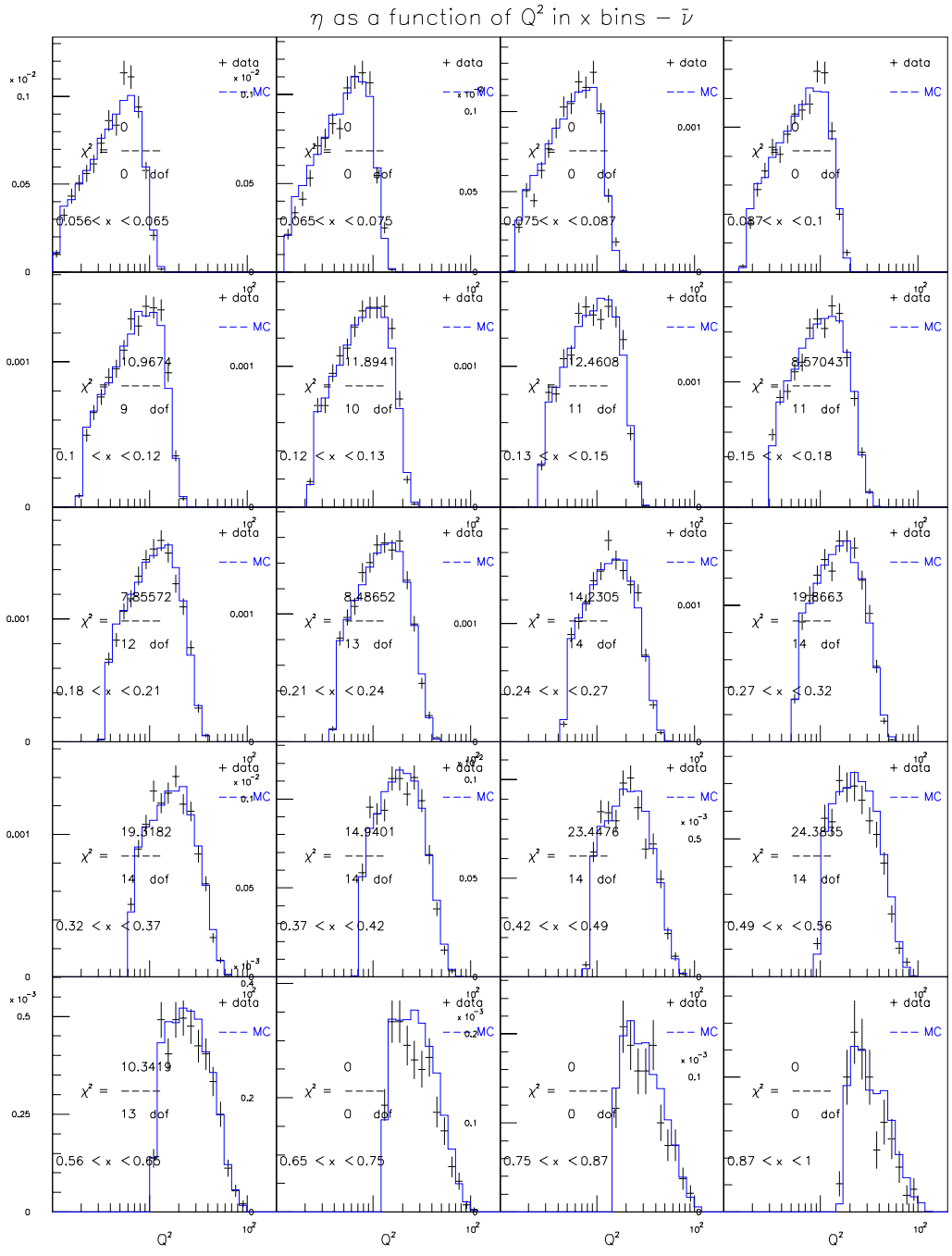

Figure E.96: GRV98LO+EMC for $85 < E_\nu < 129$ GeV ($\overline{\nu}$ mode)

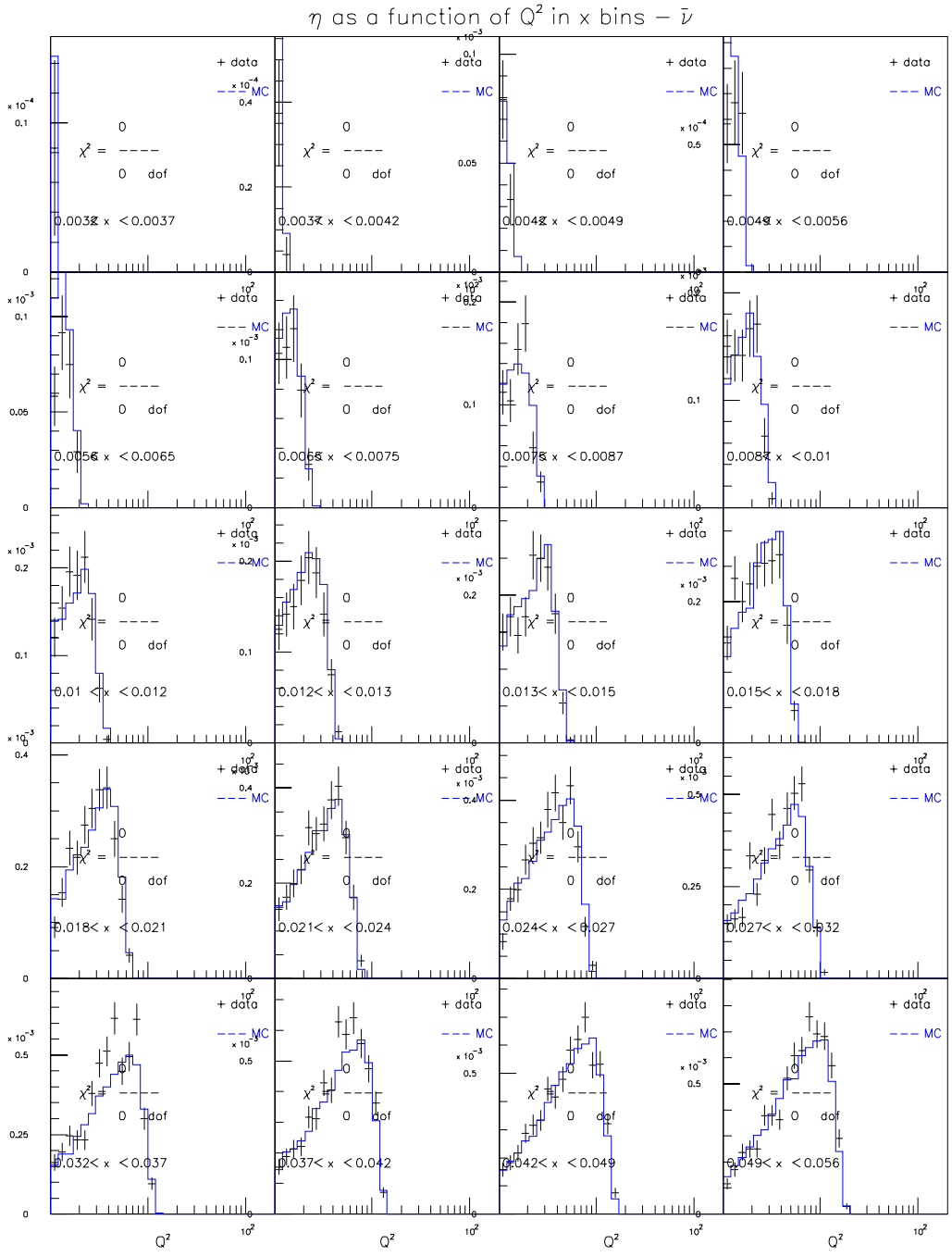

Figure E.97: GRV98LO+EMC for $129 < E_\nu < 201$ GeV ($\overline{\nu}$ mode)

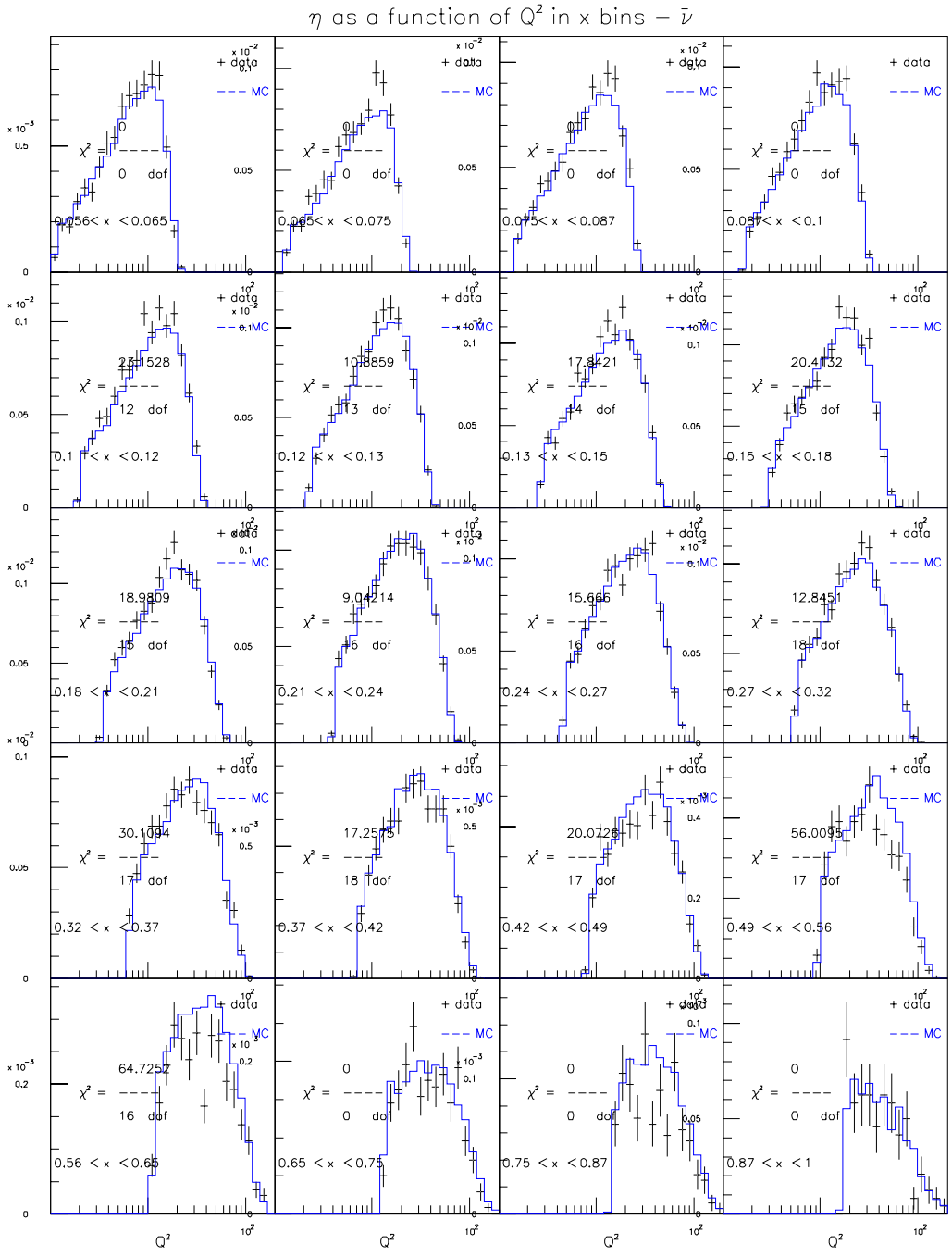

Figure E.98: GRV98LO+EMC for $129 < E_\nu < 201$ GeV ($\overline{\nu}$ mode)

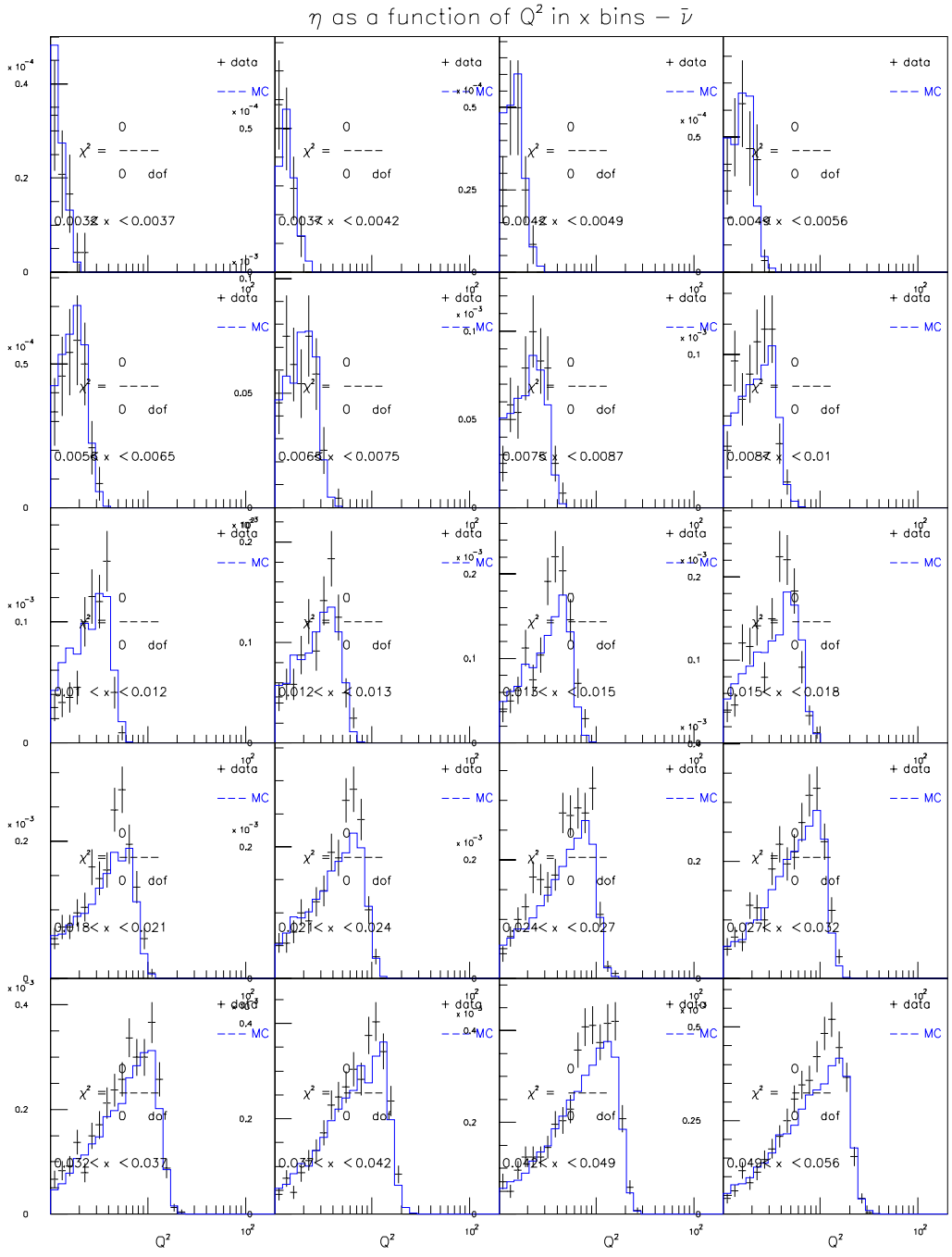

Figure E.99: GRV98LO+EMC for $201 < E_\nu < 400$ GeV ($\overline{\nu}$ mode)

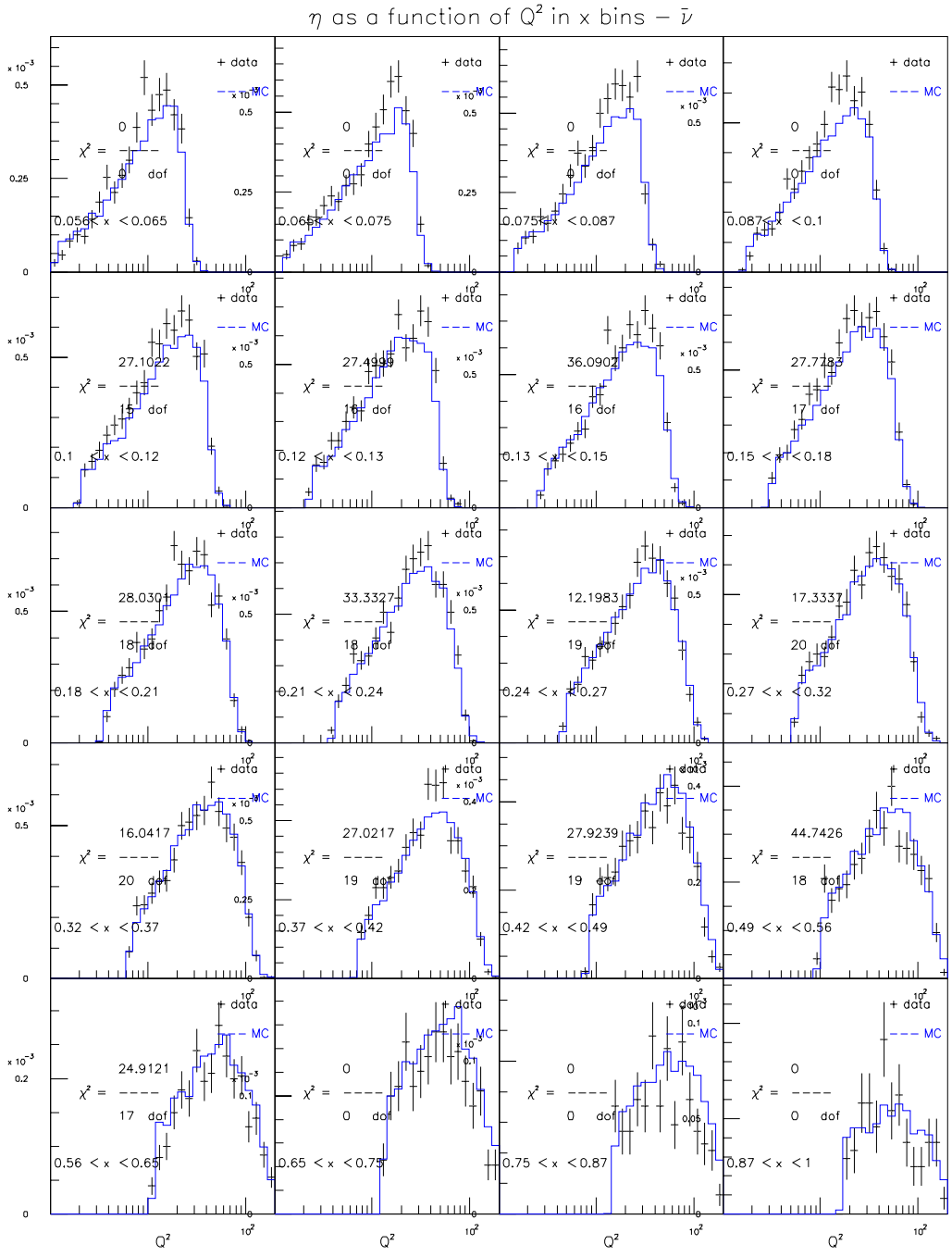

Figure E.100: GRV98LO+EMC for $201 < E_\nu < 400$ GeV ($\overline{\nu}$ mode)

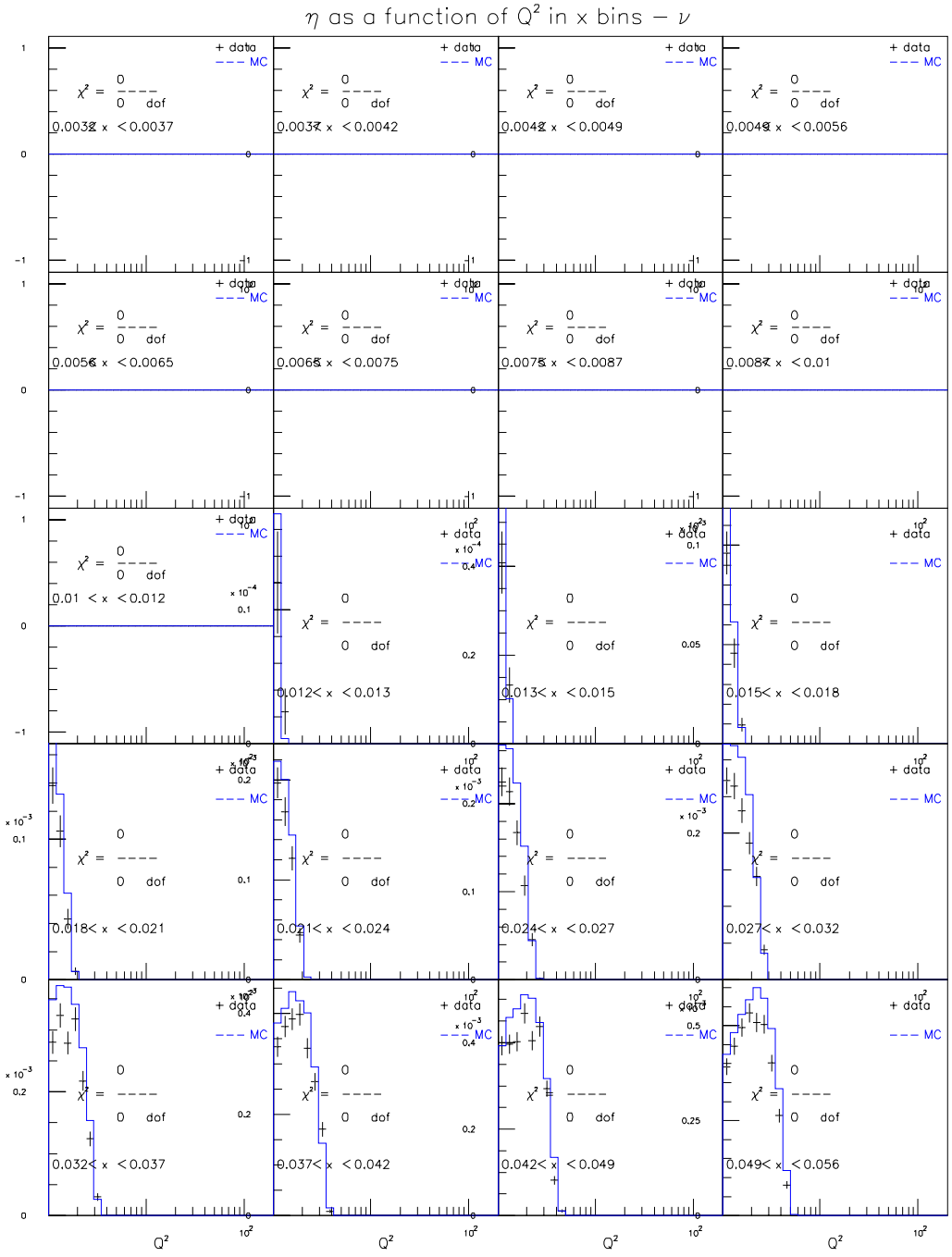

Figure E.101: BGPAR for $20 < E_\nu < 62$ GeV (ν mode)

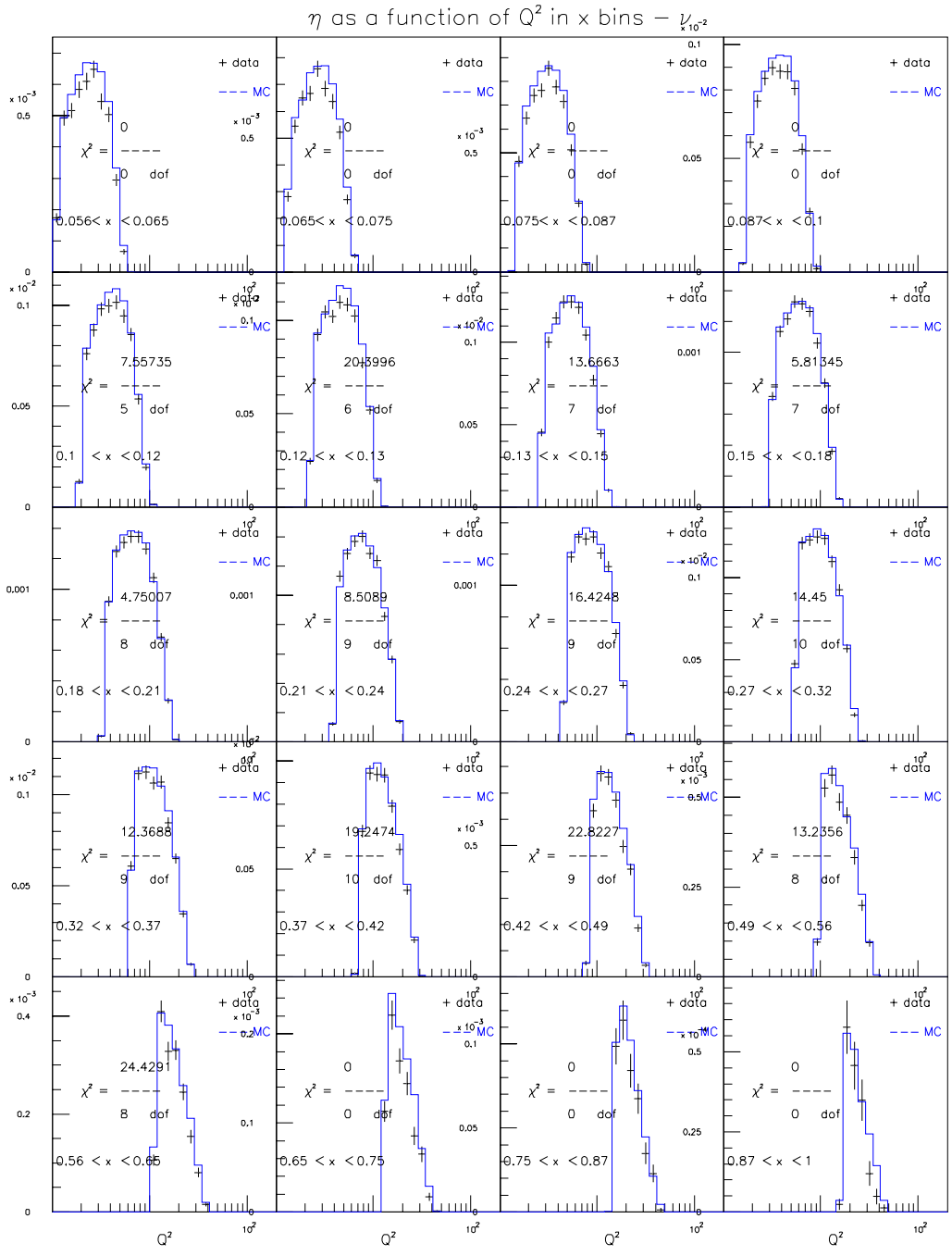

Figure E.102: BGPAR for $20 < E_\nu < 62$ GeV (ν mode)

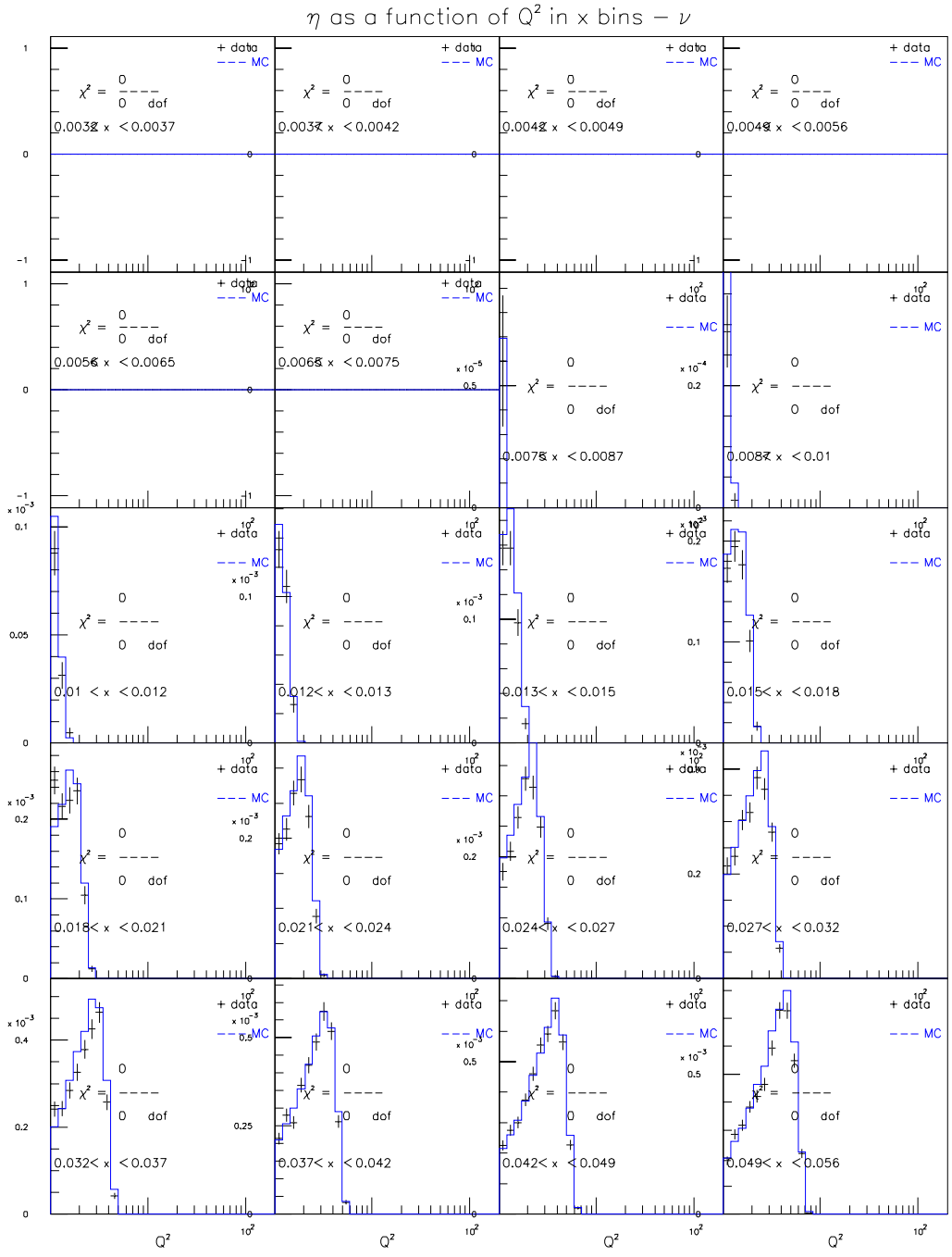

Figure E.103: BGPAR for $62 < E_\nu < 85$ GeV (ν mode)

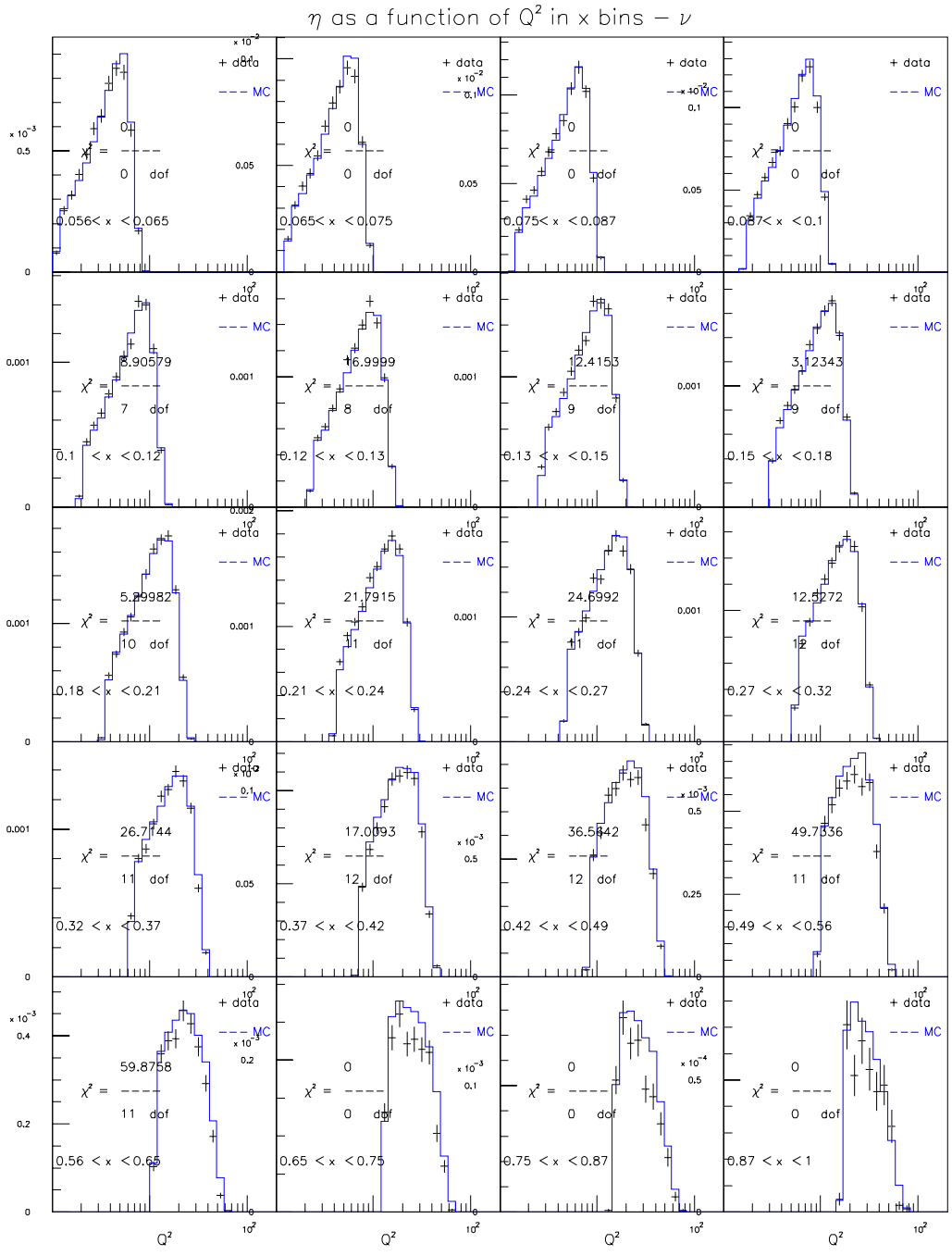

Figure E.104: BGPAR for $62 < E_\nu < 85$ GeV (ν mode)

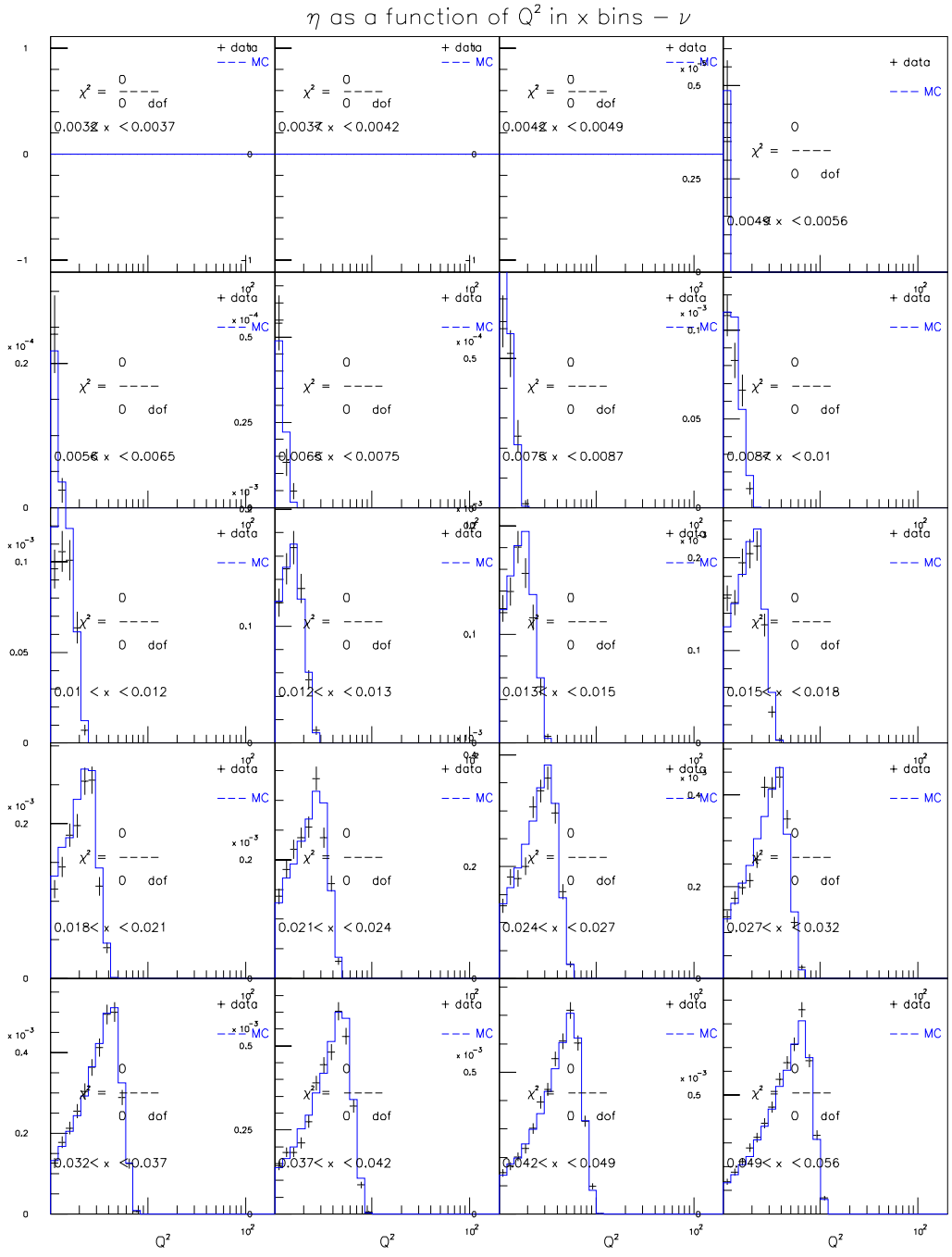

Figure E.105: BGPAR for $85 < E_\nu < 129$ GeV (ν mode)

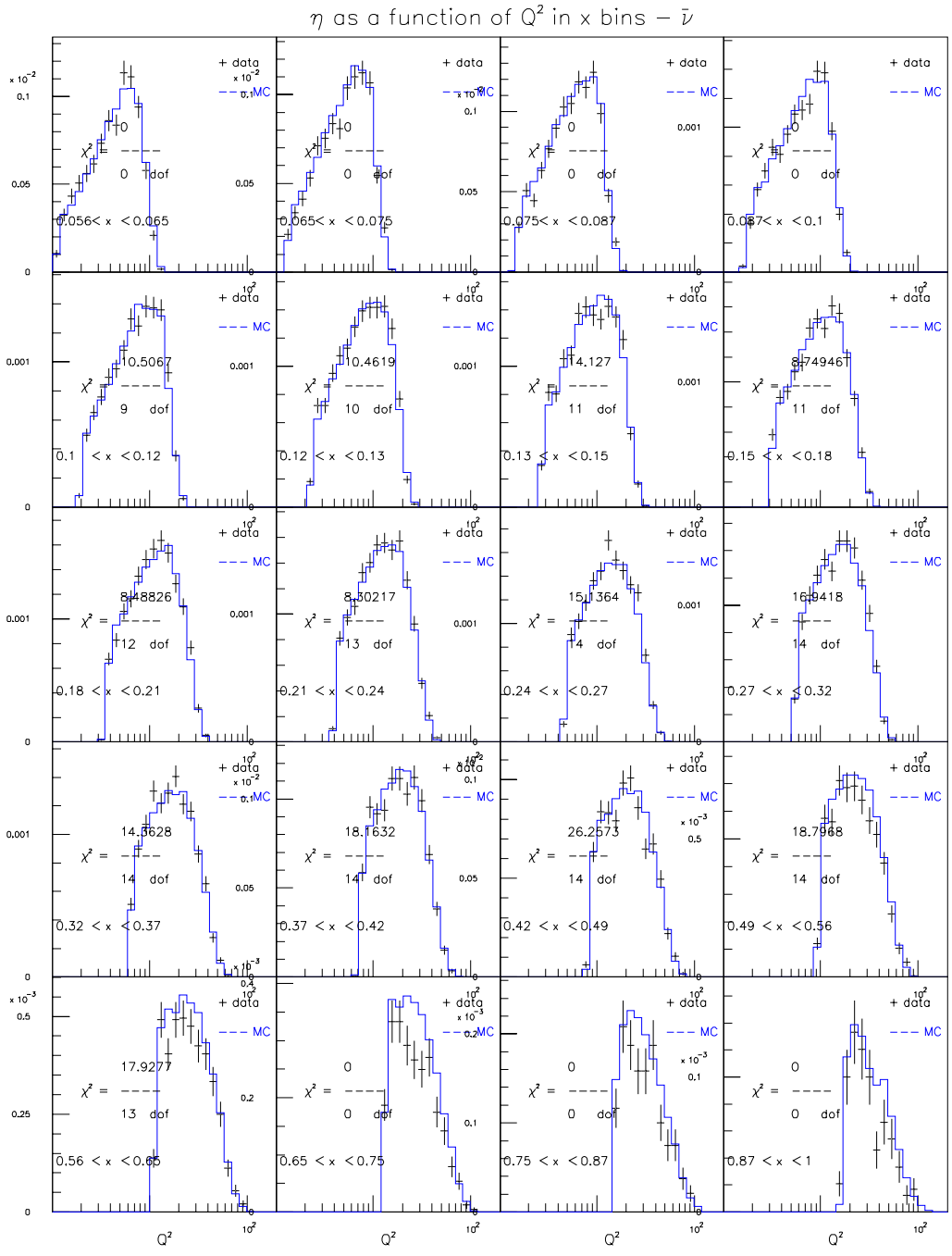

Figure E.106: BGPAR for $85 < E_\nu < 129$ GeV (ν mode)

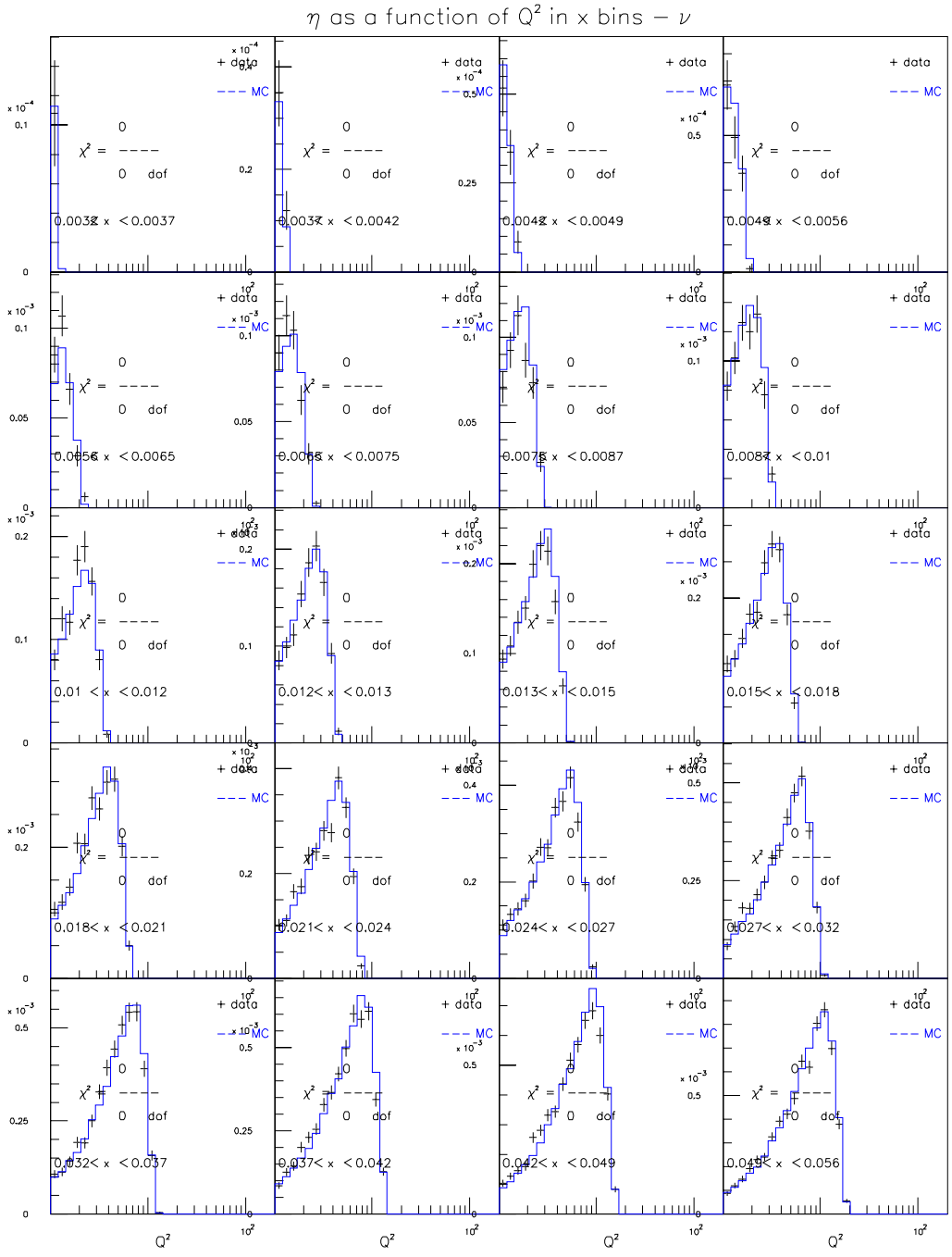

Figure E.107: BGPAR for $129 < E_\nu < 201$ GeV (ν mode)

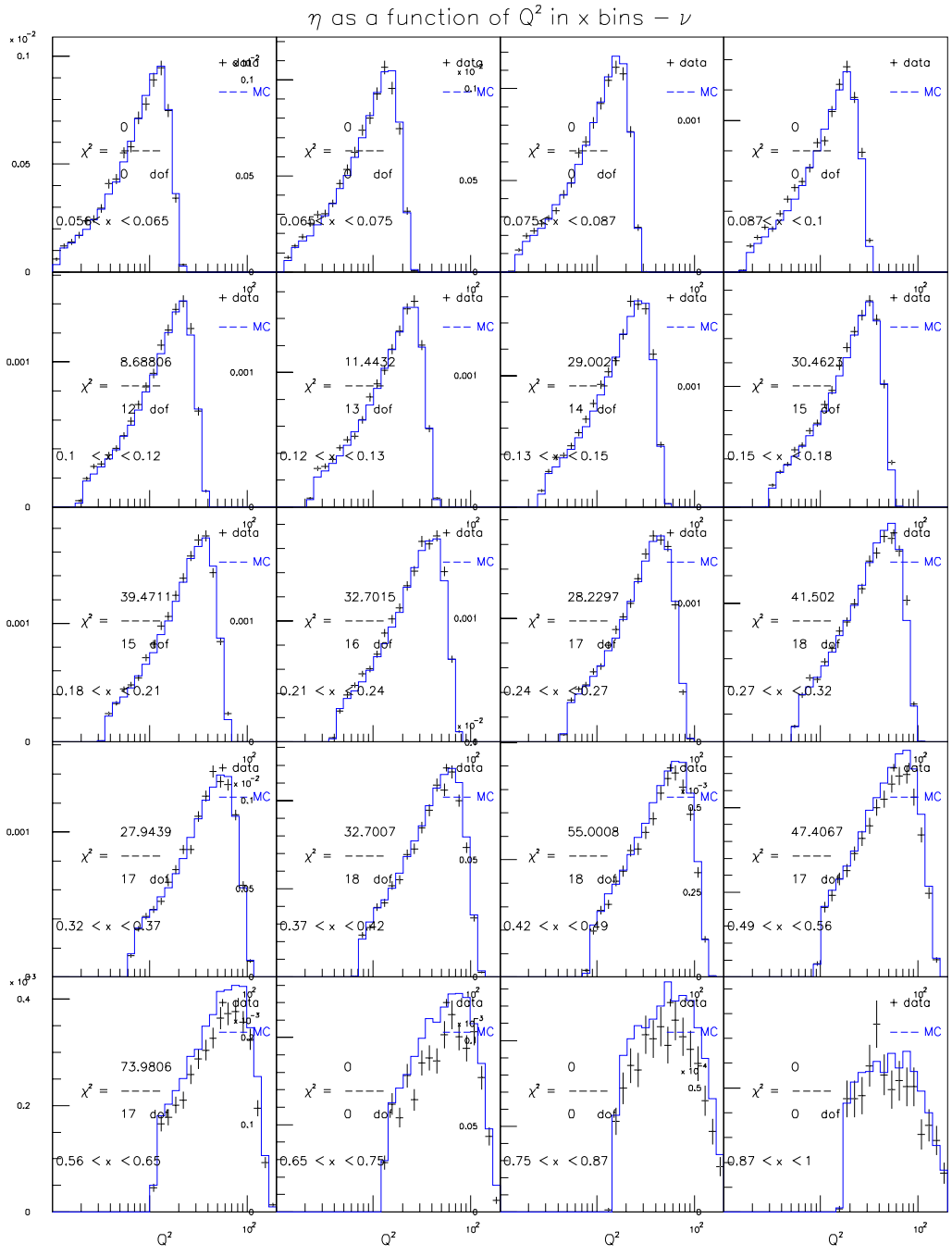

Figure E.108: BGPAR for $129 < E_\nu < 201$ GeV (ν mode)

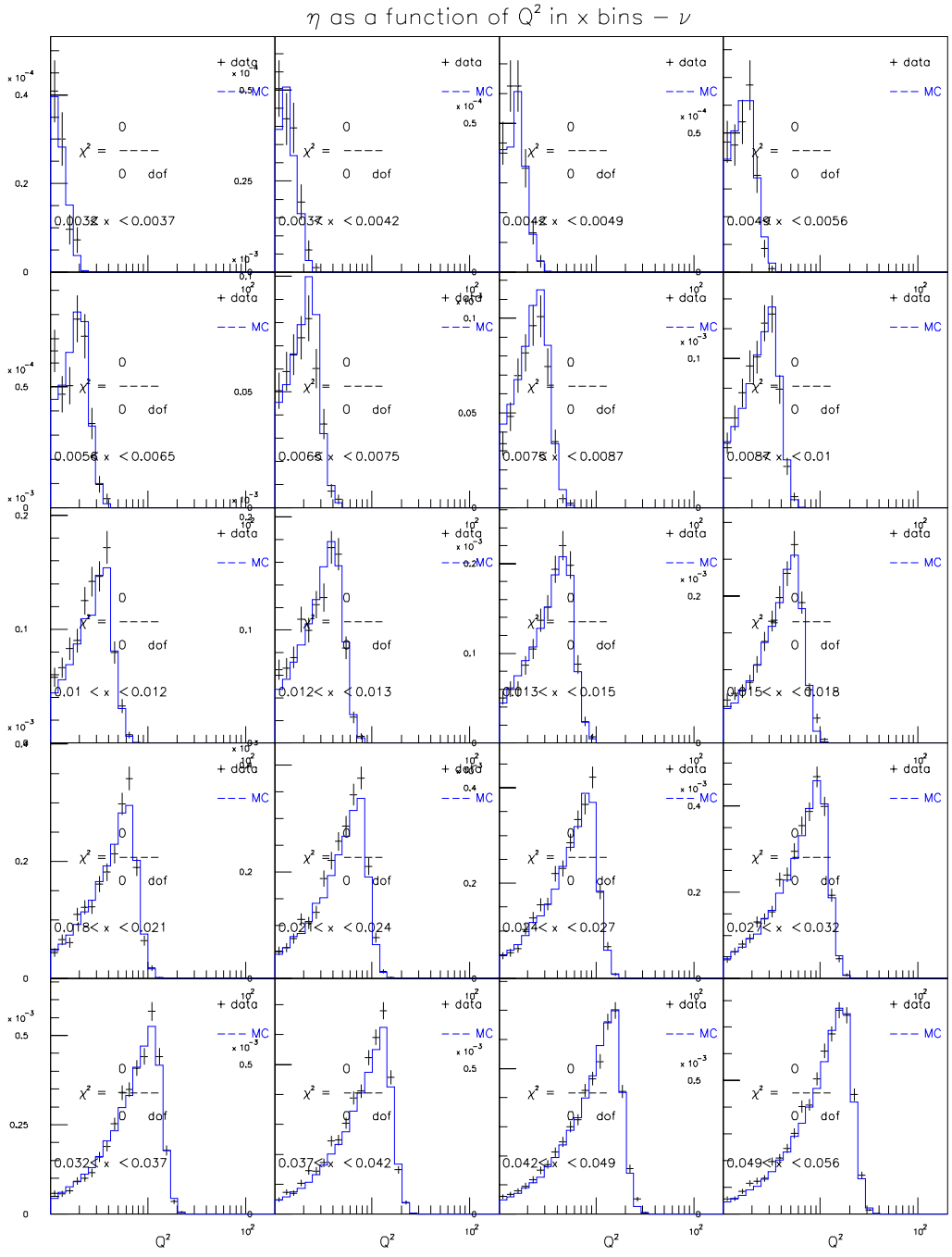

Figure E.109: BGPAR for $201 < E_\nu < 400$ GeV (ν mode)

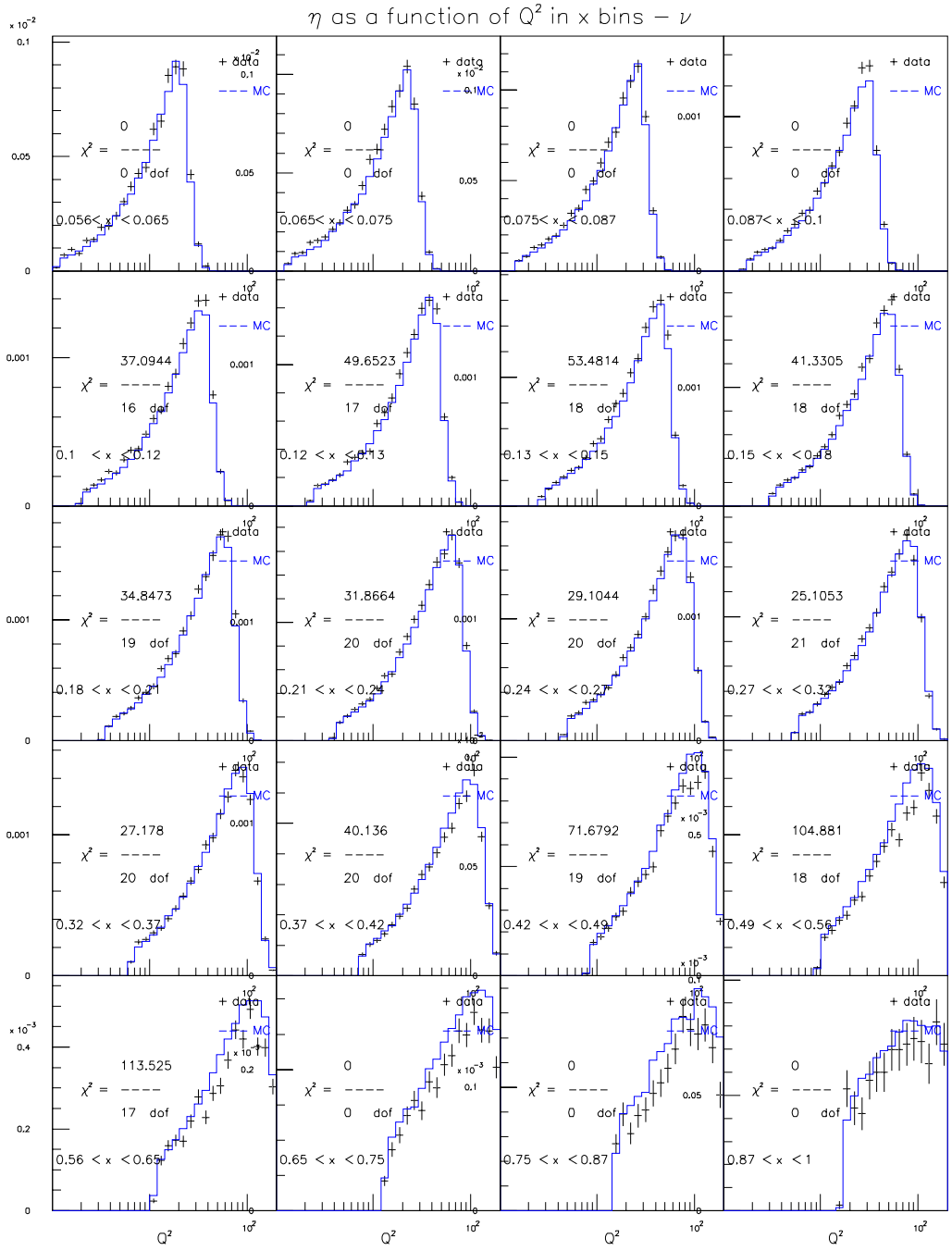

Figure E.110: BGPAR for $201 < E_\nu < 400$ GeV (ν mode)

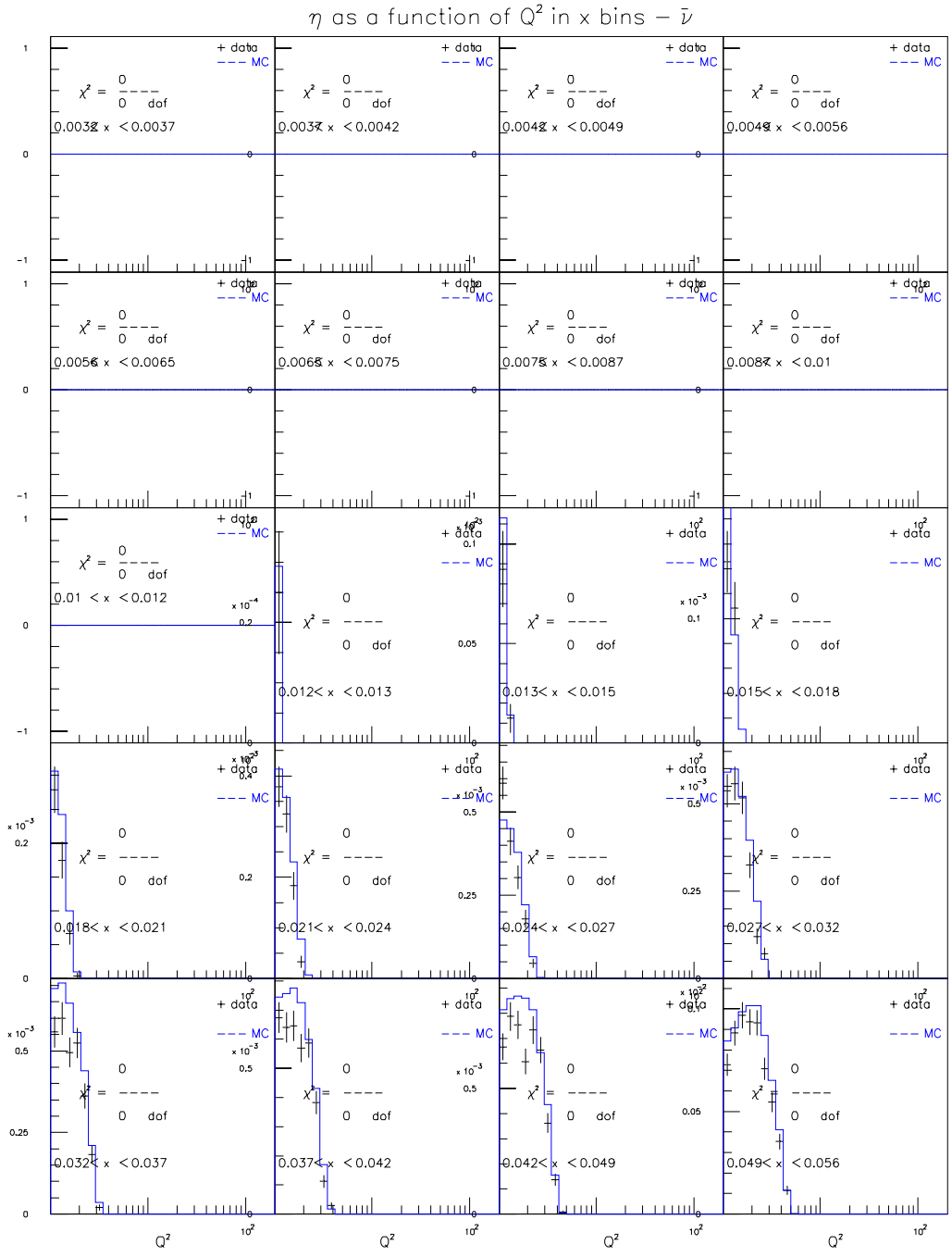

Figure E.111: BGPAR for $20 < E_\nu < 62$ GeV ($\overline{\nu}$ mode)

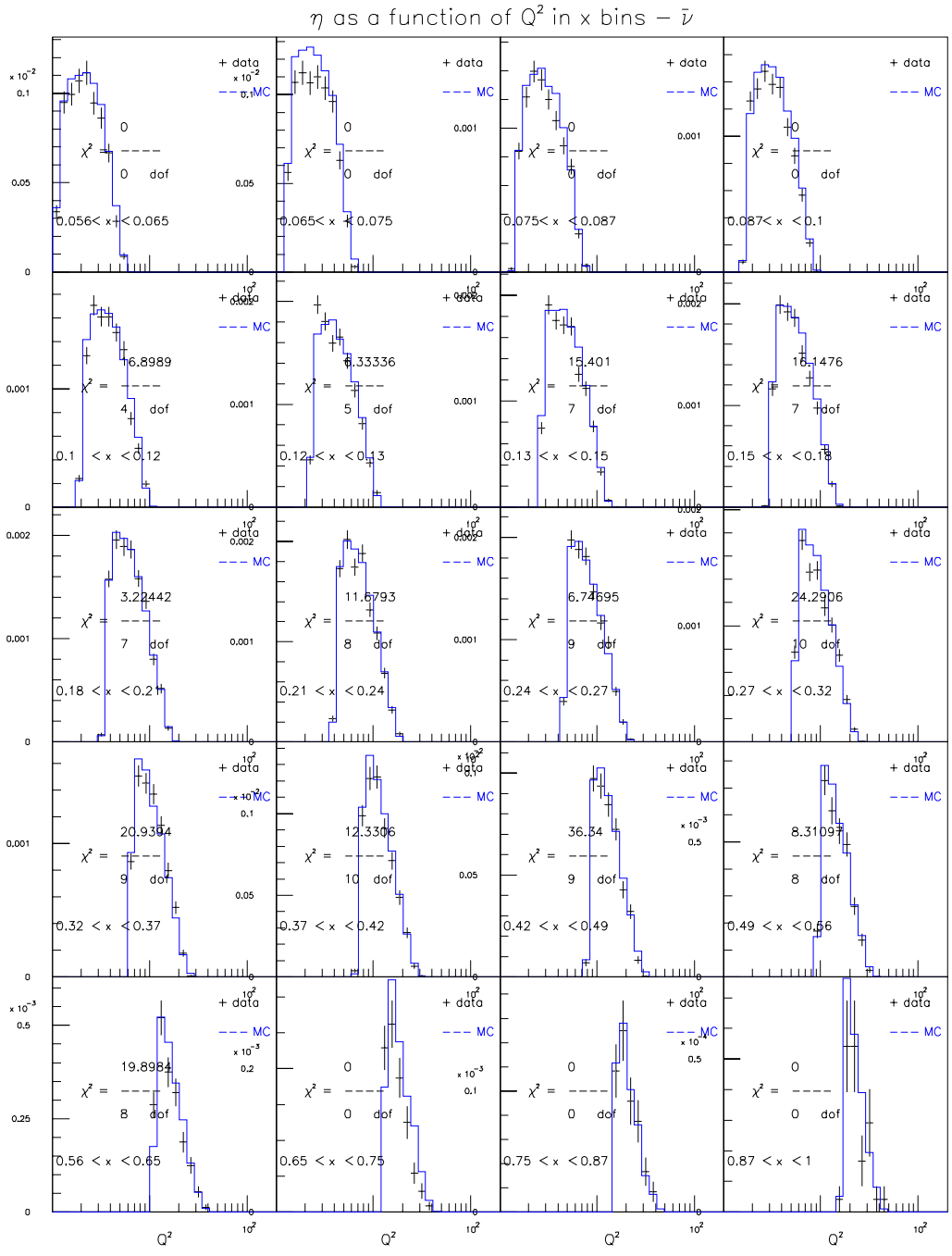

Figure E.112: BGPAR for $20 < E_\nu < 62$ GeV ($\overline{\nu}$ mode)

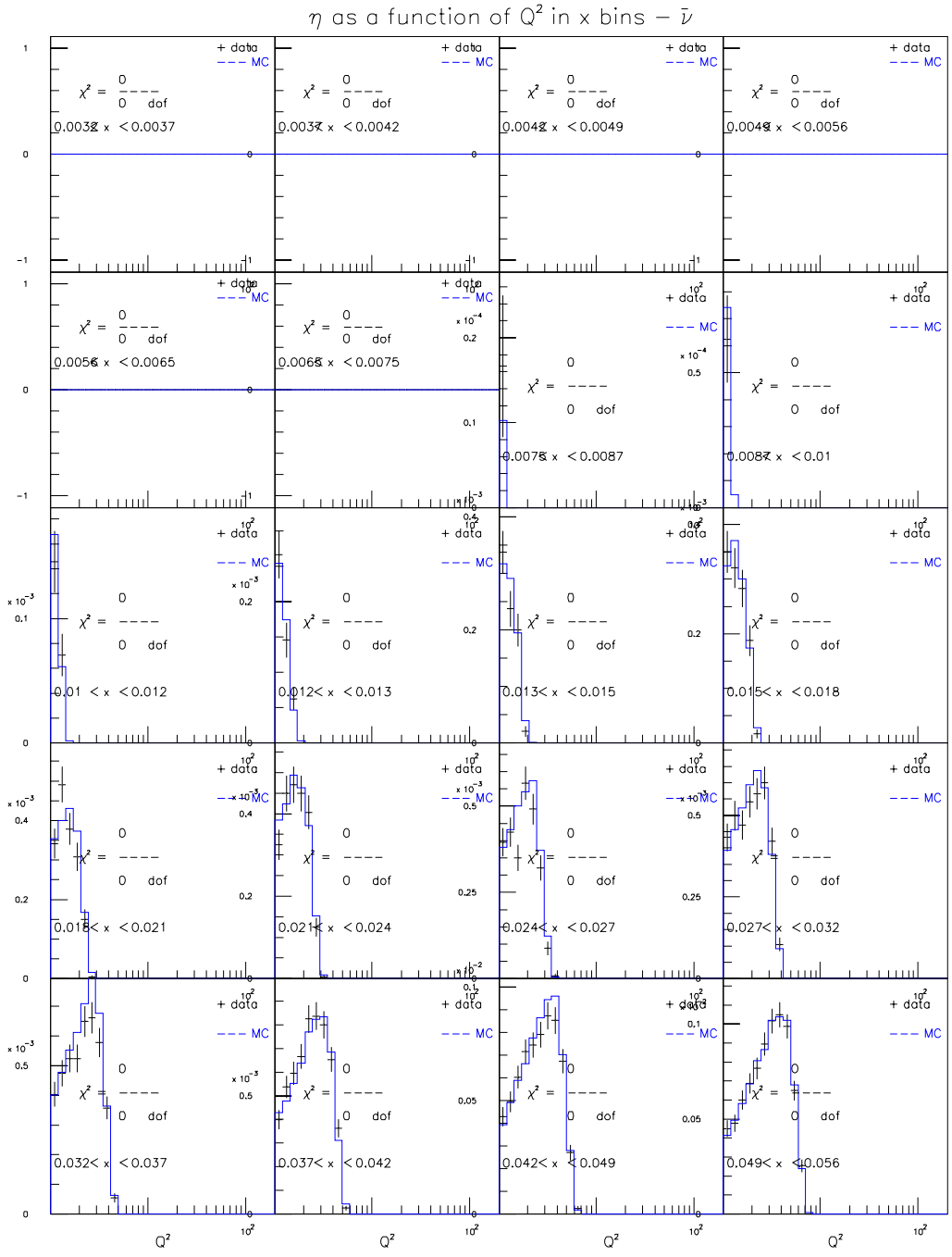

Figure E.113: BGPAR for $62 < E_\nu < 85$ GeV ($\overline{\nu}$ mode)

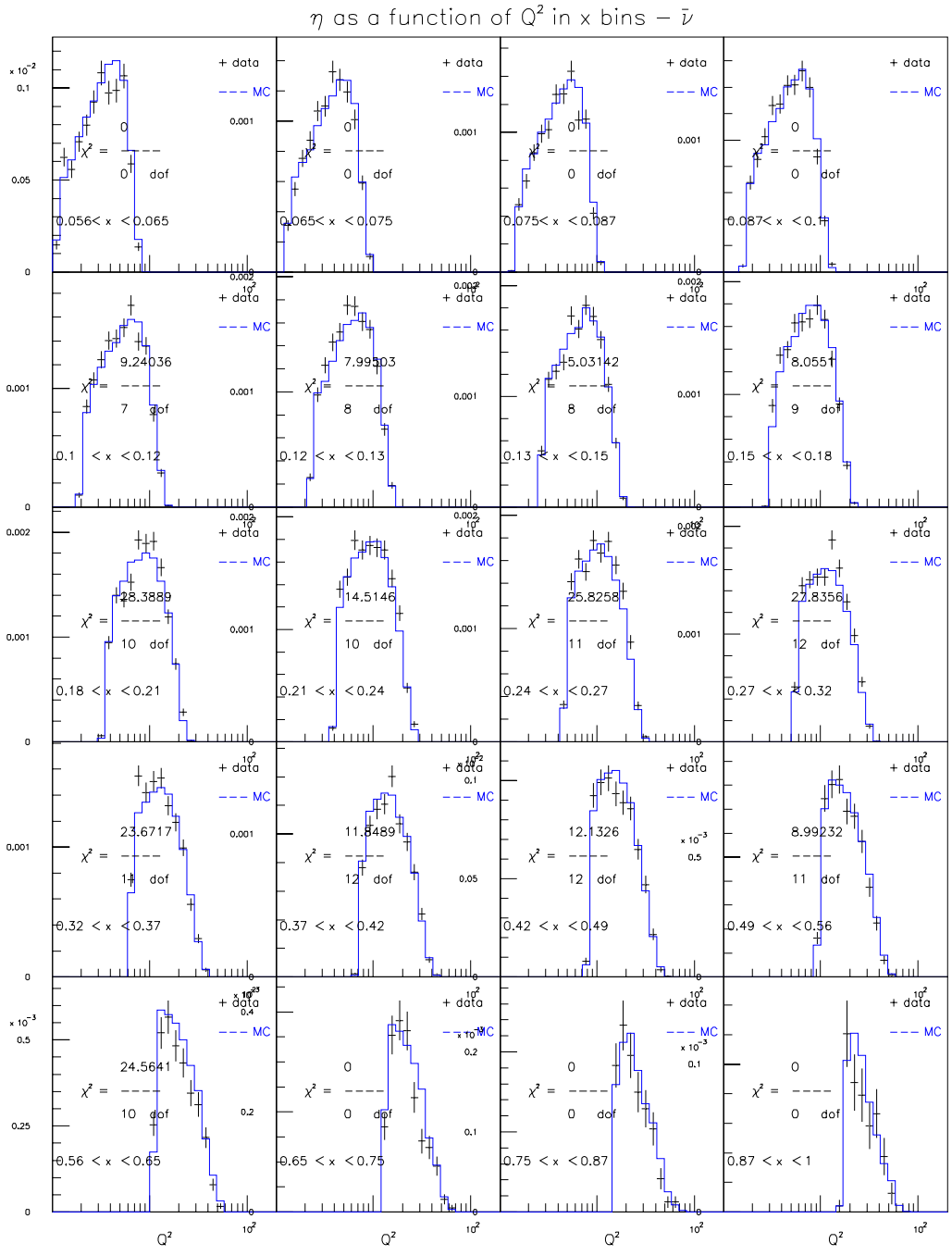

Figure E.114: BGPAR for $62 < E_\nu < 85$ GeV ($\overline{\nu}$ mode)

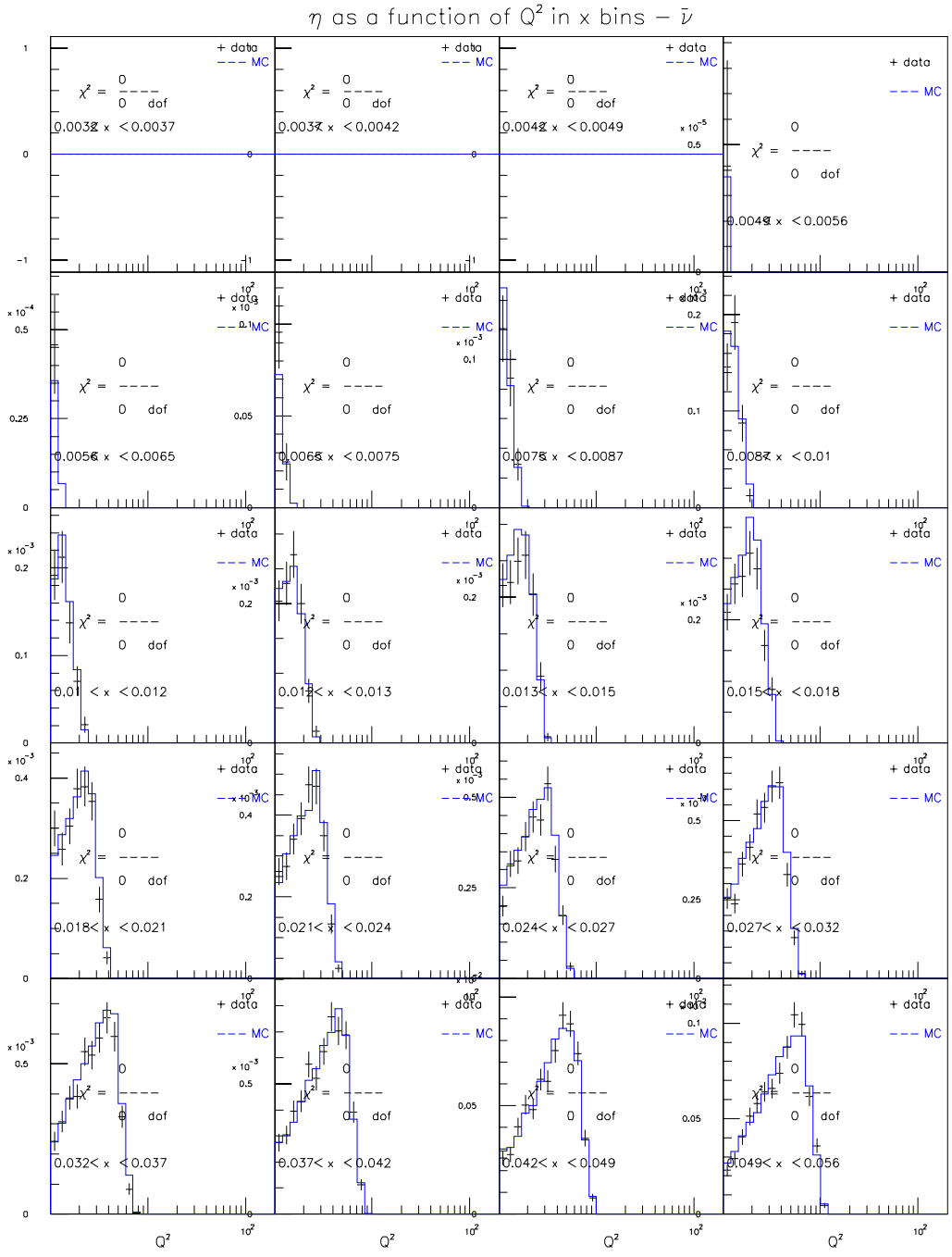

Figure E.115: BGPAR for $85 < E_\nu < 129$ GeV ($\overline{\nu}$ mode)

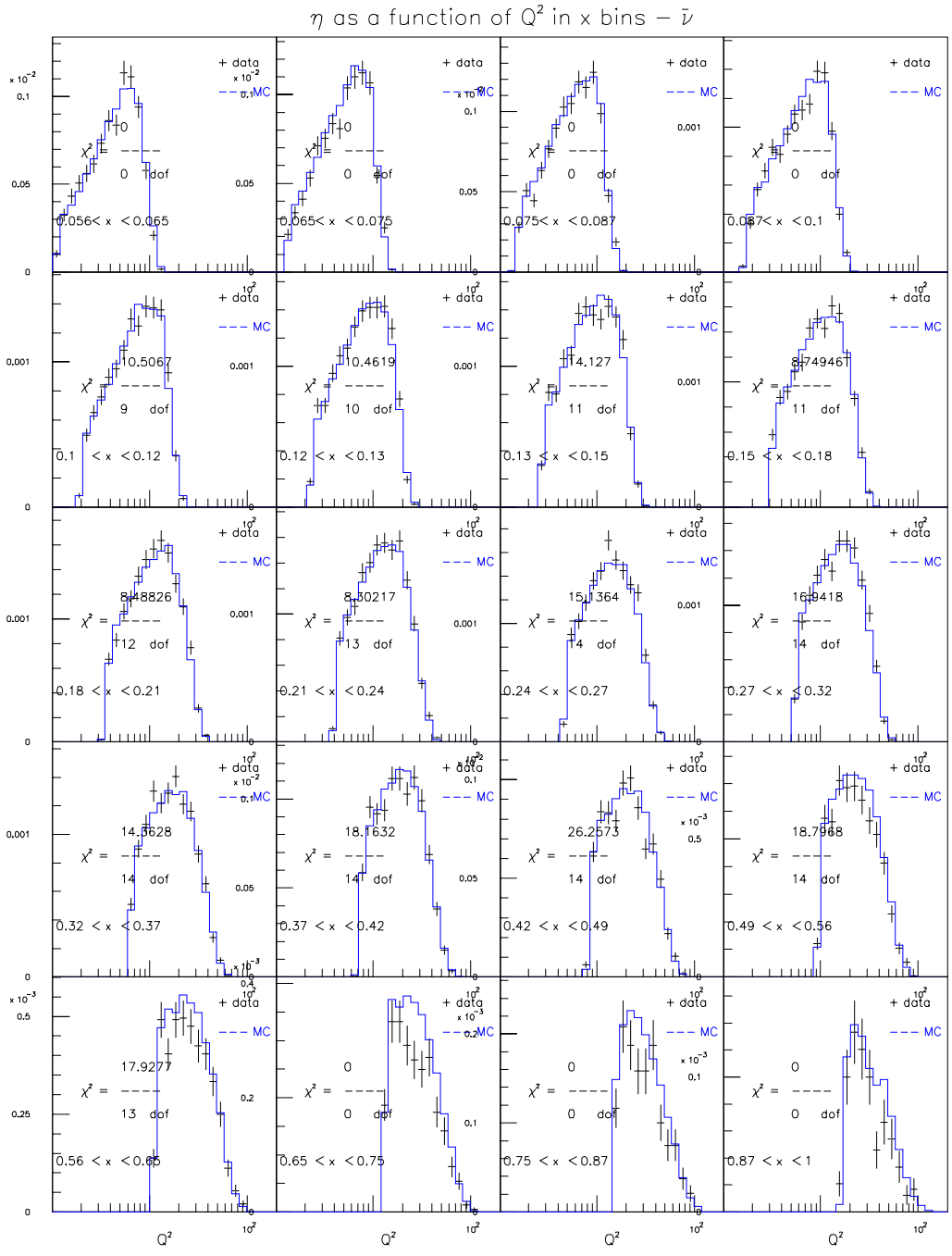

Figure E.116: BGPAR for $85 < E_\nu < 129$ GeV ($\overline{\nu}$ mode)

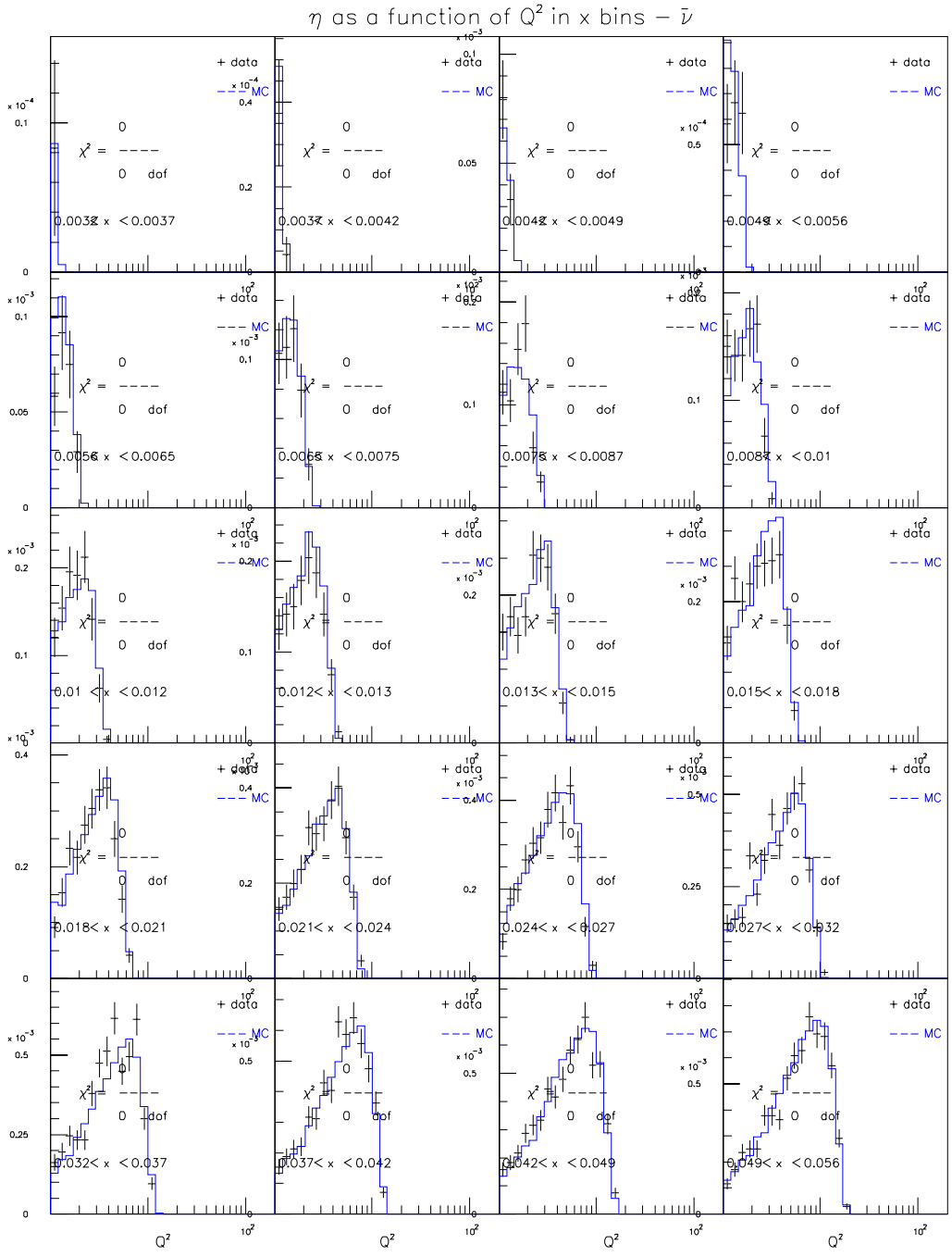

Figure E.117: BGPAR for $129 < E_\nu < 201$ GeV ($\overline{\nu}$ mode)

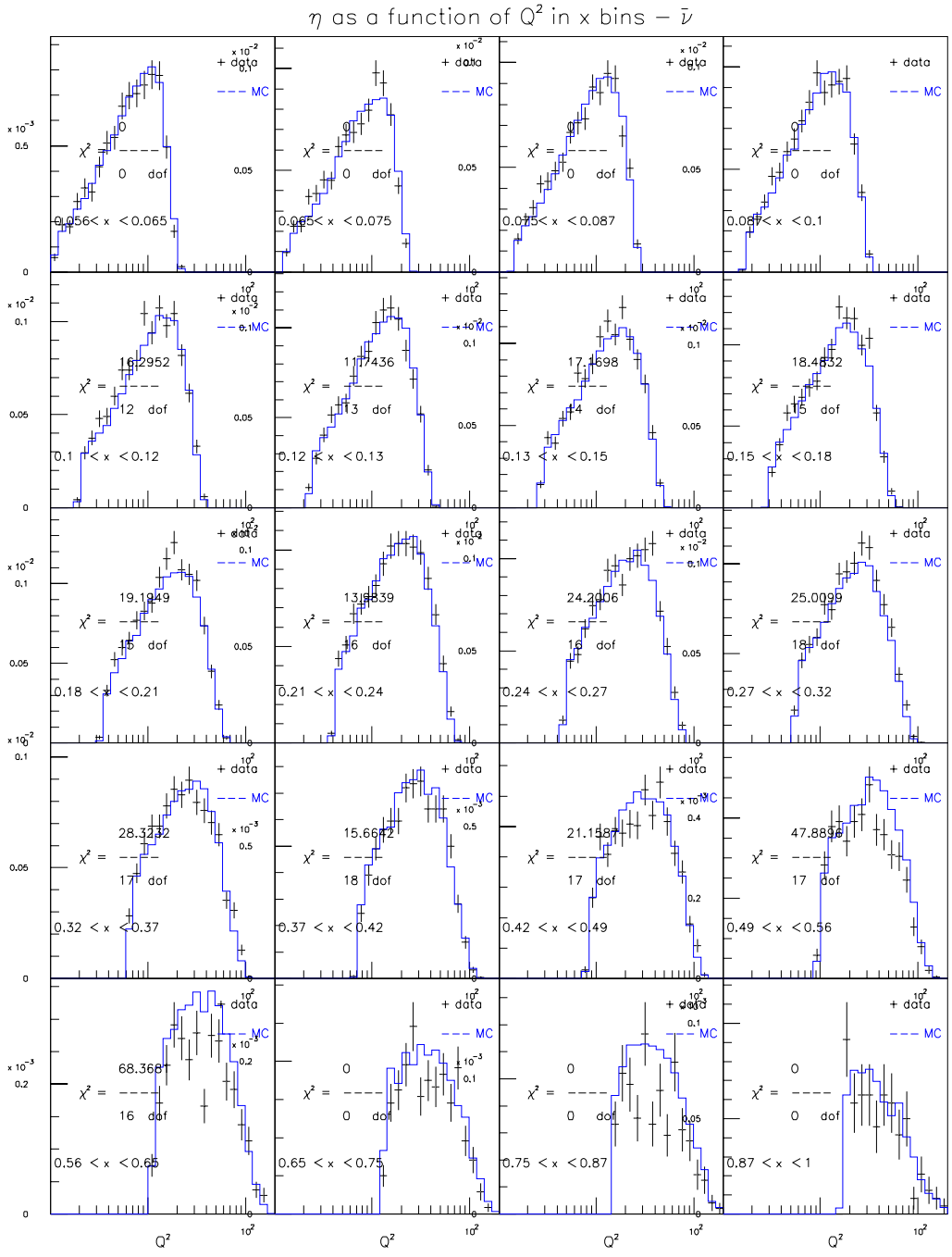

Figure E.118: BGPAR for $129 < E_\nu < 201$ GeV ($\overline{\nu}$ mode)

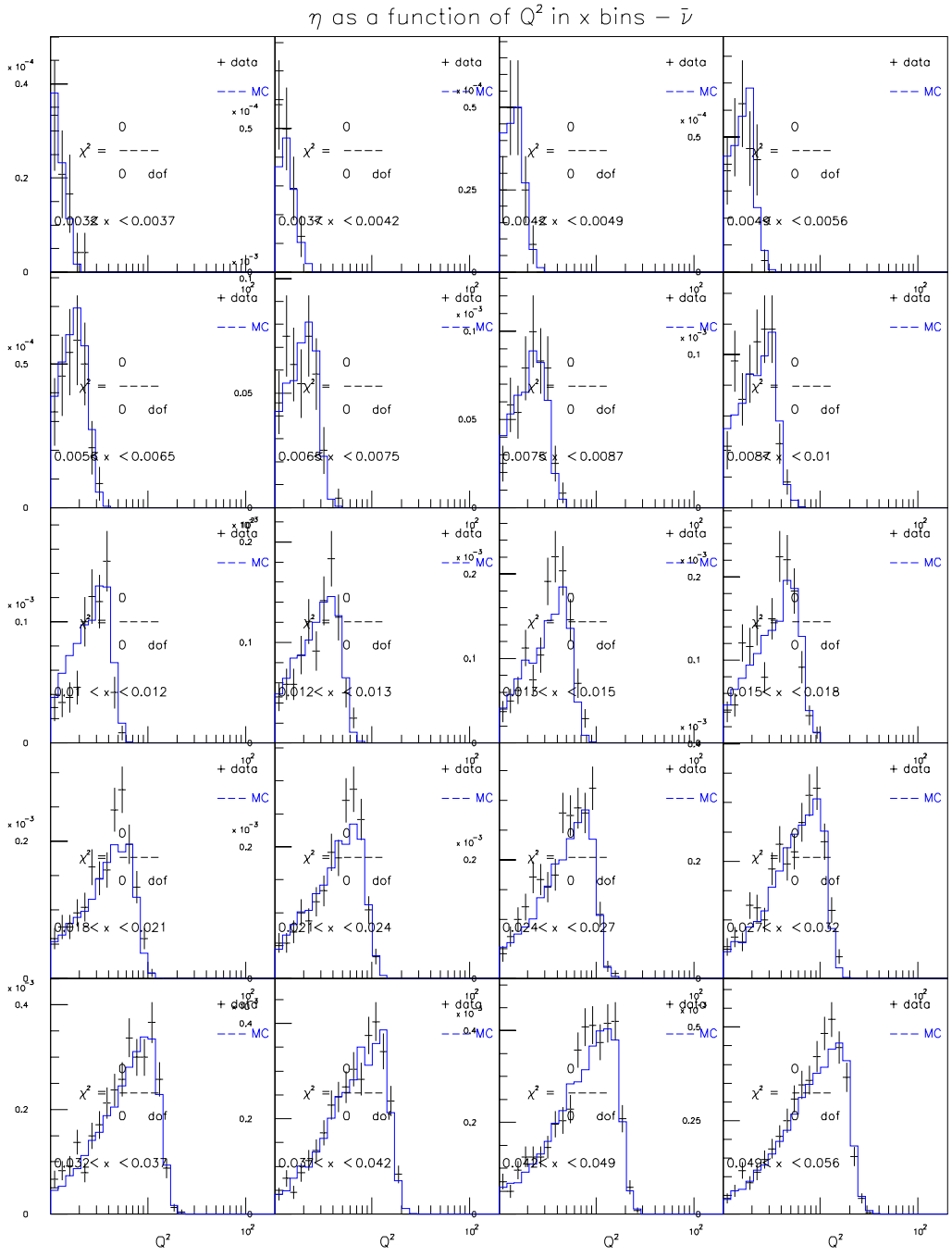

Figure E.119: BGPAR for $201 < E_\nu < 400$ GeV ($\overline{\nu}$ mode)

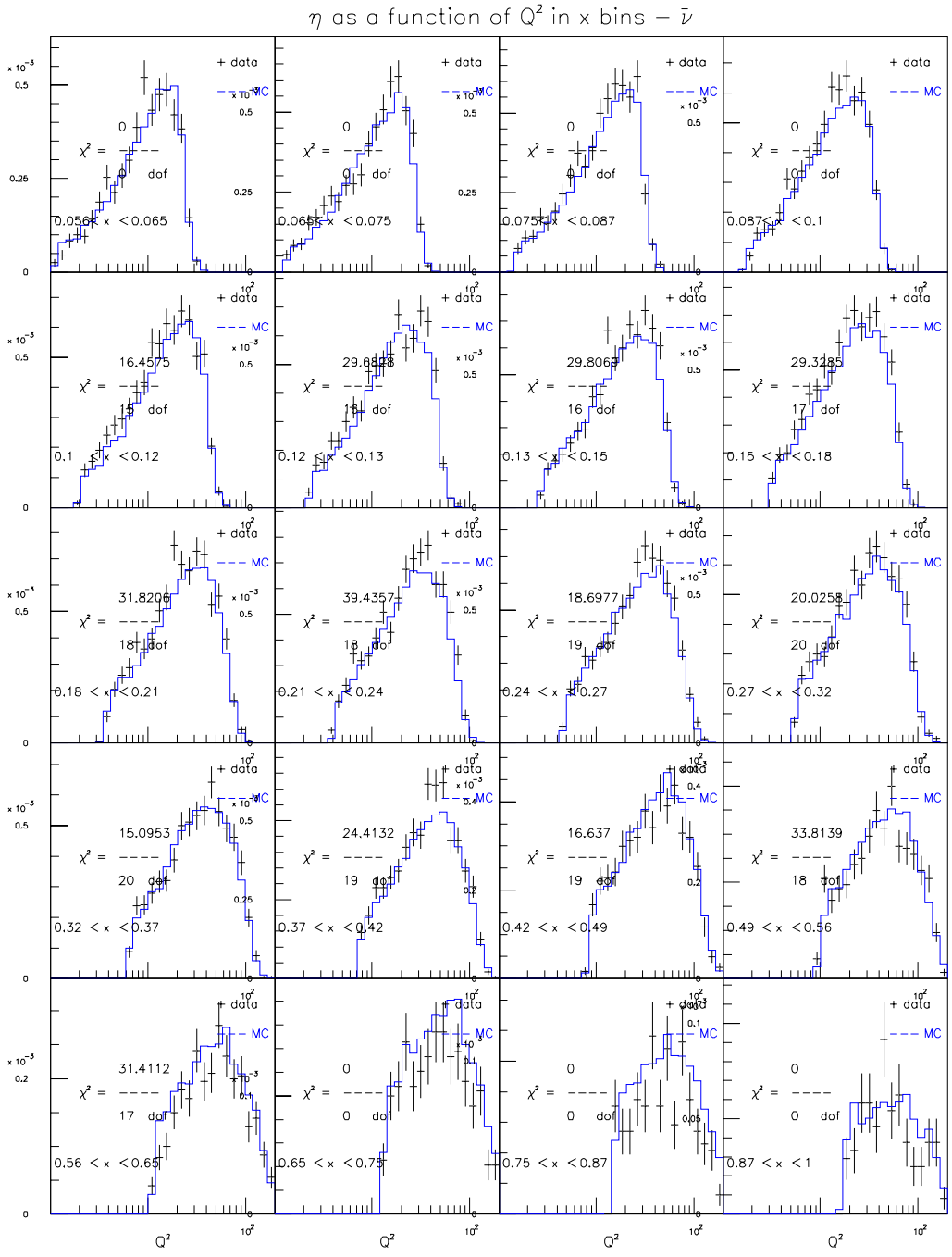

Figure E.120: BGPAR for $201 < E_\nu < 400$ GeV ($\overline{\nu}$ mode)

Appendix F

Model Comparisons in $E_\nu/x/Q^2$ Bins

This section contains model comparisons represented by χ^2/dof in a single variable. Accordingly, for each model, there are plots of χ^2/dof in E_ν bins (summed over all x and Q^2), χ^2/dof in x bins (summed over all E_ν and Q^2), and χ^2/dof in Q^2 bins (summed over all E_ν and x).

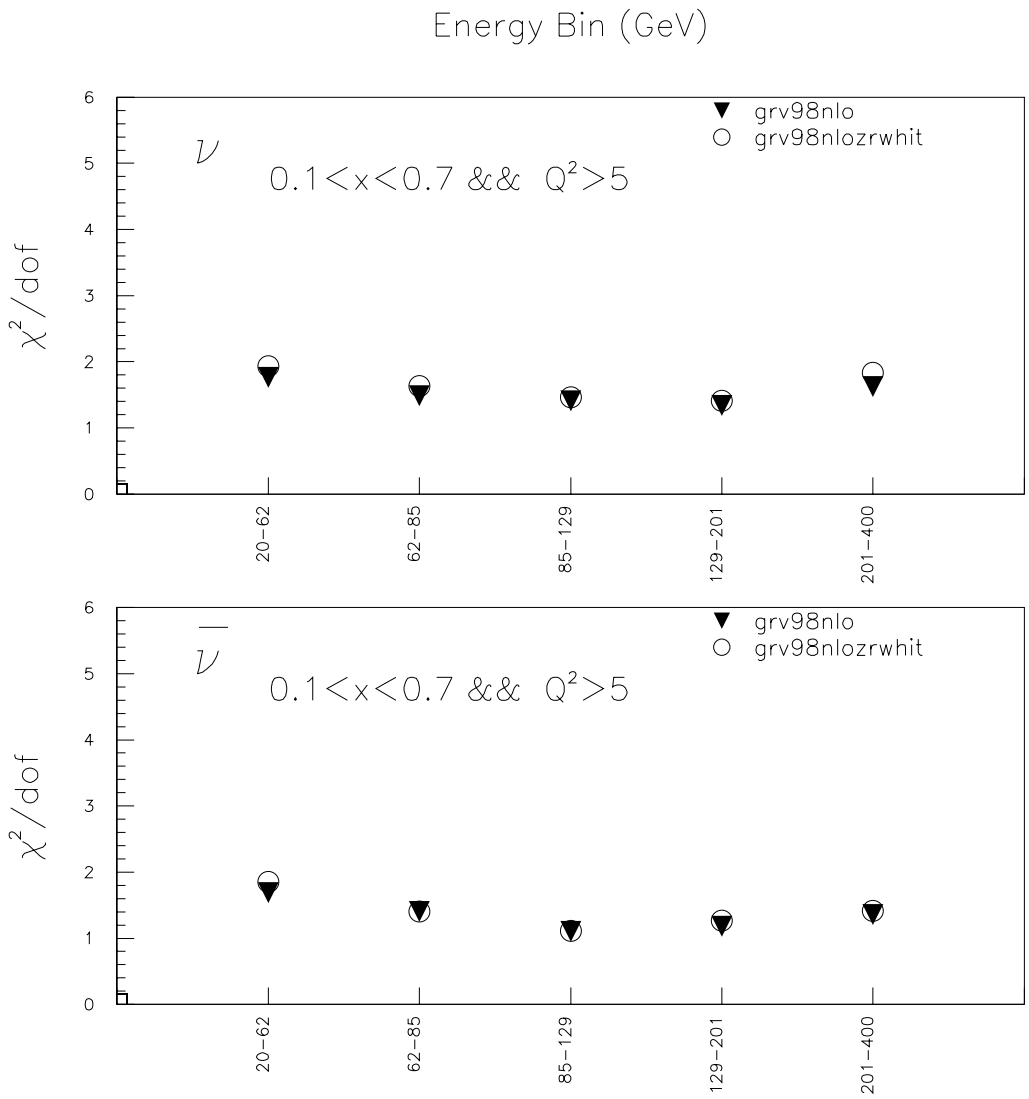

Figure F.1: GRV98NLO R_L comparison. χ^2/dof by E_ν bin

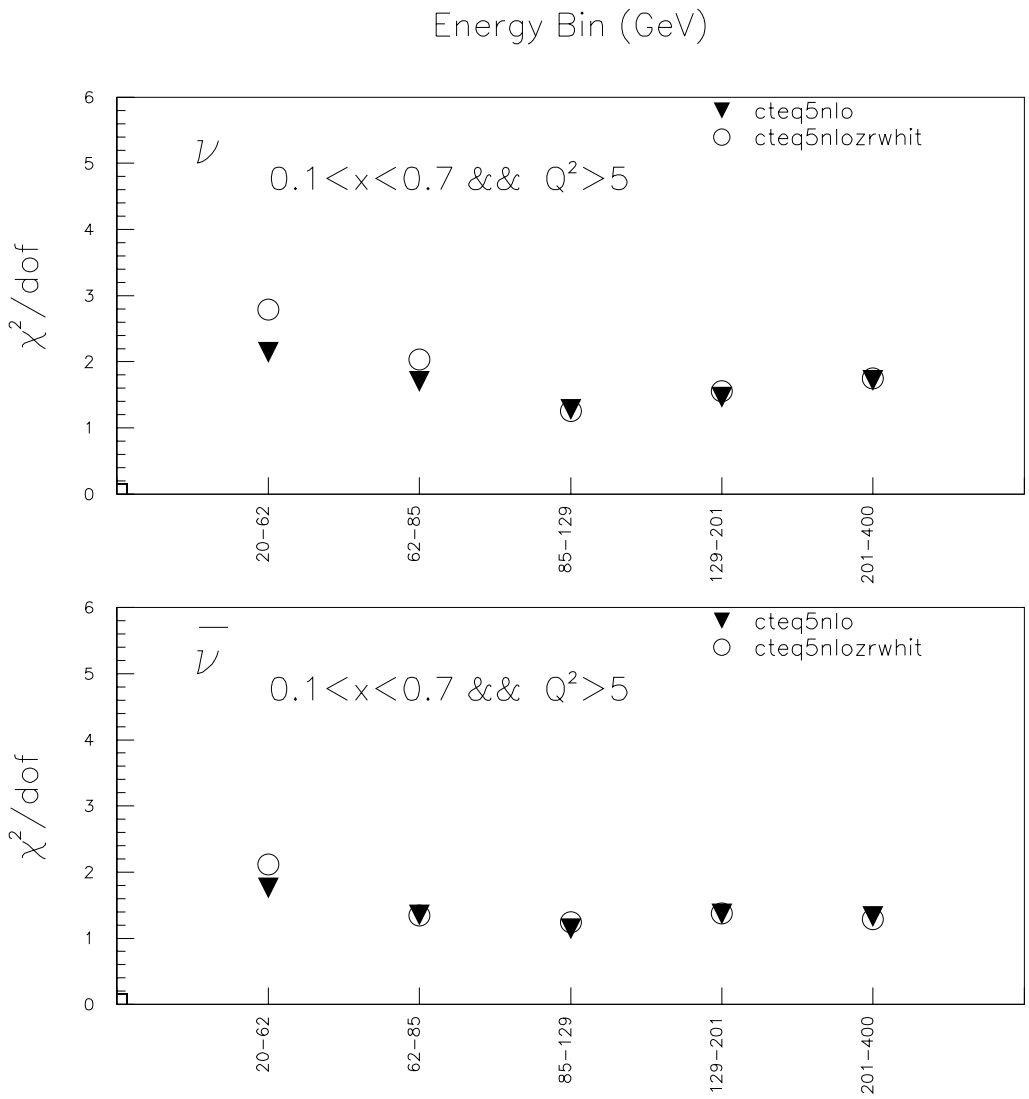

Figure F.2: CTEQ5NLO R_L comparison. χ^2/dof by E_ν bin

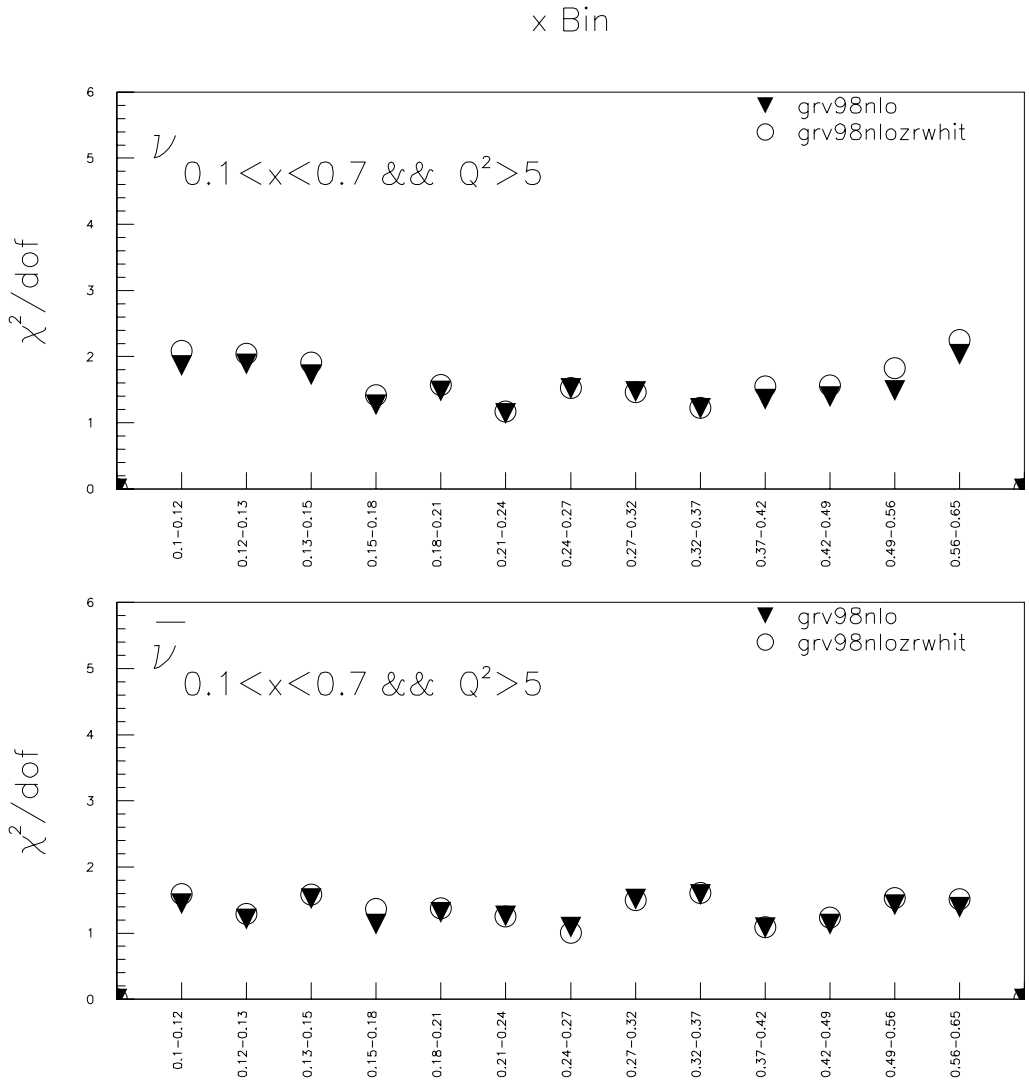

Figure F.3: GRV98NLO R_L comparison. χ^2/dof by x bin

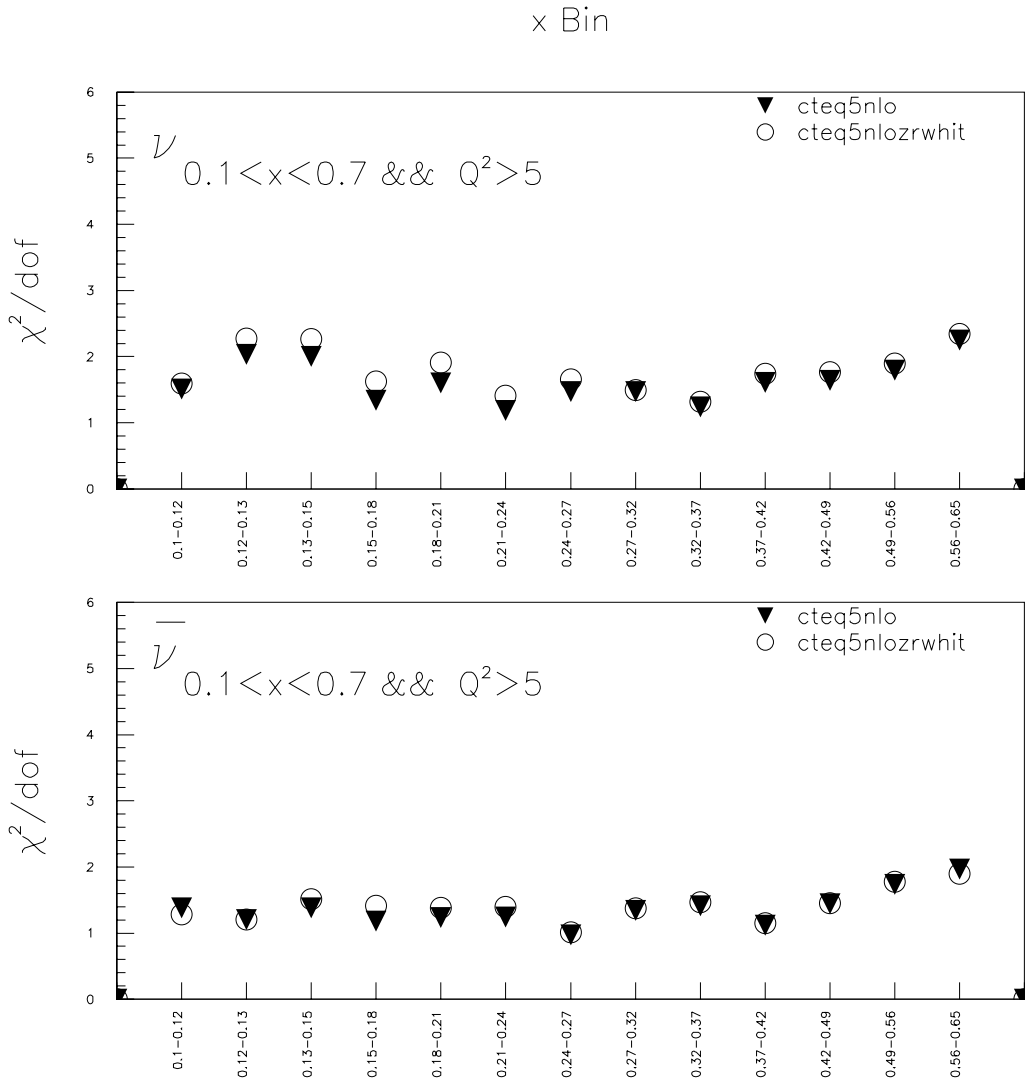

Figure F.4: CTEQ5NLO R_L comparison. χ^2/dof by x bin

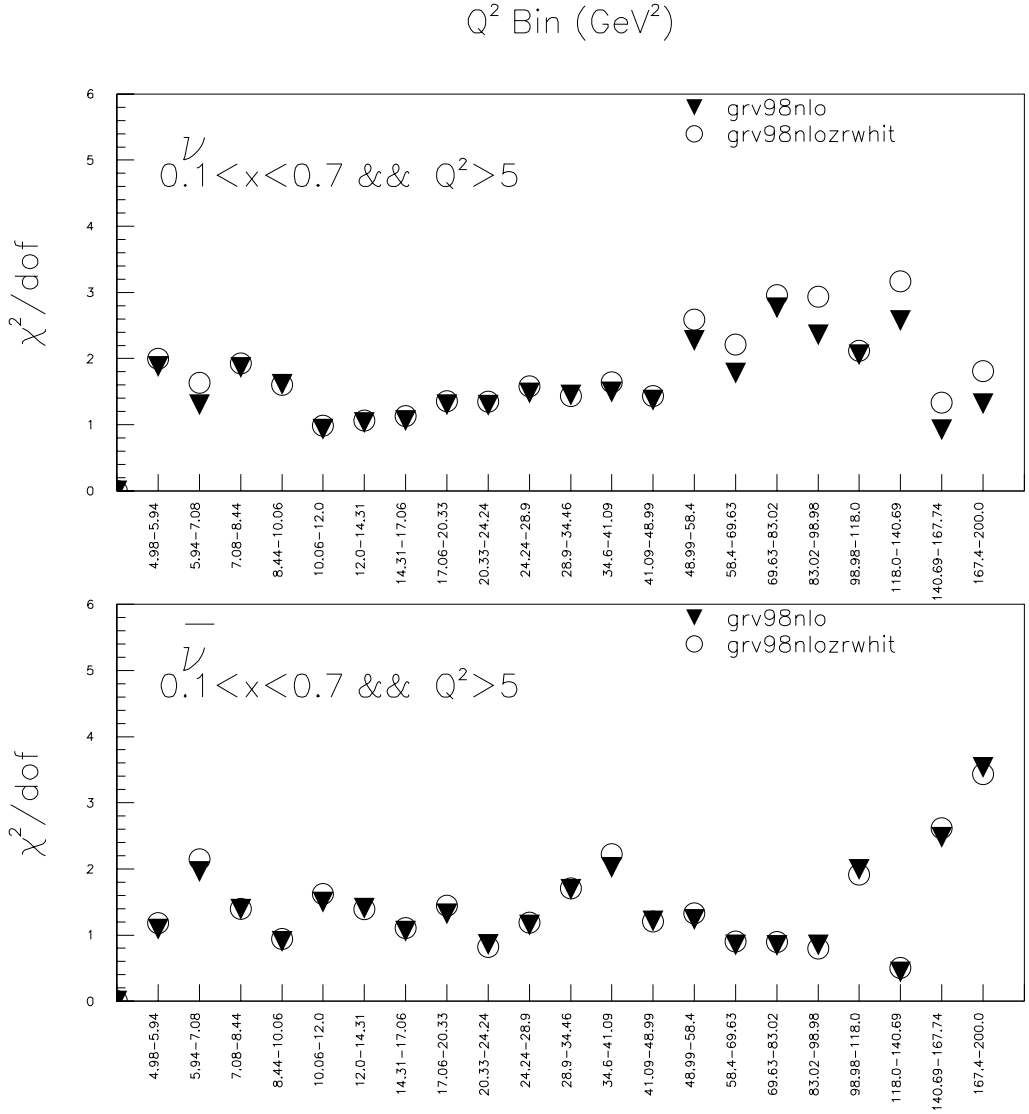

Figure F.5: GRV98NLO R_L comparison. χ^2/dof by Q^2 bin

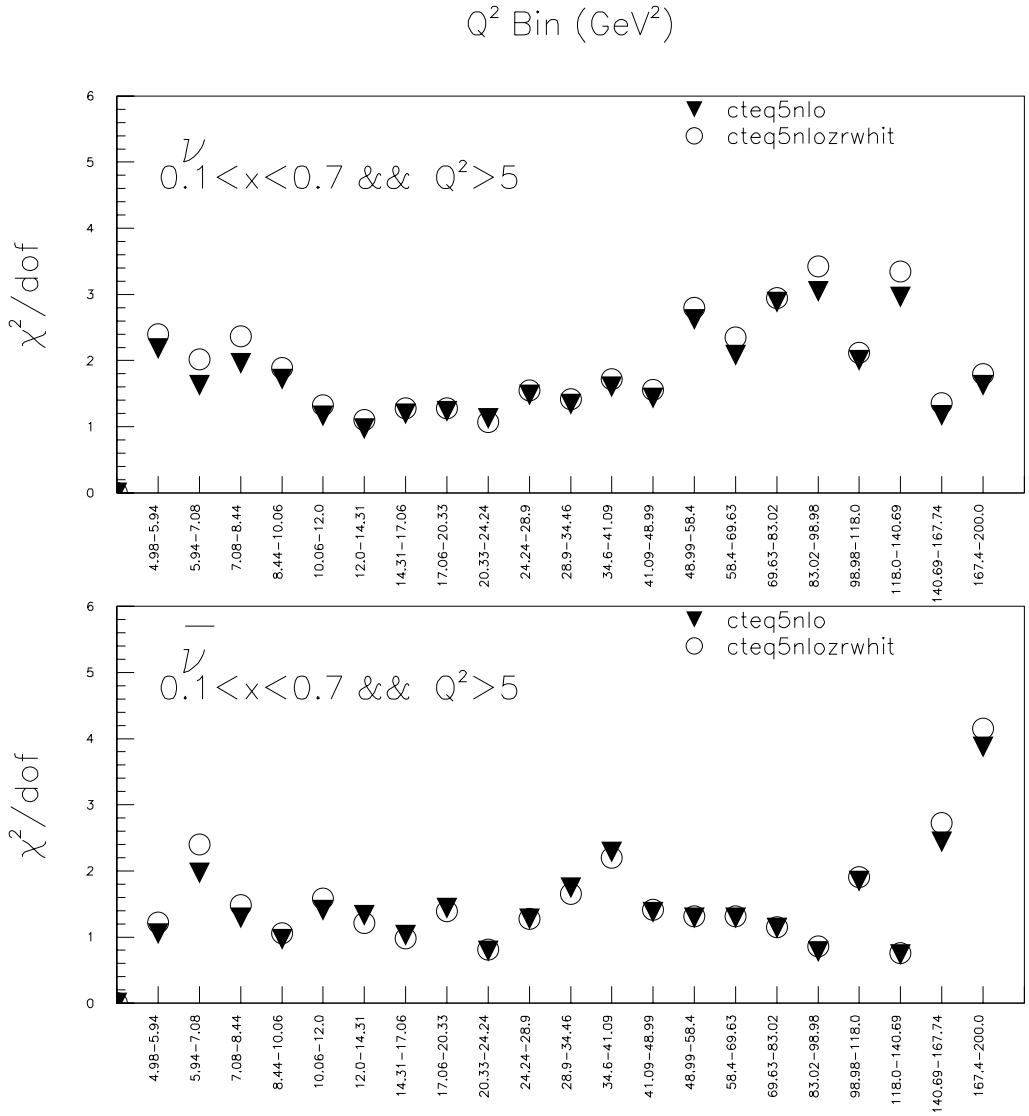

Figure F.6: CTEQ5NLO R_L comparison. χ^2/dof by Q^2 bin

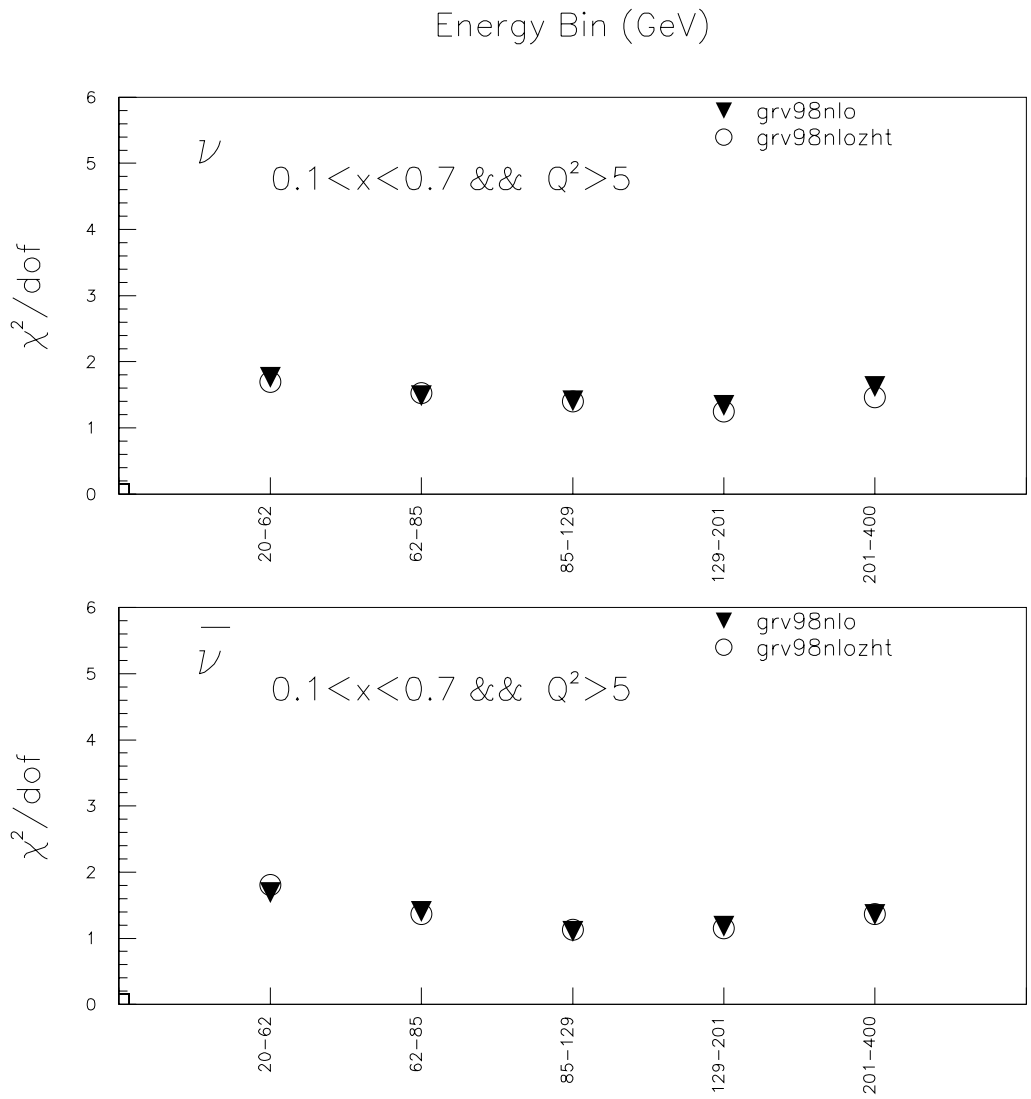

Figure F.7: GRV98NLO Higher Twist comparison. χ^2/dof by E_ν bin

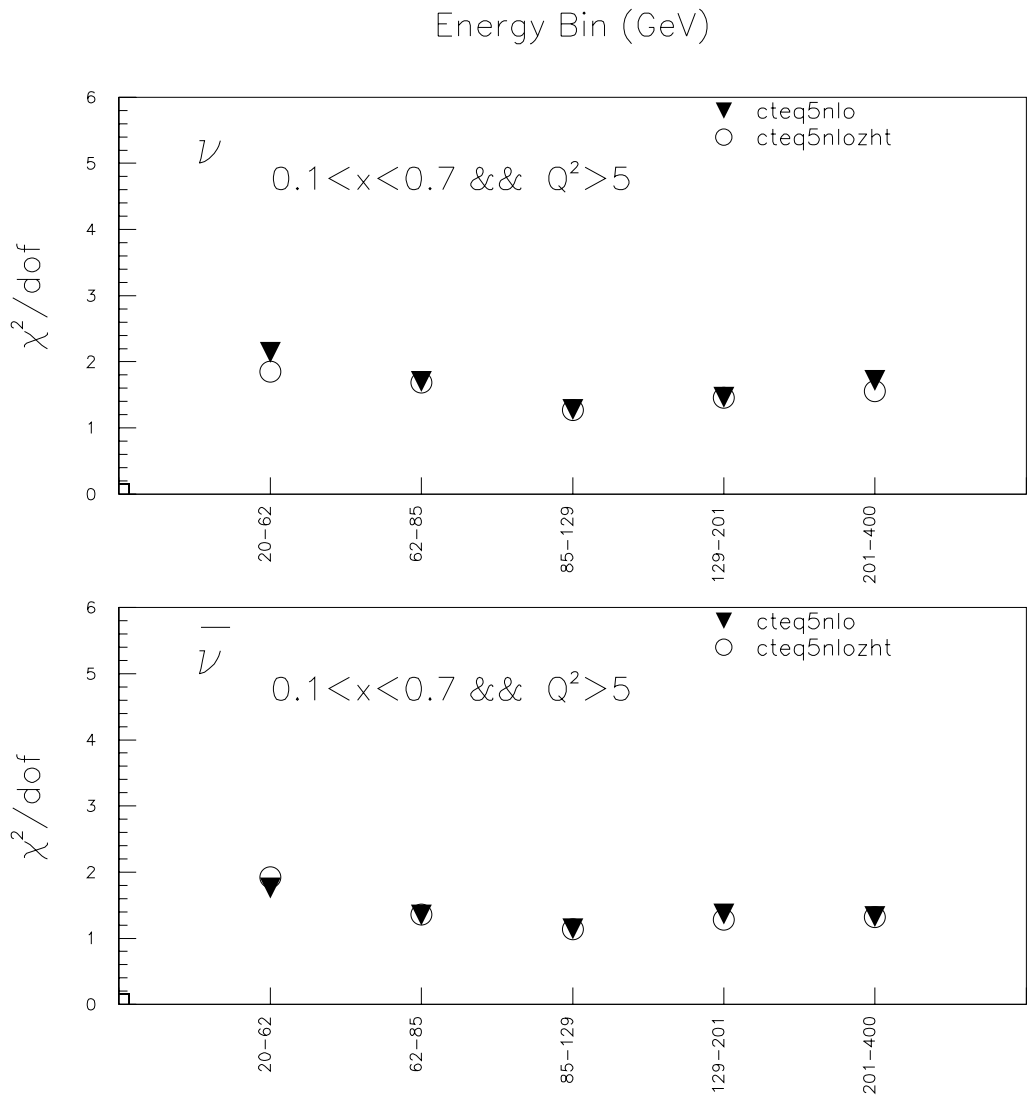

Figure F.8: CTEQ5NLO Higher Twist comparison. χ^2/dof by E_ν bin

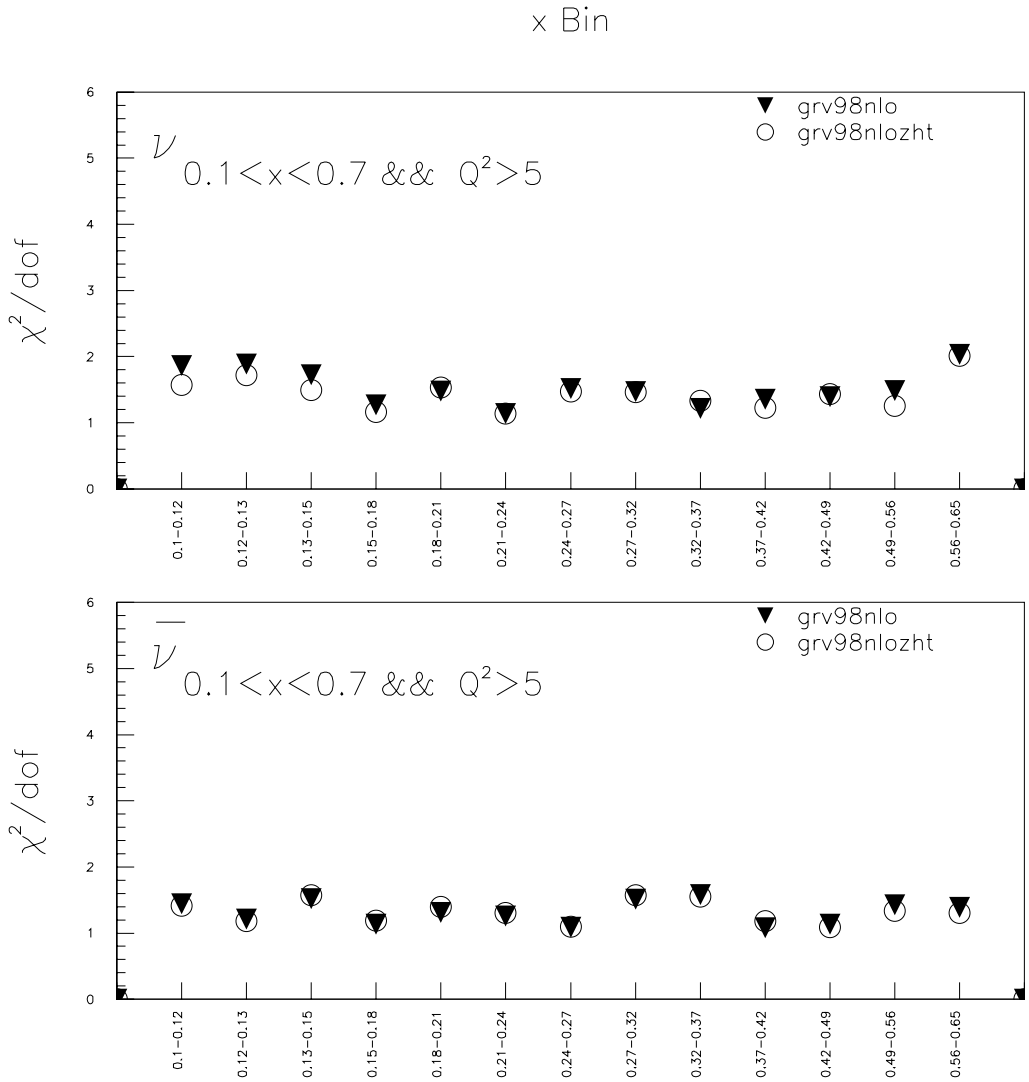

Figure F.9: GRV98NLO Higher Twist comparison. χ^2/dof by x bin

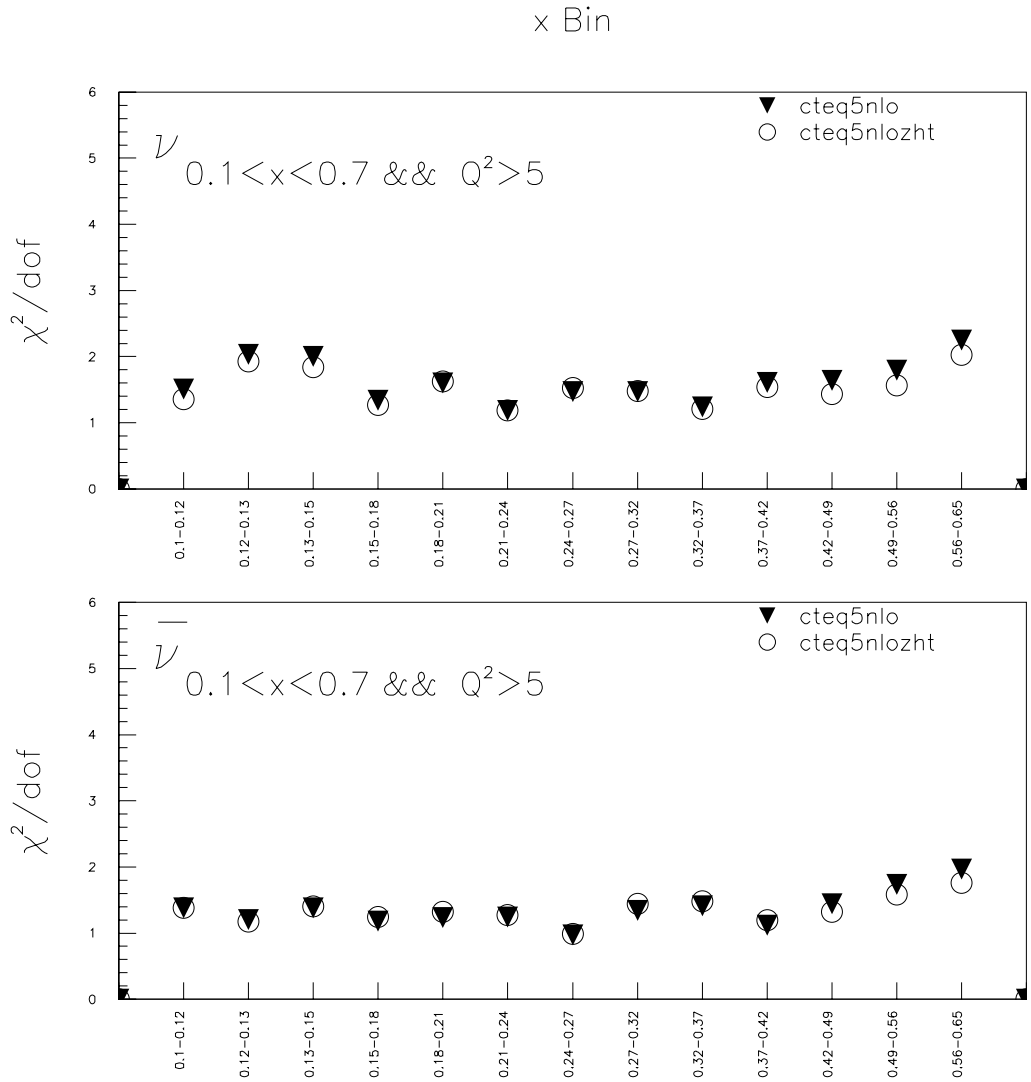

Figure F.10: CTEQ5NLO Higher Twist comparison. χ^2/dof by x bin

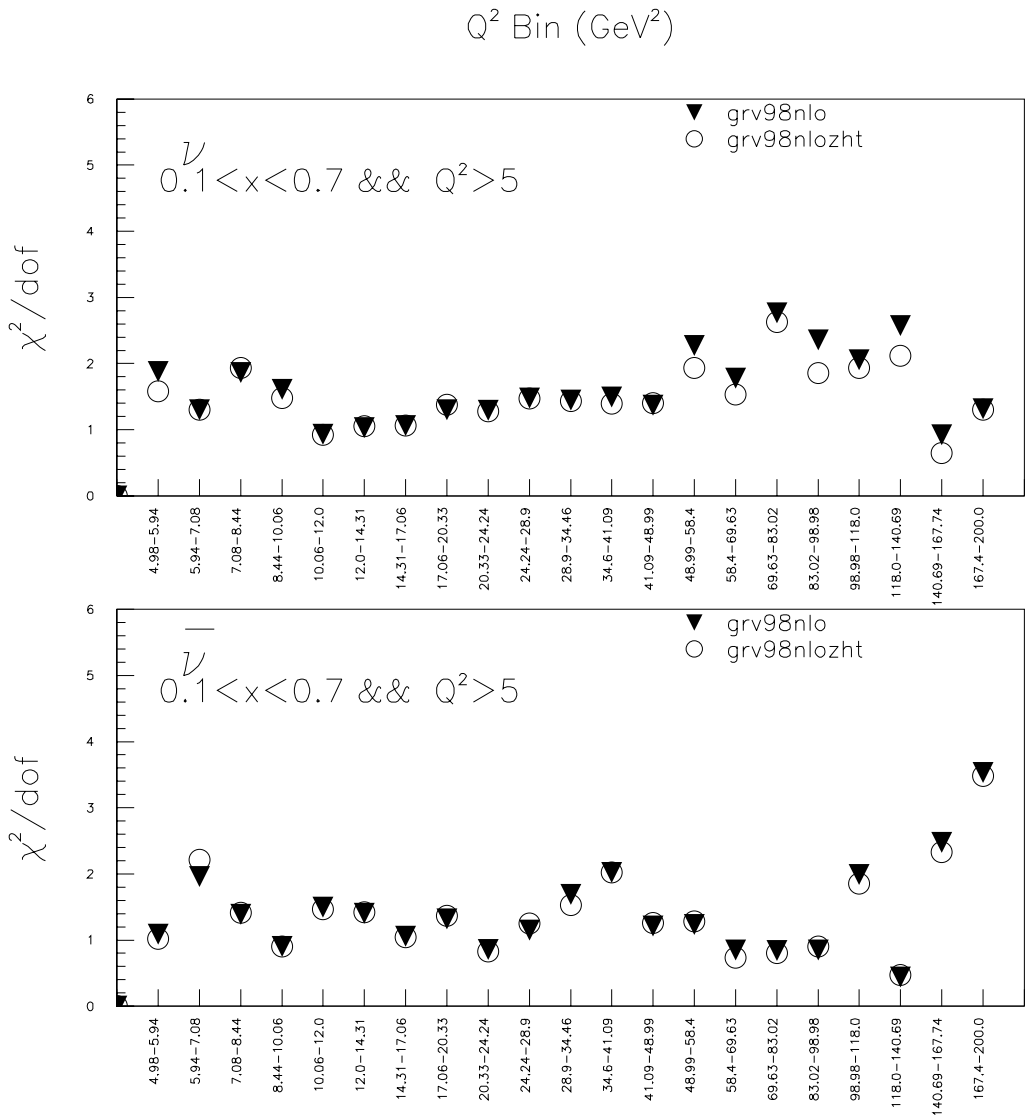

Figure F.11: GRV98NLO Higher Twist comparison. χ^2/dof by Q^2 bin

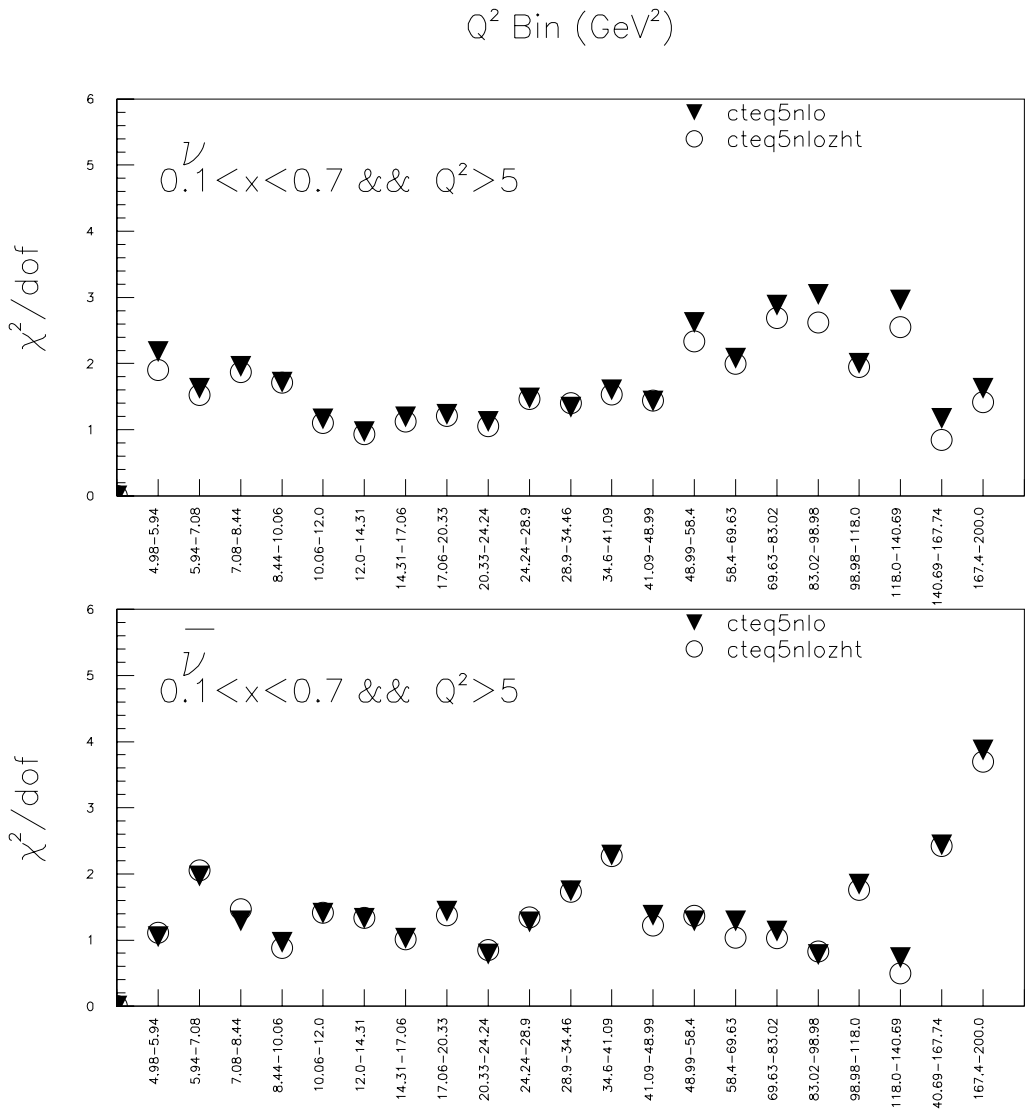

Figure F.12: CTEQ5NLO Higher Twist comparison. χ^2/dof by Q^2 bin

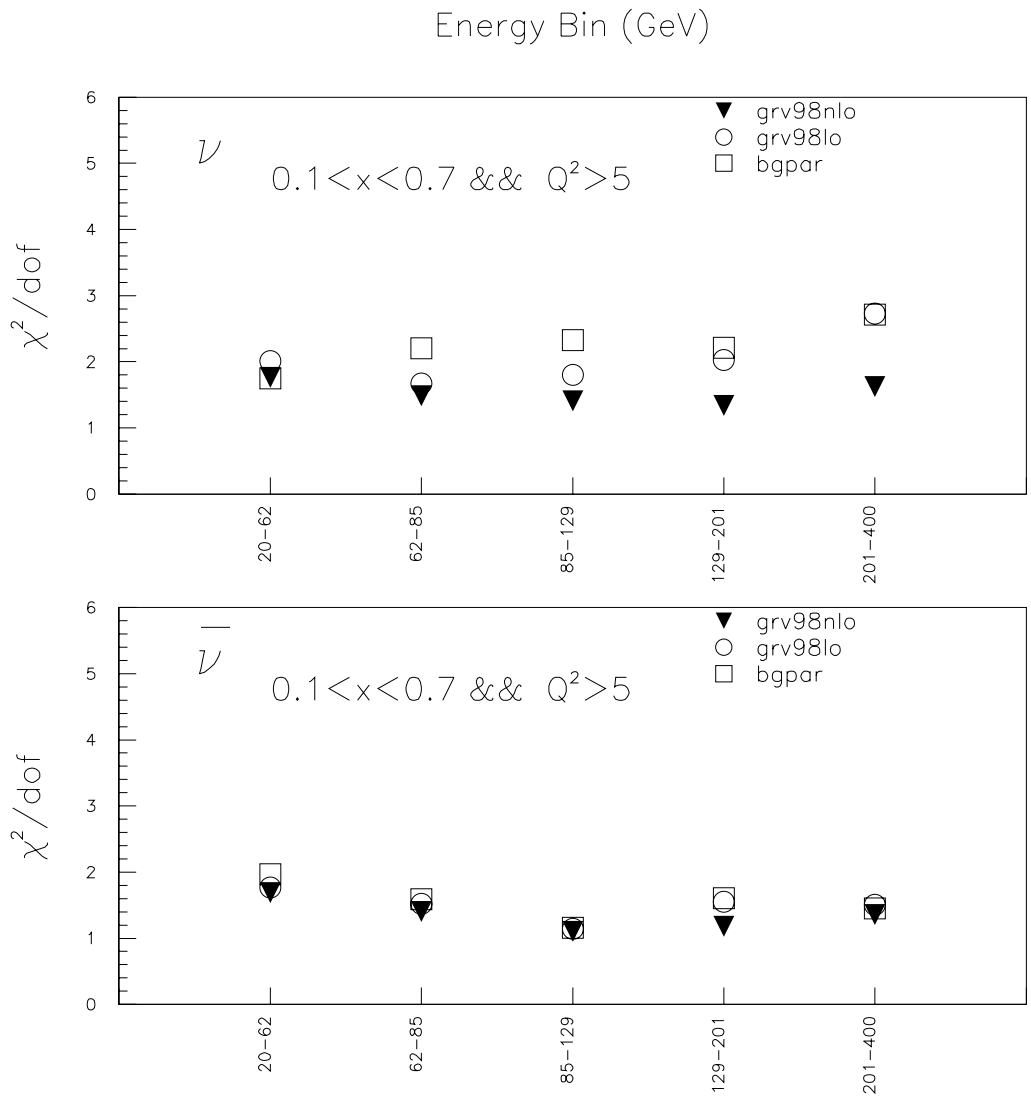

Figure F.13: GRV98 and BGPAR χ^2/dof by E_ν bin

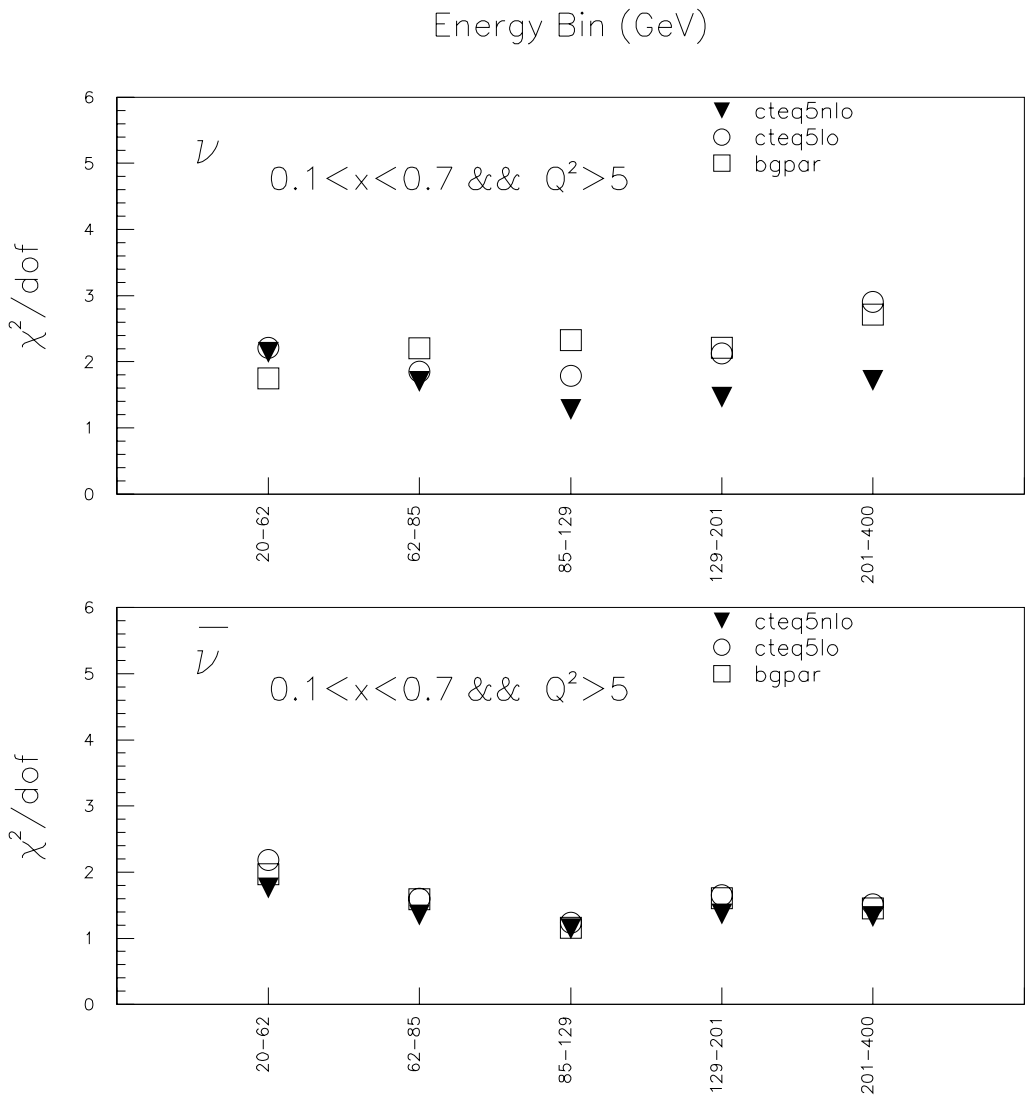

Figure F.14: CTEQ5 and BGPAR χ^2/dof by E_ν bin

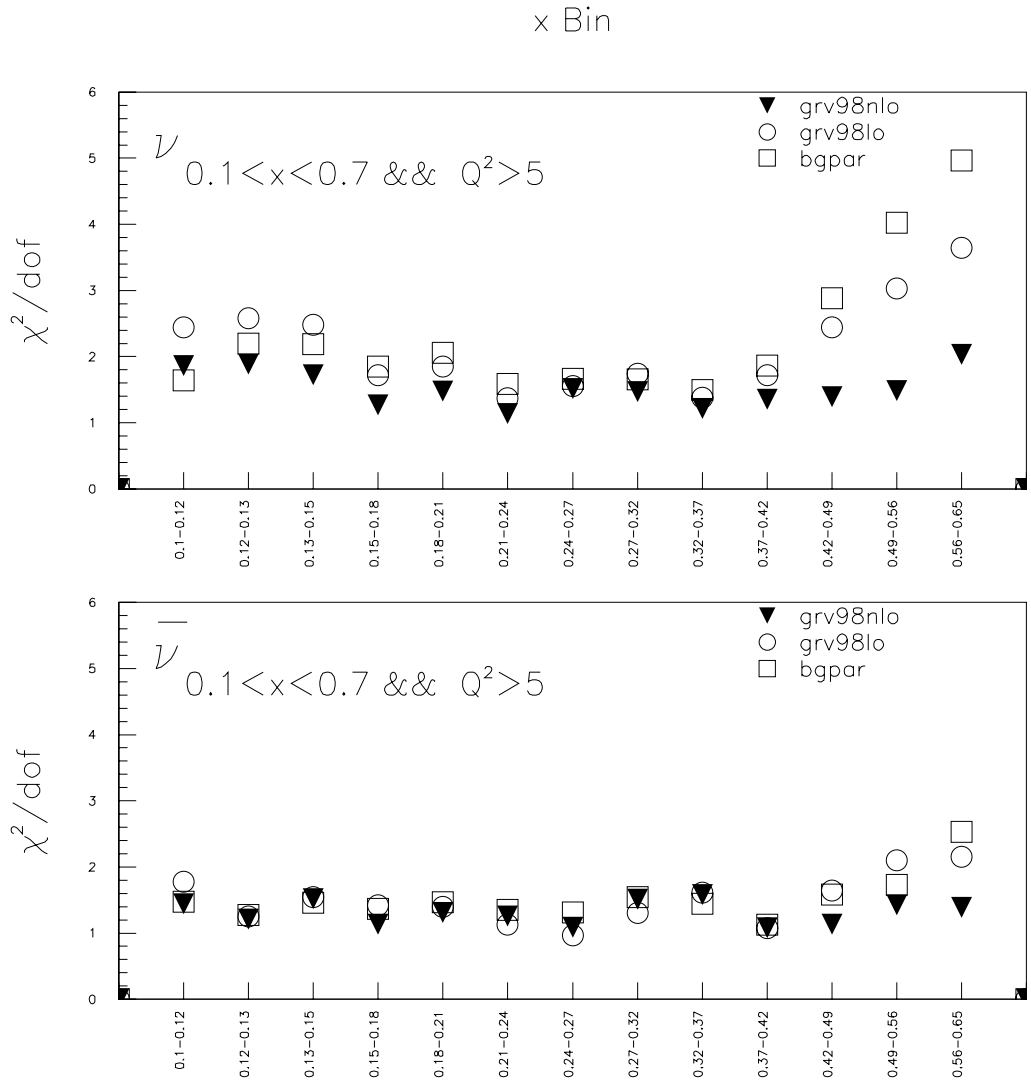

Figure F.15: GRV98 and BGPAR χ^2/dof by x bin

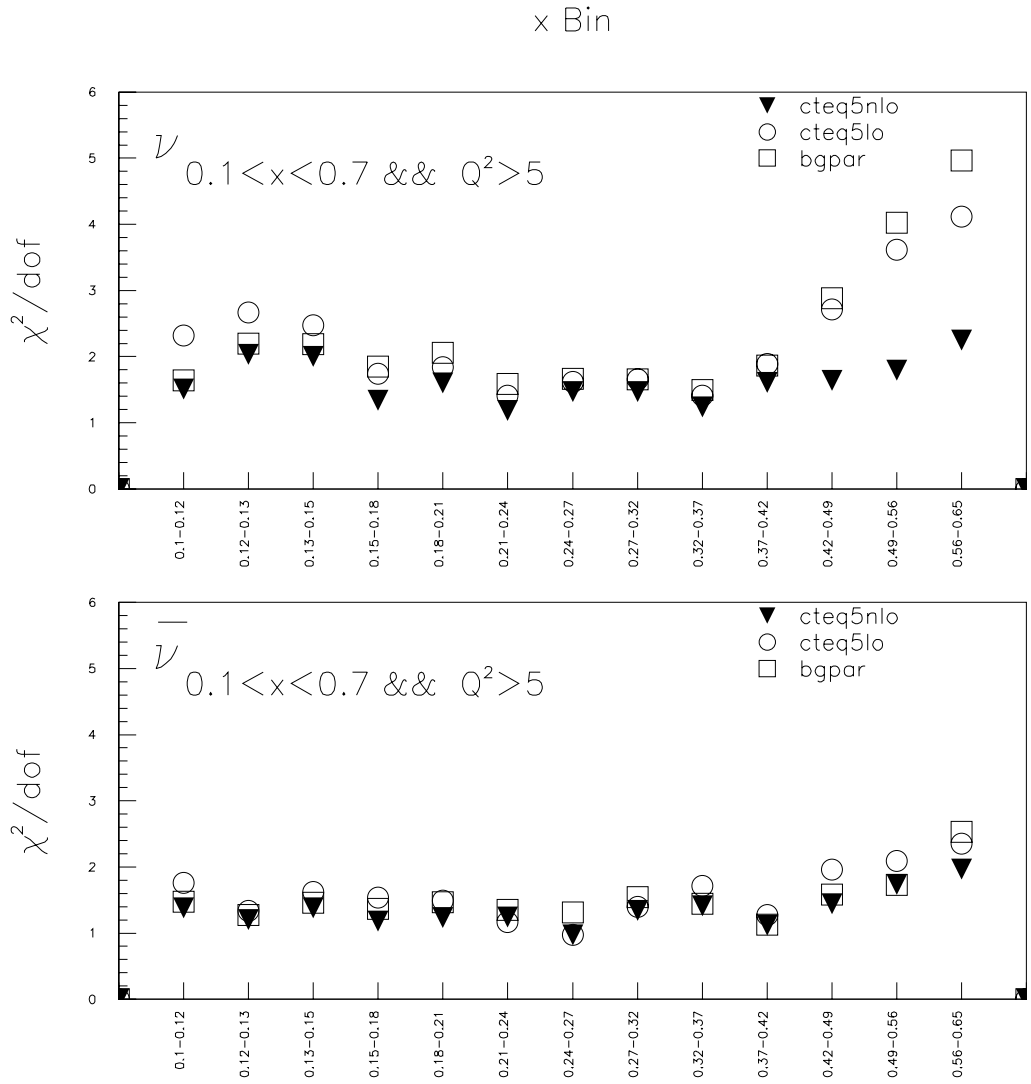

Figure F.16: CTEQ5 and BGPAR χ^2/dof by x bin

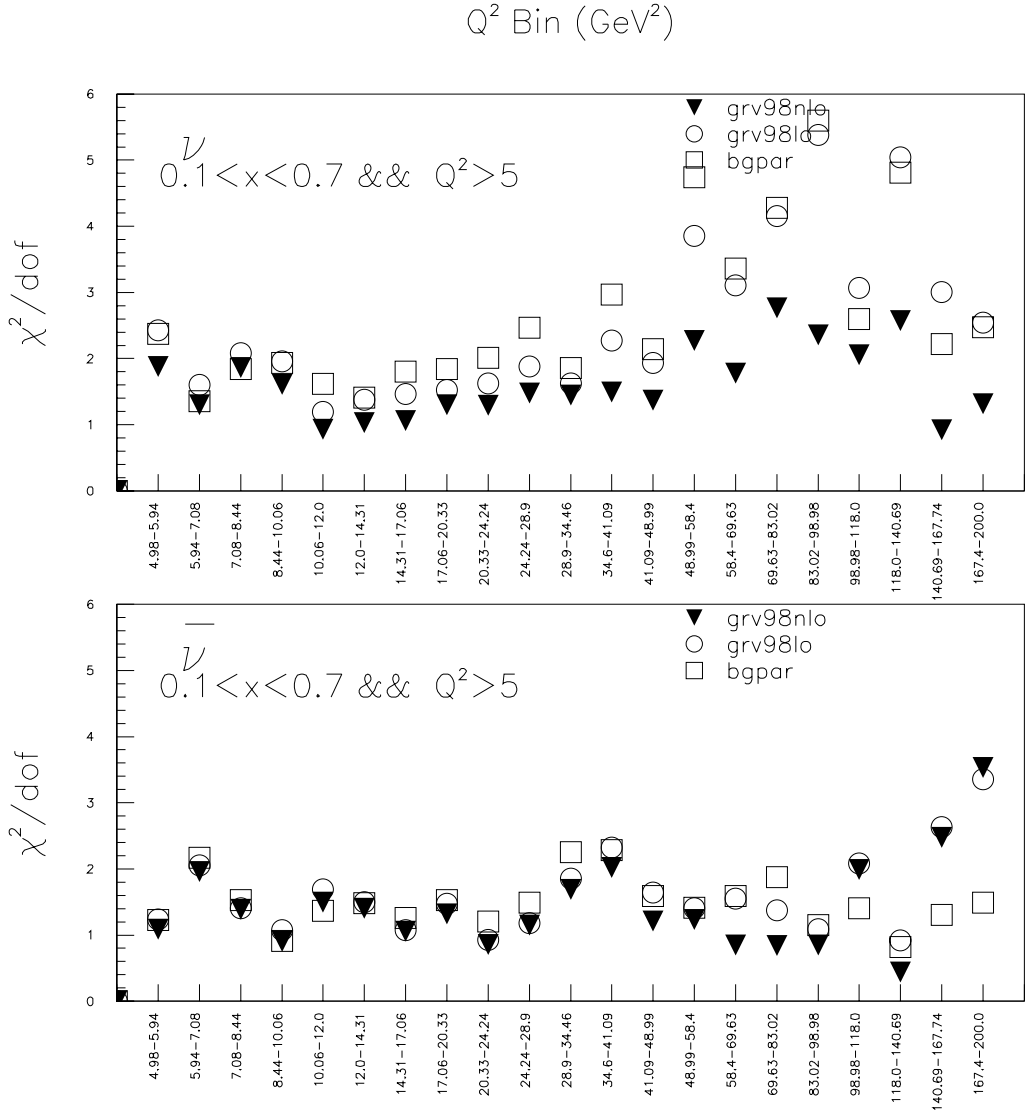

Figure F.17: GRV98 and BGPAR χ^2/dof by Q^2 bin

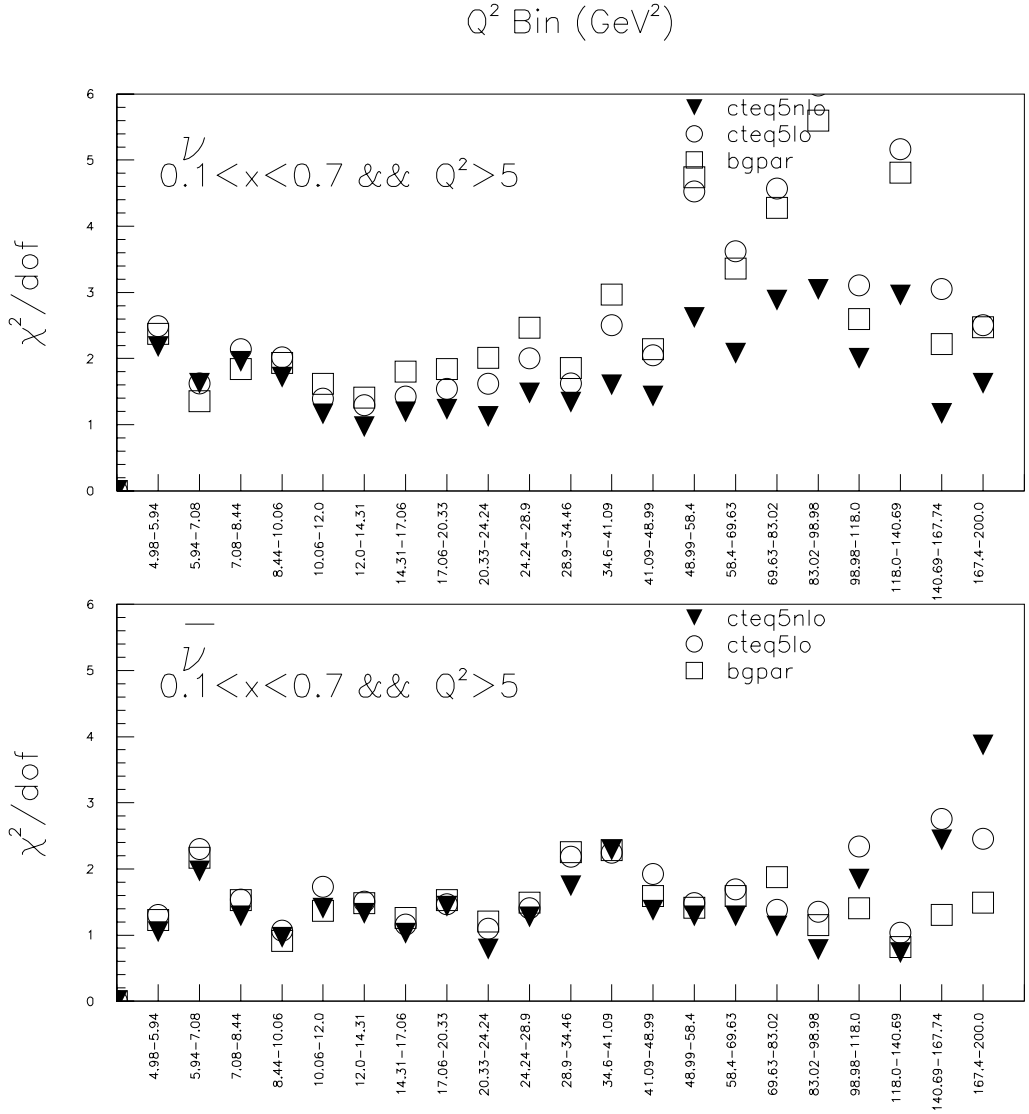

Figure F.18: CTEQ5 and BGPAR χ^2/dof by Q^2 bin

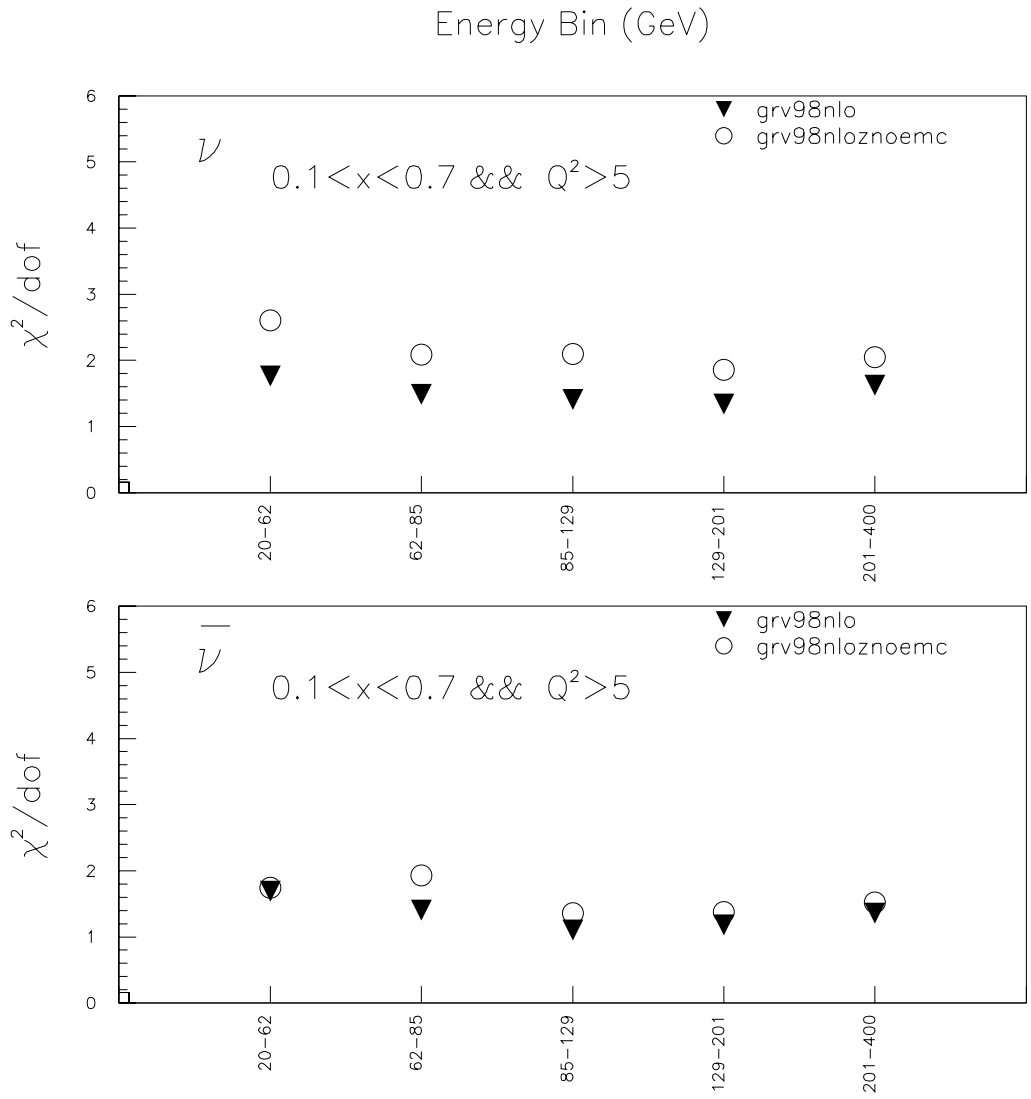

Figure F.19: GRV98NLO with and without EMC correction by E_ν bin

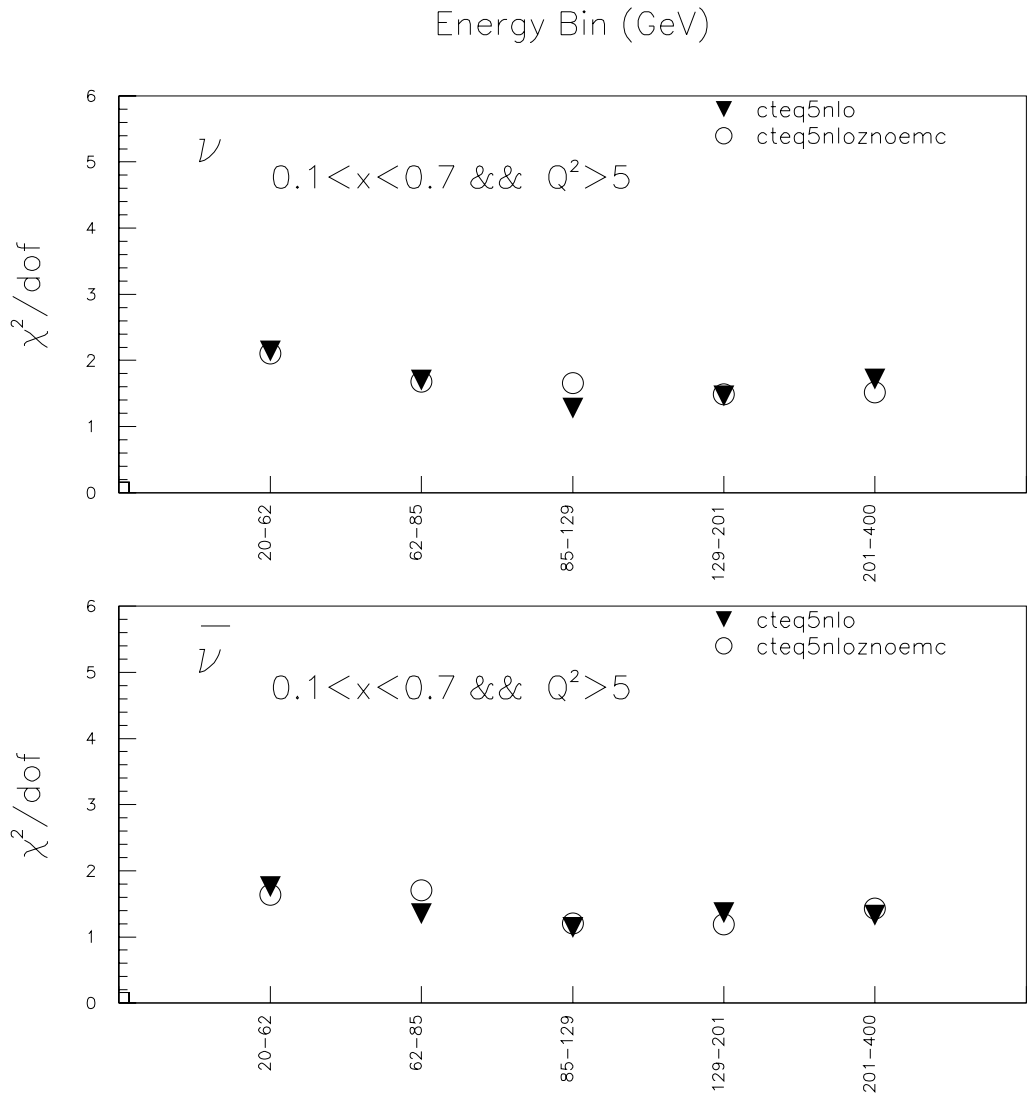

Figure F.20: CTEQ5NLO with and without EMC correction by E_ν bin

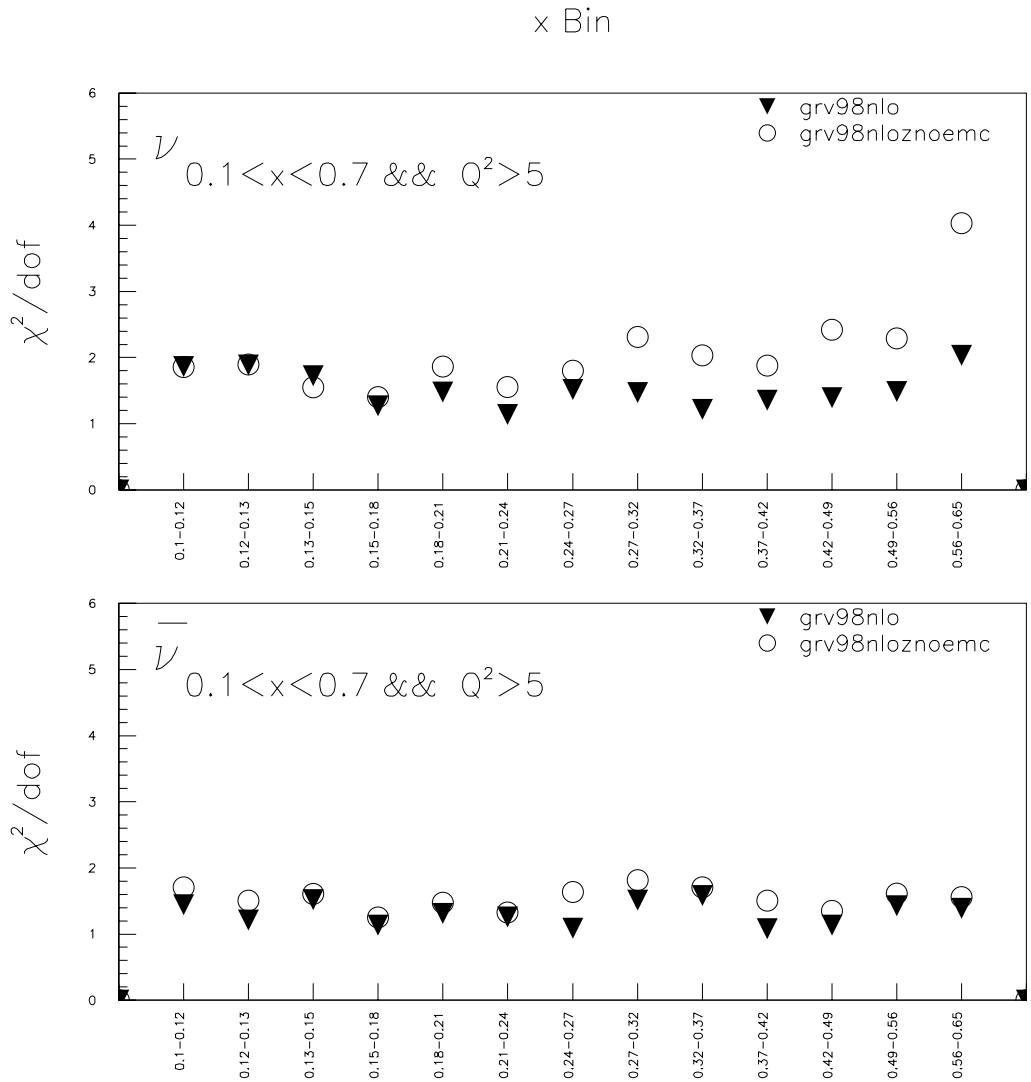

Figure F.21: GRV98NLO with and without EMC correction by x bin

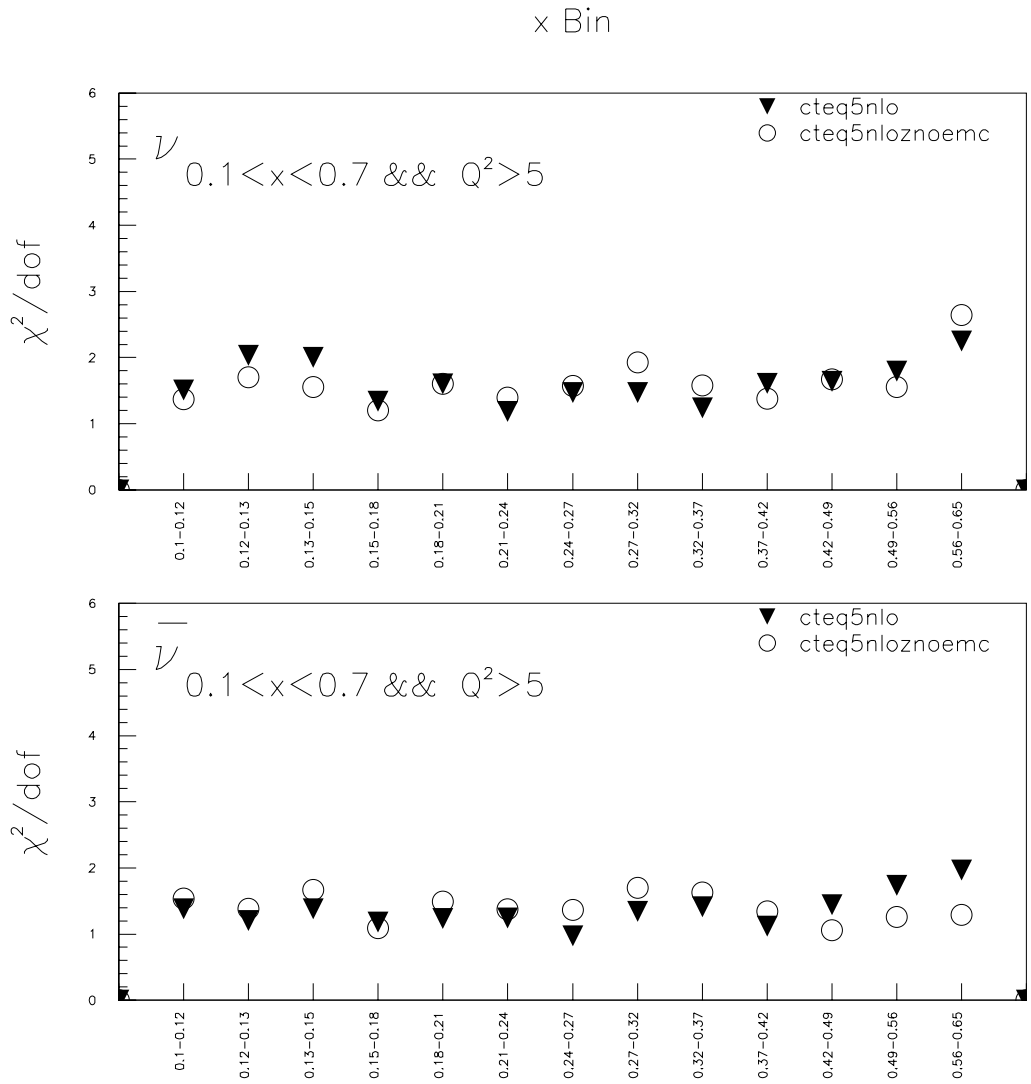

Figure F.22: CTEQ5NLO with and without EMC correction by x bin

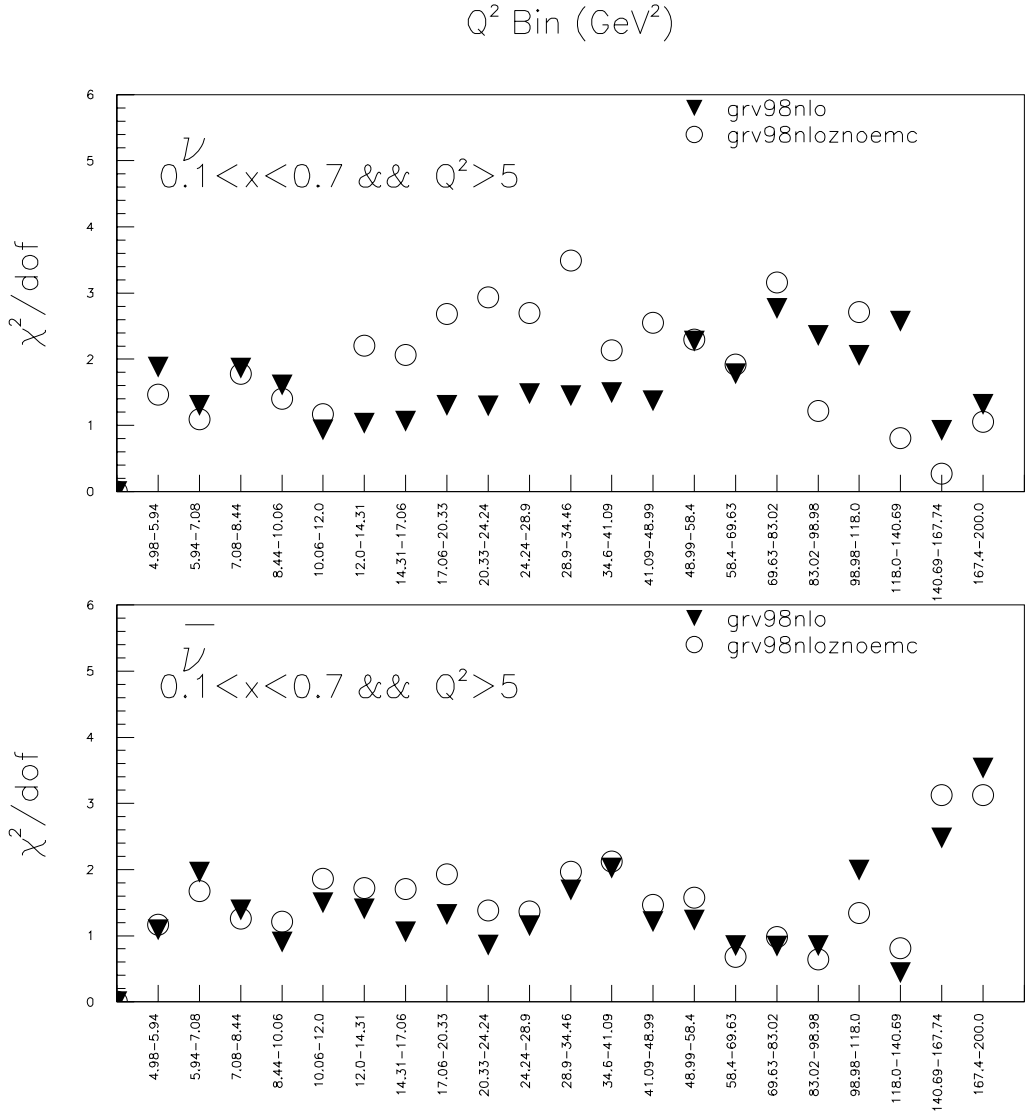

Figure F.23: GRV98NLO with and without EMC correction by Q^2 bin

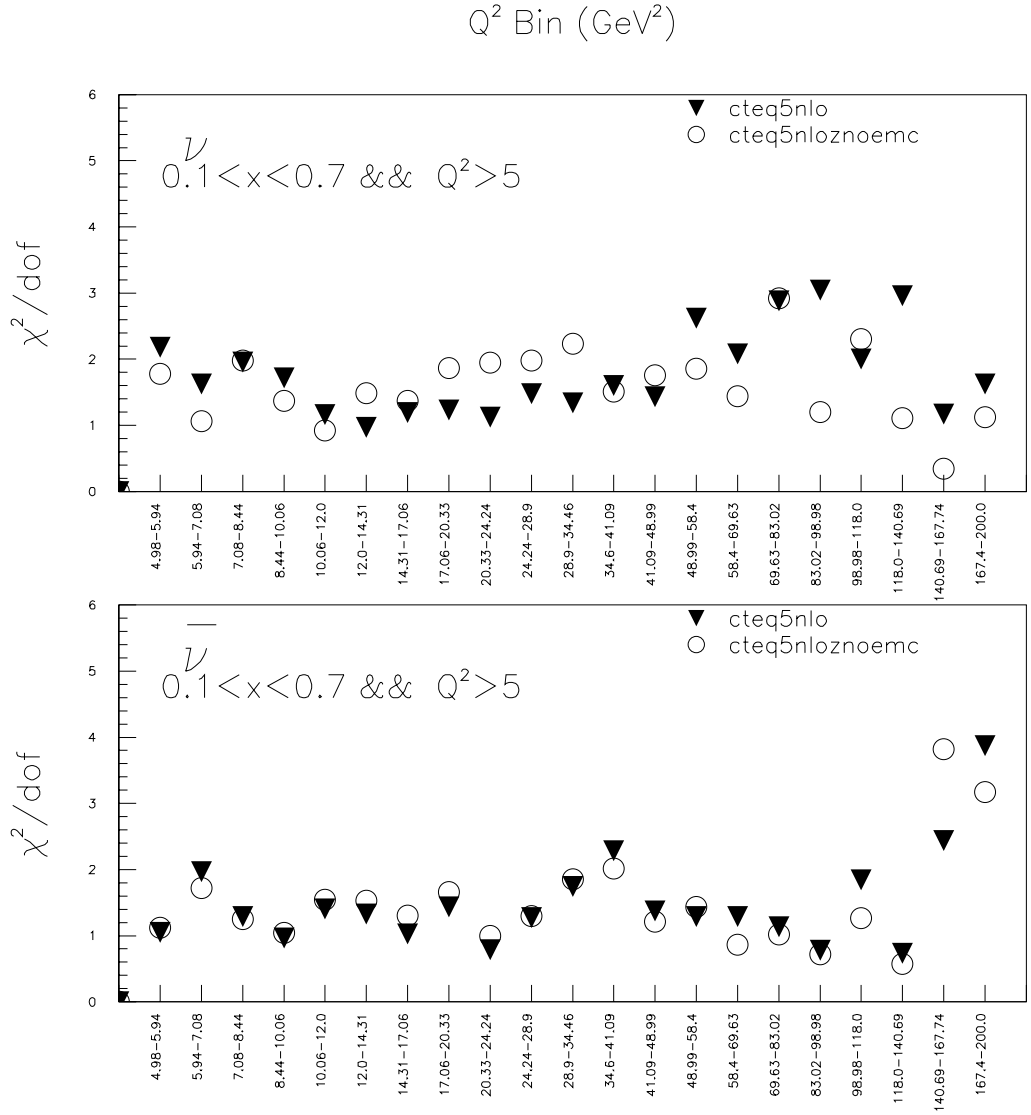

Figure F.24: CTEQ5NLO with and without EMC correction by Q^2 bin

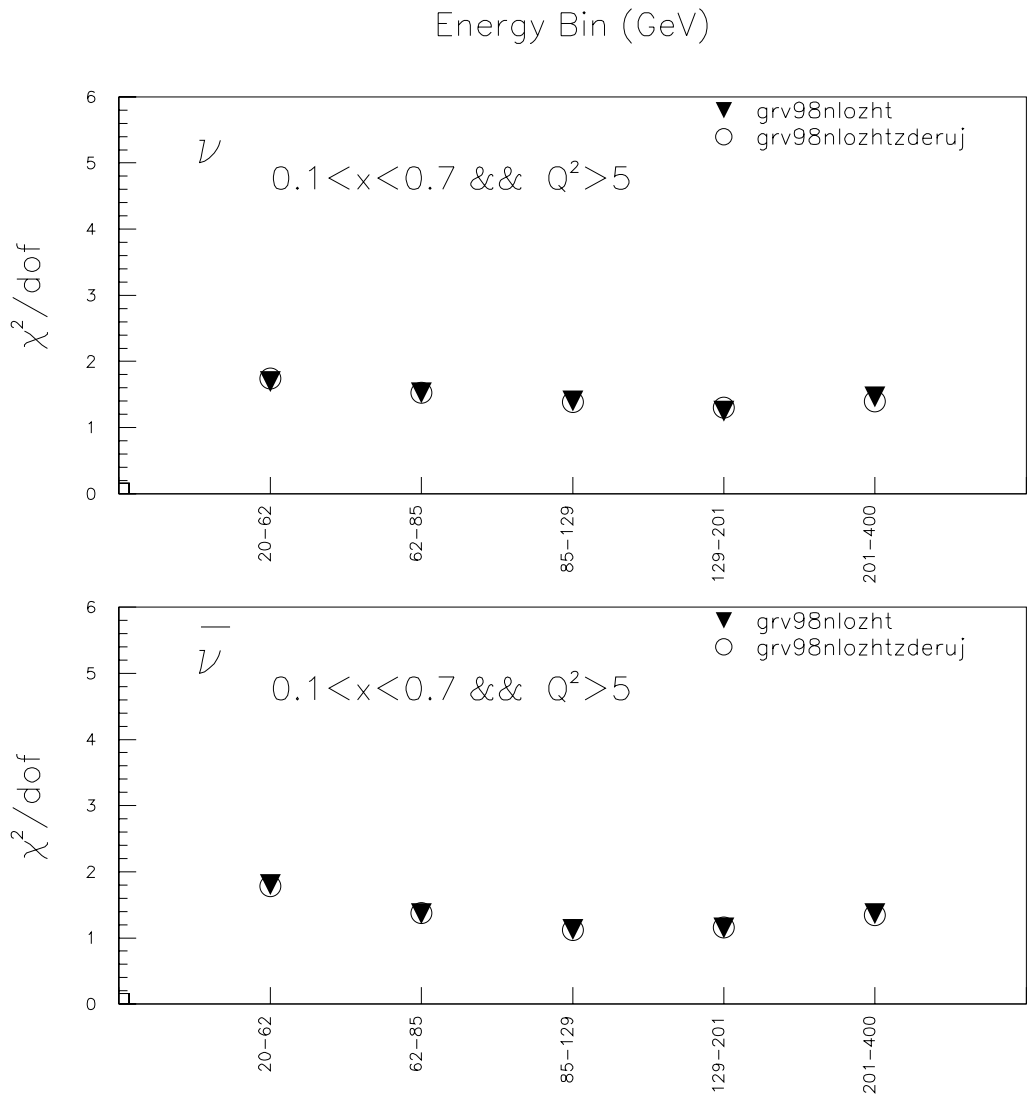

Figure F.25: GRV98NLO with and without Derujula radiative corrections by E_ν bin

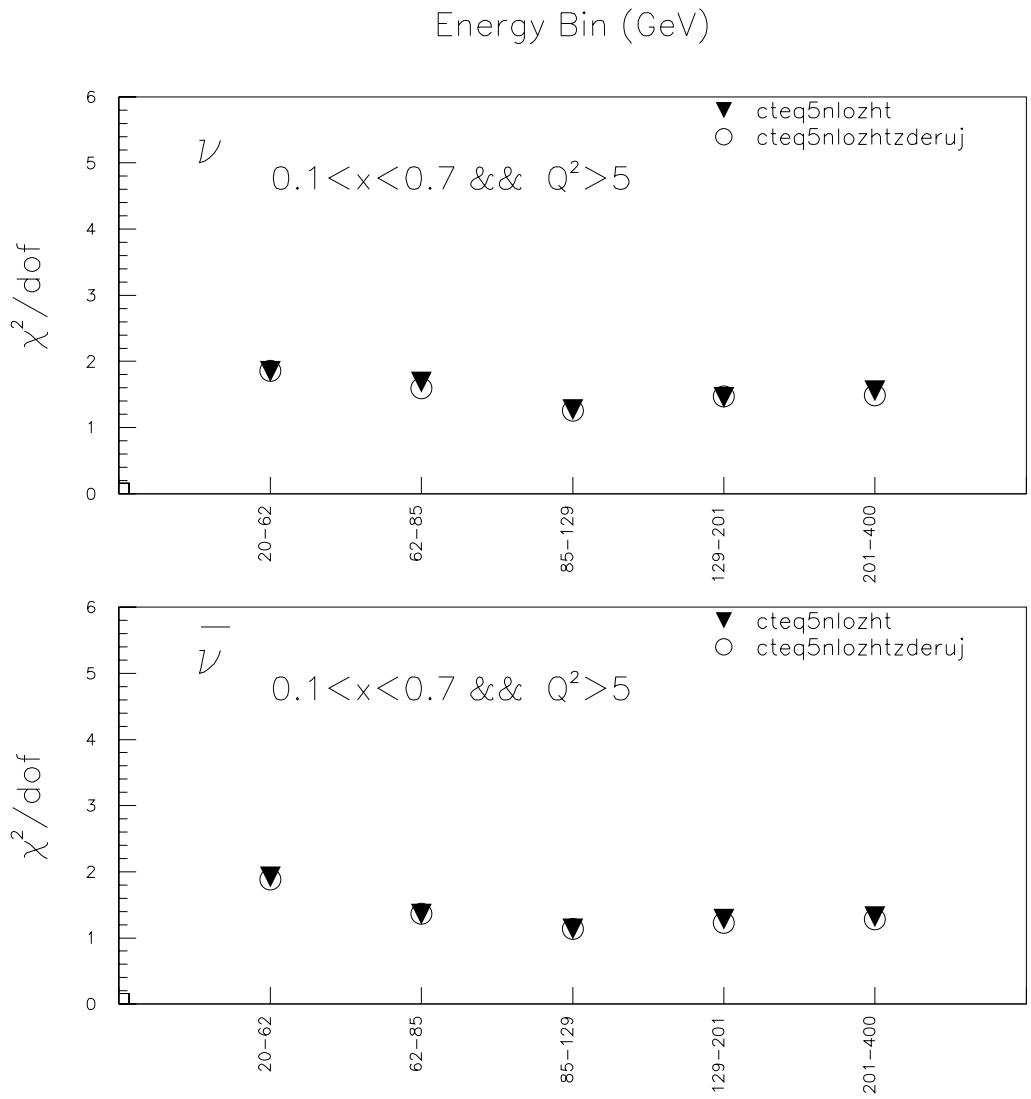

Figure F.26: CTEQ5NLO with and without Derujula radiative corrections by E_ν bin

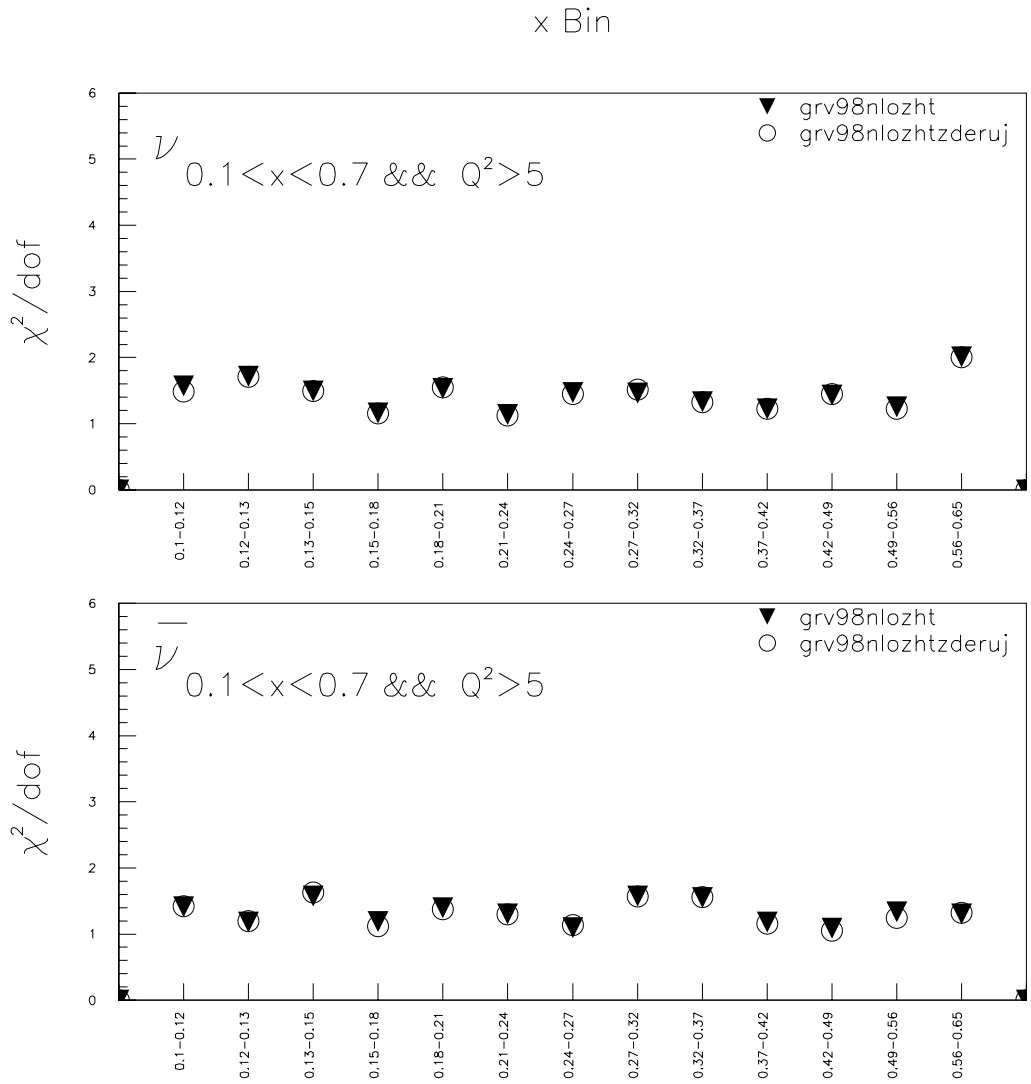

Figure F.27: GRV98NLO with and without Derujula radiative corrections by x bin

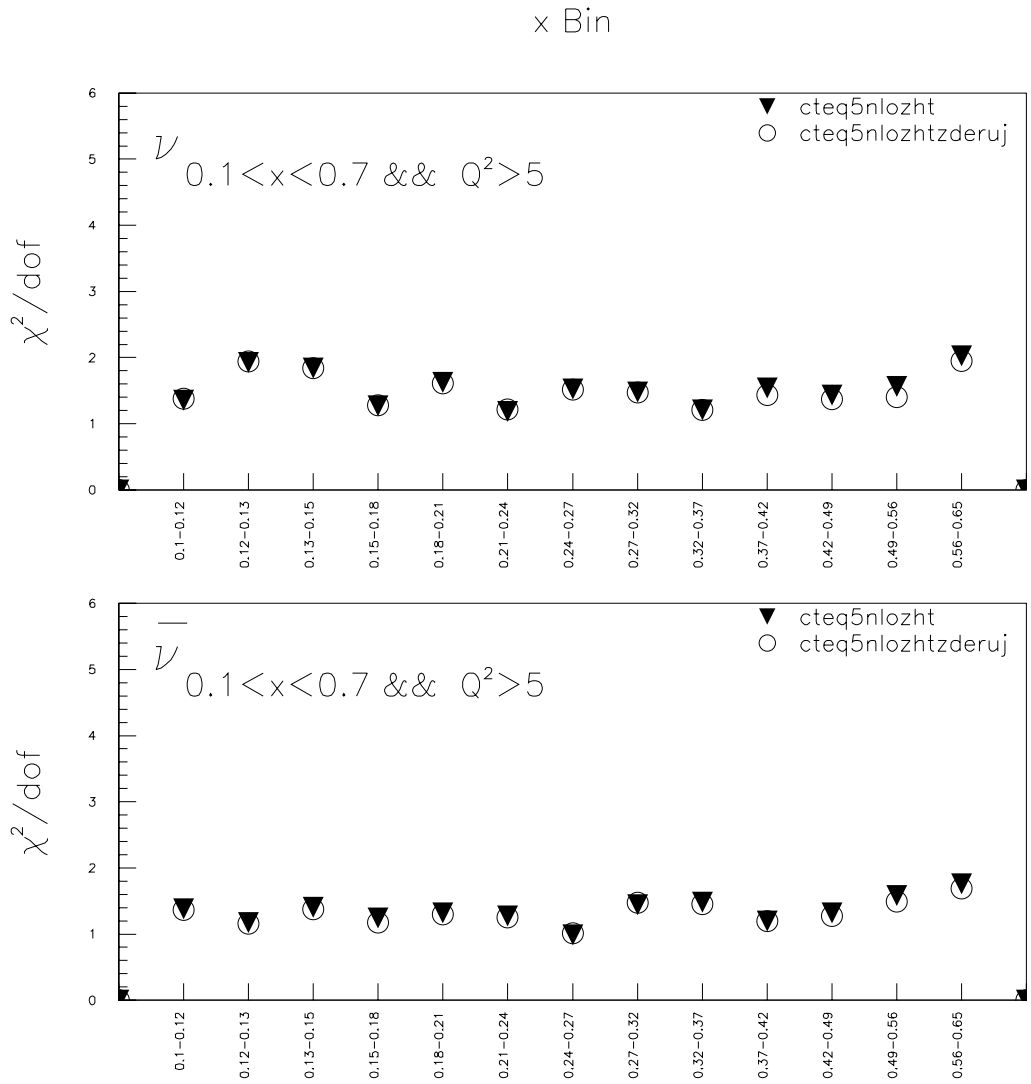

Figure F.28: CTEQ5NLO with and without Derujula radiative corrections by x bin

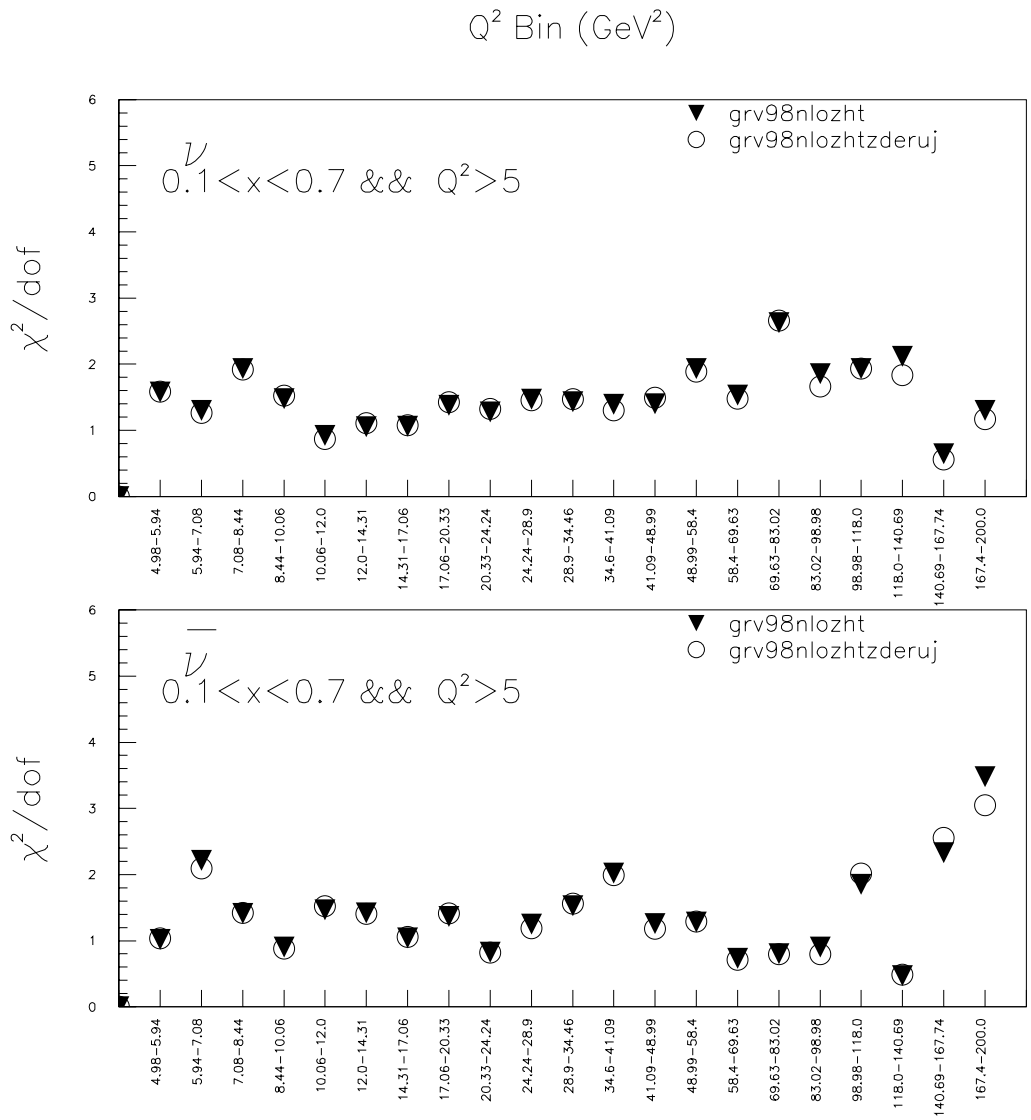

Figure F.29: GRV98NLO with and without Derujula radiative corrections by Q^2 bin

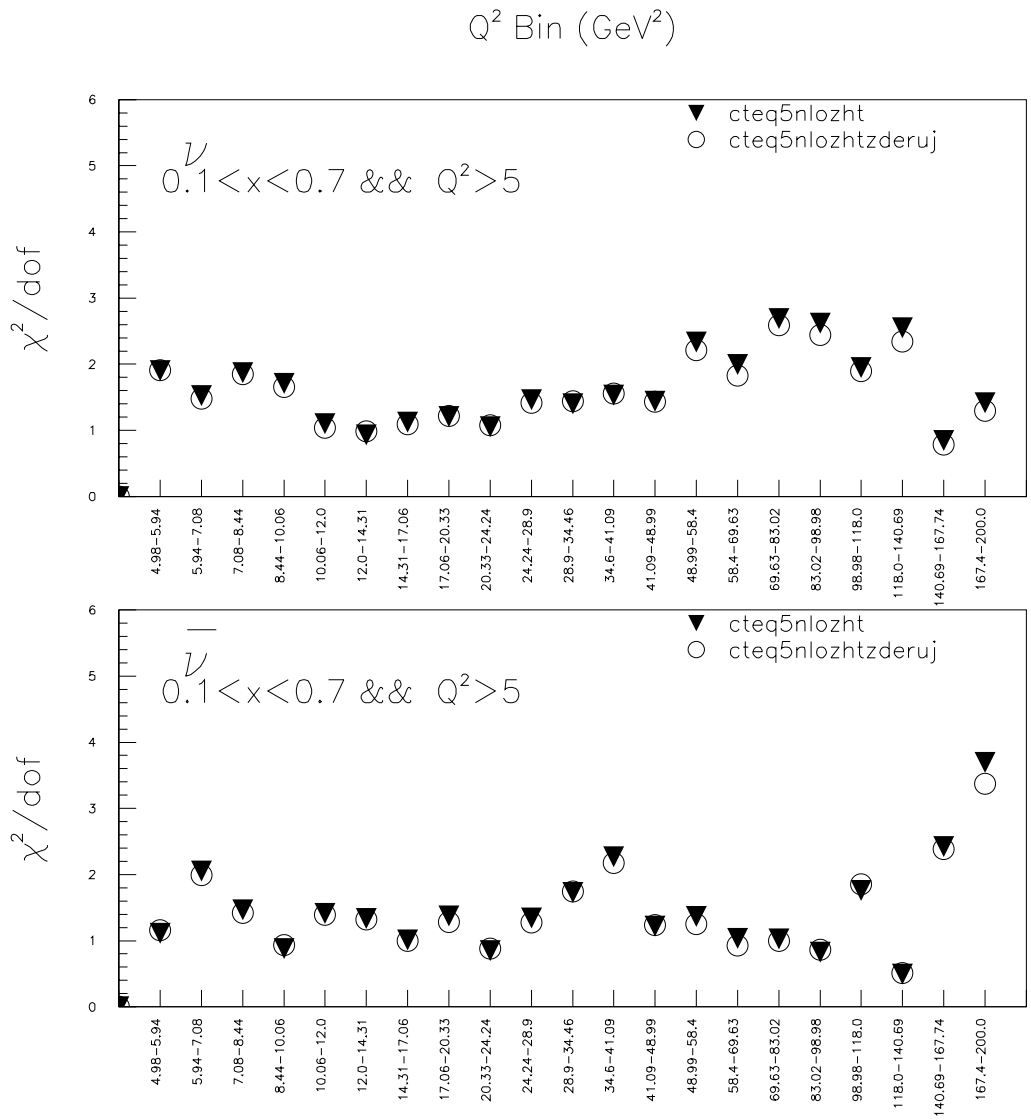

Figure F.30: CTEQ5NLO with and without Derujula radiative corrections by Q^2 bin

Bibliography

[1] David Griffiths, *Introduction to Elementary Particles*; John Wiley & Sons, 1987

[2] F.E. Close, *An Introduction to Quarks and Partons*; Academic Press, 1979

[3] Francis Halzen and Alan D. Martin, *Quarks & Leptons: An Introductory Course in Modern Particle Physics*; John Wiley & Sons, 1984

[4] R.T. Herrod and S. Wada, "Altarelli-Parisi Equation In The Next-To-Leading Order", PRL 96B, P.195

[5] T. Bolton, "SIGMCQ: A Neutrino Cross Section Model", January 11, 1995 (Internal NuTeV Memo available at www-e815.fnal.gov)

[6] A. Bazarko, "Determination of the Strange Quark Distribution from a Next-To-Leading-Order QCD Analysis of Neutrino and Anti-Neutrino Production of Charm" (Ph.D. Thesis), Columbia University, 1994

[7] "Heavy Quark and Light Parton Distributions at Collider Energies", M. Glück, R.M. Godbole and E. Reya. Sep. 1989

[8] M.Glück, S. Kretzer, and E. Reya "The Strange Sea Density and Charm Production in Deep Inelastic Charged Current Processes", DO-TH 96/06, March 1996

[9] Wu-Ki Tung, "The Heavy Quark Parton Oxymoron - A mini-review of Heavy Quark Production theory in PQCD", hep-ph/9706480

[10] Fredrick I. Olness, "Heavy Quark Production", hep-ph/9812270

[11] Fredrick I. Olness, "Leptoproduction of Heavy Quarks II", hep-ph/9312319

[12] Frank Daniel Steffen, "A Zero-Field Spectrometer: Using Multiple Coulomb Scattering to Measure the Momentum of Relativistic Muons" (M.S. Thesis), Kansas State University, 1997

[13] Eric G. Stern, "Notes On proposed E815 Dat Acquisition System" (NuTeV internal memo), October 1994

[14] William Glenn Seligman, "A Next-to-Leading-Order QCD Analysis of Neutrino-Iron Structure Functions at the Tevatron" (Ph.D. Thesis), Columbia University, 1997

[15] The CHARM II Collaboration, "Leading-Order QCD Analysis Of Neutrino-Induced Dimuon Events", Eur.Phys.J.C11:19-34, 1999

[16] E665 Collaboration, "Shadowing in Inelastic Scattering of Muons on Carbon, Calcium, and Lead at low x_{Bj}", hep-ex/9505006, May 1995

[17] The New Muon Collaboration (NMC) "A Re-Evaluation of the Nuclear Structure Function Ratios For D, He, ^{6}Li, C and Ca", hep-ph/9503291, Mar 1995

[18] J.J. Aubert et al., Phys. Lett. B123 275, 1983

[19] E.L. Berger and F. Coester, "Nuclear Effects In Deep Inelastic Lepton Scattering"i, ANL-PHY-4965, March, 1987

[20] R.G. Arnold et al., "Measurement Of The A-Dependence Of Deep-Inelastic Electron Scattering", SLAC-PUB-5813, August, 1993

[21] L.W. Whitlow, Ph.D. Thesis, Stanford University, 1989

[22] D. Duke and J. Owens, Phys. Rev., D30, 1984

[23] A. De Rujula, R. Petronzio, and A. Savoy-Navarro, "Radiative Corrections to High-Energy Neutrino Scattering", Nuclear Physics B154 394, 1979

[24] D. Yu. Bardin et al, "Electroweak Radiative Corrections To Deep Inelastic Scattering At Hera: Neutral Current Scattering", PHE 88-15, 1988

[25] D. Yu. Bardin et al, "Electroweak Radiative Corrections To Deep Inelastic Scattering At Hera: Charged Current Scattering", E2-89-145, 1989

[26] "Precision Calibration Of The NuTeV Calorimeter", D. Harris, J. Yu et al. Fermilab-Pub-99-021-E, 1999

[27] H. Wahlen, "Structure Functions In Deep Inelastic Lepton Nucleon Scattering", SLAC Summer Institute - Invited Talk, 1981

[28] M. Virchaux and A. Milsztajn, "A Measurement Of α_s And Of Higher-Twists From A QCD Analysis Of High Statistics F_2 Data On Hydrogen And Deuterium Targets", Phys. Lett. B274 221, 1992

[29] M. Dasgupta and B. R. Webber, "Power Corrections And Renormalons In Deep Inelastic Structure Functions", Phys. Lett. B382 273 1996

[30] Bruce King, "A Precise Measurement Of The Weak Mixing Angle In Neutrino-Nucleon Scattering", Ph.D Thesis, Columbia University, 1994

[31] A. Alton, "Observation Of Neutrino Induced Neutral Current Charm Events", Ph.D Thesis, Kansas State University, 2000

[32] U.K. Yang, Ph.D Thesis, University of Rochester, 2000

[33] A.J. Buras and K.J.F. Gaemers, "Simple Parametrizations Of Parton Distributions With Q^2 Dependence Given by Asymptotic Freedom", Nucl. Phys. B132:249, 1978

[34] M. Glück, E. Reya, and A. Vogt, "Dynamical Parton Distributions of the Proton and Small-x Physics", Z. Phys. C67:433, 1995

[35] I. Abt et al., "Measurement of the Proton Structure Function $F_2(x, Q^2)$ in the low x Region at HERA", Nucl. Phys. B407:515, 1993

[36] D.C. Carey, K.L. Brown, and Ch. Iselin, "DECAY TURTLE: A Computer Program for Simulating Charged Particle Beam Transport Systems, Including Decay Calculations", SLAC-246, 1982

[37] CTEQ Collaboration, "Global QCD Analysis of Parton Structure of the Nucleon: CTEQ5 Parton Distributions", Eur. Phys. J. C12:375, 2000

[38] M. Glück, E. Reya, and A. Vogt, "Dynamic Parton Distributions Revisited", Eur. Phys. J. C5:461, 1998

[39] A. Bodek and J.L. Ritchie, "Fermi Motion Effects in Deep Inelastic Lepton Scattering from Nuclear Targets", Phys. Rev. D23:1070, 1981

[40] S.A Rabinowitz, "Measurement of the Strange Sea Distribution Using Neutrino Charm Production", Phys. Rev. Lett. 70:134, 1993

[41] D.J. Gross and C.H. Llewellyn Smith, Nucl. Phys. B14:337, 1969

[42] S.A. Larin and J.A.M Vermaseren, "The α_s^3 Corrections to the Bjorken Sum Rule for Polarized Electroproduction and to the Gross-Llewellyn Smith Sum Rule", Phys. Lett. B259:345, 1991

[43] Particle Data Group, Particle Physics Booklet, July 1998.

[44] P. Astier *et al.*, "Neutrino Production of Opposite Sign Dimuons in the NOMAD Experiment", Phys. Lett. B486:35, 2000

[45] T. Bolton, "Determining the CKM Parameter V_{cd} from νN Charm Production", KSUHEP-97-04, 1997

[46] L. de Barbaro, "Muon Energy Loss Reconstruction in the Lab E Target", 1998

[47] Bonnie T. Tamminga *et al.*, "Low Q^2 Low x Structure Function Analysis of CCFR Data for F_2", Nucl. Phys. A663:344-348, 2000

[48] M. Vakili *et al.*, "Nuclear Structure Functions in the Large x Large Q^2 Kinematic Region in Neutrino Deep Inelastic Scattering", Phys. Rev. D61, 2000